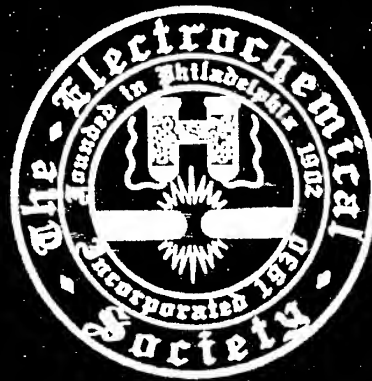


REPORT DOCUMENTATION PAGE			Form Approved OMB NO. 0704-0188	
Public reporting burden for this collection of information is estimated to average 1 hour per response, including the time for reviewing instructions, searching existing data sources, gathering and maintaining the data needed, and completing and reviewing the collection of information. Send comment regarding this burden estimate or any other aspect of this collection of information, including suggestions for reducing this burden, to Washington Headquarters Services, Directorate for Information Operations and Reports, 1215 Jefferson Davis Highway, Suite 1204, Arlington, VA 22202-4302, and to the Office of Management and Budget, Paperwork Reduction Project (0704-0188), Washington, DC 20503.				
1. AGENCY USE ONLY (Leave blank)		2. REPORT DATE 4 November 1997		3. REPORT TYPE AND DATES COVERED Final Report
4. TITLE AND SUBTITLE Proceedings of the Fourth International Symposium on Quantum Confinement: Nanoscale Materials, Devices, and Systems Proceedings Volume 97-11			5. FUNDING NUMBERS DAAG55-97-1-0155	
6. AUTHOR(S) Marc Cahay, Principal Investigator				
7. PERFORMING ORGANIZATION NAMES(S) AND ADDRESS(ES) University of Cincinnati Department of Electrical and Computer Engineering Cincinnati, Ohio			8. PERFORMING ORGANIZATION REPORT NUMBER	
9. SPONSORING / MONITORING AGENCY NAME(S) AND ADDRESS(ES) U.S. Army Research Office P.O. Box 12211 Research Triangle Park, NC 27709-2211			10. SPONSORING / MONITORING AGENCY REPORT NUMBER ARO 37354.1-EL-CF	
11. SUPPLEMENTARY NOTES The views, opinions and/or findings contained in this report are those of the author(s) and should not be construed as an official Department of the Army position, policy or decision, unless so designated by other documentation.				
12a. DISTRIBUTION / AVAILABILITY STATEMENT Approved for public release; distribution unlimited.			12 b. DISTRIBUTION CODE 19971215 093	
13. ABSTRACT (Maximum 200 words) This book is a collection of many of the papers presented at the Fourth International Symposium on Quantum Confinement: Nanoscale Materials, Devices, and Systems, held May 4-7 in Montreal, Canada, as part of the 191st Meeting of the Electrochemical Society. The symposium was sponsored by the Dielectric Science and Technology, the Electronics, and the Luminescence and Display Materials divisions of the Electrochemical Society. The symposium was organized into 8 sessions of oral presentations over a period of three days to address recent advances in nanoscale and quantum confined structures, including chemistry of nanostructures, growth and characterization of nanocrystals, optical and electrical properties of quantum dots, wires, and nanocrystals, and transport in quantum wires and devices. continued on reverse side				
14. SUBJECT TERMS			15. NUMBER OF PAGES	
			16. PRICE CODE	
17. SECURITY CLASSIFICATION OF REPORT UNCLASSIFIED	18. SECURITY CLASSIFICATION OF THIS PAGE UNCLASSIFIED	19. SECURITY CLASSIFICATION OF ABSTRACT UNCLASSIFIED	20. LIMITATION OF ABSTRACT UL	

ARO 37354.1-EL-CF

QUANTUM CONFINEMENT IV NANOSCALE MATERIALS, DEVICES, AND SYSTEMS



Edited by
Cahay
Leburton
Lockwood
Bandyopadhyay

PROCEEDINGS OF THE FOURTH
INTERNATIONAL SYMPOSIUM ON

QUANTUM CONFINEMENT: NANOSCALE MATERIALS, DEVICES, AND SYSTEMS

Editors

M. Cahay
Department of Electrical and Computer Engineering
University of Cincinnati
Cincinnati, Ohio, USA

J. P. Leburton
Beckman Institute
University of Illinois
Urbana, Illinois, USA

D. J. Lockwood
Institute for Microstructural Sciences
National Research Council
Ottawa, Canada

S. Bandyopadhyay
Department of Electrical Engineering
University of Nebraska
Lincoln, Nebraska, USA

*DIELECTRIC SCIENCE AND TECHNOLOGY DIVISION, ELECTRONICS DIVISION,
LUMINESCENCE AND DISPLAY MATERIALS DIVISION*

Proceedings Volume 97-11



THE ELECTROCHEMICAL SOCIETY, INC.,
10 South Main St., Pennington, NJ 08534-2896

DTIC QUALITY INSPECTED 8

Copyright 1997 by The Electrochemical Society, Inc.
All rights reserved.

This book has been registered with Copyright Clearance Center, Inc.
For further information, please contact the Copyright Clearance Center,
Salem, Massachusetts.

Published by:

The Electrochemical Society, Inc.
10 South Main Street
Pennington, New Jersey 08534-2896, USA

Telephone (609) 737-1902
Fax (609) 737-2743
e-mail: ecs@electrochem.org
Web site: <http://www.electrochem.org>

ISBN 1-56677-138-2

Printed in the United States of America

PREFACE

This book is a collection of many of the papers presented at the Fourth International Symposium on Quantum Confinement: Nanoscale Materials, Devices, and Systems, held May 4-7 in Montreal, Canada, as part of the 191st Meeting of the Electrochemical Society. The symposium was sponsored by the Dielectric Science and Technology, the Electronics, and the Luminescence and Display Materials divisions of the Electrochemical Society.

The symposium was organized into 8 sessions of oral presentations over a period of three days to address recent advances in nanoscale and quantum confined structures, including chemistry of nanostructures, growth and characterization of nanocrystals, optical and electrical properties of quantum dots, wires, and nanocrystals, and transport in quantum wires and devices.

Invited papers are indicated by an asterisk in the Table of Contents. The National Science Foundation Best Student Paper Award of \$500 was presented to Peter Fischer from "Otto Van Guericke" University of Magdeburg, Germany, for his paper entitled **Luminescence Characterization of Selforganized Quantum Wires: Carrier Capture and Thermalization**.

The symposium also featured on a short course **Simulation of Nanoscale Materials and Devices** which was offered on Sunday, May 4, prior to the start of the symposium. This short course was quite a success with over 25 registered people.

The editors thank all the speakers, session chairpersons, and manuscript reviewers for their contributions to the success of the symposium. We also thank the Electrochemical Society staff for their constant support and for their help in preparing the volume for publication.

Finally, we would like to express our appreciation to the Army Research Office, the National Science Foundation, and the Electro-Chemical Society for their financial support.

M. Cahay
J. P. Leburton
D. J. Lockwood
S. Bandyopadhyay

TABLE OF CONTENTS

PREFACE	iii
---------------	-----

Chemistry of Nanostructures

Self Assembling Supramolecular Materials: A Synthetic Route to Quantum Dots	3
<i>S.I. Stupp*, M. U. Pralle, P. V. Braun, G. Tew, P. Osenar, and L. S. Li</i>	
Studies of Photoredox Reactions on Nanoscale Semiconductors	16
<i>J. P. Wilcoxon, F. Parsapour, and D.F. Kelley</i>	
Platinum Nanoparticles Dispersed on Polypyrrole Nano-/micro-particles. .	28
<i>Z. Qi and P.G. Pickup</i>	
Cd_xMn_{1-x} Nanoparticles ($x < 5\%$) in Sol-Gel Silica Matrices	35
<i>G. Counio, T. Gacoin, and J.P. Boilot</i>	
Sol-Gel Template Synthesis of Semiconductor Nanostructures	47
<i>B.B. Lakshmi and C.R. Martin</i>	

Nanocrystals: Growth and Characterization

Thin-Film Nanocalorimetry for Nano-Scaled Systems	59
<i>S.L. Lai and L.H. Allen</i>	
Stability of NanoCrystalline $n-TiO_2$ and $n-TiO_2/Mn_2O_3$ Films During Photoelectrolysis of Water	65
<i>J. Akikusa and S.U.M. Khan</i>	
Semiconductor Nanocrystals by Aerotaxy Method	79
<i>K. Deppert, M.H. Magnusson, L. Samuelson, J.-O. Malm, C. Svensson and J.-O. Bovin</i>	
Gold Implanted in Porous Glass: Size and Shape Effects on the Surface Plasmon Absorption of Gold Nanocrystals	100
<i>D.O. Henderson, A. Ueda, R. Mu, Y.S. Tung, M. Wu, J. Chen, Z. Gu, C.W. White, R. Zuhr, J.G. Zhu, and Xi Li</i>	

Quantum Dots: Optical Properties

Optical Properties of Etched and Self-Assembled Quantum Dots in a Magnetic Field	117
<i>P. Hawrylak*</i>	
Fabrication and Characterization of Nanocrystalline Si Superlattice Produced by Controlled Recrystallization	134
<i>L. Tsybeskov, K.D. Hirschman, S.P. Duttagupta, P.M. Fauchet, M. Zacharias, P. Kohlert, J. McCaffrey, and D. J. Lockwood</i>	
Coupled Quantum Dot-Based InAs/GaAs Laser Structure Studied by Contactless Electroreflectance and Surface Photovoltage Spectroscopy ..	146
<i>L. Aigouy, T. Holden, F.H. Pollak, N.N. Ledentsov, V.M. Ustinov, P.S. Kop'ev, and D. Bimberg</i>	
Optical Studies of Self-Assembled Quantum Disks	155
<i>M. Potemski, D. J. Lockwood, H. J. Labbe, P. Hawrylak, H. Kamada, H. Weman, J. Temmyo, and T. Tamamura</i>	

Quantum Dots: Electronic Properties

Self-Consistent Modeling of Interface and Dopant Disorders in Delta-Doped Mesh-Gate Quantum Dot Nanostructures	165
<i>V.Y.A. Thean, S. Nagaraja, and J.P. Leburton</i>	
Electronic Structure of the Valence Band of Tetragonal Germanium Nanostructures Deposited by the Cluster-Beam Evaporation Technique .	177
<i>S. Sato, S. Nozaki, and H. Morisaki</i>	
Effect of the Interface Roughness on the Shallow Donor in a Quantum Dot	185
<i>J.-M. Shi, V.N. Freire, and G.A. Farias</i>	
Energy States in Graded Spherical GaAs/Al _x Ga _{1-x} As Quantum Dots	197
<i>V.N. Freire, J.-M. Shi, and G.A. Farias</i>	

Quantum Wires: Transport

Resistance of Molecular Nanostructures	211
<i>S. Datta*, W. Tian, and C. P. Kubiak</i>	
Demonstration of a Y-Branch Switch in Deeply Reactive Ion Etched $\text{In}_{0.53}\text{Ga}_{0.47}\text{As}/\text{InP}$ with In-Plane Gates	221
<i>J.-O.J. Wesström, K. Hieke, B. Staltnacke, T. Palm, and B. Stolz</i>	
Quantum Transport in One-Dimensional Magnetic Superlattices	231
<i>Z.-L. Ji and D.W.L. Sprung</i>	
Confined Magneto-Polariton Propagation in Quantum Wires	242
<i>A. Balandin and S. Bandyopadhyay</i>	
Generation of Ultrasonic Phonons in Parabolically Confined Quantum Wires in Tilted Magnetic Fields	255
<i>W. Xu, P. Vasilopoulos, and C. Zhang</i>	
Optical Studies of Quantum Effects in Semiconducting and Metallic Nanocrystals	269
<i>A. Stella*, V. Bellani, P. Tognigni, P. Cheyssac, and R. Kofman</i>	
Blue luminescence from Ge and GeO_2 Nanocrystallites Prepared by DC Magnetron Sputtering	287
<i>M. Zacharias, M. Schmidt, and P.M. Fauchet</i>	
Effect of Irradiant Wavelength During Porous Silicon Formation	298
<i>C. Malone and J. Jorne</i>	
A Luminescence Study of Silicon-Rich Silica and Rare-Earth Doped Silicon-Rich Silica	304
<i>A.J. Kenyon, P.F. Trwoga, and C.W. Pitt</i>	
Size Dependence of Superlinear Photoluminescence of $\text{CdS}_{0.5}\text{Se}_{0.5}$ Nanocrystallites in Glass	319
<i>E.B. Stokes and P.D. Persans</i>	
Optical Properties of Lead Sulfide Nanocrystals	331
<i>M. Sirota, E. Lifshitz, M. Folman, and R. Chaim</i>	
Quantum Confinement in Silicon	341
<i>R. Tsu, A. Filios, C. Lofgren, J. Ding, Qi Zhang, J. Morais, and C.G. Wang</i>	

Quantum Wires: Optical Properties

Nonlinear Optical Properties of Semiconductor Quantum Wires	353
<i>T. Dneprovskaya, V. Dneprovskii*, and E. Zhukov</i>	
Luminescence Characterization of Selforganized GaAs Quantum Wires: Carrier Capture and Thermalization	366
<i>P. Fischer, J. Christen, M. Takeuchi, H. Nakashima, K. Maehashi, K. Inoue, G. Austing, M. Grundmann, and D. Bimberg</i>	
Resonant Absorption of Far-Infrared Radiations in Quantum Wire at Strong Magnetic Fields	378
<i>W. Xu, P. Vasilopoulos, F.M. Peeters, and C. Zhang</i>	
Infrared Second Harmonic Generation in Magnetic-Field-Biased Quantum Wires	388
<i>A. Svizhenko, A. Balandin, and S. Bandyopadhyay</i>	
Optical Characterization of Semiconductor Nanowires Fabricated by Elec- trodeposition into Porous Alumina	402
<i>I. Avrutsky, D. Routkevitch, M. Moskovits, and J. Xu</i>	

Quantum Structures and Devices

Optical and Electrical Properties of Si/Ge Quantum Confinement Struc- tures	417
<i>Y. Shiraki*, N. Usami, H. Sunamura, E. S. Kim, A. Yutani, and S. Fukatsu</i>	
Sub-500 nm RITD Fabrication	425
<i>K. Shiralagi, R. Tsui, and H. Goronkin</i>	
Reaching the Fundamental Transistor Size Limit: MOSFETs with 10 nm Effective Channel Length	432
<i>C.H. Yang, J. Wang, M.J. Yang, B.R. Bennett, R.A. Wilson, and D.R. Stone</i>	
Bias Dependence of the Transmission Coefficient of Holes Through the Abrupt Emitter-Base Junction of a $In_{0.52}Al_{0.48}As/In_{0.53}Ga_{0.47}As$ Pnp Heterojunction Bipolar Transistor	444
<i>T. Kumar, M. Cahay, and K. Roenker</i>	

Resonant Tunneling in Quasi-One-Dimensional Multiple Well Structures with Vertically Uniform Gating	462
<i>V.R. Kolagunta, D.B. Janes, M.R. Melloch, and C. Youtsey</i>	
Scarring Effects in Open Quantum Dots	474
<i>R. Akis, D.K. Ferry, and J.P. Bird</i>	
* Invited Speaker	
AUTHOR INDEX	487
SUBJECT INDEX	491

FACTS ABOUT THE ELECTROCHEMICAL SOCIETY, INC.

The Electrochemical Society, Inc., is an international, nonprofit, scientific, educational organization founded for the advancement of the theory and practice of electrochemistry, electrothermics, electronics, and allied subjects. The Society was founded in Philadelphia in 1902 and incorporated in 1930. There are currently over 7000 scientists and engineers from more than 60 countries who hold individual membership; the Society is also supported by more than 100 corporations through Patron and Sustaining Memberships.

The Technical activities of the Society are carried on by Divisions and Groups. Local Sections of the Society have been organized in a number of cities and regions.

Major international meetings of the Society are held in the Spring and Fall of each year. At these meetings, the Divisions and Groups hold general sessions and sponsor symposia on specialized subjects.

The Society has an active publications program which includes the following:

Journal of The Electrochemical Society - The Journal is a monthly publication containing technical papers covering basic research and technology of interest in the areas of concern to the Society. Papers submitted for publication are subjected to careful evaluation and review by authorities in the field before acceptance, and high standards are maintained for the technical content of the Journal.

Interface - Interface is a quarterly publication containing news, reviews, advertisements, and articles on technical matters of interest to Society Members in a lively, casual format. Also featured in each issue are special pages dedicated to serving the interests of the Society and allowing better communication between Divisions, Groups, and Local Sections.

Meeting Abstracts (*formerly Extended Abstracts*) - Meeting Abstracts of the technical papers presented at the Spring and Fall Meetings of the Society are published in serialized softbound volumes.

Proceedings Series - Papers presented in symposia at Society and Topical Meetings are published from time to time as serialized Proceedings Volumes. These provide up-to-date views of specialized topics and frequently offer comprehensive treatment of rapidly developing areas.

Monograph Volumes - The Society has, for a number of years, sponsored the publication of hardbound Monograph Volumes, which provide authoritative accounts of specific topics in electrochemistry, solid state science, and related disciplines.

For more information on these and other Society activities, visit the ECS Home Page at the following address on the World Wide Web:

<http://www.electrochem.org>.

Chemistry of Nanostructures

**SELF ASSEMBLING SUPRAMOLECULAR MATERIALS:
A SYNTHETIC ROUTE TO QUANTUM DOTS**

S. I. Stupp^{†§*}, M. U. Pralle[†], P. V. Braun[†], G. Tew[§], P. Osenar[†], and L. S. Li[†]

Departments of Materials Science and Engineering[†] and Chemistry[§],
Beckman Institute for Advanced Science and Technology,
and Materials Research Laboratory
University of Illinois at Urbana-Champaign, Urbana, IL

ABSTRACT

The controlled synthesis of nanostructures and quantum dots is one of the goals of this work involving both organic and inorganic structures. The generation of nanostructured sulfide based semiconductors through the tight control of an organic liquid crystal template has been realized. This technique can yield differing architectures based upon the different phases of the liquid crystal template, including hexagonal and lamellar structures. Novel liquid crystalline materials have been developed which self assemble into organized three dimensional solids comprised of layers of nanoaggregate superlattices. The material exhibits polar order over many hundreds of layers and expresses a hydrophobic surface on one side of the film and a hydrophilic surface on the other. The aggregates are ~5 nanometers in diameter and have a mushroom like shape. A specially designed derivative of the molecule that forms these aggregates was used to control the morphology of cadmium sulfide semiconductor, and this produced quantum dots.

** To whom correspondence should be addressed*

INTRODUCTION

Nanotechnology has captured the interest of science because it has the potential to access new material properties and devices that remain unattainable by conventional means. Unfortunately, it is a difficult task to control feature sizes in the nanoregime and therefore the fabrication of nanoparticles has explored a gamut of synthetic pathways.(1-14) Controlling the assembly of such nanostructures into macroscopic materials is yet another challenge to be overcome in their evolution into functional, periodic structures. Nature provides us with an ideal model for controlling nanomorphology through the noncovalent interactions of folded proteins which yield highly specific nanostructured materials with long range order and site specific functionality. This example suggests that self assembling materials present a powerful synthetic route to controlled nanoscopic systems. It is in this context that we have developed materials where the nanoscale size and periodic structure are programmed into the chemical code of the system. First, we have developed nanostructured organic-inorganic composites whose size and periodicity is mediated by a lyotropic liquid crystal. Also, we have developed novel self assembling molecules that spontaneously organize into nanoaggregates which in turn pack on a superlattice. Finally, we are combining these two synthetic pathways to mediate the formation and organization of semiconductor quantum dot structures.

INORGANIC-ORGANIC COMPOSITES

Inorganic-organic interactions can play a vital role in controlling semiconductor properties and structure. Recently our group has discovered a novel technique to generate exquisitely ordered semiconductor nanostructures. We utilize the order inherent in a liquid crystal and its interaction with the growing inorganic phase to template various II-VI semiconductors.(15-17) Other groups have been able to control semiconductor-metal transitions,(18, 19) absorption and luminescence spectra,(2, 4, 20, 21) and nanostructure(5, 22-25) through organic-semiconductor interactions. In many of these systems of course, the properties and structure are intimately related.(3) Most current research and development work on semiconductor devices has concentrated on high temperature, high vacuum depositions followed by conventional lithographic techniques. Despite much work in this area, control of dimensions and properties do not rival that possible through molecular engineering of organic molecules. The calculated design of nanometer

scale structures is indeed possible for the organic and supramolecular chemists(10-12) and perhaps by coupling these concepts with semiconductor synthesis it will prove possible to access new materials. Over the last couple of years the first strides in this direction have been made. Recently several research groups have developed systems utilizing the calculated design of molecules to carefully control both structure and properties in mostly inorganic, semiconducting systems.(2, 5, 7, 25) The common thread running throughout is the absolute requirement for the presence of the organic at some time, if not at all times in the synthesis and utilization of the semiconductor. The removal of organic is often not possible, and perhaps not even desirable where it impacts the final properties. In other systems of course, the presence of organic in the final material may not be so desirable, and can be mostly removed.

Liquid crystals present an ideal system for three dimensional control. Through tight chemical specificity the system can be varied in dimension, symmetry, and internal structure. Lyotropic liquid crystals, composed of an amphiphilic molecule and solvent (not necessarily limited to water), are capable of dissolving various ions while retaining their structure. Several of these metal ions are reactive with H_2S gas, yielding an inorganic product. The most important result of this synthetic methodology is the retention of the nano- and microstructure of the liquid crystal in the product even after removal of the bulk organic phase. Our work in this area involves the direct templating of CdS, CdSe, and ZnS in the preordered environment of a nonionic amphiphilic mesophase, generating a semiconductor-organic superlattice containing both the symmetry and long-range order of the precursor liquid crystal. In general, the semiconductor is grown in a water-containing liquid crystal by the reaction of H_2S with a dissolved metal salt (providing the cation for the semiconductor). Through this work we have shown the importance of the amphiphile's chemical nature and structure in the direct templating process. In fact, the order obtained in the nanostructured systems was even found to depend on the chemical nature of the anion of the salt.(17)

Two different systems have been studied, the first, a hexagonal liquid crystal composed of an oligo(ethylene oxide) based amphiphile and ion doped water,(15, 17) and the second, a lamellar system of an oligo(vinyl alcohol) based amphiphile and water.(16) In both, the order seen in the semiconductor product is a direct template of the liquid crystal, although the amount of organic retained in the two systems is quite different. The oligo(ethylene oxide) system generates hexagonally faceted semiconductor particles (CdS, CdSe, and ZnS) which have a hexagonal array of rod-like nanopores of identical symmetry and dimension as the liquid crystal template (figure 1). These features could be eventually used to exploit

antidot modification of electronic materials.(26-28) They retain a small amount ($\leq 15\%$ by volume) of organic after work up, and because the particles consist of an inorganic continuum they are entirely morphologically stable even after removal of most of the organic. In contrast, semiconductor growth in the lamellar system results in a layered semiconductor-organic composite particle. This structure is approximately 50% by volume organic, with the remainder CdS. Surprisingly this morphology, even though it does not contain a continuous mineral framework, is stable to repeated sonication in good solvents for the organic amphiphile, always retaining the lamellar structure (figure 2). The strong affinity of the highly polar oligo(vinyl alcohol) segments of the amphiphile for the CdS must stabilize the nanostructure. In both systems, the nano- and microstructure of the resulting semiconductor is directly controlled by the liquid crystal template. In essence, the nano- and microstructure is generated because the semiconductor growth is excluded from the nonpolar regions of the liquid crystal, rod-like regions in the hexagonal system, and sheet-like regions in the lamellar system. These results demonstrate the versatility of the direct templating process, opening up a variety of synthetic avenues to the formation of novel nanostructures. There are a large number of amphiphilic liquid crystals, with different phases and lattice constants ranging from a few nanometers to tens of nanometers. One such liquid crystal, the triblock rodcoil molecule, recently emerged from our laboratory.(29) Its solid state structure capitalizes on the self assembly of rigid organic rods.

SELF ASSEMBLING NANOSTRUCTURED MATERIALS

A challenge of materials chemistry is to create supramolecular nanostructures with shape and functional specificity. There has been limited success in this area mostly due to the complex interplay of thermodynamics, kinetics, and chemical functionality. Lehn and co-workers(10) followed by Mathias et al.(11) and Seto et al.(12) demonstrated some of the early efforts by creating small aggregates of molecules. Our work in this field has concentrated on a novel class of molecules we have named triblock rodcoil molecules. Their synthesis was inspired by block copolymer chemistry with the incorporation of an important architectural duality along the backbone; a rigid rod moiety followed by a flexible oligomeric sequence (coil portion). Specifically, the rigid rod unit is a three biphenyl ester segment covalently linked to an atactic block of oligoisoprene followed by an atactic block of oligostyrene.(29)

This molecular structure yields a material with a wide range of properties due to the unique three dimensional organization the

molecules attain. The novel structure is a direct result of the interplay between two opposing thermodynamic forces. The rigid rods desire to aggregate and crystallize but this process is frustrated by the amorphous, atactic coils. The average cross section of the coil is larger than that of the rod causing hard-core repulsive forces as the molecules aggregate. We believe these two opposing energies balance when ~100 of these molecules aggregate together. These aggregates are highly monodisperse with a 5 nanometer cross section and 200 kilodalton molecular weight. The objects take on an unusual configuration similar to a mushroom with the crystallized rods forming the stem and the random coils splaying out to make the mushroom cap.

Films cast from chloroform spontaneously form these nanoaggregates as can be seen in the transmission electron micrograph shown in figure 3. The black regions are the nanocrystals of rods and the light regions are the amorphous coils. Since no electron stains were used, the contrast derives from the diffraction of the crystallized rods as well as the phase contrast between the rods and coils. Closer inspection reveals that the nanostructures are packed in an oblique two dimensional superlattice with a characteristic angle of 110° and a 66\AA by 70\AA periodicity. Small angle x-ray scattering and cross-sectional TEM have both shown that the 2-D array of mushrooms layer with a repeat distance equal to the molecular length (figure 4).

The three biphenyl rod is terminated with a phenolic group giving it hydrophilic character. When cast on water the nanoaggregates align with the stems of the mushroom down onto the water surface, maximizing the hydrophilic interactions of the phenolic group with the water. Interestingly, the top surface of this film expresses the hydrophobic character of the oligostyrene coil suggesting that the films stack in a polar arrangement. Proof of this comes from second order nonlinear optical measurements which show a linear relationship between the film thickness and the second harmonic generation of the material. This precludes a centrosymmetric or bilayer arrangement which would not exhibit dipolar second harmonic activity. Such a polar arrangement is very surprising and rarely seen in nature because it forces the hydrophilic phenolic groups to interface with the hydrophobic oligostyrene and generates a net dipole moment in the material. However one possible explanation for this arrangement is that a thermodynamic minimum is achieved due to the high energy associated with nature's abhorrence of a vacuum. The polar stacking of mushroom structures minimizes the free volume in the system which we believe outweighs the hydrophobic/hydrophilic contact energetics. It is interesting to note that solid state infrared spectroscopy studies show a presence of trapped solvent

even at high temperatures, thus suggesting that space filling by nanostructures is an important issue in the observed order.

The rodcoil's ability to control its own organization through three hierarchical levels of structural order, packing into supramolecular aggregates, forming continuous two dimensional structures from the aggregates and finally layering into macroscopic polar films, gives these systems great potential as multifunctional materials. The surface properties expressed by the polar films makes these materials ideal for adhesion to solid surfaces. Recently, derivatives of this molecule were synthesized with differing functionalities built into the rodcoil theme.

One such derivative incorporates the rigid *trans* conformation phenylene vinylene, with its interesting electronic and photonic properties, into the rod portion of the structure (figure 5). We have been able to vary the terminal functionality as well as the length of the phenylene vinylene segment incorporated into the triblock rodcoil structure. These molecules retain all of the unique features of the original triblock system in addition to their new photonic properties. Small angle x-ray scattering studies suggest these molecules form films composed of monolayer structures of the type required for polar order. When films of these molecules are annealed at 140 °C for 8 h, SAXS patterns for the molecule depicted in figure 5a show (001) and (002) reflections corresponding to a layer spacing of 78 Å, while the molecules in figure 5b and 5c show one reflection at 76 Å and 85 Å, respectively. Initial investigations into the photoluminescence behavior of these molecules is quite interesting. Not surprisingly, the molecules are fluorescent in dilute solutions with 5a, 5b and 5c showing emissions at 450 nm, 420 nm, and 487, respectively when excited with 331 nm light. However, a comparison of the quantum efficiency in the solid state of these molecules with that of poly(phenylene vinylene) suggests the nanostructured rodcoil molecules have a much higher efficiency. Detailed experiments to quantify the quantum efficiencies from our triblock rodcoil molecules are currently under way. In addition, preliminary UV/Visible spectroscopy experiments suggest for the first time the formation of aggregates in solution. With these molecules we have demonstrated the ability to integrate luminescent functionality into the rodcoil construct, yet maintain the unique mushroom structure and polar order.

QUANTUM DOT STRUCTURES

An immediate application of such mushroom structures might be as templates for the formation of semiconductor quantum dot arrays. Such structures are of profound importance in single electron devices as well as

in optoelectronic applications. Most of the work in this area has concentrated on novel lithographic techniques to sculpt intricate nanomorphologies.⁽¹⁾ A simpler approach might exploit the power of self assembly to control and template the evolving structure. By utilizing the self assembling rodcoils as a template for the precipitation of sulfide based semiconductors, it might be possible to synthesize quantum dot structures. Recently, rodcoil molecules were synthesized which replaced the oligostyrene-isoprene coil with an oligo(ethylene oxide) coil.^(30, 31) These molecules exhibit similar properties to their styrene-isoprene relative, packing into nanoaggregates with the oligoethylene oxide segments splaying out from the stem.

Since PEO can bind cadmium ions it is possible to dope the coil regions of the nanostructure and selectively precipitate CdS within the PEO portion of the nanoaggregate. Specifically this was accomplished by drying a cadmium chloride doped rodcoil/ethanol solution followed by an anneal under vacuum to remove residual ethanol and equilibrate the system. The doped material was then exposed to H₂S gas in order to precipitate the CdS nanostructures. This process yielded quantum dot structures with a diameter of 2-5 nanometers (figure 6). The nanoparticles were not oriented in a superlattice but rather were randomly arranged. Further work in this area is ongoing in order to control the organizational behavior of the quantum dot structures.

CONCLUSIONS

Controlling nanomorphology will remain a challenge for science for a long time but this work has demonstrated some powerful synthetic methodologies that could spawn future developments in this field. Molecular and supramolecular nanostructures of the type described here provide the intriguing ability to combine form and function previously unattainable by other materials in this size regime. The ability to selectively define chemical functionality in these assemblies makes them versatile systems for a wide variety of applications. By exploiting this chemical diversity it is possible to mediate the architecture of inorganic compounds to generate periodic nanostructures. This may prove useful in the formation of materials containing a large array of quantum dots and anti-dots for new device technologies.

REFERENCES

1. T. C. Shen, et al., *Science* **268**, 1590 (1995).
2. J. H. Fendler, *Membrane-Mimetic Approach to Advanced Materials* (Springer-Verlag, Berlin, 1994).
3. J. H. Fendler, F. C. Meldrum, *Adv. Mater.* **7**, 607-632 (1995).
4. N. Herron, J. C. Calabrese, W. E. Farneth, Y. Wang, *Science* **259**, 1426-1428 (1993).
5. C. B. Murray, C. R. Kagan, M. G. Bawendi, *Science* **270**, 1335-1338 (1995).
6. "Nanostructures," *Chem. Mater.* **8**, 1569-1882 (1996).
7. M. P. Pileni, *J. Phys. Chem.* **97**, 6961-6973 (1993).
8. H. Weller, *Angew. Chem. Int. Ed. Engl.* **32**, 41-53 (1993).
9. C. J. Brinker, G. W. Scherer, *Sol-Gel Science* (Academic Press, New York, 1990).
10. J. M. Lehn, *Supramolecular Chemistry* (YCH Press, New York, 1995).
11. J. P. Mathias, E. E. Simanek, G. M. Whitesides, *J. Am. Chem. Soc.* **116**, 4326 (1994).
12. C. T. Seto, J. P. Mathias, G. M. Whitesides, *J. Am. Chem. Soc.* **115**, 1321 (1993).
13. J. M. J. Fréchet, *Science* **263**, 1710 (1994).
14. D. A. Tomalia, *Aldrichimica Acta* **26**, 91 (1993).
15. P. V. Braun, P. Osenar, S. I. Stupp, *Nature* **380**, 325-328 (1996).
16. P. Osenar, P. V. Braun, S. I. Stupp, *Adv. Mater.* **8**, 1022 (1996).
17. V. Tohver, P. V. Braun, M. U. Pralle, S. I. Stupp, *Chem. Mater.*, in press.
18. D. B. Mitzi, S. Wang, C. A. Feild, C. A. Chess, A. M. Guloy, *Science* **267**, 1473-1476 (1995).
19. D. B. Mitzi, C. A. Feild, W. T. A. Harrison, A. M. Guloy, *Nature* **369**, 467-469 (1994).
20. T. Vossmeier, et al., *Science* **267**, 1476-1479 (1995).
21. Y. Tian, C. Wu, N. Kotov, J. H. Fendler, *Adv. Mater.* **6**, 959-962 (1994).
22. B. O. Dabbousi, C. B. Murray, M. F. Rubner, M. G. Bawendi, *Chem. Mater.* **6**, 216-219 (1994).
23. J. Yang, J. H. Fendler, *J. Phys. Chem.* **99**, 5505-5511 (1995).
24. Z. Y. Pan, G. J. Shen, L. G. Zhang, Z. H. Lu, J. Z. Liu, *J. Mater. Chem.* **7**, 531-535 (1997).
25. X. Peng, T. E. Wilson, A. P. Alivisatos, P. G. Schultz, *Angew. Chem. Int. Ed. Engl.* **36**, 145-147 (1997).
26. D. Weiss, et al., *Phys. Rev. Lett.* **66**, 2790-2793 (1991).
27. R. Fleischmann, T. Geisel, R. Ketzmerick, *Phys. Rev. Lett.* **68**, 1367 (1992).

28. W. Kang, H. L. Stormer, L. N. Pfeiffer, K. W. Baldwin, K. W. West, *Phys. Rev. Lett.* **71**, 3850-3853 (1993).
29. S. I. Stupp, et al., *Science* **276**, 384-389 (1997).
30. W. Eck, S. I. Stupp, *in preparation*.
31. L. S. Li, S. I. Stupp, *in preparation*.

ACKNOWLEDGEMENTS

This work was supported by the Department of Energy Center of Excellence for the Synthesis and Processing of Advanced Materials, the Department of Energy (DEFG02-91ER45439 obtained through the Materials Research Laboratory of the University of Illinois), the National Science Foundation (DMR 93-12601), the Office of Naval Research (N00014-96-1-0515), and the Army Research Office (DAAH0-96-1-0450).

4

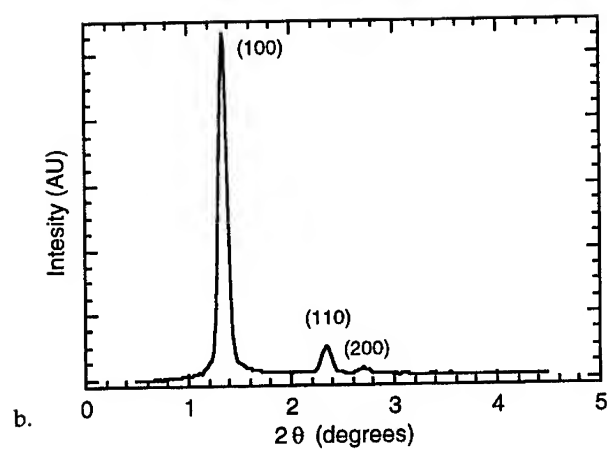
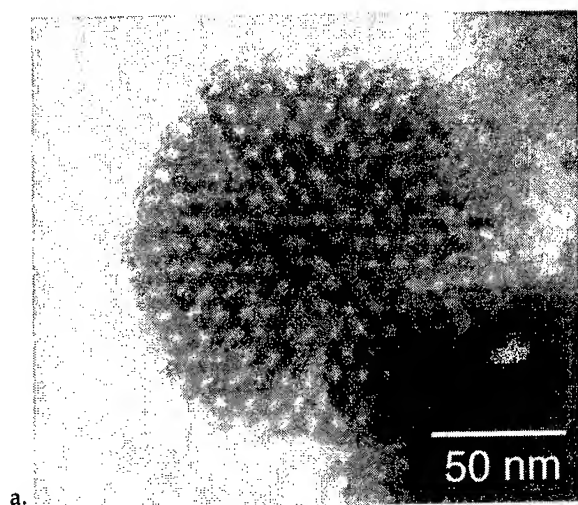


Figure 1. (a) ZnS nanostructured particle with a hexagonal array of 3 nm cylindrical pores spaced ~ 8 nm apart. (b) A hexagonal SAXS pattern of the zinc doped mesophase with lattice constant of $a=7.6$ nm, nearly identical to the spacing in the TEM micrograph in (a).

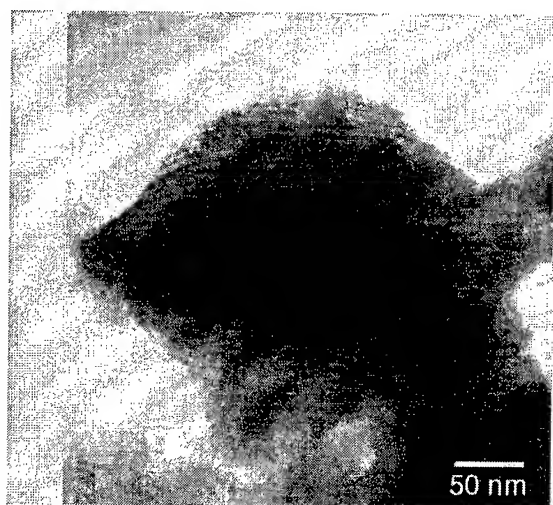


Figure 2. A TEM micrograph of the lamellar nanostructured CdS/organic composite.

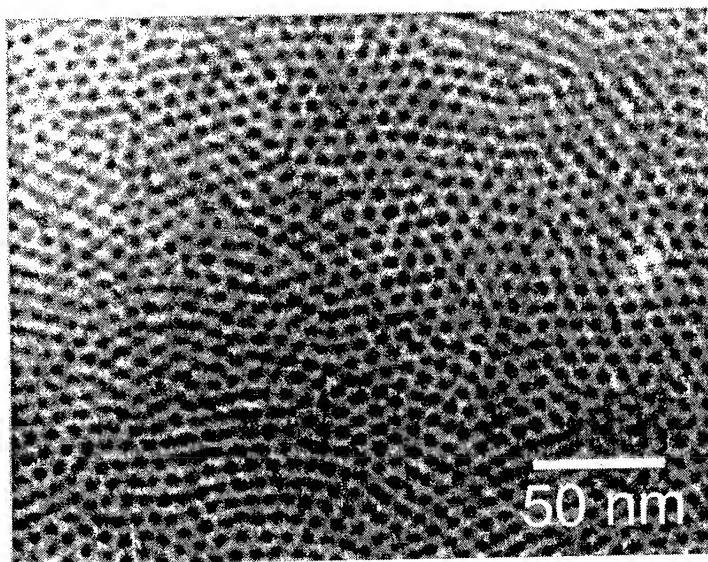


Figure 3. A monoclinic superlattice of mushroom shaped nanostructures.

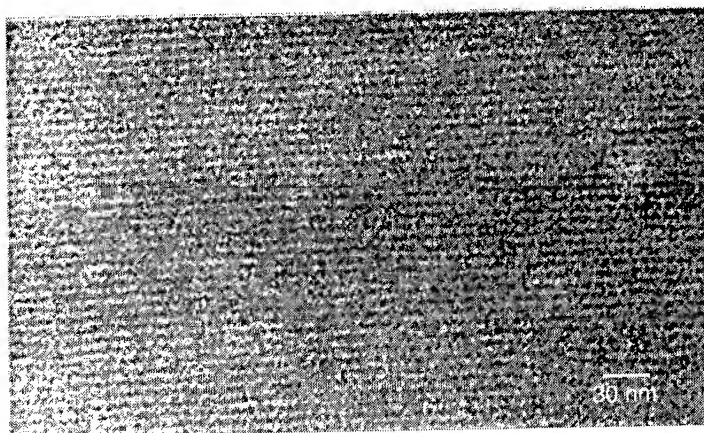


Figure 4. A cross sectional TEM micrograph of a thick rodcoil supramolecular film. The layer spacing equals the thickness of a monolayer.

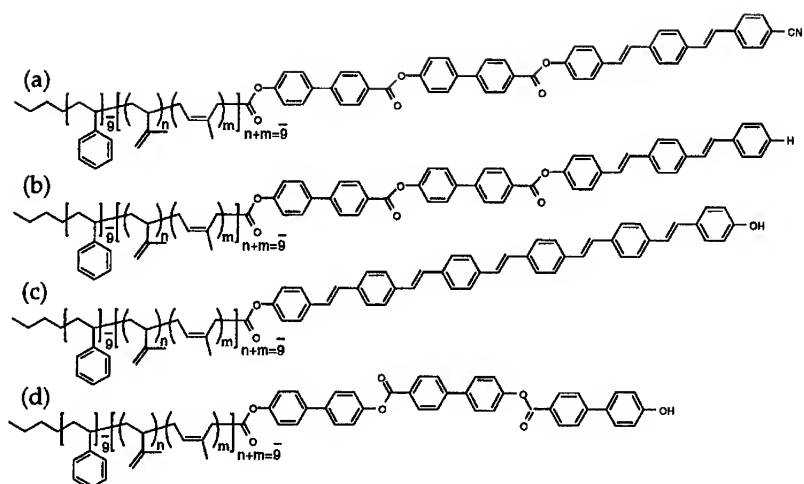


Figure 5. Examples of designed molecules programmed to form supramolecular units.

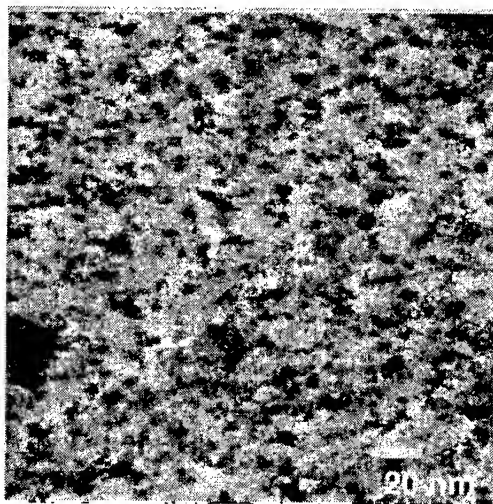


Figure 6. A nonperiodic array of CdS quantum dots.

STUDIES OF PHOTOREDOX REACTIONS ON NANOSIZE SEMICONDUCTORS

Jess P. Wilcoxon, Sandia National Laboratories, Org 1152, Albuquerque, NM; F. Parsapour, D.F. Kelley, Colorado State U., Dept. of Chemistry, Fort Collins, Co.

ABSTRACT

Light induced electron transfer (ET) from nanosize semiconductors of MoS_2 to organic electron acceptors such as 2,2'-bipyridine (bpy) and methyl substituted 4,4',5,5'-tetramethyl-2,2'-bipyridine (tmb) was studied by static and time resolved photoluminescence spectroscopy. The kinetics of ET were varied by changing the nanocluster size (the band gap), the electron acceptor, and the polarity of the solvent. MoS_2 is an especially interesting semiconductor material as it is an indirect semiconductor in bulk form, and has a layered covalent bonding arrangement which is highly resistant to photocorrosion. ET occurs following photoexcitation of the direct band gap. Quantum confinement results in the smaller nanoclusters having higher conduction band energies, and therefore larger ET driving forces. The ET reaction energies may be varied by changing the electron acceptor, by varying the size of the MoS_2 nanocluster or by varying the polarity of the solvent. In addition, varying the polarity of the solvent affects the reorganization energy and the barrier to electron transfer. TMB is harder to reduce, and thus has a smaller ET driving force than bpy. The solvent polarity is varied by varying the composition of acetonitrile/benzene mixed solvents.

INTRODUCTION

Scientists have had a long-standing interest in photosynthetic chemical reactions and in understanding the underlying mechanisms of photooxidation and reduction. This interest is fueled by the obvious practical advantages of using abundant small molecules such as water, N_2 , or CO_2 as starting materials in the artificial photosynthesis of useful fuels or chemical feedstocks such as hydrogen, ammonia, or methane. There has also been a fair amount of research in light-driven oxidation processes for the destruction of complex, sometimes toxic, organic chemicals (e.g. biphenols, chlorinated hydrocarbons, polycyclic aromatics, even coal) to form harmless products such as CO_2 and dilute mineral acids.

Although such photooxidation processes occur readily under intense UV illumination from lamp sources, it would be of major importance to develop photocatalysts which would allow the direct use of sunlight. Unfortunately, the number of catalytic materials which are sufficiently photostable and also absorb in the visible

regime is quite limited. As a compromise scientists have been forced to investigate primarily wide-bandgap metal oxides such as TiO_2 , which only absorbs light with wavelengths shorter than ~ 400 nm, about 3-7% of the typical solar spectrum.

MoS_2 is an especially interesting semiconductor material as it is an indirect semiconductor in bulk form and has a layered covalent bonding arrangement, which resists photocorrosion. Its most common industrial applications include thermal catalysis to remove sulfur compounds from crude oil and as an excellent high temperature lubricant (e.g. axle grease).

However, because MoS_2 is an indirect gap, black, IR absorbing material, it has no application as a photocatalyst. We have demonstrated that when synthesized in nanosize form, the absorption edge of MoS_2 can be significantly blue shifted.[1] This increase in the band gap energy, due to quantum confinement, is accompanied by significant shifts in both conduction and valence band energies, and implies that nanosize MoS_2 is capable of light induced electron and hole transfer (photoredox) reactions, just as are well known direct gap materials such as CdS . Experimentally, there is evidence that as MoS_2 is made smaller, the excitation becomes more like a direct transition, presumably due to the increasing importance of surface and lack of long-range translational symmetry in the lattice.

MoS_2 is also the most important hydrotreating catalytic material because it resists poisoning by sulfur during the desulfurization process so vital to fuel refining. Because the basal sulfur planes are relatively inactive toward substrates, it is thought that catalysis occurs primary at Mo edge sites. Therefore, one could imagine that synthesis of nanosize MoS_2 would vastly increase the relative numbers of such sites and thus the catalytic activity. The same type of advantage applies to possible photocatalytic applications of MoS_2 .

In this paper we report on static and dynamic photoluminescence measurements of nanosize MoS_2 and show that the observed increases in the bandgap energy with decreasing nanocluster size, are accompanied by increases in the conductance band potential which permit electron transfer electron to acceptor organic molecules. The rate of electron transfer is found to be dependent on both nanocluster size and solvent polarity. The fastest rates are observed in solvents of high polarity.

EXPERIMENT

Synthesis, Processing, and Physical Characterization

Nanosize MoS_2 is prepared by dissolving an anhydrous MoX_4 salt ($\text{X}=\text{Cl}, \text{Br}, \text{or I}$) in a water and air-free inverse micelle solution. (A typical inverse micelle solution would consist of 5-10% by weight of a quaternary ammonium surfactant in an aliphatic hydrocarbon such as octane).[2] This precursor solution is then exposed to a source of sulfide, typically H_2S gas injected through a septum in a known amount (slightly greater than 2:1 S:Mo) while rapidly stirring the solution. A brightly colored, transparent solution is formed which is then purified by extraction into an oil-immisible phase solvent, typically acetonitrile (ACN). Alternatively, we have developed high pressure liquid chromatographic (HPLC) procedures to both separate the nanoclusters from the surfactants and ionic byproducts in the solution and optically characterize the purified nanoclusters on-line.[3] Gas-Chromatography/Mass Spectrometry is used to ascertain that the organic byproducts have been removed from the reaction mixture.

The purified MoS_2 clusters have been investigated using HRTEM and shown to be nanocrystalline. The larger nanoclusters have been shown to have the bulk hexagonal lattice structure by electron diffraction, but the smallest clusters (diameter, $D < 3$ nm) have too few atoms to give unambiguous structural information based upon diffraction. However, lattice fringe images are consistent with d spacings found in the bulk material. Evidence indicates that the clusters are not spherical in shape, but are disc-like. The sandwich-like structure of MoS_2 consists of successive S-Mo-S tri-layers, with a weak Van-der-Waals interaction between layers. This graphite-like structure is responsible for the good lubricating properties of bulk MoS_2 , since these planes can readily slide past one another.

Dynamic light scattering is complementary to measurements of cluster cross-sectional size by TEM since it measures the translational diffusion of the cluster in the acetonitrile solution, and via Stokes law provides an equivalent sphere hydrodynamic diameter. This diameter is comparable to the cross-sectional area for nanoclusters with $D \sim 3.0$ nm, but is smaller for the $D \sim 4.5$ nm clusters, implying the thickness of the latter clusters is somewhat less than the cross-sectional TEM measurement.

Liquid Chromatographic Analysis of Nanosize MoS_2

Extraction of the nanosize MoS_2 from the oil phase where it is synthesized into the more hydrophilic ACN phase also extracts small amounts of the ionic byproducts and a small amount of the surfactant (0.5-1% by weight

typically). To eliminate these other chemicals and create a known, controlled environment for optical and PL studies, we perform HPLC purification and analysis of the MoS₂ clusters. The nanoclusters have a highly structured optical spectrum with a characteristic peak for D=3.0 nm cluster near 360 nm. Examination of the absorbance vs. elution time chromatogram at 350 nm shows a single sharp peak whose wavelength-dependent absorbance features may also be collected in real time. Concomitant detection of organic molecules using an differential refractive index detector shows that the surfactant is separated from the clusters quantitatively by the reverse phase c18 column used (the mobile phase is ACN with 0.1% cationic surfactant added to prevent the nanoclusters from aggregating during the chromatography).

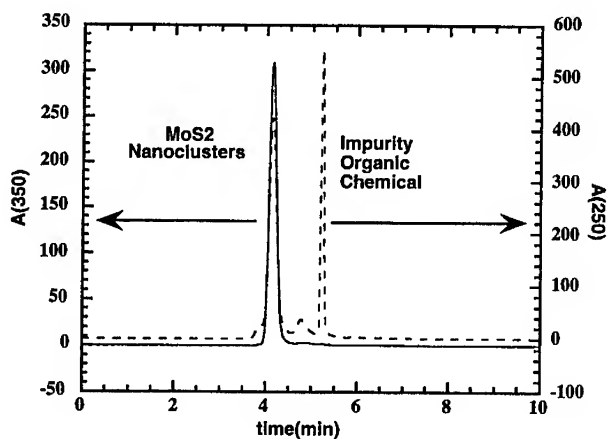


Figure 1. Coplot of the optical absorbance at 350 nm and at 250 nm shows the MoS₂ nanoclusters to be a single sharp elution peak well separated from the organic impurities which absorb at 250 nm.

It is also possible to use HPLC to study the binding and/or chemical reactions of other organic chemicals (e.g. bpy) to nanosize MoS₂. We have observed some quite interesting effects. For example, though bpy is readily separated from the MoS₂ nanoclusters at a completely different elution time under the chromatographic conditions described above and can be detected with a sensitivity exceeding $1 \times 10^{-4} \text{M}$, we observed no unbound bpy in the solutions of D=3 nm MoS₂ in ACN until the amount of bpy added exceeds $4 \times 10^{-3} \text{M}$, a level nearly twice as large as the known molybdenum concentration. Further, despite further additions of bpy, an absence of bpy amounting to $\sim 2 \times 10^{-3} \text{M}$ is always observed. However, neither the elution time, peak area, nor the spectral characteristics of the

nanocluster MoS₂ peak is changed, arguing that the MoS₂ is simply acting like a catalyst. It is clear that the bpy is being chemically altered by the presence of the nanoclusters, and indeed a white precipitate can be visually observed at high levels of added bpy. Prior to the formation of a white precipitate, new chromatographic peaks appear and grow as more bpy is added to the solution. A complete discussion of this interesting phenomena is beyond the scope of this paper, but these observations indicate the power and utility of HPLC studies of nanocluster photochemistry.

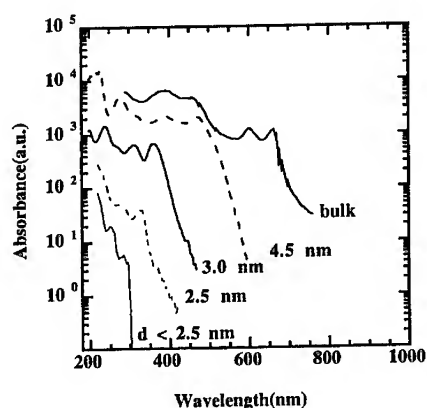


Figure 2. Absorbance vs. wavelength for a series of nanosize MoS₂ crystals in ACN is compared to that observed from bulk single crystals.

MoS₂ Optical Properties and Electronic Structure

Bulk MoS₂ is an indirect band-gap semiconductor, with a band gap of 1.23 eV.[4] As in the case of other indirect materials such as Si and Ge, no room temperature photoluminescence can be observed. Studies of thin crystalline films of MoS₂ reveal that the first direct absorbance in MoS₂ occurs at 1.88 eV, corresponding to ~660 nm. In bulk form, the top of the valence band is composed primarily of Mo d_{z²} orbitals, and the bottom of the conduction band is composed of Mo D_{x²-y²} and d_{xy} orbitals. As a result, excitation to create hole-electron pairs is metal intraband in nature and no Mo-S bonds are weakened, giving this material strong resistance to photocorrosion.[5] In contrast, II-IV semiconductors such as CdS have valence band orbitals consisting mainly of S 3p states, so that direct excitation across the gap to conduction band Cd 5s states leads to weakening of the chemical

bonds holding the material together and accounts for the observed significant photocorrosion in these semiconductors.

As MoS_2 is made smaller, the momentum selection rules due to the long-range translational symmetry of the lattice are relaxed. In effect, the material becomes more like a direct band-gap material. The blue shift of the absorbance with size is shown in figure 2 where three sizes of nanocluster MoS_2 are compared with measurements obtained by others[6] on bulk single crystals. This shift in bandgap with size is quite dramatic and an analysis of the structured featured shown in this figure is given elsewhere.[3] Also, as shown in figures 3 and 4 quantum confinement results in increased room temperature photoluminescence and larger optical extinction in the visible region. (The extinction coefficients can be obtained from figures 3 and 4 by multiplying by 1000 since the $[\text{MoS}_2] \sim 2 \times 10^{-3} \text{M}$, and are in the 10^4 to $10^5 \text{ cm}^{-1} \cdot \text{mol}^{-1}$ range, comparable to nanosize direct bandgap materials such as CdS)

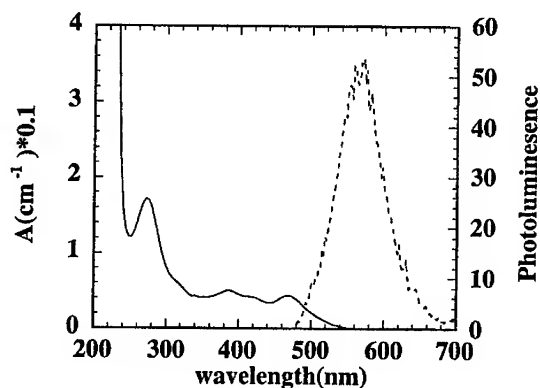


Figure 3. Absorbance (A, solid curve), and photoluminescence (excitation at 348 nm, dashed curve) from $D=4.5 \text{ nm}$ MoS_2 nanoclusters.

A significant portion of the observed luminescence occurs to the red of the absorbance band-edge indicating that recombination is occurring primarily from sub-band-gap trapped states at the surface of the nanocluster. Addition of an electron acceptor such as bpy to the MoS_2 nanoclusters will decrease the lifetime of these deep trap states by funneling some of the electrons created by direct excitation to the electron acceptor bpy, from which recombination with the hole on the MoS_2 nanocluster will also occur. This allows us to follow the electron transfer

kinetic indirectly. A more direct alternative approach to following the ET kinetics involves measurement of the change in the bpy absorbance due to ET as a function of time. We are currently pursuing such studies.

A result of making smaller MoS₂ nanoparticles is the blue shift of the absorbance edge shown in figures 2-4 a corresponding blue shift of the emission, and an increased quantum efficiency for luminescence.

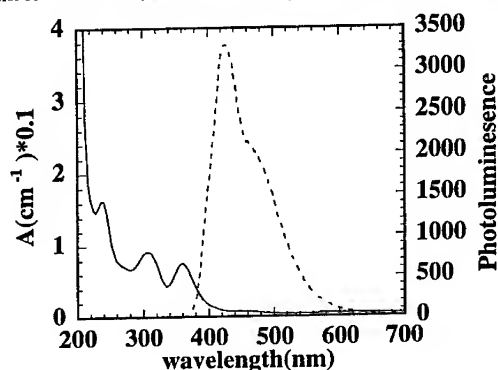


Figure 4. Absorbance (A, solid curve), and photoluminescence (excitation=348 nm, dashed curve) from D=3.0 nm MoS₂ nanoclusters.

We can roughly estimate the conduction and valence band energies of our nanosize MoS₂ clusters by using the known potentials of the bulk material of +0.1 V and +1.33 V (vs. NHE) respectively. If we attribute most the band-gap shift observed in figure 2 to changes in the conduction band potential (because of the lower electron compared to hole mass) then we estimate a value of -.66 V and -1.46 V vs. NHE for the D=4.5 nm and D=3.0 nm samples.[7] By photoexciting at the direct point we produce conduction band electrons with about 0.25 eV higher energies (more negative potential) than the above values. So nanoclusters will have a significant driving force for electron transfer compared to the bulk material.

Static PL Quantum Efficiency

Table I summarizes the results of PL integrated area, PL(area), normalized by the cluster absorbance (abs) at the excitation wavelength indicated for one size, D=3.0 nm of nanocluster. Very similar trends were observed for other sizes of cluster. Also shown in this table are the results for Coumarin 500 dye (nearly 100% Q.E. for PL) under identical instrumental conditions.

We note the very significant decrease in radiative recombination (PL) as the solvent polarity decreases from ethylene glycol to o-xylene. This effect is greatest for excitation at the first direct absorbance (~340 nm, see figure 4) compared to excitation at the band edge (~400 nm). Furthermore, we observe an interesting *decrease* in PL by 5-fold when bpy is bound to the nanocluster and excitation is at 340 nm. Band edge excitation, on the other hand, actually *increases* the yield by ~15% when bpy is bound. Additionally, changing the solvent can alter the overall wavelength dependence of the PL for excitation at the first absorbance feature. (There is little effect for excitation at the band edge) Basically, solvating the clusters in very non-polar solvents such as toluene increases the amount of light emitted from trapped surface states, effectively red-shifting the PL peak by ~20 nm compared to polar solvents such as ethylene glycol. Table I. Effect of Solvent Polarity on PL Quantum Efficiency for MoS₂ nanoclusters

Table I. Size, Excitation Wavelength, and Solvent Dependence of the PL of nanosize MoS₂

Size(nm)	solvent	l(excitation)	l(emission)	PL(area)/abs
Coumarin 500	methanol	350	497	1.5×10^{10}
3.0	Ethylene Glycol	350	465	1.0×10^7
3.0	DMF	340	481	5.8×10^4
3.0	acn	340	456	2.2×10^5
3.0	acn/bpy	340	461	4.1×10^4
3.0	hexanol	340	462	5.9×10^5
3.0	octanol	340	460	4.2×10^5
3.0	toluene	340	482	2.1×10^4
3.0	o-xylene	340	483	8.4×10^3
Coumarin 500	methanol	400	496	2.1×10^{10}
3.0	Ethylene Glycol	400	485	1.9×10^7
3.0	dmf	400	485	2.5×10^6
3.0	acn	400	484	1.3×10^7
3.0	acn/bpy	400	480	1.5×10^7
3.0	hexanol	400	478	7.0×10^6
3.0	octanol	400	479	6.1×10^6
3.0	toluene	400	486	8.2×10^5
3.0	o-xylene	400	481	2.1×10^5

ET Studies

The layer-like structure of both bulk and nanosize MoS₂ has important implications for its use as a photocatalyst. The basal planes of sulfur atoms are relatively inert and bifunctional electron donating ligands such as bipyridine (bpy) (used in the present study) will bind to the Mo at

edge sites of the disc-like MoS₂ nanoclusters. Such binding can be demonstrated to be quite strong as a MoS₂/bpy complex elutes as a single entity during HPLC up the [bpy]:[Mo] ratios of ~1:1.[6] It has been further demonstrated that the molar ratio of Mo to bpy at full edge site occupation is about 2:1, and so this was the chosen concentration for bpy, and tetramethyl substituted bpy (tmb) used in our studies. Interestingly, other mono-functional ligand dyes such as phenylthiozine (a good hole acceptor) do not bind irreversibly to MoS₂ and can be separated from nanosize MoS₂ by HPLC, indicating that the presence of two nitrogen electron donating groups in bpy is critical to its strong binding to MoS₂.

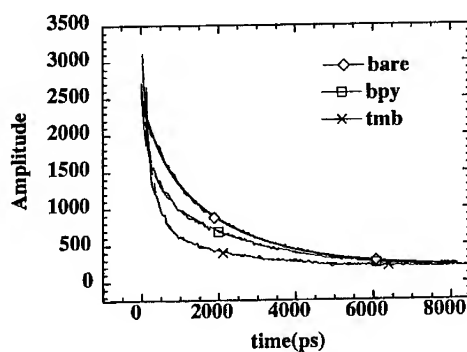


Figure 5. The decay of the photoluminescence of D=3.0 nm MoS₂ nanoclusters for various electron acceptors added.

The actual reduction potentials of bpy and tmb are quite sensitive to the type of metal to which they are bound and the chemical environment (solvent polarity etc.). Never-the-less, the difference of potential of 0.29 V between the two acceptors (tmb, is more difficult to reduce), remains quite constant. So, by adding these electron acceptors to the two different sized MoS₂ nanocluster samples and observing the changes in the PL decay curves shown in figure 5 and 6, one can estimate this potential. All PL relaxations were obtained with 315 nm excitation while detection was at 420 nm for the D=3.0 nm sample and 560 nm for the D=4.5 nm sample. The decay times do depend on the detected wavelength somewhat. Addition of tmb to the MoS₂, D=4.5 nm sample results in a very small change in the PL decay curve of figure 6, and we conclude that the potentials of tmb and bpy for reduction in acetonitrile are ~-0.7 V and ~-0.41 V vs. NHE respectively. (The decay curve of bound tmb overlaps the bare nanocluster curve of figure 6 and so is not shown).

Since the decay curves obtained are very non-exponential and represent a very wide range of decay rates, one can obtain excellent fits to these data by using a stretched exponential form, $Ae^{-(t/\tau)^b}$ from which the decay rate G can be extracted. A complicating factor is that the stretched exponential exponent b changes along with G when bpy is bound to the cluster, as well as when different solvents are used. This implies that the various mechanisms for radiative recombination for a given size cluster are influenced by the details of the cluster interface. Complete details for such energy calculations and the underlying assumptions are given elsewhere [7].

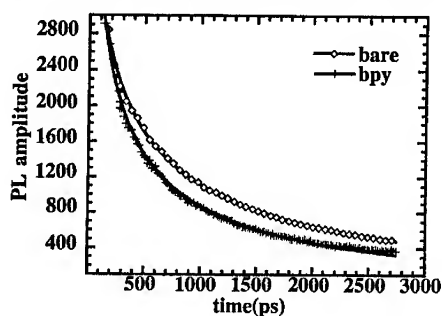


Figure 6. The decay of the photoluminescence of bare, $D=4.5$ nm MoS_2 nanoclusters and MoS_2 with bpy.

From analysis of the blue shifts of the absorbance spectra and our ET kinetics for nanosize MoS_2 , we have estimated the conduction band potential of the $D=3.0$ and $D=4.5$ nm nanoclusters to be -1.71 V and -0.91 V, respectively, in acetonitrile.[7] If we recall the estimated potential in the bulk material is $+0.1$ V, we can see that quantum size effects have made these nanoclusters into very strong reducing agents.

Size Dependence

Some of the results of our studies on ET kinetics are summarized in figure 7. We first note that for a constant solvent polarity (e.g. in acetonitrile, acn), the smallest clusters with the largest conduction band potentials are capable of driving the electron transfer to both bpy and tmb at faster rates. In fact, the larger $D=4.5$ nm clusters cannot effectively transfer electrons to tmb, the more difficult-to-reduce an electron acceptor. We have not shown the $D=4.5$ nm, tmb ET rates in figure 6 since they are so slow.

Solvent Dependence

Examination of the data of figure 7 shows that reduction of bpy to bpy radical anion is so facile for the smallest MoS₂ nanoclusters that solvent polarity has a very minor effect on ET kinetics. For the more difficult to reduce substrate, tmb, the smaller D=3.0 nm clusters show significantly slower ET once the mole fraction of the non-polar solvent, benzene is greater than 0.5. In the case of the D=4.5 nm clusters reducing the solvent polarity slows down the ET dramatically, since lower polarity solvents are less able to stabilize the charge separated state. In fact, effectively no ET to bpy occurs for solvent mixtures of greater than 20 mole% benzene.

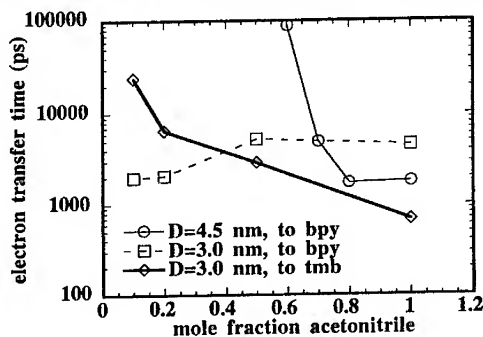


Figure 7. Effect of nanocluster size and solvent in the ET decay times (acetonitrile/benzene mixture).

CONCLUSIONS

We have shown how quantum confinement in an indirect semiconductor material can shift the conduction band potential and allow facile electron transfer to two types of substrate. Smaller clusters were demonstrated to have improved ET rates. It was also demonstrated that maximizing the solvent polarity increases the ET rate by stabilizing the charge separated state.

ACKNOWLEDGMENT

This work was supported by the U.S. dept. of Energy under contract DE-AC04-94AL85000. Sandia is a multiprogram lab operated by Sandia Corporation, a Lockheed-Martin Company, for the U.S. Dept. of Energy.

REFERENCES

- [1] J.P. Wilcoxon and G.A. Samara, Phys. Rev. B **51**, R7299, (1995).

-
- [2] J.P. Wilcoxon, G. Samara, and P. Newcomer, in Nanocrystalline Semiconductors, Ed. P. Jena, (Mat Res Soc Proc, Boston, MA., 1994), pp. 277-81.
- [3] J.P. Wilcoxon, P.P. Newcomer, and G.A. Samara, J. Appl. Phys., in press, (1997).
- [4] B.L. Evans in Optical and Electrical Properties (of Materials with Layered Structures), ed P.A. Lee, D. Reidel Publ, Boston, 1976, Chapt. 1, pg 1.
- [5] H. Tributsch, Z. Naturforsch **32a**, 972, (1977).
- [6] B.L. Evan and P.A. Young, Proc. Roy. Soc. A **284**,402,(1965).
- [7] F. Parsapour, D.F. Kelley, S. Craft, and J.P. Wilcoxon, J. Chem. Phys., **104**, 1, (1996).

PLATINUM NANOPARTICLES DISPERSED ON POLYPYRROLE NANO-/MICRO-PARTICLES

Zhigang Qi and Peter G. Pickup*

Department of Chemistry, Memorial University of Newfoundland
St. John's, NF A1B 3X7, Canada

Platinum and platinum oxide nanoparticles were chemically deposited on polypyrrole nano-/micro-particles by three different methods. Size-controllable polypyrrole particles were produced in the presence of polystyrenesulphonate by varying the concentrations of pyrrole and the ferric oxidant. The conducting polymer supported catalysts were characterized by transmission electron microscopy and conductivity measurements.

INTRODUCTION

Supported noble metal catalysts play an important role in many industrially important chemical reactions (1). The support enables the metal particles to be highly dispersed and thermostable to retard sintering so that they can be used with high efficiency. Traditionally, the selection of a support is based on certain characteristics such as inertness, stability, mechanical properties, surface area, porosity, and cost (2). The most widely used supports are C, SiO₂, Al₂O₃, TiO₂, ZrO₂, and zeolites. Carbon is unique within this group because it is electronically conductive.

Conducting polymers have generated great research interest since the 1980s (3). The electrochemical deposition of metals on a conducting polymer modified electrode results in the distribution of metal particles within the polymer matrix (4). Such metallized conducting polymer films have been used in electroanalysis and catalysis. However, electrochemical deposition is not suitable for producing large amounts of supported catalyst, and the metal particles are normally larger than 100 nm. In order to avoid these problems, we are developing chemical methods for the deposition of metal particles on conducting polymer particles. Here we describe two methods for the deposition of Pt nanoparticles on polypyrrole, and a method for the deposition of PtO₂ nanoparticles.

Conducting polymer particles have some very useful properties that none of the conventional supports possess. They can be both electronically and ionically conductive, and these conductivities are electrochemically and chemically controllable (7). Our primary interest in using conducting polymer supported catalysts arises from their potential application

in polymer electrolyte fuel cells. The ideal catalyst support in such fuel cells would be gas and water permeable, and conduct both protons and electrons (8-10). Unlike conventional catalyst supports, conducting polymers can be designed to possess all of these properties.

RESULTS AND DISCUSSION

Polypyrrole Particles

Polypyrrole particles were produced chemically in the presence of polystyrenesulphonate using ferric compounds as oxidants. Pyrrole was dissolved in an aqueous polystyrenesulphonate solution for a few minutes, then a solution of the oxidant was added causing the pyrrole to polymerize quickly. After ca. one hour, the polymer particles were separated from the reaction medium by centrifuging, washed with water, and dried at room temperature overnight under vacuum.

The size of the PPy particles could be easily controlled from as small as 40 nm to as large as 900 nm by varying the concentrations of pyrrole and the oxidant. The higher the concentrations, the smaller the resulting polymer particles. Figure 1 shows a scanning electron micrograph (SEM) of PPy particles prepared at low reagent concentrations ([PSS] = 0.0015 M, [pyrrole] = 0.0035 M, and $[\text{Fe}^{3+}] = 0.010 \text{ M}$). The particles have an average diameter of ca. 850 nm. The presence of PSS is essential in the size-control process. Without PSS, it is very difficult to control the shape and size of PPy. It was found that pyrrole polymerized much faster in the presence of PSS, with very little deposition on the surface of the reaction vessel. It is believed that PSS functions as a molecular template (11). Pyrrole is accumulated around the PSS chains via a hydrophobic interaction with the PSS backbone, resulting in a higher local concentration. When a ferric salt is added, the mixture becomes cloudy immediately due to the coagulation of PSS by Fe^{3+} . The coagulated particles blackened quickly because of pyrrole polymerization. The coagulation implies that the electrostatic interaction between $-\text{SO}_3^-$ and Fe^{3+} concentrates the latter around the PSS chains. The local preconcentration of both pyrrole and Fe^{3+} results in faster polymerization than in the absence of PSS.

Deposition of Pt Nanoparticles on PPy by Reduction of $\text{Pt}(\text{NH}_3)_4\text{Cl}_2$ with Formaldehyde

The deposition of Pt nanoparticles on PPy particles was carried out by the reduction of $\text{Pt}(\text{NH}_3)_4\text{Cl}_2$ with formaldehyde under reflux. In a typical procedure, the PPy particles were dispersed in formaldehyde by heating at reflux for 1 hour. $\text{Pt}(\text{NH}_3)_4\text{Cl}_2(\text{aq})$ was then added with 30 min of stirring at RT. The mixture was then heated at reflux for 150 min.

Figure 2 shows a transmission electron micrograph (TEM) of the resulting Pt/PPy. A large number of Pt nanoparticles with diameters of ca. 4 nm were produced, and their distribution is quite homogeneous. It was found that few Pt particles were produced when the reflux time was shorter than 1.5 hours. Longer reflux times did not significantly affect the Pt particle size. Since conducting polymers are microporous, it is likely that some Pt would deposit within the PPy particles, although it is difficult to confirm this from the TEMs. Four point probe conductivity measurements indicated that the electronic conductivity of the Pt/PPy was only 10^{-4} S/cm, which is about 3 orders of magnitude lower than that of the original PPy sample. This decrease could be due to irreversible reduction of the PPy by formaldehyde.

Deposition of Pt Particles on PPy by Reduction of K_2PtCl_4 with H_2

Another way of depositing Pt on the conducting polymer particles was through the hydrogen reduction of K_2PtCl_4 . Smaller PPy particles (ca. 40 nm) prepared at higher reagent concentrations ([PSS] = 0.042 M, [pyrrole] = 0.14 M, and $[Fe^{3+}] = 0.70$ M) were used here. PPy (69 mg) was suspended in 50 mL of aqueous K_2PtCl_4 (3 mM). The mixture was purged with H_2 for 6 min and stirred under H_2 overnight. The catalysed polymer was centrifuged, washed with water, and dried at RT under vacuum.

Gravimetric analysis by burning the sample at ca. 850 °C for 30 min showed that it contained 35% Pt. The PPy sample initially had an electronic conductivity of 3 S cm^{-1} , but this decreased to 0.3 S cm^{-1} after Pt deposition. This appears to result from hydrogenation of the polypyrrole, since exposure of the catalysed PPy particles to H_2 in a gas-diffusion electrode caused a further decrease in conductivity, that could not be reversed by electrochemical oxidation. Figure 3 shows a TEM of the catalysed polymer. The Pt particles (larger dark spots) are distributed in the polymer matrix, and attached to the polymer. The average Pt particle size was ca. 200 nm.

Deposition of PtO_2 Nanoparticles on PPy by Oxidation of $Na_6Pt(SO_3)_4$ with H_2O_2

Deposition. Platinum oxide (simplified here as PtO_2 but the actual composition is unclear (6)) nanoparticles were deposited on PPy particles via the oxidation of $Na_6Pt(SO_3)_4$ by H_2O_2 (6). $Na_6Pt(SO_3)_4$ was synthesized from H_2PtCl_6 according to a literature method (6). PPy and $Na_6Pt(SO_3)_4$ were stirred in water for 5 min, then 1 M H_2SO_4 was added dropwise to adjust the pH from ca. 4 to 2.0. The pH was then adjusted to 3.0 by the dropwise addition of 0.5 M NaOH and 30% H_2O_2 was added. The mixture was stirred for 1 h and then boiled. The PtO_2 /PPy particles were separated from the reaction medium by centrifuging, washed with water, and dried at room temperature overnight under vacuum. The

electronic conductivity of the resulting material was 10^{-5} S/cm; five orders of magnitude smaller than that of the original PPy. Figure 4 shows a TEM of the resulting PtO₂/PPy particles. The PtO₂ nanoparticles are ca. 1.2 nm in diameter and evenly distributed on and within the PPy particles.

FTIR. The decreased conductivity following PtO₂ deposition is believed to result from the overoxidation of the polymer by H₂O₂. Figure 5 shows FTIR absorption spectra of the PtO₂/PPy and the original PPy sample. The new absorption peaks at 1707 and 1620 cm⁻¹ in the PtO₂/PPy spectrum can be assigned to carbonyl and carboxylic acid groups resulting from overoxidation of the PPy.

Polarization. PtO₂/PPy was tested for oxygen reduction in a gas-diffusion electrode. The electrode was prepared by applying a mixture consisting of 8.3 mg of PtO₂/PPy, 19 mg of PTFE solution (15%), and 13.4 mg of 1.3% H₂SO₄(aq) to a 4 cm² area of Toray TGPH090 carbon fibre paper containing ca. 10% PTFE (Ballard Power Systems). Electrodes were bonded to Nafion 117 membranes at 120-130 °C and 3000 psi for 90 s. 1 cm² circular sections were used for the electrochemical studies. The Pt loading of the electrode was estimated to be ca. 0.15 mg/cm².

The test was performed in a cell designed to approximate the conditions at the cathode of an ambient temperature polymer electrolyte fuel cell. Oxygen gas was supplied to the back of the porous carbon paper at atmospheric pressure, while ionic contact to the membrane was made by a 1 M H₂SO₄(aq) solution containing a reference (SCE) and counter electrode (Pt wire). Polarization data were collected after a period of 3 s at each potential.

Figure 6 shows a polarization curve for oxygen reduction at a PtO₂/PPy electrode. The open circuit voltage was 0.79 V which was similar to carbon-supported Pt catalysts. Since the polymer was not particularly conductive, the electrode had a high-frequency resistance of 1.9 Ω, measured by impedance spectroscopy. For a carbon-supported catalyst electrode the resistance is normally as small as 0.3 Ω. Although this high resistance limited the current in the gas-diffusion electrode, the performance of the electrode was quite encouraging, with a current density of 50 mA/cm² being reached at 0 V vs. SCE (ca. 0.25 V vs SHE).

CONCLUSIONS

Highly dispersed Pt and PtO₂ nanoparticles with diameters of 4.0 and 1.2 nm, respectively, have been chemically deposited on polypyrrole nano-/micro-particles of dimensions between 40 and 850 nm by the reduction of Pt(NH₃)₄Cl₂ with formaldehyde under reflux and oxidation of Na₂Pt(SO₃)₄ with H₂O₂, respectively. However, the Pt particles were as large as 200 nm when they were produced by the reduction of K₂PtCl₆ with hydrogen. The

size control of polypyrrole particles was achieved by varying the reagent concentrations in the presence of polystyrenesulphonate. A significant problem encountered in this work has been the damage of the polymer by the Pt or PtO₂ deposition methods. Significant decreases in conductivity are caused by irreversible reduction of polypyrrole by the reducing agents (H₂ and formaldehyde), and overoxidation of polypyrrole by H₂O₂.

ACKNOWLEDGEMENTS

Financial support from NSERC and Memorial University, and donation of materials by Ballard Power Systems Inc. are gratefully acknowledged.

REFERENCES

1. G.C. Bond, Ed., *Heterogeneous Catalysis: Principles and Applications*, 2nd ed. Clarendon Press, Oxford (1987).
2. C.N. Satterfield, Ed., *Heterogeneous Catalysis in Practice*, McGraw-Hill, New York (1980).
3. T.A. Skotheim, Ed., *Handbook of Conducting Polymers*, vol. 1, Marcel Dekker, New York (1986).
4. M.E.G. Lyons, *Analyst*, 119, 805 (1994).
5. T.S. Ahmadi, Z. Wang, T.C. Green, A. Henglein, and M.A. El-Sayed, *Science*, 22, 1924 (1996).
6. H.G. Petrow and R.J. Allen, US Patent 4,044,193 (1977).
7. X. Ren and P.G. Pickup, *J. Phys. Chem.*, 97, 5356 (1993).
8. S. Srinivasan, D.J. Manko, H. Koch, M.A. Enayetullah, and A.J. Appleby, *J. Power Sources*, 29, 367 (1990).
9. D.S. Watkins, in *Fuel Cell Systems*, L.J.M.J. Blomen and M.N. Mugerwa, Eds., p. 493, Plenum, New York (1993).
10. K.B. Prater, *J. Power Sources* 51, 129 (1994).
11. Z. Qi, *Synthesis of Conducting Polymer Colloids, Hollow Nanoparticles, and Nanofibers*, Ph.D. thesis, McGill University, Montreal (1996).



Fig.1. SEM of polypyrrole particles.

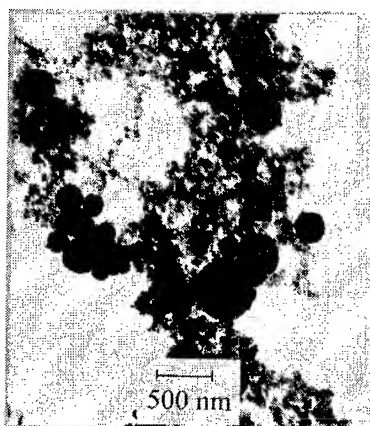


Fig.3. TEM of Pt/PPy produced by the reduction of K_2PtCl_4 with hydrogen.

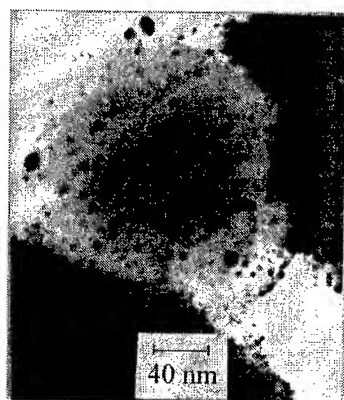


Fig.2. TEM of Pt/PPy produced by the reduction of $Pt(NH_3)_4Cl_2$ with formaldehyde.

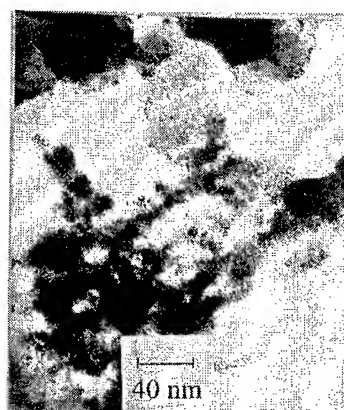


Fig.4. TEM of PtO_2/PPy produced by the oxidation of $Na_6Pt(SO_3)_4$ with H_2O_2 .

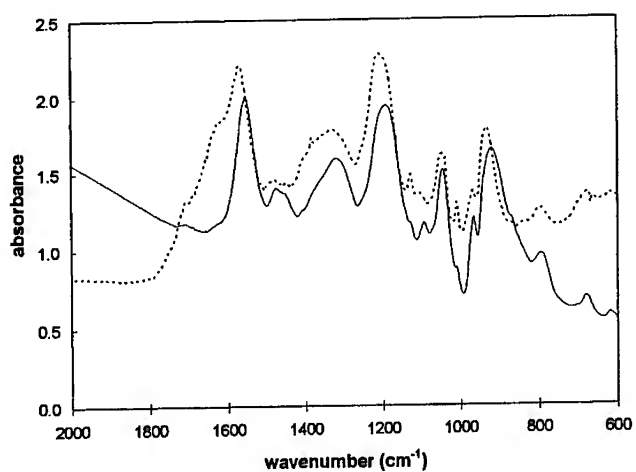


Fig. 5. FTIR spectra of PPy before (—) and after (···) the deposition of PtO₂ by the oxidation of Na₆Pt(SO₃)₄ with H₂O₂.

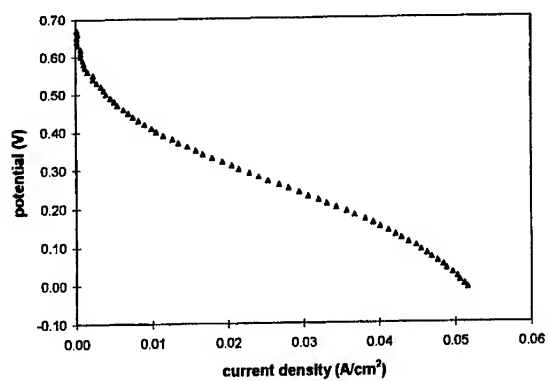


Fig. 6. Polarization curve for oxygen reduction at a PtO₂/PPy gas-diffusion electrode.

Cd_{1-x}Mn_xS NANOPARTICLES ($x \leq 5\%$) IN SOL-GEL SILICA MATRICES

G. Counio, T. Gacoin and J.P. Boilot

Laboratoire de Physique de la Matière Condensée, CNRS URA D1254
École Polytechnique, Route de Saclay, 91128 Palaiseau Cedex, France.

Abstract

We report the synthesis and the chemical characterization of Cd_{1-x}Mn_xS nanoparticles embedded in transparent matrices. In each sample, the mean size of the nanocrystals is constant and equal to 2.5 nm. Manganese concentration is controlled and can be varied up to $x_{Mn} = 5\%$. The manganese distribution between the particles follows a binomial law. The evolution of the photoluminescence properties with the number of manganese ions per particule is studied: only particles doped with a single Mn²⁺ ion contribute to the yellow luminescence peaking at 2.16 eV, whereas more doped CdS nanocrystallites are responsible for the red luminescence at 1.2 - 2 eV.

I. Introduction

Diluted magnetic semiconductors such as the (Cd, Mn) or (Zn, Mn) chalcogenide solid solutions display unusual properties caused by the half filled d-shell of the magnetic cation. At low Mn²⁺ concentrations ($x_{Mn} \leq 1\%$), a yellow luminescence band located at 2.16 eV is observed.¹ At higher manganese concentrations, the capture of the excitation energy by radiative transition centers related to manganese pairs dramatically decreases the quantum efficiency of the luminescence and leads to the appearance of new emission bands between 1.2 and 2.0 eV.² Moreover, the exchange interaction between the unpaired electrons of the magnetic cation and the band structure of the semiconducting host is responsible for remarkable magnetic or magneto-optical effects, such as a giant Zeeman splitting or Faraday rotation.³

The synthesis of semiconductor nanoparticles which display quantum confinement effects gives the opportunity to study the evolution of these properties

with the size of the crystallite. In a previous work,⁴ we have developed a synthesis process leading to CdS or ZnS nanoparticles doped with about 1 Mn²⁺ ion per particule, and studied their luminescence properties. This concentration was too low to detect magneto-optical effects. In this paper, we present an original synthesis path leading to Cd_{1-x}Mn_xS nanocrystals where the mean number of Mn²⁺ ions per particle can be tuned between 0 and 5 (Mn/Cd ratio $\leq 5\%$) which should display magneto-optical properties.

The first part of this paper is dedicated to the description of this synthesis. The crystallites can be obtained as a powder, as a colloidal suspension in an organic solvent, or embedded in a mixed organic-inorganic silica matrix obtained using sol-gel chemistry. Then, since the size of the nanocrystallites and the chemical composition of the particules are of primary importance in this system, both parameters are carefully determined. The third part of this paper is dedicated to the optical properties of these systems: the evolution of the photoluminescence and excitation spectra with manganese concentration will allow us to precise the manganese distribution between the particles.

II. Synthesis

1. Background

In order to obtain narrow size distributions and to control the surface of the particles, we choose to obtain the crystallites through a colloidal chemistry route. However, the coprecipitation of manganese and cadmium sulfide is restricted by the difference in solubility constants ($pK_{CdS} = 28$ and $pK_{MnS} = 15$ in water)⁵ which does not support a homogeneous coprecipitation of these sulfides.

In our previous work,⁴ the coprecipitation of the sulfides was achieved in water-in-oil microemulsions stabilized by a surfactant molecule. The precipitation of manganese sulfide was only possible if a basic precursor of S²⁻ ions such as sodium sulfide was used. However, in water and at high pH, Mn²⁺ ions easily react to form hydroxide species which are rapidly oxidized. This reaction is in competition with the coprecipitation of cadmium and manganese sulfides, and it appeared that we could only synthesize CdS nanocrystals doped with no more than one Mn²⁺ ion. Therefore, a completely different method has been developed to synthesize Cd_{1-x}Mn_xS nanoparticles with higher manganese concentrations.

2. Coprecipitation of the sulfurs in ethylene glycol

We choose to achieve the coprecipitation of those sulfides in ethylene glycol. The chelating properties of the two alcohol functions should damp the difference in solubility products between CdS and MnS. Moreover, the anhydrous nature of this solvent prevents the formation of manganese hydroxides. $\text{Cd}_{1-x}\text{Mn}_x\text{S}$ nanocrystals are obtained by the simple mixing of two ethylene glycol solutions: the first one containing the metallic cations (Cadmium acetate concentration is kept constant and equal to $[\text{Cd}^{2+}] = 0.1 \text{ mol}\cdot\text{L}^{-1}$ and the manganese acetate concentration $[\text{Mn}^{2+}]$ was varied between 0 and $0.4 \text{ mol}\cdot\text{L}^{-1}$) and the second one containing sulfur ions (sodium sulfide concentration was kept equal to $[\text{Cd}^{2+}] + [\text{Mn}^{2+}]$). The resulting nanoparticles are aggregated and a turbid yellow-orange suspension is obtained. We now have to separate the particles in order to have stable and non-diffusive nanocrystallite solutions.

The ethylene glycol solution is centrifuged and the crystals washed in methanol, suspended in triethylphosphate and heated at 215°C under nitrogen. After one hour, it is found that the solution is no longer turbid. The exact chemical mechanism of this redispersion is not completely understood yet. It seems that the disjunction of the particles occurs through the complexation of their surface with triethylphosphate molecules.⁶ The colloidal solution is destabilized upon the addition of heptane and pyridine, and the resulting powder can be redispersed in various solvents such as methanol, ethanol or pyridine.

The incorporation of the crystallites in a transparent silica matrix is achieved using the opportunities given by the sol-gel chemistry.⁷ In a typical experiment, a colloidal suspension of $\text{Cd}_{1-x}\text{Mn}_x\text{S}$ nanocrystals in methanol is added to a solution of silica gels precursors just before the sol-gel transition. After this transition, the careful drying of the gel at ambient temperature gives the final material either as bulk disks of a few centimeters in diameter or as thin films previously deposited onto various substrates (glass, ITO, etc.).

III. Characterization: particle size and Mn^{2+} concentration

1. Size determination

To determine the mean size of the nanocrystals, X-ray diffraction experiments were performed on crystallites powders. A typical X-ray diffraction pattern is presented

on figure 1. In order to determine the coherence length of the particles, the diffraction peaks were fitted using Scherrer's law.⁸ The coherence length of all samples was found to be constant and estimated to be equal to 1.8 nm, which yields an approximative size of 2.4 nm.

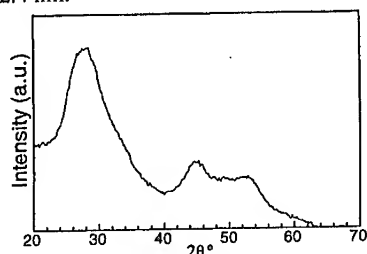


Figure 1: X-Ray diffraction pattern (Cu K α) of Cd_{0.95}Mn_{0.05}S nanoparticles.

In the case of pure CdS nanoparticles, a more reliable determination of the average size of such nanocrystals is possible by comparing the shift of the UV-visible absorption band due to the small size of the particles with the correlation established by Wang et al.⁹ Moreover, we have shown in our previous work that the presence of one Mn²⁺ ion per particle does not significantly affect the value of the energetic band gap.⁴ Using this alternative method for lightly doped and undoped samples (see figure 2), we confirm that these samples have a mean size of 2.5 nm. However, when x_{Mn} increases, the excitonic structure on the absorption spectrum of the nanoparticles gradually vanishes, probably because a distribution of chemical composition is paired with the normally observed size distribution of the nanocrystallites.

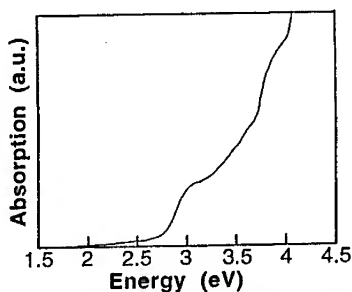


Figure 2: Absorption spectrum of a colloidal suspension of Cd_{0.99}Mn_{0.01}S crystallites.

2. Manganese concentration measurements

In order to suppress unreacted Mn^{2+} ions and MnS like by-products, the crystallites are washed in an aqueous solution acidified with HCl down to $\text{pH } 2.5$. x_{Mn} was determined by the ratio of the number of Mn^{2+} ion per mass unit to the number of S^{2-} ions per mass unit. The dissolution of a known mass of pure nanocrystallite powder in concentrated acid yields an aqueous solution of Cd^{2+} , Mn^{2+} and S^{2-} ions. Manganese concentrations are then measured by comparing the intensities of the ESR signal of this frozen solution with a reference. Sulfur concentrations are measured using the colorimetric method proposed by Mecklenburg et al.¹⁰. Since CdS nanoparticles of 2.5 nm in size have approximately 250 atoms,¹¹ the mean number of manganese per particle is then determined by :

$$N_{\text{Mn}} = x_{\text{Mn}} \cdot \frac{250}{2}$$

3. ESR characterization of $\text{Cd}_{1-x}\text{Mn}_x\text{S}$ nanocrystallites

When $x_{\text{Mn}} \leq 1\%$, the majority of the nanocrystals is doped with less than one manganese ion. Therefore, no exchange interaction exists between the paramagnetic centers. In this case, our previous study has shown that ESR spectroscopy gives an insight into the homogeneity of the coprecipitation⁴. Figure 3a shows the ESR spectrum of a powder of $\text{Cd}_{0.99}\text{Mn}_{0.01}\text{S}$ nanoparticles collected at 4.2K. This spectrum is composed of two superimposed signals: The first one encompasses six intense lines and intermediate weaker bands. We associate it to Mn^{2+} ions located in the core of the nanocrystal. The second one is a broad slightly dissymmetric signal, and is characteristic of Mn^{2+} ions who have four sulfur neighbors but are in the two or three last atomic layers of the particle.

The intensity ratio of these two signals provides an easy tool to characterize the homogeneity of the coprecipitation: for Mn^{2+} ions occupying random sites in particles of 2.5 nm in size, it is very close to one. The experimental ratio are about 40 for particles synthesized in water-in-oil microemulsions⁴ and 7 for nanocrystals prepared in ethylene glycol. Both indicate a Mn^{2+} -poor nanoparticle core. We note that even if the coprecipitation in ethylene glycol is still heterogeneous, the nanocrystals synthesized that way are more homogeneous than those obtained in our previous study.

This point is consistent with the damping of the difference in solubility products we evoked while describing the synthesis.

Figure 3b presents the ESR spectrum of $\text{Cd}_{0.95}\text{Mn}_{0.05}\text{S}$ nanoparticles recorded at 4.3 K. The ESR spectrum does not significantly vary with temperature and is composed of a broad dissymmetric band 17 mT wide, without any fine structure. These results can be compared to wide lines obtained by other authors on bulk $\text{Zn}_{1-x}\text{Mn}_x\text{S}$ powders or thin film structures for $x_{\text{Mn}} \approx 1\%$ and attributed to Mn^{2+} rich regions.¹² Therefore, dipolar interactions between manganese ions located in the same nanoparticle are probably responsible for the observed broadening.

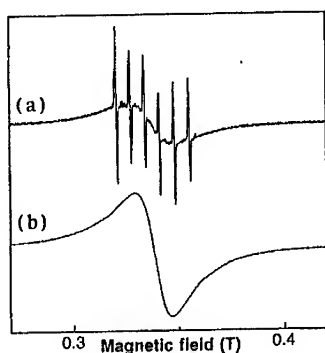


Figure 3: ESR spectrum of $\text{Cd}_{0.99}\text{Mn}_{0.01}\text{S}$ (a) and $\text{Cd}_{0.95}\text{Mn}_{0.05}\text{S}$ (b) nanoparticle powders

IV. Luminescence properties

Photoluminescence, excitation and phosphorescence spectra (recorded 2 ms after extinction of the excitation) were performed at room temperature on doped nanocrystals dispersed in methanol, silica xerogels or thin films deposited onto glass slides. The main point is to study the evolution of the luminescence properties of $\text{Cd}_{1-x}\text{Mn}_x\text{S}$ nanoparticles with increasing manganese concentration. Quantum yield evaluations were made by comparing the integrated intensity of the luminescence of our samples with those of standards of known efficiency.

1. Pure CdS nanocrystallites: $x_{Mn}=0$

Luminescence of pure CdS nanoparticles in solution or embedded in a solid transparent matrix is presented in figure 4a. The photoluminescence excitation roughly follows the absorption spectrum. The luminescence spectrum can be interpreted after a model developed by Hässelbarth et al.¹³: after the absorption of a photon by the semiconductor, the electron-hole pair is localized in deep surface traps, and the broad luminescence band results from the radiative recombination of the charge carriers trapped at the surface of the nanocrystals. The luminescence efficiency of this recombination path rarely exceeds 1%, and its lifetime varies with the detection energy but is always in the nanosecond time range.¹⁴ We note that, in our samples, there is no direct band to band recombination that would result in a narrow peak located near the excitation band gap.

2. Lightly doped CdS nanocrystallites: $x_{Mn} \leq 1\%$

Typical luminescence, phosphorescence and excitation spectra of such nanocrystals are presented figure 4b. The excitation spectrum roughly follows the absorption spectrum of the sample. Previous time resolved experiments have shown that the photoluminescence spectrum is the superimposition of two contributions:¹⁴ a broad band centered around 1.8 eV which is attributed to surface recombination commonly observed in the case of pure CdS nanoparticles, and a sharper and intense yellow band peaking at 2.16 eV. The latter is characteristic of the Mn^{2+} internal ${}^4T_1 \rightarrow {}^6A_1$ transition. The radiative lifetime of the Mn^{2+} emission is about 2 ms. The quantum yield of the 2.16 eV Mn^{2+} emission is more than one order of magnitude higher than the surface recombination of pure CdS nanoparticles, and can be as high as 20%. Our previous study has shown that the mechanism of the Mn^{2+} luminescence in sulfide nanoparticles is an energy transfer between surface trapped excited carriers and the manganese ions located in the outer shells of the nanocrystal.³

In the case of bulk compounds, the highest quantum efficiency obtained for this yellow Mn^{2+} luminescence is observed when the Mn^{2+} ions are infinitely diluted.¹⁵ When the size of the crystal is lowered down to a few nanometers, this concentration is obtained when only one Mn^{2+} ion dopes the CdS nanoparticle. Therefore, we interpret this band as originating from crystallites containing a single manganese ion.

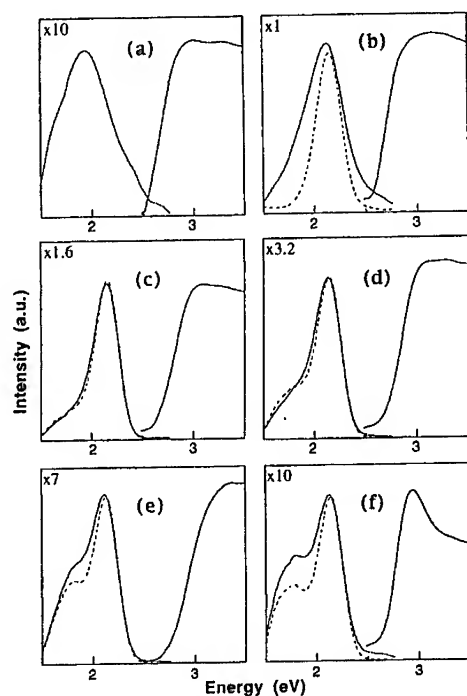


Figure 4: Luminescence, excitation (plain lines) and phosphorescence (dotted lines) spectra of $\text{Cd}_{1-x}\text{Mn}_x\text{S}$ colloidal suspensions in methanol with various x_{Mn} : 0 (a), 0.008 (b), 0.013 (c), 0.025 (d), 0.039 (e), 0.048 (f). The spectra are recorded peak to peak.

3. CdMnS solid solutions: $x_{\text{Mn}} \geq 1\%$

Luminescence, phosphorescence and excitation spectra of $\text{Cd}_{1-x}\text{Mn}_x\text{S}$ nanoparticles with x_{Mn} ranging from 1.3 to 4.8% are presented in figure 4c-4f. As soon as the mean number of Mn^{2+} ions per particle passes beyond one, the luminescence of pure CdS nanocrystals becomes negligible. We also note the emergence of a new phosphorescence band centered at about 1.77 eV. This band has the same excitation spectrum and lifetime (see figure 5) as the Mn^{2+} internal ${}^4T_1 \rightarrow {}^6A_1$ transition.

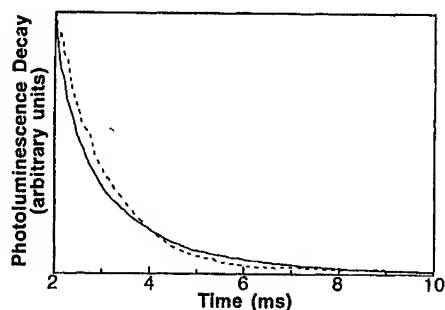


Fig. 5: Luminescence decays detected at 2.16 eV (plain line) or 1.77 eV (dotted line)

Similar studies allow to compare the luminescence of $\text{Zn}_{0.95}\text{Mn}_{0.05}\text{S}$ bulk compounds with the spectrum we obtained for $\text{Cd}_{0.95}\text{Mn}_{0.05}\text{S}$ nanoparticles:² Both display the two bands located at 1.77 and 2.16 eV, and with a similar intensity ratio. In the case of bulk crystals, the red emission at 1.77 eV is believed to occur after the capture of the excitation energy by so called "red emission centers". It is not clear whether these centers are Mn^{2+} pairs or Mn^{2+} ions located in perturbed environments¹⁶. In any case, we attribute this red band to the luminescence of particles containing two Mn^{2+} ions or more.

4. Variation of the luminescence properties with the number of Mn^{2+} ions per particle

The luminescence emitted by a particle is the fingerprint of the number of manganese ions it contains: either the emission wavelength or the radiative life time allows the determination of the proportion of particles containing 0, 1 or 2 and more Mn^{2+} ions. Therefore, the quantum yield variations of each band with x_{Mn} allows to survey the manganese repartition among the particles. The results are presented in figure 6.

Figure 6-a gives the variation of the quantum yield of the yellow emission band characteristic of CdS particles doped with a single manganese ion. This variation is compared to the proportion of particles containing exactly one manganese ion, in the case of a random distribution of manganese among particles of 2.5 nm in size (binomial distribution). The ratio of the proportion of particles containing exactly one

Mn^{2+} ion to the quantum yield of the sample allows to compute the radiative transition probability for such crystals, which is roughly equal to 60%.

The same analysis is applied to the red luminescence band: first, we consider that the contribution of particles having a given number of manganese dopants to the global luminescence is proportional to their population. Furthermore, the relaxation path of particles containing more than one Mn^{2+} ion is characterized by a competition between the so-called red luminescence and the loss of the excitation energy through a non radiative process. These non radiative paths are favoured in the case of CdS particules doped with a large number of manganese ions. This effect was taken into account by setting a cutoff: the best agreement was obtained when particles with 6 manganese ions or more were considered non luminescent and discarded. Figure 6-b compares the quantum yield of the red luminescence band with the proportion of CdS particules doped with between 2 and 5 manganese ions when a random distribution of the manganese among the particles is assumed. The radiative transition probability for such crystals is roughly equal to 1%.

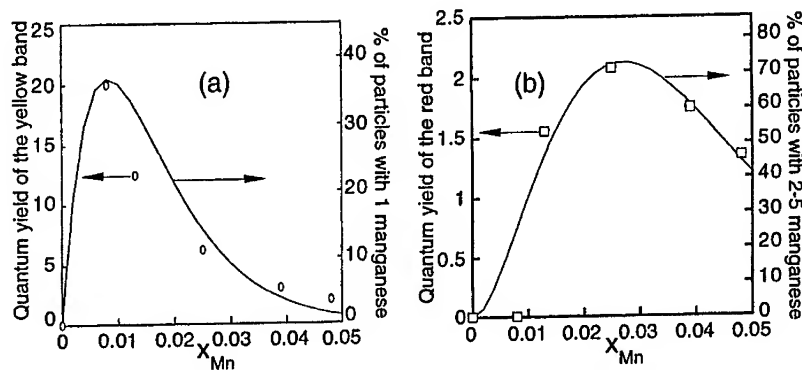


Figure 6: Correlation between the quantum yield (markers) and the proportions of particles with a given number of Mn^{2+} ions if a binomial distribution is assumed (plain line)

IV. Conclusion

In this paper, we have presented an original synthesis route to process $\text{Cd}_{1-x}\text{Mn}_x\text{S}$ nanoparticles dispersed in organic solvents or in a transparent dielectric matrix. The manganese concentration is precisely measured using ESR spectroscopy and can be continuously tuned between $x_{\text{Mn}}=0$ and $x_{\text{Mn}}=4.8\%$. The size of the crystallites is independent of the manganese concentration and is found to be 2.5 nm. The nanoparticles are incorporated in a sol-gel silica matrix in order to enhance their stability and to handle easily these materials.

The luminescence properties of an assembly of $\text{Cd}_{1-x}\text{Mn}_x\text{S}$ nanoparticles is the sum of three contributions:

- Pure CdS nanoparticles yield a broad luminescence band centered at about 1.90 eV. Its quantum efficiency is about 1% and its radiative lifetime is in the nanosecond time scale.
- CdS crystallites doped with a single Mn^{2+} ion give a bright yellow band with a quantum yield of 60%. The radiative lifetime of this contribution is in the millisecond time scale.
- When the nanoparticles contain two manganese ions or more, they emit a broad red band. Its quantum yield is about 1%, and its radiative lifetime is also in the millisecond timescale.

Since the luminescence emitted by a particle is characteristic of the number of manganese ions it contains, the relative intensities of these three contributions can be used to measure the mean Mn^{2+} concentration and the repartition of the manganese ions among the particles. In our case, this distribution is in agreement with a binomial law, characteristic of a random repartition between the crystallites.

The manganese concentrations reached to date will allow to study the effects of tridimensional quantum confinement on the magneto-optical properties of diluted magnetic semiconductors (Faraday rotation, giant Zeeman splitting...). Prospective applications include optical and magneto-optical devices.

References

- 1 D. Curie, C. R. Acad. Sci. **258** 1964 p3269
- 2 Dang Dinh Thong, W. Heimbrodt, D. Hommel and O. Goede, Phys. Stat. Sol. (a) **81** 1984 p695
W. Busse, H.-E. Gumlich, M. Krause, H.-J. Moros, J. Schliwinski and D. Tschierse, J. Lum. **31/32** 1984 p421
C. Ehrlich, W. Busse, H.-E. Gumlich and D. Tschierse, J. Cryst. Growth **72** 1985 p371
- 3 J. A. Gaj, R.R. Galazka and N. Nawrocki, Solid State Comm. **25** 1978 p193
- 4 G. Counio, S. Esnouf, T. Gacoin and J.-P. Boilot, J. Phys. Chem **100(51)** 1996 p20021
- 5 J. Bjerrum, G. Schwarzenbach and L.S. Gunnar in "Stability constants, part II : Inorganic Ligands", the Chemical Society, London 1958
- 6 C.B. Murray, D.J. Norris and M.G. Bawendi, J. Am. Chem. Soc. **115** 1993 p8706
- 7 T. Gacoin, L. Malier, G. Counio, S. Esnouf, J.-P. Boilot, L. Audinet, C. Ricolleau and M. Gandais, Mat. Res. Soc. Symp. Proc **435** 1996 p643
- 8 A. Guinier in "Théorie et technique de la radiocristallographie" 3^{eme} ed. Dunod, Paris 1964
- 9 Y. Wang and N. Herron, Phys. Rev. B **42(11)** 1990 p7253
- 10 W. Mecklenburg and F. Rosenkranzer, Z. Anorg. Chem. **86** 1914 p143
- 11 P.E. Lippens and M. Lanoo, Phys. Rev. B **39** 1989 p10935
- 12 J. Kreissl and W. Gehlhoff, Phys Stat Sol (b) **124** 1984 p343
- 13 A. Hässelbarth, A. Eychmüller and H. Weller, Chem. Phys. Let. **203(2)** 1993 p271
- 14 M.A. Chamarro, V. Voliotis, R. Grousson, P. Lavallard, T. Gacoin, G. Counio, J.-P. Boilot and R. Cases, J. Cryst. Growth **159** 1996 p853
- 15 O. Goede and Dang Dinh Thong, Phys. Stat. Sol (b) **81** 1984 p343
- 16 O. Goede and W. Heimbrodt, Phys. Stat. Sol (b) **146** 1988 p11

Sol-Gel Template Synthesis of Semiconductor Nanostructures.

Brinda B. Lakshmi & Charles R. Martin
Department of Chemistry
Colorado State University
Fort Collins, CO 80526.

ABSTRACT

The template method of synthesizing nanostructures involves synthesis of the desired material within the pores of a nanoporous membrane. Nanofibers or nanotubules can be obtained within each pore of the membrane. A number of synthetic routes have been used to synthesize these nanostructures. We have used sol-gel chemistry to synthesize semiconductor nanostructures by template synthesis. Synthesis of TiO_2 and Co_3O_4 is reported. The high surface area offered by TiO_2 nanofibrils has been used for photocatalysis of salicylic acid in sunlight. The TiO_2 synthesized is the anatase form and interestingly, smaller diameter fibrils are single crystals.

INTRODUCTION

We have been exploring a general method for preparing nanomaterials which entails synthesis of the desired material within the pores of a nanoporous membrane or other solid.¹⁻³ The membranes used contain cylindrical pores with monodisperse diameters, and a nanoscopic fibril or tubule of the desired material is synthesized within each pore. This method has been used to make tubules and fibrils composed of polymers, metals, semiconductors, carbons, and Li-ion-intercalation materials.¹⁻³ Methods used to synthesize such materials within the pores of the template membranes include electroless metal deposition, electrochemical methods, and in situ polymerization.

Sol-gel chemistry has recently evolved into a general and powerful approach for preparing inorganic materials.^{4,5} This method involves the hydrolysis of a precursor to obtain a sol which aggregates to give a gel which could be heated to give the desired material. We have recently used this combination of sol-gel and template methods to prepare fibrils and tubules of a variety of inorganic semiconducting materials.^{6,7} We report in this paper the preparation of TiO_2 and Co_3O_4 nanostructures and discuss some electron diffraction results. The high surface area offered by the fibrillar TiO_2 nanostructures has been utilized for photocatalysis of salicylic acid in sunlight.

EXPERIMENTAL.

Materials. Titanium isopropoxide, and salicylic acid (from Aldrich), $\text{Co}(\text{NO}_3)_2$ and citric acid (Mallinckrodt), ethanol (McCormick Distilling Co.), and concentrated HCl (Mallinckrodt) were used as received. Purified water was obtained by passing house-distilled water through a Milli-Q (Millipore) water purification system. The alumina template membranes were either obtained commercially (Whatman Anopore filters, Fisher) or prepared in house. The commercial membranes had 200 nm-diameter pores, and the in-house-prepared membranes had 22 nm-diameter pores.

Synthetic Methods. Titanium isopropoxide (5 mL) was added to 25 mL of ethanol, and the resulting solution was stirred in an ice bath. To a second 25 mL

portion of ethanol were added 0.5 mL of water and 0.5 mL of 0.1M HCl. The titanium isopropoxide solution was removed from the ice bath and the ethanol/HCl/water solution was slowly added and the temperature was maintained at 15° C.

After ca. 60 sec the resulting mixture turned white (sol formation). The alumina template membrane was immediately dipped into this solution for an immersion time that was varied between 5 and 60 sec. After the desired immersion time, the membrane was removed from the sol and dried in air for 30 min. at room temperature. The membranes were then heated to 400°C.

Cobalt oxide sol was prepared by dissolving 1g of $\text{Co}(\text{NO}_3)_2$ and 0.1g of citric acid in 20 ml water.⁸ This sol takes at least two days to gel. The aluminum oxide membrane (200 nm) was dipped in the sol for 10 sec and dried for 30 min before it was heated to 500° C for 24h.

Electron Microscopy. Scanning electron microscopic (SEM) images of the 200 nm-diameter tubules and fibrils were obtained as follows: One surface layer was removed by polishing with 1500 grit sand paper, and the membrane was glued (using Torr-Seal Epoxy, Varian) to a piece of paper towel. The membrane was glued with the polished face up. The resulting composite was immersed into 6 M aqueous NaOH for 10 min in order to dissolve the alumina. The resulting sample was imaged using a Phillips 505 microscope.

Transmission electron microscopic (TEM) images and the electron diffraction of the semiconductor nanostructures were obtained by removing both the surface layers and dissolving the membrane in NaOH and collecting the fibers on a carbon coated TEM grid. The accelerating voltage of the electron beam was 100 kV and the camera length was 120 cm. A gold single crystal was used as a standard to check the camera length.

Photocatalysis. The photocatalytic activity of the sol-gel synthesized TiO_2 fibrils was evaluated using salicylic acid as the organic molecule to be decomposed. Salicylic acid was chosen because the compound has a high extinction coefficient and easy to monitor by UV-vis. Samples in which the TiO_2 fibrils protruded from an epoxy surface were prepared as described for the SEM analyses. The area of epoxy surface used for these photocatalysis studies was 1 cm^2 ; this area contained ca. 10^9 200 nm-diameter TiO_2 fibrils. After removal of the alumina template membrane in NaOH, the TiO_2 fibrils were rinsed in 5 portions of water to ensure complete removal of the NaOH. The fibrils were then immersed (overnight and in the dark) in 15 mL of 0.5 mM aqueous salicylic acid in order to allow organics present in the epoxy to leach out prior to the photocatalysis experiments.

The samples pretreated in this way were then immersed into a beaker containing 15 mL of fresh 0.5 mM aqueous salicylic acid. A quartz lid was placed over the top of the beaker, and the beaker was placed on the roof of the chemistry building in direct Colorado sunlight. Two controls were run at the same time and place as the fibrillar TiO_2 samples. The first consisted of an identical beaker with the same amount of salicylic acid solution; however, a thin film (200 nm thick) of TiO_2 , prepared under identical conditions as the fibrillar sample, was used as the photocatalyst. The second control was also identical but contained no photocatalyst.

The concentration of salicylic acid in the three solutions was determined every 5 minutes for a total of 30 min. The salicylic acid concentration was determined from its characteristic UV absorbance (296 nm), using a calibration curve obtained from solutions of known concentration.

RESULTS AND DISCUSSION.

Figure 1 shows SEM images of TiO_2 tubules and fibrils prepared in the alumina membrane with 200 nm-diameter pores. Tubules were obtained if the membrane was immersed into the sol for a brief period (5 sec, Figure 1a), whereas solid TiO_2 fibrils were obtained after long immersion times (60 sec, Figure 1c). Intermediate immersion times yield tubules with very thick walls (25 sec, Figure 1b). In all cases the tubules and fibrils were 50 μm long (the thickness of the alumina template membrane) and had an outside diameter of 200 nm (the diameter of the pores in the membrane). The mechanism of formation of these nanostructures has been discussed elsewhere.⁶

Electron diffraction. Figure 2a shows a transmission electron microscopic (TEM) image of the TiO_2 nanostructures synthesized in the alumina membrane with 22 nm diameter pores. Figure 2b shows the indexed electron diffraction pattern obtained from a fibril bundle. Superimposing the electron diffraction on the fibril bundles show that the c^* axis is along the fibril axis. The phase has been indexed to anatase form of TiO_2 .

Photocatalysis. TiO_2 is a semiconductor with a large bandgap of 3.2 eV. The photocatalytic and photoelectrochemical properties of TiO_2 are well documented.⁹⁻¹¹ When exposed to UV light of energy greater than the bandgap, electrons are excited to the conduction band forming electron-hole pairs. These react with water to yield hydroxyl and superoxide radicals which are good oxidizing agents. This makes TiO_2 an excellent photocatalyst for the decomposition of organic pollutants.

TiO_2 exists in more than one form; the important phases being rutile and the metastable anatase.¹² Anatase has been found to be the best phase for photocatalysis.¹² It has been shown that high surface area anatase allows for greater photocatalytic efficiency. For this reason, suspension of anatase powder have been investigated as possible photocatalysts.^{10,11} However, such suspensions are difficult to handle, and sampling to determine the photocatalytic efficiency requires separation of the particles from the solution. The ideal system would be to immobilize a high surface area anatase catalyst on a solid support. Sol-gel template synthesis allows us to prepare such a high surface area immobilized TiO_2 photocatalyst.⁶

The catalyst investigated was an ensemble of 200 nm-diameter TiO_2 fibers that protrude from an epoxy surface like the bristles of a brush (Figure 1C). Aqueous solutions of salicylic acid were used to explore the photodecomposition efficiency of this catalyst. Sunlight was used as the light source.⁶ Figure 3 shows plots of salicylic acid concentration vs time of exposure to sunlight. The upper curve is for a solution that contained no photocatalyst, and no decomposition of salicylic acid is observed. The middle curve is for a sol-gel

synthesized thin film TiO₂ photocatalyst; catalytic decomposition of salicylic acid is now observed. However, the rate of decomposition is an order of magnitude lower than for the fibrillar TiO₂ photocatalyst (Figure 3).⁶

The increase in the decomposition rate observed with the TiO₂ fibers is due to their higher surface area (relative to the thin film). A 1 cm² area of thin film was used. The area of the epoxy support for the fibrillar catalyst was also 1 cm², but the total surface area of the TiO₂ fibrils protruding from this catalyst is ~315 cm². Given this dramatically higher surface area it is surprising that an enhancement in photodecomposition rate of only one order of magnitude is observed. This is because, as shown in Figure 1, the TiO₂ fibers lean against each other and thus shade each other from the incident sunlight. This suggests that an optimum length and density of fibers must be identified so as to maximize the surface area of the fibers exposed to the light. Finally, quantitative analysis on the rate of decomposition shows pseudo-first order kinetics with a rate constant of 0.03 min⁻¹ for the fibers as opposed to 0.003 min⁻¹ for thin film.⁶

Cobalt oxide: Cobalt forms a citrate complex which hydrolyzes to form the sol. Figure 4a shows the SEM image of the cobalt oxide fibers immobilized on Torr seal epoxy. The fibers are uniform and are seen to have grown the entire length of the pore. The surface of the fibers are smooth.

A TEM image of a single cobalt oxide fiber is shown in Figure 4b. Interestingly, while the SEM images suggest that these are continuous fibers with reasonable mechanical strength, the TEM images show that these fibers are, in fact, microporous. Longer sintering times (up to 48 hours) did not remove this microporosity. The corresponding electron diffraction pattern shows continuous rings which were indexed to the spinel Co₃O₄ (Figure 4c). The rings are sharp and continuous which shows that, although the fibers are highly crystalline, they are not single crystals, and the various crystalline domains show no preferred orientation.

CONCLUSION

Sol-gel template synthesis has been used to synthesize nanostructures of semiconductor oxides like TiO₂ and Co₃O₄. The condition has been optimized to obtain tubes and fibers of TiO₂. The nanofibers of TiO₂ immobilized on Torr seal epoxy offer a high surface area which has been utilized for photocatalysis of salicylic acid in sunlight. The Co₃O₄ fibers are microporous as seen in the TEM. The applications of these microporous nanofibers of Co₃O₄ are being investigated.

REFERENCES

- 1) Martin, C. R. *Science* **1994**, *266*, 1961.
- (2) Martin, C. R. *Acc. Chem. Res.* **1995**, *28*, 61.
- (3) Martin, C. R. *Chem. Mater.* **1996**, *8*, 1739.
- (4) Brinker, C. J.; Scherer, G. W. *Sol-gel Science*; Academic Press Inc.: New York, 1990.
- (5) Hench, L. L.; West, J. K. *Chem. Rev.* **1990**, *90*, 33.
- (6) Lakshmi, B. B.; Dorhout, P.K.; Martin, C. R. *Chem. Mater.* **1997**, *9*, 857.

-
- (7) Lakshmi, B.B.; Patrissi, C.J.; Martin, C.R. *Chem. Mater.* (communicated).
(8) Zhecheva, E.; Stoyanova, R.; Gorova, M.; Alcantara, R.; Morales, J.; Tirado, J.L. *Chem.Mater.* **1996**, *8*, 1429.
(9) Fujishima, A.; Honda, K. *Nature* **1972**, *37*, 238.
(10) Matthew, R. W. *J.Phys.Chem.* **1987**, *91*, 3328.
(11) Kraeutler, B.; Bard, A.J. *J.Am.Chem.Soc.* **1978**, *100*, 5985.
(12) Linsebigler, A. L.; Lu, G.; Yates, J. T. *Chem.Rev.* **1995**, *95*, 735.



Figure 1 SEM images of TiO₂ nanostructures at various immersion times A) 5s
B) 25s C) 60s.

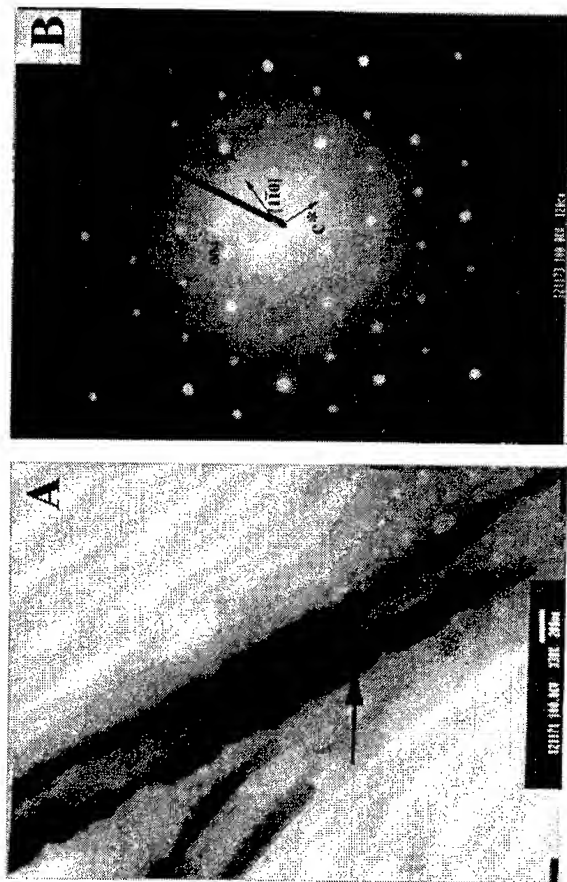


Figure 2 A) TEM image of 22 nm TiO_2 bundle of fibers. B) Corresponding electron diffraction (The arrow indicates the region from which electron diffraction was obtained).

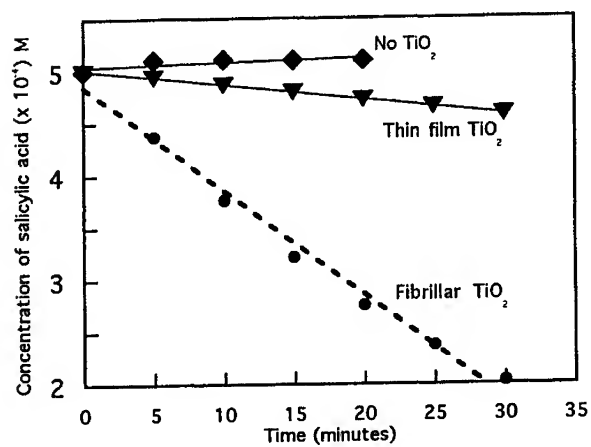


Figure 3 Photodecomposition of salicylic acid in sunlight with Thin film TiO_2 and fibrillar TiO_2 .

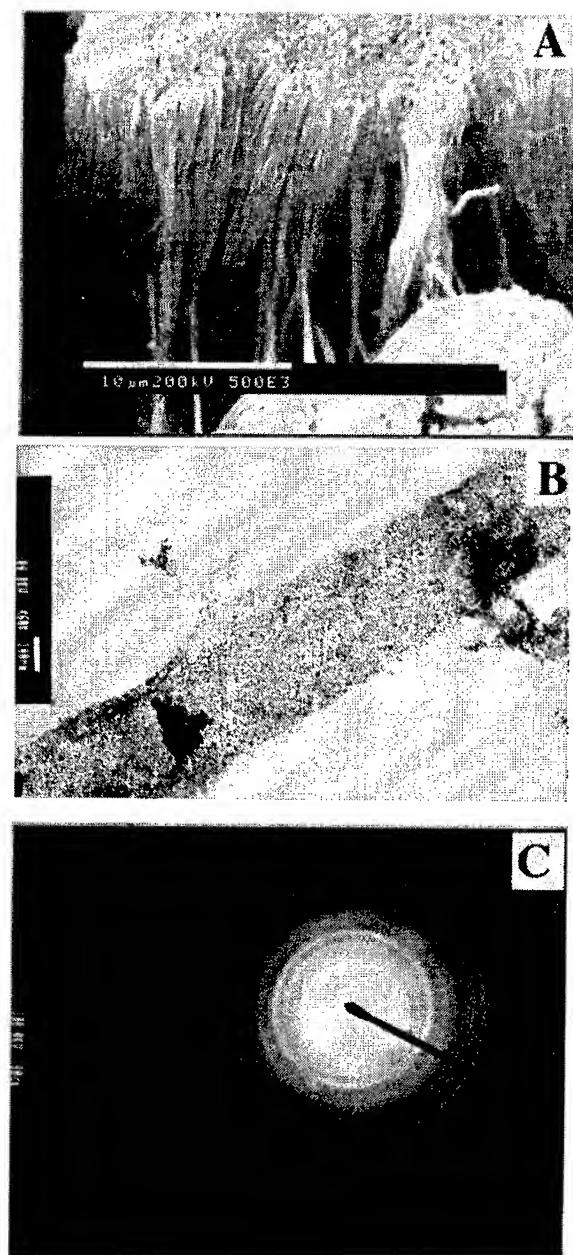


Figure 4 A)SEM image of Cobalt oxide fibers B)TEM image of the cobalt oxide fiber. C) Corresponding electron diffraction.

Nanocrystals: Growth and Characterization

Thin-film Nanocalorimetry for Nano-scaled Systems

S.L. Lai and L.H. Allen

*Department of Materials Science and Engineering
University of Illinois at Urbana-Champaign, Urbana, IL 61801*

ABSTRACT

We have developed an ultra-sensitive thin-film differential scanning calorimetric (TDSC) technique which is capable of measuring energy involved in materials processes at nano-joule scale. In the calorimeter, a metal (Ni) thin film functions as a heater and thermistor, a thin Si_3N_4 membrane provides the basic mechanical support for heater and sample. Melting point depression and coalescence of self-assembled nano-sized Sn particles have been investigated by means of heat capacity measurements using this calorimeter, and thus have demonstrated the sensitivity of the calorimeter. This thin-film nanocalorimetry technique can provide for the first time direct measurements of the energy evolved during materials processes of nano-scaled systems.

I. INTRODUCTION

Knowledge on atomic/molecular processes of clusters and nanostructures are of fundamental importance in the advance of science and technology. The energy associated with atomic/molecular processes is a key factor in characterizing materials systems, including the growth of semiconductors with nanoscale dimensions, the formation of texture in thin films and the growth of critical size second phase nuclei in silicides[1]. However, unlike structural characterization where many techniques (e.g., TEM, SEM, AFM, STM, RDX, etc.) are available, measurement of the energy at the nano-joule scale is extremely rare due to the lack of experimental techniques.

Currently, conventional differential scanning calorimetry (DSC) is the most widely used method for measuring the enthalpy of formation, e.g. reaction couples and crystallization energy of amorphous materials. However, conventional DSC is

usually not sensitive enough for more detailed measurements, such as the study of the initial stages of nucleation or for the direct measurement of the melting point of nanostructured islands on a surface. This is because the amount of heat generated during such material process is too small and the heat capacity of the calorimeter is too large.

In this paper, we discuss a novel thin-film nano-calorimetry technique for the measurement of the very small amount of energy associated with phenomenon of nano-scaled systems, in particular the size-dependent melting point depression of small Sn particles and the coalescence process of small particles. We refer to our technique as scanning *nanocalorimetry* due to the fact it is capable of measuring the dynamics of energy exchange at the level of 0.2 nano-joules[2, 3]. This level of sensitivity of energy is equivalent to the chemisorption of 1/1000 monolayer of oxygen on a W surface[4].

II. CALORIMETER AND MEASUREMENT PROCEDURE

A. Calorimeter:

The thermal mass of a calorimeter limits its sensitivity. Therefore, we utilize the thin film membrane processing technology available at Cornell University to fabricate our calorimeter so as to reduce its thermal mass[5, 6]. Figure 1 illustrates the basic layout of the measurement components of the calorimeter fabricated on silicon wafer. A metal (Ni) thin film with thickness below 500 Å functions as a heater. When an electrical current passes through the Ni film, its temperature will increase by Joule heating. The Ni film also function as a thermistor by knowing the real-time resistance and the resistance-temperature relationship. A Si₃N₄ membrane with thickness below 1000 Å provides mechanical support as well as a chemical and electrical barrier between the heater and sample of interest. The effective heat capacity of the calorimeter is as low as 6×10^{-7} J/K at 300 K, approximately 2-3 orders of magnitude smaller than conventional DSC calorimeter[2].

B. Measurement Procedure:

An example of the nanocalorimetry technique is a study characterizing the physical properties and energy exchange dynamics of ultra-thin films of Sn. The Sn sample was thermally evaporated onto the Si₃N₄ membrane side, aligned with the heater through a shadow mask during deposition. The base pressure for deposition was $1-2 \times 10^{-8}$ Torr and the deposition rate was about 1 Å/s. Immediately after the deposition, the calorimetric measurement was performed *in situ*. The

experimental condition prevents oxidation and minimizes heat loss during calorimetric measurement.

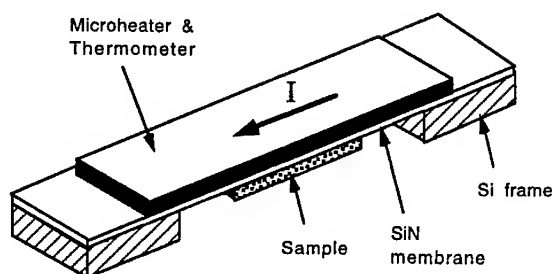


FIG. 1. Schematic of the thin-film scanning calorimeter. A metal thin film of Ni (300-500 Å in thickness) functions as heater and thermistor. A Si_3N_4 membrane (~1000 Å in thickness) provides mechanical support, as well as chemical and electrical barrier between the heater and sample.

The measurement was initiated by passing a controlled dc current pulse through the Ni thin film heater. Joule heating causes the temperature of heater to increase. Since the membrane between heater and sample is very thin and thermal-conductive, the temperature of sample is almost equal to that of heater at any time point of measurement. Evaluation of temperature can be made by measuring the real-time resistance of the heater with four-point probe configuration and the resistivity-temperature relationship beforehand[5]. The primary measured parameters are the current (I) through the heater and the voltage across the heater (V). With I and V , the temperature and heat capacity of sample can be known following data analysis procedure discussed previously[2].

III. MELTING POINT DEPRESSION

As described earlier[2], the heat capacity as a function of temperature, namely $C_p(T)$, can be measured for the entire heating cycle. If sample melts during this heating cycle, a melting peak will be developed in the measured $C_p(T)$ curve, as shown in the inset of Fig. 2. Our earlier work has demonstrated that Sn film of small thickness deposited on an inert substrate form self-assembled particles. Measurements of Sn particle size with TEM and SEM have revealed an

approximately Gaussian distribution for the particle size. Such distribution results in the broadened melting peak as shown in the inset. Therefore, the melting point determined from the melting peak position can be taken as the melting of Sn particles of the mean size r . In Figure 2, the melting points for Sn particles of various size is plotted. Clearly, T_m decreases progressively from the 232 °C, the melting point of bulk Sn, as Sn film thickness decreases. The lowest observed melting temperature for Sn is ~120 °C. This phenomenon is size dependent melting-point depression[3, 7].

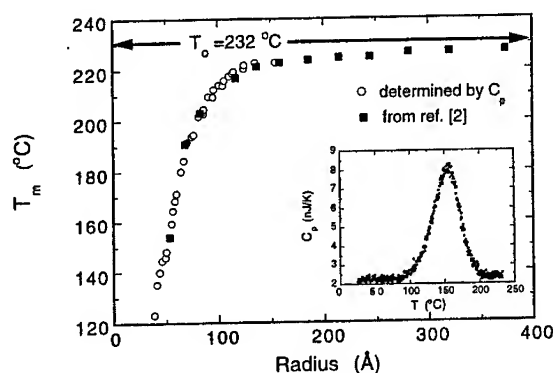


FIG. 2. Melting point as a function of Sn film thickness. The inset shows the measured heat capacity C_p for Sn sample with thickness of 5 Å.

The generally accepted model for the melting point depression phenomenon is that each particle consists of a solid core surrounded by a thin liquid shell[8]. This molten surface layer is resulted from the surface melting occurred at relatively low temperature[9]. Even though the exact nature of this surface layer is still unknown and is generating a debate about whether the shell layer is amorphous or liquid, nanocalorimetry promises to play a key role as a new experimental thrust to understand this system.

IV. ENERGY OF COALESCENCE

Another important materials process relevant to thin-film growth is coalescence[10,11]. The overall thermodynamic driving force for the growth

process is the Gibbs-Thompson effect: the reduction of surface and interface energy. To investigate the coalescence process of small particles, we have designed an experiment with multiple evaporation and annealing cycles[12]. Immediately after each deposition of 2 Å of Sn, the sample was annealed several times from 20 °C to 300 °C by dc current pulses. A full set of calorimetry data for $C_p(T, t)$ is acquired during each pulse. Using this data, we not only obtain values for T_m , but also obtain values for the coalescence energy ΔE_c — energy released as the clusters combine with islands.

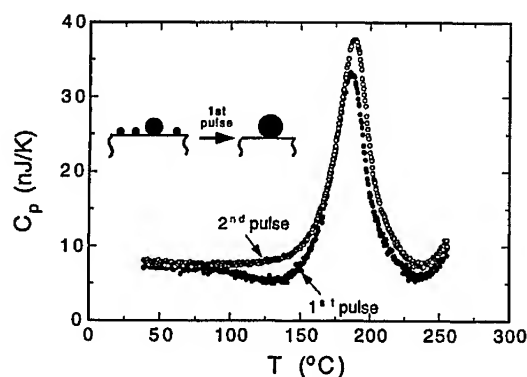


FIG. 3. $C_p(T)$ of two consecutive TDSC pulses after 2 Å of Sn was deposited on a substrate which already supports a set of large pre-existing islands. Note the difference during the first pulse. C_p during the pulses thereafter is on top of each other.

Results of one particular deposition/annealing cycle are shown in Figure 3, where the first two TDSC scans of a single evaporation cycle are displayed. Note the depression in C_p beginning at ~100 °C during the first pulse as compared with the successive pulse. This depression corresponds to a net positive flow of heat ΔE_c from the sample to the heater, this heat is generated as the net surface energy is reduced during the heating step. Complete analysis of the coalescence process is ongoing, however, an estimated value for ΔE_c can be obtained by integrating the difference between the first and second pulses: $\Delta E_c = \int (C_{p2} - C_{p1}) \cdot dT$. For example in the case of one monolayer of Sn deposited on SiN surface there will be 75 nJ of surface energy released when the average radius changes from 20 Å to 30 Å as a result of coalescence. Our preliminary results suggests that surface energy is also

size-dependent, as predicted theoretically many years ago[13,14]. To our knowledge, this is the first experimental data of its kind.

V. CONCLUSIONS

In summary, we have developed a scanning nanocalorimetry technique which is capable of measuring the dynamic of energy exchange at the level of 0.2 nano-joule. The thin-film differential scanning calorimeter (TDSC) is fabricated utilizing thin membrane processing technology: a metal thin film of Ni functions as a heater and thermistor, a Si_3N_4 membrane of 1000 Å or less in thickness provides the physical support for the heater and sample. The effective thermal mass of the TDSC is extremely small, thus the intrinsic sensitivity of the calorimeter can be extremely high. The application of the nanocalorimeter has been demonstrated by investigating the melting properties of nano-sized Sn particles. We have discovered the melting point depression using the thin-film calorimeter. We also have used the ultra-sensitive calorimeter to study the coalescence process of Sn particles. The energy released during coalescence due to the surface energy change can be measured.

ACKNOWLEDGMENT

This work is supported by NSF Grant SGER DMR 94-19604 and the Joint Service Electronics Programs under contract JESP N00014-90-1-129.

References

- [1] Z. Ma and L.H. Allen, Phys. Rev. **B 49**, 13501(1994).
- [2] S.L. Lai, G. Ramanath, L.H. Allen and P. Infante, Appl. Phys. Lett. **70**, 43(1997).
- [3] S.L. Lai, J.Y. Guo, V. Petrova, G. Ramanath and L.H. Allen, Phys. Rev. Lett. **77**, 99(1996).
- [4] D.E. Ibbotson, T.S. Wittrig and W.H. Weinberg, J. Chem. Phys. **72**, 4885(1980).
- [5] S.L. Lai, G. Ramanath and L.H. Allen, Appl. Phys. Lett. **67**, 1229(1995).
- [6] L.H. Allen and S.L. Lai, patent disclosure at UIUC, June 1996.
- [7] M. Tagagi, J. Phys. Soc. Jpn. **2**, 359(1954).
- [8] K.-J. Hanszen, Z. Phys. **157**, 523(1960).
- [9] J.W.M. Frenken, and J.F. van der Veen, Phys. Rev. Lett. **54**, 134(1985).
- [10] M. Zinke-Allmang, L.C. Feldman and M.H. Grabow, Surf. Sci. Rep. **16**, 377(1992).
- [11] A. Zangwill, *Physics of Surfaces*, (Cambridge University Press, New York, 1988).
- [12] S.L. Lai and L.H. Allen, unpublished.
- [13] R.C. Tolman, J. Chem. Phys. **17**, 333(1949).
- [14] J.C. Melrose, Ind. Eng. Chem. **60**, 53(1968).

Stability of Nanocrystalline n-TiO₂ and n-TiO₂/Mn₂O₃ Films During Photoelectrolysis of Water

by

Jun Akikusa and Shahed U. M. Khan
Department of Chemistry and Biochemistry
Duquesne University
Pittsburgh, PA, 15282

ABSTRACT

The bare n-TiO₂ film electrode was found to be unstable during photoelectrolysis of water. Significant improvement of stability was observed for Mn₂O₃-covered n-TiO₂, i.e., n-TiO₂/Mn₂O₃, film electrodes. The Mn₂O₃ layer also enhanced the rate of oxygen evolution instead of H₂O₂ formation, due to its catalytic effect. The highest photoresponse was found in n-TiO₂ film prepared at 850 °C for 13 min by thermal oxidation. The bandgap energy of both n-TiO₂ and n-TiO₂/Mn₂O₃ films was found 2.85 eV. X-ray diffraction (XRD) results indicate rutile structure for the n-TiO₂ film. The flat-band potential of the n-TiO₂ film was found to be - 1.13 V/SCE from the intercept of the Mott-Schottky plot. The highest potential-assisted photoconversion efficiencies, 5.1% and 4.1%, and the corresponding *practical* photoconversion efficiencies, 2.0% and 1.6%, were obtained for photoelectrolysis of water by n-TiO₂ and n-TiO₂/Mn₂O₃ films, respectively.

INTRODUCTION

Photoelectrochemical behavior of n-TiO₂ semiconductor films have been studied extensively (1-7). However, the stability of n-TiO₂ film electrodes during photoelectrolysis of water has not been thoroughly tested. It has been reported that the photoresponse of n-TiO₂ films decreases with time (3, 8).

Furthermore, on bare n-TiO₂, the rate of oxygen evolution is slower compared to the rate of generation of hydrogen peroxide (H₂O₂) during photoelectrolysis of water (8, 9). Thus, it is essential to study surface modification of n-TiO₂ that will stabilize its surface and as well as enhance the rate of oxygen evolution instead of H₂O₂ formation. This can be done by depositing a stable oxide layer onto n-TiO₂ film. Previously, it was reported (10) that Mn₂O₃ stabilized n-GaAs single crystal during water-splitting reactions. It is also well known that Mn acts as a catalyst to convert hydrogen peroxide to oxygen. In this study, we examined the stability and

photoresponse of bare n-TiO₂ and the Mn₂O₃-covered n-TiO₂, i.e., n-TiO₂ /Mn₂O₃ films during photoelectrolysis of water.

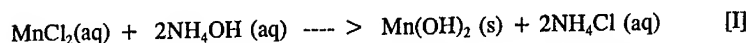
EXPERIMENTAL

Synthesis of n-TiO₂ Films by Thermal-Oxidation:

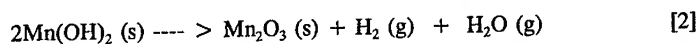
The Ti metal sheet (0.127 mm thick, 99.7 % pure) was obtained from Aldrich Co. The metal sheets was cut to an area of 1.00 cm². Various samples of pyrolytically formed n-TiO₂ were made by heating Ti metal sheet at several temperatures (700 to 1200 °C) and for different lengths of time (1 to 16 min.); a torch burner fueled by natural gas in the presence of oxygen instead of air. The temperature of the flame was measured by a digital thermocouple (Thermolyne Co., model PM- 20700).

Deposition of Manganese Oxide to Protect n-TiO₂ Films:

An n-TiO₂ film was immersed in a deposition bath containing 0.03 M MnCl₂, 0.25 M NH₄Cl, and 1.4 M NH₄OH aqueous solutions (10). The solution was stirred continuously at room temperature. After a few minutes, a light brown precipitate of Mn(OH)₂ started to form according to the reaction,



The sample was left in the bath for 15 min. After the completion of the reaction, the sample was washed in triply distilled water and, after drying, transferred to a pyrex glass tube that was evacuated to 2×10^{-5} mm Hg and sealed. This vacuum-sealed sample was then annealed in an oven at 250°C for 15 min to form a manganese oxide layer on the n-TiO₂ surface. The annealing in the vacuum resulted in the loss of water and hydrogen gas, thereby, leaving a thin film of manganese oxide (Mn₂O₃) on the n-TiO₂ surface behind, according to the reaction,



Formation of Mn₂O₃ film was identified earlier by x-ray photoelectron spectroscopic (XPS) analysis (10).

X-ray Analysis:

X-ray diffraction (XRD) of n-TiO₂ and n-TiO₂/Mn₂O₃ films was measured using a Philips diffractometer, type PW 1830/00, No DY 1050 with PW 3710 mpd control. The n-TiO₂ films prepared at 850 °C for 13 min were used for the XRD analysis. The incident X-ray angle of 2 degrees with respect to the horizontal

plane of the film was used during the measurement to avoid the contribution from Ti metal substrate underneath the $n\text{-TiO}_2$ film.

Preparation of $n\text{-TiO}_2$ and $n\text{-TiO}_2/\text{Mn}_2\text{O}_3$ Film Electrodes:

The oxide layer on the back side of the Ti sheet was removed by a file in order to have a resistance free contact between Ti metal and the copper wire. A copper wire was connected to the Ti metal substrate on the back of the film electrode using a conductive silver-epoxy adhesive. The back side of the film electrode was then covered by a nonconductive epoxy adhesive.

Photocurrent-Potential Measurements:

The photocurrent response at each $n\text{-TiO}_2$ and $n\text{-TiO}_2/\text{Mn}_2\text{O}_3$ film electrodes was measured using a scanning potentiostat (EG & G. Model 362) and recorded by an X-Y recorder (EG & G model RE 0092) using a saturated calomel electrode (SCE) as a reference electrode, and a Pt wire as a counter electrode in 5 M KOH solution in a one compartment cell. The $n\text{-TiO}_2$ and $n\text{-TiO}_2/\text{Mn}_2\text{O}_3$ electrodes were illuminated by a 150 W Xe arc lamp (Hanovia Co.) with a power supply (Kratos LPS 251 HR). The light intensity was measured by a photometer (International Light Inc., model IL 1350) and was adjusted to give 50 mW cm^{-2} by changing the distance of the light source from the film electrode. The reflection and absorption of light by the window of the photoelectrochemical cell was taken into account in the measurement of light intensity. The film electrodes were placed close enough to the window of the cell (distance: 5 mm) to minimize the error from the absorption of light by the solution. The monochromatic photocurrent-wavelength measurements were carried out by placing a monochromator (Kratos model GM 100-1) in front of the xenon light source.

AC-Impedance Measurements:

The AC-impedance of the $n\text{-TiO}_2$ and $n\text{-TiO}_2/\text{Mn}_2\text{O}_3$ film electrodes was measured using an EG & G Two Phase Lock-in Analyzer model 5208 equipped with EG & G Potentiostat/ Galvanostat model 273. These instruments were computer controlled by an EG & G electrochemical impedance software model 378 that automatically adjusted the phase angle during each measurement. AC amplitude of 10 mV was used for all of the measurements, a Pt mesh electrode was used as a counter electrode, and each of the $n\text{-TiO}_2$, and $n\text{-TiO}_2/\text{Mn}_2\text{O}_3$ film electrodes were used as the working electrode. These measurements were performed in the dark using 5 M KOH electrolyte solution. The capacitance, C , was calculated using the following expression of impedance, Z , for a serial capacitor-resistor model,

$$Z = Z' + iZ'' \quad [3]$$

where Z' is the real part of impedance and Z'' is the imaginary part of impedance from which capacitance, C , can be obtained using $Z'' = i / \omega C$, with $\omega = 2\pi f$, $i = (-1)^{1/2}$, and f is the AC frequency in Hz.

RESULTS AND DISCUSSION

Photoresponse of n-TiO₂ and n-TiO₂/Mn₂O₃ Films:

The dependence of the photocurrent density at n-TiO₂ film electrodes (prepared using different oxidation temperatures) on applied potential are given in Fig. 1. Highest photocurrent density was observed for the sample prepared at an oxidation temperature of 850 °C for 13 min (see Fig. 1). The photoresponse of n-TiO₂/Mn₂O₃ film was found to be slightly lower as compared to that of the bare n-TiO₂ film (see Fig. 2). This decrease in the photocurrent density can be attributed to absorption (blocking) of light by the Mn₂O₃ layer.

The onset potential of the n-TiO₂/Mn₂O₃ film electrode shifted approximately 50 mV in the anodic direction, however, the shape of the curve did not change (see Fig. 2). This indicates that Mn₂O₃ acts only as a protective layer and does not affect the nature of the n-TiO₂ semiconductor.

Quantum Efficiency n-TiO₂ and n-TiO₂/Mn₂O₃ Films:

The quantum efficiency (spectral response), $\eta(\lambda)$ was calculated using the relation (8),

$$\eta(\lambda) = j_p(\lambda) / eI_0(\lambda) \quad [4]$$

where $j_p(\lambda)$ is the monochromatic photocurrent density, e is the electronic charge and $I_0(\lambda)$ is the flux of incident photon at wavelength, λ .

The quantum efficiencies (spectral response), $\eta(\lambda)$ under monochromatic light illumination on both n-TiO₂ and n-TiO₂/Mn₂O₃ films are shown in Fig. 3. The decrease in quantum efficiency from 60% to 54% at 330 nm for Mn-oxide covered samples (n-TiO₂/Mn₂O₃ films) can be attributed to the absorption of the photon by the Mn₂O₃ layer. Two absorption maxima were observed for both films indicating the presence of a mixed band in these nanocrystalline films.

Bandgap Energy and the Structure of n-TiO₂ Films:

The bandgap energy, E_g , of the semiconducting n-TiO₂ and n-TiO₂/Mn₂O₃ films can be determined using the following equation (11, 12),

$$\eta(\lambda)h\nu = A(h\nu - E_g)^n \quad [5]$$

where, $\eta(\lambda)$ is the quantum efficiency (spectral response), A is a constant, n equals either 0.5 for allowed direct transition or 2 for allowed indirect transitions (13). The allowed direct transition of an electron from the valence band to the conduction band by light energy, $h\nu$, is not phonon assisted because such a transition does not require a change in momentum (momentum is conserved). For the indirect bandgap, the transition of an electron is phonon assisted because such a transition involves change in energy and momentum (13). In the case of indirect transition, momentum is conserved via a phonon interaction because light photons cannot provide a change in momentum (13). Equation 5 is appropriate to use to determine the bandgap energy when the applied potential is far from the flatband potential, so that the transport of photogenerated carriers inside the semiconductor becomes rate determining (14).

Figure 4 shows the bandgap of pyrolytically prepared n-TiO₂ films obtained from the intercept of $[\eta(\lambda)h\nu]^{1/2}$ versus $h\nu$ plot. It shows an indirect bandgap energy of approximately 2.85 eV which is close to the earlier reported values of 2.9 eV (15). No change in bandgap energy for Mn₂O₃ covered n-TiO₂, i.e., n-TiO₂/Mn₂O₃ film was observed. Several values of bandgap energy have been reported; approximately 3.0 eV for the rutile structure and 3.2 eV for the anatase structure of n-TiO₂ films (16). The observed values of bandgap energy indicate that the n-TiO₂ films that we prepared pyrolytically have a rutile structure.

Figure 5 shows the X-ray diffraction (XRD) spectrum of the n-TiO₂ film prepared at 850 °C. The peaks of this XRD spectrum also confirm a rutile structure. No difference between XRD peaks of n-TiO₂ and n-TiO₂/Mn₂O₃ films was observed because the Mn₂O₃ layer was too thin (≤ 5 nm) to provide observable XRD signals (7).

Flatband Potential and the Donor Density from the Mott-Schottky plots:

It is well-known that the flatband potential (V_{fb}) of a semiconductor can be obtained from the intercept of the Mott-Schottky plot, using the relation (17),

$$1/C^2 = (2/\epsilon\epsilon_0 N_d e)(V - V_{fb} - kT/e_0) \quad [6]$$

where C is the space charge capacitance, ϵ is the dielectric constant of the

semiconductor, ϵ_0 is the permittivity of the vacuum, e is the electronic charge, N_d is the donor density, V is the applied potential with respect to a reference electrode, and kT/e is the temperature-dependent term in the Mott-Schottky equation. A value of 120 was used for the dielectric constant of polycrystalline n-TiO₂ film (17).

Figure 6 shows the Mott-Schottky plot for the capacitance measured at the AC frequency of 1000 Hz for both n-TiO₂ and n-TiO₂/Mn₂O₃ films prepared at 850 °C for 13 min. From the intercept, the flatband potential for bare n-TiO₂ film is found to be - 1.13 V/SCE, when the kT/e term is included. For the n-TiO₂/Mn₂O₃ film, a non-linear Mott-Schottky plot was observed. Similar non-linearity of the Mott-Schottky plot was reported for a passive film of γ -Fe₂O₃ on Fe₃O₄ film (18). This non-linearity can be attributed to the partial potential drop between the n-TiO₂ film and the Mn₂O₃ layer when an external potential is applied to the electrode. At the AC frequency of 1000 Hz, the donor density for the n-TiO₂ film was found to be $3.9 \times 10^{19} \text{ cm}^{-3}$ from the slope of the Mott-Schottky plot.

Stability of n-TiO₂ and n-TiO₂/Mn₂O₃ Films:

(i) Bare n-TiO₂ Films:

To determine the stability of a bare n-TiO₂ film electrode (prepared at the pyrolysis temperature of 850 °C for 13 min), the photocurrent density was measured and plotted as a function of time (see Fig. 7). One n-TiO₂ electrode was used successively for three periods to study the photoresponse with an interval of 16 hours in dry condition prior to each successive run. The photocurrent density decreased with time, and the rate of decrease of photocurrent density increased in the second and third runs (see Fig. 7); however, the photocurrent densities were higher at the beginning of the second and the third runs. This suggests that the n-TiO₂ film regained some of its photoactivity during the 16 hour rest period between each run due to restructuring of its surface in the dry condition. This indicates that the degradation of n-TiO₂ film is responsible for the decrease of the photocurrent density with time. This observation agrees with earlier results (3, 4).

(ii) n-TiO₂/Mn₂O₃ Film:

In order to enhance the stability of n-TiO₂ film, a newly prepared n-TiO₂ film was covered by a Mn₂O₃ layer by chemical deposition. The stability of the Mn₂O₃-covered n-TiO₂, i.e., n-TiO₂/Mn₂O₃ film is also shown in Fig. 7. The photocurrent density at n-TiO₂/Mn₂O₃ film electrode shows no decrease for the eight hour test period. No successive tests were made for this film. However, the photocurrent density at n-TiO₂/Mn₂O₃ film is approximately 19% lower than that of the n-TiO₂ film electrode.

It should be noted that the deposition of the Mn-oxide (MnO) layer by annealing the $\text{Mn}(\text{OH})_2$ in the ambient condition according to the reaction,



did not improve the stability of n-TiO₂ films.

The Amount of H₂ and O₂ Gases Evolved:

The amount of H₂ gas evolved at the counter Pt electrode during illumination of both n-TiO₂ and n-TiO₂/Mn₂O₃ film electrodes is shown in Fig. 8. Potentials of -0.45 V/SCE and -0.30 V/SCE were applied to n-TiO₂ and n-TiO₂/Mn₂O₃ film electrodes, respectively, to obtain an equal photocurrent density of 2.5 mA cm⁻² at both electrodes in 5.0 M KOH solution. After 180 min, 3.4 ml of hydrogen gas (= 1.37 x 10⁻⁴ mol H₂) was collected at 21 °C at atmospheric pressure of 740.5 mm Hg and vapor pressure of water of 14.3 mm Hg at each of these film electrodes. The coulomb passed through the circuit was 27.0 C, and the coulomb calculated from the amount of hydrogen gas was 26.4 C; its experimental error was ± 2.1%. This indicates that the amount of H₂ gas is proportional to the current density and the current efficiency for the hydrogen production was 97.9 ± 2.1%.

Figure 8 also shows the amount of oxygen evolved at the bare and Mn₂O₃-covered n-TiO₂ electrodes. The amount of O₂ gas collected at the bare n-TiO₂ film was much less than the theoretical amount, and the H₂: O₂ ratio was 1 : 0.30. This indicates that oxygen is not the only product, and that some of the charges are utilized to form H₂O₂ or the corrosion products of the n-TiO₂ film. This is consistent with the earlier reports that one of the main products at n-TiO₂ electrode under illumination is H₂O₂ (8, 9).

However, the amount of O₂ evolved at the n-TiO₂/Mn₂O₃ film electrode increased significantly; the ratio of hydrogen gas to oxygen gas was found to be 1 : 0.49 which is close to the theoretically expected ratio of 1 : 0.50. This result indicates that Mn₂O₃ not only stabilizes the n-TiO₂ photoelectrode, but also promotes oxygen evolution by its catalytic effect.

Potential-Assisted Photoconversion efficiency at n-TiO₂ and n-TiO₂/Mn₂O₃ Film Electrodes:

The potential-assisted photoconversion efficiency for the photoelectrolysis of water in the presence of an external applied potential can be calculated using the relation,

$$\begin{aligned} \% E_{\text{eff}} &= (\text{Power output} / \text{Power input}) \times 100 \\ &= [j_p \times V_{\text{rev}}] / (I_0 + j_p \times V_{\text{applied}}) \times 100 \end{aligned} \quad [8]$$

The percentage of potential-assisted photoconversion efficiencies at applied potential of 0.75 V becomes 5.1% and 4.1% at n-TiO₂ and n-TiO₂/Mn₂O₃ film electrodes, respectively. For this, the observed photocurrent densities, $j_p = 2.15 \text{ mA cm}^{-2}$ and 1.71 mA cm^{-2} were used at applied potential, $V_{\text{applied}} = 0.75 \text{ V}$ between the working and the counter electrode for n-TiO₂ and n-TiO₂/Mn₂O₃ film electrodes, respectively. $V_{\text{rev}} = 1.23 \text{ V}$ and I_0 (light intensity) = 50 mW cm^{-2} were also used in Eq. (8).

However, the potential-assisted practical photoconversion efficiency, E_{eff} (practical) can be calculated by taking into account the regeneration of power loss due to use of external potential, V_{applied} . Thus, the potential-assisted practical photoconversion efficiency can be expressed as (19),

$$\begin{aligned} \% E_{\text{eff}}(\text{practical}) &= [(\text{Power output} - \text{power lost}) / (\text{Power input})] \times 100 \\ &= [j_p \times V_{\text{rev}} - j_p \times V_{\text{applied}}] / (I_0 + j_p \times V_{\text{applied}}) \times 100 \quad [9] \end{aligned}$$

The potential-assisted practical photoconversion efficiencies at both bare and Mn₂O₃-covered n-TiO₂ film electrodes at different applied potentials are shown in Fig. 9. The practical photoconversion efficiency becomes zero at $V_{\text{applied}} = 1.2 \text{ V}$ and negative when V_{applied} is higher than 1.2 V because at these higher applied potentials the power loss becomes more than the power output from photoconversion (see Fig. 9).

The highest potential-assisted practical photoconversion efficiencies for the photoelectrolysis water, 2.0 % and 1.6 % are obtained at applied potential of 0.75 V for n-TiO₂ and n-TiO₂/Mn₂O₃ film electrodes, respectively (see Fig. 9).

CONCLUSIONS

The following conclusions can be made from this study:

1. It is essential to optimize the temperature and the time of oxidation to obtain the best photoresponse of n-TiO₂ films prepared by thermal oxidation.
2. Chemical deposition of Mn₂O₃ highly improves the stability of n-TiO₂ film electrodes during photoelectrolysis of water.
3. Mn₂O₃ deposition also enhances the oxygen evolution close to that of the theoretical amount due to its catalytic effect.
4. Deposition of Mn₂O₃ does not affect the bandgap energy of n-TiO₂ films.

ACKNOWLEDGMENT

The authors are grateful to Dr. Jean Blachere, University of Pittsburgh, Department of Material Science for obtaining the X-ray data for the n-TiO₂ and n-TiO₂/Mn₂O₃ films. We also gratefully acknowledge the partial financial support of this work by the Alcoa Foundation.

REFERENCES

1. S. E. Lindquist, A. Lindgren, and Z. Yan-Ning, *J. Electrochem. Soc.*, **132**, 623 (1985).
2. J. Akikusa and S. U. M. Khan, *Electrochemical Society Proceeding*, **95-8**, 109 (1995).
3. R. Vogel, P. Hoyer, and H. Weller, *J. Phys. Chem.*, **98**, 3183 (1994).
4. Q. W. Choi and S. M. Park, *J. Electrochem. Soc.*, **139**, 1803 (1992).
5. O. R. Camara and C. P. De Pauli, *J. Appl. Electrochem.*, **25**, 247 (1995).
6. M. Mikula, J. Blecha, and M. Ceppan, *J. Electrochem. Soc.*, **139**, 3470 (1992).
7. I. Saeki, N. Okushi, H. Konno, and R. Furuichi, *J. Electrochem. Soc.*, **123**, 2226 (1996).
8. J. Augustynski, *Electrochim. Acta*, **38**, 43 (1993).
9. E. Yesodharan and M. Gratzel, *Helvetica Chimica Acta*, **66**, 2145 (1983).
10. R. C. Kainthla, B. Zelenay, and J. O'M. Bockris, *J. Electrochem. Soc.*, **134**, 241 (1987).
11. J. O'M. Bockris, M. Szklarczyk, A. Q. Contractor, and S. U. M. Khan, *Int. J. Hydrogen Energy*, **9**, 741 (1984).
12. C. Searson and R. M. Latanision, *J. Electrochem. Soc.*, **135**, 1358 (1988).
13. J. I. Pankove, *Optical Processes in Semiconductor*, Dover Pub., New York, Chapter 3, 1971.
14. J. O'M. Bockris and S. U. M. Khan, *Surface Electrochemistry*, Plenum Press, Chapter 5, New York, 1993.
15. D. Zane, F. Decker, and G. Razzini, *Electrochim. Acta*, **38**, 37 (1993).
16. T. D. Burleigh, *Corrosion*, **45**, 464 (1989).
17. F. Mollers, H. J. Tolle, and R. Memming, *J. Electrochem. Soc.* **121**, 1160, (1974).
18. B. D. Cahan and C. T. Chen, *J. Electrochem. Soc.*, **129**, 474 (1982).
19. S. U. M. Khan and S. A. Majumder, *Int. J. Hydrogen Energy*, **14**, 653 (1989).

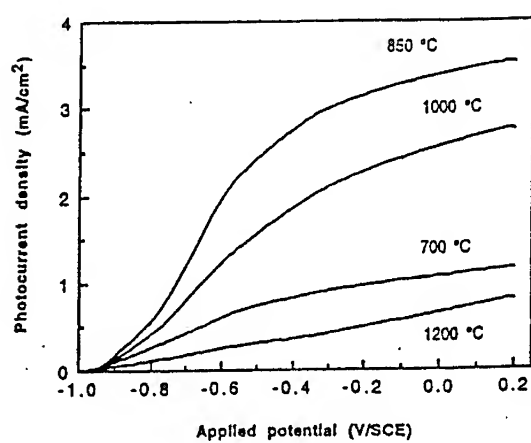


Figure 1. Photocurrent density versus applied potential for n-TiO₂ films prepared at different temperatures. Solutions: 5 M KOH, light intensity: 50 mW cm⁻².

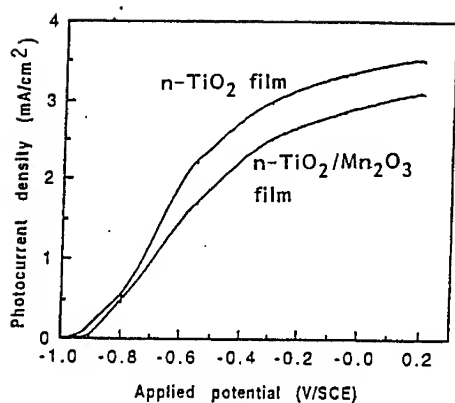


Figure 2. Photocurrent density versus applied potential for both n-TiO₂ and n-TiO₂/Mn₂O₃ film electrodes prepared at 850 °C for 13 min. Solutions: 5 M KOH, light intensity: 50 mW cm⁻²

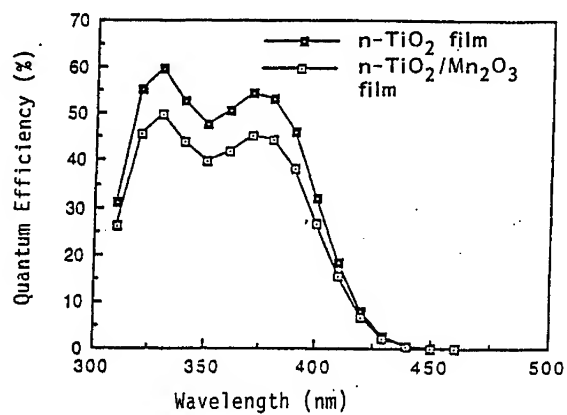


Figure 3. The quantum efficiencies (spectral response) for both n-TiO₂ and n-TiO₂/Mn₂O₃ films at applied potential of - 0.24 V/SCE.

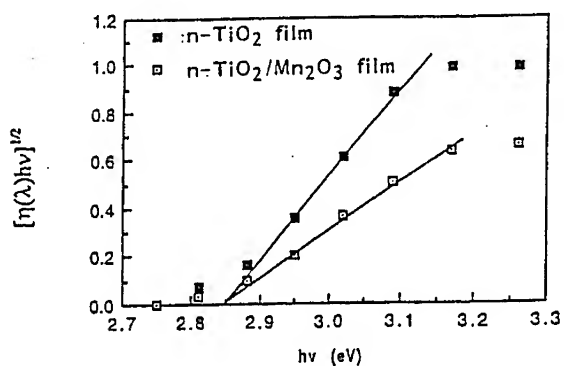


Figure 4: The plot of $[\eta(\lambda)h\nu]^{1/2}$ vs $h\nu$ to determine the bandgap energy of n-TiO₂ and n-TiO₂/Mn₂O₃ film electrodes.

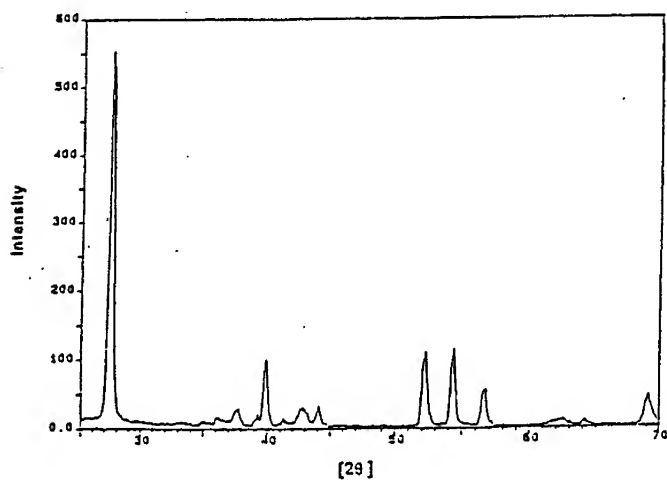


Figure 5. X-ray diffraction (XRD) spectrum of n-TiO₂ film prepared at oxidation temperature of 850 °C for 13 min.

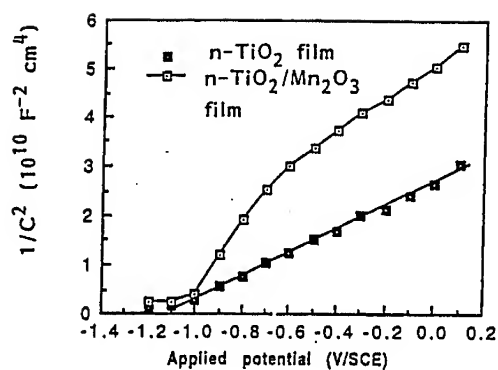


Figure 6. Mott-Schottky plot of both $n-TiO_2$ and $n-TiO_2/Mn_2O_3$ film electrodes measured at AC frequency of 1000 Hz.

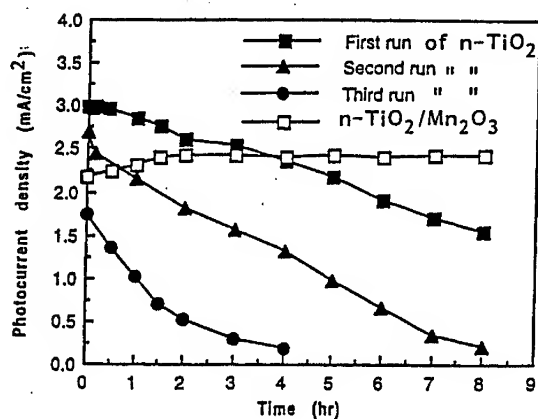


Figure 7. The photocurrent densities at $n-TiO_2$ and $n-TiO_2/Mn_2O_3$ film electrodes at applied potential of - 0.30 V/SCE versus time to show the stability of the films. The $n-TiO_2$ film electrode was run three times with rest period of 16 hours in the dry condition between the runs.

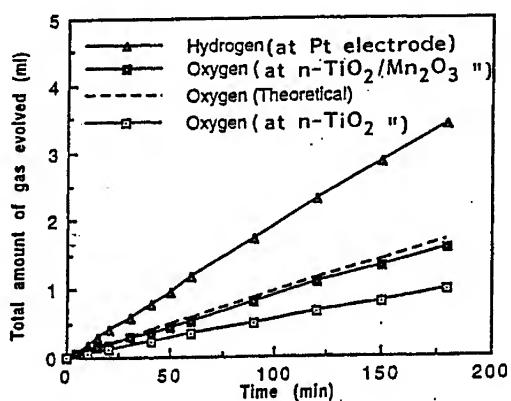


Figure 8. The total amount of hydrogen gas and oxygen gas evolved versus time of illumination having a constant photocurrent density of 2.5 mA cm^{-2} at both n-TiO_2 and $\text{n-TiO}_2/\text{Mn}_2\text{O}_3$ film electrodes.

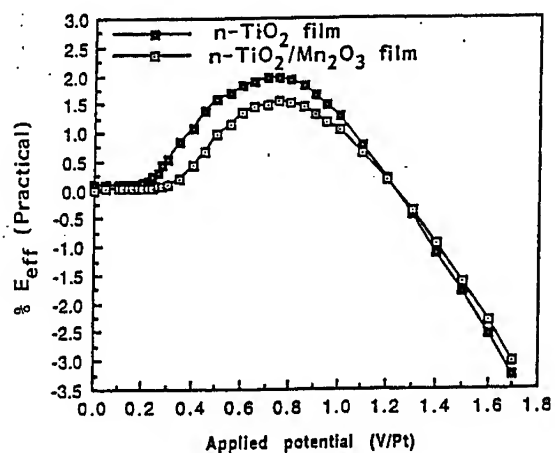


Figure 9. The plot of practical photoconversion efficiencies, E_{eff} (practical) vs V_{applied} for both n-TiO_2 and $\text{n-TiO}_2/\text{Mn}_2\text{O}_3$ films during photoelectrolysis of water.

Semiconductor nanocrystals by aerotaxy method

Knut Deppert, Martin H. Magnusson, and Lars Samuelson
Lund University, Solid State Physics, Box 118, S-221 00 Lund, Sweden

Jan-Olle Malm, Chatrin Svensson, and Jan-Olov Bovin
Lund University, Inorganic Chemistry 2, Box 124, S-221 00 Lund, Sweden

ABSTRACT

In this paper we present a fabrication route to produce size-selected III-V semiconductor nanocrystals via a simple, reliable, and efficient aerosol route. Since this approach includes the reaction of aerosol particles and a self-organized growth of a new compound, all in the aerosol phase, we call this process aerotaxy. Size-selected nanocrystals of different III-V compounds in a diameter range below 20 nm were fabricated using this method. Utilizing the reaction of either arsine or phosphine with either gallium or indium droplets, GaAs and InP clusters were formed. Our approach opens the possibility to produce size-selected nanocrystals of compound semiconductor materials with considerable freedom in composition and size.

INTRODUCTION

Semiconductor crystals with dimensions in the nanometer-scale are of substantial interest due to their electronic quantum-size effects. However, the fabrication of such structures remains difficult. The strong demand for very narrow size distribution is especially challenging since the quantum-size effect will otherwise be averaged out. Several attempts have been made to produce this type of nanocrystals for instance by: homogeneous nucleation in a vapor-phase epitaxy reactor [1], pulverization of bulk crystal [2], spark processing [3], sol-gel processes [4,5], organometallic vapor deposition into porous glass [6], solution phase synthesis [7,8], and utilizing the Stranski-Krastanow epitaxial growth mode [9]. One reported attempt via the aerosol route uses a rather complicated chemical reaction [10]. All these attempts are characterized by the fact that the nanocrystals are bound in one or the other way to surrounding material, and most of these methods result in nanocrystals with wide size distributions. In this letter we present the fabrication of size-selected, contamination-free nanocrystals of III-V semiconductor material in the size range below 20 nm via a simple, reliable, and efficient aerosol route.

In short, an aerosol of a group-III component is formed by condensation from a vapor the metal evaporated. Thereafter, a size selection of the particles takes place. The monodisperse group-III aerosol is mixed with a group-V containing gas and sent

into a second tube furnace for reaction. Figure 1 shows a schematic diagram of the set-up. Since this approach includes the reaction of aerosol particles and a self-organized growth of a new nanocrystalline compound, all in the aerosol phase, we call this process aerotaxy [11].

EXPERIMENTAL

The nanocrystals are produced with an aerosol generator set-up similar to that used in previous studies [12], based on a common aerosol generator [13]. The fabrication route utilizes the formation of an aerosol of ultrafine metal particles. In this study, gallium and indium were used as the group-III metals. Experiments were performed with the first furnace, for the metal evaporation, at a temperature between 1090 and 1130°C, resulting in a sufficiently large number of particles with a diameter below 20 nm. Since quantum-size effects for semiconductor nanocrystals are to be expected at sizes of about 10 nm and smaller, this study has been concentrated on particles with a diameter of about 10 nm. Palladium-purified hydrogen was used as a carrier gas for the formation of the metal aerosol. This gas flow through the first furnace was kept constant at either 1.68 or 2 l/min. To charge the aerosol particles, a charger is placed after the furnace including a ^{85}Kr source emitting β -particles. The size selection takes place in a differential mobility analyzer (DMA). A DMA apparatus exploits the fact that the electrical mobility of singly charged particles is a monotonically decreasing function of particle size. This is valid for the particle sizes characterized in this study, as particles below 20 nm in diameter can only be charged by one elementary charge unit by the charger used in this study. While sending a flow of electrically charged particles in a perpendicular electric field, the field causes particles to be attracted to one capacitor plate. Particles with higher electrical mobility will be precipitated on the nearest portion of the plate and those with lower mobility will be carried along with the main flush flow. Only those particles with the correct mobility, and hence particle size, will be attracted to the vicinity of a sampling slit where they are swept out by the small gas stream flowing through the slit [14]. The DMA is widely used in aerosol technology, both for measuring size distributions of aerosols and for producing monodisperse test aerosols, with a standard deviation down to a few percent.

The size-selected metal aerosol is then mixed with a group-V containing gas, here either phosphine (PH_3) or arsine (AsH_3) with electronic grade purity, and sent into a second furnace for reaction. The hydride flow was kept small, thus not altering the aerosol flow conditions. However, the ratio of the number of hydride molecules to the total number of metal atoms in the reaction zone was of the order of 10^6 to 10^7 . The reaction furnace was operated at settings from room temperature up to 650°C, a temperature range in which one may expect reaction of the hydride with the metal droplet to form a compound. A second DMA was utilized to measure the size distribution after the reaction, thus monitoring the reaction process. Since only charged particles pass the DMA, an electrometer functioned to determine the particle

concentrations. At each temperature setting, a scan was recorded of the size distribution of the aerosol particles leaving the reaction furnace. The maximum of the size distribution curve was used as a measure for the mean particle diameter. Both DMAs were run at 10 l/min N₂ flush gas (purity better than 99.995%). After the reaction furnace, the particles produced may be deposited on a substrate by means of an electric field.

The ratio of the flows in the DMAs gives a theoretical spread in the size distribution of 16% or 20% for the two different flow ratios used in this study. However, the use of hydrogen as aerosol carrier and nitrogen as sheath gas implies some deviation from the normal DMA operation, thus making the calculation of the particle diameter a difficult issue. The error, however, is a systematic offset and can be solved, e. g. by calibration with transmission electron microscopy (TEM). Any given particle diameter in this letter is taken from the calculation using the ideal transfer function of the DMA. An earlier TEM study showed that those diameters may be up to 50% too large [11].

Samples have been prepared for high-resolution transmission electron microscopy at certain conditions of the reactions by depositing particles on a standard grid for electron microscopy after the reaction furnace. By investigation of those samples, high-resolution images of single particles could be obtained. For a few samples it was possible to acquire energy-dispersive x-ray spectroscopy data, as well as electron diffraction patterns of the particles.

RESULTS AND DISCUSSION

The present work focuses on the change in the aerosol particle characteristics with respect to (i) the temperature in the reaction furnace, and (ii) the hydride flow for the reaction of gallium particles with arsine and of indium particles with phosphine. The reaction results in a change in size distribution which depends on both the temperature and the hydride flow. The characteristic shape of the size distribution, however, does not change with temperature. Thus, the maximum of this curve can well be taken as a measure of the mean particle diameter. The changes to be observed with increasing temperature are connected with changes in the particle diameter. In the following, the two different material combinations dealt with in this study will be discussed.

Gallium with arsine

Plotting the mean particle diameter against temperature, figure 2 is one example, reveals a four step process: (a) slight decrease, (b) strong and step-wise increase, (c) steady state, and (d) moderate increase of the particle diameter. Studying the relative value of the mean particle diameter with respect to room temperature conditions reveals an almost identical behavior of the three different inlet diameters used in this study of 10, 12, and 14 nm, respectively. Figure 3 shows the change of the relative

mean diameter for one inlet diameter but with different arsine flows. The observed curves are similar and, in case of higher arsine flows, identical.

The four characteristic temperature ranges observed for the reaction of Ga particles with arsine can be attributed to the following processes. Temperature region (a) is characterized by a slight decrease of the particle diameter between room temperature and about 200°C. The shrinking of the particles is insignificant in this temperature range. This process can be understood in terms of evaporation of Ga atoms from the particles. Evaporation phenomena are widely observed in aerosol technology [15]. In our case, the evaporation is affected by adsorption of arsine molecules on the Ga particles. This is clearly revealed in the variation of the slope for different arsine input flows in this temperature region. Higher arsine flows may suppress Ga evaporation, as can be seen from figure 3. Still, a reaction between the Ga in the drop and the attached arsine is not expected for such low temperatures.

The next temperature region (b) is characterized by a strong and linear increase of the particle diameter. It reveals a reaction of the adsorbed arsenic containing species with the gallium in the particle. Here, GaAs particles are formed. This growth over a temperature range of about 50°C is nearly linear. Figure 3 shows a clear dependence of this step on the arsine flow. For lower arsine inputs, it starts and ends at higher temperatures. The reaction, under all conditions, started at remarkably low temperatures, lower than expected from investigations of vapor-phase growth processes [16].

In step (c), after the saturated reaction, a stable phase can be observed over a temperature range of more than 100°C in which the size of the particles remains constant. The fact that the particle size after the reaction is almost constant, suggests a built-in self-limitation of the reaction. The particles created can only be GaAs, as judged from the phase diagram of the Ga-As system. The steady state behavior indicates that the reaction is complete, and that all of the Ga in the particles has been converted into the stoichiometric III-V compound. Transmission electron micrographs, figure 4 shows one example, indicate the good crystallinity of the particles, as would be expected only for stoichiometric particles. Furthermore, electron diffraction shows clearly the pattern expected from GaAs, as illustrated in figure 5.

Gallium has a density of 6.095 g/cm³ at 30°C [17], while GaAs has a density of 5.316 g/cm³ at the same temperature [18]. Converting 1 mol of Ga, with a volume of 11.44 cm³, into 1 mol of GaAs, with a volume of 27.21 cm³, leads to a change in volume of 2.38. The change of the densities with temperature are similar for Ga and for GaAs at the temperatures used in this study, allowing us to assume a temperature independent volume ratio. For spherical particles this volume ratio gives a diameter ratio of 1.33. We observed ratios between 1.2 and 1.3; the bigger the particles the larger this ratio. This ratio is somewhat lower as the calculated value and may be caused by inaccuracies in the DMA measurement for such small particles and the fact that the particles are not completely spherical.

In the final temperature region (d), after the steady state step, the particle diameter increases again. This process starts at about 400°C, independent of the initial Ga particle diameter. It can be attributed to arsine cracking, homogeneously in the gas phase and/or heterogeneously on the already existing GaAs particle surfaces, and subsequent condensation of arsenic atoms on the particles. The set-up used does not include the possibility to detect particles composed of pure As, formed by the cracking of arsine in the reaction furnace. Only charged particles can pass the DMA and be detected in the electrometer, and there is no additional charging device between the reaction furnace and the electrometer. Since there might be a possibility that some freshly formed As particles are charged, these would be added to the total number of particles. Indeed, going to higher temperatures than 500°C in the reaction furnace, results in an increased broadening of the particle size distribution.

This description of the reaction, derived from tracing the particle diameter with reaction temperature and precursor flow, is supported by the investigations made with electron microscopy. A limited study of the composition of the particles produced in this temperature region was carried through, using electron beam induced x-ray analysis. For this, a special series of experiments was prepared with larger particles to enable this investigation with reasonable signal-to-noise ratio. Figure 6 shows a comparison between the particle diameter, as determined by the TEM, and the arsenic content of the particles, as determined by x-ray analysis, as a function of temperature for the aerotaxy process of gallium and arsine. At low temperatures the particles consist out of gallium only. When the temperature in the reaction furnace exceeds 250°C, arsenic can be detected in the particles, increasing in parallel with the particle diameter with increasing temperature. When the diameter for the fully reacted gallium droplet is reached, the arsenic content reaches also its maximum value of 48.5%. This means a stoichiometric composition within the uncertainty of the measurement technique for such small particles.

The larger particles used for this special investigation also exhibit another interesting feature. Since the number of gallium atoms in those particles is larger, it takes longer time to react, and also their surface is larger allowing the reaction to start at several places. Due to these multiple reaction sites, the spherical droplets become misshaped. This is illustrated in figure 7, where the diameter of the particles is plotted together with their circularity. The circularity of a particle measures, on a scale from 0 to 1, how circular a particle is. It is determined by comparing the area with the perimeter of the projection of the particle. Due to the projection in the electron microscope the circularity indicated is only a measure in two dimensions, that is only an approximation of the three-dimensional sphericity of a particle. In the temperature region where the reaction occurs the circularity decreases. Recrystallization processes may be the cause for the circularity increase at higher temperatures.

Indium with phosphine

In the case of indium droplets reacting with phosphine the observations are similar to those made in the gallium-arsine case. Figure 8 gives an example of the change in size distribution with temperature for a certain inlet diameter of the indium particles and different phosphine flows. Several observations can be made from these plots. First, a difference in the plots concerning whether phosphine is present or not, second, a pattern in the diameter development with non-zero phosphine flows, and third, some difference for different phosphine flows.

The difference in the behavior of the particles is striking concerning whether phosphine is present or not. Without phosphine the particle diameter decreases, at first slowly until about 500°C and then at an increased rate. This can be attributed to the evaporation process the pure indium particles undergo. A simple model of the evaporation process [19] shows a good agreement with the measured decrease in particle diameter when the temperature increases.

As soon as phosphine is added to the aerosol flow this evaporation process is suppressed and the reaction of indium droplets with phosphine can be followed. The overall picture of the reaction is similar for all phosphine flows investigated in this study. Step (a), between room temperature and about 280°C, is characterized by an almost constant particle diameter. Above this temperature (b), the diameter increases drastically and reaches a steady state value (c), between 380 and 500°C. Increasing the temperature further (d), leads to a steady increase in diameter. This behavior is similar to the one of gallium droplets reacting with arsine to form GaAs [20].

The four steps can be attributed to the same processes as discussed in the gallium-arsine case: (a) suppressed evaporation, (b) reaction between the indium droplets and the phosphine gas to form InP particles, (c) stable InP particles, and (d) catalytic cracking of the phosphine molecule. The constant diameter in step three indicates that all indium in the particle has reacted and no further change to it seems to take place. The densities for Indium and InP at room temperature are 7.30 g/cm³ [21] and 4.81 g/cm³ [18], respectively. This difference in density can be transformed into a volume ratio between a particle consisting solely out of In and one where the In has reacted completely into InP. Assuming spherical particles, this volume ratio gives a diameter ratio of 1.25, the InP particle being the larger one. In our experiments, the diameter ratios between the room-temperature value and the value at step three in the diameter curve lay between 1.18 and 1.24, close to the calculated value with the same argumentation for the deviation as in the gallium-arsine case.

This description of the reaction derived from tracing the particle diameter with reaction temperature and precursor flow is supported by the investigations made with electron microscopy. Almost all particles passing the furnace at temperatures below 300°C exhibit an amorphous structure, and the composition is characterized as being mainly indium with nearly no phosphorus. As indium metal has a low melting point (156°C), observations of such small particles in the electron microscope, due to the

strong interaction of the electron beam with the particle, will melt or at least affect this type of particles. Figure 9 shows an example of a TEM picture of such a sample.

The next step, the reaction itself, is difficult to follow by electron microscopy. Samples studied exhibit agglomerates of crystalline as well as of amorphous particles. Obviously, during the reaction process, some of the particles may react to form InP while other particles may pass the reaction zone without being reacted. This description is supported by looking at the full width at half maximum of the size distribution curves versus temperature. This parameter exhibits a doubling of its value at the temperatures where the reaction takes place. After this reaction step, a steady state situation is visible in the diameter development, with an almost constant value. Here, the electron microscopy reveals that the reaction between indium and phosphine is completed, and thus the diameter is expected to be constant. However, recrystallization processes may still take place. For instance, 17 nm indium particles reacted with 8 ml/min phosphine are mainly amorphous at a reaction temperature of 422°C and are mainly monocrystalline at 519°C. Figure 10 shows an example of such a particle reacted at 519°C.

It is possible to get electron diffraction from these particles as shown in figure 11. The diffraction pattern constitutes clear evidence that the particles created are InP. Furthermore, x-ray spectroscopy on such particles reveals their composition to be close to 50% In and 50% P. No decisive electron microscopy observations were possible for particles created at even higher temperatures. The heavy decomposition of phosphine and the subsequent deposition of phosphorus on the sample grid makes a reasonable microscopy as well as interpretation of x-ray spectroscopy data impossible.

SUMMARY

We performed experiments in which ultrafine group-III metal particles of selected diameters, and under controlled conditions, reacted in a self-limited fashion with group-V hydrides to form monodisperse III-V nanocrystals. This approach, called aerotaxy, thus allows the formation of size-selected nanocrystals of a binary compound. Nanocrystals of almost any binary compound should be possible to produce using this fabrication route. Investigations have been carried out concerning the evolution of particle diameter of the primary metal particles with reaction temperature and hydride flow for the reaction of gallium droplets with arsine and indium droplets with phosphine. This analysis leads to a consistent picture and good understanding of the mechanisms involved. Investigations of produced nanocrystals by electron microscopy supports this picture. Our approach opens the possibility to produce a sufficient number of size-selected semiconductor nanocrystals and it will allow new types of self-assembly and control of quantum dots.

ACKNOWLEDGMENT

This work was performed within the Nanometer Structure Consortium in Lund and was supported by grants from NUTEK, NFR and TFR.

REFERENCES

- [1] P. C. Sercel, W. A. Saunders, H. A. Atwater, K. J. Vahala and R. C. Flagan, *Appl. Phys. Lett.* 61 (1992) 696.
- [2] S. Juen, K. F. Lamprecht, R. Rodrigues and R. A. Höpfel, *Solid-State Electronics* 37 (1994) 1163.
- [3] M. H. Ludwig, R. E. Hummel and S.-S. Chang, *J. Vac. Sci. Technol. B* 12 (1994) 3023.
- [4] L. Butler, G. Redmond and D. Fitzmaurice, *J. Phys. Chem.* 97 (1993) 10750.
- [5] A. J. Nozik, H. Uchida, P. V. Kamat and C. Curtis, *Israel J. Chem.* 33 (1993) 15.
- [6] D. G. Hendershot, D. K. Gaskill, B. L. Justus, M. Fatemi and A. D. Berry, *Appl. Phys. Lett.* 63 (1993) 3324.
- [7] S. S. Kher and R. L. Wells, in: *Proc. Molecularly Designed Ultrafine/Nanostructured Materials Symp.*, 1994, p 293.
- [8] A. A. Guzelian, J. E. B. Katari, A. V. Kadavanich, U. Banin, K. Hamad, E. Juban, A. P. Alivisatos, R. H. Wolters, C. C. Arnold and J. R. Heath, *J. Physical Chem.* 100 (1996) 7212.
- [9] W. Seifert, N. Carlsson, M. Miller, M.-E. Pistol, L. Samuelson and R. Wallenberg, *Progr. Crystal Growth Charact.* 33 (1996) 423.
- [10] O. V. Salata, P. J. Dobson, P. J. Hull and J. L. Hutchinson, *Appl. Phys. Lett.* 65 (1994) 189.
- [11] K. Deppert, J.-O. Bovin, J.-O. Malm and L. Samuelson, *J. Crystal Growth* 169 (1996) 13.
- [12] K. Deppert, I. Maximov, L. Samuelson, H.-C. Hansson and A. Wiedensohler, *Appl. Phys. Lett.* 64 (1994) 3293.
- [13] H. G. Scheibel and J. Porstendörfer, *J. Aerosol Sci.* 14 (1983) 113.
- [14] Detailed descriptions of the device can be found in: F. Bademosi, Ph. D. Thesis, University of Minnesota, Minneapolis, 1971; E. O. Knutson, Ph. D. Thesis, University of Minnesota, Minneapolis, 1971; B. Y. H. Liu and D. Y. H. Pui, *J. Colloid Interface Sci.* 47 (1974) 155.
- [15] W. C. Hinds, *Aerosol Technology: Properties, behavior, and measurement of airborne particles* (John Wiley & Sons, New York, 1982).
- [16] G. B. Stringfellow, *Organometallic Vapor-Phase Epitaxy: Theory and Practice* (Academic Press, San Diego, 1989).

- [17] C. J. Smithells, Smithells metals reference book (Butterworth-Heinemann, Oxford, 1992).
- [18] R. Blachnik and O. Madelung, in: Physics of Group IV Elements and III-V Compounds, Landolt-Börnstein, Vol. 17a, Ed. O. Madelung, M. Schulz and H. Weiss (Springer, Berlin, 1982) 247.
- [19] M. H. Magnusson, M.Sc. Thesis, Lund University, Lund, 1996.
- [20] K. Deppert and L. Samuelson, Appl. Phys. Lett. 68 (1996) 1409.
- [21] CRC Handbook of Chemistry and Physics (CRC Press, Boca Raton, 1984).

FIGURE CAPTIONS

- Fig.1: Schematic diagram of the aerotaxy process.
- Fig.2: Plots of the mean particle diameter of the reaction of gallium droplets with arsine for different temperatures. Particles of three different diameter, together with 2.69 ml/min arsine, were sent into the reaction furnace.
- Fig.3: Plots of the relative mean particle diameter with respect to room temperature of the reaction of gallium droplets with arsine for different arsine flows and temperatures. Particles with a diameter of 12 nm were into the furnace.
- Fig.4: Transmission electron micrograph of a GaAs particle.
- Fig.5: Electron diffraction pattern from an area covered with GaAs particles.
- Fig.6: Comparison of diameter and arsenic content as a function of temperature of the reaction of gallium droplets with arsine. The arsine flow was 5.38 ml/min, the initial particle diameter was 57 nm.
- Fig.7: Comparison of diameter and circularity of the reaction of gallium droplets with arsine as a function of reaction temperature. Reaction conditions as for fig. 6.
- Fig.8: Plots of the mean particle diameter of the reaction of indium particles with phosphine for different temperatures and varying phosphine flow.
- Fig.9: Transmission electron micrograph of an indium particle passing the reaction furnace at 153°C.
- Fig.10: Transmission electron micrograph of a InP particle reacted at 512°C.
- Fig.11: Electron diffraction pattern from an area covered with InP particles.

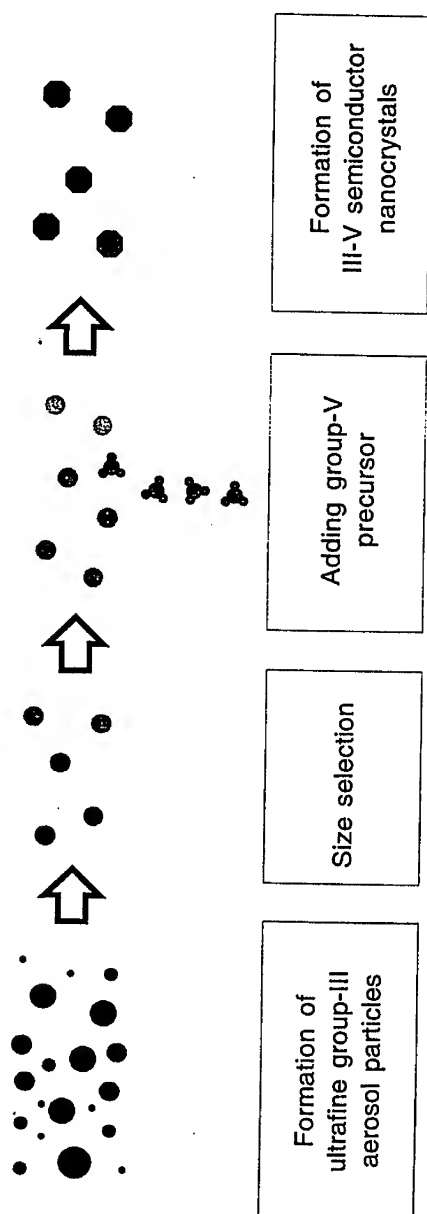


Fig.1

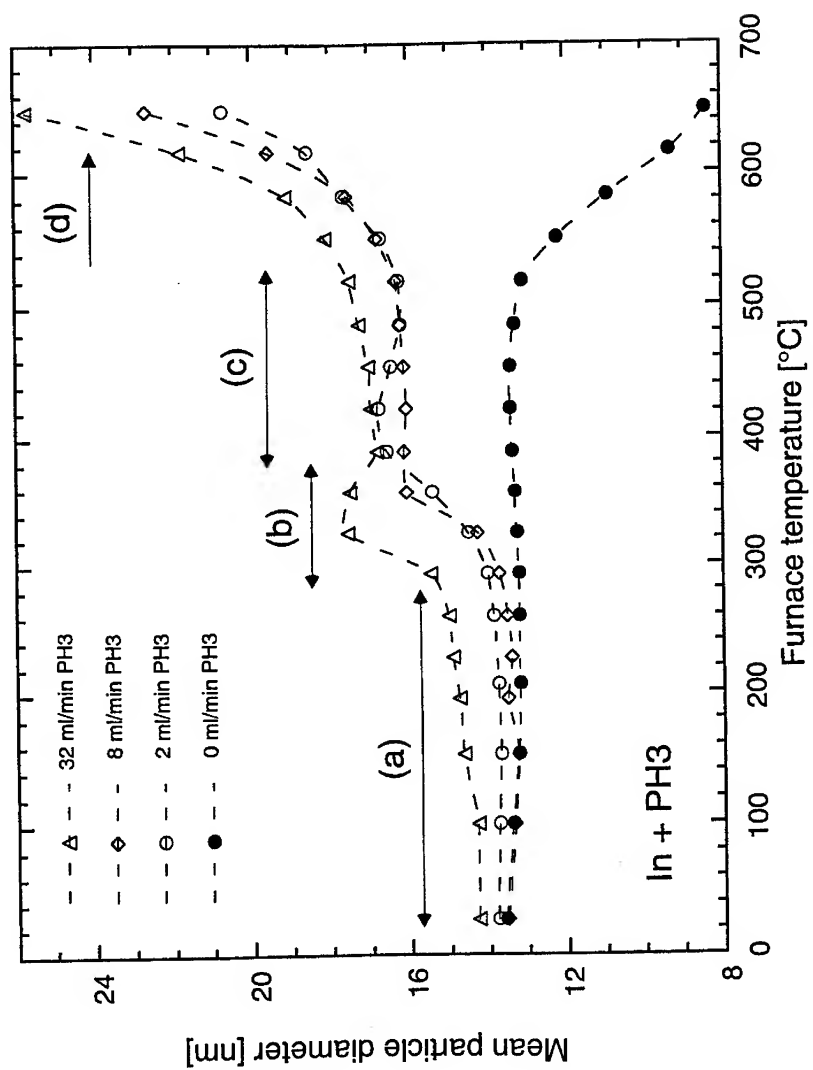


Fig.2

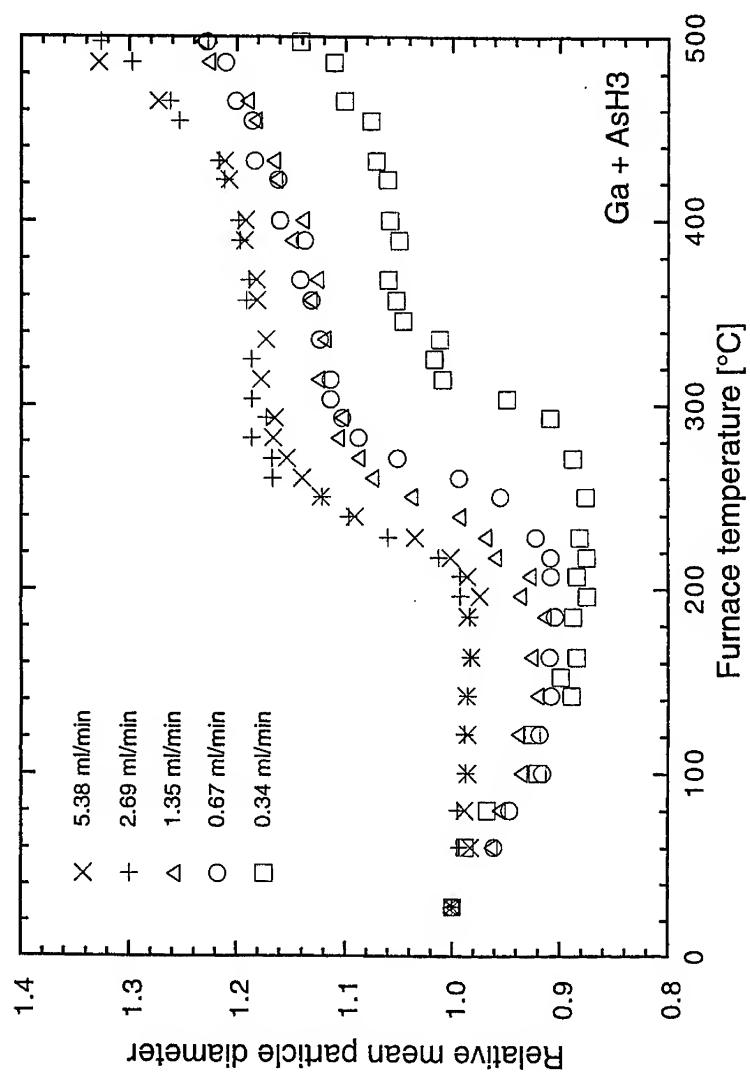


Fig.3

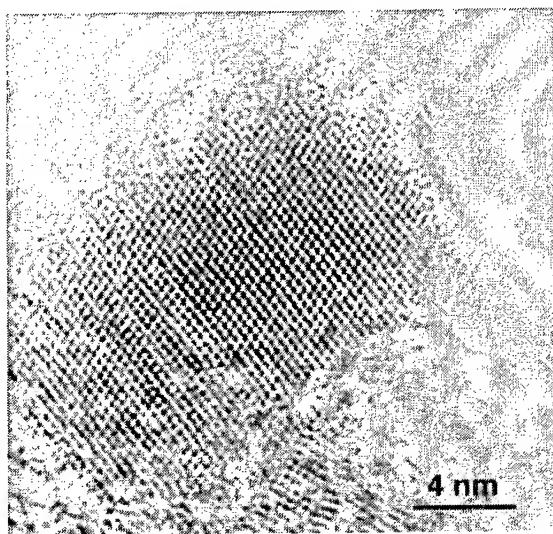


Fig. 4

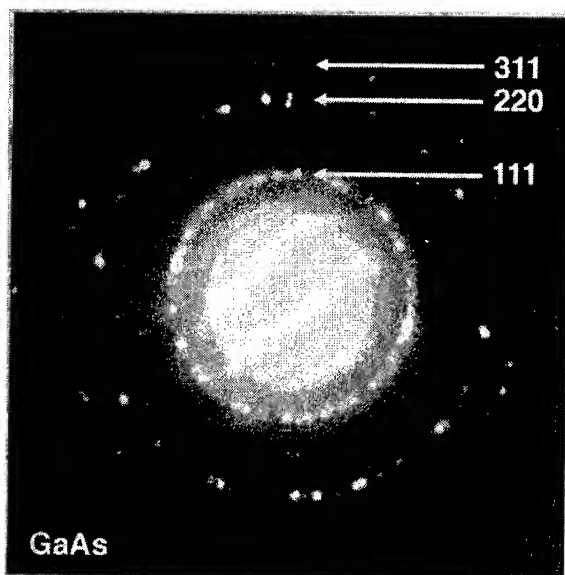


Fig.5

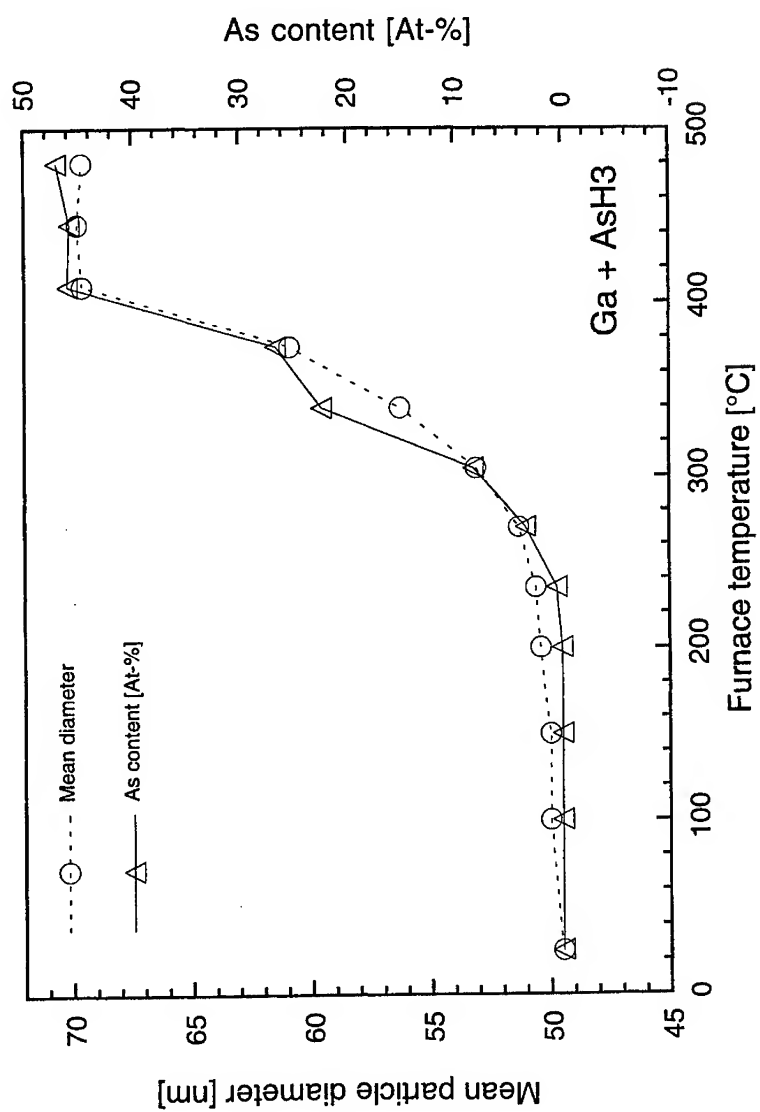


Fig.6

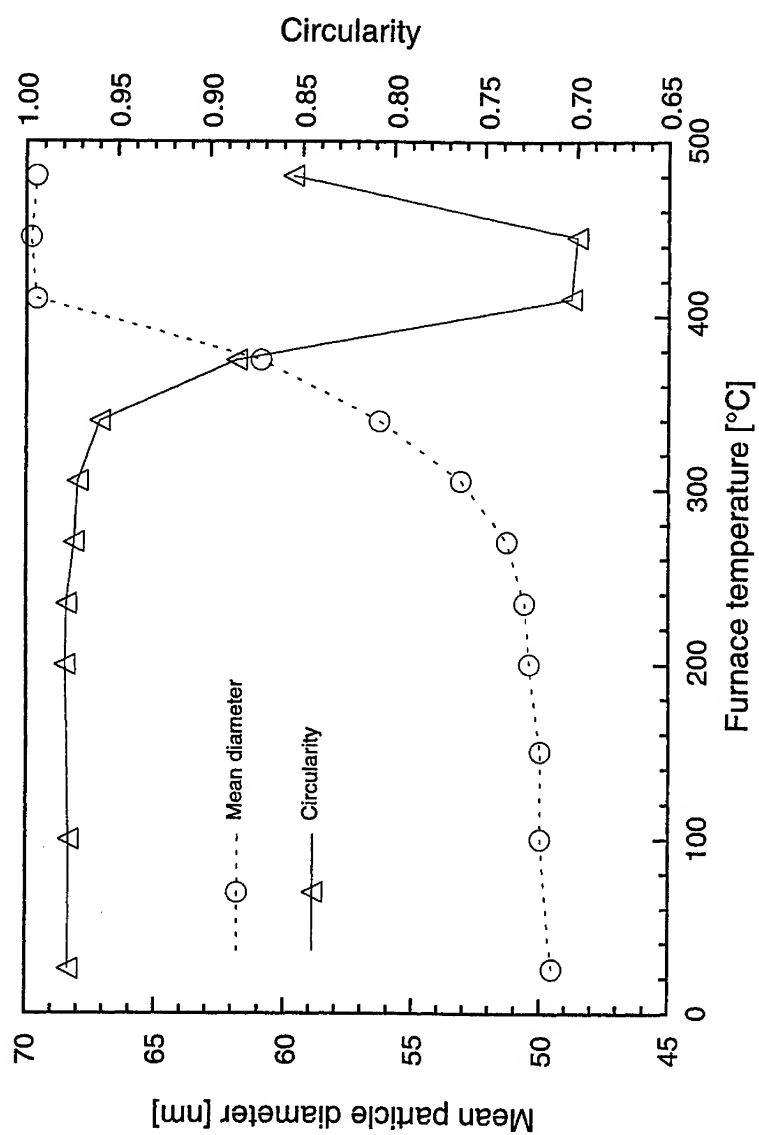


Fig.7

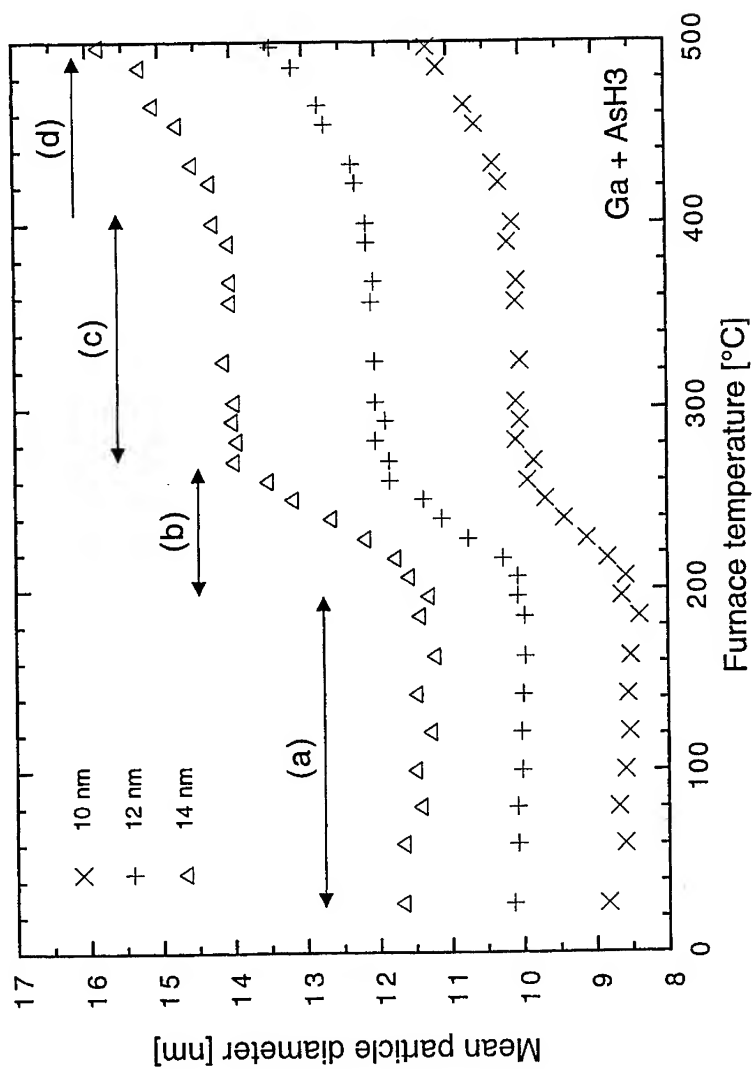


Fig.8

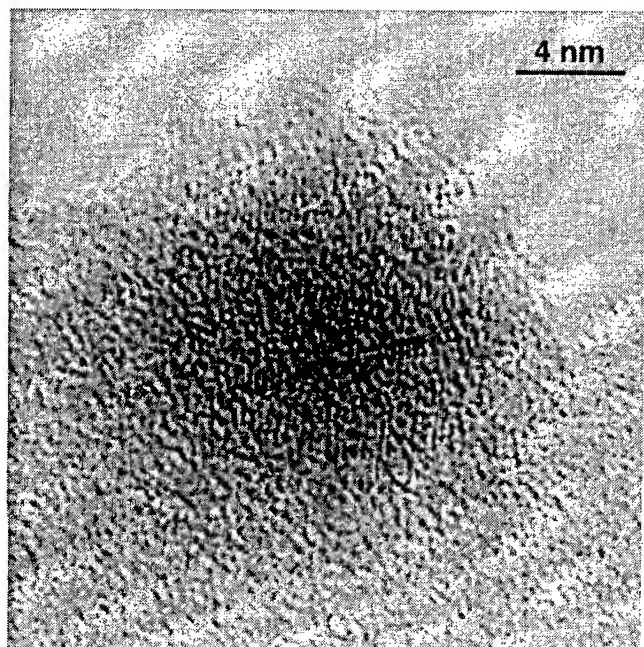


Fig.9

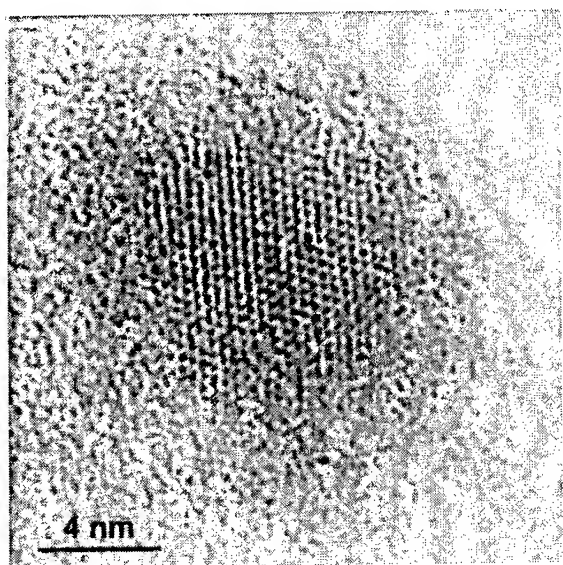


Fig.10

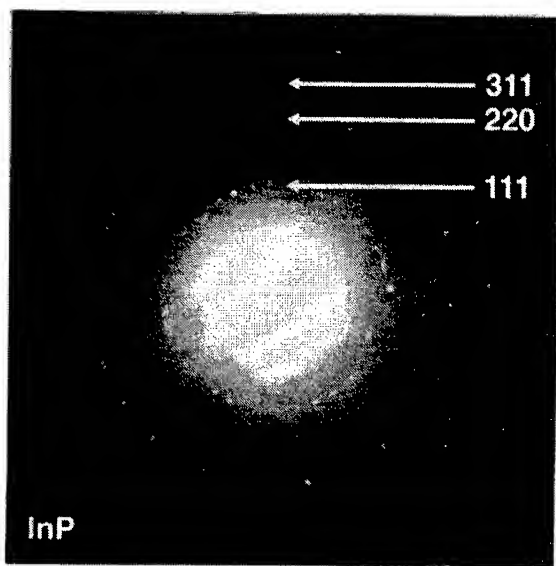


Fig. 11

GOLD IMPLANTED IN POROUS GLASS: SIZE AND SHAPE EFFECTS ON THE SURFACE PLASMON ABSORPTION OF GOLD NANOCRYSTALS

D. O. Henderson*, A. Ueda*, R. Mu*, Y. S. Tung*, M. Wu*, Jinli Chen*, Z. Gu*, C. W. White**, R. Zuhr**, Jane G. Zhu** and Xi Li***

*Chemical Physics Laboratory, Physics Department, Fisk University, Nashville, TN 37208

**Oak Ridge National Laboratory, Solid State Division, P. O. Box 2008, Oak Ridge, TN 37831

***Department of Chemistry Jilin University, Changchun, 130023, China

ABSTRACT

Gold is implanted into porous Vycor glass cylindrical substrates at an energy of 1.1 MeV and at doses of 1, 3, 6 and 10×10^{16} ions/cm². The Rutherford backscattering (RBS) measurements show that the gold concentration profile for the as-implanted samples is approximately Gaussian with a maximum appearing at 0.5 μm below the surface with a FWHH of $\sim 0.4 \mu\text{m}$. Subsequent annealing of the implanted samples at 1000–1100°C resulted in the appearance of a second peak attributed in the RBS spectra at $\sim 1.0 \mu\text{m}$ below the surface. The relative intensities of the two peaks (0.4 and 1.0 μm) are found to depend on the implanted ion dose. Peaks at 2.34 eV (530 nm) and 1.4 eV (800 nm) observed in the electronic spectra for the annealed samples and are attributed to the surface plasmon resonances along the minor and major axes of prolate ellipsoid gold nanocrystals. The infrared reflectance spectra for the as-implanted samples show an increase in intensity of the longitudinal and transverse optical modes that arise from ion beam induced densification of the porous glass. Thermal densification of the porous substrates is found to be anisotropic with shrinkage dominated in the radial direction as compared to the axial. This anisotropy, we propose is the mechanism for the formation of non-spherical gold particles that nucleate and grow during annealing (during annealing, the densification is dominated along the radial direction) and can also account for the two peaks observed at 530 and 800 nm in the electronic spectra.

INTRODUCTION

The optical properties of metal nanocrystals have been a subject of scientific investigation for many years. This interest can be traced to their intriguing optical response that differs from that of bulk material. This is particularly expressed in the visible to ultraviolet part of the spectrum where a collective mode, the surface plasmon resonance is observed for many metals.¹ Predictions of the surface plasmon resonance are based on Mie scattering theory² and effective medium theories (Maxwell-Garnett³, Bruggeman⁴, for e.g.) which indicate that the frequency of the surface plasmon resonance depends on the dielectric constant of the medium surrounding the nanocrystal. Mie theory also predicts that more than one resonance is observed for particles that are non-spherical. For a sphere, the geometrical depolarization factors L_i are degenerate with $L_i = 1/3$ ($\sum_i L_i = 1$). However, when the degeneracy is removed, say for a spheroid, ($L_x = L_y \neq L_z$), an additional mode is observed. Clearly then, particle shape is an important factor in controlling the frequency of the surface plasmon absorption. In addition, the intensity of the surface plasmon absorption depends on the volume filling fraction and the FWHH depends inversely on the nanocrystal size. Based on Mie and effective medium theories, the particle shape, volume filling fraction and particle size are the key factors that determine the lineshape and position of the surface plasmon resonance.

Interest in metal nanocrystals has also centered around their nonlinear optical properties, because they are expected to have a large third order nonlinear susceptibility, $\chi^{(3)}$.⁵ The large $\chi^{(3)}$

expected for these metal nanocrystals stems from the large polarization of metal nanocrystals that leads to an enhancement in $\chi^{(3)}$. In addition, the metal nanocrystals have ultrafast polarization relaxation times, which makes them attractive candidates for all optical switching and other devices based on optical bistability. Such potential devices strongly depend on the wavelength of the driving laser and consequently it is advantageous to be able to tune the position and intensity of the surface plasmon absorption into or near the resonance of the surface plasmon absorption for controlling the resonant or off-resonant enhancement of $\chi^{(3)}$.

To explore the possibility of tuning the surface plasmon resonance of metal nanocrystals, we have taken the approach to implant gold into porous Vycor glass substrates and exploit the anisotropy of glass densification during annealing to exercise control over particle shape. Using porous Vycor glass also allows for a simple method for increasing the volume filling fraction of the metal nanocrystals by as much as 30%, (the void volume of the porous glass) that occurs when the pores collapse upon thermal annealing.

EXPERIMENT

The porous Vycor substrates used for gold implantation were purchased from Corning. The average void space is 28% of the volume and the average pore diameter is 4 nm. The porous glass is composed of 96% SiO_2 , 3% B_2O_3 , 0.4% Na_2O and the remaining balance is predominately metal oxide impurities. The porous glass substrates were cleaned according to a standard procedure before ion implantation⁶. Gold ions were implanted at room temperature at an energy of 1.1 MeV and at doses of 1, 3, 6, and 10×10^{16} ions/cm². The samples were annealed in a tube furnace at temperatures between 800-1100°C in a 95% Ar + 5% H_2 atmosphere. Depth profiles of the implanted ions were determined from RBS measurements for the as-implanted and annealed samples using 2 MeV He^{2+} ions.

Infrared reflectance spectra were collected with a Bomem MB-102 interferometer at a resolution of 1 cm⁻¹. An angle of incidence of -7° is used for all reflectance measurements. Typically, coaddition of 100 interferograms were collected to acquire spectra in the 4000 - 200 cm⁻¹. All reflectance spectra were normalized against an aluminum mirror. The electronic spectra were recorded using a dual beam Hitachi 3501 spectrophotometer. All absorption measurements were normalized against virgin porous Vycor glass annealed under the same conditions as the implanted sample.

RESULTS

The results of the RBS measurements are shown in figs. 1a, 1b, 1c and 1d. The as-implanted samples show, for all ion doses, a well defined peak at 0.5 μm below the surface with a FWHH of $\sim 0.4 \mu\text{m}$. Annealing the samples at 900°C leads to little change in the depth profile. However, annealing the implanted substrates at 1000°C causes a decrease in the intensity of the peak located at 0.5 μm and the development of a new peak located at $\sim 1.0 \mu\text{m}$ below the surface. It is also evident that the relative intensities of the two peaks, $I_{1.0 \mu\text{m}}/I_{0.5 \mu\text{m}}$, decrease with ion dose, i.e., for the lowest dose sample, the peak at 1.0 μm is more intense than the peak located at 0.5 μm . Annealing the substrates implanted with 1 and 3×10^{16} ions/cm² at 1100°C causes the peak at 0.5 μm to completely vanish, while the peak at 1.0 μm increases. The samples implanted with 6 and 10×10^{16} ions/cm² do not exhibit such dramatic changes in their depth profiles, but do show a shift in the peak located near 0.5 μm to 0.6 μm . Also, the peak near 1.0 μm appears to shift to a depth of 1.1 μm for the two highest dose samples⁷.

The electronic spectra for the as-implanted samples together with the spectrum of the virgin porous glass are illustrated in fig. 2. The absorption in the region between 2 and 6 eV is found to increase with increasing ion dose and a peak begins to develop at 2.5 eV for the substrates dosed with 6 and 10×10^{16} ions/cm². The inset in the figure displays the region between 1.0 and 2.0 eV and reveals that a peak at 1.3 eV is beginning to develop for the two highest dose samples. Fig. 3 depicts the spectra for all ion doses annealed at 900°C. The peak near 2.5 eV that was weak for the 6 and 10×10^{16} ions/cm² for the as-implanted samples has now increased significantly and is also observed for the samples dosed with 1 and 3×10^{16} ions/cm². The 1.0 - 2.0 eV region shown in the inset shows that the peaks at 1.2 eV observed for the two highest dose samples have increased in intensity and additional peaks are present at 1.5 and 1.7 eV for the samples containing 3 and 1×10^{16} ions/cm². It is noteworthy that the development of the peaks near 1.3 eV correlate with the intensity increase of the peaks located at 2.5 eV. Fig. 4 shows the time dependence for the development of the 2.5 eV band for a sample implanted with 6×10^{16} ions/cm² and annealed at 900°C for up to 27 hours. This plot clearly demonstrates that the intensity of the peak increases with annealing time.

The infrared reflectance spectra are shown in fig. 5 for the virgin porous glass annealed at temperatures ranging from 800 to 1100°C. There is nearly a three-fold increase in the reflectivity in the 1250-900 cm⁻¹ region for the substrates annealed at 1000°C as compared to the reflectance of the unannealed virgin porous glass. The infrared spectra for the as-implanted samples are depicted in fig. 6 and show that there is an increase in the reflectance in the 1250-900 cm⁻¹ that is comparable to the reflectivity increase observed for the unimplanted porous glass annealed at 1000°C. The spectra of the annealed samples are shown in fig. 7. The reflectivity of the peaks near 1200, 1100 and 450 cm⁻¹ exhibit a further increase as compared to the as-implanted samples with a maximum value of ~55% for the highest dose sample.

DISCUSSION

Ion implantation has recently been developed as a technique for fabricating metal and semiconductor nanocrystals in dielectric matrices by implanting high ion doses. The as-implanted substrates, when annealed under the proper conditions, can lead to the formation of gold clusters by atom diffusion in the implanted layer. Diffusion of the clusters can later fuse to form precipitated metal colloids or semiconductor nanocrystals. We have reported on the optical properties of gold nanocrystals isolated in various matrices and now have extended this approach to investigate the use of porous Vycor glass as a host material. In all previous investigations the host matrix was completely densified, for example, implantation of Au into CaF₂ <111>⁸, Muscovite mica <100>⁹, MgO <100>¹⁰, Al₂O₃ <0001>¹¹ and optical grade fused silica¹². Annealing gold implanted substrates leads to very little, if any change in the density of the substrate and consequently the profile of the implanted layer shows no difference before and after the annealing treatments. On the other hand, porous Vycor glass has a 30% porosity and consequently, annealing these implanted substrates can lead to dramatic changes in the material density, that in turn may change the concentration profile of the implanted ions. Also, because of the porosity of the host, it is expected that diffusion of gold atoms in the pores during an annealing cycle may cause a significant redistribution of the gold concentration in the substrate. These are some of the considerations that must be taken into account when analyzing the optical properties and RBS of the implanted porous substrates.

We shall first discuss the infrared reflectance spectra of unimplanted, and annealed porous glass substrates. Three prominent peaks at 1220, 1100, and 450 cm⁻¹ are observed in the reflectance spectra for the unimplanted annealed samples and have previously assigned to the LO, TO and Si-O-

Si bending vibrations for fused silica. Based on comparison of the fused silica spectra with those for porous Vycor, we make the same assignments. The reflectivity of the unimplanted, annealed porous glass substrates are expected to increase as the material densifies when the annealing temperature is near 1000°C. It is at this temperature the pores begin to collapse and as a result the substrate increases in density. It is also known that when the porous glass densifies the effective refractive index increases due to the fact that amount of air (the lower index material) within the pores has decreased. Such an increase in density and effective refractive index would then account for the increased reflectivity that is observed in fig. 5 for the samples annealed at 1000 and 1100°C. The infrared spectra for the as-implanted samples also exhibit an increased reflectivity that is comparable to that observed for the virgin substrates that were annealed at 1000°C. This observation leads us to conclude that the ion implantation process leads to densification of the porous substrate in the implanted region. Annealing the implanted samples leads to a further increase in reflectivity of the three peaks observed in the 400-1200 cm⁻¹ region. This increase is 50% greater as compared to the virgin samples annealed at 1000°C and must also be attributed to an increase in the substrate density. It is significant to note that gold implantation in fused silica causes a decrease in reflectivity for the three peaks observed between 400 and 1300 cm⁻¹. This decrease has been interpreted in terms of ion beam damage that ruptures the Si-O-Si linkages that make up the glass network structure¹³. As a consequence, the number of oscillators that are sampled by the incident infrared beam are reduced which leads to a decreased reflectivity. The fact that the opposite trend is observed for porous glass is consistent with the assertion that the ion beam causes densification of the porous glass.

The electronic spectra of metal nanocrystals often have resonances in the ultraviolet-visible part of the spectrum and are attributed to the surface plasmon absorption. The energy of the absorption depends on the dielectric constant of the surrounding medium and on the particle shape, while the intensity of the absorption depends on the volume filling fraction of the metal nanocrystals.

The electronic spectra for the as-implanted samples show a peak that begins to develop at 2.5 eV as the ion dose increases and a further increase in intensity is observed for the annealed samples. The energy of this absorption is very close to that observed for the surface plasmon absorption observed for gold nanocrystals isolated in fused silica¹² and therefore we attribute this band to the surface plasmon resonance of gold nanocrystals. However, the band between 1.3 and 1.8 eV observed for gold implanted in the annealed porous glass substrates is not present or is very weak for gold implanted in fused silica and must be assigned.

The particle shape of metal nanocrystals is a critical factor in determining the position of the surface plasmon absorption. It is known from Mie theory that spherical metal particles embedded in a dielectric medium give a single peak in the UV-Vis part of the spectrum which is assigned to the first order term (dipole excitation) in the multipole expansion. However, departure from spherical symmetry removes the degeneracy of the geometrical depolarization factors, L_i with $i = a, b, c$ ($L_a = L_b = L_c$ for sphere) and activates new resonances along the principal axes when $L_a \neq L_b \neq L_c$, i.e. for a general ellipsoid. It is conceivable that the peak that appears near 1.3 eV after annealing could arise from gold nanocrystals that have a symmetry lower than that of a sphere. One possible mechanism that could account for the reduced symmetry of the gold nanocrystals is the anisotropic densification of the porous substrate that occurs during annealing. That is, the as-implanted samples have been densified along the ion beam axis, and when the substrates are thermally annealed, there is densification that occurs principally along the axes normal to the ion beam direction. Under these conditions, it is expected that the spheres would be deformed into prolate ellipsoids and could

therefore account for the appearance of the new peak observed at 1.3 eV. Other possible explanations accounting for the appearance of the peak at 1.3 eV such as particle aggregation, or the growth of a continuous distribution of randomly oriented ellipsoids are not likely since these processes lead to broad band absorption with no well defined peaks and are therefore considered as an unlikely interpretation for the 1.3 eV peak.

In order to further investigate the plausibility of the attributing the peak near 1.3 eV to a dipole mode of the surface plasmon resonance along one of the principal axes of a prolate ellipsoid, we have modeled our experimental data using Maxwell-Garnett effective medium theory for a gold prolate ellipsoid embedded in an SiO₂ matrix. For a spherical particle, the absorption coefficient is given as

$$k = \frac{18\pi f \epsilon_m^{3/2} \epsilon_2}{\lambda (2\epsilon_m + \epsilon_1)^2 + \epsilon_2^2} \quad (1)$$

where k is the absorption coefficient, f is the volume filling fraction of the gold nanocrystals, ϵ_m is the dielectric function of silica, ϵ_1 and ϵ_2 are the real and imaginary parts of the dielectric function for gold. From eqn. 1, it is clear that k will be a maximum (the dipole surface plasmon resonance) when $-2\epsilon_m = \epsilon_1$. However, for a non-spherical particle, depolarization factors along the principal axes must be included in the form

$$\epsilon = -\frac{1 - L_i}{L_i} \epsilon_m \quad (i=a,b,c) \quad (2)$$

This expression indicates that additional resonances will occur when $L_i(L_i - 1)\epsilon_m = 0$. Applying eqns. 1 and 2 we have simulated the experimental spectra using depolarization factors for a prolate ellipsoid with a geometrical aspect ratio of 0.23 for the principal axes ($a=b \neq c$). The model fit is illustrated fig. 8 and shows good agreement with the experimental results and successfully reproduces the two modes that would be expected for a prolate ellipsoid. In addition, the resonance occurring near 1.3 eV is very close to that reported for prolate gold ellipsoids with an aspect ratio of 0.17¹⁴ indicating that 0.23 is a reasonable value for the geometrical aspect ratio. However, the aspect ratio of 0.23 appears to be too small if it is compared to the value of 0.5 estimated from compressing a sphere by 20% into a prolate ellipsoid while conserving the volume. Based on this observation, it is expected that another mechanism is also operative in forming the prolate ellipsoids. We suggest that the pore acts as a confining geometry, that in part, restricts the particle shape during growth by atom or very small cluster diffusion. The geometrically confined particle shape is expected to be rod-like and is consistent with model that treats the gold particles as prolate ellipsoids.

CONCLUSION

Annealing of the gold implanted porous Vycor glass produces peaks at 2.5 and 1.3 eV. The peaks are assigned to the surface plasmon absorption of gold prolate ellipsoids embedded in the Vycor matrix. It is suggested that anisotropic densification of the implanted Vycor glass together with the pore acting as a confining geometry leads to the formation of prolate ellipsoidal gold nanocrystals.

The electronic spectra are simulated by Maxwell-Garnett effective medium theory for prolate ellipsoids in silica matrix and give a good fit to the experimental. The quality of the fit supports the claim that the isolated gold nanocrystals are of a prolate ellipsoid shape.

ACKNOWLEDGMENTS

The work at Fisk was supported under DOE Grant No. DE-FG05-94ER45521. Oak Ridge National Laboratory is managed by Lockheed Martin Energy Research Corp. For U.S. Department of Energy under contract number DE-AC05-96OR22464.

REFERENCES

1. J. A. Creighton and D. G. Eadon, *J. Chem. Soc. Faraday Trans. 87*, 3881 (1991).
2. G. Mie, *Ann. Phys.* 25, 377 (1908).
3. J. C. Maxwell Garnett, *Phil. Trans. Roy. Soc. (London) A* 203, 385 (1904).
4. D. A. G. Bruggeman, *Ann. Physik* 5. Folge 24, 636 (1935).
5. R. F. Haglund, R. H. Magruder, S. H. Morgan, D. O. Henderson, R. A. Weller, L. Yang, and R. A. Zuhr, *Nucl. Instr. & Meth. B* 65, 405 (1992).
6. R. Mu, F. Jin, S. H. Morgan, D. O. Henderson and E. Silberman, *J. Chem. Phys.* 100, 7749 (1994).
7. A detailed analysis of the RBS results in terms of diffusion of gold in porous Vycor glass will be presented in a forthcoming publication.
8. D. O. Henderson, Y. S. Tung, A. Ueda, R. Mu, Y. Xue, C. Hall, W. E. Collins, C. W. White, R. A. Zuhr, J. G. Zhu, P. W. Wang, *J. Vac. Sci. Technol. A* 14, 1199 (1996).
9. D. O. Henderson, R. Mu, A. Ueda, Y. S. Tung, C. W. White, R. A. Zuhr, and J. G. Zhu, *J. Non-cryst. Solids* 205, 788 (1996).
10. A. Ueda, R. Mu, Y. S. Tung, D. O. Henderson, C. W. White, R. A. Zuhr, J. G. Zhu, and P. W. Wang, *Materials Science Forum* 239-241, 675 (1997).
11. D. O. Henderson, R. Mu, Y. S. Tung, M. A. George, A. Burger, S. H. Morgan, C. W. White, R. A. Zuhr, and R. H. Magruder, *J. Vac. Sci., Technol. B* 13, 1198 (1995).
12. C. W. White, J. D. Budai, J. G. Zhu, S. P. Withrow, D. M. Hembree, D. O. Henderson, A. Ueda, Y. S. Tung, and R. Mu, *Mat. Res. Soc. Symp. Proc.* 396, 377 (1996).
13. D. O. Henderson, S. H. Morgan, R. Mu, W. E. Collins, R. H. Magruder, C. W. White, and R. A. Zuhr, *Mat. Res. Soc. Symp. Proc.* 316, 451 (1994).
14. M. J. Bloemer, M. C. Buncick, R. J. Warmack, and T. L. Ferrell, *J. Opt. Soc. Am. B* 5, 2552 (1988).

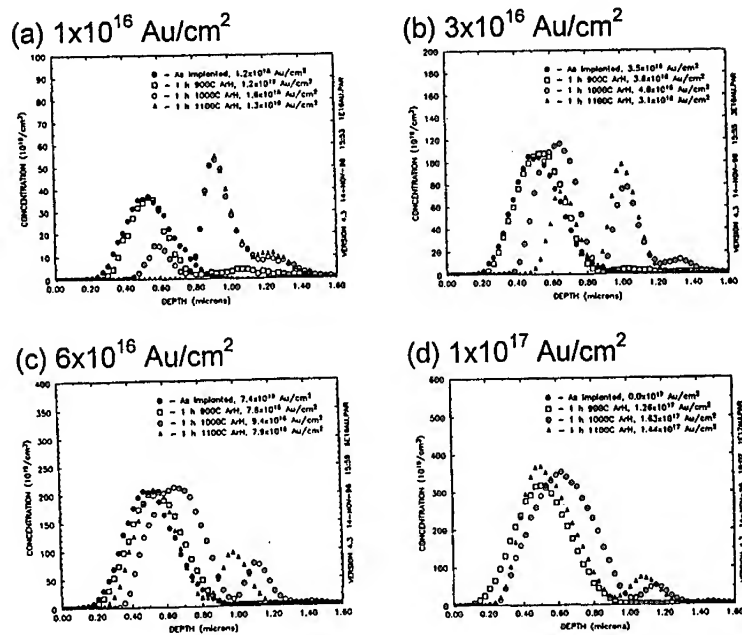


Figure 1. Rutherford backscattering spectra for gold as-implanted in porous Vycor and after annealing at different temperatures as indicated in the figure.

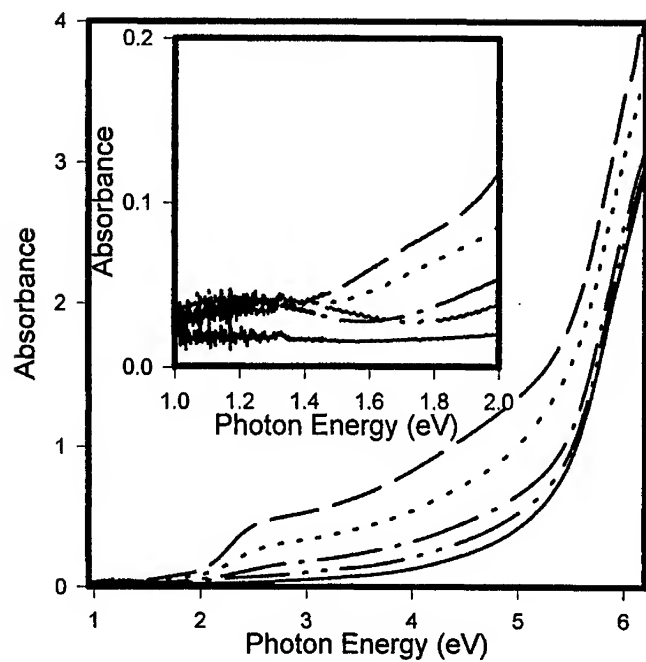


Figure 2. Absorbance spectra for various doses of gold as-implanted in porous Vycor glass .
 Virgin Vycor (—); 1×10^{16} ions/cm² (—•—•—); 3×10^{16} ions/cm² (—•—•—);
 6×10^{16} ions/cm² (•••••); 1×10^{17} ions/cm² (—•—•—).

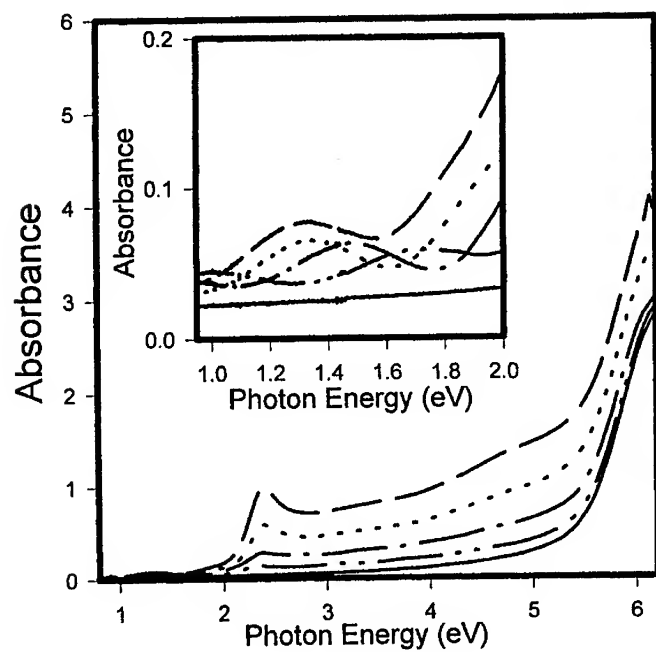


Figure 3. Absorbance spectra for gold implanted in porous Vycor glass at various doses and annealed at 900C. Virgin Vycor (—); 1×10^{16} ions/cm² (— · — · —); 3×10^{16} ions/cm² (— · — · —); 6×10^{16} ions/cm² (· · · · ·); 1×10^{17} ions/cm² (— · — · —). The inset shows the peak attributed to the surface plasmon resonance occurring along the major axis of the ellipsoid.

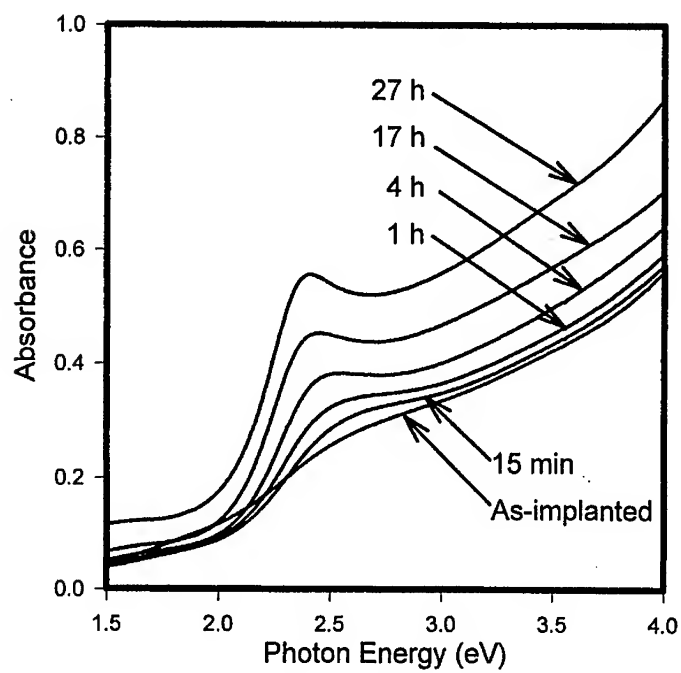


Figure 4. Spectra showing the time dependent development of surface plasmon absorption of gold implanted in porous Vycor glass at dose of 6×10^{16} ions/cm².

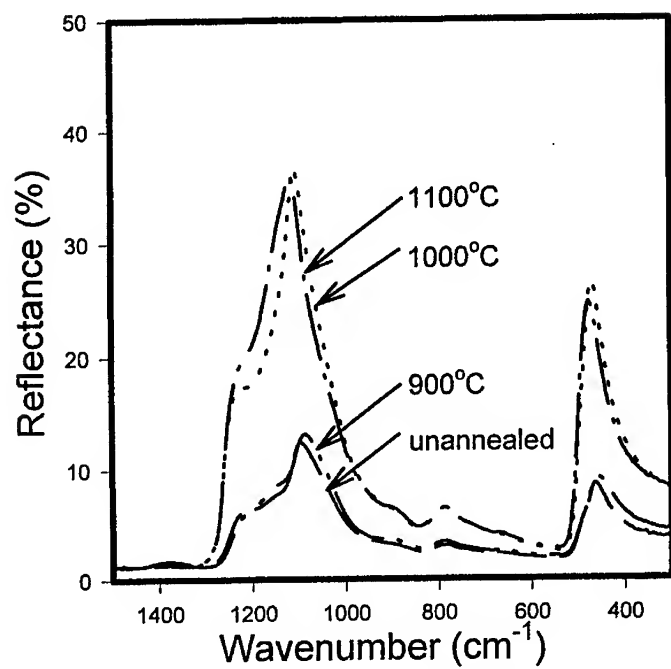


Figure 5. Infrared reflectance spectra of virgin porous Vycor glass annealed at temperatures from 900°C to 1100°C

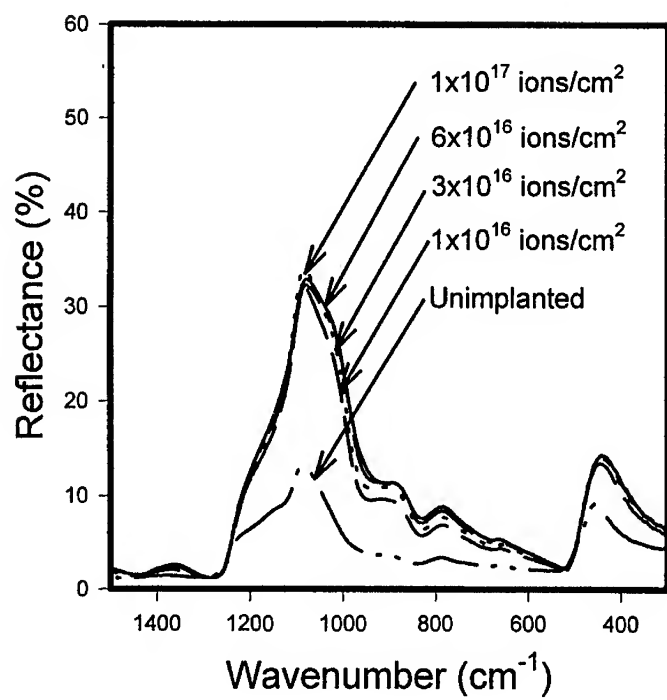


Figure 6. Infrared reflectance spectra for as-implanted porous Vycor glass at different ion doses.

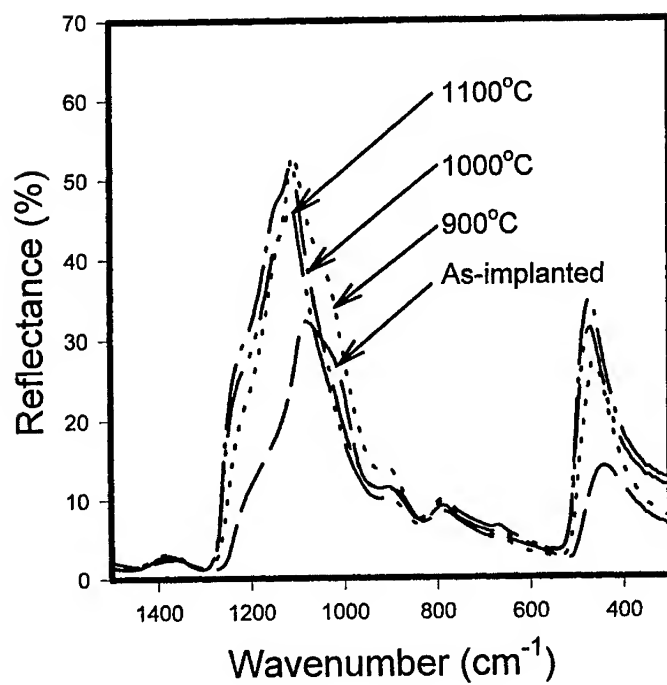


Figure 7. Infrared reflectance spectra for porous Vycor glass implanted with 1×10^{17} ions/cm² and annealed from 900°C to 1100°C.

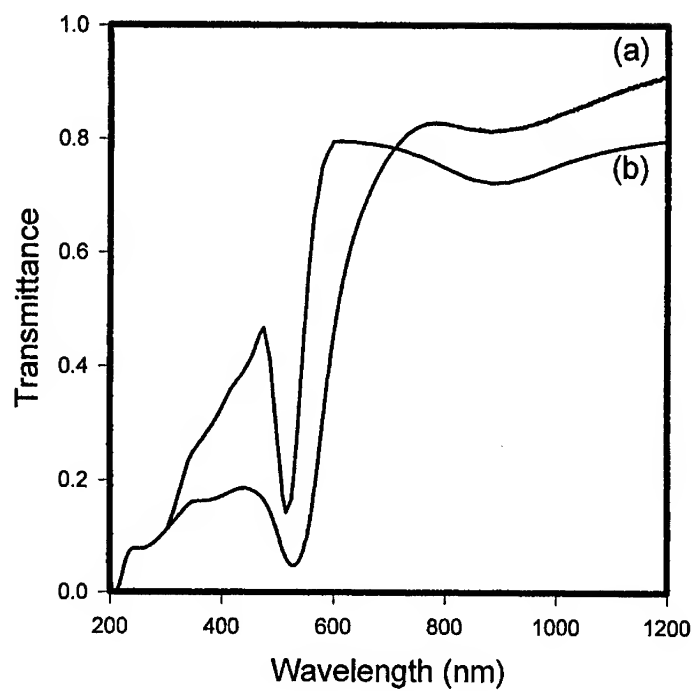


Figure 8. Comparison of the experimental (a) and simulated (b) spectra using Maxwell-Garnet theory for a gold prolate ellipsoid embedded in a silica matrix.

Quantum Dots: Optical Properties

OPTICAL PROPERTIES OF ETCHED AND SELF-ASSEMBLED QUANTUM DOTS IN A MAGNETIC FIELD

Pawel Hawrylak
Institute for Microstructural Sciences
National Research Council of Canada
Ottawa, K1A 0R6, Canada
(May 27, 1997)

Theory of optical properties of etched and self-assembled quantum dots containing electrons or excitons is reviewed. Optical processes such as infrared absorption, photoluminescence, and inelastic light scattering are discussed. The ground state properties and charge and spin excitations are obtained through Hartree, Hartree-Fock, and exact diagonalization techniques. The calculations are compared with existing experiments.

I. INTRODUCTION

Optical probes such as infrared absorption, photoluminescence, and inelastic light scattering provide useful information about low dimensional semiconductor structures. The reduction in size of electronic and opto-electronic devices leads to Quantum Dot (QD) based single-electron transistors (QSET) [1] and single-exciton lasers (QDL) [2]. Because of reduced dimensionality electrons neither can avoid each other nor their number is sufficiently large for statistical behaviour to take effect. Therefore the interaction among carriers in QD is of paramount importance. We use Hartree, Hartree-Fock, and exact diagonalization methods to study ground state properties and elementary excitation in quantum dots as a function of the number of free carriers N . Varying N often leads to drastic changes in electronic and optical properties of QSET and QDL. To understand these changes it is necessary to calculate the coupling of elementary excitations to external probes. In the intraband far infrared spectroscopy absorption of photons couples to the center of mass motion, and through boundaries or imperfections, to relative motion of electrons. The relative motion is determined by electron-electron interactions. In interband spectroscopy excess electrons interact with an exciton. An electron component of an exciton can be viewed as a charge and spin excitation of the electron system. In inelastic light scattering one probes directly charge and spin density excitation spectrum of a confined electron gas. In a quantum dot laser adding/removing an exciton can be viewed as a one-particle probe of the many-exciton excitation spectrum.

We review here briefly our work on electrons and excitons in quantum dots and their coupling to optical probes. The calculated response functions are compared with available far infrared, photoluminescence and electronic Raman experiments.

II. ETCHED AND GATED DOTS IN A MAGNETIC FIELD

In gated and etched nanostructures with significant density of surface states, trapped electrons produce long range potentials. The effective confining potential is smooth and weak, i.e. of the order of few meV. The effects of electron-electron interactions and magnetic fields are significant [1,3,4]. One can think of electrons as forming quantum Hall droplets, with magnetic field driving the droplets through different filling factors. In the filling factor regime $1 \geq \nu \geq 2$ interesting behavior of the spin polarization is expected [5]. In the filling factor regime $\nu = 1$ the system is expected to form a chiral Fermi liquid. The transitions between different filling factors

in this regime involve reconstructions of edges through condensation of edge-magnetorotons [6]. The edge reconstruction is expected to lead to new absorption lines [6]. In the fractional quantum Hall regime the low energy excitations of the droplet are governed by the chiral Luttinger liquid theory [5,7] with non-Fermi liquid behaviour.

A. SINGLE ELECTRON CAPACITANCE SPECTROSCOPY

Single electron capacitance spectroscopy (SECS) was developed by Ashoori et al. [4] to measure changes in capacitance of a single quantum dot due to the addition of a single electron. Hence SECS measures the dependence of the chemical potential of the confined electron gas on the number of electrons N . SECS was capable of detecting changes in the spin and angular momentum of the ground state of few-electron complexes [3].

B. MAGNETOOPTICAL MEASUREMENT OF GROUND STATE ENERGY

The magnetic field induced transitions of quantum Hall droplets imply changes in the ground state. It turns out that the ground state energy can be measured optically by measuring the mean photon energy $\langle \omega \rangle$ of the acceptor related recombination line [6,8,9]. Experiments in this direction have been reported by Patel et al. [9].

C. RAMAN SCATTERING OFF DEEP ETCHED MODULATION DOPED DOTS

Inelastic light scattering measures the excitation spectrum of a QD [10-13] and, in principle, can provide direct evidence of the discrete nature of excitations in zero-dimensional (0D) systems. The electron-electron interactions play a significant role in determining these excitations. For example, in a strong magnetic field the gap in the excitation spectrum of the Hall droplet is determined by electron-electron interactions. The origin of the gap is similar to the origin of the gap in the incompressible Laughlin fluid [3]. Changing the magnetic field leads to a collapse of the gap at special values of the magnetic field i.e. to a compressible Hall droplet. One could in principle observe this behaviour as soft modes in Raman spectra [10]. However, the wavelength of the perturbation necessary to excite electrons of the droplet across the gap has to be much smaller than the physical size of the droplet. In typical Raman experiments on 2DEG this wavelength was of the order of few thousand angstroms i.e. much larger than the size of the droplet. Nevertheless, a number of groups [11,12] have undertaken inelastic light scattering studies of quantum dots. Strentz et al. [11] measured the resonant electronic Raman spectrum from shallow etched QD's with sizes down to 400nm. Lockwood et al. [12] measured the resonant electronic Raman spectrum of deep etched modulation-doped QD's with sizes down to 100nm and in a magnetic field. Both groups attributed observed structures in the Raman spectra to the 0D density of states. These observations were possible due to patterning, and hence surface roughness, of the samples.

The samples studied by Lockwood et al. [12] were GaAs/GaAlAs quantum dots prepared in the form of disks of radius R . Disks with radii in the range $50\text{nm} < R < 100\text{nm}$ were etched from a modulation doped multi-quantum well structure [13] with carrier density $n_s = 8.5 \cdot 10^{11}\text{cm}^{-2}$. The near-resonant electronic Raman spectra (in a backscattering geometry) were measured in magnetic fields up to 12 T at 2K.

1. SELF-CONSISTENT ELECTRONIC STATES IN A MAGNETIC FIELD

To understand the measured electronic Raman spectra we need to know the electronic states. To calculate the wavefunctions, energies and Single Particle Excitation (SPE) spectra we approximate the quantum dots as disks of radius R and thickness t , confined by infinite potential barriers. The positive charges of ionized donors are modeled as a disk with uniform density, separated by a distance d from the plane of the dot. For such a high density multiple-quantum well system, we assumed that electrons trapped in surface states represent a very small fraction of the free electrons.

We start by considering the Hamiltonian of N electrons in the conduction band, moving on a 2D disk in the presence of a perpendicular magnetic field:

$$H = \sum_{i=1}^N \left[\frac{1}{2m^*} (\vec{p}_i + \frac{e}{c} \vec{A}(\vec{r}_i))^2 + V_c(\vec{r}_i) + V_+(\vec{r}_i) + g\mu S_z^i \right] + \sum_{i < j, i,j=1}^N V_{ee}(|\vec{r}_i - \vec{r}_j|) \quad (1)$$

The vector potential is given in the symmetrical gauge, g is the effective g-factor, m^* is the effective mass, μ_B is the Bohr magneton, S_z^i is the z-component of the i th particle spin, and $V_c(\vec{r}_i)$, $V_+(\vec{r}_i)$, and $V_{ee}(|\vec{r}_i - \vec{r}_j|)$ are the confining potential, the potential produced by the positive charge, and the electron-electron interaction potential.

In the Hartree approximation the many electron Hamiltonian is replaced by a Hamiltonian of a single particle moving in a self-consistent potential V_H :

$$H = \left[\frac{1}{2m^*} (\vec{p} + \frac{e}{c} \vec{A}(\vec{r}))^2 + V_c(\vec{r}) + V_H(\vec{r}) + g\mu S_z \right], \quad (2)$$

where Hartree potential is determined by the electron density $n_-(r)$ and a positive charge density $n_+(r)$ as

$$V_H(\vec{r}) = \int d\vec{r}' [V_{ee}(\vec{r} - \vec{r}') n_-(\vec{r}') - V_+(\vec{r} - \vec{r}') n_+(\vec{r}')], \quad (3)$$

and density is given in terms of occupied eigenstates Ψ_ν of Eq.2 as $n_-(r) = \sum_{\nu, occ} |\Psi_\nu(r)|^2$. Hartree procedure is implemented for a disk of radius R with $V_c(r < R) = 0$ and $V_c(r > R) = \infty$. The energies and distances are measured in relative Rydbergs, $Ry = m^* e^4 / 2\hbar^2 \epsilon^2$, and in the relative Bohr radius, $a_0 = \epsilon \hbar^2 / m^* e^2$, units.

The Hamiltonian of the Hartree particle is rotationally invariant, therefore we seek a solution for each angular momentum channel in the form $\Psi(\rho, \theta) = f(\rho) \frac{e^{im\theta}}{\sqrt{2\pi}}$, where $f(\rho)$ is the solution of the radial Schrodinger equation

$$\left[-\frac{1}{\rho^2} \frac{d}{d\rho} \rho \frac{d}{d\rho} + \frac{m^2}{\rho^2} + \gamma m + \frac{1}{4} \gamma^2 \rho^2 + V_H(\rho) \right] f(\rho) = E f(\rho), \quad (4)$$

with $\gamma = \omega_c / 2Ry$, $m = -\infty, \dots, 0, \dots, +\infty$, $0 < \rho < R$, and boundary conditions requiring $f(\rho = 0) = \text{finite}$ and $f(\rho = R) = 0$.

From the expansion of the plane wave $e^{ikr} = \sum_{m=-\infty}^{m=+\infty} i^m e^{im\theta} J_m(k\rho)$ the normalized eigenstates of the single particle Hamiltonian in zero magnetic field in a given angular momentum channel m can be written as:

$$f_{m,i}(\rho) = \frac{\sqrt{2}}{R |J_{m+1}(k_i R)|} J_m(k_i \rho). \quad (5)$$

Here $k_i R$ are the zeros of the m -th Bessel function ($J_m(k_i R) = 0$), and the energy spectrum in a given channel is given by $E_i = k_i^2$. The eigenstates of the radial equation for $m < 0$ are the

same as for $m > 0$ and the energy spectrum $E_{m,\nu}$ for $m < 0$ is related to the energy spectrum for $m > 0$ by $E_{m<0,\nu} = E_{m>0,\nu} - 2\gamma m$.

The eigenfunctions of Eq.4 are written as a combination of the non-interacting eigenfunctions for a given angular momentum channel m :

$$\Psi_\nu(\rho) = \sum_i C_i^\nu f_{m,i}(\rho), \quad (6)$$

where ν is the index of the self-consistent states. The coefficients C_i^ν satisfy a self-consistent equation for each angular momentum channel:

$$[E_i + \gamma m]C_i^\nu + \sum_{i'} \langle m, i | \frac{1}{4}\gamma^2 \rho^2 + V_H(\rho) | m, i' \rangle C_{i'}^\nu = E_\nu C_i^\nu. \quad (7)$$

The Hartree potentials depend on the actual charge density in the disk, with matrix elements due to the electron-electron repulsion given by:

$$\langle m, i | V_H^{ee} | m, i' \rangle = \sum_\sigma \sum_{jj'} \sum_{l, \nu_l} \langle m, i | V_{ee} | l j', m i' \rangle C_{i,j}^\nu C_{i',j'}^\nu g_{l, \nu_l, \sigma} n_{l, \nu_l, \sigma}, \quad (8)$$

where $g_{l, \nu_l, \sigma}$ and $n_{l, \nu_l, \sigma}$ are the degeneracies and occupations of exact states ν_l .

The Coulomb matrix elements $\langle m, i | V_{ee} | l j', m i' \rangle$ can be evaluated using an expansion of the Coulomb potential in terms Bessel functions

$$\frac{1}{\sqrt{|\vec{r} - \vec{r}'|^2 + t^2}} = \int_0^\infty \frac{dq q}{2\pi} v(q) e^{-qt} \sum_m e^{im(\theta - \theta')} J_m(q\rho) J_m(q'\rho) \quad (9)$$

where $v(q) = \frac{2\pi\epsilon^2 e^{-qt}}{\epsilon_0 q}$ is the Fourier transform of the Coulomb interaction (including finite well thickness $\approx t$) and matrix elements are given in terms of integrals over dimensionless variable Q :

$$\langle m, i | V_{ee} | l j', m i' \rangle = \frac{2}{R} R/t \int_0^\infty dQ e^{-Q} G_{m,m}^{i',i}(QR/t) G_{l,l}^{i',i}(QR/t). \quad (10)$$

The form factor $G(Q)$ is given in terms of an integral over Bessel functions:

$$G_{m,m}^{i',i}(QR/t) = \frac{2}{J_{m+1}(k_i R) J_{m+1}(k_i R)} \int_0^1 dx x J_m(k_i R x) J_m(k_i R x) J_0(QR/t x). \quad (11)$$

Coulomb matrix elements are integrated via Gauss-Legendre quadrature over a set of 10 special points Q_i using matrix $G_{m,m}^{i',i}(Q_i R/t)$ as an input. The matrix $G_{m,m}^{i',i}(Q_i R/t)$ is evaluated numerically on a set of 10 special points. The integrand is rapidly oscillating and the integration consists of identifying all zeros of the integrand and using standard IMSL adaptive routines to integrate between zeros.

The electron-positive background interaction matrix elements are evaluated for a disk of positive charge separated by a distance d from the plane of the disk:

$$\langle m, i | V_+ | m, i' \rangle = \frac{2}{R} (R/t) \int_0^\infty dQ e^{-Q} G_{m,m}^{i',i}(QR/t) e^{(-Q(d/t-1))} G_+(QR/t), \quad (12)$$

where

$$G_+(QR/t) = 2\pi R^2 \int_0^1 dx x n_+(x) J_0(QR/t x). \quad (13)$$

The Coulomb matrix elements $\langle m, i | V_+ | m, i' \rangle$ are evaluated using the same numerical procedure as described above.

D. RESULTS AND SPE SPECTRA

In numerical results the following parameters were used: $R = 70\text{nm}$, $N_e = 124$, $d = 30\text{nm}$, $t = 8\text{nm}$. These parameters correspond to a disk with diameter of 140nm and density $n_s \approx 8 \cdot 10^{11}\text{cm}^{-2}$. In calculating Coulomb interactions we have also assumed a uniform dielectric constant of GaAs and neglected the effects due to image charges associated with the semiconductor-vacuum interface.

In Figure 1 we show the calculated Hartree potential V_H and Hartree density $n(r)$. Due to the spatial separation of the positive background from the disk the electron charge density is depressed inside the disk and enhanced at the edges of the disk. The Hartree potential is therefore repulsive in the center of the dot, a situation very similar to Hartree potentials in modulation doped quantum wells.

The calculated Hartree density of states for different values of the magnetic field is shown in Fig. 2. The Hartree energy spectrum is discrete and hence the 0D density of states (DOS) consists of a series of peaks. For $B = 0$ there is a typical single particle energy spacing $\delta E \approx 0.1 - 0.5\text{meV}$ within each peak and an overall arrangement of peaks in the DOS reminiscent of the shell structure of atoms, with a typical energy spacing of $\approx 5\text{meV}$.

When compared with the DOS of noninteracting electrons we find that the modulation is enhanced by electron-electron interactions. This is due to the spatial separation of the positive background from the disk. Since electrons repel each other very effectively, the electron charge density is depressed inside the disk and enhanced at the edges of the disk. The Hartree potential is therefore repulsive in the center of the dot, a situation very similar to Hartree potentials in modulation doped quantum wells. The shell structure is enhanced by the degeneracy of states with the same absolute value of angular momentum m . This degeneracy is removed by magnetic field, leading to a splitting of energy levels. For small values of the magnetic field a rapid rearrangement and crossing of levels takes place. For higher magnetic fields, $B > 4\text{T}$, Landau bands begin to form.

Experimental spectra for a dot with a nominal radius $R=75\text{nm}$ and nominal density $n_s = 8.5 \cdot 10^{11}\text{cm}^{-2}$ in magnetic fields $B=0-5\text{T}$ are shown in Fig. 3a. The $B=0$ spectra show clearly broad peaks separated by approximately $\omega_0 = 6\text{meV}$ as indicated by arrows. Up to three peaks were observed. On top of the broad structure a number of sharper peaks, especially at low energies, is also visible. Similar structure was observed previously [11,13] in other dot structures. As the magnetic field increases, the spectrum evolves in a complicated way. For example, the lowest peak appears to split and evolve into two peaks $\Omega_{+/-}$ as indicated by arrows. However, the Ω_+ peak at $B=5\text{T}$ is split into a number of peaks, and an additional low energy peak appears. This complicated behavior can only be understood by a comparison of experiment with realistic calculations of Raman spectra.

The exciting light is scattered by a 2D array of pillars, each containing ten QD's. Not surprisingly [14], the spectra do not show the wavevector conservation and clear polarization dependence found in quantum well experiments. Thus the spin density (SDE) and charge density (CDE) excitations are not resolvable from the single particle excitations (SPE), which dominate the electronic Raman spectrum of the unpatterned quantum wells. In the interpretation of the experimental spectra, we initially restrict ourselves to the analysis of the dominant SPE based on Hartree calculations. In the absence of the wavevector conservation the cross section $I(\omega)$ is averaged over all possible wavevector transfers $q = k_f - k_i$ of the incident (k_i) and scattered (k_f) light: $I(\omega) \approx \sum_q W(q) I(q, \omega)$. The function $W(q)$ depends on the structure of individual dots and the structure of an array of pillars on the sample surface. The Raman cross section $I(q, \omega)$ for a given wavevector transfer q and frequency ω is proportional to the imaginary part of the polarizability $\Pi(q, \omega)$ of the system [15]:

$$I(q, \omega) \approx \sum_{m, m', \nu, \nu'} | \langle m', \nu | \rho_q | m, \nu \rangle |^2 (1 - f(m', \nu')) f(m, \nu) \delta(E_{m', \nu'} - E_{m, \nu} - \omega), \quad (14)$$

where the density operator $\rho_q = e^{i\vec{q}\cdot\vec{r}}$, and $f(m, \nu)$ is the Fermi occupation function for a state ν with angular momentum m and energy E_m^ν . The coupling through the density fluctuation operator $e^{i\vec{q}\cdot\vec{r}} = \sum_m i^m e^{im\theta} J_m(qr)$ induces transitions between different angular momenta m and different single particle states ν .

We now summarize in Fig.3 the evolution with magnetic field of calculated SPE Raman spectra. In Fig.3 we show the representative calculated SPE spectra for small ($qR = 0.7$; $q = 1 \cdot 10^5 \text{ cm}^{-1}$) and large ($qR = 3.5$; $q = 5 \cdot 10^5 \text{ cm}^{-1}$) wave-vectors involved in the scattering process. For comparison with experiment the calculated energies have been multiplied by a factor of 1.3 to account for a decrease in the effective dielectric constant due to the vacuum. The calculated spectra for $q = 1 \cdot 10^5 \text{ cm}^{-1}$ and $B=0$ show only one peak while spectra for $q = 5 \cdot 10^5 \text{ cm}^{-1}$ consist of three main transitions with a spacing of the order of 6 meV in good agreement with experiment. If we follow the evolution of the calculated SPE spectrum as a function of the magnetic field we see that the $q = 5 \cdot 10^5 \text{ cm}^{-1}$ spectra are in better agreement with the measured spectra. For example, at $B=0\text{T}$ we see two peaks, while at $B=3\text{T}$ we see three peaks. At $B=5\text{T}$ the agreement is also encouraging, especially with respect to the emergence of a very low energy excitation associated with the Fermi level crossing a quasi-Landau level band. The measured spectra are, of course, an average over many such calculated spectra.

In summary, the experimental spectra show a magnetic field behavior consistent with that calculated for single particle excitations within the Hartree approximation. The excitation spectrum reflects the formation of electronic shells within quantum dots and exhibits a complex evolution with magnetic field. This now opens up the possibility to study collective excitations from a range of strongly correlated ground states in QD's in a strong magnetic field [10].

III. SELF-ASSEMBLED DOTS

Self-Assembled Dots (SAD) [16] are small quasi-two-dimensional semiconductor structures formed spontaneously during epitaxial growth of strained layers. Because they can be grown in-situ and require no processing, they offer an interesting alternative to etched nanostructures. Dots in the shape of pyramids [17,18], disks [19], and lenses [20-23] have been reported, although the actual determination of the shape is not definite. The SADs described here are the lens-shaped structures formed on a narrow InGaAs wetting layer (WL) and surrounded by the GaAs barriers [20-23]. The dependence of energy levels of SAD on size, depth of confining potential, and the magnetic field has been studied in Ref. [24]. The effects of electron-electron and electron-hole interactions on electronic and optical properties of SAD containing many electrons and/or excitons have been investigated theoretically [25,26] and experimentally [17,23,27,28]. The Single Electron Capacitance (SECS), far-infra-red (FIR), and photoluminescence/absorption spectra were calculated as a function of the number of particles, the size, and the magnetic field [25]. Results were compared with SECS and FIR experiments [20,21] and PL experiments by Raymond *et al.* [23].

A. SINGLE PARTICLE STATES

A schematic picture of a lens-shaped $\text{In}_{0.5}\text{Ga}_{0.5}\text{As}$ SAD is shown in Fig. 4. The dot forms on a wetting layer (WL) of thickness t_w in the form of a part of a sphere with fixed height h and radius at the base s . The carriers, confined to a narrow WL quantum well are further localized in the area of the dot due to the effectively increased thickness of the layer. The effective 2D potential acting on carriers is shown in Fig. 4. Its radial dependence can be very well approximated by a parabola, and electronic states can be approximated by Fock-Darwin states. This is shown in Fig. 5 where numerically calculated energy levels are shown as a function of angular momentum. The calculated levels tend to bunch into groups, forming well separated shells. When electrons

occupy degenerate shells there are many ways to form degenerate configurations. In such case, as illustrated in Fig. 5 for $N = 4$, unusual configuration spin configurations are possible.

The spacing of energy levels and the wavefunctions are very well fitted by Fock-Darwin energy levels, as discussed below. The FD states $|nm\rangle = (a^\dagger)^n (b^\dagger)^m |00\rangle / \sqrt{n!m!}$ are those of a pair of harmonic oscillators with energies $\Omega_\pm = \frac{1}{2}(\Omega \pm \omega_c)$, where: $\Omega^2 = \omega_0^2 + 4\omega_c^2$, $\omega_c = eB/cm_e$ is the cyclotron energy, and ω_0 measures the effective confinement energy. Associating index n with frequency Ω_+ and index m with frequency Ω_- , the energy E_{nm}^e and orbital angular momentum R_{nm} of the state $|nm\rangle$ are: $R_{nm} = m - n$ and $E_{nm}^e = \Omega_+(n + \frac{1}{2}) + \Omega_-(m + \frac{1}{2})$. The Zeeman energy is very small and can be neglected. The eigenstates are doubly degenerate due to spin σ . The valence band holes are treated in the effective mass approximation as positively charged particles with angular momentum $R_{nm}^h = n - m$, opposite to the electron, and FD energies $E_{nm}^h = \Omega_+(n + \frac{1}{2}) + \Omega_-(m + \frac{1}{2})$ (ignoring the semiconductor gap E_G). The knowledge of single particle states allows us to proceed to the calculation of many-body effects.

B. MANY-PARTICLE STATES

With a composite index $j = [m, n, \sigma]$ describing the FD states the Hamiltonian of the interacting electron (electron-hole) system may be written in a compact form:

$$H = \sum_i E_i^e c_i^\dagger c_i + \sum_i E_i^h h_i^\dagger h_i - \sum_{ijkl} \langle ij|v_{eh}|kl\rangle c_i^\dagger h_j^\dagger h_k c_l + \frac{1}{2} \sum_{ijkl} \langle ij|v_{ee}|kl\rangle c_i^\dagger c_j^\dagger c_k c_l + \frac{1}{2} \sum_{ijkl} \langle ij|v_{hh}|kl\rangle h_i^\dagger h_j^\dagger h_k h_l. \quad (15)$$

The operators $c_i^\dagger(c_i), h_i^\dagger(h_i)$ create (annihilate) the electron or valence band hole in the state $|i\rangle$ with the single-particle energy E_i . The two-body Coulomb matrix elements are $\langle ij|v|kl\rangle$ for electron-electron (ee), hole-hole (hh) and electron-hole (eh) scattering, respectively [29,30].

The eigenstates $|\nu\rangle$ of the electron(electron-hole) system with N electrons(excitons) are expanded in products of the electron and hole configurations $|\nu\rangle = (\prod_{i=1}^N c_i^\dagger)(\prod_{k=1}^N h_k^\dagger)|\nu\rangle$. Up to 30 single particle states per dot, including spin, were used in calculations. The electronic configurations were labeled by total angular momentum R_{tot} and z-th component of total spin S_z^{tot} . For electrons, numerical diagonalization of up to $N = 6$ electrons was carried out for Hilbert spaces with different total angular momentum. For excitons, we concentrated on the optically active subspace of $R_{tot} = 0$ and $S_z^{tot} = 0$. A combination of exact diagonalization techniques (for up to $N = 6$ excitons) in configuration space coupled with the Hartree-Fock approximation extended calculations up to $N = 20$ excitons.

C. ELECTRONIC SHELLS

Due to the large quantization of kinetic energy the electronic shells correspond to the minimum kinetic energy configuration. In case of partially filled shells i.e. degenerate states, the configurations with maximum total spin and maximum individual momentum form the ground state. The calculated evolution of the total angular momentum and spin of the ground state as a function of the number of electrons is shown in Fig. 5. For example, we fill up the d shell orbitals with spin down electrons as $|2, 0\rangle, |0, 2\rangle, |1, 1\rangle$ etc. This trend is in agreement with Hund's rules.

The role of degeneracies, spin, electron-electron interactions and the magnetic field can be illustrated for $N = 4$ electrons, i.e. two electrons in a partially filled p -shell. For low magnetic fields the two "core electrons" of the s -shell are frozen in a spin singlet state while the two

electrons on the p -shell occupy degenerate FD orbitals $|01\rangle$ and $|10\rangle$. The ground state is a spin triplet, zero total angular momentum state $R = 0$, $S = 1$. The triplet state lowers its energy by exchange-interaction term $\langle 01;10|V_{ee}|01;10\rangle$ while the spin singlet state $R = 0$, $S = 0$ increases its energy by the same amount. With increasing magnetic field the triplet state $R = 0$, $S = 1$ begins to compete with a finite angular momentum spin singlet state $R = 2$, $S = 0$. In the $R = 2$ state both p electrons occupy the lower energy orbital $|10\rangle$. At $B \approx 2.8$ Tesla the gain in exchange energy of the triplet configuration $R = 0$, $S = 1$ is overtaken by an increase of kinetic energy and the system makes a transition into a spin singlet lower kinetic energy configuration. Should the dot be asymmetric, the splitting of the two p levels would prevent the formation of the spin triplet configuration.

D. INFRA-RED SPECTROSCOPY

Drexler *et al.* [20] and Fricke *et al.* [21] reported FIR absorption measurements of self-assembled dots in a magnetic field. The dots were charged with up to $N = 6$ electrons filling the s and p electronic shells. The infra-red spectroscopy was used to study the electronic excitations of the dots as a function of the number of electrons and the magnetic field.

The excitations of SAD reflect the electronic structure and the number of electrons in the dot. For an infinite parabolic confinement only the center of mass excitations with frequencies Ω_+ and Ω_- (generalized Kohn's theorem) [1,31] can be measured in FIR. In SAD, a finite number of confined FD levels leads to additional transitions in the IR spectrum related to the magnetic field induced changes in the GS, e.g. spin triplet to spin singlet transition discussed above.

The FIR absorption for N electrons can be conveniently expressed in terms of the FD creation/annihilation operators a and b [30,32]:

$$A(\omega) \propto \sum_f |\langle f | \sum_{j=1}^N (a_j + a_j^\dagger + b_j + b_j^\dagger) | i \rangle|^2 \delta(E_f - E_i - \omega), \quad (16)$$

where $|i\rangle$ is the initial (ground) state and the summation is over all bound final states $|f\rangle$. IR radiation connects only the states with the same S_z^{tot} and total angular momenta different by ± 1 . We show in Fig. 6a the magnetic field evolutions of the IR spectra calculated for the SAD with $N = 4$ electrons. The area of each circle is proportional to the intensity $A(\omega)$. The solid lines show the transition energies Ω_\pm of the noninteracting system and a vertical line marks the spin transition in the GS. The GS and two excited single particle configurations for $B \geq 2.8T$ are shown in Fig. 6b. The two excited configurations responsible for the splitting of the transition for $N = 4, 5$, are coupled through Coulomb interactions. Experiments by Fricke *et al.* [21] indeed showed the predicted here splitting which illustrates the desired sensitivity of the optical transitions to the number of electrons N .

E. MANY EXCITONS IN HIGHLY EXCITED DOTS

To understand the operation of a quantum dot based laser one must understand the effect of exciton-exciton interaction on optical properties of highly excited SAD. We shall loosely refer to excitons as interacting electron-hole pairs. Calculations were carried out [26] for SAD with 15 bound states which can be filled with up to 30 electrons and holes [23]. Due to the large confinement, the lowest kinetic energy configurations are an excellent approximation to the ground state in the case of filled shells. When electrons and holes partially fill up a degenerate shell the states and energies are completely determined by their mutual interactions and exact numerical calculations are necessary. However, a simple interpretation of results is possible due to "hidden symmetries" in the problem [26].

For most quantum dots where electrons and holes are confined in the same physical area, the electron and hole interactions turn out to be symmetrical. For example, in the sample calculated here $v_{ee}/v_{eh} = v_{eh}/v_{hh} = 1.04$. For almost symmetrical interactions, when the Hamiltonian is restricted to a single degenerate shell t , the commutator of the Hamiltonian and the interband polarization operator $P^+ = \sum_i c_{it}^\dagger h_{it}^\dagger$ can be approximated as $[H_t, P^+] \approx E_X^t P^+$, where $E_X^t = E_t^e + E_t^h - \sum_{jk} g_{ij}^{-1} \langle jj|v_{eh}|kk \rangle$ is an approximate exciton binding energy. The quantum number j ($-t \leq j \leq t$) denotes the angular momentum on a given shell. This commutation relation is a manifestation of hidden symmetry [33]. One can construct coherent N exciton states $(P^+)^N |v\rangle$ as eigenstates of P^2 . Due to hidden symmetry these states are also eigenstates of the shell Hamiltonian with energies $E(N) = NE_X^t$. The energy of these states is just the sum of energies of noninteracting excitons. These coherent states turn out to be excellent approximations of exact ground states with corresponding overlaps of 100% for shells s and p , and 99.8% and 99.2% for shells d and f .

In a QDL one needs to add/subtract an exciton to/from a dot already packed with excitons. In Fig. 7a we show the numerically calculated energy to add an exciton to N excitons present in the isolated f shell. The maximum number of excitons in an f shell is $N = 8$. The addition energy is almost a constant, independent of the number of excitons, in agreement with the "hidden symmetry" argument. In Fig. 7b we allow excitons to scatter to higher shells. We see that the addition energy is lowered and that it is split into two lines. The splitting corresponds to the interaction among excitons and is equal to the singlet bi-exciton binding energy in an f shell [26]. Finally, in Fig. 7c we show the same addition energy into the f shell but this time including interaction of excitons in the f shell with empty shells at higher energy and filled shells at lower energy. The electrons and holes in filled shells can exchange with those in an f shell. This leads to a sizeable bandgap renormalization but the weak dependence of the chemical potential on the exciton number in a partially filled shell survives. This means that there are steps in the chemical potential of the interacting system corresponding to single-particle shells. The emission spectrum of an exciton droplet corresponds to a spectral function of a "missing" (removed) exciton. This spectral function [26] describes the spectrum of charge excitations of an exciton droplet. The spectral function peaks at the highest energy (chemical potential). Hence the recombination spectrum of highly excited dots, averaged over many different exciton populations with e.g. up to $N = 20$ excitons will consist of only 4 distinct energies, corresponding to steps in the chemical potential.

An application of the magnetic field destroys the hidden symmetry responsible for this behaviour, as demonstrated by Raymond et al. [23]. The blueshift of the chemical potential was also evident in a SAD red-emitting laser structure studied by Fafard et al. [2].

The interaction of excess electrons with an exciton i.e. the recombination spectrum of modulation doped SADs has been studied recently [34].

IV. CONCLUSIONS

The ground state properties and charge and spin excitations in self-assembled and deep etched dots were obtained through exact diagonalization techniques, Hartree-Fock, and Hartree calculations. The calculations of far infrared, interband, and inelastic light scattering spectroscopies were compared with experiments.

ACKNOWLEDGEMENT

Collaboration with A. Wojs, D. J. Lockwood, A. Pinczuk, J. A. Brum, M. Potemski, S. Fafard, and S. Raymond is acknowledged.

- [1] For recent reviews and references see M.Kastner, *Physics Today*, **24**, January 1993; T. Chakraborty, *Comments in Cond.Matter Physics* **16**,35(1992); R. C. Ashoori, *Nature* **370**,413 (1996).
- [2] S. Fafard et al. *Science* **274** 1350 (1996)
- [3] P. Hawrylak, *Phys. Rev. Lett.* **71**, 3347 (1993).
- [4] R. C. Ashoori, et. al, *Phys. Rev. Lett.* **71**, 613 (1993).
- [5] A. Wojs and P. Hawrylak, submitted to *Phys. Rev. B*
- [6] P. Hawrylak, A. Wojs, and J. A. Brum, *Solid State Commun.* **98**, 847 (1996); *Phys. Rev. B*, **54**, 11 397 (1996).
- [7] X. G. Wen, *Phys. Rev. B* **41**,12 838 (1990); C. de Chamon and X.-G. Wen, *Phys.Rev. B* **49**, 8227 (1994)
- [8] P. Hawrylak and D. Pfannkuche, *Phys. Rev. Lett.* **70**, 485 (1993)
- [9] S. Patel, A. S. Plaut, P. Hawrylak, H. Lage, P. Grambow, D. Heitmann, K. von Klitzing, J. P. Harbison and L. T. Florez *Solid State Comm.* (in press)
- [10] P.Hawrylak, *Solid State Commun.* **93**, 915(1995).
- [11] R.Strenz et al., *Phys. Rev. Lett.* **73**, 3022 (1994).
- [12] D. J. Lockwood, P. Hawrylak, P. D. Wang, C. M. Sotomayor-Torres, A. Pinczuk, and B. S. Dennis, *Phys. Rev. Lett.* **77**, 354 (1996).
- [13] P. D. Wang et al., *Superl. and Microstr.* **15**, 23 (1994).
- [14] C.Dahl et al., *Phys. Rev.* **51**, 17211 (1995).
- [15] A. Pinczuk and G. Abstreiter in *Light Scattering in Solids*, edited by M. Cardona and G. Guntherodt (Springer,Berlin 1989)p.153; P. Hawrylak et al., *Phys. Rev. B* **32**, 5169 (1985).
- [16] P. M. Petroff and S. P. Denbaars, *Superlattices and Microstructures* **15** 15 (1994); for a recent review see *Proceedings of International Conference on Modulated Semiconductor Structures*, Madrid, 1995.
- [17] M. Grundmann, et. al, *Phys. Stat. Sol.* **188**, 249 (1995).
- [18] J. Y. Marzin, G. Bastard, *Solid State Comm.* **92**, 437 (1994).
- [19] R. Notzel,et. al, *Appl.Phys.Lett.* **66**, 2525 (1995).
- [20] H. Drexel, et. al, *Phys. Rev. Lett.* **73**, 2252 (1994).
- [21] M. Fricke, A. Lorke, J. P. Kotthaus, G. Medeiros-Ribeiro, and P. M. Petroff, *Europhys. Lett.* **36**, 197 (1996).
- [22] S. Fafard, et. al, *Appl. Phys. Lett.* **65**, 1388 (1994); R. Leon, et. al, *Appl. Phys. Lett.* **67**, 521 (1995); S. Fafard, et. al, *Phys. Rev. B* **52**, 5752 (1995).
- [23] S. Raymond, S. Fafard, P. J. Poole, A. Wojs, P. Hawrylak, S. Charbonneau, D. Leonard, R. Leon, P. M. Petroff, and J. L. Merz, *Phys. Rev. B*, **54**, 11 548 (1996). S. Raymond et al, *Solid State Commun.* (in press)
- [24] A. Wojs, P. Hawrylak, S. Fafard, L. Jacak; *Phys. Rev. B*, **54**, 5604 (1996).
- [25] A. Wojs and P. Hawrylak, *Phys. Rev. B*, **53**, 10 841 (1996)
- [26] A. Wojs and P. Hawrylak, *Solid State Comm.* **100**, 487 (1996). P. Hawrylak and A. Wojs, *Proceedings of International Winter School in Solid State Physics*, Mauterndorf, 1996 .
- [27] U. Bockelmann, et al. *Phys.Rev.Lett.* **76**,3622 (1996).
- [28] M. Bayer, et. al, *Phys. Rev. Lett.* **74**, 3439 (1995).
- [29] A. Wojs and P. Hawrylak, *Phys. Rev. B* **51**, 10 880 (1995).
- [30] P. Hawrylak, *Solid State Comm.* **88**, 475 (1993).
- [31] W. Kohn, *Phys. Rev.* **123**, 1242 (1961); L. Brey, N. Johnson, B. Halperin, *Phys. Rev. B* **40**, 10 647 (1989); P. Maksym, T. Chakraborty, *Phys. Rev. Lett.* **65**, 108 (1990).
- [32] D. Pfannkuche, V. Gudmundsson, P. Hawrylak, R. R. Gerhards, *Solid State Electronics* **37**, 1221 (1994).
- [33] I. V. Lerner, Yu. E. Lozovik, *Zh. Eksp. Teor. Fiz.* **80**, 1488 (1981) [*Sov. Phys. JETP* **53**, 763 (1981)]; D. Paquet, T. M. Rice, K. Ueda, *Phys. Rev. B*, **32**, 5208 (1985); A. H. MacDonald, E. H. Rezayi, *Phys. Rev. B* **42**, 3224 (1990); Yu. A. Bychkov and E. I. Rashba, *Phys. Rev. B*, **44**, 6212 (1991).
- [34] A. Wojs and P. Hawrylak, submitted to *Phys. Rev. B*.

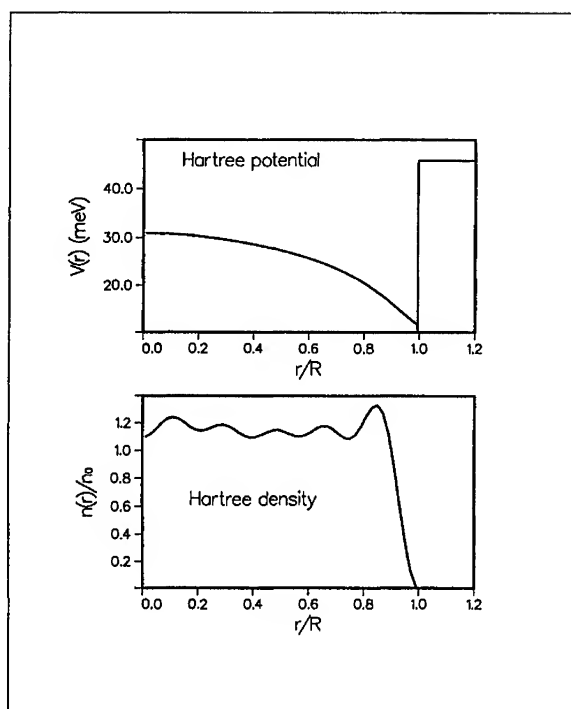


FIG. 1. Calculated Hartree potential and charge density for a dot with carrier density $n_s = 8.0 \cdot 10^{11} \text{ cm}^{-2}$ ($N=124$) and radius $r = 70 \text{ nm}$.

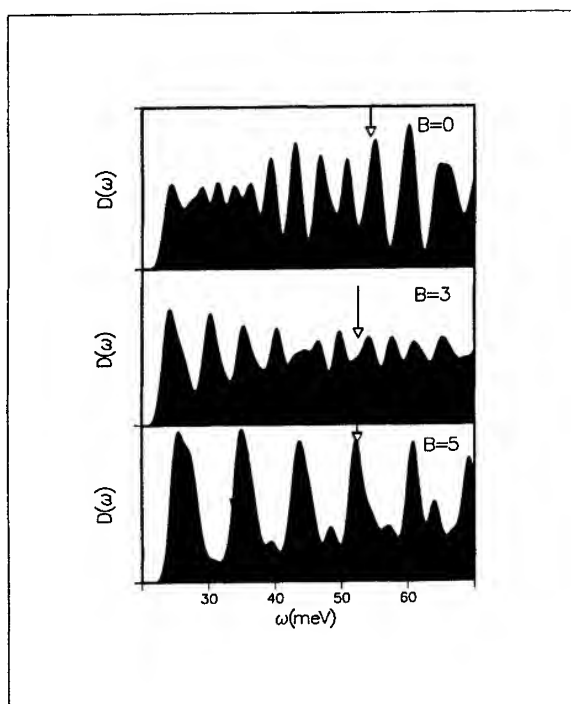


FIG. 2. Calculated density of states of a dot with carrier density $n_s = 8.0 \cdot 10^{11} \text{ cm}^{-2}$ ($N=124$) and radius $r = 70 \text{ nm}$ for different values of the magnetic field.

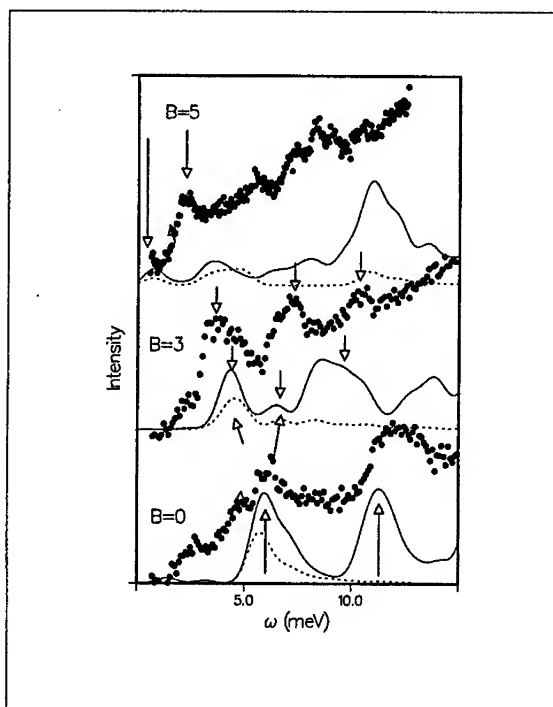


FIG. 3. measured and calculated Raman spectra of quantum dots with nominal carrier density $n_s = 8.5 \cdot 10^{11} \text{ cm}^{-2}$ and radius $r = 75 \text{ nm}$ for magnetic fields $B = 0 - 5 \text{ T}$. Calculated SPE spectra $I(q, \omega)$ are for $q = 1 \cdot 10^5 \text{ cm}^{-1}$ (dashed line) and $q = 5 \cdot 10^5 \text{ cm}^{-1}$ (solid line). The arrows point out related peaks in experiment and theory for each magnetic field.

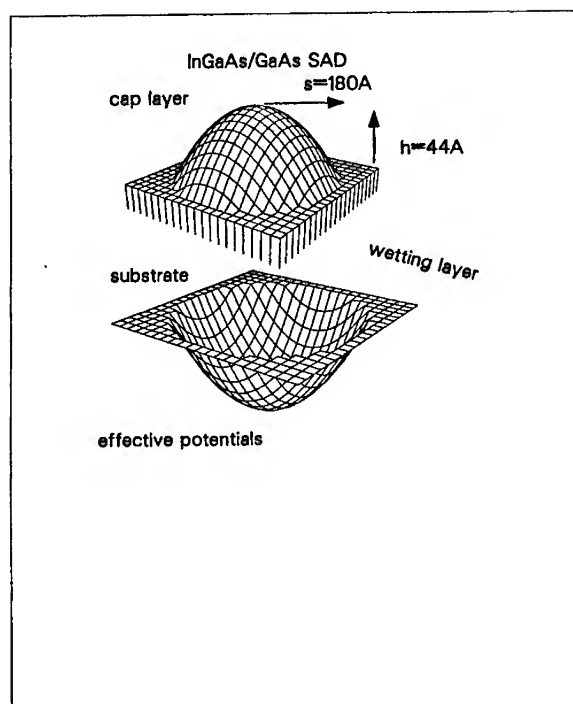


FIG. 4. (a) schematic picture of the InGaAs/GaAs self assembled dot (b) effective lateral confining potential for electrons

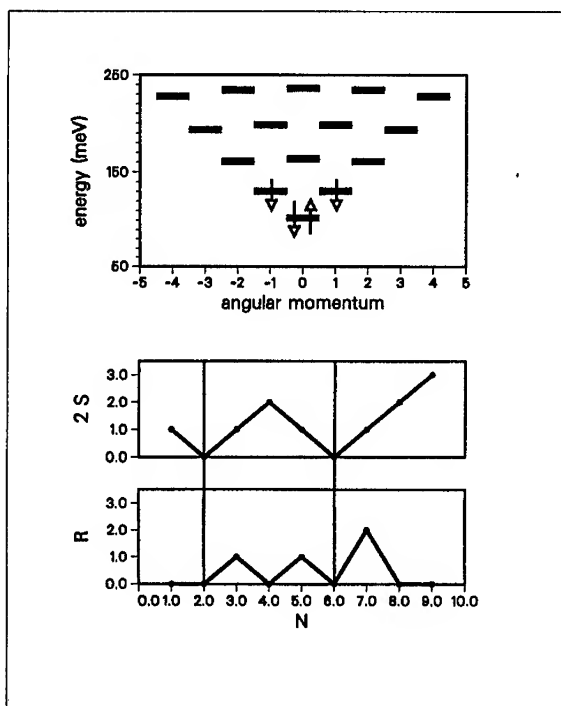


FIG. 5. Calculated energy levels as a function of angular momentum. Arrows indicate spin configuration of $N = 4$ electrons. Spin and angular momentum dependence of the ground state of SAD on the number of electrons N

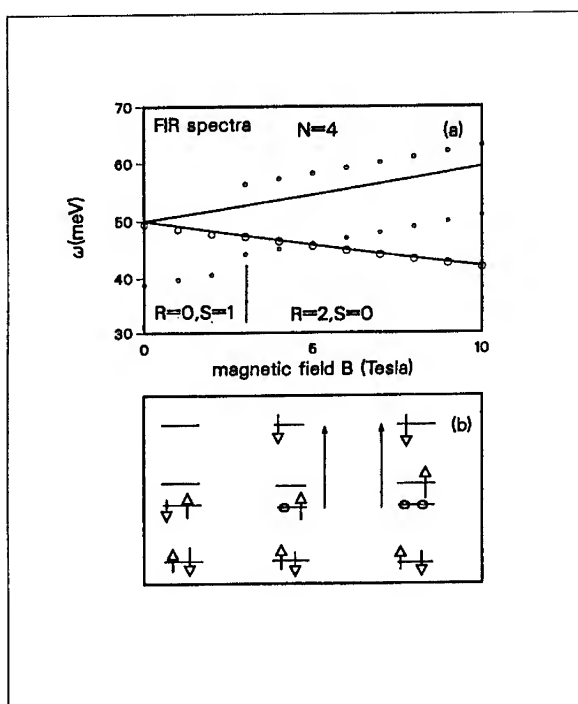


FIG. 6. (a) FIR spectra of SAD with $N=4$ electrons (b) ground state and excited single particle configurations with arrows indicating transitions

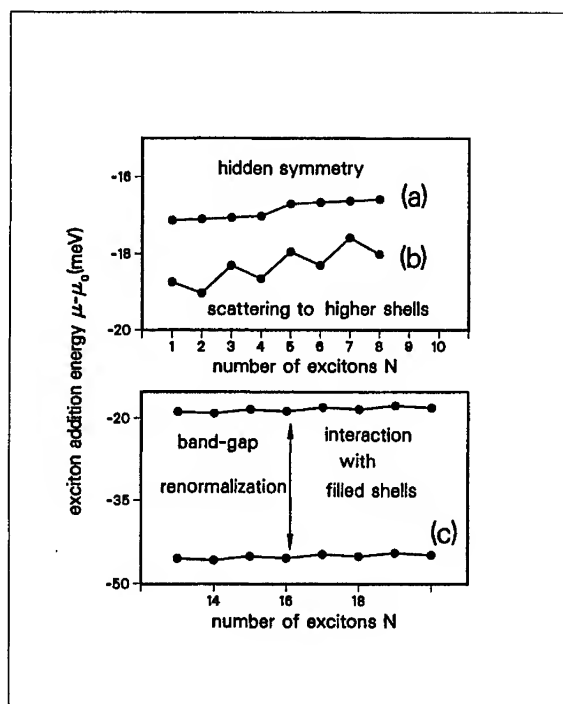


FIG. 7. Addition spectrum as a function of the number of excitons (excluding kinetic energy) (a) isolated f -shell (b) f -shell and scattering to g -shell (c) exchange with all filled shells Inset shows the behaviour of the chemical potential, including Coulomb and kinetic energy.

FABRICATION AND CHARACTERIZATION OF NANOCRYSTALLINE SILICON SUPERLATTICES PRODUCED BY CONTROLLED RECRYSTALLIZATION

L. Tsybeskov, K. D. Hirschman, S. P. Duttagupta, and P. M. Fauchet

Department of Electrical Engineering, University of Rochester, Rochester, NY, USA

M. Zacharias and P. Kohlert

Institute for Experimental Physics, Otto-von-Guericke University, Magdeburg, Germany

J. P. McCaffrey and D. J. Lockwood

Institute for Microstructural Sciences, National Research Council, Ottawa, Canada

We report the fabrication of Si quantum dots by plasma-assisted chemical vapor deposition (PECVD) or magnetron sputtering of nanometer-thick amorphous Si (a-Si) layers followed by high-temperature recrystallization. The recrystallization has been performed in two steps (rapid thermal pulse annealing and slow ramp-up furnace annealing) and has been monitored by Raman scattering. The fabrication technique is able to control the size and packing density of Si nanocrystals in the nc-Si/SiO₂ superlattices. Room temperature intrinsic photoluminescence is approaching a quantum efficiency of 0.3%. Preliminary results on the doping of Si nanocrystals are discussed.

I. INTRODUCTION

Since the discovery of efficient light emission in anodically etched Si or porous Si (PSi) [1], the room temperature photoluminescence (PL) in Si nanocrystals has been a hot research topic. Silicon nanocrystals can be produced not only by anodic etching but also by selective-size precipitation [2], spark-erosion [3], ion implantation [4] and chemical vapor deposition [5]. Recently, efficient light-emitting devices (LEDs) based on different types of nanocrystalline Si (nc-Si) have been reported [6-10]. However, several problems need to be solved. Although the role of quantum confinement has been demonstrated [11], the recombination mechanism in nc-Si is not completely understood yet. In contrast to the well developed manufacture of II-VI and III-V semiconductor nanocrystals [12], a fabrication technique that is able to control the distribution of sizes, surface passivation, and packing density of the Si nanocrystals has never been reported. Also, current studies of light-emitting nc-Si are focused on the PL in the visible and on nanocrystals with sizes significantly smaller than the Bohr exciton radius [2,13]. The regime of strong quantum

confinement, where the bandgap upshift is ~ 1 eV is extremely sensitive to the shape and the size of the nanocrystals, and the reported PL spectra are broad and featureless.

Recently, we demonstrated room temperature $1.1 \mu\text{m}$ luminescence in Si nanograins prepared by the recrystallization of PSi [14]. The PL spectra are very similar to c-Si bandedge luminescence, but the PL temperature dependence is unusually weak. We suggested that the room temperature PL at $1.1 \mu\text{m}$ is due to recombination of electron-hole pairs weakly confined within the recrystallized Si nanograins with a size larger than the size of the exciton.

In this work we will show that light-emitting nc-Si can also be produced by thermal recrystallization of amorphous Si (a-Si). In addition, nc-Si can be prepared in the form of nc-Si/SiO₂ superlattices similar to the amorphous Si/SiO₂ superlattices reported in Ref. 15. We will discuss the fabrication and characterization of the nc-Si/SiO₂ superlattices produced by controlled recrystallization. We will also show the advantage of weak quantum confinement when the nc-Si maintains physical properties similar to bulk c-Si but with efficient room temperature PL.

II. SAMPLE PREPARATION & CHARACTERIZATION

a). Sample preparation

Amorphous Si/SiO₂ multilayers were grown at Rochester by plasma enhanced chemical vapor deposition (PECVD) or by magnetron sputtering. Decomposition of silane and nitrous oxide was done at a pressure of 400-500 millitorr with an RF power of 40 W. The PECVD grown samples were deposited at 250°C on (100) c-Si substrates with 100-1000 Å SiO₂ sublayers. We prepared 20-period a-Si/SiO₂ multilayers with a thickness of 112 Å and 35 Å for the a-Si and SiO₂ layers respectively. The magnetron sputtering of the a-Si/SiO₂ multilayers was performed in a Perkin-Elmer 2400 sputtering system by RF sputtering and plasma oxidation. In the sputtered samples, the a-Si thickness ranges from ~ 40 Å to 250 Å and that of the SiO₂ from 50 Å to 60 Å. The number of periods varies from 10 to 40 in order to keep the total thickness of the samples approximately the same. The recrystallization in both types of samples was performed by rapid (40-60 seconds) thermal annealing (RTA) at 800°C-900°C followed by furnace annealing. In the furnace annealing step, the temperature increases by ~ 10 degrees per minute from 600°C to 1050°C. This annealing was defined as quasi-equilibrium annealing (QEA). All annealing steps were done in a N₂ atmosphere. An FTIR analysis of the annealed samples indicated that hydrogen, carbon, and other contaminants were absent. We do not find any significant difference between our PECVD grown and sputtered samples after recrystallization. However, the magnetron sputtering is easier to use for samples with thin (< 100 Å) a-Si layers because of the linearity of the deposition process.

b). Thermal recrystallization

Figure 1 shows the TEM picture of an as-deposited a-Si/SiO sample (Fig. 1a.) The amorphous halo in the selected area electron diffraction patterns (Fig. 1b) confirms the absence of crystallinity. The annealing process was monitored by Raman scattering. Figure 2 shows the evolution of the Raman spectra with different annealing steps. The Raman spectrum of the as-deposited sample has broad features near $\sim 480 \text{ cm}^{-1}$ and $\sim 320 \text{ cm}^{-1}$ due

to scattering by TO and LA phonons respectively [16]. Thermal recrystallization occurs after ≤ 60 seconds of RTA at temperatures 800°C-850°C, and the Raman spectra clearly show the coexistence of amorphous and crystalline phases (Fig. 2). The recrystallization of the layered structures requires a higher temperature compared to a single a-Si film for which the typical recrystallization temperature is near 600°C. The trace of a residual amorphous phase (at 320 cm^{-1} and an additional contribution at 480 cm^{-1}) can be seen even after QEA at 1050°C, but the signal due to the crystalline phase near 520 cm^{-1} is predominant. A preliminary study shows that strain in the layered structures is responsible for an increase of the recrystallization temperature. The strain mostly depends on the volume ratio between silicon and silicon-oxide; a-Si layers thinner than 60 Å were only partially recrystallized (Fig. 2b). The main Raman peak is shifted to smaller wavenumbers ($\sim 518 \text{ cm}^{-1}$) and broadens compared to the Raman signature of c-Si. A quantitative analysis of the Raman lineshape is difficult due to the presence of the amorphous phase, the broadening related to nc-Si, the contribution from c-Si substrate and the possible influence of strain [17].

The thermal recrystallization of Si/SiO₂ multilayers is controlled by several factors. Silicon has a very low diffusivity in SiO₂ and the initial RTA process forms nanocrystals without distorting the periodic structure. The shape of the Si nanoclusters is expected to be close to spherical due to the competition between surface and volume tension. The strain in nc-Si/SiO₂ multilayers can be released by QEA using a slow temperature increase. High-temperature annealing also results in a decrease of the Si/SiO₂ interface defect density (see Ref. 18 for details).

The TEM image (Fig. 3a) of a 20-period nc-Si/SiO₂ superlattice with 112 Å thick nc-Si sublayers confirms our expectations: the nc-Si/SiO₂ periodic structure is not damaged by annealing, recrystallization occurs in the Si layer, and the shape of the Si nanocrystals is almost spherical. The selected area electron diffraction patterns also confirm the presence of a nanocrystalline phase (Fig. 3b). A small amount of residual amorphous tissue remains between the Si nanocrystals within the Si layers. A quantitative analysis of the nc-Si size distribution is difficult, but the difference between recrystallized spheres is not greater than a few monolayers.

The role of the double-step annealing is to create crystalline nuclei by RTA (nucleation stage) and to complete the crystallization of the Si nanocrystals and improve their surface passivation by QEA (growth stage). After nucleation, the nanocrystalline nuclei are surrounded by an amorphous coverage with a nc-Si/a-Si ratio near 0.2-0.3 (estimated from Raman scattering). After furnace annealing and completed crystallization, the ratio of nc-Si/a-Si was found to be ~ 0.9 -0.95 in samples with Si nanocrystals greater than 70-80 Å.

c). The size of the Si nanocrystals and the effect of quantum confinement

This growth technique makes it possible to control the size of the Si nanocrystals and their packing density. The size of the Si nanocrystals within the sublayers is near the thickness of the a-Si layer while the packing density is controlled by the thickness of the SiO₂. Figure 4 shows data of X-ray diffraction in several samples with a wide range of Si nanocrystal sizes. The clear separation of the (220) and (311) crystalline peaks demonstrates the crystalline structure of the samples.

However, if the a-Si layer is thinner than 60 Å, the thermal recrystallization in the a-Si/SiO₂ multilayers is difficult to complete, possibly because of a strain. The minimum SiO₂ thickness (> 10 Å) limits the size of Si nanocrystals to larger than 30-35 Å. Figure 2b shows the Raman spectra of samples with different thicknesses for the a-Si layers. The contribution from residual a-Si in the recrystallized samples is increased when the Si layer thickness decreases. The X-ray diffraction and Raman data reveal a contribution of amorphous silicon for samples with nanocrystals of smaller (< 40 Å) sizes (Fig. 4).

The transformation of the band structure related to quantum confinement in c-Si has been calculated by a number of authors (for example, Refs. 19 and 20). Different calculations predict a continuous increase of the fundamental bandgap as $\Delta E_g \sim 1/d^n$, with $1.4 < n < 2$, when the size d of the nanocrystals is 150 Å and smaller. The value of the fundamental bandgap can be estimated from optical absorption. Our samples were deposited on c-Si substrates and the measurements of optical transmission above the c-Si bandgap are complicated. Also, an accurate estimation of the gap, especially in case of an indirect bandgap semiconductor, requires a relatively thick (>100 µm) sample. In the case of nc-Si/SiO₂ superlattices, such a thickness cannot be achieved. On the other hand, the optical reflection measurements in the region of the critical points do not require such thick samples, and sharp features are observed near the direct transitions of c-Si. Figure 5 shows reflection spectra of several nc-Si/SiO₂ samples with different Si nanocrystals sizes. The blue shift for the critical point near 3.4 eV is not strong but clearly observed. In the case of smaller sizes (< 60 Å), the singularity in the reflection near the critical point is less observable due to the contribution from residual a-Si.

III. PHOTOLUMINESCENCE

It is accepted that c-Si is a poor light emitter because of its indirect bandgap and the low probability of phonon-assisted radiative recombination. That was confirmed by the observation of a long radiative lifetime (of the order of milliseconds) in intrinsic c-Si samples with a very low density of surface states [21]. The PL in c-Si is due to the recombination of an exciton and, if the exciton is bound to an impurity, the recombination need not be phonon assisted. The wavefunction of a deep level is spread over the entire Brillouin zone and the selection rules are relaxed: a fast and relatively efficient (> 1 %) PL in c-Si can be produced by isoelectronic impurities [22], but only at low temperatures. The major reason for this limitation is the low binding energy of excitons in c-Si (~ 11 meV). The probability of radiative recombination of the exciton captured by a deep level is high, but the exciton dissociation time must be longer than the trapping time.

There are two major directions available to increase the efficiency of radiative recombination in silicon. The first one is to relax the selection rules. This has been predicted in Si nanocrystals having a size much smaller than the Bohr exciton diameter [18]. However, recent studies have demonstrated that the phonon-assisted processes in nc-Si with sizes as small as 30 Å are dominant [2,11]. The second direction is to increase the exciton binding energy. This can be done by a spatial confinement of the electron-hole pairs in Si nanocrystals with sizes close to the exciton diameter [20]. The exciton dissociation within a nanocrystal is not irreversible; in the case of a good surface passivation, the electron and the hole will eventually be close enough to form an exciton again.

Figure 6 shows the PL spectrum in nc-Si/SiO₂ superlattices with a nanocrystal size of ~ 12 nm (Fig. 7a). Its temperature dependence is also compared to that of c-Si (Fig. 6b). The

external quantum efficiency is higher (up to 0.3 %) and the temperature dependence of the PL is weaker. The low-temperature PL phonon replicas are very similar to those in bulk c-Si, except that all of the PL lines are slightly broader. The PL in c-Si is extremely sensitive to the presence of impurities because radiative recombination of a bound exciton is preferable to recombination of a free exciton. The positions of all phonon replicas clearly show that the PL originates from free excitons in the high-purity silicon clusters produced by thermal recrystallization. This suggests that thermal recrystallization is accompanied by the self-purification of the Si. The small broadening of the PL bands is attributed to non-uniform strain. No PL band at ~ 0.8 eV, which would be attributed to structural defects [14], is found in our samples, indicating their high crystalline quality.

Non-radiative Auger recombination is one of the limitations of the PL efficiency in bulk c-Si. It is responsible for the PL intensity saturation with increasing excitation intensity [21]. In nc-Si, the effect should be reduced due to a possible increase in the oscillator strength for radiative recombination and the spatial isolation of the electron-hole pairs. Indeed, we observed no saturation of the PL intensity over more than three orders of magnitude of injected carrier densities.

The increase of electron-hole wavefunction overlap due to confinement in a region comparable to the size of the exciton can be observed as an increase of the intensity of the no-phonon (NP) PL line at ~ 1.16 eV. In nc-Si/SiO₂ superlattices with nanocrystals of ~ 12 nm size, the NP PL line is observed very clearly (Fig. 7a), but no significant changes in the relative ratio of TA-phonon/NP PL is found. In the vicinity of the NP PL line, we observe a PL line that can be attributed to an anti-Stokes TO-phonon replica with a shift of ~ 60 meV. We also observe an unknown line at ~ 1.5 eV with a Stokes TO-replica (Fig. 7b). A decrease of the Si nanocrystal size down to 70-80 Å changes the PL structure and makes the TO- and TA-phonon PL lines much broader. In addition, a broad PL line with a maximum near ~ 1.2 - 1.3 eV appears. This case of strong quantum confinement in nc-Si, with sizes below 70-80 Å, will be discussed elsewhere.

The nc-Si/SiO₂ superlattice is a relatively simple system. There is no detectable chemical contamination, the size distribution is very narrow, and the PL is due to the well-defined phonon-assisted free-exciton recombination [19]. The PL external quantum efficiency can be as high as 0.3% at room temperature. The increase of the PL external quantum efficiency is at least in part due to a decrease of the refractive index and reflectivity compared to c-Si. We have not found any changes in the PL spectra which can be associated with an increase of direct recombination probability. Practical applications require a room-temperature quantum efficiency greater than 1% and a nanosecond PL radiative lifetime. These requirements can be met by doping the nanocrystals. The exciton dissociation time is expected to increase due to spatial confinement; the relaxation of the selection rules by recombination via the dopant's deep levels leads to a decrease of radiative lifetime and an increase of the PL quantum efficiency. As a first step, we implanted carbon into the nc-Si/SiO₂ superlattices. The PL spectrum was drastically changed. We observed a strong and narrow PL at ~ 0.8 eV, with a low-temperature quantum efficiency close to 1% (Fig. 8). The origin of the PL is not absolutely clear, but one possible explanation involves carbon-oxygen complexes, which are known to be responsible for the PL at 790 meV in c-Si [22]. The PL persists up to room temperature, but its intensity decreases significantly.

IV. CONCLUSION

In conclusion, nc-Si/SiO₂ superlattices containing Si nanoclusters confined between SiO₂ sublayers have been fabricated by controlled thermal recrystallization. Room temperature free exciton luminescence in Si nanocrystals with sizes comparable to the size of the Bohr exciton was demonstrated and explained by the recombination of spatially confined electron-hole pairs. The high PL quantum efficiency ($\leq 0.3\%$) makes it possible to examine the spectral region in the vicinity of the NP PL line. However, the spatial confinement does not increase the probability of direct band-to-band recombination in the Si nanocrystals. Doping of the nc-Si has been demonstrated.

This work was supported by the U.S. Army Research Office. L. Tsybeskov would like to thank D. G. Hall, Al. L. Efros, A. P. Alivisatos, R. S. Williams and J. R. Heath for useful discussions and attention to this work.

References

1. L. T. Canham, Appl. Phys. Lett. **57**, 1046 (1990)
2. W. L. Wilson, P. J. Szajowski, and L. E. Brus, Science **262**, 1242 (1993)
3. R. E. Hummel and S.-S. Chang, Appl. Phys. Lett. **61**, 1965 (1992)
4. T. Shimazu-Iwayama, S. Nakao, and K. Saitoh, Appl. Phys. Lett. **65**, 1814 (1994)
5. H. Takagi, H. Ogawa, Y. Yamazaki, A. Ishizaki, and T. Nakagiri, Appl. Phys. Lett. **56**, 2379 (1990)
6. J. Linnros and N. Lilic, Appl. Phys. Lett. **66**, 3048 (1995)
7. A. Loni, A. J. Simons, T. I. Cox, P. D. J. Calcott, and L. T. Canham, Electron. Letters **31**, 1288 (1995)
8. L. Tsybeskov, K. D. Hirschman, S. P. Duttagupta, and P. M. Fauchet, Appl. Phys. Lett. **68**, 2058 (1996)
9. L. Tsybeskov, S. P. Duttagupta, K. D. Hirschman, and P. M. Fauchet, in *Advanced Luminescent Materials*, edited by D. J. Lockwood, P. M. Fauchet, N. Koshida and S. R. J. Brueck (Electrochemical Society, Pennington, NJ) 1996, 34-47
10. K. D. Hirschman, L. Tsybeskov, S. P. Duttagupta, and P. M. Fauchet, Nature **384**, 338 (1996)
11. P. D. J. Calcott, K. J. Nash, L. T. Canham, and M. J. Kane, in *Microcrystalline and Nanocrystalline Semiconductors*, edited by R. W. Collins, C. C. Tsai, M. Hirose, F. Koch and L. Brus (Mater. Res. Soc. Symp. Proc. **358**, Pittsburgh, PA, 1995), p. 465
12. A. P. Alivisatos, Science, **271**, 933 (1996)
13. S. Schuppler et al., Phys. Rev. Lett. **72**, 2648 (1995)
14. L. Tsybeskov, K. L. Moore, D. G. Hall, and P. M. Fauchet, Phys. Rev. B **54**, R8361, (1996)
15. Z. H. Lu, D. J. Lockwood, and J.-M. Baribeau, Nature **378**, 258 (1995)
16. J. S. Lannin, in *Semiconductors and Semimetals*, v. 21, Hydrogenated Amorphous Silicon, Part B, editor J. I. Pankove, Academic Press Inc., London, 1984, p. 159
17. P. M. Fauchet and I. H. Campbell, Crit. Rev. Solid State and Mater. Sc. **14**, S79 (1988)
18. In: *The Physics and Chemistry of SiO₂ and the Si-SiO₂ Interface*, edited by C. R. Helms & B. E. Deal, Plenum Press, New York and London, 1988, p.556
19. M. S. Hybertsen, Phys. Rev. Lett. **72**, 1514 (1994)
20. T. Takagahara and K. Takeda, Phys. Rev. B **46**, 15579 (1992)
21. E. Yablonovitch et al., Phys. Rev. Lett. **57**, 249 (1986)
22. G. Davis, Physics Reports **176**, 83 (1989)

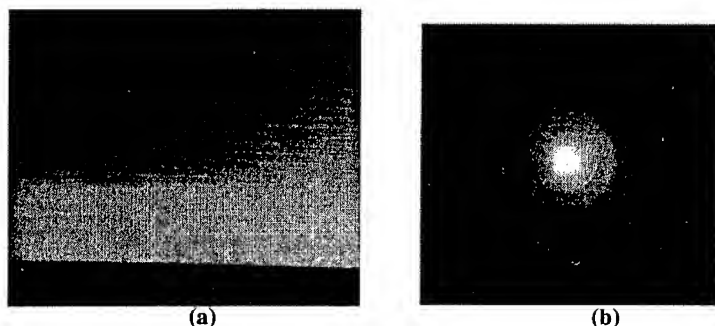


Figure 1. The (a) TEM image and (b) selected area electron diffraction patterns of an as-deposited 112Å a-Si /35Å SiO₂ superlattice on ~ 800Å thermally grown SiO₂. The sample was prepared by PECVD.

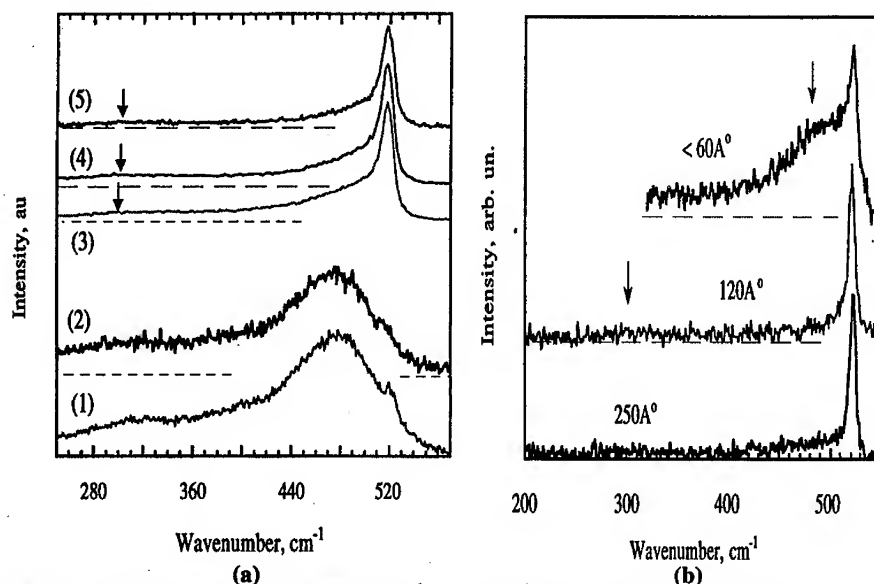


Figure 2. Raman spectra of a 20 period 112Å nc-Si /35Å SiO₂ superlattice (Fig. 2a): (1) as deposited; (2) after RTA at 700°C; (3) after RTA at 900°C, (4) after RTA at 1100°C, and (5) after 1050°C furnace annealing. The RTA time was 60 s. The arrows show a contribution from the residual amorphous phase in the annealed samples. The contribution from the residual amorphous phase at ~ 320 cm⁻¹ and at ~ 480 cm⁻¹ is clearly seen in nc-Si/SiO₂ superlattices with smaller sizes of Si nanocrystals after thermal recrystallization for 30 min at 1050°C (Fig. 2b). The poorer recrystallization in thinner a-Si layers is attributed to a higher strain.

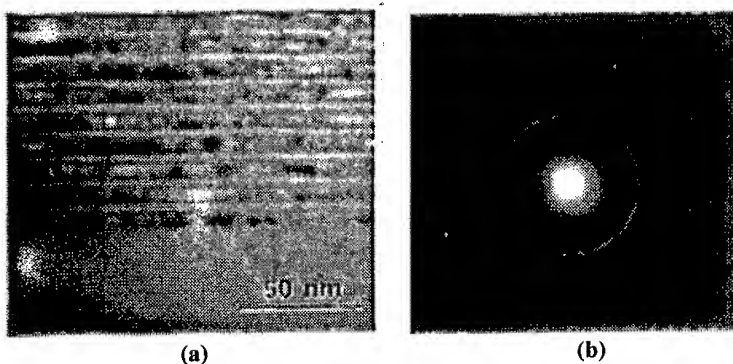


Figure 3. The (a) TEM image and (b) selected area electron diffraction patterns of recrystallized 112Å nc-Si /35Å SiO₂ superlattice.

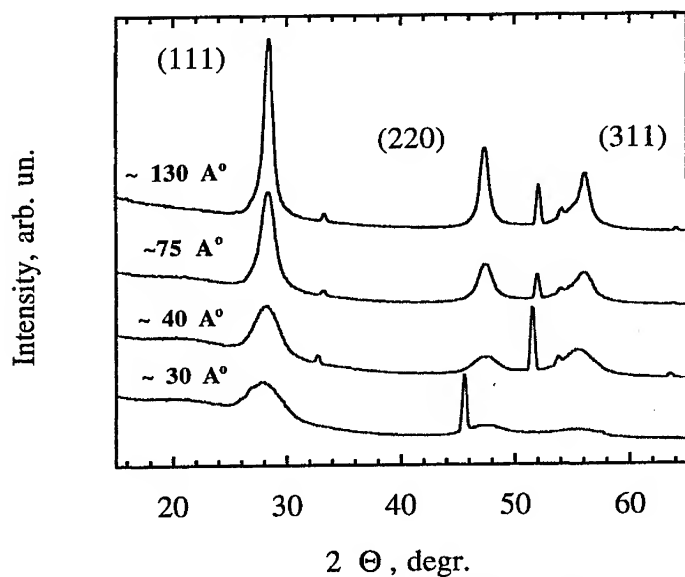


Figure 4. X-ray diffraction in nc-Si/SiO₂ superlattices with different silicon nanocrystal sizes. The radiation source is Cu-K α and the size of nanocrystals is obtained using the Scherrer multiple peak method.

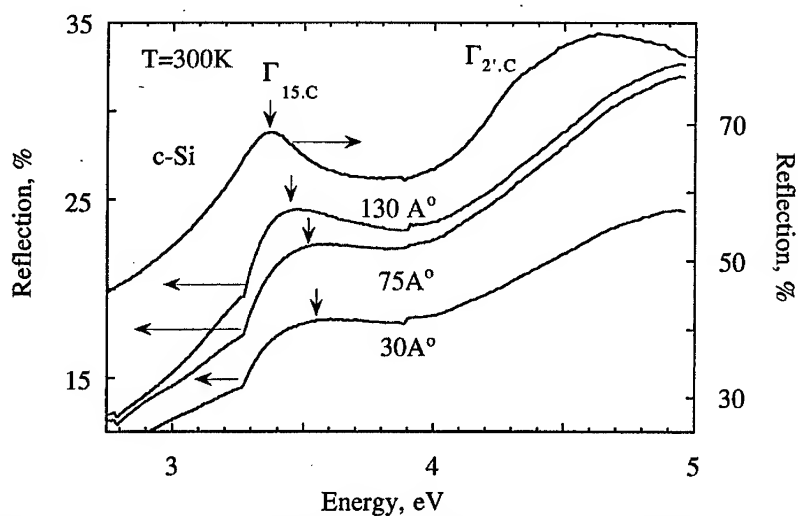


Figure 5. Reflection spectra in nc-Si/SiO₂ superlattices and in c-Si. The Si nanocrystal sizes are indicated. The arrows show the shift of the peak associated with the transition at the vicinity of the Γ critical point at ~ 3.4 eV.

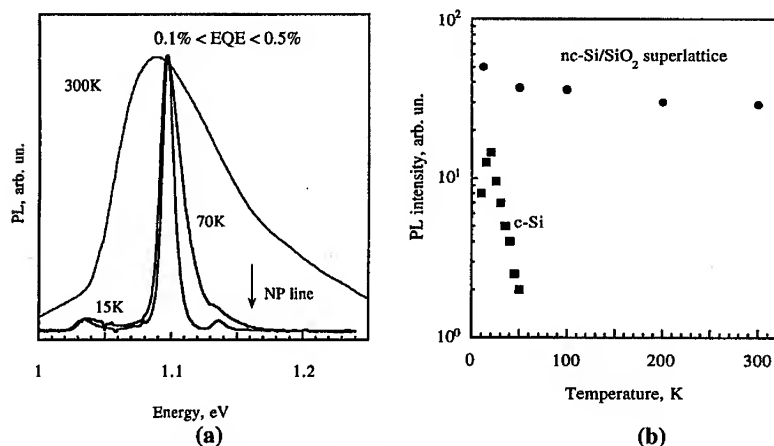


Figure 6. The (a) PL spectra and (b) temperature dependence of PL integrated intensity in a nc-Si/SiO₂ superlattice with ~ 130 Å Si nanocrystals. The PL temperature dependence of c-Si is shown for comparison [21].

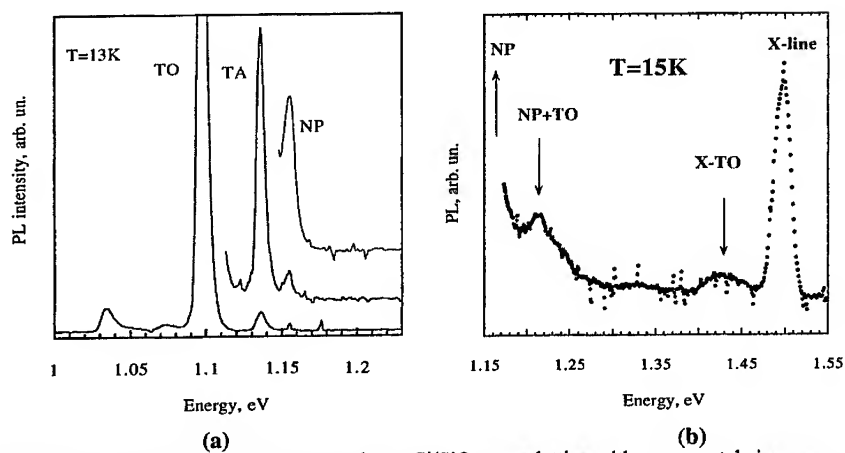


Figure 7. Low temperature PL spectra of a nc-Si/SiO₂ superlattice with nanocrystal sizes near 130Å. The major phonon lines are indicated (Fig. 8a). The PL spectrum above the Si energy gap shows the anti-Stokes TO-phonon replica of the NP-line and an unknown line at ~ 1.5 eV with a Stokes TO-phonon replica (Fig. 8b).

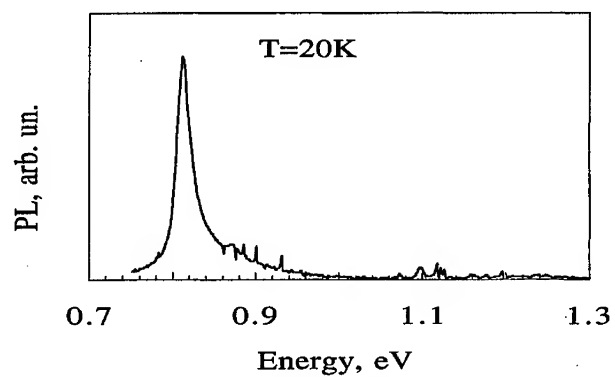


Figure 8. The PL spectrum of a C-implanted nc-Si/SiO₂ superlattice. The PL efficiency is estimated to be $\leq 1\%$.

**Coupled Quantum Dot-based InAs/GaAs Laser Structure Studied by
Contactless Electreflectance and Surface Photovoltage Spectroscopy**

Lionel Aigouy, Todd Holden ^(a) and Fred H. Pollak ^(a,b)
Physics Department and New York State Center for Advanced Technology in
Ultrafast Photonic Materials and Applications
Brooklyn College of the City University of New York
Brooklyn, New York 11210

and
N.N. Ledentsov ^(c), V.M. Ustinov and P.S. Kop'ev
A.F. Ioffe Physical-Technical Institute
Politekhnikeskaya 29
195251 St. Petersburg, Russia

and
D. Bimberg
Technische Universität Berlin, Hardenbergstrasse 36,
D10623 Berlin, Germany

ABSTRACT

We have performed a contactless electreflectance (300K and 20K) and surface photovoltage spectroscopy (103K) investigation of the optical transitions in a vertically coupled InAs/GaAs quantum dot (VECOD)-based laser structure. Signals have been observed from all the relevant regions of the sample including the quantum dots (QDs), InAs wetting layer (WL) and GaAs sections. Two of the energies of the QD transitions are related to the vertical coupling between the dots while a weaker feature at lower energies is in agreement with a lateral coupling between neighboring dots on the upper rows. The two observed WL features correspond to transitions involving heavy- and light-hole excitons in an InAs quantum well, formed by the WL, with an effective thickness of about one monolayer.

I. INTRODUCTION

A worldwide research effort has been devoted in the last ten years to the growth and the characterization of nanometer scale entities like quantum dots. This trend is strongly motivated by the technological issues associated with these small objects. Among them, stimulated emission of InAs/GaAs quantum dot (QD)-based laser devices has recently been investigated¹⁻³. These structures exhibit excellent lasing characteristics in agreement with theoretical predictions⁴, such as low threshold current densities, high material gains, and high temperature stabilities of the threshold current, making them able to compete

with quantum well-based laser devices². Although the optical properties of InAs QDs have been widely investigated by photoluminescence (PL)^{2,3,5-9}, photoluminescence excitation spectroscopy (PLE)⁶⁻⁸, time-resolved photoluminescence (TRPL)¹⁰, and calorimetric absorption spectroscopy (CAS)^{3,6,7}, very little work has been done on QDs using either modulation spectroscopy^{11,12} or surface photovoltage spectroscopy.¹³

In this article we present a contactless electroreflectance (CER)¹⁴ (300K and 20K) and SPS (103K) investigation of the optical transitions in a vertically coupled InAs/GaAs quantum dot (VECOD)-based laser structure. Signals have been observed from all the relevant portions of the sample including the quantum dots (QDs), wetting layer (WL) and GaAs sections. We have fit the CER and numerical derivative (with respect to photon energy) of the SPS spectra from the QDs and WL to the first derivative of a Gaussian profile to accurately determine the energies and linewidths of the observed features. The GaAs portion of the signal was accounted for on the basis of a band-to band third-derivative functional form. The energies of the QD transitions provides evidence for both lateral as well as vertical coupling. The two observed WL features correspond to the fundamental conduction to heavy- and light-hole transitions of a single InAs/GaAs quantum well approximately one monolayer in thickness. The temperature dependence of the energies of the InAs QD transitions is different from that of the two WL features.

II. EXPERIMENTAL DETAILS

The laser structure studied in this report was grown on a (001) oriented *n*-doped GaAs substrate by molecular beam epitaxy. The active region of the laser consists of InAs/GaAs quantum dots. After the deposition of an InAs WL [which forms a quantum well (QW)] on a GaAs layer, the strong lattice mismatch between the two compounds induces the formation of InAs pyramids. The VECODs are then self-organized during alternate short period GaAs-InAs depositions. For this sample, the number of periods was set equal to 10. The active region is embedded between two 400Å-thick GaAs layers, themselves inserted between two GaAs/Ga_{0.7}Al_{0.3}As short period cladding superlattices and GaAlAs cladding layers. The whole structure is sandwiched in a GaAs *p-n* junction. More details of the growth conditions are described elsewhere.³

In CER electromodulation is accomplished by placing the sample in a capacitor-like system, one of plates being semi-transparent to allow the illumination of the sample and collection of the reflected light from its surface.¹⁴ Besides being contactless CER does not necessitate a pump beam such as employed in photoreflectance, thus avoiding the strong PL background often encountered in the study of nanostructures at low temperatures. The modulating voltage was ~1 kV peak-to-peak at 200Hz. The SPS data were acquired using

a Kelvin probe, which is a contactless form of photovoltage, where the variations of the surface potential are measured as a function of the incident monochromatic light.¹³

III. EXPERIMENTAL RESULTS AND DISCUSSION

The experimental CER spectra of the laser structure at 300K and 20K are displayed in Figs. 1(a) and 1(b) by the dotted lines, respectively. In Figs. 2(a) and 2(b) we show an expanded plot of the spectra in the region of the QD features at 300K and 20K, respectively. The electromodulation signals from bound states such as those in QDs or QWs can be fit to the first derivative of either a Lorentzian or a Gaussian profile, depending on whether the broadening is homogeneous or inhomogeneous, respectively.¹⁴ We found that the first derivative of a Lorentzian lineshape did not fit the relevant experimental data (QDs and WL) in our case. On the other hand, a very good fit was obtained using the first derivative of a Gaussian lineshape. This observation indicates that

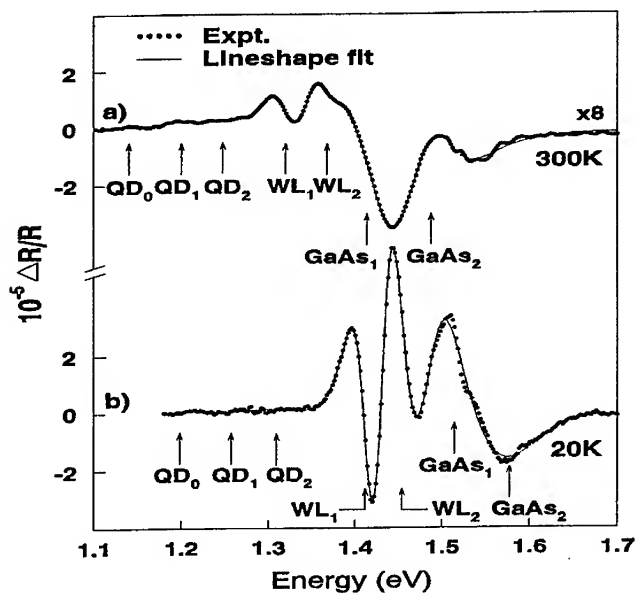


Fig.1 Experimental CER spectra (dotted lines) of the InAs/GaAs quantum dot-based laser structure at (a) 300K and (b) 20K. The solid line is a lineshape fit.

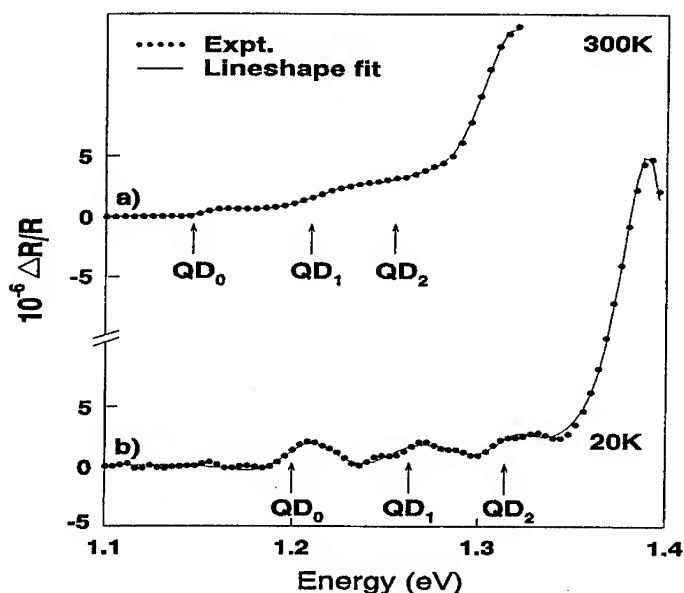


Fig. 2 Experimental high resolution CER spectra (dotted lines) of the laser structure in the vicinity of the quantum dot transitions at (a) 300K and (b) 20K. The solid line is a lineshape fit.

the broadening in these structures is inhomogeneous and is probably due to fluctuations in the size and the thickness of the nanostructures, as it was previously observed by photoluminescence⁵. The features originating in the GaAs portions of the sample were fit to a band-to-band third-derivative functional form.¹⁴

Shown by the solid lines in Figs. 1(a), 1(b), 2(a) and 2(b) are least square fits of the experimental data to the relevant lineshape functions. The obtained energies are indicated by arrows. The low energy features, labelled QD₀, QD₁ and QD₂, originate from the QDs while in the mid-energy region of the spectra the resonances designated W₁ and W₂ correspond to the *1C-1H* and *1C-1L* transitions the QW formed by the WL, respectively. The notation *mC-nH(L)* denotes a transition between the *m*th conduction and *n*th valence state of heavy (*H*)-or light-*(L)* hole character, respectively. Although the oscillator strength of the QD features is small compared to the WL resonances, they are clearly visible even at 300K.

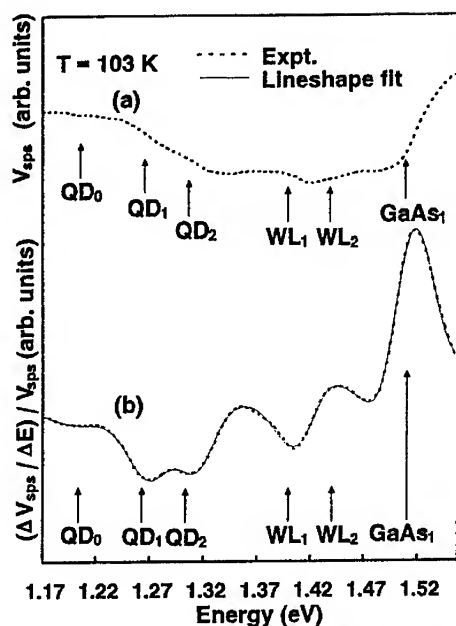


Fig. 3 The dashed lines are the (a) SPS spectrum and (b) normalized derivative of the SPS spectrum with respect to photon energy. The solid line is a lineshape fit.

Displayed by the dashed line in Fig. 3(a) is the SPS spectrum (V_{SPS}) of the sample at 103K. Figure 3(b) shows the normalized numerical derivative with respect to photon energy [$(V_{\text{SPS}}/\Delta E)/V_{\text{SPS}}$] (dashed line) and a least-squares fit (solid line) using a lineshape function similar to that employed for the CER data. The obtained values of the energies of the various features are indicated by the arrows and are listed in Table I.

On the high energy side of the spectra of Figs. 1(a) and 1(b), the two additional lines designated by GaAs_1 and GaAs_2 are attributed to GaAs-related transitions. The GaAs_1 transition at both 300K and 20K corresponds to the bandgap energy of GaAs and probably comes from the undoped 400Å-thick GaAs layers which envelop the QD region. The GaAs_2 feature is most likely related to the p -doped 6000Å-thick GaAs cap layer. The heavy doping of this layer induces a Burstein-Moss blue shift of the bandgap.¹⁵

The complete values of the CER and SPS transition energies are presented in Table I. For a comparison, data obtained by CAS and PL are also

listed. The energies of the three QD features seen by CER at 20K are in good agreement with the CAS and PL measurements. The strong 20K CER resonances at 1.265 eV and 1.318 eV are attributed to the ground and first excited state transitions in the VECOD. The weaker structure at 1.2 eV corresponds to the low energy tail of the PL emission and is attributed to lateral coupling between neighboring dots on the upper rows. The PL peak at similar energies becomes clearly visible for $N > 10$.⁹ This is due to the higher probability for lateral coupling and association of the QDs as the QD lateral size gradually increases with N , as verified by TEM.

With regard to the WL features we have performed an envelope function calculation of the $1C-1H$ and $1C-1L$ transition energies of strained layer InAs/GaAs QW system using the values of the band gaps, effective masses, deformation potentials, elastic constants and band offsets given in Ref. 16. We find very good agreement between experiment and theory for an InAs QW thickness of 1.4 ML, as listed in Table I. This value of the InAs QW thickness also is consistent with the results of previous optical measurements of thin InAs/GaAs QWs.^{17,18}

If we interpret the difference between $GaAs_1$ and $GaAs_2$ features (≈ 60 meV) as being due to the Burstein-Moss shift, then based on previous electroreflectance measurements¹⁹ the related p -type carrier concentration is $\approx 5 \times 10^{18} \text{ cm}^{-3}$, in good agreement with the intended p -doping level of $7 \times 10^{18} \text{ cm}^{-3}$ in the uppermost cap layer.

The temperature dependence of the $GaAs_1/GaAs_2$ and WL_1/WL_2 features are very similar while the energy of the QD resonances have a smaller variation with temperature. The temperature dependence of the former set of features is equal to that of bulk GaAs. It has been found for both lattice-matched ($GaAs/GaAlAs$ ¹⁴) and strained layer ($InGaAs/GaAs$ ¹⁴ and $Ge/SiGe$ ²⁰) QWs that the temperature variation of the quantum transitions is essentially the same as that of the bulk material. We find that while the temperature shift of the energies of the QD features is quite close to that of bulk InAs²¹ this is not true of the WL features.

The Gaussian nature of the QD and WL peaks indicates an inhomogeneous broadening that is probably due to fluctuations in the size and thickness of the nanostructures. As can be seen in Figs. 1(a), 1(b), 2(a) and 2(b) the linewidth of these features exhibits almost no temperature dependence.

IV. SUMMARY

In summary, we have performed a CER (300K and 20K) and SPS (103K) investigation of the transition energies in a InAs/GaAs QD laser structure. At both temperatures signals have been observed from all the relevant portions of the sample. From a detailed lineshape fit we have accurately determined the

energies of the various features and their temperature dependence. The energies of the QD transitions provides evidence for both lateral as well as vertical coupling. The temperature shift of these features is essentially the same as bulk InAs. The experimentally determined positions of the two observed WL features, corresponding to *1C-1H* and *1C-1L*, agree very well with an envelope function calculation of a 1.4 ML InAs/GaAs QW. The Gaussian nature of the lineshape and temperature independence of the linewidths of the QD and WL features indicates that the broadening is inhomogeneous and is probably due to fluctuations in the QD size and WL thickness, respectively. The energy of the GaAs₂ feature is in good agreement with a Burstein-Moss shift corresponding to the doping level in the upper *p*-type GaAs contact layer.

ACKNOWLEDGEMENTS

The authors LA, TD and FHP acknowledge the support of U.S. Army Research Office contract # DAAHO4-94-G-0153, National Science Foundation grant #DMR-9414209, PSC/BHE grant #666424 and the New York State Science and Technology Foundation through its Centers for Advanced Technology program. The authors>NNL, VMU, PSK and DB acknowledge the support of the Volkswagen Foundation and INTAS (Grant # 94-1028).>NNL also wishes to thank the Alexander von Humbolt Foundation.

REFERENCES

- (a) Also at the Graduate School and University Center of the City University of New York, New York, NY 10036
- (b) E-mail address: FHPBC@CUNYVM.CUNY.EDU
- (c) Also at Technische Universität Berlin
1. N.N. Ledentsov et al, Solid State Electronics **40**, 785 (1996); D. Bimberg et al, Jpn. J. Appl. Phys. **35**, 1311 (1996).
2. N. Kirstaedter et al, Appl. Phys. Lett. **69**, 1226 (1996).
3. N.N. Ledentsov et al, Phys. Rev. B **54**, 8743 (1996); N.N. Ledentsov et al, Mat. Res. Soc. Symp. Proc. **421**, 133 (1996).
4. Y. Arakawa and H. Sakaki, Appl. Phys. Lett. **40**, 939 (1982); M. Asada, M. Miyamoto and Y. Suematsu, IEEE J. Quantum Electron. **QE-22**, 1915 (1986).
5. L. Goldstein et al, Appl. Phys. Lett. **47**, 1099 (1985); J.Y. Marzin et al, Phys. Rev. Lett. **73**, 716 (1994); D. Leonard et al, J. Vac. Sci. Tech. **B12**, 2516 (1994); G.S. Solomon et al, Phys. Rev. Lett. **76**, 952 (1996); R. Rinaldi et al, Phys. Rev. Lett. **77**, 342, (1996); M. Grundmann et al, Appl. Phys. Lett. **68**, 979 (1996).
6. R. Heitz et al, Appl. Phys. Lett. **68**, 361 (1996).
7. M. Grundmann et al, Phys. Rev. Lett. **74**, 4043 (1996).

8. K.H. Schmidt et al, Phys. Rev. B **54**, 11346 (1996).
9. A.F. Tsatsul'nikov et al, Semiconductors, vol. 31 (1997), in print.
10. S. Raymond et al, Phys. Rev. B **54**, 11548 (1996); U. Bockelmann et al, Phys. Rev. B **55**, 4456 (1997).
11. H. Qiang et al, Appl. Phys. Lett. **64**, 2830 (1994); G. Gumbs et al, Phys. Rev. B **50**, 10962 (1994); Y.S. Tang et al, J. Electron. Mat. **24**, 99 (1995).
12. See, for example, K.L. Stokes and P.D. Persans, Phys. Rev. B **54**, 1892 (1996) and references therein.
13. L. Kronik, N. Ashkenasy, M. Leibovitch, Y. Shapira, S. Gorer, and G. Hode, submitted to J. Electrochem. Soc.
14. F. H. Pollak and H. Shen, Mater. Sci. Eng. Rep. **R10**, 375 (1993); O.J. Glembocki and B.V. Shanabrook, *Semiconductors and Semimetals*, edited by D.G. Seiler and C.L. Littler (Academic, New York, 1992), Vol. 67, p. 222.
15. J.I. Pankove in *Optical Processes in Semiconductors* (Dover, New York, 1971) p. 39.
16. S.H. Pan et al, Phys. Rev. B **38**, 3375 (1988).
17. R. Cingolani et al, Phys. Rev. B **42**, 3209 (1990); O. Brandt, H. Lage and K. Ploog, Phys. Rev. B **43**, 14285 (1991).
18. A. Ksendsov et al, Mat. Res. Soc. Symp. Proc. **221**, 459 (1991); also, Phys. Rev. B **43**, 14574 (1991).
19. M. Cardona, K.L. Shaklee and F.H. Pollak, Phys. Rev. **154**, 696 (1967).
20. Y. Yin et al, Phys. Rev. B **52**, 8951 (1995).
21. *Numerical Data and Functional Relationships in Science and Technology*, ed. by O. Madelung, M. Schulz and H. Weiss, Landolt-Börnstein, New Series, Group III, Vol. 17 (Springer, New York, 1982).

Table I. Summary of the transition energies observed in CER (300K and 20K) and SPS (103K). Also listed are results from CAS, PL and an envelope function calculation for the WL.

Spectral Feature	CER (300K) (eV)	CER (20K) (eV)	SPS (103K) (eV)	CAS (0.5K) (eV)	PL (eV)	Calculation (eV)
QD ₀	1.140±0.005	1.200±0.003	1.203±0.004	1.2 ^(a,b)	1.2 ^(c)	
QD ₁	1.219±0.010	1.265±0.004	1.263±0.005	1.258 ^(a)	1.268 ^(a,d)	
QD ₂	1.260±0.010	1.318±0.004	1.305±0.005	1.306 ^(a)	1.32 ^(a,d)	
WL ₁	1.337±0.003	1.415±0.002	1.400±0.005	1.405 ^(a)		1.347 ^{(e)/1.445^(f)}
WL ₂	1.373±0.003	1.455±0.002	1.450±0.005	1.445 ^(a)		1.388 ^{(e)/1.487^(f)}
GaAs ₁	1.434±0.010	1.509±0.010	1.512±0.010	1.5 ^(a)		
GaAs ₂	1.50±0.010	1.57±0.010				

(a) Ref. 3
(f) 20K

(b) Weak shoulder

(c) Ref. 9 at 77K

(d) 8K

(e) 300K

OPTICAL STUDIES OF SELF-ASSEMBLED QUANTUM DISKS

M. Potemski^{1,2}, D.J. Lockwood¹, H.J. Labbé¹, P. Hawrylak¹, H. Kamada³, H. Weman⁴,
J. Temmyo³, and T. Tamamura³

¹Institute for Microstructural Sciences, National Research Council, Ottawa, ON, Canada K1A 0R6

²Grenoble High Magnetic Field Laboratory, MPI/FKF and CNRS, 38042 Grenoble, France

³NTT Opto-electronics Laboratories, Atsugi, Kanagawa 243-01, Japan

⁴Dept. of Physics and Measurements Technology, Linköping University, 581 83 Linköping, Sweden

We have investigated the optical response of a self-assembled quasi-zero-dimensional semiconductor system in magneto-luminescence and inelastic light scattering experiments. The quantum disk sample was grown on a (311)B GaAs substrate using low-pressure metalorganic vapor phase epitaxy. The $\text{Ga}_{0.8}\text{In}_{0.2}\text{As}$ nanostructures buried in a $\text{Ga}_{0.5}\text{Al}_{0.5}\text{As}$ barrier are of disk shape ~80 nm across and 5 nm thick. Luminescence excitation spectra obtained for magnetic fields up to 20 T indicate the presence of confined electrons in the disks. Polarization-resolved inelastic light scattering spectra have been obtained under nonresonant as well as resonant conditions with excited disk states. When approaching resonance, the phonon-related scattering increases by more than one order of magnitude and the development of weaker sharp structure on the low-energy side of the main longitudinal-optical phonon peak is observed. Resonant enhancement of phonon related scattering is accompanied by the appearance of an extremely intense wing feature in a range of energies from -40 to +60 cm^{-1} either side of the laser line. This spectrum, peaking at the laser line, is strongly polarized and is likely the signature of electron-acoustical phonon and electron-electron interactions.

INTRODUCTION

The maturity in semiconductor crystal-growth and lithographic technologies now makes it possible to produce laterally confined quantum structures such as wires and dots in the 10–100 nm range (1,2). Once the size uniformity of the quantum wires and dots can be controlled, they may lead to new devices for future optoelectronic and microelectronic applications. In particular, quantum boxes fabricated in such a way give atomic-like discrete densities-of-states (3), which may allow for a greater improvement in their optoelectronic properties. Also, from a physics point of view, these systems now offer a very attractive field to study the basic physical properties of fully quantized electrons and holes (3,4). Recently a Stranski-Krastanov method, which avoids any lithographic and etching processing and thus eliminates the possible introduction of damage, has been adopted to fabricate self-assembled quantum dots; this is by controlled islanding during the epitaxial growth of

strained layers (5,6). More recently Nötzel *et al.* have reported a new strain-driven spontaneous islanding phenomenon where strained InGaAs/AlGaAs films grown on misoriented (311)B-GaAs substrates by metalorganic vapor phase epitaxy (MOVPE) form very-well-ordered high-density confined InGaAs disk arrays. The use of the term *disk* originates from its geometrically anisotropic shape with the thickness of a typical quantum well and the lateral diameter ranging from 100 nm down to less than 30 nm. A striking feature of this strain-driven islanding phenomenon is that the InGaAs disks are completely enveloped by spontaneous coverage with the AlGaAs initially grown before the InGaAs films. The smallest size of the quantum disks attainable by simply increasing the In composition to increase the initial strain energy is 20 nm, and the photoluminescence (PL) is characterized by narrow linewidths and well-resolved intense exciton resonances in PL and excitation (PLE) spectroscopy (8).

Following the discovery of this spontaneous crystal reorganization, we examine the effects of lateral confinement on the quantum disk system. Since a magnetic field applied perpendicular to the quantum well plane serves as an additional lateral confining potential, we use the magnetic field as a variable probe on the spatial extent of the built-in lateral potential. Therefore, the study of the optical properties of the strained InGaAs quantum disks under high magnetic fields is extremely valuable. To study the electronic structure of the quantum disks and to clarify how the lateral confinement affects the excitonic properties, we have measured magneto-luminescence and magneto-luminescence excitation spectra of the InGaAs quantum disks with diameters ranging from 100 nm down to 20 nm (9). Here, we focus on doped quantum disks in the intermediate size range where the size of the disks is several times larger than the exciton in-plane Bohr radius (10 nm), and the center-of-mass motion can be separated from the internal exciton motion. We report experimental PL, PLE, and inelastic light scattering data concerning the quasi-0D electronic excitations with and without an applied magnetic field.

EXPERIMENTAL DETAILS

The sample used for this study was grown in a low-pressure MOVPE reactor on a GaAs (311)B substrate using trimethyl-gallium (TMG), -aluminum (TMA), -indium (TMI), and arsine as gas sources. The growth rate was typically 0.6 $\mu\text{m/h}$ for InGaAs, and 1.2 $\mu\text{m/h}$ for AlGaAs. The buffer layer comprises 100 nm of $\text{Al}_{0.5}\text{Ga}_{0.5}\text{As}$. The growth temperature was varied between 720 and 750°C. Isolated quantum disks investigated in this study were obtained with a nominal In content of 0.2 and a nominal InGaAs layer thickness of 5 nm giving rise to disk diameters ~ 80 nm.

PL and PLE spectra were measured in a 10 MW resistive Bitter magnet in fields up to 20 T. For the PL measurements we used the 488 nm line from an Ar ion laser and for the PLE measurements a Ti:sapphire laser. The emitted light from the sample was dispersed

through a 1.5-m Jobin Yvon spectrometer and detected with a cooled GaAs photomultiplier. The magnetic field was applied parallel to the growth direction (normal to the quantum disk) in the Faraday configuration. Spin-resolved components of the electron heavy and light hole transitions were obtained with circularly polarized light using a photoelastic modulator.

Resonance Raman spectra were excited with 10 or 50 mW of Ti:sapphire laser light, analyzed with a Spex 14018 double monochromator, and detected with a cooled RCA 31034A GaAs photomultiplier. The incident laser light (along X) was at 94° or 66° to the normal to the sample surface, and the scattered light (along Y) was collected at 90° to the incident light. In opaque semiconductors, this would correspond to a quasi-backscattering geometry, but it should be noted that the $\text{Al}_{0.5}\text{Ga}_{0.5}\text{As}$ barrier layer is transparent to the Ti:sapphire wavelengths used in this study. The disk sample was mounted on the cold finger in the He exchange-gas space of a Thor S500 variable temperature cryostat. The sample was masked with In to ensure that the same region of the sample was investigated in the various runs at 10 K.

RESULTS AND DISCUSSION

Figures 1 and 2 show the PL and PLE spectra taken at 10 K in zero magnetic field. The PL emission at 1.419 eV, with a linewidth of 4.4 meV, is identified as the ground state electron-heavy-hole $1s(1e-1hh)$ exciton transition in the quantum disks. A weak peak is observed on the high energy side of the quantum disk peak, near 1.5 eV, that is due to emission from the GaAs substrate, and another peak found at 1.38 eV is due to the emission from a 15-nm thick $\text{In}_{0.2}\text{Ga}_{0.8}\text{As}$ layer used as an initiation layer for the quantum disk formation. The ground state electron-heavy-hole $1s(1e-1hh)$ exciton is well resolved in PLE with the absorption onset at 1.44 eV. Higher energy exciton transitions are observed at 1.52 and 1.61 eV (see Fig. 2) that are associated with the GaAs substrate and the first excited subband of the quantum disks. It is very opportune for the resonance Raman study to have another higher-lying confined state within the disk, as a consequence of the high $\text{Al}_{0.5}\text{Ga}_{0.5}\text{As}$ barrier potential.

PLE spectra measured in magnetic fields up to 20 T indicate the presence of confined electrons in the disks. From the spectra, the carrier density is estimated to be 6×10^{11} electrons/cm². The presence of these carriers is accounted for by unintentional doping of the $\text{Ga}_{0.5}\text{Al}_{0.5}\text{As}$ embedding layer. At high magnetic fields ($B > 10$ T), the luminescence fan diagram (9) resembles that of a two-dimensional (2D) electron gas, as could be expected for doped disks.

Inelastic light scattering spectra have been obtained when approaching resonance at the optical gap at 1.44 eV and also with the first excited subband at 1.61 eV. Typical spectra

are given in Figs. 3 and 4.

When approaching resonance with the first excited subband, the phonon scattering due to longitudinal optic (LO) phonons in the disks increases by more than an order of magnitude in intensity and a weaker band of scattering is observed on the low-energy side of the main LO phonon peak. The side band to lower energy exhibits a varying lineshape depending on the laser excitation energy and exhibits sharp structure. This lower energy band is tentatively attributed to phonons confined in smaller-sized disks resulting from a nonuniform size distribution. Resonant enhancement of the phonon-related scattering is accompanied by the appearance of an extremely intense, broad feature in the range of energies -40 to $+60$ cm^{-1} either side of the laser exciting line. These Raman spectra show a strong linear polarization dependence in both the wing feature and the phonons. For the quasi-backscattering geometry, the main LO phonon peak in the disks is expected to be strong in $X(YX)Y$ polarization and weak in $X(YZ)Y$ polarization, as observed experimentally (see Fig. 3).

A similar inelastic wing feature is seen on the anti-Stokes and Stokes sides of the laser exciting line for excitation energies near 1.44 eV, but in this case the scattered light is depolarized (see Fig. 4). However, the intensity of the scattering exhibits a strong resonant enhancement as the laser exciting energy approaches the optical gap at 1.44 eV. At excitation energies ~ 1.42 eV, the PL emission dominated the Raman scattering.

CONCLUSION

These PL, PLE, and inelastic light scattering measurements on doped self-assembled quantum disks have shown the strong effect of confinement on the electrons. The PLE spectrum revealed a higher energy confined state in the disks. Resonance Raman scattering with this state revealed a broad inelastic peak with a strong polarization dependence, which is tentatively attributed to electron-acoustical phonon scattering and electronic excitations of the electron gas within the disk.

REFERENCES

1. D.J. Lockwood and A. Pinczuk, *Optical Phenomena in Semiconductor Structures of Reduced Dimensions* (Kluwer, Dordrecht, 1993).
2. D.J. Lockwood, *Physics of Semiconductors* (World Scientific, Singapore, 1995).
3. D.J. Lockwood, P. Hawrylak, P.D. Wang, C.M. Sotomayor Torres, A. Pinczuk, and B.S. Dennis, *Phys. Rev. Lett.* **77**, 354 (1996).
4. P. Hawrylak and A. Wojs, *Semicond. Sci. Tech.* **11**, 1516 (1996).
5. J. Ahopelto, A. Yamaguchi, K. Nishi, A. Usui, and H. Sakaki, *Jpn. J. Appl. Phys.* **32**, L32 (1993).

6. N. Hoguchi and K. Ishige, *Jpn. J. Appl. Phys.* **32**, 2052 (1993).
7. R. Nötzel, J. Temmyo, and T. Tamamura, *Nature* **369**, 131 (1994).
8. R. Nötzel, J. Temmyo, and T. Tamamura, *Jpn. J. Appl. Phys.* **33**, L275 (1994).
9. H. Weman, H. Kamada, M. Potemski, J. Temmyo, R. Nötzel, and T. Tamamura, *Solid State Electron.* **40**, 379 (1996).

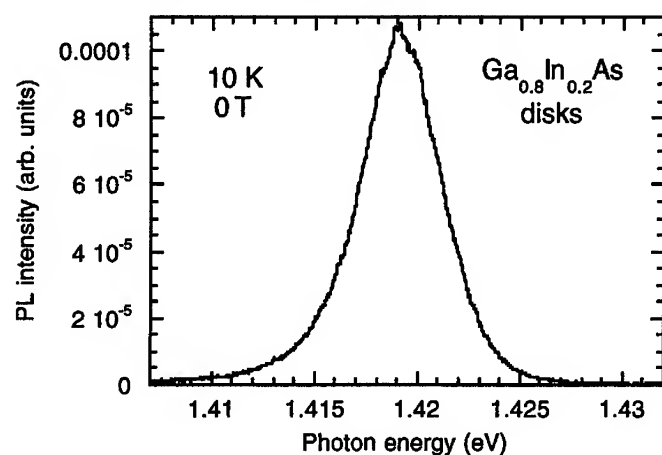


Figure 1. PL spectrum of the disk sample at 10 K.

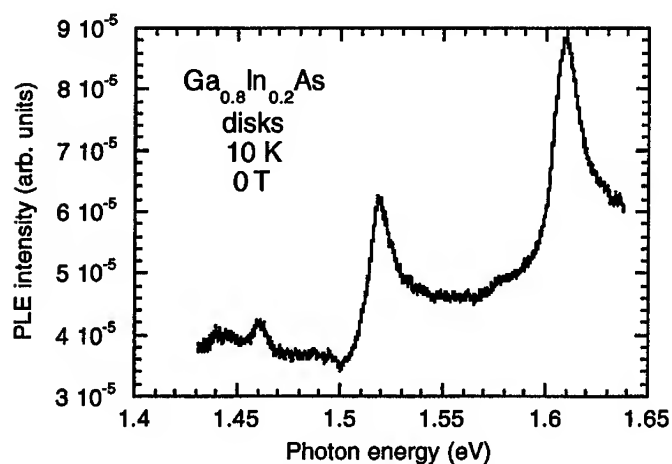


Figure 2. PLE spectrum of the disk sample at 10 K.

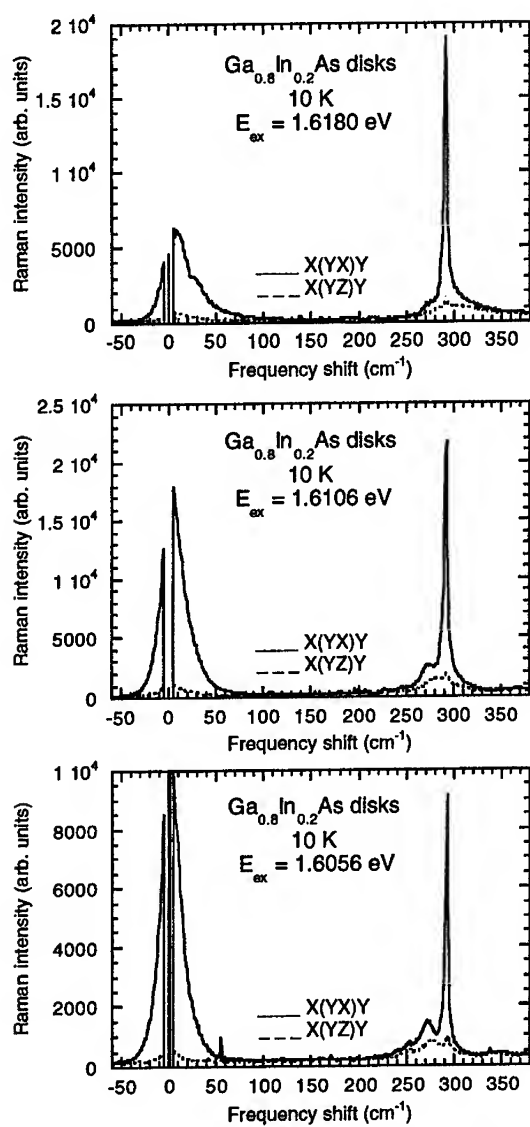


Figure 3. Raman spectra of the disk sample at 10 K recorded with laser excitation energies E_{ex} close to the first excited subband at 1.61 eV.

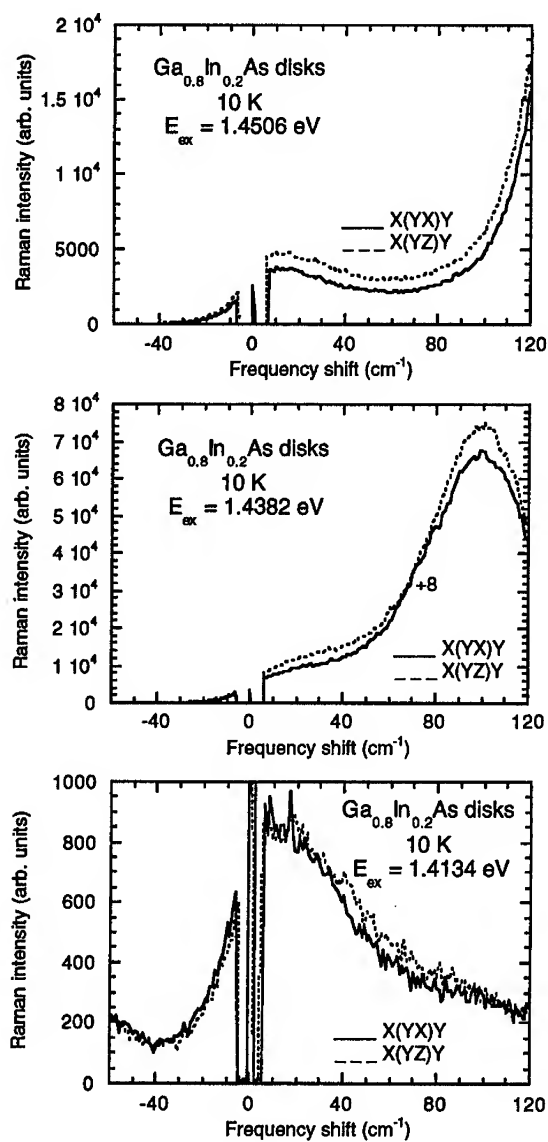


Figure 4. Raman spectra of the disk sample at 10 K recorded with laser excitation energies E_{ex} close to the optical gap at 1.44 eV.

Quantum Dots: Electronic Properties

Self-Consistent Modeling of Interface and Dopant Disorders in Delta-Doped Mesh-Gate Quantum-Dot Nanostructures

V.Y. Thean, S. Nagaraja and J.P. Leburton
*Beckman Institute for Advanced Science and Technology and
Coordinated Science Laboratory,
University of Illinois, Urbana, Illinois 61801*

ABSTRACT

The influence of material interface disorder on the potential and fluctuations in the coulombic impurity charge distribution in a δ -doped $\text{Al}_{1-x}\text{Ga}_x\text{As} - \text{GaAs}$ quantum dot mesh gate device at $T=4.2\text{K}$ is investigated with a self-consistent 3-D Poisson and 1-D Schrödinger computer simulation. Sensitivity analysis of the device shows that various disorder mechanisms can result in fluctuations in the charging energy of as much as 50% from device to device.

I. INTRODUCTION

Advances in nanofabrication techniques in recent years have permitted the making of ultrasmall structures such as semiconductor quantum dots with potential in future device applications[1]. As devices are made smaller, sensitivity to material randomness and dopant disorder is expected to become a major issue for device reproducibility. However relatively few experiments and theoretical studies have focused on the effects of granular disorders in these nanostructures[3],[4]. Previous analysis have shown that low-dimensional devices like quantum wires and quantum dots, are very sensitive to influences of potential fluctuations[5],[6]. In order to assess the sensitivity of quantum dot structures to various kinds of material disorder, a quasi-atomistic analysis is desirable as the virtual-crystal model becomes inadequate.

In this paper, we present an investigation of interface and dopant disorder in

periodic mesh-gate quantum dot nanostructures. In order to analyze the influence of various disorder mechanisms, we perform self-consistent simulations of the device by solving the 3-D Poisson and 1-D Schrödinger's equations for the strong vertical confinement in the dot and by taking into account the influence of random structural and doping disorder[2]. The charging behavior of the device is obtained by computing the number of electrons in the quantum dot simulation at different gate bias.

The remaining presentation of this paper will be organized into three main sections. In section II, the basic device structure is described. The approach based on the self-consistent solution of the Poisson-Schrödinger equations with pertinent boundary conditions will be presented. We will also describe the models for interface roughness and dopant disorders and their incorporation into the simulation of the basic device structure. In addition, a new model to treat disordered boundary conditions which replaces the zero-Neumann conditions for ideal devices, will be introduced. Section III will be devoted to the presentation and discussion of our results and Section IV will be our conclusion.

II. APPROACH

A. Device Structure and Model

The periodic grid gate quantum dot device is fabricated with a mesh-like metal gate on top of a GaAs and $\text{Al}_{1-x}\text{Ga}_x\text{As}$ heterostructure(Fig. 1). A 50Å GaAs cap layer is followed by a 450Å thick undoped $\text{Al}_{1-x}\text{Ga}_x\text{As}$, which contains a n^+ δ -doped layer that is approximately 10Å thick, with a sheet density of $1.5 \times 10^{12} \text{ cm}^{-2}$. This $\text{Al}_{1-x}\text{Ga}_x\text{As}$ layer is grown on top of a lightly p-doped GaAs substrate with a background dopant density of $1 \times 10^{14} \text{ cm}^{-3}$, forming a modulation doped structure. A quantum well containing a 2-D electron layer is induced at the $\text{Al}_{1-x}\text{Ga}_x\text{As}/\text{GaAs}$ heterojunction in the device, approximately 100Å from the dopant plane. By applying a negative gate bias, the quantum well regions between the gate and the substrate will be depleted, except for the material beneath the gate aperture, creating a quantum dot.

In this analysis we simulate a unit cell of the grid gate structure and focus on the role of disorder on the electronic properties of the quantum dot.

Since device symmetry is broken due to material disorders and charge fluctuations from cell to cell, new disordered boundary condition on the electric fields, instead of the zero-Neumann conditions, will be introduced and discussed in subsection B.4.. At the gate interface, Dirichlet boundary condition is imposed for the potential given by a constant gate bias. The bulk conditions in the GaAs substrate are simulated by relaxing the energy bands, far away from the heterojunction, to

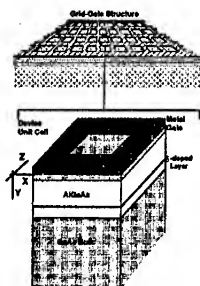


FIG. 1. Schematic of the grid gate structure with the unit cell of the device.

the flat band condition.

The device is discretized by using a nonuniform finite-difference mesh, consisting of $26 \times 26 \times 197$ grid points. The discretized Poisson's equation in finite-difference form is solved by Newton-Raphson technique and the solution process is accelerated with successive over-relaxation[7]. The finite-difference 1-D Schrödinger's equation is transformed into symmetrical tridiagonal form[8], and solved by direct method using a QR algorithm[10]. A self-consistent loop is employed to iterate between the two equations until convergence is achieved. The solution process is accelerated by using successive over-relaxation.

B. Models of Disorder

In this work we considered three major sources of material disorder: interface roughness, dopant density fluctuations for densely-doped and sparsely-doped regions and finally the random coulombic influence of neighboring cells.

B.1 Interface Roughness

In our analysis, interface roughness is considered as monolayer fluctuations of the $\text{Al}_{1-x}\text{Ga}_x\text{As}/\text{GaAs}$ interface which is modelled by intermixed monolayered material clusters of $\text{Al}_{1-x}\text{Ga}_x\text{As}$ and GaAs of various dimensions and shapes at the heterojunction, as revealed in the growth kinetics of adatom nucleation on the surface by AFM and STM studies[9].

The simulated clusters are constituted from a random mixture of tiles and points(Fig. 2). Small islands are first constructed from randomly assigned tiles of $200 \times 200 \times 5 \text{ \AA}$. Larger clusters are formed from filling the smallest inter-island spacings using tiles and points. The height of these clusters is approximately 1

monolayer($\sim 2.5\text{\AA}$) away from the mean interface position. The roughness of the interface is then characterized by the averaged cluster size. Figure 2 shows the material profile of the heterointerface generated with average cluster size of $800 \times 800\text{\AA}$. We see a series of AlGaAs plateaus and GaAs troughs surrounded by rougher regions made up of alternating AlGaAs and GaAs. The plateaus and troughs would represent smoother regions of desired monolayered growth while the surrounding rougher profile simulate regions where extensive adatoms coalescence had not occurred. Previous work have found that using $800 \times 800\text{-}5\text{\AA}$ clusters to simulate interface roughness can reproduce resonant-tunneling features in GaAs/ $\text{Al}_{0.3}\text{Ga}_{0.7}\text{As}$ device structure observed experimentally[3]. These clusters are simulated as spatial fluctuations in the band offset $\Delta E_c(y)$ and the material permittivity $\epsilon(x, y, z)$ at the heterojunction. This gives rise to potential fluctuations in the solution of Poisson's equation(1) at the heterointerface and also modulated the confinement potential that appears in Schrödinger's equation(2).

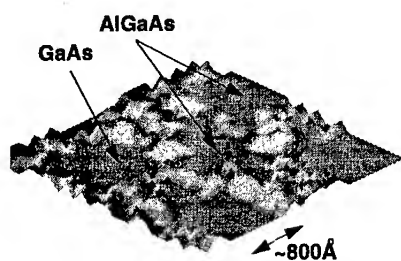


FIG. 2. Simulated AlGaAs/GaAs interface roughness at the quantum well.

B.2. Disorder in Densely-doped Regions

We have assumed that the spreading in the dopant profile obeys a gaussian-type histogram, centered at the intended position of the δ -doped layer, with a periodicity corresponding to the lattice constant(Fig.3). Thus the dopant density, $\overline{N_d}(y)$, of each crystal monolayer in the histogram follows the distribution:

$$\overline{N_d}(y = na_o) = \frac{A}{\sigma_o} \exp\left[-\frac{1}{2}\left(\frac{y - y_o}{\sigma_o}\right)^2\right] \quad (1)$$

Here, y_o is the nominal position of the δ -doping, and the distance y from y_o is given in terms of integer multiples n of the monolayer thickness a_o . The normalization constant is given by $A = \frac{N_o}{\sum_y \overline{N_d}(y)}$ where N_o is the nominal sheet density of the δ -doped layer. We have estimated that the standard deviation of the spread to be

$\sigma_o = 4.8\text{\AA}$, for the doping density considered here. The dopant density $\overline{N_d(y)}$ in each monolayer of the δ -doped profile used as the mean value for statistical random assignment of dopant densities at every (x,z) point in the dopant monolayer plane.

As such we have chosen to randomize the dopant density on each grid point according to a normal probability distribution derived from a Poisson process. At each lateral point (x, z) of the dopant plane, a random number, r between 0 and 1 is generated. The value r represents a probability value that corresponds to a unique dopant number n_d obtained from a gaussian probability function. Hence, a specific doping number $n_d(x, y, z)$ at a point is picked corresponding to the random number r and n_d is distributed spatially according to some statistical distribution P , ie. $n_d(x, y, z) = P^{-1}(r)$. The probability distribution for N_d at any point on the $x - z$ plane is gaussian,

$$P(n_d) = \int_{-\infty}^{n_d} \frac{1}{\sigma\sqrt{2\pi}} \exp\left[-\frac{1}{2}\left(\frac{n - \overline{n_d}}{\sigma}\right)^2\right] dn \quad (2)$$

The mean number of dopants at each point is computed with $\overline{n_d}(x, y, z) = \overline{N_d(y)}\Delta x\Delta y\Delta z$. According to Poisson statistics, the standard deviation at each point is the square root of the mean number of dopants at the point, $\sigma(x, y, z) = \sqrt{\overline{n_d}(x, y, z)}$. Then the dopant density to be assigned to each point is given by $\frac{n_d(x, y, z)}{\Delta x\Delta y\Delta z}$. Hence, the resulting distribution of the dopants in each layer of the δ -doping will fluctuate about the mean dopant density corresponding of the layer, $\overline{N_d(y)}$.

Inset(a) of Figure 3 shows the x - z spatial profile of the dopant density fluctuation at the center of the δ -doped layer ($y = y_o$). Inset(b) is a frequency plot of the dopant density $N_d(x, z)$ on the same x - z plane ($y = y_o$). The plot shows the distribution of the point-to-point dopant density with the mean $\overline{N_d}(y = y_o) = 6.5 \times 10^{19} \text{cm}^{-3}$. Also, the total number of dopants within the δ -doping ($n_d^{total} = \sum N_d(x, y, z)\Delta x\Delta y\Delta z$) will fluctuate too. The spatial fluctuations in $N_d(x, y, z)$ enters into the simulation through Poisson's equation(1) as a disordered dopant profile.

B.3. Disorder in Sparsely-Doped Regions

A sparsely-doped region occurs at the tails of the n -type δ -doping(Fig. 3) and in the bulk substrate regions where unintentional p -type doping results in very low doping concentrations($\sim 1 \times 10^{14} - 1 \times 10^{16} \text{cm}^{-3}$). For the donor profile used in this simulation, the tails of the δ -doping occur beyond 6\AA from the peak, where the donor concentration drops far below $\sim 1.8 \times 10^{18} \text{cm}^{-3}$ and falls into the 10^{16}cm^{-3} range. In these sparsely-doped regions the dopant atoms are spaced much further apart ($\sim 2000\text{\AA}$) than in the densely δ -doped regions. If we assume

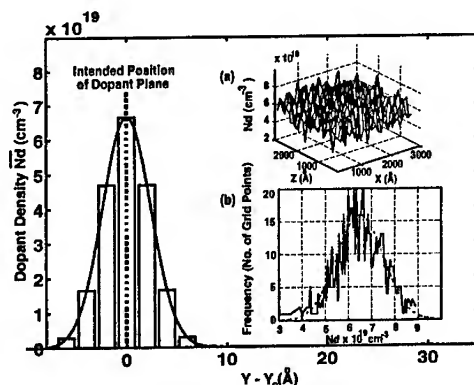


FIG 3. Spreading of the δ -doped layer simulated by a gaussian-fitted histogram with the nominal position at Y_0 . Inset(a): x-z dopant density distribution on the dopant plane at Y_0 . Inset(b): frequency plot of the x-z dopant density on the dopant plane at Y_0 .

that these dopant atoms fall only on the grid points specified for the model, we can model the dopant atoms as randomly distributed point charges. Similarly, since the average separation between the acceptors in the lightly p-doped substrate is large, isolated negative ions are used to simulate the sporadic background acceptors. An isolated point charge at any point (x, y, z) is simulated by assigning a charge density corresponding to a single dopant atom at that point eg. $N_d(x, y, z) = \frac{1}{\Delta x \Delta y \Delta z}$. This charge density then enters into the Poisson's equation(1) as part of the overall dopant profile. The number of dopants to be assigned is determined from the background doping and the volume of the device. $n(\text{dopants}) = \overline{N_d(y)} \Delta y(y) A$, where A is the cross-sectional area of the device.

B.4. Disordered Periodic Boundary Condition

In the absence of disorder, the description of the ideal device can be reduced to just a quadrant of a cell through symmetry considerations with periodic zero-Neumann boundary conditions. Also, the field lines are mirrored across the cell boundary, satisfying the periodic boundary conditions. However, the influence of disorder breaks the translational invariance of the grid-gate device in the x-z plane and consequently the lateral symmetry of the device structure. This means that the periodic boundary conditions, that requires the lateral electric field across the virtual device boundaries to be strictly zero, are no longer applicable. In this case, there are residual fluctuating electric field lines traversing the virtual boundaries,

in and out of the device(Fig 4).

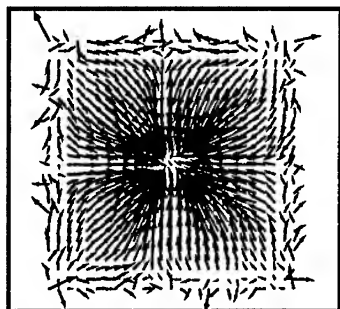


FIG 4. Lateral (x-z) electric field mappings of an device unit-cell with random boundary conditions.

The magnitude of these field fluctuations and the degree of field disorder in any region should be proportional to the amount of charge located in the region. However, from a statistical point of view, the fields across the entire virtual boundaries should average zero because of the periodic nature of the structure. As such, these requirements determines the boundary conditions on the electric fields in the device.

The random residual fields at each point on the virtual surface is assigned in a manner similar to the assignment of dopant density fluctuations, ie. with a gaussian probability distribution,

$$P(E_x) = \int_{-\infty}^{E_x} \frac{1}{\sigma(y,z)\sqrt{2\pi}} \exp\left[-\frac{1}{2}\left(\frac{E'_x}{\sigma(y,z)}\right)^2\right] dE'_x \quad (3)$$

The electric field at any point on the virtual boundary is picked according to a random number r , between 0 and 1, i.e. $E_x(y,z) = P^{-1}(r)$. The mean of the distribution is zero, which will result in zero electric field being statistically dominant at the virtual boundaries. The standard deviation, which measures the degree of disorder in the field from point to point, is position dependent, $\sigma(y,z)$. We have chosen it to be proportional to the the field lines $E_x^{stand-alone}(y,z)$ of a stand-alone unit cell, which removed from the periodic lattice and is now surrounded by bulk semiconductor.

The magnitude of the the fields in various regions is a direct indication of the amount of charge in the region. We exploit this field profile, which is specific to this device structure to assign a distribution of disordered fields at the virtual boundaries of a non-ideal device.

By using a scaled field profile of a stand-alone cell as the standard deviation of the random distribution, $\sigma(y) = k E_x^{Stand-alone}(y, z)$ (k : scaling factor), will give us greater variations of field lines in regions containing high charge and much smaller variations in regions of low charge density. Figure 4 shows the field profile of a device with disordered residual fields across the virtual boundaries of the unit cell. The non-zero fields at the boundaries simulate the electrostatic influence from neighboring cells.

III. RESULTS

The fluctuating material boundary due to interface roughness results in random shifts of the energy levels as well as distortions in the 1-D electron wavefunctions at the interface. A 5Å fluctuation in the quantum well size results in approximately 0.2meV shifts in the energy levels. Though potential distortions due to material offsets are localized in regions close to the interface, the distortion of the electron density occurs over a distance of $\sim 10\text{\AA}$. Hence, the overall effect of interface roughness on device behavior is relatively small. Comparing the charging characteristics of the devices with average cluster size of 400Å and 800Å, we find that the averaged fluctuations in the threshold voltage are only about 1 to 2mV, for our configuration. Distortions in the charging characteristics are most prominent when the quantum dot is empty or barely populated. This corresponds to the condition when the dot size is the smallest and close to the spatial extent of the roughness.

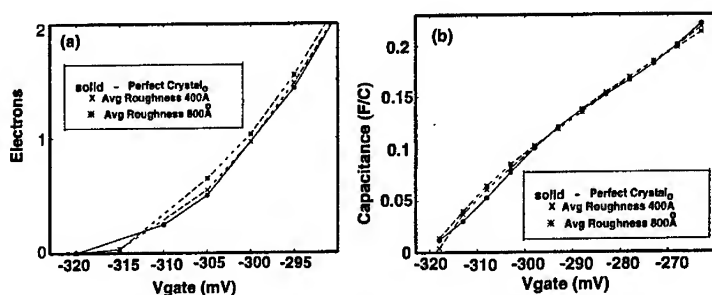


FIG 5. (a) Device charging behavior for 3 different interfaces. (b) Corresponding device capacitances

The effects of remote dopant distribution on potential fluctuations are illustrated in figure 6, for which two different dopant configurations are considered.

The first simulation is for a particular dopant profile in the densely-doped regions of the δ -doped layer ($N_d \sim 10^{19} - 10^{18} \text{ cm}^{-3}$); the sparsely-doped tail region which includes discrete point charges is not included. Figure 6(a) shows the 2-D x-z contour plot of the conduction band which indicates that closely spaced charges result in smaller spatial fluctuations of the potential, even though the mean value of the potential has been changed due to the overall effect of the fluctuating charge density. This is due to the fact that the $1/r$ potential tails of closely positioned charges produce a coherent distortion of the potential, bending the conduction band in a collective manner, thereby causing an overall shift of the potential over a larger spatial extent. Hence, the magnitude of the short order spatial fluctuations that affect the potential are reduced. It should be pointed out that these short-ranged potential fluctuations have a weak remote influence over the electrons in the quantum dot because they can be easily offset by electron screening.

The second simulation shown in figure 6(b) has been performed with a particular dopant configuration where the sparsely-doped tails in the δ -doped layer contains discrete point charges distributed according to dopant densities less than $\frac{1}{100}$ times the peak δ -doped density. Though the discrete charges are located at only 5\AA - 10\AA of the quantum dot, they seem to produce more dramatic modulations of the potential in the quantum well. A comparison of the conduction band edge to the dopant profile in the tail, reveals strong correlations between the point charges and the potential modulations, with a significant disorder in the potential surface. On average, the isolated point charges do not change the average potential value very much, but induce pronounced fluctuations which has a drastic effect on local regions within the potential well. This implies that the positions of the remote ions in the δ -doped tail has a more important effect on the shape of the well than the positioning of remote ions in the densely-doped regions.

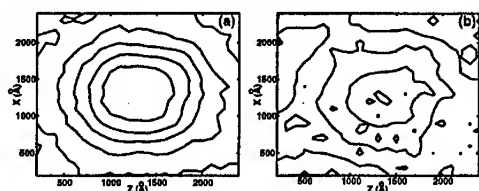


Fig 6. Contour plots of the Conduction Band in the Quantum Well, parallel to the AlGaAs/GaAs Interface.

The dopant density fluctuations in the densely-doped region of the δ -doped layer have a different effect on the device behavior. We have simulated the same device with different random distribution of the dopant density in the densely-doped regions which also results in fluctuations in the total number of dopants in

the δ -doped layers. For all these configurations, we have intentionally excluded the sparsely-doped tail of the dopant layer to remove the effects of isolated point charges. The different charging curves for each configuration with the total number of dopant atoms are shown in figure 7. The charging characteristic for a perfect device with uniform dopant density is also shown for comparison (Fig. 7 (solid line)). As expected the general trend is a shift to the left of the charging curves of quantum dot with increasing number of donors, since the threshold voltage decreases. There is an approximate 5mV shift in threshold voltage for a difference of 1 dopant/dot in the δ -doped layer. However, the shifts are not proportional to the variations of donor atom numbers, which could be explained by the weaker dependence of the charging characteristics on the distribution of the dopants in the δ -doped layer as well. This can be seen in the comparison of the perfect crystal with a disordered configuration containing the same number of dopants (1218 donors) (Fig7). The disordered device, with dopant density fluctuations, deviates slightly from the perfect crystal, by about 2mV. Hence, we have demonstrated that both potential fluctuations in different distributions of dopant ions and the fluctuations in the total number of dopant ions in the quantum dot affects, in their own way, the threshold voltage of the device.

The presence of discrete acceptor dopants in the quantum well region also distorts the shape of the confining potential, causing drastic variations in the electron wavefunctions.

The acceptor impurity is placed 150Å away from the interface at the center of the gate aperture where the electron density peaks. It is progressively moved from the center to regions under the gate. We obtain the charging behavior for each position. Fig. 8(b) shows that the screening of the acceptor ion when the acceptor is located close to the center of the aperture, the charging curves converges for high electron numbers. However, when the acceptor sits under the gate, depleted of electrons, the charging curve suffer greater distortion.

IV. CONCLUSIONS

In summary, the short-ranged disorder introduced by interface roughness which is localized near the interface modulates the electron density over the extent of the wavefunction (100Å to 200Å). However, the overall charging characteristic of the device only experiences an averaged fluctuation of 1 to 2mV. On the other hand, long-ranged potential modulations due to random dopant impurities in the δ -doped layer extend deeper into the quantum dots. These fluctuations depend strongly on the averaged separations between the ions. Ions that are closely spaced (eg. in the densely-doped regions) might not necessarily produce larger spatial fluctuations of

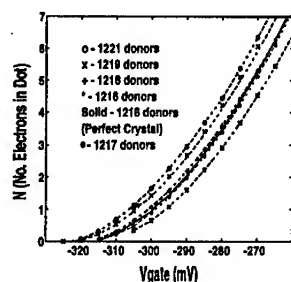


FIG 7. Charging curves for configurations with different number of δ -dopant atoms. The charging curve for the perfect crystal device with uniform doping density in the δ -doped layer is plotted for comparison.

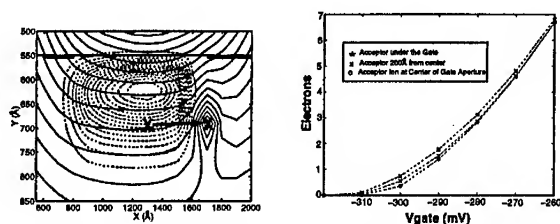


FIG 8. (a) Solid lines: shows the x-y contour plot of the potential. Dashed lines: shows the corresponding electron density contour. (X marks show the movement of the point charge ion from the center of aperture to regions under the gate.) (b) The corresponding variation in the device charging curves as acceptor point charge is moved.

the long-range potential due to the convolution effects of the $1/r$ potential tails. Thus lead to rapid attenuation by charge screening in regions of high electron population. Local point charges in the quantum well produce more dramatic effects on the electronic bound state energies and the wavefunctions. As the active region is small, electron population in the well is unable to screen the much larger potential spike. The largest variation in device behavior seems to be due to variation in dopant number rather than potential fluctuations.

ACKNOWLEDGEMENT

This work is supported by NSF Grant ECS 95-09751 and the Joint Services Electronics Program.

References

- [1] U.Meirav, E.B.Foxman, Semicond. Sci. Technol 10 (1995) 255-284.
- [2] V.Y.Thean, S.Nagaraja and J-P.Leburton J. Appl. Phys., To be published.
- [3] D.Jovanovic & J.P. Leburton, Phys Rev B 50 5412 (1994).
- [4] M.Stopa, Phys Rev B, 54 767 (1996).
- [5] J.H.Davies and J.A.Nixon, Phys Rev B, 39 7929 (1989).
- [6] M.Macucci, K.Hess & G.J.Iafrate, Phys Rev B, 48 354 (1993).
- [7] D.Jovanovic & J.P. Leburton, Phys Rev B 49 7474 (1994).
- [8] I-H. Tan, G.L. Snider, L.D. Chang, and E.L. Hu, J. Appl. Phys. 68 4071 (1990).
- [9] C.Orme, M.D.Johnson, K.T. Leung, B.G.Orr, P.Smilauer, D.Vvedensky, Journal of Crystal Growth 150 128 (1995).
- [10] Numerical Recipes in Fortran, The Art of Scientific Computing, W.H.Press, S.A.Teukolsky, W.T.Vetterling, B.P.Flannery. Cambridge University Press, 1992.

**ELECTRONIC STRUCTURE OF THE VALENCE BAND OF
TETRAGONAL GERMANIUM NANOSTRUCTURES DEPOSITED
BY THE CLUSTER-BEAM EVAPORATION TECHNIQUE**

S. Sato, S. Nozaki and H. Morisaki
Department of Communications and Systems
The University of Electro-Communications,
1-5-1, Chofugaoka, Chofu-shi, Tokyo 182,
Japan

ABSTRACT

The electronic structure of the valence band of germanium (Ge) nanostructures deposited by cluster-beam evaporation were analyzed with X-ray photo-emission spectroscopy (XPS). The XPS spectrum has shown an excellent agreement with the density of states of tetragonal (ST-12) Ge, suggesting that the Ge nanostructures have an ST-12 structure, distinct from the crystal structure of bulk Ge. The optical absorption spectrum in the region from near infrared to near ultraviolet also shows that the film has an ST-12 Ge structure.

Although the ST-12 Ge structure is known to be metastable, the obtained Ge nanostructures have the density of states of the ST-12 Ge even after annealing at 700°C and are considered to be thermally stable.

I. INTRODUCTION

Much attention has been drawn to semiconductor clusters because of their unique physical and chemical properties. Computer simulations of the crystallographic structures and of the electronic states of small clusters containing up to 10^2 atoms have been performed, (1) while those of giant clusters containing up to $10^3 \sim 10^4$ atoms are hindered by a lack of an efficient theoretical model. A giant cluster, which is an intermediate phase between a small cluster and a bulk crystal, is expected to show novel properties distinct from those of a small cluster or a bulk crystal. The theoretical calculation of silicon (Si) clusters predicts that their crystal structures are more close-packed than for bulk structures in order to

reduce the number of dangling bonds (1). It suggests that the structure of Si clusters is closely related to the high pressure form of Si. This is also true for germanium (Ge) clusters. We have recently found evidence that Ge nanostructures fabricated by cluster-beam evaporation are stable by taking a simple tetragonal structure with 12 atoms in the unit cell (ST-12), (2) which is well known as a high-pressure form of Ge: the theoretical density is 5.91 g/cm³, as compared to 5.32 g/cm³ for diamond Ge (3). Joannopoulos and Cohen (4) made a theoretical calculation using the empirical-pseudopotential method and predicted that the ST-12 Ge structure would have a direct band gap of 1.47 eV. An experimental study also confirmed that ST-12 structured Ge is a semiconductor with an electrical resistivity that decreases when the temperature rises (3). The ST-12 Ge structure can, therefore, become an attractive material for a wide range of device applications including light emitting devices on condition that the structure is thermally stable under atmospheric pressure at relatively elevated temperature. Unlike Si and compound semiconductors, Ge has been regarded as a less interesting material because of its band gap, that is small and indirect.

In this study, we present the density of states (DOS) of the valence band of Ge nanostructures determined by the X-ray photo-emission spectroscopy (XPS). Our results suggest presence of an ST-12 structure. We also show the optical absorption spectra of them to support the result of the XPS analysis. It should be emphasized that the analysis of the crystal structure of nano-sized materials by X-ray or electron-beam diffraction is often difficult because the diffraction peak intensities become substantially weaker and broader as the size decreases.

II. EXPERIMENTAL

The cluster-beam evaporation technique, which was described in detail elsewhere, (2) was employed to deposit films consisting of Ge nanostructures on Si and quartz substrates. During the deposition, the substrate temperature was kept at room temperature. Hereafter, we refer to the obtained Ge films as Ge-RT films.

The electronic structure of the valence bands of the Ge-RT films was

analyzed with an XPS spectrometer (Shimadzu ESCA K-1). In order to avoid effects of the surface contamination and to remove the native oxide on the surface, the samples were sputtered with Ar ions before the measurement. The individual Ge nanostructure was identified by a ultra-high vacuum scanning tunneling microscope (UHV-STM), and the optical absorption measurements were carried out with a Shimadzu UV-3100PC to estimate the band gap and to support DOS data obtained by XPS analysis.

III. RESULTS AND DISCUSSION

Figure 1 shows the UHV-STM image of a Ge-RT film on a Si substrate. The film consists of giant clusters whose diameters are $3 \sim 4$ nm, corresponding to $\sim 10^4$ Ge atoms in a cluster. The size distribution appears to be narrow, and the clusters are dense.

A typical XPS spectrum of an as-deposited Ge-RT film is shown by the curve (a) in Fig. 2. The detailed analysis of the DOS by XPS is described elsewhere (5). We have extended the analysis of the XPS data for amorphous Si and Ge developed by Joannopoulos and Cohen (4) to compare the XPS data with the theoretical DOS for the ST-12 Ge structure. In Fig. 2, the theoretical DOS curves (b), (c), (d) and (e) are for the diamond structure, for the hexagonal structure with four atoms in the unit cell (2H-4), for the body-centered cubic structure with eight atoms in the unit cell (BC-8), and for the ST-12, respectively. Here, the theoretical curves have been smoothed out by averaging the DOS values over the range of ± 0.1 eV in order to compare with the experimental data which have a minimum energy resolution of 0.05 eV. The curve (f) in Fig. 2 is the experimental XPS spectrum of amorphous Ge.

Joannopoulos and Cohen (4) studied the band structures of the 2H-4, BC-8 and ST-12 forms of Ge to clarify the electronic properties of amorphous Ge. In order to discuss the electronic properties of the long-range disordered Ge, they considered these high-pressured forms composed of strained tetrahedral bondings. Among them, only the ST-12 structure has five-fold rings in the network, which is a characteristic feature of amorphous Ge and Si. The DOS curves reflect this feature: two

peaks are observed at about 1 eV and 8 eV for the ST-12 structure, as compared with three peaks at about 2 eV (known as the *p*-like peak), 7 eV and 10 eV (known as the *s*-like peaks) for the other crystal structures. Therefore, it is rather easy to identify the ST-12 structure. These features in the DOS curves are, therefore, quite useful to determine the crystal structure of Ge clusters.

The XPS spectrum of the Ge-RT film in Fig. 2 is in good agreement with the theoretical DOS curve of the ST-12 structure: both show two broad peaks at about 1 eV and 8 eV.

Figure 3 shows the XPS spectra of Ge-RT films annealed at various temperatures. The spectra of the samples annealed at temperatures lower than 700°C show two peaks, resembling the theoretical DOS curve of the ST-12 structure, while the spectrum of the Ge-RT film annealed at 800°C shows a distinct difference and rather resembles the DOS curve of the diamond structure. The phase transformation of the Ge nanostructures in the Ge-RT film from the ST-12 to the diamond structure was previously studied by Raman spectroscopy (6). It was found that the ST-12 structure in the Ge-RT film was more thermally stable than that in the Ge film deposited by the gas-evaporation technique and requires a higher annealing temperature for the phase transformation into the diamond structure. The critical temperature of the phase transformation found by the Raman study was 800°C and is consistent with that by obtained with the DOS investigation.

The solid curve in Fig. 4 is the optical absorption spectrum of the as-deposited Ge-RT film near the band edge. Although the construction of the absorbance curve from the theoretical absorption-coefficient curve requires accurate thickness, the shape of the absorbance curve is rather different from that for the diamond-structured Ge. The absorption starts to rise at 0.6 ~ 0.8 eV but increases sharply only at ~1.6 eV.

Since the optical absorption spectrum of amorphous Ge (curve (b) in Fig. 4) is in good agreement with the experimental curve in the low energy region, the Ge-RT film contains the amorphous phase. However, the optical absorption spectrum in the higher energy region is distinct from those of the diamond or amorphous phase. A simple addition of the optical

absorption spectra of the amorphous and ST-12 phases with adjusting parameters for thicknesses well reproduces that of the Ge-RT film. Here, although theoretical construction of the absorbance curve of Ge nanostructures consisting of the amorphous and ST-12 phases requires each thickness, the thicknesses were adjusted to see whether the constructed curve can fit to the experimental curve. This suggests that the absorption in the energy region higher than 1.6 eV is mainly from the ST-12 phase. One may argue that the band gap of the Ge-RT film consisting of the ST-12 structure of Ge should be much higher than 1.47 eV (the theoretical band gap of the bulk ST-12 structure) because of the quantum size effect. However, we do not expect the carrier confinement, simply because an individual Ge nanostructure physically touching adjacent ones, as clearly observed in Fig. 1, causes overlap of the electron wave functions in two nanostructures.

IV. SUMMARY

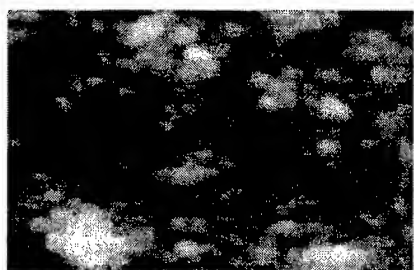
In the UHV-STM image, the Ge-RT film deposited by cluster-beam evaporation consists of Ge nanostructures whose diameters are 3~4 nm with a narrow size distribution. They are dense enough for an individual nanostructure to touch adjacent ones. The XPS spectrum of the Ge-RT film resembles the theoretical DOS of the ST-12 Ge structure, suggesting that the Ge nanostructures have a ST-12 structure. The optical absorption spectrum of the Ge-RT film also supports that the crystal structure of the Ge nanostructures in the Ge-RT film is not the diamond but the ST-12 structure. The DOS study of Ge-RT films annealed at various temperatures shows that the ST-12 structure in the films is thermally stable.

ACKNOWLEDGMENT

One of the authors (S. Sato) greatly appreciates a grant from the Sasakawa Science Foundation. This study was partly supported by the Yazaki Science Promotion Foundation and the Mechanical Industry Development & Assistance Foundation, and also by Grant-in-Aid for Scientific Research (B) of the Ministry of Education Science and Culture.

REFERENCES

1. M. F. Jarrold, *Science* **252**, 1085 (1991).
2. S. Sato, S. Nozaki, H. Morisaki, and M. Iwase, *Appl. Phys. Lett.* **66**, 3176 (1995).
3. F. P. Bundy and J. S. Kasper, *Science* **139**, 340 (1963).
4. J. D. Joannopoulos and M. L. Cohen, *Phys. Rev. B* **7**, 2644 (1973).
5. G. Margaritondo and J. H. Weaver, *Solid State Physics: surfaces*, ed. R. L. Park and M. G. Legally, (Academic Press, New York 1985), pp. 127-185.
6. S. Nozaki, S. Sato, H. Ono, H. Morisaki, and M. Iwase, *Mat. Res. Soc. Symp. Proc.* **405**, 223 (1996).



20 nm

Fig. 1. Ultrahigh vacuum scanning tunneling microscope (UHV-STM) image of a Ge-RT film.

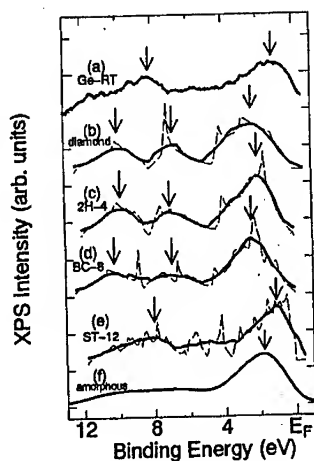


Fig. 2. XPS and DOS curves. The curve (a) is the XPS spectrum of an as-deposited Ge-RT film. The broken curves (b), (c), (d) and (e) represent the theoretical DOS curves of the diamond, the 2H-4, the BC-8 and the ST-12 structures, respectively. By considering the step width of the XPS measurements, we smoothed out the curves in (b), (c), (d) and (e) by averaging the adjacent data in the range of ± 0.1 eV (solid curves). The curve (f) is the experimental XPS curve of amorphous Ge. The spectra in (b)~(f) are from Ref. 4.

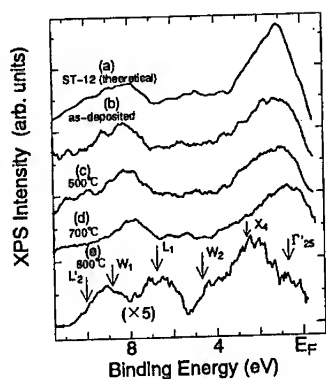


Fig. 3. The XPS spectra of annealed Ge-RT films. The theoretical spectrum of the ST-12 structure is also shown in curve (a). The curves (b), (c), (d), and (e) are the spectra of the as-deposited sample, samples annealed at 500°C, 700°C, and 800°C, respectively. The singular points of the diamond structured Ge are shown in the spectrum of the sample annealed at 800°C.

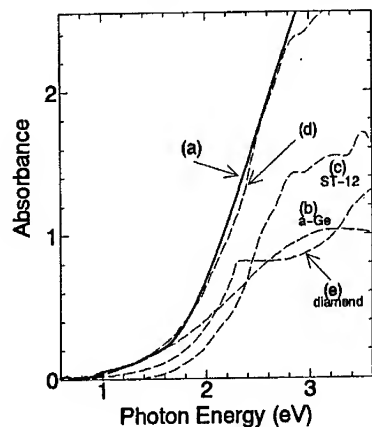


Fig. 4. The optical absorption spectrum of an as-deposited Ge-RT film (a). The spectrum of an amorphous film and the theoretical absorption spectrum are shown in curves (b) and (c), respectively. The curve (d) is the spectrum obtained by addition of the curves (b) and (c).

EFFECT OF THE INTERFACE ROUGHNESS ON THE SHALLOW DONOR IN A QUANTUM DOT

Jian-Min Shi, Valder N. Freire, and Gil A. Farias
Departamento de Física, Universidade Federal do Ceará,
C.P. 6030, Campus do Pici, 60455-760 Fortaleza, Ceará, Brazil

ABSTRACT

A theoretical study is presented of interface roughness effects on a shallow donor in a graded GaAs/ $\text{Al}_x\text{Ga}_{1-x}\text{As}$ spherical quantum dot. Such roughness is simulated by a linear variation of the Al molar fraction in the interface region. The ground state of the shallow donor located at an arbitrary position has been calculated by a variational approach. A detailed comparison of our results is performed with those obtained in the corresponding structures having sharp interfaces. We find that the existence of the interface roughness enhances the energy of the donor state. In some cases this enhancement is observable in experiments. The intensity of the broken spherical symmetry of the system due to the off-center donor becomes stronger with the increase of the interface influence. The effect of band nonparabolicity on the donor state is discussed within a simple Kane model, and shown to be important for strong confinement systems.

I. INTRODUCTION

In recent years, impurity states in both bulk semiconductors and confined structures such as quantum wells, superlattices, quantum wires, and quantum dots have been an interesting subject for theoretical and experimental investigations [1-4] because the properties of impurities are of particular importance to the design of devices. Among the most extensively studied systems are those consisting of GaAs and $\text{Al}_x\text{Ga}_{1-x}\text{As}$ doped with Si atoms. Since the optical and transport properties are strongly influenced by both these dopants and the type of low dimensional confinement structures, the knowledge of the effect of the confinement potential

on the impurity state is very helpful.

Most of previous theoretical calculations of the donor states in low dimensional systems address an ideal interface between different semiconductors, *i.e.*, the interface is absolutely sharp, and the conduction band can be expressed by a square-well potential. However, recent experiments have shown that the interface between GaAs and $\text{Al}_x\text{Ga}_{1-x}\text{As}$ is nonabrupt, and they extend along the growth axis through a region between two and four GaAs unit cells [5]. A simple model including such interface roughness has been proposed to study free electrons in a graded quantum well [6], and later this method was used to discuss a shallow donor in the same structure [7]. Recently we have found that the effect of such graded interface is more pronounced for an electron in a quantum dot than in a quantum well due to the stronger confinement [8].

In this work, we study the ground state of a Si shallow donor in a graded spherical GaAs/ $\text{Al}_x\text{Ga}_{1-x}\text{As}$ quantum dot. Since the Schrödinger-like equations can not be solved exactly for the donor away from the dot center, a variational approach is used to calculate the energy level and the wave function of the donor ground state, in which the spatial dependence of the electron effective mass on the Al concentration is included. The binding energy shift of the donor state due to the existence of the interface roughness is obtained. It is found that such shift should be observable by optical measurements in strong confinement quantum dots. The influence of band nonparabolicity on the binding energy of the donor included with a standard Kane model [9] is shown also to be important for the system under study.

II. VARIATIONAL CALCULATION

The system considered here consists of a Si dopant located at position \vec{R}_0 measured from the center (0,0,0) of a graded spherical quantum dot. This structure is a GaAs dot of radius R surrounded by a bulk $\text{Al}_x\text{Ga}_{1-x}\text{As}$ semiconductor, and a graded GaAs/ $\text{Al}_x\text{Ga}_{1-x}\text{As}$ interface of width W ($R > W$) extending from $R-W$ to R . Based on the standard effective-mass approximation, the Hamiltonian describing this system can be written as

$$H = \vec{p} \frac{1}{2m^*(r)} \vec{p} - \frac{e^2}{\epsilon_0 |\vec{r} - \vec{R}_0|} + V(r), \quad (1)$$

where \vec{p} and \vec{r} are, respectively, the momentum and position operator for the donor electron, $-e$ is the electronic charge, $\epsilon_0 = 12.5$ is the dielectric constant of GaAs [10] assumed to be uniform in the whole structure. In Eq. (1), the graded spherical confinement potential depends on the distribution of the Al concentration in the

structure, that is taken here to be [11]

$$V(r) = \begin{cases} 0, & r < R - W \\ 0.693y + 0.222y^2 \text{ (eV)}, & R - W < r < R \\ 0.693x + 0.222x^2 \text{ (eV)}, & r > R, \end{cases} \quad (2)$$

where

$$y = x \frac{r + W - R}{W} \quad (3)$$

describes a linear interfacial Al molar fraction variation. This type of dependence was assumed early in previous work for different systems [6,7]. The quantity $m^*(r)$ is the electron effective mass, which changes also with the variation of the Al concentration in the samples according to the following expression [10]

$$m^*(r)/m_e = \begin{cases} 0.067, & r < R - W \\ 0.067 + 0.083y, & R - W < r < R \\ 0.067 + 0.083x, & r > R, \end{cases} \quad (4)$$

with m_e the electron mass in vacuum. Since the present work aims at studying the interface effect on the donor state, we will pay attention mainly to strong confinement quantum dots, as well as to dots having not very small radii in order to allow some space for change in the interface width. The Al concentration $x = 0.3$ in the $\text{Al}_x\text{Ga}_{1-x}\text{As}$ alloy is fixed in this work, and the electron band offset is considered to be 60% of the total band-gap difference between the two semiconductors.

For the system with donor position $\vec{R}_0 \neq 0$, the spherical symmetry is broken. Therefore, the Schrödinger-like equations in such case can not be solved exactly. A variational calculation for the ground state of the donor will be given. Because in general the electron energy related to the quantum dot potential is much larger than the Coulomb energy, one can explicitly factor out the associate solution to an electron in the same structure in the absence of any impurities [3]. Consequently, the variational wave function of the donor state can be written as the product of two functions,

$$\Psi(\vec{r}, \vec{R}_0) = \psi(\vec{r}) \exp \left[-\alpha \sqrt{\rho^2 + \beta^2(z - R_0)^2} \right], \quad (5)$$

where the donor position has been chosen as $\vec{R}_0 = (0, 0, R_0)$, ρ is the distance of the electron in the x - y plane, and $\psi(\vec{r})$ is the lowest-energy (E_e) wave function of a free electron (here a free electron implies that the electron is free from any Coulomb interaction) in the same structure. In actual calculation, we have approximated the variation of the potential energy and of the electron effective mass in the interface region by a multistep function [12]. This simple approximation allows one to obtain the wave function of the free electron state and to determine its energy

level through the solution of a transcendental equation. The detailed calculation of this solution has been given in our other paper in the same volume [8].

The second factor on the right-hand side of Eq. (5) describes the Coulomb interaction between the donor electron ($-e$) and the donor ion ($+e$). It has two variational parameters α and β which are determined such that they minimize the energy E_D of the donor according to the following equation

$$E_D = \frac{\langle \Psi(\vec{r}, \vec{R}_0) | H | \Psi(\vec{r}, \vec{R}_0) \rangle}{\langle \Psi(\vec{r}, \vec{R}_0) | \Psi(\vec{r}, \vec{R}_0) \rangle}. \quad (6)$$

We have examined the accuracy of this approach by comparison of our result with an exact solution obtained in Ref. [7], and found that the difference of the binding energy E_B , which is defined by

$$E_B = E_c - E_D, \quad (7)$$

between these two methods is very small, less than one percent for the donor located at the center of an abrupt GaAs/Al_xGa_{1-x}As quantum dot with $x = 0.3$ and $R = 50$ Å.

It is well known that in strong confinement systems and/or in the presence of an external electric and magnetic field, band nonparabolicity becomes important to the donor energy level [2,3]. The effect of band nonparabolicity is included in the calculation by using the standard Kane model [13] given by

$$E_{np} = \frac{E_g}{2} \left(\sqrt{1 + \frac{4E_p}{E_g}} - 1 \right), \quad (8)$$

where E_{np} and E_p are, respectively, the donor (or free electron) energy with and without the effect of band nonparabolicity, and $E_g = 1.52$ eV is the band gap of GaAs. This expression has been used to successfully describe band nonparabolicity for the electron and donor energy levels in bulk GaAs [2] as well as in GaAs/Al_xGa_{1-x}As superlattices [3] at high magnetic fields.

III. NUMERICAL RESULTS

A numerical calculation has been performed of the energy level and the wave function of a shallow donor located in a graded spherical quantum dot with $x = 0.3$ for different dot radii and various donor positions. In actual calculation, we have used the natural units of GaAs: the effective Bohr radius $a_0^* = \hbar^2 \epsilon_0 / m^*(0) e^2 = 98.7$ Å as the unit of length, and the effective Rydberg $R^* = e^2 / 2 \epsilon_0 a_0^* = 5.83$ meV as the unit of energy.

In order to simply describe the donor state, we plot in Fig. 1 the two variational parameters α and β as a function of the interface width for quantum dots with

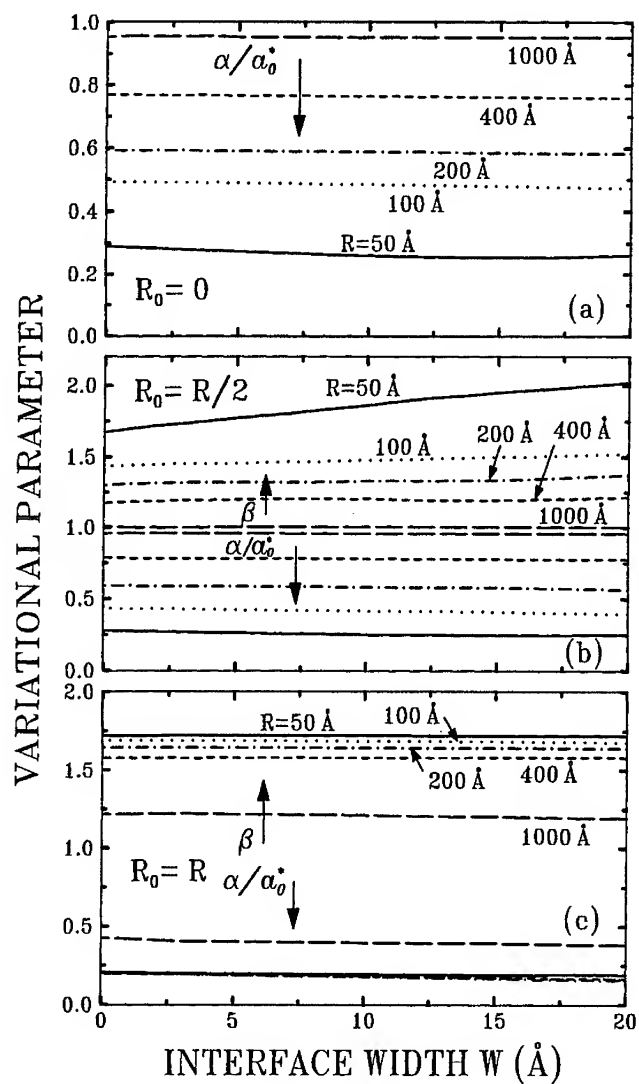


Figure 1: Behaviour of the two variational parameters α and β as a function of the interface width for graded quantum dots with five different radii and three typical donor positions: (a) $R_0 = 0$, (b) $R_0 = R/2$, and (c) $R_0 = R$.

radii $R = 50 \text{ \AA}$ (solid), 100 \AA (dotted), 200 \AA (dot-dashed), 400 \AA (short-dashed), and 1000 \AA (long-dashed curves), and also for the donor located: (a) at the dot center $R_0 = 0$; (b) at the midpoint $R_0 = R/2$ between the dot center and the interface; and (c) in the interface $R_0 = R$. In doing so, we have limited ourselves to the variational calculation which determines the energy level and the values of α and β since the solution of the free electron can be found exactly [8]. Note that the parameter α has the dimension of the reverse of length, while β is dimensionless.

For the dot-center donor, β is constant and equal to 1 due to the fact that such system has always spherical symmetry. It is not plotted in Fig. 1(a). The value of α decreases with the increase of the quantum dot confinement (decrease of the dot radii) since the Coulomb interaction becomes relatively less important in this case. When R is going to infinite, the situation of a three-dimensional hydrogen-like atom is recovered, which can be seen clearly in the case of an $R = 1000 \text{ \AA}$ dot where α is approaching to 1. When the donor is located away from the dot center, the spherical symmetry of the system is broken. The intensity of such break is described by β , whose value is always larger than 1. This indicates that β follows the direction of the donor-center movement in which the Coulomb interaction is stronger than in others. The interface effect on the intensity of the symmetry breaking becomes stronger with the donor center moving away from the dot center and becomes weaker when the donor is close to the interface [compare Figs. 1(a) and 1(c) to Fig. 1(b)]. This is due to the fact that the dot-center donor does not break the symmetry of the system and the very far-away donor has little influence on the electron probability distribution for strong confinement quantum dots. Therefore, the disturbance of the Coulomb interaction on the system symmetry must not be a monotonous function of the donor position. The value of α decreases with increasing the distance R_0 between the donor center and the dot center since the Coulomb interaction is becoming weaker.

The binding energy of the shallow donor can be obtained by the use of Eq. (7). Two calculations are performed in this work: one is for the ground state of the shallow donor in the quantum dot, and the other for that of a free electron in the same structure. Figure 2 depicts the binding energy for a shallow donor as a function of the interface width in the same system as shown in Fig. 1. Increasing confinement in the quantum dot forces the electron closer to the impurity center when it is located inside the dot. As a consequence, the Coulomb interaction between the donor ion and the electron will become stronger, which enhances the binding energy. This can be seen for the case of quantum dots with different radii. The interface effect is shown clearly only for the strong confinement system when the donor is located around the dot center. For graded quantum dots with radii larger than 200 \AA , such effect can be neglected even when one has an interface with width up to 20 \AA , which corresponds roughly to the length of four GaAs unit cells. However, for small quantum dots the interface roughness influences strongly

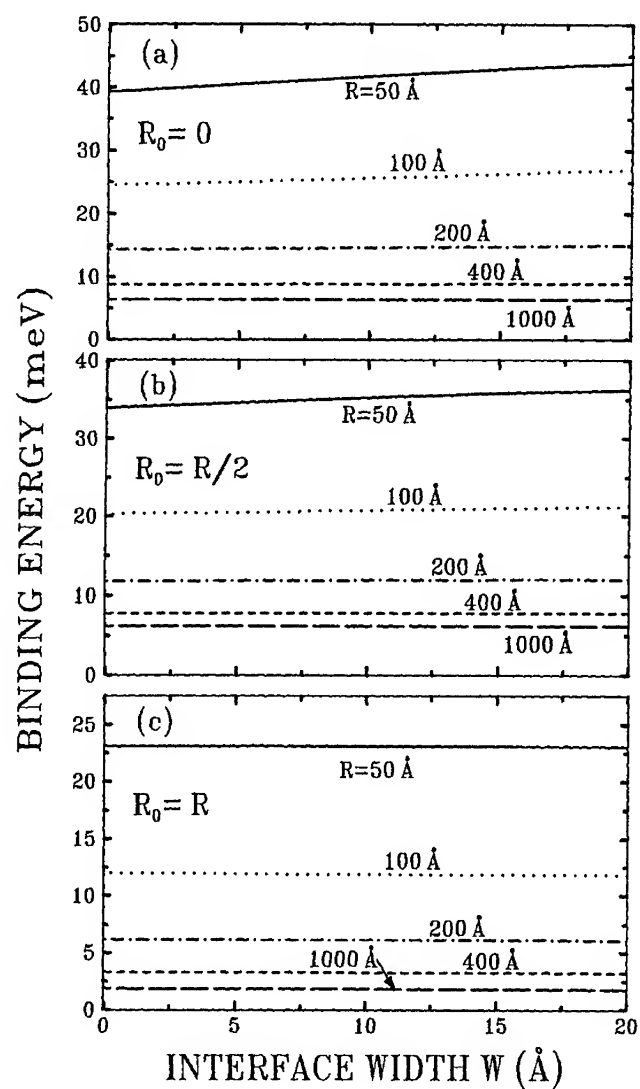


Figure 2: Binding energy of the donor ground state as a function of the interface width for graded quantum dots with five different radii and three typical donor positions: (a) $R_0 = 0$, (b) $R_0 = R/2$, and (c) $R_0 = R$.

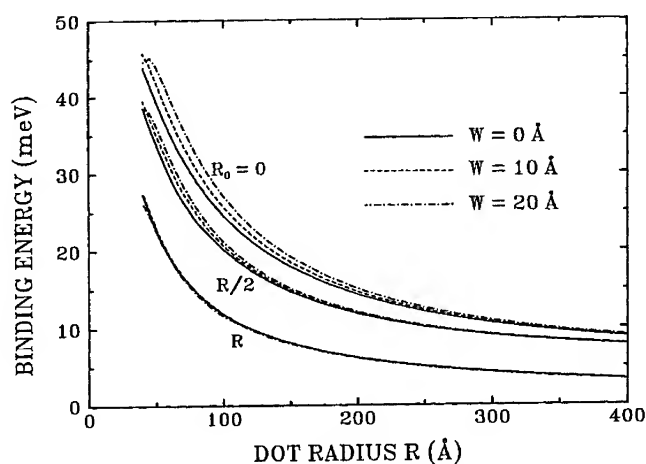


Figure 3: Dot-radius dependence of the binding energy of a donor at three typical positions in the graded quantum dots with three different interface widths.

the binding energy of the shallow donor. For instance, due to the existence of the interface roughness the binding-energy shift of the dot-center donor in the $R = 50$ Å ($R = 100$ Å) quantum dot is about 2.5 (1.1) meV for $W = 10$ Å, and about 4.6 (2.5) meV for $W = 20$ Å, respectively, as compared to the corresponding results for the sharp-interface quantum dots. For the $R_0 = R/2$ donor in the same quantum dot, the binding-energy shift decreases and is about a half of that for the dot-center donor: 1.3 (0.47) meV for $W = 10$ Å, and 2.3 (1.0) meV for $W = 20$ Å for the dot with $R = 50$ Å ($R = 100$ Å). The accuracy of recent optical measurements is as high as 2 cm^{-1} [2] which is about 0.25 meV. Therefore, the measurement of the binding energy of the shallow donor near the dot center will provide useful information on the roughness of interfaces. Notice that in the limit of bulk GaAs, the correct behavior of the donor state is recovered: the binding energy of the shallow donor approaches that of a donor in bulk GaAs with increasing dot radii R for the cases of $R_0 = 0$ and $R_0 = R/2$, while the $R_0 = R$ donor will act as an interface donor in a GaAs/ $\text{Al}_x\text{Ga}_{1-x}\text{As}$ heterostructure, having a binding energy less than one effective Rydberg.

In Fig. 3, we have plotted again the binding energy of a shallow donor which is located at three typical positions $R_0 = 0$ (upper-), $R_0 = R/2$ (middle-), and $R_0 = R$ (lower-group curves) in a graded quantum dot as shown in Fig. 2, but now as a function of the dot radius for three different interface widths: $W = 0$ Å (solid) $W = 10$ Å (dashed), and $W = 20$ Å (dot-dashed curves). It is clear that the effect

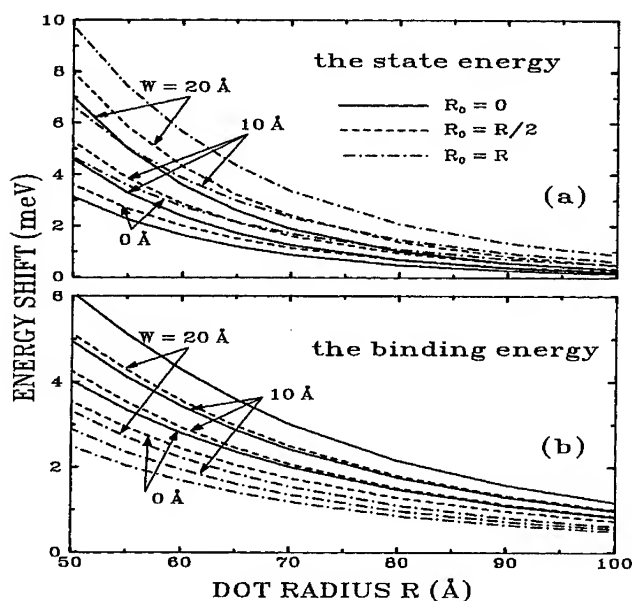


Figure 4: Dot-radius dependence of the energy shifts due to band nonparabolicity for a donor at three typical positions in the graded quantum dots with three different interface widths. (a) is for the ground state energy, and (b) for the binding energy.

of the interface roughness increases the binding energy of the donor which is close to the dot center, and changes little in the case of the interface donor. When the dot radius goes to infinite, the states of the dot-center ($R_0 = 0$) donor and the $R_0 = R/2$ donor degenerate. They behave as a donor in bulk GaAs. On the other hand, the interface donor ($R_0 = R$) is always in contact with two different semiconductors. As a result, the potential of the barrier pushes the electron away from the donor center so that its binding energy is less than that of a donor in bulk GaAs, and depends on the barrier height. In our case ($x = 0.3$), we found that the binding energy of the interface donor approaches to a quarter of that for bulk GaAs. Notice that the binding energy of the donor state decreases when the quantum-dot radius turns to be very small. This is due to the finite height of the barrier which makes the system to change from strong confinement to bulk $\text{Al}_x\text{Ga}_{1-x}\text{As}$ when $R \rightarrow 0$ [14].

We present in Fig. 4 the numerical results for the dot-radius dependence of

the energy shift ($E_p - E_{np}$) due to band nonparabolicity for: (a) the state energy and (b) the binding energy of the donor located at the positions $R_0 = 0$ (solid), $R_0 = R/2$ (dashed), and $R_0 = R$ (dot-dashed curves) in graded quantum dots with interface widths $W = 0$ Å, $W = 10$ Å, and $W = 20$ Å, respectively. The effect of band nonparabolicity is shown to decrease the donor energy [see Fig. 4(a)]. It becomes more important with increasing confinement (such as decreasing the dot radius, increasing the interface width, and also with the donor moving away from the dot center), so that the energy difference of the donor without (E_p) and with (E_{np}) band nonparabolicity becomes larger. The influence of band nonparabolicity on the binding energy of the donor, which is also large enough to be measurable by experiments, shows the same behavior as that on the state energy (both decrease) with increasing dot radius. But this effect gives an opposite dependence on the donor position for the binding energy and the state energy, *i.e.*, the binding (state) energy shift decreases (increases) with the donor moving further away from the dot center. The binding energy shift due to band nonparabolicity is about 3 (0.5) meV for a dot-center donor in an $R = 50$ Å (100 Å) quantum dot in the absence of any effect of the interface roughness, which is comparable with the shift due to the existence of a graded interface, as can be seen in Fig. 4(b).

Therefore, in order to correctly predict and/or describe measurements of the binding energy of a shallow donor in the actual system the effect of both interface roughness and band nonparabolicity should be taken into account.

IV. CONCLUSIONS

We have performed a theoretical study of a shallow donor in a graded GaAs/ $\text{Al}_x\text{Ga}_{1-x}$ spherical quantum dot. Using a variational approach, we have studied the ground state of a shallow donor which can be located at an arbitrary position in the quantum dot. A detailed comparison of our results has been done with those obtained for the corresponding structures having sharp interfaces. We found that: (i) the existence of the interface roughness enhances the energy of the donor state as well as its binding energy. In strong confinement systems this enhancement can be observable in experiments; (ii) the break of the spherical symmetry of the system becomes stronger with the donor moving away from the dot center and then turns to be weaker when the donor reaches the interface region, while the interface roughness increases the intensity of such break; and (iii) the effect of band nonparabolicity on the donor state is also important for small dot systems, which is comparable with the effect of the interface roughness for the case under study. Further study on the same structure but for the donor excited states and in the presence of an external electric and magnetic field is in progress.

ACKNOWLEDGEMENT

One of us (J.M.S.) was supported by FUNCAP (Ceará, Brazil) and would like to thank Universidade Federal do Ceará for the hospitality. V.N.F. and G.A.F. would like to acknowledge financial support from FINEP and CNPq (Brazil).

References

- [1] A. A. Reeder, J. M. Mercy, and B. D. McCombe, IEEE J. Quantum Electron. **QE-24**, 1690 (1988), and references therein.
- [2] J. P. Cheng, B. D. McCombe, J. M. Shi, F. M. Peeters, and J. T. Devreese, Phys. Rev. B **48**, 7910 (1993).
- [3] J. M. Shi, F. M. Peeters, and J. T. Devreese, Phys. Rev. B **50**, 15 182 (1994).
- [4] D. S. Chu, C. M. Hsiao, and W. N. Mei, Phys. Rev. B **46**, 3898 (1992).
- [5] See, *e.g.*, A. Ourmazd, D. W. Taylor, J. Cunningham, and C. W. Tu, Phys. Rev. Lett. **62**, 933 (1989).
- [6] V. N. Freire, M. M. Auto, and G. A. Farias, Superlatt. Microstruct. **1**, 17 (1992).
- [7] J. L. Zhu, D. L. Lin, and Y. Kawazoe, Phys. Rev. B **54**, 16 786 (1996).
- [8] V. N. Freire, J. M. Shi, and G. A. Farias, in this Symposium.
- [9] See, *e.g.*, X. G. Wu, F. M. Peeters, and J. T. Devreese, Phys. Rev. B **40**, 4090 (1989).
- [10] S. Adachi, J. Appl. Phys. **58**, R1 (1985).
- [11] H. J. Lee, L. Y. Juravel, J. C. Wolley, and A. J. Springthorpe, Phys. Rev. B **21**, 659 (1980).
- [12] Y. Ando and T. Itoh, J. Appl. Phys. **61**, 1497 (1987).
- [13] G. Ambrazevicins and M. Cardona, Phys. Rev. Lett. **63**, 2288 (1989).
- [14] F. M. Peeters, J. M. Shi, and J. T. Devreese, Physica Scripta. **T55**, 57 (1994).

ENERGY STATES IN GRADED SPHERICAL GaAs/Al_xGa_{1-x}As QUANTUM DOTS

Valder N. Freire, Jian-Min Shi, and Gil A. Farias
Departamento de Física, Universidade Federal do Ceará,
C.P. 6030, Campus do Pici, 60455-760 Fortaleza, Ceará, Brazil

ABSTRACT

We perform a theoretical study of the interface effect on the energy states of a single electron in graded spherical GaAs/Al_xGa_{1-x}As quantum dots. The spatial dependence of the graded dot potential and the electron effective mass is calculated by assuming a linear variation of the aluminium molar fraction in the interface region. A multistep potential approximation is employed to accurately solve Schrödinger-like equations. The energy levels of the ground state (1s-like) and the two lowest excited states (2p- and 2s-like) have been obtained as a function of the quantum dot radii as well as the interface width. We find that the existence of the interface roughness blue shifts the energy levels of the electron states. These blue shifts become larger when the electron confinement in the quantum dot and/or the interface width increase. The existence of a graded interface with a 6 Å width in a quantum dot of radius 50 Å can preclude the presence of all the electron excited states, a result which seems to support recent experimental findings. We show that the interface effect on the intersubband transition energies of the electron states can be measurable by optical experiments.

I. INTRODUCTION

Due to advances in crystal-growth techniques such as molecular-beam epitaxy and metalorganic chemical vapor deposition, the investigation of the confinement states of electrons in low-dimensional structures has attracted a lot of theoretical and experimental attention in recent decades [1,2]. Important optical and electronic properties of low-dimensional semiconductors such as quantum wells, superlattices, quantum wires, and quantum dots are strongly influenced by the

confinement degree of the systems as well as by their heterointerfaces [3,4]. Chemical imaging results have shown that interfaces between GaAs and $\text{Al}_x\text{Ga}_{1-x}\text{As}$ have at least a width of two GaAs lattice parameters [5,6], containing substantial atomic roughness on scales finer than suggested by optical measurements. The interface effect on the energy levels of an electron in a quantum well has been shown to increase considerably the electron energy [7]. In the present work, we study the effect of an interface on the electron energy levels in a quantum-dot structure. Because our aim is to investigate the interface effect, the calculations are performed for small quantum dots. As a consequence, we are enabled to use the nearly independent particle limit for a single electron in these structures [8].

For a single electron confined in a spherical quantum dot with an abrupt interface, the Schrödinger equation can be solved exactly [9]. However, an analytical solution is not possible to be obtained when the existence of interfaces is considered because of the spatial dependence of the electron effective mass. Therefore, we have used a multistep potential approximation [10] to solve numerically Schrödinger-like equations that take into account the interfacial potential and the non-uniform electron effective mass. With this approach, the wave functions of the electron can be expressed analytically, and the energy levels are determined by a transcendental equation. The numerical solution can be calculated with high accuracy by use of suitable different multisteps. The program of this approach can be easily generalized to a system with an arbitrary potential. We have found that the effect of the graded interface is more important for an electron in a quantum dot than in a quantum well [7] due to the stronger confinement, and that the interface influence on the ground state is weaker than on the excited states. A graded interface with a 6 Å width in a quantum dot of radius 50 Å can preclude the presence of all the *bound* excited states of the electron, which is consistent with recent experimental findings [11,12]. The existence of the interface roughness increases the transition energy of the electron from the ground state to the excited states. The transition-energy blue shift due to the interface can be measurable by experiments.

This paper is organized as follows. In Section II, we describe our approach to solve the Schrödinger equations for an electron in a graded GaAs/ $\text{Al}_x\text{Ga}_{1-x}\text{As}$ spherical quantum dot within the multistep potential approximation. In Section III, the numerical results of the calculation are given as a function of the quantum dot radius and the interface width. The transition energies as well as the electron energy shifts related to the interface effects are also presented. Section IV is devoted to our main conclusions.

II. CALCULATION APPROACH

The quantum dot immersed in a bulk $\text{Al}_x\text{Ga}_{1-x}\text{As}$ alloy we consider here

consists of a GaAs sphere of radius R surrounded by a cap which is a graded interface with a finite width W ($R > W$). In doing so, we have chosen the dot center as the origin of our coordinates. An electron located in this nonabrupt quantum dot will be confined by a potential, which is dependent on the distribution of the Al concentration in the structure and is given here by [13]

$$V(r) = \begin{cases} 0, & r < R - W \\ 0.693y + 0.222y^2 \text{ (eV)}, & R - W < r < R \\ 0.693x + 0.222x^2 \text{ (eV)}, & r > R, \end{cases} \quad (1)$$

where

$$y = x \frac{r + W - R}{W} \quad (2)$$

describes a linear variation of the Al concentration in the interface region between GaAs and $\text{Al}_x\text{Ga}_{1-x}\text{As}$ as proposed by Freire, Auto, and Farias [4] for a nonabrupt GaAs/ $\text{Al}_x\text{Ga}_{1-x}\text{As}$ heterojunction. Furthermore, the effective mass of the electron in the system, which is also dependent on the interface variation of the Al molar fraction in the samples, is expressed by [14]

$$m^*(r)/m_e = \begin{cases} 0.067, & r < R - W \\ 0.067 + 0.083y, & R - W < r < R \\ 0.067 + 0.083x, & r > R, \end{cases} \quad (3)$$

with m_e the electron mass in vacuum.

In our calculation, we divide the interface variation of the Al molar fraction into N segments. In each of these segments, the Al concentration can be taken as a constant. Thus the interfacial potential is replaced by a multistep square-well potential. But its continuous change can be recovered provided that the segments become finer and finer (*i.e.*, $N \rightarrow \infty$). Therefore, equations (1) and (2) for the confinement potential and the electron effective mass in the interface region are approximated, respectively, by the multistep functions

$$V(r) \rightarrow V_j = V\left(\frac{r_{j-1} + r_j}{2}\right), \quad (4)$$

and

$$m^*(r) \rightarrow m_j^* = m^*\left(\frac{r_{j-1} + r_j}{2}\right), \quad (5)$$

for $r_{j-1} < r < r_j$ with $j = 0, 1, 2, \dots, N, N + 1$. Notice that $j = 0$ corresponds to the $y = 0$ region where $V(r) = 0$, and $j = N + 1$ to the $y = x$ region in which $V(r) = V_{\text{MAX}} = 0.693x + 0.222x^2$ eV. Since our system has a spherically symmetric potential, it is convenient to use the spherical polar coordinates to study the electron states. In the present work, we will limit ourselves to the ground (1s-like) state, and the two lowest excited (2p-like and 2s-like) states, which will be

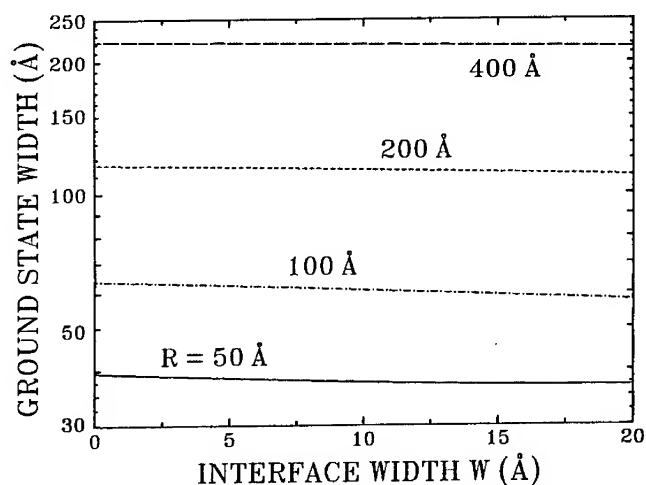


Figure 1: Ground state width of an electron in various GaAs/Al_{0.3}Ga_{0.7}As quantum dots as a function of the interface width.

mass approximation can be broken down if the height of the confinement potential is enhanced, *e.g.*, for the case of small quantum dots with an infinitely-high potential.

III. ENERGY LEVELS AND THEIR SHIFTS

We have performed the numerical calculation of the energy levels and the wave functions of an electron in graded spherical GaAs/Al_{0.3}Ga_{0.7}As quantum dots with different dot radii and various interface widths. In actual calculation, we have used the natural units of GaAs: the effective Bohr radius $a_0^* = \hbar^2 \epsilon_0 / m^* e^2 = 98.7$ Å as the unit of length, and the effective Rydberg $R^* = e^2 / 2 \epsilon_0 a_0^* = 5.83$ meV as the unit of energy.

The calculated energy levels of the *1s*-, *2p*-, and *2s*-like states of an electron in the graded quantum dots are plotted in Fig. 2(a) as a function of the dot radii for three typical interface widths $W = 0$ Å, 10 Å, and 20 Å, in which $W = 0$ Å corresponds to the dot having an abrupt interface. Although quantum dots have some features similar to shallow donors, the character of the confinement potentials for electrons is different in these two structures. The artificial confinement potential in the quantum dot takes the role of the Coulomb interaction between

shown to be most important in the structures under investigation. Although we have used the notation of the hydrogen-atom states for indicating our electron states, these states have quite different properties due to the type of confinement potential.

In the standard effective mass approximation and neglecting the angular part of the electron probability distribution, the radial part of the wave function $\{\psi_{\mu,j}(r)\}$ of an electron in the μ -th state with momentum $k_{\mu,j} = [2m_j^*(E_\mu - V_j)/m_e]^{1/2}/\hbar$ and energy E_μ in the j -th region of the structure can be expressed by the following form

$$\psi_{\mu,j}(r) = \frac{1}{r} [A_{\mu,j} \exp(ik_{\mu,j}r) + B_{\mu,j} \exp(-ik_{\mu,j}r)] \quad (6)$$

for the 1s- and 2s-like states with angular momentum quantum number $l = 0$, and

$$\psi_{\mu,j}(r) = A_{\mu,j} \frac{1}{r} \left(1 + \frac{1}{k_{\mu,j}r}\right) \exp(ik_{\mu,j}r) + B_{\mu,j} \frac{1}{r} \left(1 - \frac{1}{k_{\mu,j}r}\right) \exp(-ik_{\mu,j}r) \quad (7)$$

for the 2p-like state with $l = 1$. Considering the continuity of both $\psi_{\mu,j}(r)$ and $(1/m_j^*)(d\psi_{\mu,j}/dr)$ at each boundary of all the steps, the normalization of the wave function, and that $\psi_{\mu,j}(r) \rightarrow 0$ when $r \rightarrow \infty$, one can determine all the coefficients $A_{\mu,j}$, $B_{\mu,j}$ and the energy E_μ of the μ -th state from a multiplication of $N+1$ (2×2) matrices [10].

As is well known, the effective mass approximation is applicable only for weakly bound states. In general, it requires an average radius larger than 20 Å for an bound electron in most of semiconductors [15]. The effective Bohr radius of an electron bound to a shallow donor in bulk GaAs is about 100 Å. However, such average radius of the electron in a GaAs-based quantum dot must decrease when the confinement potential of the structure becomes stronger. In order to verify whether this approximation may still be suitable to our system, we plot in Fig. 1 the state width of the 1s-like electron, which is defined as $\langle r^2 \rangle^{1/2}$, as a function of the interface width up to 20 Å for four different quantum dots with radii $R = 50$ Å, 100 Å, 200 Å, and 400 Å, respectively. In this work, the Al concentration is fixed as $x = 0.3$, and the electron band offset as 60% of the total energy-band-gap difference between the two materials. It is clearly shown that the potential of the quantum dot confines the electron wave function considerably, and this confinement increases with decreasing the dot radii. The state width of the 1s electron in a quantum dot of radius 50 Å with a graded interface of width 20 Å still has a value larger than 35 Å. Therefore, the standard effective mass approximation is reliable for the present study. By the way, we have found that as the dot radius decreases further, the state width of the ground-state electron will increase due to the finitely-high barrier of the system which is moving from the quantum-dot structure into bulk $\text{Al}_{0.3}\text{Ga}_{0.7}\text{As}$. There are no bound states for a quantum dot with radius $R < R_{\text{MIN}} = \pi\hbar/[8m^*V_{\text{MAX}}]^{1/2}$ [9]. On the other hand, the effective

helps the eliminations.

The energy-level shifts of the electron states due to the presence of a finitely-wide interface is displayed in Fig. 2(b), which shows us that in most of the cases the higher the state energy, the stronger the interface effect on it, and that the interface effect will become negligible for $R > 300 \text{ \AA}$ when interface widths up to 20 \AA are considered. However, the situation will be changed when the electron states are going from the quasi-zero-dimensional system to the three-dimensional $\text{Al}_x\text{Ga}_{1-x}\text{As}$, which can be seen for the case of small quantum dots: the energy shifts of the two excited states have maximum values for certain dot radii, and also there are some crossings for the energy shifts of the $2p$ and $2s$ states. The most important is that the energy shift due to the interface effect in strong confinement dots is as large as about 20 meV for $W = 10 \text{ \AA}$ (roughly equal to two GaAs lattice constants) and about 40 meV for $W = 20 \text{ \AA}$. Such large differences should be easily measured by optical experiments.

In Fig. 3, we depict the energy levels of the $1s$ (a), $2p$ (b), and $2s$ (c) states as a function of the interface width for an electron in graded quantum dots with radii $R = 50 \text{ \AA}$, 60 \AA , 75 \AA , 100 \AA , 150 \AA , and 200 \AA , respectively. It is clear that the effect of the interface roughness increases the electron energy, and this effect becomes weaker with the increase of the quantum dot radii. Notice that the energy shifts of the excited states are larger than those of the ground state, which is due to the fact that most of the electron probability of the ground state is more localized around the dot center (further away from the interface) as compared to that of the excited states. As a consequence, the influence of the interface is weaker on the ground state than on the excited states. All the excited states, which may occur in quantum dot structures with sharp interfaces, can be precluded to exist in the bound states when the interface width is large enough. For instance, the $2s$ state disappears in graded quantum dots with radii $R = 50 \text{ \AA}$ and $R = 60 \text{ \AA}$ when the interfaces have widths $W = 3 \text{ \AA}$ and $W = 20 \text{ \AA}$, respectively. A graded interface of only $W = 6 \text{ \AA}$ in a quantum dot with $R = 50 \text{ \AA}$ can turn the $2p$ state into an unbound one, *i.e.*, there are no bound excited states in the system anymore. This interesting result can explain qualitatively the recent experimental observation of the existence of only one photoluminescence peak from a single quantum dot published by two groups [11,12].

In order to predict possible experimental results for the structures studied here, we display in Fig. 4(a) the dot-size dependence of the intersubband transition energies between the ground state ($1s$) and the $2p$ and $2s$ states of the electron, while that of the transition-energy shifts due to the interface effect are depicted in Fig. 4(b). Theoretically, the transition $1s \rightarrow 2s$ for a shallow donor and also for the present system is forbidden. However, actual man-made systems have not a *perfect* spherical symmetry, so there must be a mixing of the states with different quantum numbers. Such mixture will lead the initially forbidden transitions to become

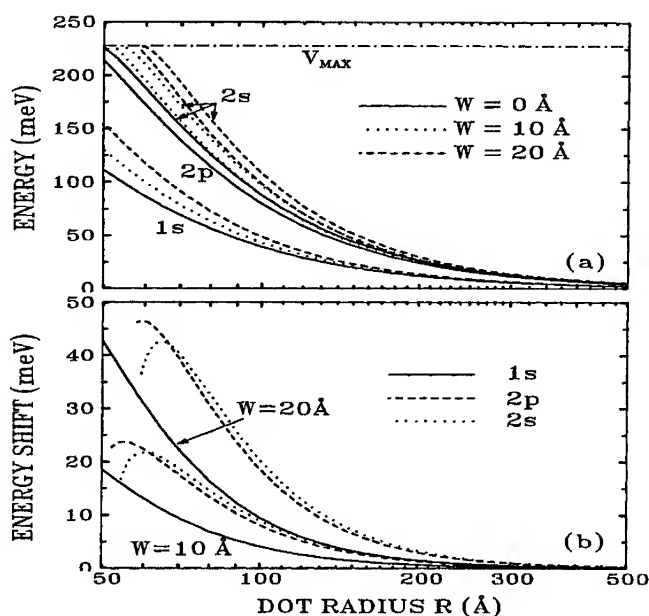


Figure 2: Dot-radius dependence of (a) the energy levels and (b) the energy shifts for the electron states $1s$, $2p$, and $2s$. The shifts are due to the graded interface with $W = 10 \text{ Å}$ and $W = 20 \text{ Å}$.

the hydrogen-like ion and an electron. The $2p$ -like state in the present system has no degeneracy [9], while the $2p$ hydrogenic state has a three-fold degeneracy, (*i.e.* $2p_x$, $2p_y$, and $2p_z$); and the $2s$ -like state in the quantum dot has a zero value at the dot center, while the $2s$ state of the hydrogen atom has a zero-value circle around the dot center. It is clear that with increasing dot radii all the electron states become degenerate with state energy zero. This is not the case for the hydrogen atom where the degenerate states are always dependent on their principal quantum numbers. The confinement intensity of the different electron states in the quantum dot changes due to the different spatial symmetries of these states. It is shown in Fig. 2(a) that: (i) the $2s$ state has always a higher energy than the $2p$ state, which indicates that the $2p$ state is the *lowest* excited state; (ii) considering abrupt quantum dots ($W = 0 \text{ Å}$) with a decrease in the dot radii, all the excited states can be eliminated when $R < 2R_{MIN}$ [9], and the ground state too when $R < R_{MIN}$. That is different from the case for the electronic subbands in quantum wells where the lowest subband is always bound; and (iii) the effect of the interface roughness

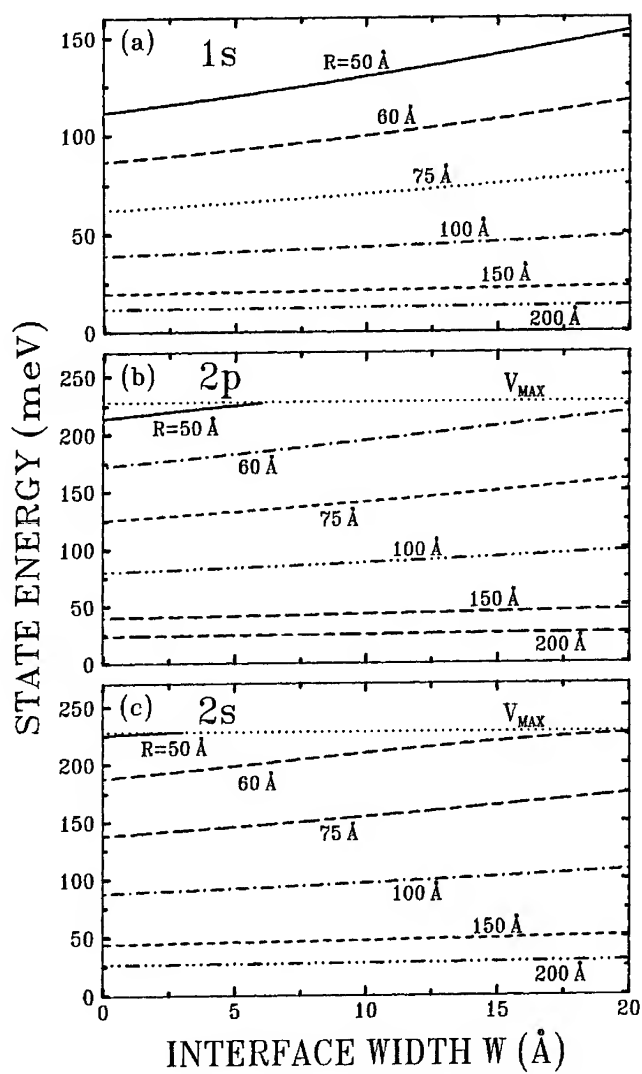


Figure 3: Energy levels of the electron states 1s (a), 2p (b), and 2s (c) as a function of the interface width for six quantum dots with different radii.

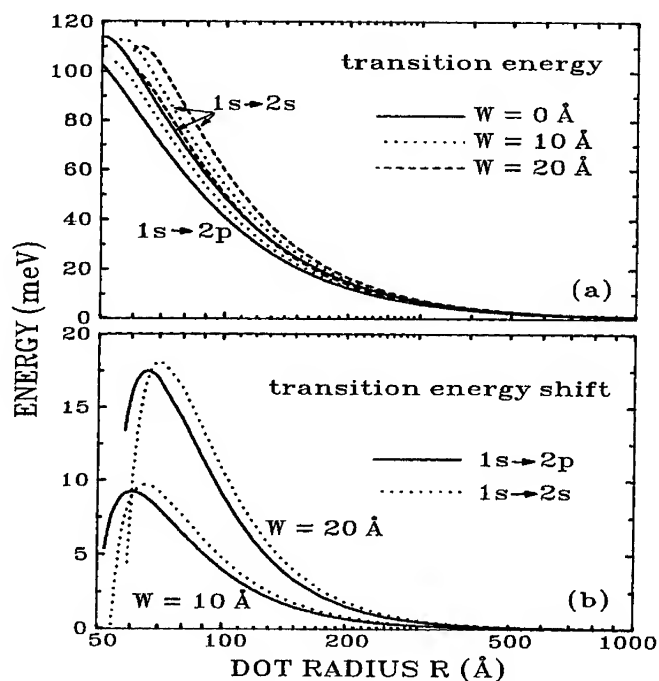


Figure 4: The same as shown in Fig. 2 but now for the intersubband transition energy (a) and their energy shift (b).

weakly possible. Similar forbidden transitions, *e.g.*, $1s \rightarrow 2s$ and $1s \rightarrow 3d^{-2}$ for a hydrogen-like donor in GaAs, were observed in magneto-optical experiments [16], and the explanation for their existence and a good agreement with theoretical results were given in Ref. [17] and [18], respectively. It is found from Fig. 4(a) that all the transition energies go to zero when the dot radii increase since the system is becoming bulk GaAs in this limit, while in the opposite direction the transition energies decrease also due to the system becoming the $\text{Al}_{0.3}\text{Ga}_{0.7}\text{As}$ semiconductor in this case.

The transitions between the bound states disappear for dot radii smaller than certain values (see Fig. 3) since the excited states are no longer bound in this case. The interface effect on the transition energy is shown again to be very important for the strong confinement quantum dots ($R < 200 \text{ Å}$). Shifts of the transition energies due to the interface roughness reach the maximum value for the dot radii

around 65 Å. An interface width $W = 10$ (20) Å enhances the transition energy as much as about 10 (15) meV. Such large enhancement must be also measurable by experiments. As compared to the shifts of the state-energy levels [see Fig. 2(b)], the intersubband transition-energy shifts are relatively small because of the energy-shift cancellation of the ground state and the excited states.

IV. CONCLUSIONS

We have performed a theoretical study of the electron states in graded GaAs/ $\text{Al}_x\text{Ga}_{1-x}\text{As}$ spherical quantum dots. The graded interface between the two semiconductors was simulated by a linear interfacial Al molar fraction variation. A multistep potential approximation in actual calculation was developed to accurately solve Schrödinger-like equations to obtain the wave functions and the energies of the electron states. The energy levels of the ground state (1s-like) and of the two lowest excited states (2p- and 2s-like), as well as the intersubband transition energies of $1s \rightarrow 2p$ and $1s \rightarrow 2s$ have been calculated as a function of the quantum dot radius as well as the interface width. We have found that the existence of the interface roughness blue shifts the energy levels of the electron states, and these blue shifts increase with both decreasing the quantum dot radius and increasing the interface width. A graded interface with width of only 6 Å in a quantum dot of radius 50 Å can preclude the presence of all the electron excited states, a result which seems to support recent experimental findings [11,12]. Our results for the intersubband transition energies are expected to motivate new experiments.

ACKNOWLEDGEMENT

One of us (J.M.S.) was supported by FUNCAP (Ceará, Brazil) and would like to thank Universidade Federal do Ceará for the hospitality. V.N.F. and G.A.F. would like to acknowledge financial support from FINEP and CNPq (Brazil).

References

- [1] T. Ando, A. B. Fowler, and F. Stern, *Rev. Mod. Phys.* **54**, 437 (1982).
- [2] T. Chakraborty, *Comm. Conden. Matter Phys.* **16**, 35 (1993).
- [3] M. A. Herman, D. Bimberg, and J. Christen, *J. Appl. Phys.* **70**, R1 (1991).
- [4] V. N. Freire, M. M. Auto, and G. A. Farias, *Superlatt. Microstruct.* **1**, 17 (1992).
- [5] A. Ourmazd, D. W. Taylor, J. Cunningham, and C. W. Tu, *Phys. Rev. Lett.* **62**, 933 (1989).
- [6] O. Albrektsen, D. J. Arent, H. P. Meier, and H. W. M. Salemink, *Appl. Phys. Lett.* **57**, 31 (1990).
- [7] E. C. Ferreira, J. A. P. da Costa, G. A. Farias, and V. N. Freire, *Superlatt. Microstruct.* **17**, 397 (1995).
- [8] U. Merkt, *Physica B* **189**, 165 (1993).
- [9] See, *e.g.*, J. Irving and N. Mullineux, *Mathematics in Physics and Engineering*, (Academic, New York, 1959) Sec. 6.2., p. 345.
- [10] Y. Ando and T. Itoh, *J. Appl. Phys.* **61**, 1497 (1987).
- [11] Y. Nagamune, H. Watabe, M. Nishioka, and Y. Arakawa, *Appl. Phys. Lett.* **67**, 3257 (1995).
- [12] S. A. Empedocles, D. J. Norris, and M. G. Bawendi, *Phys. Rev. Lett.* **77**, 3873 (1996).
- [13] H. J. Lee, L. Y. Jurel, J. C. Wolley, and A. J. Springthorpe, *Phys. Rev. B* **21**, 659 (1980).
- [14] S. Adachi, *J. Appl. Phys.* **58**, R1 (1985).
- [15] W. Kohn, *Solid State Phys.* **5**, 257 (1957).
- [16] J. P. Cheng, B. D. McCombe, J. M. Shi, F. M. Peeters, and J. T. Devreese, *Phys. Rev. B* **48**, 7910 (1993).
- [17] G. E. Stillman, D. M. Larsen, and G. M. Wolfe, *Phys. Rev. Lett.* **27**, 989 (1971).
- [18] J. M. Shi, F. M. Peeters, and J. T. Devreese, *Phys. Rev. B* **48**, 5202 (1993).

Quantum Wires: Transport

Resistance of Molecular Nanostructures

Supriyo Datta and Weidong Tian
School of Electrical Engineering

Clifford P. Kubiak
Department of Chemistry
Purdue University,
W.Lafayette, IN 47907-1285, USA.

ABSTRACT

Recent developments in nanotechnology have made it possible to measure the resistance of individual molecular wires self-assembled between two metallic pads. In this paper we present a simple expression that relates the resistance of a symmetric molecule to $N_{\text{even}} - N_{\text{odd}}$, where N_{even} and N_{odd} are the number of electrons occupying the even and odd states respectively. This relation is based on the Friedel sum rule and should be valid even in the presence of interactions. We use this relation to provide insight into the factors that affect the resistance of (1) neutral molecules and (2) molecules that have been "doped" to a fractional charge state.

Introduction

A number of experimental groups have recently reported the observation of electronic conduction through "molecular wires" attached to two metallic contacts by special functional groups at the ends that act as "alligator clips" (Fig.1) [1-7]. Some of these molecular wires are based on alkane chains and their primary application would be in making ultrathin insulating films. Others are based on conjugated polymers like poly-paraphenylene which in bulk form can be doped to attain near metallic levels of conductivity. Molecular wires in this category could, in principle, find use in constructing interconnection networks for electronic devices. However, the measured resistances to date are at least several megohms per molecule and it is important to identify the various factors affecting the molecular resistance, so that molecules with lower resistance values can be designed.

Theoretical work in this area has been based on the Landauer formula which relates the measured resistance R to the transmission function at the Fermi energy [8] :

$$R = \frac{h / 2e^2}{T(E_F)} = \frac{12.9 \text{ K}\Omega}{T(E_F)} \quad (1)$$

The transmission function is equal to the transmission probability per mode times the number, M , of transverse modes or conducting channels in the molecule (not including spin). Eq.(1) includes a factor of two to account for the two spins which, for simplicity, are assumed to act as identical independent channels. Note that Eq.(1) predicts a non-zero resistance of $(12.9 / M)$ kilo-ohms for a "ballistic" molecule with a transmission probability of one. This represents the contact resistance at the metal-molecule interface. Different authors use different methods for calculating the transmission function but their results are similar and in general agreement with the available experimental data [9-11].

The point to note is that in order to use Eq.(1) to estimate the resistance of a molecule in a given charge state, we first need to locate the Fermi energy by counting the electrons. It would clearly be much more convenient if the transmission function at the Fermi energy could be related directly to *the number of electrons*. The purpose of this paper is to show that, at least for a restricted class of molecules, there is a simple relation between the transmission function and the number of electrons. Furthermore, this relation is based on a general principle, namely the Friedel sum rule and as such should be valid even in the presence of interactions [12]. This feature could make it particularly useful in describing open-shell molecules for which correlation effects can be quite complex. In this paper we will derive this relation, illustrate it with an example and finally use it to provide

insight into the factors that affect the resistance of (1) neutral molecules and (2) molecules that have been "doped" to a fractional charge state.

Fig.1 shows a typical example of a molecular wire. The transmission function exhibits peaks at energies corresponding to the energy levels of the molecule, as we would expect. According to Eq.(1), the resistance is determined by the transmission at the Fermi energy. For a neutral molecule, the Fermi energy is located between the highest occupied molecular orbital (HOMO) and the lowest unoccupied molecular orbital (LUMO), so that the resistance is relatively high. The resistance would be much lower if charge could be transferred to the molecule, thereby moving the Fermi energy closer to the HOMO or the LUMO. One way to achieve this is to use metallic contacts with work functions that are much smaller or larger than the molecule. However, this approach appears to be limited since the amount of charge transferred has been measured experimentally for numerous metal-molecule complexes experimentally and is usually quite small. A more promising approach is to place the molecular wire in a fractional charge state through the formation of a charge transfer complex. For example, the charge transfer complex between tetrathiafulvalene and tetracyanoethylene (TTF-TCNE) possesses a ground state electronic structure with a degree of charge transfer of 0.5 ± 0.1 [13]. Many other charge transfer complexes are known involving electron donors such as hexamethylbenzene [14] and electron acceptors such as nitrosonium or carbonium ions [15, 16]. It should be possible to use such donor or acceptor molecules to transfer a fractional amount of charge into a molecular wire of the type we are discussing.

A simple expression for the transmission function

Consider a symmetric molecule connected to external reservoirs through single-mode leads. The states of such a molecule can be classified as even and odd and we use N_{even} and N_{odd} to denote the total number of electrons occupying each group of states. We will show that the transmission coefficient is given by

$$t = -i e^{-i\pi N} \sin(\pi N_d) \quad (2a)$$

$$\rightarrow T = |t|^2 = \sin^2(\pi N_d) \quad (2b)$$

$$\text{where } N_d = N_{\text{even}} - N_{\text{odd}}, \quad \text{and } N = N_{\text{even}} + N_{\text{odd}} \quad (3)$$

Eq.(2a) shows that the phase of the transmission coefficient is proportional to the total number of electrons, N , in the molecule. This is just a special case of the well-known

Friedel sum rule [17, 18]. But to our knowledge there is no such general result for the **magnitude** of the transmission coefficient. The simple result of Eq.(2) is made possible by restricting our attention to symmetric molecules with single-moded leads. The basic idea is easy to see and is outlined below; a detailed discussion has been presented elsewhere [19].

The point is that the eigenspace of a symmetric molecule with symmetric leads has an even part and an odd part which are completely decoupled from each other so that we can apply the Friedel sum rule *to each part individually*. If we excite a symmetric molecule symmetrically at the two leads with an input (1 1), the output will also be (1 1) phase-shifted by an amount that is related to N_{even} by the Friedel sum rule (see Eq.(2), Ref.12) :

$$(1 \ 1) \rightarrow (1 \ 1) e^{-i2\delta_{\text{even}}} \quad \text{where} \quad \delta_{\text{even}} = \pi N_{\text{even}} \quad (4a)$$

Similarly for an anti-symmetric input (1 -1) the phase-shift is related to N_{odd} by the Friedel sum rule :

$$(1 \ -1) \rightarrow (1 \ -1) e^{-i2\delta_{\text{odd}}} \quad \text{where} \quad \delta_{\text{odd}} = \pi N_{\text{odd}} \quad (4b)$$

But if we excite the molecule only at one lead with an input (1 0), it will transmit partially to (0 1) and reflect partially to (1 0). It is easy to see by superposing the results in Eqs.(4a) and (4b) that the amplitude for transmission from (1 0) to (0 1) is given by

$$t = \frac{1}{2} \left[e^{-i2\delta_{\text{even}}} - e^{-i2\delta_{\text{odd}}} \right] = \frac{1}{2} \left[e^{-i2\pi N_{\text{even}}} - e^{-i2\pi N_{\text{odd}}} \right] \quad (5)$$

which is readily rewritten in the form stated in Eq.(2a).

Applicability of Eq.(2)

Eq.(2) gives a simple expression for the transmission function subject to two restrictions. Firstly, the structure has to be symmetric. Many molecular wires of interest satisfy this condition and their eigenstates can be classified as even, odd or uncoupled. The amplitude of an even state is the same at both leads, while that of an odd state changes sign from one lead to the other. An uncoupled state has zero amplitude at the leads and can be ignored; it does not participate in the conduction process.

The second restriction is that the leads have to be single-moded (multi-moded leads can be handled if they are decoupled, like the two spins, for example). This is somewhat

confusing, since it may not even be clear what one means by a lead. Let us discuss this point with an example. Looking at the molecule shown in Fig.1, we can identify the sulphur atoms at the ends as the 'leads', since electrons flow out into the reservoir from these sites. Equivalently, but more formally, one could say that it is the site energies of these atoms that acquire an imaginary self-energy due to the coupling to the gold. Since a sulphur atom has one s-level and three p-levels this would mean we have a four-moded lead and strictly speaking, Eq.(2) is not applicable [20]. Luckily, however, one can often capture the essential physics by assuming that only the p_z orbitals of sulphur couple to the gold. We find that the single mode approximation works well for a variety of different molecules, at least in the energy range around the HOMO-LUMO gap [19].

How do we calculate N_{even} and N_{odd} ?

We first calculate the complex eigenenergies ($E_i = \epsilon_i + i \Gamma_i$) of the Hamiltonian (+self-energy due to the leads) using the method described in Ref.11. The real part ϵ_i tells us the energy of the eigenstate while the imaginary part Γ_i gives us the broadening of level 'i' due to the coupling to the metal. It indicates how effectively the level can empty into the metallic reservoir through the lead. Knowing ϵ_i and Γ_i , we can calculate N_{even} and N_{odd} :

$$N_{\text{even,odd}} = \sum_{\text{even,odd levels}} \left[\vartheta(E - \epsilon_i) - \frac{1}{\pi} \tan^{-1} \frac{\Gamma_i}{E - \epsilon_i} \right] \quad (6)$$

The first term (ϑ is the unit step function) gives the number of electrons that would be present if the molecule were isolated ($\Gamma_i = 0$) while the second term gives the gain or loss due to the coupling to the contacts. This relation can be obtained simply by integrating a Lorentzian of width Γ_i centered around ϵ_i , but it is valid for non-Lorentzian line shapes too. In general, once we have identified the one-particle excitation energies (ϵ_i) and their escape rates (Γ_i), we can determine $N_d(E)$ and use it in Eq.(2b) to obtain the transmission (and hence the resistance from Eq.(1)). Let us now see how this viewpoint provides insight into the resistance of (1) neutral molecules and (2) molecules that have been "doped" to a fractional charge state.

Neutral molecules

For neutral (closed-shell) molecules the total number of electrons is an even number, so that the number of electrons per spin is an integer. We can write

$$\begin{aligned} N_{\text{even}} &= \text{Integer} + \alpha \\ N_{\text{odd}} &= \text{Integer} - \alpha \quad \rightarrow \quad T = \sin^2 2\pi\alpha \end{aligned} \quad (7)$$

where α is a fractional quantity that depends on the degree of coupling to the contacts. Using Eq.(6),

$$2\pi\alpha = \sum_i p_i \tan^{-1} \frac{\Gamma_i}{E_f - \epsilon_i} \quad (8)$$

where the parity p_i is +1 for even levels and -1 for odd levels. From Eqs.(7) and (8) we can write

$$T(E_f) = \sin^2 \left(\sum_i p_i \tan^{-1} \frac{\Gamma_i}{E_f - \epsilon_i} \right) \equiv \left(\sum_i \frac{p_i \Gamma_i}{E_f - \epsilon_i} \right)^2 \quad (9)$$

The approximation indicated in Eq.(9) can be used if the Fermi energy is located in the HOMO-LUMO gap far from all the molecular energy levels ϵ_i , so that $(E_f - \epsilon_i) \gg \Gamma_i$. Note that the Fermi energy is set by the charge neutrality condition

$$0 = \sum_i \tan^{-1} \frac{\Gamma_i}{E_f - \epsilon_i} \equiv \sum_i \frac{\Gamma_i}{E_f - \epsilon_i} \quad (10)$$

Knowing the energy levels ϵ_i and their broadening Γ_i , we can use Eq.(10) to locate the Fermi energy E_f and use it in Eq.(9) to find the transmission.

If the HOMO and the LUMO are well-separated from the other levels, then we can ignore the other levels to obtain from Eqs.(9) and (10)

$$T(E_f) \equiv \sin^2 \left(\frac{2\Gamma_0}{E_g} \right) \equiv \left(\frac{2\Gamma_0}{E_g} \right)^2 \quad (11)$$

where $\Gamma_0 = \Gamma_{\text{HOMO}} + \Gamma_{\text{LUMO}}$ and we have assumed that the HOMO and the LUMO have opposite parities, as is usually the case. Eq.(11) is often not accurate because of the close proximity of other levels. But it is still useful in a qualitative sense. It shows that the resistance of neutral molecules is essentially determined by the parameter, Γ_0/E_g , equal to

the ratio of the broadening to the bandgap. This parameter is determined by the "clips" that bind the molecule to the metallic contacts.

"Doping"

We now consider molecules for which the total number of electrons per spin, $N_{\text{even}} + N_{\text{odd}}$, is fractional due to charge transfer from another species as discussed in the introduction. To estimate the resistance of such a "doped" molecule let us assume that fractional charges α_{te} and α_{to} have been transferred into the even and odd states of a molecule respectively [21]. We can then write the number of electrons *per spin* as

$$\begin{aligned} N_{\text{even}} &= \text{Integer} + (\alpha_{\text{te}} / 2) \\ N_{\text{odd}} &= \text{Integer} + (\alpha_{\text{to}} / 2) \end{aligned} \quad \rightarrow \quad T = \sin^2 \frac{\pi(\alpha_{\text{te}} - \alpha_{\text{to}})}{2} \quad (12)$$

For n-type doping, charge is transferred into the LUMO which is even : $\alpha_{\text{te}} = \alpha_{\text{t}}$ and $\alpha_{\text{to}} = 0$. For p-type doping, charge is transferred out of the HOMO which is odd : $\alpha_{\text{te}} = 0$ and $\alpha_{\text{to}} = -\alpha_{\text{t}}$. In either case $T = \sin^2 (\pi \alpha_{\text{t}} / 2)$. For some molecules we find that the LUMO (or the HOMO) has another level close by in energy having the opposite parity. The transferred charge then tends to contribute both to α_{te} and α_{to} making it difficult to dope n-type (or p-type). In some cases charge may be transferred into a level that is decoupled from the leads, thus contributing neither to α_{te} nor to α_{to} . Usually one can guess α_{te} and α_{to} from a knowledge of the energy levels ϵ_i , their broadening Γ_i and their parities p_i . Eq.(12) can then be used to estimate the resistance.

Note that we are assuming that all energy levels are spin degenerate and can accommodate two electrons. That is why the transmission is maximum when the charge transferred is one ($\alpha_{\text{t}} = 1$): the additional electron causes the Fermi energy to pin in the middle of the LUMO. But if the level broadening Γ is small, then each level might accommodate only one electron due to single-electron charging effects. We would then expect the transmission to be maximum when the charge transferred is one-half ($\alpha_{\text{t}} = 0.5$). This is what we get from Eq.(2b) if we do not assume that the levels are spin degenerate : the transmission is then given by $T = \sin^2 \pi(\alpha_{\text{te}} - \alpha_{\text{to}})$ instead of Eq.(12). However, this case requires a fuller discussion [19].

Summary

We have presented a simple expression (Eq.(2)) relating the transmission function of symmetric molecules to $N_{\text{even}} - N_{\text{odd}}$, where N_{even} and N_{odd} are the number of electrons occupying the even and odd states respectively. This relation is based on the Friedel sum rule and as such should be valid even in the presence of interactions. The main restriction is that the leads be effectively single-moded - a condition that is approximately fulfilled by many of the molecular wires of interest. We have used this relation to obtain expressions for the transmission through neutral molecules (Eq.(11)) and through molecules that have been "doped" to a fractional charge state (Eq.(12)). Possible schemes for "doping" molecular wires by fractional charge transfer are also discussed.

Acknowledgements

This work was supported by the Army Research Office under a University Research Initiative Grant No. DAAL- 03-92-G-0144.

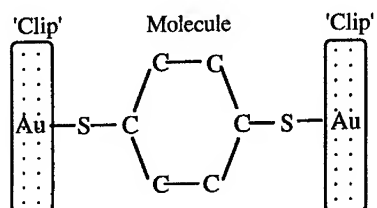
References

1. D.L. Klein, P.L. McEuen, J.E. Bowen Katari, R. Roth and A. Paul Alivisatos, Appl. Phys. Lett. **68**, 2574 (1995).
2. C. Boudas, J.V. Davidovits, F. Rondelez and D. Vuillaume, Phys. Rev. Lett. **76**, 4797 (1996).
3. L.A. Bumm, J.J. Arnold, M.T. Cygan, T.D. Dunbar, T.P. Burgin, L. Jones II, D.L. Allara, J.M. Tour and P.S. Weiss, Science **271**, 1705 (1996).
4. R.P. Andres, T. Bein, M. Dorogi, S. Feng, J.I. Henderson, C.P. Kubiak, W. Mahoney, R.G. Osifchin, R. G. Reifengerger, Science **272**, 1323 (1996).
5. R. P. Andres, J. D. Bielefeld, J. I. Henderson, D. B. Janes, V. R. Kolagunta, C. P. Kubiak, W. J. Mahoney and R. G. Osifchin, "Superlattice of Molecularly Linked Metal Clusters," Science, to appear.
6. A. Yazdani, D.M. Eigler and N.D. Lang, Science **272**, 1921 (1996).
7. M.A. Reed, C. Zhou, C.J. Muller, T.P. Burgin and J.M. Tour, " Observation of Conductance and Room Temperature Coulomb Blockade in a Molecule", submitted to Science.

8. S. Datta, *Electronic Transport in Mesoscopic Systems*, Cambridge University Press (Cambridge, 1995). See Chapter 2 and references therein.
9. M. Kemp, A. Roitberg, V. Mujica, T. Wanta and M.A. Ratner, *J. Phys. Chem.* **100**, 8349 (1996); V. Mujica, M. Kemp, A. Roitberg and M.A. Ratner, *J. Chem. Phys.* **104**, 7296 (1996).
10. C. Joachim and J.F. Vinuesa, *Europhys. Lett.* **33**, 635 (1996) and references therein.
11. M.P. Samanta, W. Tian, S. Datta, J.I. Henderson and C.P. Kubiak, *Phys. Rev.* **B53**, R7626 (1996).
12. J.S. Langer and V. Ambegaokar, *Phys. Rev.* **121**, 1090 (1961).
13. M. Meneghetti, C. Pecile, *J. Chem. Phys.* **105**, 397 (1996).
14. B.M. Britt, J.L. McHale, D.M. Friedrich, *J. Phys. Chem.* **99**, 6347 (1995).
15. E. Kim, J.K. Kochi, *J. Am. Chem. Soc.* **113**, 4962 (1991).
16. Y. Takahashi, S. Sankararaman, J.K. Kochi, *J. Am. Chem. Soc.* **111**, 2954 (1989).
17. J. Friedel, *Phil. Mag.* **43**, 153 (1952).
18. J. Callaway, *Phys. Rev.* **154**, 515 (1967).
19. S. Datta and W. Tian, *Phys. Rev.* **B55**, R1914 (1997).
20. Actually the number of modes is even larger because the orbitals on the interior atoms have some coupling to the gold. Besides we are ignoring the d-orbitals.
21. There will be some additional charge transfer ($\pm\alpha$) due to the coupling to the contacts as we have seen with neutral molecules. However, for doped molecules we expect α to be much smaller than α_t . For simplicity we have ignored it in Eq.(12).

FIGURE CAPTIONS

Fig.1. Generic structure consisting of a molecular wire attached to two metallic contacts by special functional groups like thiols that act as "alligator clips".



DEMONSTRATION OF A Y-BRANCH SWITCH IN DEEPLY REACTIVE ION ETCHED $\text{In}_{0.53}\text{Ga}_{0.47}\text{As}$ / InP WITH IN-PLANE GATES

Jan-Olof J. Wesström, Katharina Hieke, Björn Stålnacke, and Thomas Palm

The Laboratory of Photonics and Microwave Engineering, Department of Electronics, Royal Institute of Technology, Electrum 229, S-164 40 Kista, Sweden

Björn Stoltz

Opto Electronics Products, Ericsson Components AB, S-164 81 Kista-Stockholm, Sweden
(May 16, 1997)

Switching is demonstrated in a 320nm wide $\text{In}_{0.53}\text{Ga}_{0.47}\text{As}$ / InP electron Y-branch switch with in-plane gates. The device was fabricated using metalorganic vapor phase epitaxy, electron beam lithography and CH_4/H_2 reactive ion etching. The switching behavior was for certain gating-schemes consistent with coherent single-mode electron transport, but classical transport can not be ruled out.

I. INTRODUCTION

Continuing miniaturization in semiconductor processing has made it possible to fabricate structures with dimensions comparable to the electron wavelength. One of the so called electron waveguide devices is the Y-Branch Switch,¹ (YBS). The YBS in Fig. 1 is composed of three electron waveguide sections connected in a Y-shape. The incoming electron wave in the source waveguide is deflected into either of the branches by the field from an applied potential difference on two side gates. This device has two main advantages. First, electron waveguide devices can potentially show a switching voltage lower than the thermal voltage (kT/q), where k is Boltzmann's constant, T is the temperature, and q is the electron charge. Secondly, the YBS has a monotonic response. Logic designs have been proposed retaining standardized levels,² making use of this latter property. The simplest electron waveguide device, the Quantum Point Contact, QPC, is just a straight electron waveguide section between two reservoirs, as seen in Fig. 2(a). As the gate voltage is increased, more modes are populated, each increasing the source-drain conductance by $G_0 = 2q^2/h$, where h is

Planck's constant. We have fabricated and made measurements on a QPC³ as a first step towards fabricating the more complicated YBS. It has served to verify basic material and design properties such as ballistic transport and gate efficiency.

To characterize the YBS, we need to measure the elements of the conductance matrix, relating currents into the three leads, source, left drain, and right drain, I_S , I_L , and I_R , when voltages V_S , V_L , and V_R are applied:

$$\begin{pmatrix} I_S \\ I_L \\ I_R \end{pmatrix} = \begin{pmatrix} G_{SS} & G_{SL} & G_{SR} \\ G_{LS} & G_{LL} & G_{LR} \\ G_{RS} & G_{RL} & G_{RR} \end{pmatrix} \begin{pmatrix} V_S \\ V_L \\ V_R \end{pmatrix}. \quad (1)$$

A switching curve is recorded when the conductance matrix is measured while the gate voltages are swept. To do this, two simultaneous four-probe measurements were performed as in Fig. 3(b). Since no magnetic field is present, reciprocity makes the matrix symmetric. Furthermore, the sum of each column has to be zero to ensure current conservation. This reduces the degrees of freedom to three, so the whole matrix can be reconstructed if we for example know the three elements G_{LS} , G_{RS} , and G_{RL} . In a single mode three-port structure with coherent electron transport, the electron wave scattering matrix is unitary which decreases the degrees of freedom to two.² Expressed in the conductance matrix elements, this relation can be written

$$(G_{LS}G_{RS} + G_{LS}G_{RL} + G_{RS}G_{RL})^2 = -4G_0G_{LS}G_{RS}G_{RL}. \quad (2)$$

Many groups have fabricated and measured on electron waveguide devices, first on QPCs.^{4,5} At least two measurements on YBSs are also in the literature.^{6,7} These experiments on YBSs have taken place in the GaAs/AlGaAs material system with split gates defining the electron waveguides. While this method produces smooth waveguides, the split-gate technology has the disadvantage of small subband energy separation due to the smooth confining potential profile. This makes operation at higher temperature impossible, since the subband separation should be larger than the thermal energy kT . Furthermore, changing the gate voltages tend to move the waveguide sideways instead of applying an electric field to an already existing waveguide. This increases the needed switching voltage. We therefore think dry etching is the simplest way to get a better defined potential profile, while still allowing arbitrary geometries. In our design we use the 2DEG on the sides of the electron waveguide as gates as seen in Fig. 4(a). These in-plane gates, isolated from the electron waveguide by an etched groove are defined in the same lithographic step as the waveguides. This has the advantage of perfect alignment and simpler processing than when

the gates are defined in a separate step by metal deposition and lift-off. Furthermore, in-plane gates should have the best possibility to provide the needed lateral field. The $\text{In}_{0.53}\text{Ga}_{0.47}\text{As}$ / InP material system is advantageous when etching since it has shown less problems with etching induced surface states than for example GaAs.

II. FABRICATION

The 2D-samples were grown by MOVPE at 650° C and 20 mbar on a semi-insulating InP substrate. The thicknesses and compositions were as follows: 200 nm InP, 120 nm Zn-doped InP with $N_A = 10^{17} \text{ cm}^{-3}$, 600 nm InP buffer, 12 nm $\text{In}_{0.53}\text{Ga}_{0.47}\text{As}$ quantum well, 15 nm InP spacer, 10 nm Si-doped InP layer and 60 nm InP top layer. The Si doping levels were $N_D = 9 \times 10^{17} \text{ cm}^{-3}$ for sample A used for the QPC and $N_D = 1.0 \times 10^{18} \text{ cm}^{-3}$ for sample B, used for the YBS. The Zn-doped layer was grown to form a pn-junction to inhibit conduction to a Si-contaminated and parallel-conducting layer at the interface to the semi-insulating InP substrate. Hall measurements in darkness at $T \approx 23 \text{ K}$ yielded carrier concentrations of $N_{2D} \approx 4 \times 10^{15} \text{ m}^{-2}$ and $N_{2D} \approx 3 \times 10^{15} \text{ m}^{-2}$ and electron mobilities of $\mu \approx 7 \text{ m}^2/\text{Vs}$ and $\mu \approx 8 \text{ m}^2/\text{Vs}$ for the two samples respectively. From this, one can approximate the mean free path, $l \approx 7 \times 10^{-7} \text{ m}$ for both samples which is longer than the constriction in the QPC but somewhat shorter than the total length of the YBS.

The trenches between the electron waveguides and the gates were defined by electron beam lithography using a 50 kV accelerating voltage. The 950K PMMA resist was 1700 Å thick and was developed in MIBK:Isopropanol 1:1 for 30 seconds. The resist mask was transferred to a 40 nm thick SiN layer, using CF_4 RIE. After stripping off the resist, the semiconductor was deeply etched using RIE with 17% CH_4 , 83% H_2 at the power of 0.26 W/cm² under a 15 mTorr pressure during 5 minutes resulting in a calculated etch depth of 130 nm, efficiently isolating the electron waveguide from its gates. To remove polymers deposited during etching, the sample was exposed to an oxygen plasma in a barrel reactor. Oxides were in turn removed by the use of diluted HCl:H₂O in a 1:5 mixture. For ohmic contacts 80 nm AuGe, 10 nm Ni, 50 nm Ti, 50 nm Pt, and 110 nm Au was deposited after the SiN was removed locally with buffered HF. The contacts were annealed at 650°C

III. MEASUREMENTS AND DISCUSSION

To characterize the QPC, the conductance between source and drain has to be measured while the gate voltages are swept. To reduce the effect of contact resistances, a four-probe measurement was performed. The setup used is shown in Fig. 3(a).

As seen in Fig. 2(b), the conductance is quantized and increases in steps of G_0 . This shows that the electron transport is coherent in the constriction.

The switching of the YBS was measured using two simultaneous four-probe measurements as in Fig. 3(b). The measurements were done after illuminating the sample to enhance electron concentration. We have chosen to present the matrix elements G_{LS} , G_{RS} , and G_{RL} . The first two of these represent the current into the drains, when a voltage is applied on the source, and the drains are kept at a zero voltage. In Fig. 5 (a) we see how the current from the source is switched from the left to the right drain as the voltage on the left gate V_{GL} is increased and the voltage on the right gate V_{GR} is decreased, keeping $V_{GL} + V_{GR} = 0$. When both channels are open there is also a conductance between the two drains G_{RL} . It can also be seen that the pinch-off is very good for each channel when the other has maximal conductance. The measured conductances have approximately the same levels as expected for a YBS in single mode operation, all elements being below G_0 . The switching performance is also in qualitative agreement with predictions for single mode operation.

When either of the gate voltages reach values around $-3V$ there is no conductance between any leads. This probably means that the source is pinched off, in addition to the branch closest to the negative gate voltage. We have also noted that the pinch-off voltage of a QPC with different voltages on the two side gates depends almost only on the more negative of the two gate voltages. One possible explanation would be that the etched surface between the channel and gate takes the more negative of the potentials on the neighboring 2DEGs. This would be the case if one assumes some finite conductivity on the surface. Both 2DEGs are then isolated from the surface by a depletion layer close to the surface, but this barrier will be lower at the 2DEG with lower potential, allowing a small leakage current which changes the potential of the surface. A negative gate potential is then transferred to the surface which in turn depletes the channel. When a gate potential is positive, however, the surface takes the potential of the channel. Then the surface effectively screens the field from that gate.

The crossover point is at $V_{GL} - V_{GR} = -0.8V$. This reflects some asymmetry in the device due to technological inadequacies.

In Fig. 6 (a) the same three conductance matrix elements are plotted as a function of gate voltages, but now $V_{GL} + V_{GR} = 2V$, giving higher overall conductances. This may be interpreted as multimode operation or classically just as a higher electron concentration in the channels. As in the previous case when $V_{GL} + V_{GR} = 0$, all conductance is quenched when either of the gate voltages reach approximately $-3V$. Apart from higher conductance, the most visible difference is the slower relative change of the conductances.

The conductance matrix can be described by an equivalent resistive net consisting of three resistors, each of which is connected between a lead and a common center node. The conductance of these resistors may be calculated from the matrix elements when G_{LS} , G_{RS} , and G_{RL} are all non-zero. These calculated values are presented in Fig. 5(b) and 6(b). We may also rewrite the relation (2) valid for single-mode coherent transport in terms of these conductances:

$$G_S + G_L + G_R = 4G_0. \quad (3)$$

This sum is also plotted in 5(b) and 6(b). It is interesting to note that this sum is relatively close to 4. This does not however imply single-mode coherent transport. Another, classical interpretation might be that each of the branches of the YBS act as a field effect transistor. In the diagrams we then see that the source is open and has a rather constant conductance while the branches are pinched off when the neighboring gate takes a negative voltage. The fact that the mean free path determined from Hall-measurements is somewhat shorter than the length of the YBS suggests that non-ballistic transport will be significant.

IV. CONCLUSION

We conclude that switching has been demonstrated in a YBS fabricated in dry etched $\text{In}_{0.53}\text{Ga}_{0.47}\text{As}$ / InP with in-plane gates. It can not be determined whether the transport is coherent through the whole device or if the measurements should be explained by classical phenomena. To ensure coherent transport, more narrow and shorter devices should be fabricated. This could be done with samples having higher n-doping levels, thus decreasing the depletion width from the etched surfaces. Regrowing the etched trenches with InP should also remove many surface defects, increasing the mobility. This should also simplify the analysis since it would eliminate the effect of the surface current leakage.

V. ACKNOWLEDGEMENTS

This work was financed by the Swedish Board for Industrial and Technical Development and the European Commission through ESPRIT IV, Long Term Research, project number 20960, Q-SWITCH. The authors also gratefully acknowledge the help with the low temperature measurements given by Dr. Magnus Andersson at the Department of Solid State Physics, Royal Institute of Technology.

- ¹ T.Palm, L. Thylén. *Appl. Phys. Lett.*, **60**, 237 (1992).
- ² T.Palm, L. Thylén. *J. Appl. Phys.* **79**, 8076 (1996).
- ³ J.-O. J. Wesström, K. Hieke, B. Stålnacke, T. Palm, and B. Stoltz. *Appl. Phys. Lett.*, **70**, 1302 (1997).
- ⁴ B.J. van Wees, H. van Houten, C.W.J. Beenakker, J.G. Williamson, L.P. Kouwenhoven, D. van der Marel, and C.T. Foxon, *Appl. Phys. Lett.*, **60**, 848 (1988).
- ⁵ D.A. Wharam, T.J. Thornton, R. Newbury, M. Pepper, H. Ahmed, J.E.F. Frost, D.G. Hasko, D.C. Peacock, D.A. Ritchie, and G.A.C. Jones, *J. Phys. C*, **21**, L209 (1988).
- ⁶ P. Ramvall, P. Omling, T. Palm, and L. Thylén. *Proceedings of the Second International Symposium on Quantum Confinement: Physics and Applications*, Electrochemical Society. 77 (1994).
- ⁷ N. Dagli, M. Thomas, M. Rao, M. Sundaram, and A. Gossard. *Proceedings of the Second International Symposium on Quantum Confinement: Physics and Applications*, Electrochemical Society. 87 (1994).

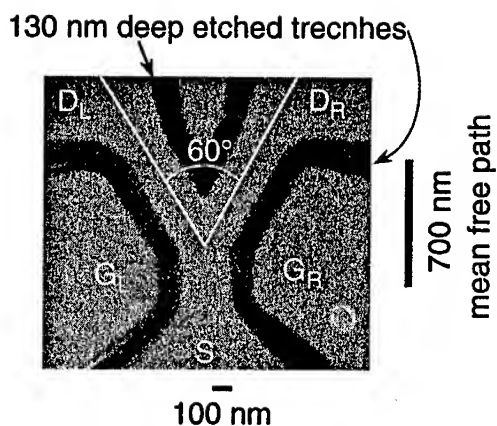


FIG. 1. Top view SEM-photograph of a 320 nm wide YBS. The silicon nitride etch mask is lighter than the etched grooves isolating the electron waveguide from its gates.

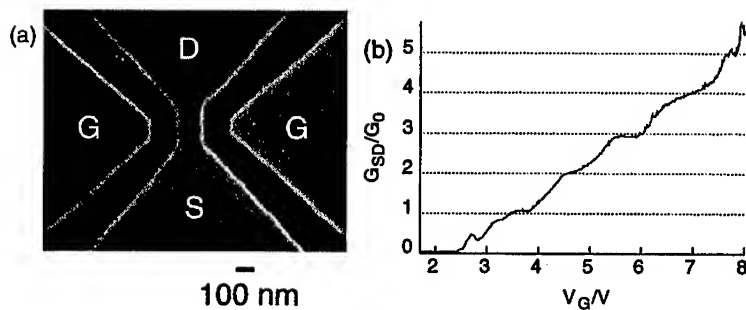


FIG. 2. (a) Top view SEM-photograph of a 140 nm wide and 200 nm long electron waveguide. The silicon nitride etch mask is lighter than the etched grooves isolating the electron waveguide from its gates. (b) Conductance as a function of gate voltage at $T=4.2$ K for the device. The source-drain voltage was 0.5 mV. The conductance was calculated from measurement assuming a series resistance of 500Ω . This value is chosen to fit the plateaus to the theory and represents the contacts.

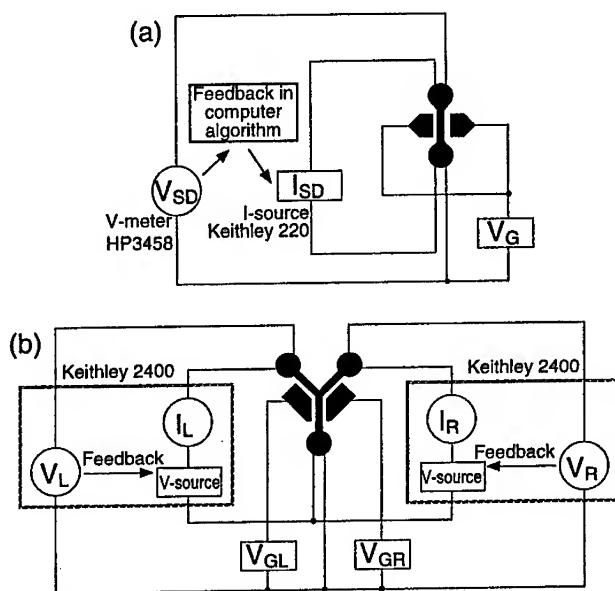


FIG. 3. (a) A four-probe measurement was performed on the quantum point contact. A current I_{SD} was fed through the structure, while the voltage V_{SD} was monitored. The computer algorithm controlling the measurement contained a feedback mechanism, keeping V_{SD} at a specified voltage of 0.5 mV. (b) To measure the conductances of the YBS, the gate voltages are swept while four-probe conductance measurements are performed between the source and each drain. The drain currents I_L and I_R and voltages V_L and V_R are measured while a feedback mechanism adjusts the voltage sources so that V_L and V_R are kept at specified voltages. By varying these voltages independently and recording I_L and I_R , all elements of the conductance matrix can be calculated.

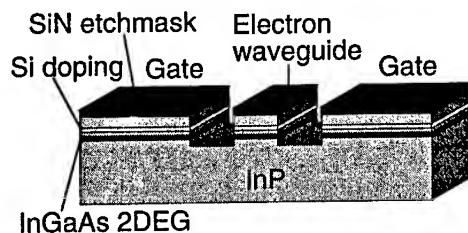


FIG. 4. Schematic drawing of cross-section of the electron waveguide with its in-plane side gates.

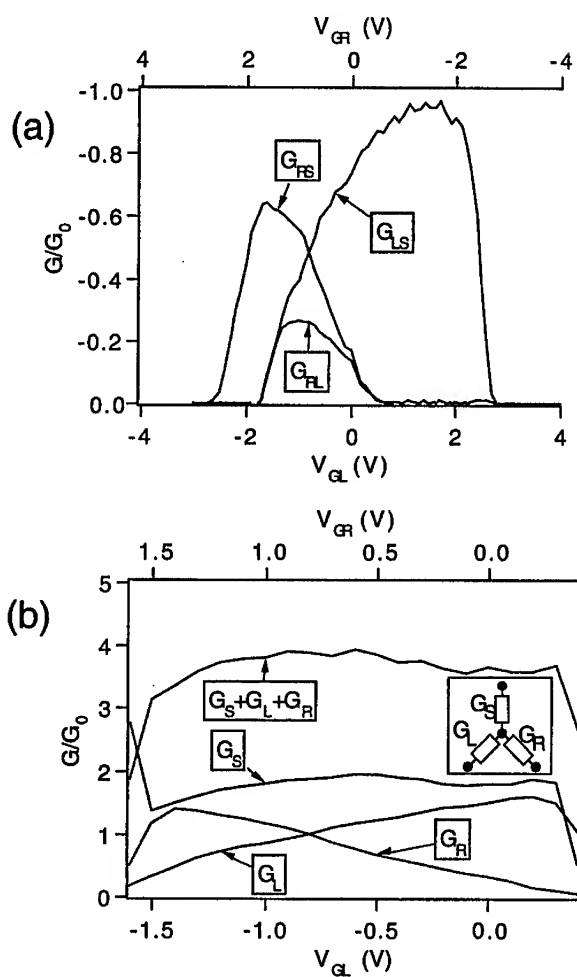


FIG. 5. (a) Measured conductance-matrix elements G_{LS} , G_{RS} , and G_{RL} as a function of the gate voltages. The sum of left and right gate voltages was 0 V. The data was taken at $T=1.5$ K. The source-drain voltages were ± 1 mV. (b) Conductances of the three resistors in the equivalent resistive net shown in the inset figure.

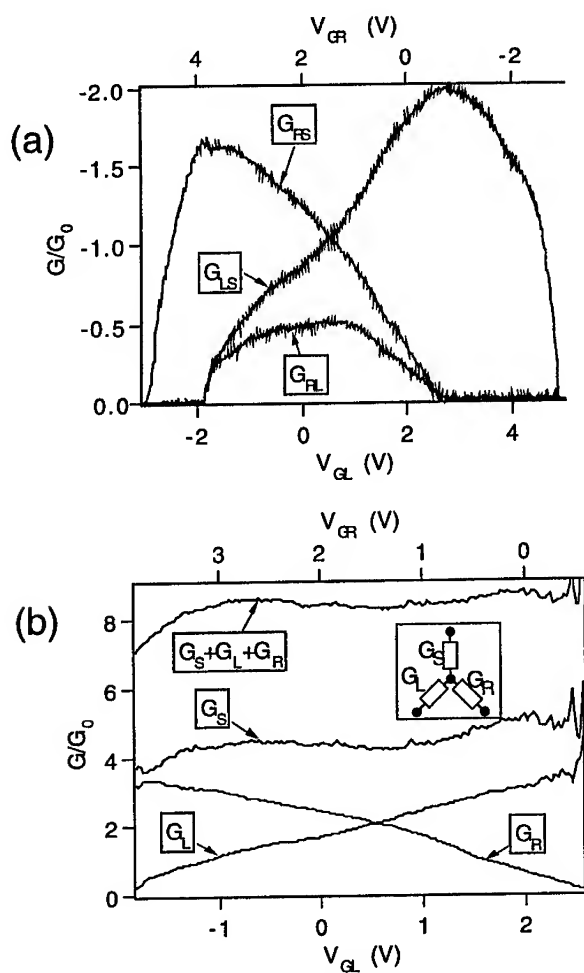


FIG. 6. (a) Measured conductance-matrix elements G_{LS} , G_{RS} , and G_{RL} as a function of the gate voltages. The sum of left and right gate voltages was 2 V. The data was taken at $T=1.5$ K. The source-drain voltages were ± 1 mV. (b) Conductances of the three resistors in the equivalent resistive net shown in the inset figure.

Quantum transport in one-dimensional magnetic superlattices

Zhen-Li Ji and D. W. L. Sprung

*Department of Physics and Astronomy, McMaster University,
Hamilton, Ontario, Canada L8S 4M1*

Abstract

The transport properties of quantum wires with a spatially periodic magnetic field are investigated. We predict that the magnetoconductance displays regular dips due to the formation of minigaps, and rapid oscillations due to electron transmission through the quasi-zero-dimensional states in the cavity region between magnetic barriers. The differences between the one dimensional (1D) *electric* superlattice and 1D *magnetic* superlattice are highlighted. We also consider the spatial distributions of currents, which are useful in elucidating many features of quantum transport in semiconductor nanostructures.

I. Introduction

Historically, Esaki and Tsu [1] proposed in 1970 a realization of energy minigaps and minibands in a synthetic superlattice, which is created by growth of alternating layers of semiconductors with different band-gap energies. Recent advances in sub-micrometer technology have made it feasible to achieve a lateral superlattice, in which the potential modulation is defined in the plane of the two-dimensional electron gas (2DEG), instead of the conventional one, in which the periodic potential is produced perpendicular to a substrate. There have been a considerable number of experimental and theoretical investigations on lateral superlattices defined by potentials in the plane of a 2DEG [2]. The formation of minibands and energy gaps in the conductance pattern of various quasi-one-dimensional periodic systems has been investigated by several authors [3, 4, 5]. These lateral superlattice effects may be studied in the linear-response regime of small applied voltage by varying the channel width or the Fermi energy E_F [6]. It has been found that the index of a quantized conductance plateau has a one-to-one correspondence

to the number of positive-velocity states in the energy band structure for the corresponding infinite modulated channel [5, 7].

It is now possible to study electronic transport in nonhomogeneous magnetic fields on the nanometer scale. Nonuniform magnetic fields can be realized, for instance, by depositing a patterned superconducting or ferromagnetic film on top of a heterojunction [8, 9] or by applying a uniform magnetic field to a nonplanar 2DEG [10]. Weiss-type oscillations were observed in the magnetoresistance, which are closely related to similar oscillations induced by 1D electrostatic potential modulation. On the theoretical side, the properties of a 2DEG in periodic magnetic fields [11, 12], and electronic transport under the influence of magnetic barriers [13, 14, 15, 16], random magnetic fields [17, 18], and a linearly varying magnetic field [19] have been investigated. It was shown that the "magnetic Weiss oscillation" is out of phase with the electric Weiss oscillation [20]. Electron tunneling through magnetic barriers is an inherently two-dimensional (2D) process, and the magnetic barriers possess wave-vector-dependent properties [16]. In a random-magnetic-field system, the localization length is not a monotonically decreasing function of magnetic-field randomness, in contrast to a random-potential system, in which it is [18].

The physics of lateral *magnetic* superlattices in an unbounded 2DEG is a topic of great current interest, and magnetotransport through spatially periodic magnetic fields has recently yielded very interesting results [8, 9, 20, 21, 22]. In this paper we point out that the experimental study of a new class of semiconductor nanostructures, the 1D *magnetic* superlattices, is now within reach, and we present theoretical predictions of their transport properties. The lower dimensionality and high degree of quantum coherence in the 1D *magnetic* superlattice are features which will make the study of these new systems rewarding. We find that the conductance shows periodic miniband and gap structures in the low plateaus, while aperiodic patterns caused by strong interchannel scattering appear in higher conductance plateaus, which is similar to the case of an *electric* superlattice. In contrast to the usual *electric* potential case, however, the form of the effective potential for magnetic barriers depends on the wave vector of the incident electron [16]. This unique feature should make the study of transmission through 1D *magnetic* superlattices very interesting.

II. Theoretical Model

Our quantum wire has width W , and a finite section which is modulated along the channel by a 1D sinusoidal magnetic field of period a , as depicted in Fig. 1.

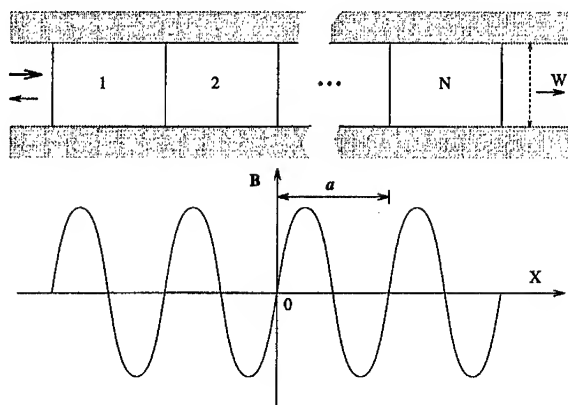


Figure 1: Schematic view of a quantum wire with hard-wall confinement of width W in the transverse direction. A finite section of which is subject to periodically varying magnetic field. Profile for the magnetic field is shown in the lower graph.

The spatial magnetic modulation can be written as

$$\mathbf{B}(x) = \begin{cases} 0\hat{z}, & |x| > L/2 \\ B_m \sin \left[K \left(x + \frac{L}{2} \right) \right] \hat{z}, & |x| \leq L/2 \end{cases} \quad (1)$$

where $K = 2\pi/a$, $L = Na$, and $N = 1, 2, \dots$ is the number of unit cells. The magnetic field is taken to point along the z direction, normal to the plane of the wire. The quantum wire consists of a finite magnetic superlattice and two straight leads, i.e., we do not bother about the details of how electrons are injected into the wire or emitted from it. For simplicity we assume that the wire is confined laterally $-W/2 < y < W/2$ by hard wall potentials. Inside the channel the potential is taken to be zero. We consider the process where electrons enter through the left lead, scatter inside the magnetic superlattice region, and then reflect back or transmit to the right lead.

For simplicity, we ignore inelastic scattering throughout the device. Spin is accounted for by twofold degeneracy in the Landauer formula and is ignored otherwise throughout the calculations. The two-dimensional time-independent Schrödinger equation for an electron with an effective mass appropriate for *GaAs*, $m^*/m_0 = 0.067$, and charge $-e$, can be written as

$$\left[\frac{(\mathbf{P} + e\mathbf{A})^2}{2m^*} + V_c(y) \right] \psi(x, y) = E_F \psi(x, y) \quad (2)$$

with

$$V_c(y) = \begin{cases} 0, & |y| < W/2 \\ \infty, & |y| \geq W/2 \end{cases}, \quad (3)$$

where \mathbf{P} is the momentum operator and $E_F = \hbar^2 k_F^2 / 2m^*$. The vector potential \mathbf{A} of the modulated magnetic field $\mathbf{B}(x)$ is chosen to be

$$\mathbf{A} = \begin{cases} (0, -\frac{B_m}{K}, 0), & |x| > L/2 \\ (0, -\frac{B_m}{K} \cos[K(x + \frac{L}{2})], 0), & |x| \leq L/2 \end{cases}. \quad (4)$$

In our calculations a numerical algorithm based on the finite element method was used. We use a finite element method to achieve numerical discretization over the modulated region, which reduces the problem of solving the Schrödinger equation to a sparse matrix problem [23, 24]. Meshes of up to 16371 nodal points were used to achieve convergence. The wave functions in the leads were calculated separately. The wave functions and their spatial derivatives were then matched at the boundaries between the leads and modulated region, after which the transmission and reflection coefficients were extracted. The conductance in the linear response regime was obtained using the two-terminal version of the Landauer formula. The details of this numerical scheme can be found in Refs. [23] and [24].

III. Results and Discussion

Figure 2 shows the conductance of a modulated quantum wire with $N = 1, 4$ and 8 unit cells, respectively. The conductance for $N = 1$ shows an incipient quantization profile. There is a dip in conductance in the region near 2.2 meV ; this dip is due to coupling between localized states and propagating modes. For a wire with $N = 4$ unit cells the conductance shows an indication of miniband formation in a periodic structure. Although the basic features of the formation of minibands and gaps are already present for wires with a few unit cells, some narrow and fine minibands and gaps reveal themselves only for a rather long modulated wire, as seen in Fig. 2 for the wire with $N = 8$ periods.

In Fig. 3(a) we show the calculated conductance of a wire with $N = 16$ and the individual transmission coefficients for each incident mode. The conductance displays dips due to the formation of minigaps, and rapid oscillations due to electron transmission through the coupled quasi-zero-dimensional states in the cavity regions between the magnetic barriers. Each group of conductance oscillations evolves into a continuous miniband in the limit of an infinitely long superlattice. The formation of minibands and minigaps in a finite lateral surface superlattice

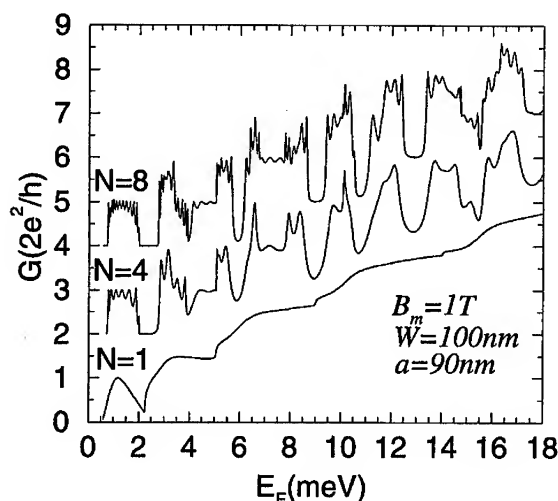


Figure 2: Conductance vs Fermi energy E_F for quantum wires with $N = 1, 4$, and 8 , respectively. Curves for $N = 4$ and 8 are vertically offset for clarity.

has been reported using split-gate structures, in which the 1D lateral surface superlattice is realized by a periodic modulation of constriction width instead of magnetic modulation [6].

In contrast to the electric modulated case [3, 4, 5], the number of oscillations in the first conduction plateau has no simple direct correspondence to the number of unit cells. This result shows that the effective potential of the magnetic barriers for electron motion in the wire is complicated [11]. The oscillations in higher plateaus are more irregular because of the strong coupling between modes. The conductance, plotted in Fig. 3(a), shows a profile of quantization in units of $2e^2/h$ [5, 7].¹ Unlike the usual quantization of a quantum point contact, however, the conductance does not increase monotonically but rather steps up and down between quantized levels. The conductance quantization is related to the band structure for the corresponding infinite system [7]. However, none of the individual modal transmission coefficients in Fig. 3(b) shows quantization by itself. See for example the region near 9 meV . The quantization occurs as the various modes are mixed by the periodic modulation.

¹In some places, the peaks are narrow and due to the accident of their position on our numerical grid, the quantized value is not achieved in the drawing. Using a finer grid does tend to increase the height of these peaks.

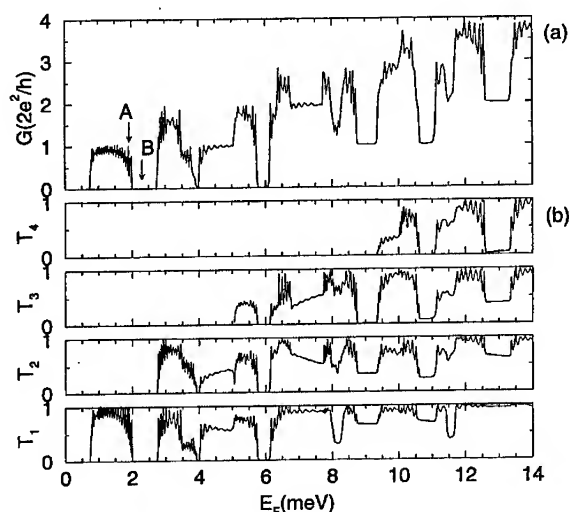


Figure 3: (a) Conductance as a function of Fermi energy E_F for a finite period magnetic superlattice with 16 unit cells. $a = 90$ nm, $W = 100$ nm, and $B_m = 1.5$ T. The arrows A and B indicate the energies corresponding to the current distributions shown in Figs. 4(a) and 4(b), respectively. (b) Transmission coefficients of individual modes for the magnetic modulated quantum wire.

In Figs. 4(a) and 4(b), we have plotted current distributions in a unit cell of the magnetic superlattice for the states labeled A and B indicated in Fig. 3(a). There is one vortex in the current patterns for states A and B, respectively. The origin of the vortices is the Lorentz force which tends to produce a circulation in the current flow. The state labeled A is in the first miniband; the transmission coefficient through each unit cell is unity. We find that there is a large amount of net current traveling from one unit cell to another even in the case of vortex formation as shown in Fig. 4(a). The state labeled B is in a minigap where the conductance essentially zero. The corresponding current profile is shown in Fig. 4(b); it is clear that little current escapes from the cell.

Nonmonotonic conductance quantization as a function of the amplitude B_m , is shown in Fig. 5(a). The conductance steps down by two-units of $2e^2/h$ and up by one-unit, then down to zero as B_m is increased. Transmission coefficients T_i of individual modes for the magnetic superlattice are shown in Fig. 5(b); the curves are vertically offset for clarity. Although the total conductance, which is the sum

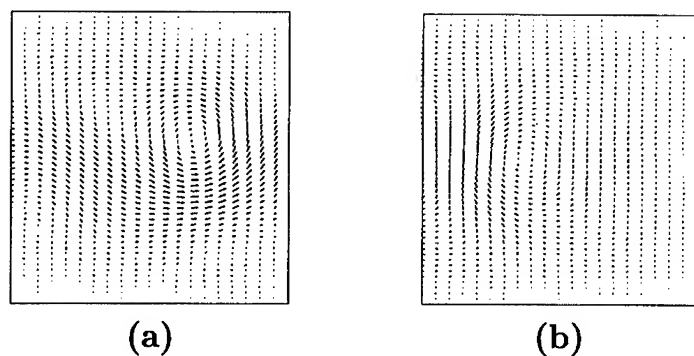


Figure 4: (a) and (b) show the current density distributions for the cases denoted by the arrows A and B in Fig. 3(a), respectively. One cell of the structure is shown.

of the modal transmissions, is essentially quantized, the individual transmissions, plotted in Fig. 5(b), show complicated dependence on B_m .

For comparison, we calculated the conductance for an *electric* superlattice with amplitude V_m and sinusoidal barriers. The geometry of the structure is otherwise the same as that of Fig. 5(a). The conductance for a 1D *electric* superlattice steps down monotonically as the propagating modes in the leads are blocked by the potential barriers with increasing electric modulation amplitude V_m , as shown in Figs. 5(c) and 5(d). No two-unit drop is seen for increasing electric modulation amplitude V_m in Fig. 5(c). Clearly, the unique features of the wave-vector-dependent effective potential for the magnetic barriers are critical for the two-unit drop in Fig. 5(a). In our calculations, the two-unit drop in conductance with increasing B_m is predominant but not universal; occasionally we find cases with a one-unit drop. The reason for this is that the effective potential of the magnetic barriers for electron motion along the quantum wire depends on the mode of the incident electron in the leads [11].

Figs. 6(a)-6(f) show the current densities in one unit cell of the magnetic and electric superlattices for the cases labeled A through F denoted in Fig. 5(a) and 5(c), respectively. Figure 6(a) corresponds to the current pattern for the case that two propagating modes are in the sample. The current pattern clearly shows that the Lorentz force allows electrons move in a meandering way. At sufficiently high magnetic fields, the current flow forms a complex pattern as shown in Fig. 6(b). In this situation, the corresponding conductance is essentially zero. As B_m is further

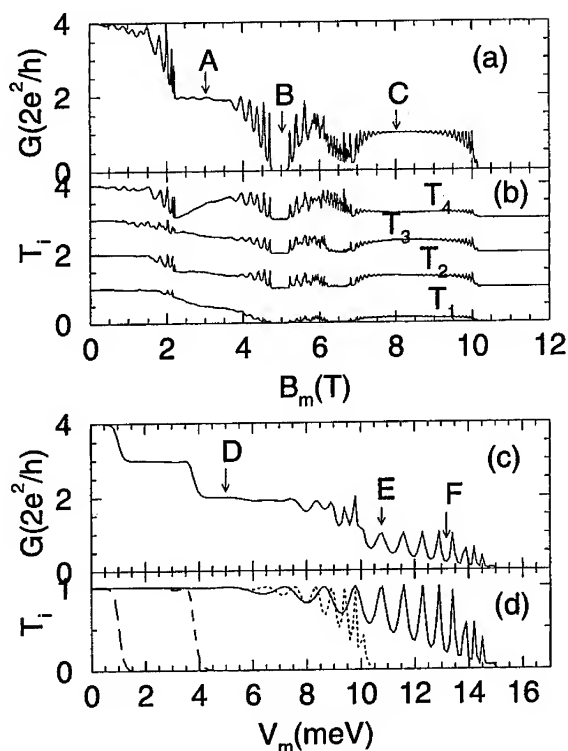


Figure 5: (a) The conductance as a function of the *magnetic* modulation amplitude B_m for a quantum wire with 16 unit cells. $a = 90$ nm, $W = 100$ nm, and $E_F = 12$ meV. (b) Transmission coefficients T_i of individual modes for the *magnetic* superlattice. The curves are offset for clarity. (c) The conductance as a function of the *electric* modulation amplitude V_m for a finite period *electric* superlattice. The other parameters are the same as (a). (d) Transmission coefficients T_i of individual modes for the *electric* superlattice. The solid, dotted, dashed, and long-dashed curves correspond to $i = 1, 2, 3$, and 4 , respectively. The arrows A-F indicate the cases corresponding to the current distributions shown in Figs. 6(a)-6(f), respectively.

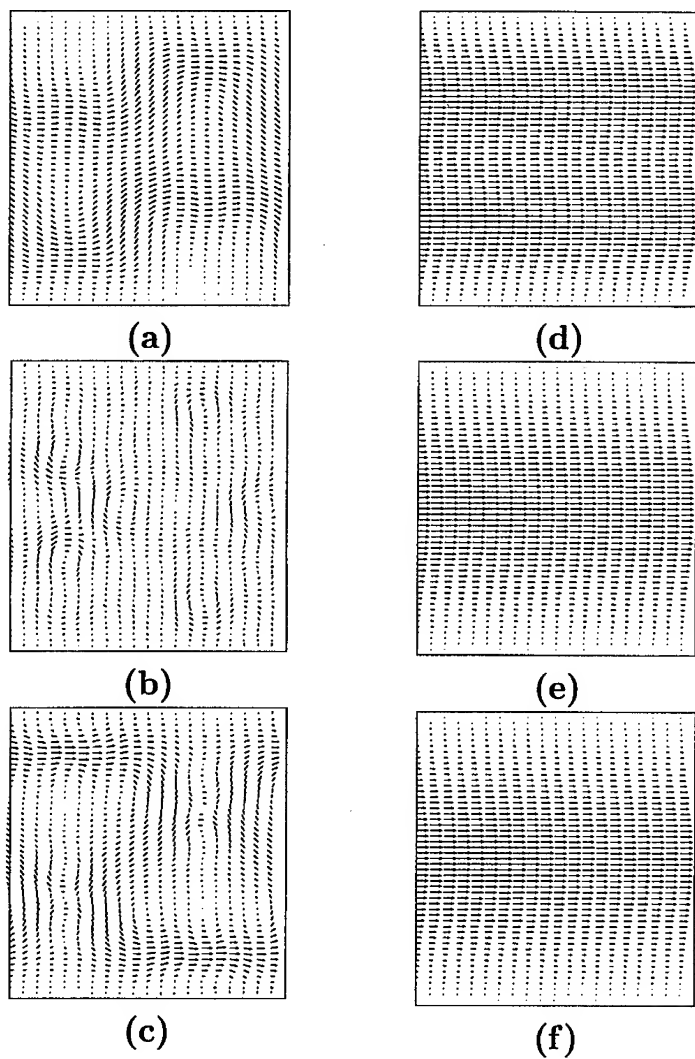


Figure 6: The current density distributions. (a)-(f) corresponding to the cases labeled A-F indicated in Figs. 5(a) and 5(c), respectively.

increased, the conductance steps up by one-unit. The corresponding current flow is shown in Fig. 6(c). The current pattern shows the electron trajectory bending first to the right and then to the left, which allows it more easily to find a path through the cell. Figs. 6(d)-6(f) show the current distributions for an electric superlattice with sinusoidal barriers. Notice that in this case, the current flows straight across the cell. This indicates that the electron transport in this electric superlattice is equivalent to a one-dimensional system, in contrast to the magnetic one, in which it is not.

IV. Conclusion

We have shown that many features of electronic transport in 1D *magnetic* superlattices differ from those of the electrostatically modulated ones. We find that unlike the electric superlattice, the number of oscillations in the first conduction plateau has no simple direct correspondence to the number of unit cells N . The conductance of 1D magnetic superlattices does not decrease monotonically with increasing B_m but rather steps up and down between quantized levels, sometimes going to zero. The spatial distributions of current density show dramatic differences between the magnetic superlattices and electric ones.

Acknowledgments

We are grateful to NSERC Canada for continuing support under research grant SAP-003198. Computations were performed on a CRAY computer at the IFM, Linköping University, Sweden.

References

- [1] L. Esaki and R. Tsu, IBM J. Res. Dev. **14**, 61 (1970).
- [2] For a review, see C. W. J. Beenakker and H. van Houten, in *Solid State Physics, Semiconductor Heterostructures and Nanostructures*, edited by H. Ehrenreich and D. Turnbull (Academic Press, New York, 1991), Vol. 44, p.1, and references cited therein.
- [3] S. E. Ulloa, E. Castaño, and G. Kirczenow, Phys. Rev. B **41**, 12 350 (1990).
- [4] D.W.L. Sprung, Hua Wu and J. Martorell, Am. J. Phys. **61**, 310 (1993).
- [5] M. Leng and C. S. Lent, Phys. Rev. B **50**, 10 823 (1994).

- [6] L. P. Kouwenhoven, F. W. J. Hekking, B. J. van Wees, C. J. P. M. Harmans, C. E. Timmering, and C. T. Foxon, *Phys. Rev. Lett.* **65**, 361 (1990).
- [7] M. Leng and C. S. Lent, *Phys. Rev. Lett.* **71**, 173 (1993).
- [8] H. A. Carmona *et al.*, *Phys. Rev. Lett.* **74**, 3009 (1995).
- [9] P. D. Ye *et al.*, *Phys. Rev. Lett.* **74**, 3013 (1995).
- [10] M. L. Leadbeater, C. L. Foden, J. H. Burroughes, M. Pepper, T. M. Burke, L. L. Wang, M. B. Grimshaw, and D. A. Ritchie, *Phys. Rev. B* **52**, 8629 (1995).
- [11] I. S. Ibrahim and F. M. Peeters, *Phys. Rev. B* **52**, 17 321 (1995).
- [12] R. Yagi and Y. Iye, *J. Phys. Soc. Jpn.* **62**, 1279 (1993).
- [13] J. Q. You and L. Zhang, *Phys. Rev. B* **54**, 1526 (1996); J. Q. You, L. Zhang, and P. K. Ghosh, *Phys. Rev. B* **52**, 17 243 (1995).
- [14] Y. Takagaki and K. Ploog, *Phys. Rev. B* **51**, 7017 (1995).
- [15] Zhen-Li Ji and D. W. L. Sprung, *Phys. Rev. B* **54**, 8044 (1996).
- [16] A. Matulis, F. M. Peeters, and P. Vasilopoulos, *Phys. Rev. Lett.* **72**, 1518 (1994).
- [17] Y. Takagaki and K. Ploog, *Phys. Rev. B* **53**, 3885 (1996).
- [18] W. L. Chan, X. R. Wang, and X. C. Xie, *Phys. Rev. B* **54**, 11 213 (1996).
- [19] S. Izawa *et al.*, *J. Phys. Soc. Jpn.* **64**, 706 (1995).
- [20] F. M. Peeters and A. Matulis, *Phys. Rev. B* **48**, 15166 (1993).
- [21] D. Yoshioka and Y. Iye, *J. Phys. Soc. Jpn.* **56**, 448 (1987).
- [22] Y. Iye, A. Endo, S. Izawa, M. Kato, and S. Katsumoto, *Physica B* **227**, 122 (1996).
- [23] M. Leng and C. S. Lent, *J. Appl. Phys.* **76**, 2240 (1994).
- [24] Y. Wang, J. Wang, and H. Guo, *Phys. Rev. B* **49**, 1928 (1994).

Confined Magneto-Polariton Propagation in Quantum Wires

A. Balandin and S. Bandyopadhyay
Department of Electrical Engineering
University of Nebraska
Lincoln, Nebraska 68588-0511 USA

Abstract

In this paper, we have calculated the refractive index of a quantum wire waveguide in the vicinity of an exciton-polariton resonance. The critical values of the exciton decay parameter, defining the onset of polariton transport regime, and the associated temperature were also found using the combination of a variational approach and a numerical solution. Our theoretical model allows us to include the effects of an external magnetic field. The results show that confinement of excitons to one dimension and the simultaneous application of a magnetic field may lead to the extension of the temperature and spatial limits of polariton transport. The magnetic field can be used to shift refractive index peaks in frequency thus providing a much-desired tuning capability.

I. Introduction

Exciton dynamics in semiconductor quantum confined structures has always been attractive because of its potential applications in optoelectronics. One of the most interesting phenomenon related to excitons in such structures is the formation of exciton-polaritons. In the spectral region around an exciton resonance, a photon, absorbed by a semiconductor, linearly couples with an exciton to create a polariton. Exciton polaritons have been studied extensively in quantum wells by measuring photoluminescence and reflection,

as well as by picosecond time-of-flight measurements.^{1,2} It was shown that polaritons are much more stable in quantum wells than in bulk,³ and they are expected to be even more stable in quantum wires since the exciton binding energy and oscillator strength tend to increase with reducing dimensionality.⁴

The formation of polaritons modifies the transport of light through the medium. In particular, the medium of propagation becomes substantially more transparent^{5,6} and the group velocity of light propagating along the waveguide approaches the speed of light in vacuum.⁷ At the same time, there is a possibility of controlling polariton transport with an external field. In this paper, we argue that a relatively weak magnetic field is particularly attractive for tuning polariton transport because it increases exciton oscillator strength thus *extending the polariton regime* of energy transfer, while an electric field would decrease exciton oscillator strength and quench polariton transport.

Although existing theoretical models recognize modification of polariton transport due to spatial confinement, they account for it by using heuristically peaked values for exciton oscillator strength and binding energy. The authors are not aware of any attempts to include an external field, particularly magnetic, into consideration.

In this work, we present a model for calculating the exciton-polariton critical decay parameter and the refractive index of a quantum wire around a polariton resonance in the presence of a magnetic field. The decay parameter determines the regime of polariton transport. To our knowledge, this is the first study where the exciton longitudinal-transverse (LT) splitting and exciton resonance frequency - which define the polariton dispersion - are found in a non-ad-hoc manner using the combination of a variational approach and an exact numerical solution of the Schrödinger equation. The calculations are performed for a quantum wire with finite lateral dimensions subjected to a magnetic field.

The rest of the paper is organized as follows. In section II, we establish the polariton dispersion relation used throughout the model; section III presents

the results of calculation of the LT splitting and oscillator strength of the exciton transition in a quantum wire subjected to a magnetic field; in section IV, we examine the exciton critical damping for the onset of the polariton transport regime and calculate refractive index of the wire in the vicinity of exciton resonance. Conclusions are given in section V of the paper.

II. Polariton dispersion

We consider an array of parallel *GaAs* quantum wires of rectangular cross section separated by infinite potential barriers so that wavefunctions of the excitons from different wires do not overlap. In such a structure, excitons are free to move along the wire axes but are confined in perpendicular directions. The lateral dimension of each wire is comparable to the exciton Bohr radius. The cladding material is assumed to have a similar refractive index so that we can ignore image charges of the exciton and associated dielectric confinement effects. Under these conditions, the dispersion relation of the exciton polaritons can be determined for each separate wire. The multiple wire structure in this case merely forms a waveguide structure analogous to that considered in Ref. [8].

Most theoretical models for exciton polaritons (both in bulk material and nanostructures) embody a semi-classical approach and utilize the dispersion relation of a polariton derived for a single electric-dipole-active exciton resonance.^{5,8} Here, we adopt the same philosophy and consider electromagnetic waves propagating through an array of quantum wires with a wavevector k parallel to the wire axis. This choice of the direction of propagation allows for a spatial dispersion of the light waves. In the opposite case of light propagating normal to the wire axis, the translational motion of excitons is suppressed and the spatial dispersion effects do not occur.

In the long-wave approximation ($kL_{y,z} < 1$, where $L_{y,z}$ are the wire lateral dimensions) the array interacts with light waves like an effective medium, and the dielectric function in the vicinity of an isolated exciton resonance can be

written as⁹

$$\epsilon(\omega, k) = \epsilon_o + \frac{2\epsilon_o\omega_{LT}\omega_o}{\omega_o^2 - \omega^2 + \hbar k^2\omega_o/M - i\omega\gamma}. \quad (1)$$

where ϵ_o is the background dielectric constant (contribution made by other resonances), ω is the frequency of light, ω_{LT} is the longitudinal-transverse splitting of the exciton related to its oscillator strength, ω_o is the exciton resonant frequency at $k = 0$, $M = m_e + m_h$ is the translational mass of an exciton, and $\Gamma \equiv \hbar\gamma$ is the exciton damping parameter. Here we have assumed parabolic wavevector dependence of the exciton frequency $\hbar\omega_t(k) = \hbar\omega_o + \hbar^2k^2/2M$, with the caveat that this is valid only in weak magnetic fields when the magnetic length $l_m (= \sqrt{\hbar/eB})$ is much larger than the transverse dimensions of the wire. In the formula above, the quantities $\omega_{LT} \equiv \omega_{LT}(L_{y,z}, B)$ and $\omega_o \equiv \omega_o(L_{y,z}, B)$ are the functions of the wire lateral dimensions and a magnetic field. The exciton damping constant is considered to be independent of the magnetic field since it is known that *energy-averaged* phonon-interaction rates in quantum wires are not terribly sensitive to a magnetic field. In any case, Eq. (1) is a good approximation when the magnetic field applied to the system is relatively weak: $l_m > L_{y,z}$. This equation relates ω and k and is the sought-after dispersion relation of a polariton.

Before we can go further into polariton transport properties, we have to calculate ω_{LT} and ω_o as the functions of wire dimensions $L_{y,z}$ and a magnetic flux density B . This is discussed in the next section.

III. Longitudinal-transverse splitting

Let us assume that the infinite potential barriers of the quantum wire are located at $y = \pm L_y/2$ and $z = \pm L_z/2$. A magnetic field is applied along the z -direction (see inset to Fig. 1). To simplify the calculations, we assume strong quantum confinement of the carriers which enables us to factorize an exciton wavefunction into the product of electron and hole wave functions. Moreover, we limit our consideration to systems with relatively large dielec-

tric constants so that all Coulomb interactions are strongly screened. This assumption, together with the hard-wall boundary condition, allows a coordinate separation. Consequently, the wave function of an exciton in the vicinity of subband bottom (with center-of-mass momentum $\vec{P}_X \approx 0$) is given by⁴

$$\begin{aligned}\Psi \equiv \Psi(x, y_e, y_h, z_e, z_h) &= g_t(x, \eta) \psi_e(y_e, z_e) \psi_h(y_h, z_h) \\ &= g_t(x, \eta) \phi_e(y_e) \phi_h(y_h) \chi_e(z_e) \chi_h(z_h),\end{aligned}\quad (2)$$

where $g_t(x, \eta)$ is chosen to be the Gaussian-type "orbital" function:

$$g_t(x, \eta) = \frac{1}{\eta^{1/2}} \left(\frac{2}{\pi}\right)^{1/4} e^{-(x/\eta)^2} \quad (3)$$

in which η is a variational parameter which defines the exciton size ("longitudinal length"), and x is the relative electron-hole coordinate. The subscripts in $x_{e,h}, y_{e,h}, z_{e,h}$ identify them as electron or hole coordinates. The variables $\chi_{e,h}(z_{e,h})$ are the z-components of the wave functions which are not affected by the magnetic field. They are given by particle-in-a-box states. The electron and hole wave functions along the y direction, $\phi_{e,h}(y_{e,h})$, are to be calculated numerically when a magnetic field is present. This is done by solving the one-particle Schrödinger equation using a finite difference method.¹⁰

In order to find an exciton "length" η , we use the variational approach of minimizing the energy given by $\langle \Psi | \hat{H}^X | \Psi \rangle$, where the exciton Hamiltonian is

$$\begin{aligned}\hat{H}^X &= \frac{\hat{P}_X^2}{2M} + \frac{\hat{p}_x^2}{2\mu} + \frac{\hat{p}_{y_e}^2 + \hat{p}_{z_e}^2}{2m_e} + \frac{\hat{p}_{y_h}^2 + \hat{p}_{z_h}^2}{2m_h} \\ &+ \frac{eB(y_e - y_h)}{M} \hat{P}_X + eB(y_e/m_e + y_h/m_h) \hat{p}_x + \frac{e^2 B^2}{2} (y_e^2/m_e + y_h^2/m_h) \\ &+ U_C(x_e, x_h, y_e, y_h, z_e, z_h) + U_S(y_e, y_h, z_e, z_h).\end{aligned}\quad (4)$$

Here we have chosen the Landau gauge $\vec{A} = (-By, 0, 0)$. The quantities m_e, m_h , are the effective masses of electrons and holes respectively, $1/\mu (= 1/m_e + 1/m_h)$ is the exciton's reduced mass, $U_C(x_e, x_h, y_e, y_h, z_e, z_h)$ is the electron-hole Coulomb interaction term, $U_S(y_e, y_h, z_e, z_h)$ is the spatial confinement potentials for electrons and holes along y and z directions.

Details of the variational procedure, calculations of η , etc., can be found in some of our earlier work.⁴

We can find the oscillator strength of the exciton transition α_o and the LT splitting by evaluating the momentum matrix element which is given as

$$|M_{cv}^X|^2 = \left| \frac{1}{2\pi} \int dk g_t(x, \eta) M_{cv}(k) \right|^2, \quad (5)$$

where M_{cv} is the valence-band to conduction-band dipole matrix element, and k is again the wave vector along the unconfined direction of the wire. When the k dependence of M_{cv} is neglected, Eq. (5) reduces to the simple expression

$$|M_{cv}^X|^2 = |M_{cv}|^2 |g_t(x=0, \eta)|^2. \quad (6)$$

The exciton oscillator strength per unit length can be written as follows

$$\alpha_o = \frac{2}{m_o \hbar \omega_o} |M_{cv}^X|^2. \quad (7)$$

Here $\hbar \omega_o = E_G + E_{e1} + E_{hh1} - \min \langle \Psi | \hat{H} | \Psi \rangle$ is the exciton ground state energy, E_G is the fundamental bandgap of the bulk material, E_{e1} , E_{hh1} are the lowest electron and the highest heavy hole magneto-electric subband bottom energies in a quantum wire measured from the bottom of the bulk conduction band and the top of the bulk valence band, and m_o is the free electron mass. The exciton LT splitting $\Omega_{LT} \equiv \hbar \omega_{LT}$ can now be written as

$$\hbar \omega_{LT} = \frac{2\pi \alpha_o \hbar \omega_o}{\epsilon_o} = \frac{4\pi}{m_o \epsilon_o} |M_{cv}^X|^2. \quad (8)$$

In Fig. 1 we present the LT splitting calculated for different wire dimensions and magnetic flux densities. The physical parameters used for the calculations correspond to a *GaAs* quantum wire with $\epsilon = 12.9\epsilon_o$, $E_G = 1.515\text{eV}$, $m_e = 0.067m_o$, $m_h = 0.5m_o$, where m_o is free electron mass and ϵ_o is electrical permittivity of free space, E_{e1} , E_{hh1} are calculated numerically following the prescriptions of Refs. [10, 11]. One can see from the figure, that the exciton splitting is sensitive to the spatial confinement and increases by about 60 % when the wire width decreases from 500 Å to 50 Å. A magnetic field

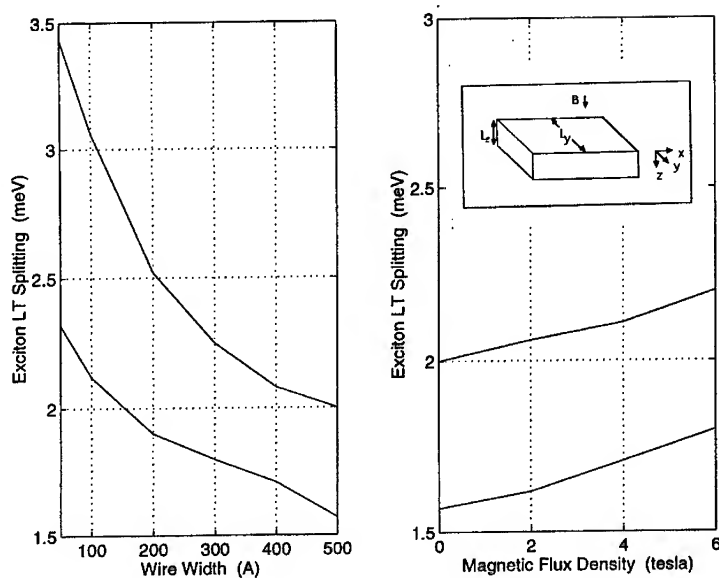


Figure 1: Longitudinal-transverse splitting of an exciton as a function of wire width (left pannel); and as a function of magnetic flux density for a 500 Å wide wire (right panel). For both panels, the upper and lower curves correspond to 200 Å and 500Å thick wires, respectively.

also increases the splitting (and oscillator strength) thus making the exciton polaritons more stable.

IV. Refractive index and decay parameter

The experimentally observed higher transparency of the medium of propagation in polariton transport regime has been attributed to certain features of the dispersion law for excitonic polaritons and to the fact that polariton transport by itself cannot cause true absorption. In order for absorption to occur, polaritons have to be scattered inelastically, e.g., by phonons. The onset of polariton transport through some structure is governed by the exciton

polariton coherence length related to the exciton decay parameter $\Gamma \equiv \hbar\gamma$. It has been shown, both experimentally and theoretically, that there exists a critical value of the exciton decay parameter, Γ_c , which corresponds to a change in the nature of absorption.^{5,6} Here we intend to examine the influence of spatial confinement and a magnetic field on this parameter and calculate the refractive index of a quantum wire in the polariton regime.

Confining ourselves to the TE waves relevant to light propagation in the medium, we can write polariton dispersion in the following form

$$\epsilon(\omega, k) = \frac{c^2 k^2}{\omega^2} \equiv n^2. \quad (9)$$

Combining this equation with Eq. (1), and after some algebra, we obtain

$$\frac{\hbar\omega_o\omega^2}{Mc^2}n^4 + (\omega_o^2 - \omega^2 - i\gamma\omega - \epsilon_o \frac{\hbar\omega_o\omega^2}{Mc^2})n^2 - \epsilon_o(\omega_o^2 - \omega^2 - i\gamma\omega + 2\omega_{LT}\omega_o) = 0. \quad (10)$$

This equation can be solved for two sets of the refractive indices, n_1 and n_2 , corresponding to different transverse polariton branches. It also follows from Eq. (10) that if the damping parameter Γ becomes larger than the critical value

$$\Gamma_c \equiv \Gamma_c(L_{y,z}, B) = 2\hbar\omega_o \sqrt{\frac{2\epsilon_o \hbar\omega_{LT}}{Mc^2}}, \quad (11)$$

then only one light wave mode can propagate in the medium, since there is only one real solution for n . This is the boundary of the polariton propagation regime. The critical value comes about because of the term $\hbar k^2 \omega_o / M$ associated with spatial dispersion effects. The physical importance of the critical damping can be illustrated by the following example. It was shown⁶ that when the damping exceeds the critical value, the integral absorption is independent of Γ and proportional to the oscillator strength of transitions (non-polariton regime). When $\Gamma < \Gamma_c$, the integral absorption depends on Γ linearly, and decreases with decreasing damping.

Using the results from the previous section, we can calculate Γ_c for different values of wire widths and magnetic field. In Fig. 2 we present the critical exciton damping (decay) parameter as a function of wire width. It is

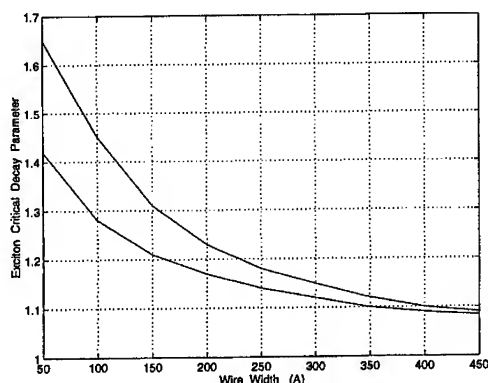


Figure 2: The critical exciton decay parameter (damping) as a function of wire width. The upper and lower curves correspond to the thickness along the z -direction of 200 Å and 300 Å, respectively.

normalized by the value of the decay parameter of a very wide wire ($L_y=700$ Å) which is wide enough to be approaching the 2D limit. For this wide wire, $\Gamma_c \approx 1.01$ meV. Combining Eqs. (7, 8, 11) we can also estimate the magnetic field dependence of the critical decay parameter using the formula $\Gamma_c(B)/\Gamma_c(0) = (\omega_o(B)/\omega_o(0))\sqrt{\omega_{LT}(B)/\omega_{LT}(0)}$. Although not shown here, the magnetic field dependence of the critical parameter is weak; it increases only 5% at a magnetic flux density of 5 tesla. The strong dependence of the critical damping on the wire width may lead to a pronounced modification of the integral (total) absorption of systems consisting of a number of narrow quantum wires.

We can now find a temperature which corresponds to the critical damping from the relation $\Gamma_c = \Gamma_o + \Gamma_{ph}(T_c)$, where Γ_o is the damping associated with the impurity and other temperature-independent elastic scattering, while $\Gamma_{ph}(T_c)$ represents interactions with acoustic and optical phonons. By increasing Γ_c one can increase T_c which defines the onset of polariton transport and, as a consequence, higher transparency.

Since there is no data available on quantum wires, we assume that the half-width at half maximum (HWHM) of the exciton resonance in a quantum wire is the same as in a 200 Å thick *GaAs/AlGaAs* quantum well. Using the approximation of Ref [11] we may write for our case (energy units are meV)

$$\Gamma_c = \Gamma_o^+ + 0.00147T_c + 4.0(e^{\hbar\omega_{ph}/k_B T_c} - 1)^{-1} + \Gamma_{imp}e^{-E_b/k_B T_c}, \quad (12)$$

where $\hbar\omega_{ph} = 36$ meV is a longitudinal optical phonon energy, k_B is the Boltzman constant, $E_b \approx 10$ meV is the average binding energy for donor impurities in GaAs, $\Gamma_{imp} = 0.75$ meV is a linewidth due to fully ionized impurity scattering, $\Gamma_o^+ \approx 0.45$ meV is the linewidth due to inhomogeneous fluctuations of the wire thickness. The values chosen for the various parameters are typical of experimental systems reported in the literature.

Table I. Critical temperature vs. wire width

$L_y, (\text{\AA})$	500	300	100
$\Gamma_c, (meV)$	1.09	1.16	1.45
$T_c, (K)$	118	138	169

Solving Eq. (12) for the temperature T_c for each value of $\Gamma_c(L_y, z, B)$, we are able to obtain the dependence of the critical temperature on the wire width. The thickness of the wire, L_z , was fixed at 200Å for this calculation. As one can see from Table I, that the critical temperature T_c , that defines the onset of polariton transport, can be controlled over a wide range by changing the wire width L_y .

Now let us assume that $\Gamma < \Gamma_c$ (exciton polariton regime) and find the refractive index of the quantum wire in the vicinity of polariton resonance. In order to do this, we make use of Pekar's additional boundary condition (total polarization is zero at the boundary) and write the effective refractive index as

$$n_{eff} = \frac{n_1 n_2 + \epsilon_o}{n_1 + n_2}. \quad (13)$$

In Fig. 3, we present the real (upper panel) and imaginary (lower panel) parts of the refractive index of a quantum wire with thickness 200 Å and

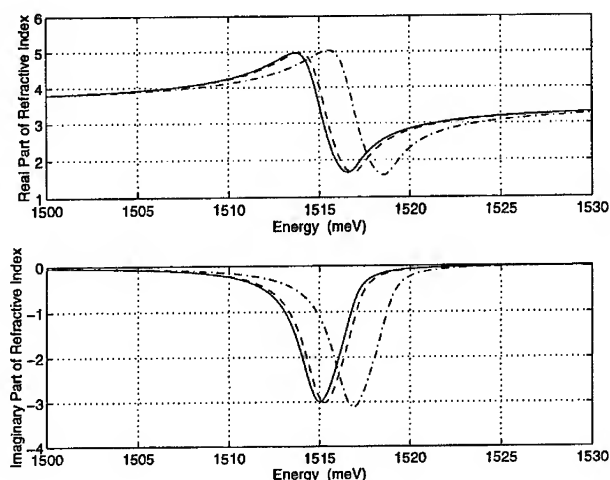


Figure 3: The refractive index of the wire in the vicinity of exciton resonance. The solid, dashed and dash-dotted curves correspond to a 0, 1, and 5 tesla magnetic flux density, respectively.

width 300 Å. An external transverse magnetic field is applied along the thickness. The decay parameter is chosen to be $\Gamma = 1\text{meV}$ which is less than Γ_c for the given wire dimensions. As one can see from the figure, the maximum of the real part of the refractive index is as large as 4.97 at zero field and 5.04 at 5 tesla magnetic field. It is about 1.4 times larger than that of the bulk material. The refractive index attains its maximum value at a photon energy slightly lower than the resonance energy $\hbar\omega_o(L_{y,z}, B)$ at any given magnetic field B . The minimum value of the refractive index, which is 1.66 for zero field and 1.59 for 5 tesla, is located at a frequency of $\omega_o(L_{y,z}, B) + \omega_{LT}(L_{y,z}, B)$. It is interesting to note that efficient waveguiding can be achieved in the spectral range where the real part of the refractive index increases. However, in this region, the imaginary part of the refractive index (extinction coefficient) also peaks and this increases the transmission

loss. The mitigating factor in all this is that the two peaks do not occur at exactly the same frequency so that an optimal region for optical waveguiding exists.

A magnetic field of 5 tesla blue-shifts the refractive index peak by 2 meV. According to Ref. [13], approximately the same magnitude of an opposite red-shift can be achieved by applying an electric field of about 4×10^4 V/cm. However, the electric field leads to a 15-20 % increase in exciton radius and a concomitant decrease in the binding energy. This, in turn, causes a decrease in exciton LT splitting and makes exciton polaritons less stable. Note that while an electric field will tend to ionize an exciton by pulling the electron and hole apart, a magnetic field has the opposite effect. It squeezes the electron and hole even tighter together and increases the binding energy. Therefore, the magnetic field can be used to advantage in this context since it shifts the peaks in frequency while actually increasing polariton stability. This frequency tuning capability, acquired without a penalty in polariton stability, is obviously very attractive and has device applications.

VI. Conclusions

In this paper, we have calculated the refractive index of a quantum wire waveguide in the vicinity of polariton resonance. The critical values of the exciton decay parameter and associated temperature were also found taking into account the effects of spatial confinement and an external magnetic field. Our results show that confinement of excitons to one dimension and the application of a magnetic field may lead to the extension of temperature and spatial limits of polariton transport. The magnetic field can be used to shift refractive index peaks in frequency - without compromising polariton stability - thus providing a much-desired tuning capability.

Acknowledgement: This work was supported by the US Army Research Office under grant number DAAH04-95-1-0527. The authors are indebted to the Electrochemical Society, Inc. for providing travel support.

REFERENCES

- [1]. E.L. Ivchenko, V.P. Kochereshko, P.S. Kopev, V.A. Kosobukin, I.N. Uraltsev, D.R. Yakovlev, *Solid State Commun.*, **70**, 529 (1989).
- [2]. K. Ogawa, T. Katsuyama, H. Nakamura, *Phys. Rev. Lett.*, **64**, 796 (1990).
- [3]. T. Katsuyama, K. Ogawa, *Semicond. Sci. Technol.*, **5**, 446 (1990).
- [4]. A. Balandin and S. Bandyopadhyay, *Phys. Rev. B*, **52**, 8312 (1995); A. Balandin and S. Bandyopadhyay, *Phys. Rev. B*, **54**, 5712 (1996).
- [5]. V.A. Kosobukin, R.P. Seisyan, S.A. Vaganov, *Semicond. Sci. Technol.*, **8**, 1235 (1993).
- [6]. N. Akhmediev, *Zh. Eksp. Teor. Fiz.*, **79**, 1554 (1980).
- [7]. K. Oimatsu, T. Iida, S. Nishimura, K. Ogawa, T. Katsuyama *Journal of Luminescence*, **48**, 713 (1991).
- [8]. T. Katsuyama, S. Nishimura, K. Ogawa, T. Sato, *Semicond. Sci. Technol.*, **8**, 1226 (1993).
- [9]. see for example E.L. Ivchenko in *Excitons* (North-Holland, Amsterdam, 1992), edited by E.I. Rashba and M.D. Sturge, p.141.
- [10]. S. Chaudhuri, S. Bandyopadhyay, *J. Appl. Phys.*, **71**, 3027 (1992).
- [11]. A. Balandin and S. Bandyopadhyay, *J. Appl. Phys.*, **77**, 5924 (1995).
- [12]. J. Lee, E.S. Koteles, M.O. Vassell, *Phys. Rev. B*, **33**, 5512 (1986).
- [13]. D.A.B. Miller, D.S. Chemla, T.C. Damen, A.C. Gossard, W. Wiegmann, T.H. Wood, C.A. Burrus, *Phys. Rev. Lett.*, **53**, 2173 (1984); *Phys. Rev. B*, **32**, 1043 (1985).

GENERATION OF ULTRASONIC PHONONS IN PARABOLICALLY CONFINED QUANTUM WIRES IN TILTED MAGNETIC FIELDS

W. Xu^{a)}, P. Vasilopoulos^{b)}, and C. Zhang^{a)}

^{a)}*Department of Physics, University of Wollongong
Wollongong, NSW 2522, Australia*

^{b)}*Department of Physics, Concordia University
Montreal, Canada H3G 1M8*

ABSTRACT

A detailed theoretical study of generation of high-frequency acoustic phonons by electrically heated electrons in a GaAs-based quantum wire (QW), subject to a strong magnetic fields B , is presented. The QW is along the y axis, B lies in the xz plane at an angle θ_B with the x axis, and the potential that confines the electrons along the x and z directions is taken parabolic. The main results are: i) the electron energy spectrum, the electron density of states, and the Fermi energy are independent of θ_B ; ii) the frequency of the acoustic-phonons generated is around $\omega_Q \sim 1$ THz and depends weakly on the strength B and on θ_B ; iii) the presence of B results in a markedly enhanced generation of acoustic phonons compared to that at $B = 0$. These results are pertinent to phonon emission experiments and to the application of QWs as high-frequency ultrasonic sources.

I. INTRODUCTION

High-frequency (HF) ultrasound waves have been of great importance in medical and industrial applications [1]. It has been realised [2] that ultrasonic sources of the highest frequencies, if they exist at all, can only be condensed matter materials. Using piezoelectric semiconductors, such as GaAs, HF ultrasonic radiations can be generated at the Gunn oscillation frequency and at its second and third harmonics [3]. Normally, the ultrasonic signals generated from bulk semiconductors are below

gigahertz (10^9 Hz or GHz) frequencies. In some device applications and scientific investigations proposed recently, such as medical imaging, space communications, non-destructive testing, non-accelerator particle physics, etc., generation of ultrasound at higher frequencies is required. Accordingly, the exploration of ultrahigh frequency ultrasonic sources (or so-called hypersonic sources [2]) has recently received a considerable attention.

The application of semiconductor-based quantum wire (QW) systems as electronic and optical devices has been intensively investigated over the past two decades. Recently it has been realised that GaAs-based QWs can also serve as acoustical devices such as HF ultrasonic generators [4] and attenuators [5]. The relevant physical mechanism is the emission and absorption of acoustic-phonons by electrons in the device system. In piezoelectric semiconductors, such as GaAs, electrons can interact strongly with acoustic phonons. Radiation and scattering of ballistic acoustic phonons from electrically heated electrons in low-dimensional semiconductor systems have been detected experimentally [6] and studied theoretically [4,7,8].

In a GaAs-based QW, the conducting electrons are confined within nanometer distances so that the relevant energies, e.g., the Fermi energy, the electron kinetic energy, the electronic subband separation, etc., are on the meV scale. As a consequence, the energy or frequency of the acoustic phonons generated through energy transfer during electronic transitions can reach the meV or terahertz (10^{12} Hz or THz) scale. Therefore, GaAs-based QWs can be used as THz ultrasonic sources. For a QW along the y axis, the electron momentum in the xz plane is absent during an electron-phonon scattering event. This leads to an enhancement of the effective electron-phonon interaction and, consequently, to an enhanced rate of acoustic-phonon generation. Furthermore, the results obtained from experimental and theoretical studies have indicated that in the presence of intersubband scattering channels in a QW, the emission of acoustic phonons is cut off at a much higher frequency than that for intrasubband processes. This favours significantly the generation of HF acoustic phonons.

Phonon generation can be detected experimentally in, e.g., phonon emission experiments (PEEs) [6,9]. In PEEs, the electrons in the device system are heated by a pulsed electric field. Then the electron gases interact strongly with lattice and emit phonons. The intensity of the phonon signal can be measured by using, e.g., superconducting tunnel junction phonon spectrometers [2] or sensitive imaging bolometers [10]. Together with time-of-flight measurements, the generated transverse (TA) and longitudinal (LA) phonon modes can be resolved because of different sound velocities for LA and TA modes.

Due to the distinctive feature of electron-phonon interactions in a dimensionally reduced electronic system, such as QW, phonon emission from a QW has a strong dependence on the angle and frequency. This is important for the detection of the phonon signals generated and the application to practical devices. The frequency

and angular distributions of acoustic-phonon emission from a QW at zero magnetic field $B = 0$ have been studied in Ref. [4]. In some device applications, it is desirable to control the frequency and the angle of the phonon emission. One scheme proposed for achieving tunable ultrasonic generation is to apply a strong B to the device system, e.g., a QW. Then the vector potential couples to the confining potential of the QW and the electronic subband structure is modified by the strength of B and its angle θ_B with respect to a certain axis. Hence, the nature of the electron-phonon interaction in the presence of a field B differs from that at $B = 0$. Thus, the generation of phonons can be controlled by an applied magnetic field.

In this paper, we present a theoretical study of the emission of acoustic phonons from a GaAs-based QW subjected to a strong magnetic field.

II. DEVICE CONFIGURATION AND ELECTRONIC STRUCTURE

We consider a parabolically confined QW along the x and z axes. The confining potential of the one-dimensional electron gas (1DEG) is modeled by

$$U(x, z) = \frac{m_0^* \omega_0^2}{2} (x^2 + z^2), \quad (1)$$

where the QW is along the y direction; m_0^* is the effective electron mass and ω_0 the confining frequency. This device system can be realised by, e.g., using nanoscale lithographic [11] or split-gate techniques [12].

To find out the conditions for the strongest phonon emission, we consider a magnetic field B applied perpendicular to the QW (y direction) but at an angle θ_B with the x axis. That is, we have $\mathbf{B} = B(\cos\theta_B, 0, \sin\theta_B)$ and $\mathbf{A} = B(0, x\sin\theta_B - z\cos\theta_B, 0)$ where \mathbf{A} is the vector potential in the Landau gauge. The eigenstates along y are plane waves $\propto \exp(ik_y y)$. Applying the transformation $X = x\cos\theta_B + z\sin\theta_B$ and $Z = -x\sin\theta_B + z\cos\theta_B - (\omega_c/\omega_B)/l_B^2 k_y$ to the free-electron Hamiltonian, the single-electron Schrödinger equation can be solved analytically. The electron wavefunction and energy spectrum are obtained, respectively, as

$$|k_y, M, N\rangle = (2^{M+N} M! N! \pi l_0 l_B)^{-1/2} e^{ik_y y} e^{-(\xi_0^2 + \xi_B^2)/2} H_M(\xi_0) H_N(\xi_B), \quad (2)$$

and

$$E_{MN}(k_y) = \frac{\hbar^2 k_y^2}{2m_B^*} + \left(M + \frac{1}{2}\right) \hbar \omega_0 + \left(N + \frac{1}{2}\right) \hbar \omega_B. \quad (3)$$

Here, k_y is the electron wavevector along the QW, $M, N = 0, 1, 2, \dots$ are quantum numbers, $l_0 = (\hbar/m_0^* \omega_0)^{1/2}$, $l_B = (\hbar/m_0^* \omega_B)^{1/2}$, $\omega_B = \sqrt{\omega_c^2 + \omega_0^2}$ with $\omega_c = eB/m_0^*$

being the cyclotron frequency, and $m_B^* = m_0^*[1 + (\omega_c/\omega_c)^2]$. Further, $H_N(x)$ are the Hermite polynomials, $\xi_0 = X/l_0$, and $\xi_B = Z/l_B$.

The corresponding density of states (DOS) for electrons at the energy level $\alpha = (M, N)$ is

$$D_\alpha(E) = \frac{g_s}{2\pi} \sqrt{\frac{2m_B^*}{\hbar^2}} \frac{\Theta(E - \varepsilon_\alpha)}{\sqrt{E - \varepsilon_\alpha}}, \quad (4)$$

where $g_s = 2$ accounts for the spin degeneracy, $\Theta(x)$ is the unit-step function, and $\varepsilon_\alpha = (M + 1/2)\hbar\omega_0 + (N + 1/2)\hbar\omega_B$.

From Eqs. (2)-(4) we see that: (1) the electronic subband energy ε_α and the DOS $D_\alpha(E)$ are independent of θ_B ; (2) the energy separation between different quantum states, the effective mass along the QW, and the DOS are enhanced by the field B ; (3) the centre of the harmonic-oscillator wave function is shifted by B ; and (4) the Fermi energy does not depend on θ_B due to the features stated in (1). Nevertheless, for a QW the presence of the tilted B does not change the 1D nature of the electronic system.

III. ELECTRON ENERGY LOSS RATE

The results obtained from experimental [6] and theoretical [13] studies have indicated that the power signals detected in PEEs can be described by the electron energy loss rate (EELR) induced by electron-phonon interactions. In this paper, we develop a simple model to calculate the phonon-induced EELR in a 1DEG. Due to the 1D nature of the electronic subband structure in the QW, we consider a steady-state Boltzmann equation for degenerate statistics ($\hbar = 1$)

$$F \frac{\partial f_\alpha(k_y)}{\partial k_y} = g_s \sum_{\alpha', k'_y} [f_{\alpha'}(k'_y)[1 - f_\alpha(k_y)]W_{\alpha\alpha'}(k_y, k'_y) - f_\alpha(k_y)[1 - f_{\alpha'}(k'_y)]W_{\alpha'\alpha}(k'_y, k_y)] \quad (5)$$

where $F = -eE$ with E the electric field applied along the QW, $f_\alpha(k_y)$ is the distribution function (DF) for an electron in a state $|k_y, \alpha\rangle$, and $W_{\alpha'\alpha}(k'_y, k_y)$ is the transition rate for an electron scattered from a state $|k_y, \alpha\rangle$ to a state $|k'_y, \alpha'\rangle$. We have $W_{\alpha'\alpha}(k'_y, k_y) = W_{\alpha'\alpha}^+(k'_y, k_y) + W_{\alpha'\alpha}^-(k'_y, k_y)$ where the first term stands for absorption and the second for emission of a phonon, respectively. Using Fermi's golden rule we obtain

$$W_{\alpha'\alpha}^\pm(k'_y, k_y) = 2\pi \sum_{q_x, q_z} \left[\frac{N_Q}{N_Q + 1} \right] C_i(\mathbf{Q}) G_{\alpha'\alpha}(\mathbf{Q}) \delta_{k'_y, k_y + q_y} \delta[E_{\alpha'}(k'_y) - E_\alpha(k_y) \mp \omega_Q]. \quad (6a)$$

Here, $\mathbf{Q} = (q_x, q_y, q_z) = Q(\sin\phi\cos\theta, \cos\phi, \sin\phi\sin\theta)$ is the phonon wavevector with ϕ the polar angle and θ the azimuthal angle (we have taken the polar axis along

the QW), ω_Q the phonon frequency, $N_Q = [e^{\omega_Q/k_B T} - 1]^{-1}$ the phonon occupation number, $C_i(\mathbf{Q})$ the electron-phonon coupling constant, and $G_{\alpha'\alpha}(\mathbf{Q}) = |\langle M', N' | e^{i(q_x x + q_z z)} | M, N \rangle|^2$ is the form factor. Using Eq. (2) we obtain

$$G_{\alpha'\alpha}(\mathbf{Q}) = C_{M',M}(a^2/2)C_{N',N}((b^2 + c^2)/2), \quad (6b)$$

where $a = l_0(q_x \cos \theta_B + q_z \sin \theta)$, $b = l_B(q_x \sin \theta_B - q_z \cos \theta_B)$, $c = (\omega_c/\omega_B)l_B q_y$, and $C_{N,N+J}(x) = [N!/(N+J)!]e^{-x}x^J[L_N^J(x)]^2$ with $L_N^J(x)$ being the associated Laguerre polynomials. As can be seen, for finite B the form factor depends on q_x , q_y , and q_z , whereas for $B = 0$ it depends only q_x and q_z , which implies that in the presence of B the phonon emission angle will differ from that at $B = 0$. It should be noted further that the effect of the angle θ_B on the emission and scattering of acoustic phonons in QWs is mainly through varying the form factor.

The EELR can be obtained from the energy-balance equation derived in the standard way from the Boltzmann equation, i.e., through multiplying both sides by $E_{NM}(k_y)$ and summing over N , M , and k_y . As for the electron DF we model it by a drifted in energy DF in the manner

$$f_\alpha(k_y) \simeq f[\varepsilon_\alpha + (k_y - m_0^* v)^2/2m_B^*] \simeq f(\varepsilon_\alpha + \varepsilon_{k_y}) - v k_y \frac{\partial f(\varepsilon_\alpha + \varepsilon_{k_y})}{\partial \varepsilon_{k_y}}, \quad (7)$$

with v the average electron velocity and $\varepsilon_k = k_y^2/2m_B^*$. This assumption is equivalent to the relaxation time approximation in linear response theory. Using electron number conservation and the expression $\sigma = -n_e e v$ where n_e is the electron density, the average EELR is given by

$$P = \sigma E^2 = \frac{m_B^*}{2\pi^3} \sum_{\alpha', \alpha} \int d^3 \mathbf{Q} \left[\frac{-N_Q}{N_Q + 1} \right] C_i(\mathbf{Q}) G_{\alpha'\alpha}(\mathbf{Q}) \frac{\omega_Q}{|q_y|} f(\varepsilon_{\alpha'\alpha}) [1 - f(\varepsilon_{\alpha'\alpha} \pm \omega_Q)], \quad (8)$$

where $\varepsilon_{\alpha'\alpha} = \varepsilon_\alpha + (\varepsilon_\alpha - \varepsilon_{\alpha'} - \varepsilon_{q_y} \pm \omega_Q)^2/4\varepsilon_{q_y}$ with $\varepsilon_{q_y} = q_y^2/2m_B^*$. Eq. (8) shows that the net energy transfer rate is the difference between phonon emission and absorption in the device system.

IV. ACOUSTIC-PHONON EMISSION

The phonon modes in a GaAs-based QW are very similar to those in GaAs. Experimental [6] and theoretical [13] studies of GaAs-based QWs have indicated that, for electron temperatures (or excitations) in the range $10 < T_e < 40$ K (or $1 < P_e < 4$ pW/electron), the electrons interact mainly with deformation-potential acoustic phonons. For GaAs only the longitudinal acoustic phonons are connected with the deformation-potential and the coupling constant is given by

$$C_{DP}(\mathbf{Q}) = \frac{E_D^2 Q}{2\rho v_l}, \quad (9)$$

which is independent of the phonon emission angle. Here, E_D is the deformation-potential constant ($E_D \simeq 11$ eV for GaAs-based low-dimensional systems), ρ is the density of the material ($\rho = 5.37$ kg/m³ for GaAs), and v_l is the longitudinal sound velocity ($v_l = 5.29 \times 10^7$ m/s for GaAs). For long-wavelength acoustic phonons we have $\omega_Q \simeq v_l Q$.

In PEEs it is possible to measure the EELR per electron induced by the emission of phonons. In our model, the EELR per electron can be written as

$$P_T = \frac{P}{n_e} = \int_0^\infty d\omega_Q \int_0^{2\pi} d\theta \int_0^\pi d\phi P(\omega_Q, \theta, \phi), \quad (10a)$$

where the frequency and angular distribution function for phonon emission is given by

$$P(\omega_Q, \theta, \phi) = \sum_{\alpha', \alpha} [(N_Q + 1) I_{\alpha' \alpha}^-(\mathbf{Q}) - N_Q I_{\alpha' \alpha}^+(\mathbf{Q})], \quad (10b)$$

with

$$I_{\alpha' \alpha}^\pm(\mathbf{Q}) = \frac{m_B^* E_D^2 \omega_Q^3}{4\pi^3 \rho n_e v_l^4} G_{\alpha' \alpha}(\mathbf{Q}) f(\varepsilon_{\alpha' \alpha}) [1 - f(\varepsilon_{\alpha' \alpha} \pm \omega_Q)] \tan \phi. \quad (10c)$$

$P(\omega_Q, \theta, \phi)$ measures the intensity of phonon emission from a QW device in the frequency and angle range (ω_Q, θ, ϕ) to $(\omega_Q + d\omega_Q, \theta + d\theta, \phi + d\phi)$, which is measurable in PEEs. Here we use a Fermi-Dirac DF characterized by an effective electron temperature T_e and the Fermi energy E_F , $f(x) = [e^{(x-E_F)/k_B T_e} + 1]^{-1}$.

V. RESULTS AND DISCUSSIONS

In the calculations, in line with PEEs, we use a lattice temperature $T = 2$ K (which depends on the usage of Al bolometers as the phonon detectors) and take $T_e = 20$ K (since at this T_e the strongest deformation-potential acoustic-phonon emission can be generated and detected [6,13]). The other parameters are $n_e = 10^8$ m⁻³ and $\hbar\omega_0 = 4$ meV.

In Figs. 1 and 2 we plot $P(\omega_Q, \theta, \phi)$ as a function of phonon frequency $\hbar\omega_Q$. As can be seen, i) the acoustic phonons are generated at a frequency $\omega_Q \sim 1$ THz; ii) the generation of acoustic phonons is enhanced markedly by the field B (Fig. 1); and iii) the angle θ_B has a strong effect on the intensity of the phonon signal (Fig. 2). These results show that the generation of acoustic phonons, and especially the intensity of the signal, depends strongly on B and θ_B . The frequency of the generated acoustic phonons is about a factor of 2 smaller than that generated from GaAs-based quantum well systems [13].

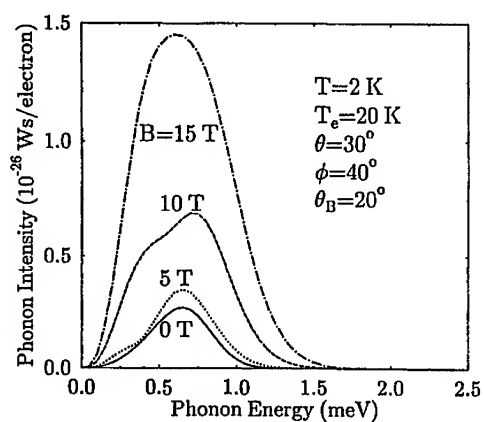


Fig. 1. Spectrum of acoustic-phonon emission, $P(\omega_Q, \theta, \phi)$, as a function of phonon frequency $\hbar\omega_Q$, detected at fixed angles θ and ϕ for different magnetic fields applied at a fixed angle θ_B to the x axis.

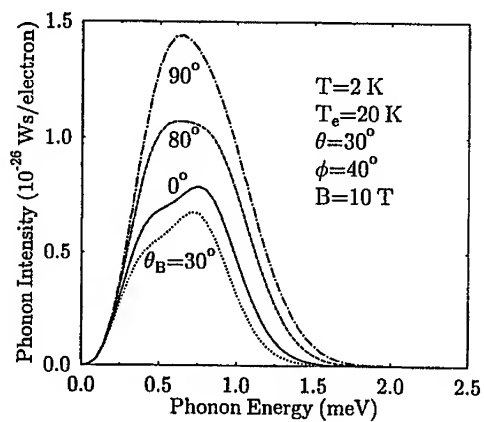


Fig. 2. Acoustic-phonon spectrum detected at fixed angles θ and ϕ for a field $B = 10$ T applied at different angles θ_B .

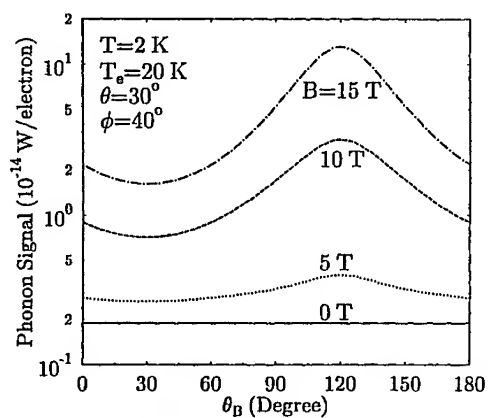


Fig. 3. Intensity of acoustic-phonon signal, defined by $P(\theta, \phi) = \int_0^\infty d\omega_Q P(\omega_Q, \theta, \phi)$ detected at angles θ and ϕ , as a function of θ_B for different strengths of B .

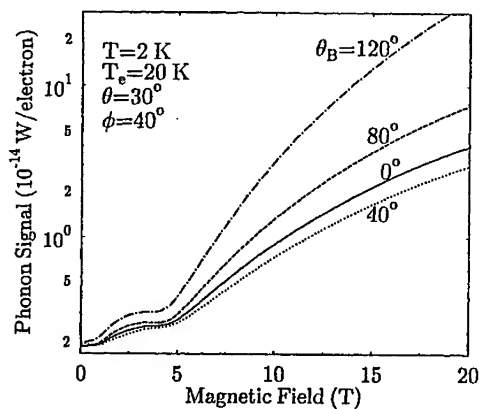


Fig. 4. Intensity of phonon signal, detected at angles θ and ϕ , as a function of the field B applied at different angles θ_B .

At present, due to technical difficulties, the PEEs can only measure the total

intensity of the phonon signal at angles θ and ϕ , i.e., the quantity $P(\theta, \phi) = \int_0^\infty d\omega_Q P(\omega_Q, \theta, \phi)$. In Figs. 3 and 4, we show the influence of B and θ_B on the intensity of the generated signal. We note that: i) a stronger dependence of the phonon emission on θ_B is obtained for stronger B (Fig. 3), as the emission increases with increasing B (see Fig. 4); ii) the strongest acoustic-phonon emission occurs at about $\theta_B = 120^\circ$. It should be pointed out that the use of Eq. (9) implies a definition of the (001) direction of a GaAs crystal as the z axis in our configuration; and iii) the increase of the phonon emission with B (Fig. 4) reflects the enhancement of the effective electron-phonon interaction through that of the effective mass and DOS at strong B . The corresponding electronic transitions for this degenerate statistics occur near the Fermi level.

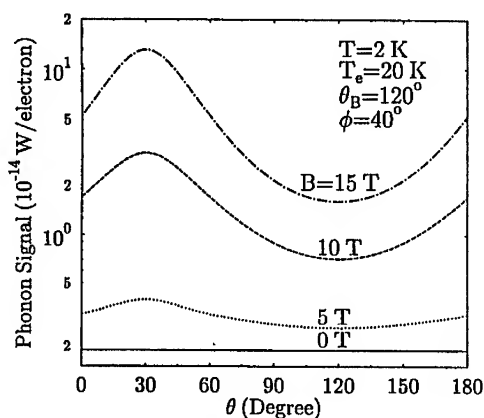


Fig. 5. Intensity of the acoustic-phonon signal, $P(\theta, \phi)$, as a function of the angle θ for different B fields applied at a fixed angle θ_B .

In PEEs it is very important to know the angle at which the strongest signal can be detected and that at which the phonon detectors should be placed. The phonon signal, as a function of the emission angles θ and ϕ , is shown in Figs. 5 and 6, respectively. The phonon emission angle is determined mainly by: i) the momentum and energy conservation during electron-phonon scattering events, ii) the interaction matrix element $C_i(\mathbf{Q})$, and iii) the form factor $G_{\alpha'\alpha}(\mathbf{Q})$. The results shown in Figs. 5 and 6 indicate that the phonon emission angle in a strong B field differs markedly from that at $B = 0$. For example (see Fig. 5), at $B = 0$ phonon emission is independent of θ , whereas at a strong B phonon emission is generated around the angle regime $\theta \sim 30^\circ$. Therefore, by varying B and/or θ_B one may control the phonon emission angles. In the present study, we have chosen

the polar axis to be along the QW and by doing so we can see clearly the difference of phonon emission at $B = 0$ and at $B \neq 0$. Moreover, because the form factor for electron-phonon interaction depends always on q_x and q_z (see Eq. (6b)), a strong dependence of phonon emission on angle ϕ can be observed over all magnetic fields (see Fig. 6).

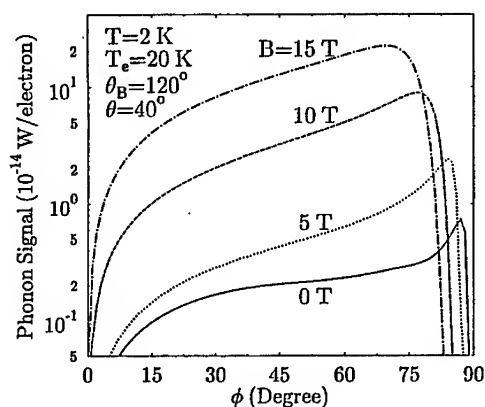


Fig. 6. Intensity of the phonon signal as a function of the angle ϕ for different B fields applied at a fixed angle θ_B .

VI. SUMMARY

We have studied the electronic subband structure in a parabolically confined quantum wire (QW), along the y direction, subjected to tilted magnetic fields in the (z, x) plane. The energy spectrum and the wave functions have been obtained analytically. We have then developed a simple model to calculate the electron-energy-loss rate induced by electron-phonon interactions in such a system. In conjunction with phonon emission experiments, we have obtained the intensity of the acoustic-phonon emission from a QW in the frequency and angle range (ω_Q, θ, ϕ) to $(\omega_Q + d\omega_Q, \theta + d\theta, \phi + d\phi)$.

In detail we have evaluated the following: (1) the frequency and angular distribution of the acoustic-phonon emission by electrically heated electrons in the QW; and (2) the dependence of the emitted acoustic-phonon signal on the strength and angle of the applied magnetic fields. The results show that one can use a QW as an ultrasonic source and control efficiently the emitted acoustic-phonon signals by changing the strength and/or the angle of the applied magnetic fields. We ex-

pect that the results will be useful in the development of high-frequency ultrasonic sources.

ACKNOWLEDGEMENT

This work was supported by the Australian Research Council (WX, CZ) and by NSERC Grant No. OGP0121756 (PV).

References

- [1] *Special Issue: Ultrasonic Electronics*, Jpn. J. Phys. **33**, Pt. 1, No. 5B (1994).
- [2] H. Kutttruff, *Ultrasonics: Fundamentals and Applications* (Elsevier, London, 1991).
- [3] M. Shur, *GaAs Devices and Circuits* (Plenum Press, New York, 1987).
- [4] W. Xu, Appl. Phys. Lett. **68**, 1353 (1996); W. Xu, M.P. Das, D.J. Fisher, S.M. Stewart, and C. Zhang, Superlattices and Microstructures **18**, 209 (1995).
- [5] C. Rodrigues and O.A.C. Nunes, J. Appl. Phys. **71**, 4635 (1992); **73**, 7163 (1993).
- [6] L.J. Challis, A.J. Kent, and V.W. Rampton, Semicond. Sci. Technol. **5**, 1179 (1990); for a recent work, see, e.g., P. Hawker, A.J. Kent, N. Hauser, and C. Jagadish, *ibid.* **10**, 601 (1995), and references therein.
- [7] R. Mickevičius and V. Mitin, Phys. Rev. **B 51**, 1609 (1995); R. Mickevičius, V. Mitin, V. Kochelap, M.A. Strosio, and G.J. Iafrate, J. Appl. Phys. **77**, 5095 (1995), and references therein.
- [8] F.T. Vasko, G. Balev, and P. Vasilopoulos, Phys. Rev. **B 47**, 16433 (1993).
- [9] V. Narayanamurti, Science **213**, 717 (1981); J.C. Hensel, R.C. Dynes, and D.C. Tsui, Phys. Rev. **B 28**, 1124 (1983).
- [10] D.C. Hurley, G.A. Hard, P. Hawker, and A.J. Kent, J. Phys. **22**, 824 (1989).
- [11] R. Cheung, S. Thoms, M. Watt, M.A. Foad, T.C.M. Sotomayor, C.D.W. Wilkinson, U.J. Cox, R.A. Cowley, C. Dunscombe, and R.H. Williams, Semicond. Sci. Technol. **7**, 1189 (1992).
- [12] See, e.g., M.A. Reed, Sci. American, p.98, Jan. 1993.
- [13] W. Xu, Phys. Rev. **B 51**, 13294 (1995); **B 54**, 2775 (1996); W. Xu and C. Zhang, Appl. Phys. Lett. **68**, 823 (1996).

Optical Properties of Nanocrystals

**OPTICAL STUDIES OF QUANTUM EFFECTS IN SEMICONDUCTING
AND METALLIC NANOCRYSTALS**

A. Stella, V. Bellani and P. Tognini

Istituto Nazionale per la Fisica della Materia - Dipartimento di Fisica "A. Volta",

Università di Pavia, Via Bassi 6, 27100 Pavia, Italy

P. Cheyssac and R. Kofman

Laboratoire de Physique de la Matière Condensée. Université de Nice-Sophia

Antipolis, Parc Valrose, 06108 Nice Cedex 2, France

ABSTRACT

Nanocrystals, which are systems characterized by crystal order and are confined in the three space dimensions, are assuming an increasingly major role. The optical investigation of the properties of metallic and semiconducting nanocrystals embedded in dielectric matrices presents several aspects of relevant importance, as it will be shown with a few examples and in particular: i) Concerning Ge, the study of the different behavior of the E_1 and E_2 structures in the dielectric constant under quantum confinement, in relation to their different nature inside the Brillouin Zone; ii) In the case of metals, the attention is focused on solid and liquid Ga nanoparticles having sizes of the order of a few nm. The plasmon

lineshapes in the transmission and reflection spectra are investigated with evidence of their blue shift due to size decrease

INTRODUCTION

The growing interest for the nanoscale systems is strongly motivated not only by the peculiarity of their basic properties, which show remarkable deviations from bulk behavior, but also by their potential applications mainly in the field of electronic devices [1]. Among such systems, in recent years the interest in the study and application of the properties of nanocrystals has been growing very rapidly [2]. These systems, which are characterized both by crystal order and sizes of the order of few nm, show a behavior which: i) is somewhat intermediate between that of single atoms and bulk solids; ii) can be tailored as a function of size (i.e. number of constituent atoms). [3]

Some specific applications particularly related to light emitting diodes [4], lasers fabrication [5], non linear optical response [6], appear to be very promising.

The investigation of the systems and structures in the nanometer domain presents rather challenging aspects in term of experimental characterization [7] and theoretical calculations [8] for prediction and/or interpretation of their basic properties. To summarize in one sentence it can be stated that space confinement plays a key-role in modeling and tuning the physical properties of the nanoparticles in general, and nanocrystals in particular. This statement can be endorsed with a few considerations:

-
- Limitation of the validity of effective mass approximation below a given size [9] and of the ab-initio molecular dynamics approach above a certain number of constituent atoms ($\sim 10^2$) with the related size.
 - Strong redistribution of the electronic density of states and blue shift of the main spectral structures when the size is smaller than the excitonic radius [6].
 - Concerning the phonon behavior in confined systems, the breaking of the $\vec{k} = 0$ selection rule due to the uncertainty principle $\Delta x \cdot \Delta k = 1$ (where Δx and Δk are the uncertainty on position and wave vector, respectively) and possibility of exploring the ω vs k dispersion curve also away from $\vec{k} = 0$ [10].
 - Strong modification of the thermodynamic properties when N_s/N (where N_s is the number of surface atoms and N the overall number of atoms) becomes relevant [11].
 - Strong effects of surface scattering in the ultrafast electron dynamics when the size is much smaller than the mean free path and consequence on the thermalization times of the electron gas [12].
 - Concomitant modification of surface plasmon peak energy position due to space confinement [13].

EXPERIMENTAL DETAILS

We investigated Ga and Ge nanoparticles embedded in amorphous matrix (Al_2O_3 and SiO_x) grown by an evaporation-condensation self-organization technique in a ultra-high-vacuum UHV chamber. The samples were prepared on carefully cleaned sapphire substrates. Ga or Ge were condensed over a previously evaporated thin layer (some tens of Å thick) with a consequent nucleation and growth of nano-particles in the liquid state; in fact during the nucleation process the temperature of the substrate is maintained sufficiently high. The particles become solid after a slow temperature decrease, and then another layer of the dielectric material is deposited to cover and protect them. In this way one obtains an amorphous matrix of Al_2O_3 (or SiO_x) in which nanocrystals of the selected material are embedded. Moreover this deposition process can be repeated several times, so that multilayers of the matrix material with nano-particles of the desired thickness can be obtained. More details on the growth can be found in Ref. [14]; the main advantages of this growth technique are the regular shape (generally truncated spheres) and the possibility of varying size of the nanocrystals which can be previously selected in a wide range. [14]

The size dispersion of the nanoparticles is $\leq 20\%$. The size distribution is typically bimodal with a 95% peaking around the average radius and a polydispersed tail toward zero radius. For Ge the good crystalline nature of the

nanoparticles was clearly evidenced by transmission electron microscopy both in the dark field and high resolution configuration. No relevant presence of impurities and defects was detected [15]. Evidence of the structure characteristics and crystalline order of the Ga nanostructures has been given elsewhere [12].

The various samples had an average size of the nanocrystal between 9 and 60 nm for the Ga and between 2 and 13 nm for the Ge. The characteristics of all the sample studied in this work are reported in Tables I, II and III.

Optical transmission at near-normal incidence and reflectance measurements between 77 and 300 K were performed using a Varian Cary 5 spectro-photometer, in the 0.6-6 eV range with a measurement accuracy better than 0.01 eV.

GERMANIUM

In the case of semiconductor nanocrystals, relevant and well identified quantum effects show up due to space confinement in the three dimensions, below a given size which depends on the properties of the material: for this reason the systems are currently called quantum dots. A typical signature of quantum behavior due to space confinement is the blue shift either of the gap or of typical structures of the density of states above the band gap which are driven by the size reduction of the dots. Such effects in Ge quantum dots have been studied, through the shift of the absorption and reflection peaks related to the main interband structures E_1 and E_2 .

In previous works [15] we discussed the presence of quantum confinement effects on nanoparticles with average diameter from about 130 Å down to about 20 Å (table I and Fig. 1, Fig. 2). Here we intend to concentrate the attention on the behavior of the nanoparticles in the size domain below 30 Å. The difference between the transmission spectrum of a reference sample without nanoparticles and that of the samples containing Ge nanoparticles (table II) is reported in Fig. 3 for a new series of samples. As one can note, the main absorption structures fall roughly at the same energy in both Fig. 1 and Fig. 3; this proves that the growth procedure is not substantially influenced by spurious parameters and the response is strictly related to the nature of the material. Note that the energy position of E_2 at room temperature and for diameters larger than 120 Å is nearly coincident with that of the bulk [15].

In this work the blue shift of the E_2 absorption peak is investigated in detail and it is found to increase by reducing the size down to diameters of ≈ 24 Å; below this value there is a progressive reduction of the shift (Fig. 2 and Fig. 4), which is evident in the two series here presented.

This effect deserves a more extended analysis which requires a careful coupling of absorption with electron microscopy and Raman spectroscopy data. On preliminary grounds, one can speak in terms of attenuation of the quantum confinement effects which, in principle, are amenable to details of the process of

aggregation and coalescence of the liquid state atoms in nanoparticles in the early stages of growth.

GALLIUM

We investigated the effect of the reduced dimensionality, i.e. of the limitation of the electronic mean free path, on the Ga surface plasma peak, both in the metallic solid and liquid state. We recall that the nanoparticles are here embedded in an amorphous matrix, and their structural characteristics are summarized in table III.

It is well known that in the case of systems confined in the 3 spatial dimensions the plasma frequency ω_p is given by the expression [16]

$$\omega_p = \frac{\omega_B}{\sqrt{(1 + 2\varepsilon_m)}} \quad (1)$$

where ω_B is the bulk plasma frequency and ε_m the dielectric constant of the embedding medium at the plasma frequency.

The limitation of the electron mean free path, with a good approximation, changes the imaginary part of the dielectric constant of the nanoparticle in the following way [16]

$$\varepsilon_2(\omega, r) = \varepsilon_2(bulk) + \frac{3}{4} \frac{\omega_p^2}{\omega^3} \frac{v_F}{r} \quad (2)$$

where v_F is the Fermi velocity of the electrons and r the radius of the nanoparticles. The effect due to the presence of the additional term in the above expression is a decrease of the peak height and an increase of its width when the size is reduced.

The overall consequence of size reduction (taking into account also the effect on the real part of ε) is a shift of the maximum toward higher energies and a broadening of the band.

Under a given size value, which depends on the material, and in our case is about 10 nm, the behavior shows a deviation from predictions of equations (1) and (2), since the bulk dielectric function undergoes important modifications.

In Fig. 5 the difference between the transmission of a reference sample without Ga and that of the samples with nanoparticles is reported. The surface plasma peak is evident, in agreement with the prediction of Eq. 1 in the case of the biggest nanoparticles [12]. As one can see in Fig. 5 and in Fig. 6, there is a blue shift of the peak position by reducing the nanoparticle size.

In Fig. 7 the reflectivity spectra (ratio between the reflectivity of the samples containing nanoparticles and the reference one) are reported.

It is worthwhile noting that nanoparticles both in the solid and in the liquid state yield very similar curves. This can be explained on the following grounds: i) the electron mean free path is comparable or larger than the dimensions of the nanoparticles, so that bulk plasmons (strictly related to the crystal order in the solid state) play a minor role in the scattering mechanism which are responsible for the width of the plasma lineshape; ii) a major role in such processes can be attributed instead to the presence of the interface between particle and matrix. The latter statement has been confirmed by measurements on ultrafast electron dynamics [12], which show that the electron thermalisation process is reduced when the size is smaller than the mean free path.

In previous works [11] it has been noted that the process of melting and solidification is characterized by an hysteresis cycle in reflectivity at a given wavelength (inset Fig. 8). In Fig. 8 we give evidence of the solid-to-liquid transition with transmission data taken at different temperatures around the nanocrystals melting point in the energy range 2 - 4 eV.

CONCLUSIONS

The main conclusions can be summarized as follows:

- We report on specific novel aspects of the growth technique based on self organisation, valid both for metals and semiconductors.

- Evidence is given of space confinement as a driving mechanism for important new features both in Ge and Ga nanocrystals.
- Examples which show new and basic achievements in the optical properties of semiconducting (Ge) and metallic (Ga) systems in the nanoscale domain are here illustrated in detail.

REFERENCES

- [1] A.P. Alivisatos, *Science* 271, 933 (1996).
- [2] L. Banyai and S. Koch, *Semiconductor Quantum Dots*, World Scientific, Singapore (1993).
- [3] A. Stella, P. Cheyssac, and R. Kofman in *Science and Technology of Thin Films* (World Scientific, Singapore, 1995).
- [4] V.L. Colvin, M.C. Schlamp, A.P. Alivisatos, *Nature* 370, 354 (1994).
- [5] R.F. Service, *Science* 271, 920 (1996).
- [6] L. Brus, *Appl. Phys. A* 465 (1991).
- [7] E. Palange, G. Cappellini, L.D. Gaspare and F. Evangelisti, *Appl. Phys. Lett.* 68, 2982 (1996).
- [8] L.-W. Wang and A. Zunger, *Phys. Rev. Lett.* 73, 1039 (1994).
- [9] D.M. Wood, A. Zunger, *Phys. Rev. B* 53, 7949 (1996)

-
- [10] C. E. Bottani, C. Mantini, P. Milani, M. Manfredini, A. Stella, P. Tognini, P. Cheyssac and R. Kofman, *Appl. Phys. Lett* 69, 2409 (1996).
- [11] P. Cheyssac, R. Kofman, G. Mattei, P. G. Merli, A. Migliori and A. Stella, *Superlatt. Microstruct.* 17, 47 (1995).
- [12] M. Nisoli, S. Stagira, S. De Silvestri, A. Stella, P. Tognini, P. Cheyssac, R. Kofman, *Phys. Rev. Lett.* (in press, 1997).
- [13] H. Hovel, S. Fritz, A. Hilger, U. Kreibig, M. Vollmer, *Phys. Rev. B* 48, 18178 (1993).
- [14] E. Sondergard, R. Kofman, P. Cheyssac, A. Stella, *Surf. Sci.* 364, 467 (1996).
- [15] P. Tognini, L.C. Andreani, M. Geddo, A. Stella, P. Cheyssac, R. Kofman, A. Migliori, *Phys. Rev. B* 53, 6992 (1996).
- [16] C.F. Bohren and D.R. Huffman, *Absorption and Scattering of Light by Small Particles* (Wiley, New York, 1982)

TABLES

Table 1: Series 1 (substrate sapphire, matrix amorphous Al_2O_3)

Name	Equivalent thickness (\AA) of each layer deposited	Number of layers	Nanoparticles average radius (\AA)
Ge8	8	5	12
Ge12	12	5	13
Ge15	15	5	15
Ge35	35	5	48
Ge50	50	5	65

Table 2: Series 2 (substrate sapphire, matrix amorphous Al_2O_3) In this table only the equivalent layer is reported since nanoparticle nucleation is not expected to be complete.

Name	Equivalent thickness (Å) of each layer deposited	Number of layers
Ge6.6	6.6	12
Ge8	8	10
Ge10	10	8
Ge13.3	13.3	6
Ge16	16	5

Table 3: Series 3 (substrate sapphire, matrix amorphous SiO_x , $x \sim 1$)

Name	Equivalent thickness (nm)	Average radius (nm)
Ga2	2	5
Ga3	3	7
Ga4	4	9
Ga5	5	13
Ga10	10	21.5
Ga15	15	30.5

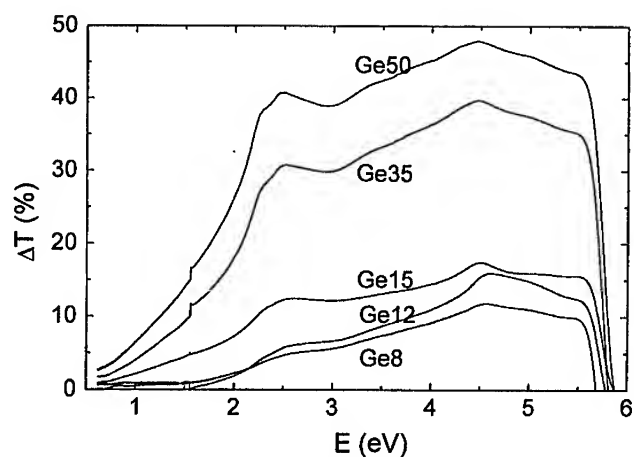


Fig. 1: Difference between the transmission of a reference sample without Ge and that of the samples containing Ge nanoparticles for the samples of series 1. Ref. [15].

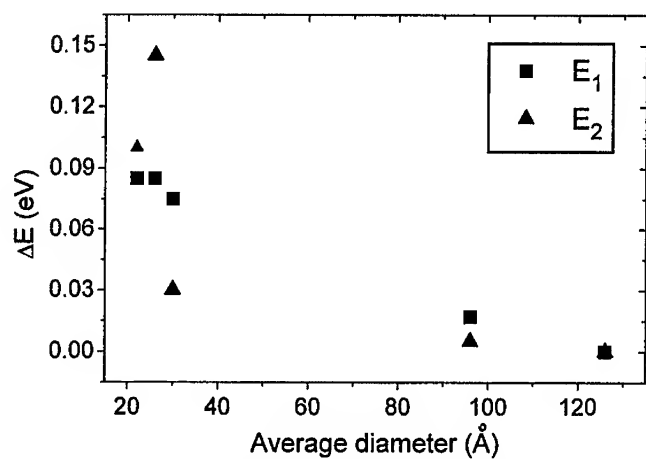


Fig. 2: Blue shift of the E1 and E2 absorption peaks reported in Fig. 1 with respect to the bulk value.

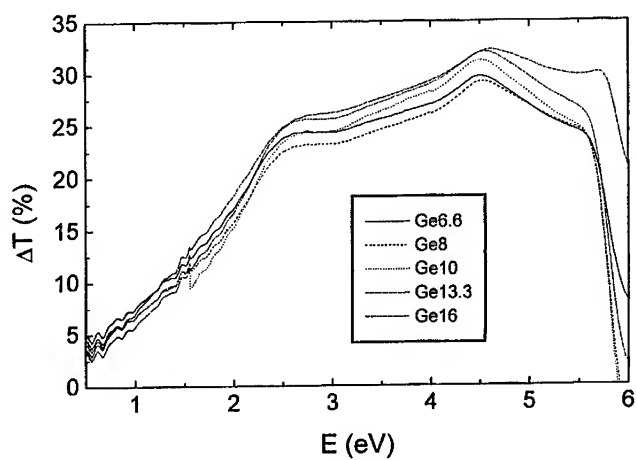


Fig. 3: Difference between the transmission of a reference sample without Ge and that of the samples containing Ge nanoparticles for the series 2.

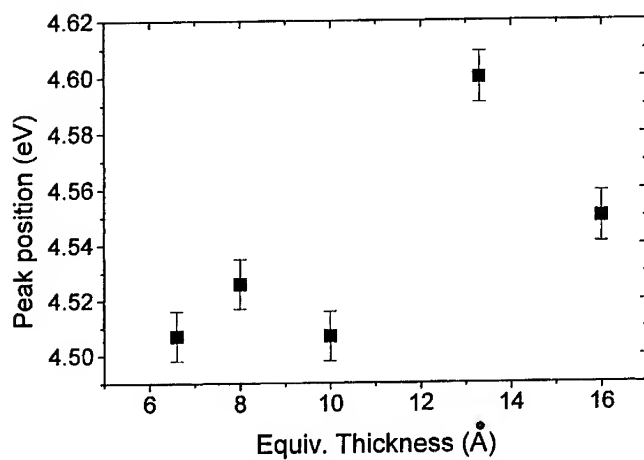


Fig. 4: Shift of the E2 absorption peak reported in Fig. 3 versus the equivalent thickness of each layer deposited.

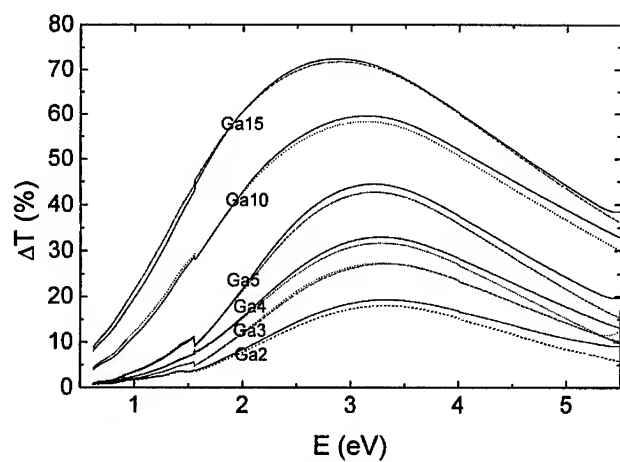


Fig. 5: Difference between the transmission of a reference sample without Ga and that of the samples containing nanoparticles for the series 3. Solid curves: RT measurements; dashed curves: LNT measurements.

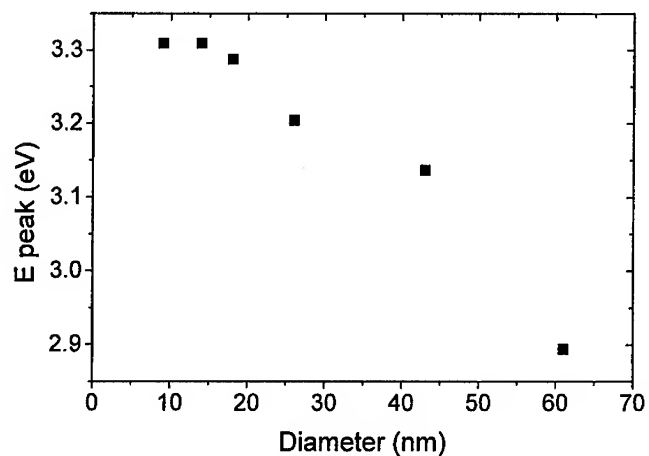


Fig. 6: Shift of the Ga nanocrystals plasma peak as a function of the average size of the nanoparticles.

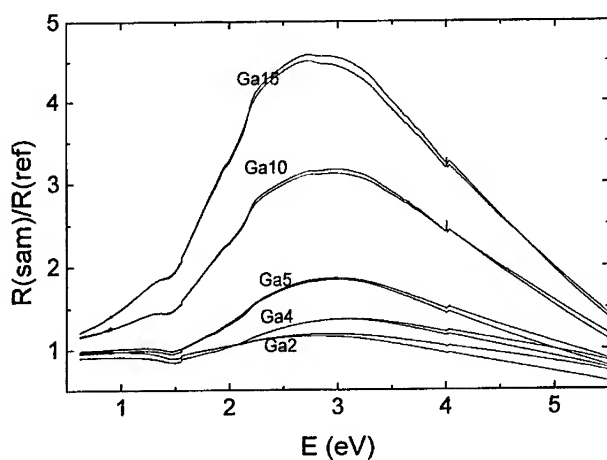


Fig. 7: Ratio between the reflectivity of the samples containing Ga nanoparticles and that of a reference sample without Ga (series 3).

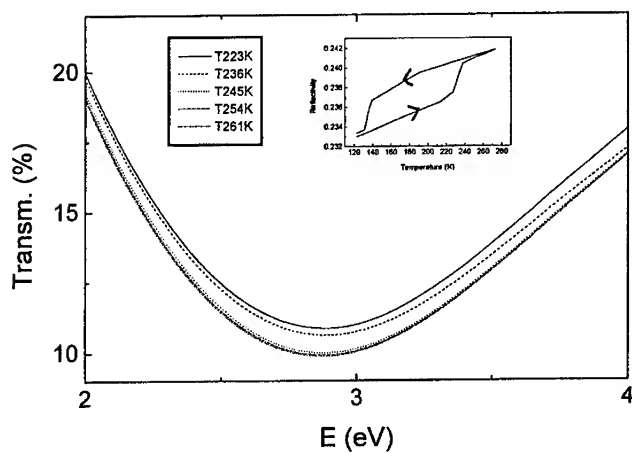


Fig. 8: Liquid and solid state Ga transmission spectra of the sample Ga15. In the inset the hysteresis cycle at a wavelength of 600 nm is shown. One can notice a sizeable difference in the optical response of the nanoparticles in the two states, in the temperature range corresponding to the solid-to-liquid transition.

**BLUE LUMINESCENCE FROM Ge AND GeO₂ NANOCRYSTALLITES
PREPARED BY DC MAGNETRON SPUTTERING**

M. Zacharias^{1,2}, M. Schmidt², and P. M. Fauchet¹

¹Department of Electrical Engineering, University of Rochester, Rochester NY 14627,
USA

²Institute of Experimental Physics, Otto-von-Guericke University, Magdeburg,
PF 4120, 39016 Magdeburg, Germany

The results of a comprehensive investigation of films containing Ge or GeO₂ nanocrystals prepared by dc magnetron sputtering are presented. The as-prepared films show a precipitation of amorphous Ge or GeO₂ nanoclusters and exhibited negligible luminescence. After annealing, X-ray, Raman and TEM investigations show that nanocrystals of Ge and GeO₂ have been formed in the oxide matrix with a size closed to the cluster size. The nanocrystals are randomly distributed in the amorphous matrix or show a self-organized layer structure as demonstrated by TEM investigations. Under UV excitation, both types of films luminesce around 3.1 eV, with identical lineshapes and subnanosecond PL dynamics. The strongest PL intensity was found for the films containing GeO₂ crystals and for the largest nanocrystals. These results are the first clear indication that although the blue luminescence is correlated with the formation of Ge (or GeO₂) nanocrystals, it is not produced by the radiative recombination of excitons confined in the nanocrystals. Possible mechanisms for the luminescence include defects at the nanocrystal/matrix interface or in the matrix itself.

Introduction

Group IV nanocrystals embedded in a SiO₂ matrix have been studied extensively because of their potential for integrated optoelectronic devices on silicon substrates. Luminescent Ge nanocrystals (nc-Ge) have been fabricated by several groups using rf co-sputtering, ion implantation, dc sputtering in a reactive oxygen environment or oxidation of SiGe alloys, and subsequent thermal annealing to induce the crystallization (1-5). The usual photoluminescence (PL) spectrum is a broad band centered at 2.1-2.4 eV (2,6). However, there is no clear evidence for a size dependent blue shift of the PL peak, as expected from carrier quantum confinement in quantum dots (7).

Nanocrystals (nc) exhibit spatial confinement in three dimension. Our understanding of these crystallites, or clusters, is more than primitive. Some rather elementary calculations have been published, and the reported optical spectra are the contribution of different sizes and shapes. Most of these calculations are limited to direct gap semiconductors and well saturated interfaces.

In bulk semiconductors of indirect gap, the electron-hole recombination is coupled with phonon emission or absorption because of the wave-vector difference between the

bottom of the conduction-band and the top of the valence-band. One of the possibilities to convert an indirect gap semiconductor into a direct gap semiconductor might be to form low-dimensional structures like superlattices or isolated quantum dots (7). In the case of the superlattices the size of the Brillouin zone is reduced and the bottom of the conduction-band is expected to be folded onto the Γ point, resulting in a direct-gap behavior. For isolated quantum dots the periodicity due to a bulk semiconductor or a superlattice structure is absent and the electronic states are completely discrete as in molecules or atoms. The optical matrix element between such discrete states must be calculated to identify if the optical transition is optically allowed or not. However, in most cases and for not too small nanocrystals, the model of the folding onto the Γ point is approximately valid. On the other hand, there is a relative large surface-to-volume ratio in small quantum dots which affects the luminescence. Luminescence can involve highly localized states. In the case of nanocrystals, these states may originate in the crystal surface, which contains a large fraction of the total number of the atoms in the nanocrystals (8). Chemical modification of the nanocrystal surface can result in a fast trapping of the carrier to the surface, and thus surface dominated luminescence is expected (9). Chemical modifications of the nanocrystal surfaces is not reported to change the absorption, it probes the interior states of the nanocrystals. The absorption features follow simple confinement rules and the band structure.

In the following discussion some of the models describing quantum-size effects in semiconductor microcrystals and their limits are summarized (9-13). The effective-mass approximation (EMA) is derived from the parabolic expansion of the bulk band structure. It is valid for large systems (≥ 40 Å) and can be extended to incorporate band mixing (14-16). The kinetic operator is replaced by an effective-mass operator and the microscopic quasi-periodic potential by a constant potential. Instead of using parabolic bands, the truncated crystal method uses the actual dispersion relation of the bulk band structure (17,18). The quantum dot wave functions are approximated by the sum of bulk Bloch wave functions of a single band at different wavevectors. The model is valid only for quantum dots of simple geometries and ignores band mixing. On the other hand, direct molecular calculations avoid the approximation of the above methods (19). The used microscopic Hamiltonian consists of the full kinetic energy and the quasi periodic Hamiltonian, but the Hamiltonian or its basis representation are usually simplified. Versions of this model are the widely used tight binding model (20), the linear combination of the atomic orbitals (21) or the empirical pseudopotential method (18). However, only Takagahara et.al. (7) represents calculation applied to Ge quantum dots based on the effective-mass theory which will be used for discussion of our experimental results.

We report here for the first time the investigation of Ge and GeO₂ nanocrystals showing a blue-PL band centered at 3.1 eV and stronger in intensity than the orange-green band around 2.3 eV. The structure of the Ge and of GeO₂ nanocrystals embedded in an oxide matrix was studied by X-ray diffraction, Raman investigation and TEM. We will

discuss possible mechanisms for the blue room temperature luminescence, including defects.

Experimental

The samples were deposited with dc magnetron sputtering under various powers (50-150 W) to change the average crystal radius R from 25 to 1.5 nm (8,23). Subsequent thermal annealing at 800°C for 30 min. in a quartz tube under Ar atmosphere induced the crystallization of the Ge or GeO₂ precipitation. Raman spectra were measured in backscattering geometry. An Ar⁺ ion laser was used as a light source. The laser power below 20mW was small enough to avoid sample heating. The spectra were analyzed using the model of the Raman line shape of semiconductor nanocrystals (24). The as-prepared and annealed films were investigated with wide angle X-ray scattering and the results were analyzed with the Scherrer multiple peak method.

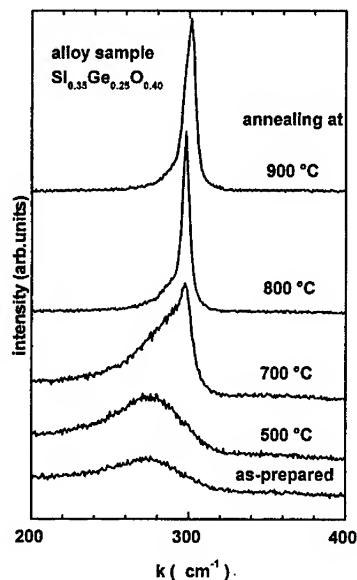


Fig. 1: Raman spectra of the as-prepared and annealed film demonstrating the crystallization process (22). The as-prepared film contains random distributed Ge nanocluster in the SiO_x matrix. The crystallization of the Ge is observed by the narrowing and disappearing of the broad amorphous peak around 270 cm⁻¹ and the onset of the sharp phonon peak around 300 cm⁻¹. While increasing the annealing temperature, the Raman peak shifted towards higher frequencies with a peak position direct correlated to the average size of the nanocrystals. We calculated a size of 4.0-5.0 nm (700°C), 5.5-7.0 nm (800°C) and above 15 nm (900°C). The doubling in size can be interpreted as a recrystallization of agglomerates.

Infrared transmission (IR) measurements were performed from 300 to 4000 cm⁻¹ with a conventional IR double-beam spectrometer using the thin film deposited onto polished silicon substrate. The absorption-free transmission baseline was calculated by

means of an optical model (25) as a function of the film thickness, the refractive index and the wavenumber. In this way, the absorption spectra were determined without errors due to interference fringes. The incorporation of the radicals and ions resulting from the decomposition of the water in the sputtering plasma leads to a variety of oxygen-related infrared absorption bands.

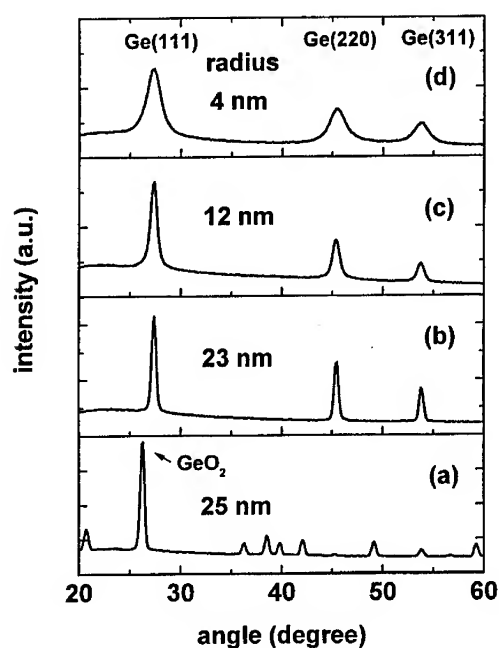


Fig. 2: X-ray diffraction under grazing incidence gives clear evidence for the crystal structure of the films. The films annealed at 800°C contain large hexagonal GeO_2 nanocrystals (a) or cubic Ge nanocrystals (b-d) with sizes down to 4nm. The size of the nanocrystals is defined by the sputtering conditions, i.e. the sputtering power, the partial pressure of the reactive gases and the number of Ge pieces (8).

For PL measurements, thin films were deposited onto roughened silicon substrates to avoid interference effects and total internally reflection at the surface. The steady state PL at room temperature was excited with a HeCd laser using the 325 and 441.6 nm lines with a laser intensity below 100 mW/cm². The PL was recorded using a Spex M500 grating monochromator and a signal detection with a nitrogen cooled CCD detector head with UV coating. All PL spectra were corrected for the spectral response of the detecting system. The time-resolved PL was excited by the frequency-doubled output of a cavity-dumped dye laser pumped by the second-harmonic of a cw mode-locked Nd:YLF laser. The 6 ps-long pulses were tunable around 350 nm. The overall temporal resolution of the

photon counting system was better than 100 ps. All measurements were performed at room temperature.

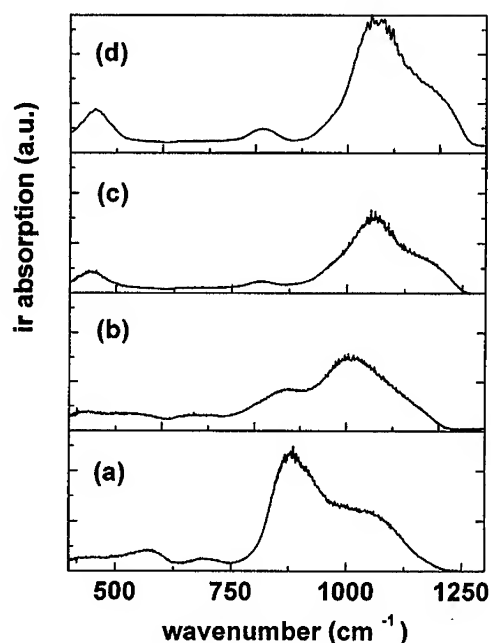


Fig. 3: IR absorption spectra of different as-prepared films prepared with increasing sputtering power, (a) 50W, (b) 75W, (c) 125W, (d) 150W. Film (a) is dominated by the Ge-O stretching mode at 860 cm^{-1} and contains large GeO_2 clusters. When the sputtering power increases the films contain more Si preferentially bonded in SiO_2 configurations (band near 1050 cm^{-1}). Then pure Ge nanocluster are precipitated in the SiO_2 matrix.

Results and discussion

Fig. 1 demonstrates the Raman spectra of the as-prepared amorphous and nanocrystalline state of a sample with an average nanocrystal size of 5.5-7 nm after annealing at 800°C (22). The broad Raman peak around 270 cm^{-1} is the signature of the amorphous Ge-Ge mode. The Ge nanoclusters remain amorphous up to 500-600°C. While increasing the annealing temperature to 700°C, a sharp Raman peak with an asymmetric shoulder at the low frequency side is found shifting towards 300 cm^{-1} . In bulk unstrained Ge crystals the Ge-Ge peak is symmetric and centered around 300.5 cm^{-1} . Analyzing peak position and full-width at half maximum of the nc-Raman peak allows an calculation of the average size of the nanocrystals by using the model of the Raman line shape of semiconductor nanocrystals (24).

X-ray diffraction spectra of selected annealed samples are presented in Fig. 2. These films are prepared with increasing the sputtering power from 50 to 150 W which changes size and chemistry of the as-prepared nanoclusters in the SiO_2 matrix (8). The Ge crystallization is indicated by the splitting of the Ge (220) and (311) peaks. A increase in sputtering power results in a decrease of the average Ge nanocrystal radius from 25 nm down to ~ 1.5 nm. The partial water pressure is the second parameter which has an important influence on the size and the composition of the nanocrystals. The combination of a high partial water pressure and a very low sputtering power can produce large GeO_2 nanoclusters embedded in the as-prepared films which, after annealing, form hexagonal GeO_2 crystals (Fig.2, sample (a)). Further details of the X-ray analysis will be published elsewhere (26).

The IR spectra shown in Fig. 3 demonstrate the strong influence of the sputtering conditions on the atomic bonding in the films. There is a clear trend for an decrease of the 860 cm^{-1} vibration assigned to the Ge-O stretch mode (27) and an increase of the 1050 cm^{-1} vibration assigned to the Si-O asymmetric stretching band (28) with increase of the sputtering power. This can be explained as follows: At low sputtering power the SiO_2 coverage of the Si target can not be removed with the low energy particle bombardment resulting in an preferential sputtering of the Ge pieces. The resulting film contains only a limited amount of Si. Oxygen bonded preferential to silicon forming the amorphous SiO_2 matrix. The enthalpy of GeO_2 formation is 128.1 kcal/mol in comparison to the value of SiO_2 (203.4 kcal/mol) and GeO_2 is not stable in the same manner as SiO_2 (27).

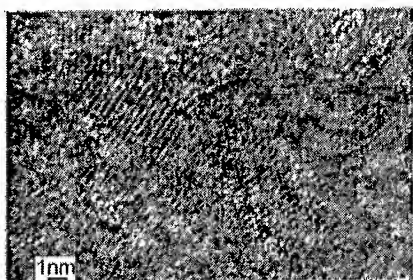


Fig. 4a: High resolution images of random distributed Ge nanocrystals.

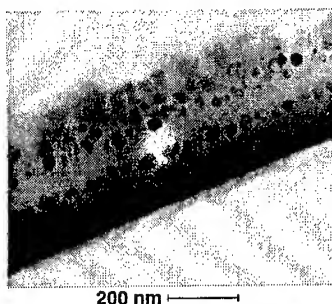


Fig. 4b: TEM images of large Ge nanocrystals self-organized in layers.

The arrangement of the nanocrystals is either random or self ordered in layers as can be demonstrated by TEM (see Fig. 4a, b). A higher sputtering power in combination with a lower water partial pressure results in a strong decrease of the crystal sizes down to 2 nm and in a random distribution of the Ge nanocrystals as seen in Fig. 4 (a). An self-arrangement of larger nanocrystals in a layer structure only is found in films deposited at

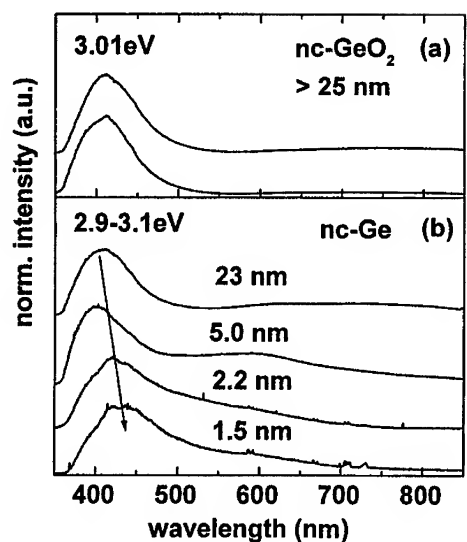


Fig. 5: Room temperature photoluminescence spectra excited with the 325nm line of a HeCd laser. Fig. 5 (a) demonstrates the PL of two films containing large GeO₂ nanocrystals. PL spectra of samples with a wide range of Ge nanocrystal sizes are shown in (b). With decreasing the size the PL slightly shifted to the red contrary to the expected blue shift. An increased Ge/GeO₂ content is correlated with stronger PL.

the extremely low deposition rate of ~ 0.2 nm/s which is on the limit of the sputtering process stability.

Samples that do not contain Ge and as-prepared amorphous Si_xGe_yO_z samples show no significant luminescence. Thus, the blue luminescence near 3.0 eV shown in Fig. 5 is without a doubt correlated with the formation of the nanocrystals. The absolute intensity of the blue luminescence increases with the size of the nanocrystals. The brightest samples are those with the largest crystallites and an increased Ge content. The PL intensity varies by a factor of ~ 80 , with the strongest PL found in the films containing GeO₂ crystals (Fig. 5a). In all our samples excitation at 441.6 nm results in a PL band with a lower intensity centered ~ 2.1 eV. The 2.1 eV peak position is in agreement with results reported previously (1,2,29). However, we can not confirm a systematically shift of this orange/green band. Our results for both PL bands are thus in contradiction with the predictions of the quantum confinement model. Fig. 6 shows the observed peak positions of a large set of samples including the nc-GeO₂ and the energy of the lowest transition calculated using the effective-mass model.

The time-resolved photoluminescence in selected samples were investigated. The blue-PL band decays with a characteristic time slightly less than 1 nsec (8). The PL decay is approximately described as single exponential having a time constant independent of the excitation intensity. Our experiments were performed on samples containing GeO₂

crystals of $R \sim 25$ nm and Ge crystals of 23 and 1.5 nm resulting in decay times of 0.87, 0.84, 0.66 nsec. According to the theory, a decrease of the carrier lifetime should be seen with decreasing size. Hence, our result for the decay time is again in contradiction with the predictions of the confinement theory. With increasing detection wavelength from 390 to 650 nm, the PL decay time increases from ~ 1 nsec to ~ 1.8 nsec, and a long-lived but weak PL background becomes detectable, typical of a slow decay ($>> \mu\text{sec}$).

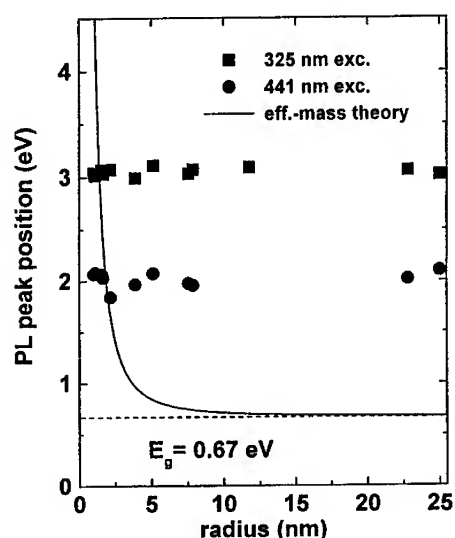


Fig. 6: Peak position of the room temperature PL of a large set of samples (8). The blue luminescence is visible by eye using an excitation at 325 nm. Excitation with 441.6 nm results in a weaker orange-green band. The peak position of both bands remains constant over a wide range of sizes which is incompatible with a quantum confinement origin.

In the following discussion we will consider three possible models for the blue and orange-green emission from films containing Ge or GeO_2 nanocrystals. It has been reported that Ge nanocrystals excited with an Ar laser at 488 nm luminesce at 2.2 - 2.3 eV independent of the size in the 6 - 14 nm range (29). The reported PL decay was ~ 0.9 nsec, nearly identical to our results with the blue PL. However, a fast decay is not an indication of a transition from indirect-gap to direct-gap behavior as suggested in Ref. (29): In all our films, the orange-green PL near 2.1-2.3 eV ($\lambda_{\text{exc}} = 441.6$ nm) and the blue PL near 3.0 eV exhibit a similar nsec PL decay over a wide distribution of sizes. Thus, our PL is not produced by the radiative recombination of excitons confined in the Ge or GeO_2 nanocrystals.

The second possibility is that the luminescence may originate from the oxide matrix itself. Indeed, SiO_2 is known to luminesce efficiently in the visible after excitation

with photon energies larger than 5 eV (30) which creates carriers into deep defect states (4.7 eV, 2.7 eV bands). We can not rule out that an increased number of defects in the nonstoichiometric SiO_x matrix exist and may be responsible for the orange-green PL. It is consistent with the increased intensity of the orange-green PL in some samples where the Si is not fully oxidized and the band gap of the matrix is decreased due to the oxygen deficit. The band gap of the nonstoichiometric SiO_x is smaller (1.8-4 eV) and depends strongly on the oxygen content (31, 32). A correlation between the intensity of the PL centered at 2.6 eV and the intensity of the infrared absorption related to Si-O-Si bridges has been established in thermally and chemically oxidized porous silicon (33). Different types of defects in silicon dioxide (i.e., non-bridging oxygen hole center) could be responsible for the visible PL around 2.3 eV (34). In contrast, we can rule out defects in the matrix as the source of the blue PL, since the PL intensity of the blue component increases by a factor of around 15-80 when the Si content of the films decreases from 35at.% to ~7at.%. When the Si content decreases, the matrix contains more GeO_x nanoclusters as demonstrated with our IR results (see Fig. 3). Indeed, some of the as-prepared films containing GeO_x clusters show an extremely weak blue PL peak. There might be a small amount of Ge-O related defects in the GeO_x clusters of the kind discussed below.

We propose that the large number of highly disturbed bonds in the inhomogeneous strain field of the Ge or GeO_2 surfaces is responsible for the appearance of the PL after annealing. The crystallization process is associated with cleaning and reconstruction which causes the out-diffusion of the last traces of oxygen during the growth of the Ge nanocrystals. The growth of the hexagonal GeO_2 crystals should be correlated with a reconstruction of the bond angle and bond length of the O-Ge-O inside of the crystals and with oxygen defects on the surfaces. The facts that the presence of both Ge and O is necessary for the PL and that there is a clear trend of stronger blue PL with increasing $[\text{O}]/[\text{Ge}]$ ratio support this interpretation. GeO_2 defects containing two non-bonding electrons have been reported by Ginzburg (35) for Ge-doped silica glass fibers. Such defects form a ground state singlet level (S_0), an excited singlet level (S_1) and a triplet level (T_1). In this energy scheme, a blue luminescence ~ 3.1 eV has been attributed to the T_1 to S_0 transition. The value of the PL lifetime reported in (35) is found to be very large as typical for spin-forbidden triplet-to-singlet transitions. Our fast PL decay is not in agreement with a spin-forbidden transition. The inhomogeneous strain field at the nanocrystal/matrix interfaces makes the forbidden transition of the Ginzburg defect at least partially allowed and this shorten the lifetime sufficiently.

Conclusion

Raman spectra demonstrate the crystallization process with increasing annealing temperature up to 900°C. X-ray diffraction proves the crystallization into Ge or GeO_2 nanocrystals. TEM images show the random distributed arrangement of the nanocrystals. A self organized layer structure only was found in case of a very low deposition rate. The

change in the oxygen bonding with the preparation conditions is monitored with IR spectroscopy. We have observed a strong room temperature photoluminescence near 3.0 eV in alloy films containing Ge or GeO₂ nanocrystals. The characteristic decay time is found to be ~1 nsec. We have established a correlation between the blue-PL and the [O]/[Ge] ratio in the films. The experimental facts lead us to conclude that the blue PL is not produced by the radiative recombination of excitons confined in the nanocrystals. After examination of several models, we suggest that the origin for the fast blue-PL band is a Ge/O-related defect.

We acknowledge P. Veit for TEM investigation of the films, J. Bläsing, P. Kohlert for X-ray investigation and R. Weigand for help in PL measurements. Financial support by the Deutsche Forschungsgemeinschaft and the Kultusministerium of Sachsen-Anhalt and the NSF Science and Technology Center on Photoinduced Charge Transfer is gratefully acknowledged.

References

1. Y. Maeda, N. Tsukamoto, Y. Yazawa, Y. Kanemitsu, Y. Masumoto, Appl. Phys. Lett. 59, 3168 (1991).
2. Y. Maeda, Phys. Rev. B51, 1658 (1995).
3. C.M. Yang, K.V. Shcheglov, M.L. Brongersma, A. Polman, H.A. Atwater, MRS Symp.Proc. 358, 181 (1995).
4. M. Zacharias, J. Bläsing, M. Löhmann, J. Christen, Thin solid films 278, 32 (1996).
5. D.C. Paine, C. Caragianis, Y. Shigesato, Appl. Phys. Lett. 60, 2286 (1992).
6. D.C. Paine, C. Caragianis, T.Y. Kim, Y. Shigesato, Appl. Phys. Lett. 62, 2842 (1993).
7. T. Takagahara, K. Takeda, Phys. Rev. B46, 15578 (1992).
8. M. Zacharias, P.M. Fauchet, Appl. Phys. Lett. in press (1997).
9. R.W. Schoenlein, D.M. Mittleman, J.J. Shiang, A.P. Alivisatos, C.V. Shank, Phys. Rev. Lett. 70, 1014 (1993).
10. L.-W. Wang, A. Zunger, J. Chem.Phys. 98, 2158 (1994).
11. Y. Kayanume, Phys Rev. B38, 9797 (1988).
12. Y. Kayanuma, Phys. Rev. B38, 9797 (1988).
13. A.I.L. Efros, A.L. Efros, Sov. Phys.-Semicond. 16, 772 (1982).
14. J.M. Luttinger, W. Kohn, Phys. Rev. B97, 869 (1955).
15. L. Brus, J. Chem.Phys. 80, 4403 (1984).
16. L. Brus, J. Chem.Phys. 90, 2555 (1986).
17. M.V. Rama Krishna, R.A. Friesner, Phys. Rev. Lett. 67, 629 (1993).
18. C.Y. Yeh, S.B.Zhang, A. Zunger, Appl. Phys. Lett. 63, 3455 (1993).
19. L.-W. Wang, A. Zunger, J. Phys. Chem. 98, 2158 (1994).
20. P.Y. Yu, M. Cardona, *Fundamentals of Semiconductors*, Springer-Verlag Berlin, 78ff. (1996)
21. B.J. Delley, J. Chem. Phys. 94, 7245 (1991).

22. M. Zacharias, R. Weigand, B. Dietrich, F. Stolze, J. Bläsing, P. Veit, T. Drüsedau, J. Christen, J. Appl. Phys. 81, 2384 (1997).
23. M. Zacharias, J. Bläsing, J. Christen, U. Wendt, J. of Non-Cryst. Solids 198-200, 919 (1996).
24. P.M. Fauchet, *Light Scattering in Semiconductor Structures and Superlattices*, ed. by D.J. Lockwood and J.F. Young, Plenum, New York, 229 (1991).
25. N. Maley, Phys. Rev. B46, 2078 (1992).
26. J. Bläsing, P. Kohlert, M. Zacharias, P. Veit, submitted (1997).
27. M. Zacharias, J. Bläsing, Phys. Rev. B52, 14018 (1995).
28. G. Lucovsky, M.J. Mantini, J.K. Srivastava, E.A. Irene, J. Vac. Sci. Techn., B5, 530, (1987).
29. Y. Kanemitsu, H. Uto, Y. Masumoto, Y. Maeda, Appl. Phys. Lett. 61, 2187 (1992).
30. L. Skuja, J. of Non-Cryst. Solids 167, 229 (1994).
31. H.R. Philipp, J. Phys. Chem. Solids 32, 1971 (1971).
32. M. Zacharias, D. Dimova-Malinovska, M. Stutzmann, Phil. Mag. 73, 799 (1996).
33. L. Tsybeskov, J.V. Vandyshev, and P.M. Fauchet, Phys. Rev. B49, 7821 (1994).
34. M. Stutzmann, Phys. Stat. Sol. (b) 192, 273 (1995).
35. L.P. Ginzburg, A.A. Gordeev, A.P. Gorchakov, A.P. Jilinsky, J. Non-Cryst. Solids 183, 234 (1995).

EFFECT OF IRRADIANT WAVELENGTH ON POROUS SILICON FORMATION

Crona Malone and Jacob Jorné
Dept. of Chemical Engineering
University of Rochester
Rochester, NY 14627

In an effort to determine the correct formation and luminescence mechanism of porous silicon (PS), photoelectrochemical etching experiments were conducted, using various wavelengths of irradiant light. The crystallite size decreases as the etching process proceeds, resulting in a blueshift of the photoluminescence (PL) spectrum. At a crystallite size of approximately 2.5nm, a saturation point is reached at which the PL peak wavelength remains constant. A further reduction in crystallite size does not result in a lower peak wavelength. Experimental results suggest that the surface state model is responsible for this luminescence process.

INTRODUCTION

The realization that light emission is possible from porous silicon (1) has resulted in tremendous possibilities for the use of silicon in the microelectronics industry. The ability to use optical rather than electrical interconnects will improve the performance of advanced integrated circuits. Extensive research is also being conducted on the use of porous silicon in optoelectronic devices and displays. Numerous experimental and theoretical studies have been performed in order to determine the origin and mechanism of the luminescence process. This dilemma has still not been fully solved. To date, the only two models which have not been discredited are the pure quantum confinement model (2) and the "smart" quantum or surface state model (3).

Previous heat treatment experiments (4) and studies involving reversible shifts of the PL spectrum by selected chemical treatments (5), have provided reason to doubt the quantum confinement model. In this paper we report further experimental results which cannot possibly be explained by the pure quantum confinement effect, thus providing further evidence for the surface state theory. The surface states, positioned within the bandgap of the porous silicon, control the process by which light is emitted. These lower energy states result from a relaxation and restructuring of the surface in accordance with its chemical environment. The energy of the emitted light is less than the bandgap energy by an amount which is too large to be attributed to Stokes shift.

EXPERIMENTAL

The experimental set-up for the photoassisted etching process is shown in figure 1. The porous microstructure depends critically on the electrolyte composition, anodization parameters and the type and doping level of the silicon crystal. Two types of wafers were used in this study : n-type 0.7-1.3 Ω cm and p-type 1-10 Ω cm. A thin layer of aluminum was deposited on the back side of the silicon wafer in order to provide a good electrical contact. The anodization was carried out in a solution of hydrofluoric acid (48wt%), deionized water and ethanol at a constant current density of 30mA/cm². Ethanol is used as it minimizes the formation of hydrogen bubbles and enhances deeper penetration into the pores. The etching time ranged from 0-45min. The irradiant light source during the experiments was either an Argon laser (514nm and 476nm lines) or a Tungsten - Halogen lamp which was connected to a power supply variac in order to control the lamp's illumination intensity and irradiant wavelength. After the formation process the PS samples

were rinsed with deionized water and blown dry with Nitrogen. All PL spectra were taken using a SPEX FLUOROLOG-2 series spectrofluorometer.

RESULTS

According to the formation process proposed by Lehmann (2), the higher the irradiating energy during the formation process, the smaller the crystallite size which in turn results in a larger bandgap energy. Figure 2 shows the PL peak wavelengths plotted as a function of etching time for n-Si samples prepared under different irradiant conditions. Similar results were shown for p-Si samples. As expected, a blueshift, or move to higher energies, results as the etching process proceeds. This is due to a reduction in the size of the silicon crystallites, hence an increase in the level of confinement. However, after a certain amount of time, a saturation point is reached below which no further blueshift is possible.

There are two major features to notice from Figure 2. Firstly, there is no considerable difference between the results for the 476nm irradiated sample and the one for 514nm sample. One might expect that irradiating with a higher energy light source would result in a smaller crystallite size, a larger bandgap and hence a higher energy PL peak. Clearly, this does not occur in this case. Secondly, the final peak wavelength at saturation, in all cases, is not that of the irradiant wavelength used during the formation process. If the mechanism of luminescence is via pure quantum confinement, as proposed by Canham (1), then the irradiant energy should correlate with the energy of the PL peak position. Based on these results, the pure quantum confinement model is questioned.

The bandgap of porous silicon was determined using previous experimental and theoretical results (3,6,7) based on the position of the second luminescence line in the infrared spectral region. Theory suggests that the ratio of the shift of the valence and conduction band should be equal to 2 (8). The bandgap, E_g , can be calculated using the following equation (4) :

$$E_g = 1.17\text{eV} + (IR - 0.82)(1 + (\Delta E_v / \Delta E_c)) \quad [1]$$

The estimated bandgap values for n-Si samples, which were subjected to 20 minutes of etching under various irradiating energies, are tabulated in Table I. The effective bandgap energies are comparable with the irradiant energies hence confirming that the formation mechanism is via quantum confinement. However, there is a significant difference between the bandgap energies and the PL peak energies which is too large to be explained by Stoke's shift.

In order to confirm these bandgap values, Transmission Electron Microscopy pictures were studied to determine the size of the silicon crystallites. The size was then related to the bandgap of the porous silicon sample (8,9). The crystallite size was determined using NIH Image software analysis. A n-Si wafer, having been etched for 15 minutes under 80V (548nm, 2.26eV) illumination yielded a crystallite size of 2.7nm, which correlates to a bandgap of 2.2eV. A sample which was irradiated with a wavelength of 476nm (2.6eV) during etching, for 10 minutes, resulted in a size of 2.2nm, which corresponds to a bandgap of 2.6eV. These results confirm that the bandgap energy is equal to the energy of the irradiant light used during the formation process. The emitted energy is less than this value.

The full width at half maximum (FWHM) is thought to be related to the size distribution of the silicon crystallites. Figure 3 shows two n-Si spectra taken after 5 minutes and 30 minutes of etching. The FWHM is estimated at around 100nm. After 30 minutes the formation process is thought to be completed and hence each of the crystallites should be of a similar size. The fact that there is no difference in the width of this peak to the width after 5 minutes suggests that the size distribution is not the only contributing factor. The samples which were irradiated with monochromatic light show similar values for the FWHM. Murayama et al (10) proposed that the emission process also contributes to this broad luminescence band. This suggestion seems reasonable in light of the present work.

DISCUSSION

The fact that the PL peak position is always lower than the estimated bandgap questions the validity of the pure quantum confinement effect in modeling the mechanism of luminescence. Based on the outcome of this study, the "smart" quantum model appears to be the only model capable of explaining the experimental results. Changes in the electronic structure of the solid will result in induced stresses on the surface of the silicon crystallite leading to energy level modifications of the electronic states. Some of these states will lie within the bandgap of the silicon crystallites. Electrons will become trapped in these states and recombination will result in an emitted energy less than the bandgap.

The surface state model is also useful in explaining the saturation effect which is observed in figure 2. During the formation process, as the bandgap enlarges, the surface positions change with it, a condition also noted by Petrova-Koch et al (7). This effect will continue until a critical size of the silicon crystallite is reached. It is suspected that once this size is attained, the surface states take on a predominant role in the emission process. This size was estimated to be approximately 2.5nm. Any further decrease in size will result in the surface effects becoming more pronounced since the surface area of the crystallite is increasing. More surface states will be created and the emitted energy will remain constant despite an increase in the bandgap. The illustration in figure 4 clarifies this model.

CONCLUSION

Irradiation during the electrochemical etching process will determine the bandgap of porous silicon, confirming that the formation mechanism is predominantly due to quantum confinement. The surface state model, recently proposed by many workers (3,12) explains why there is such a large difference between the bandgap energy and the energy of the emitted light obtained from a PL spectrum. This model can be used to explain the mechanism of luminescence. The emitted PL peak energy will be dependent on the surface states that form within the bandgap and the crystallite size determines if the saturated value has been attained. Saturation occurs at a size of approximately 2.5nm (~2eV)

ACKNOWLEDGMENTS

The financial support of the Electric Power Research Institute is gratefully acknowledged.

REFERENCES

1. L. Canham, *Appl. Phys. Lett.*, **57**, 1046 (1990)
2. V. Lehmann, *Mat. Res. Soc. Symp. Proc.*, **283**, 28 (1993)
3. F. Koch, V. Petrova-Koch, T. Muschik, A. Nikolov and V. Gavrilenko, *Mat. Res. Soc. Symp. Proc.*, **283**, 197 (1993)
4. V. Petrova-Koch, T. Muschik, A. Kux, B.K. Meyer, F. Koch and V. Lehmann, *Appl. Phys. Lett.*, **61**, 943 (1992)
5. C. Peng, L. Tsybeskov, P. M. Fauchet, *Mat. Res. Soc. Symp. Proc.*, **283**, 121 (1993)
6. A. Kux and M. Ben Chorin, *Phys. Rev. B* **51**, 17535 (1995)
7. V. Petrova-Koch, T. Muschik, G. Polisski and D. Kovalev, *Mat. Res. Soc. Symp. Proc* **358**, 483 (1995)
8. S. Y. Ren and J. D. Dow, *Phys. Rev. B*, **45** 6492 (1992)
9. J. P. Proot, C. Delarue and G. Allan, *Appl. Phys. Lett.*, **61**, 1948 (1992)
10. K. Murayama, S. Miyazaki and M. Hirose, *Jpn. J. Appl. Phys.* **31**, L3158 (1992)
11. V. Lehmann and U. Gosele, *Appl. Phys. Lett.*, **58**, 856 (1991)
12. P. M. Fauchet, E. Ettudgui, A. Raisanen, L. J. Brillsor, F. Seifferth, S. K. Kurinec, Y. Gao, C. Peng and L. Tsybeskov, *Mat. Res. Soc. Symp. Proc.*, **298**, 271 (1993)

Table I. Estimated bandgaps of porous silicon based on the position of the second luminescence line in the infrared spectral region.

Irradiant Energy (eV)	PL Red Peak (eV)	PL Infrared Peak (eV)	Bandgap (eV)
2.26	1.95	1.15	2.22
2.36	2.03	1.18	2.3
2.41	2.05	1.19	2.34
2.60	2.07	1.20	2.37

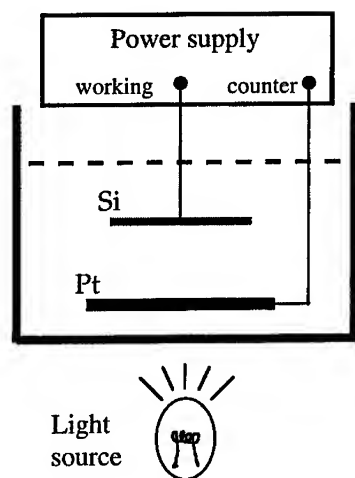


Figure 1. Experimental Setup.

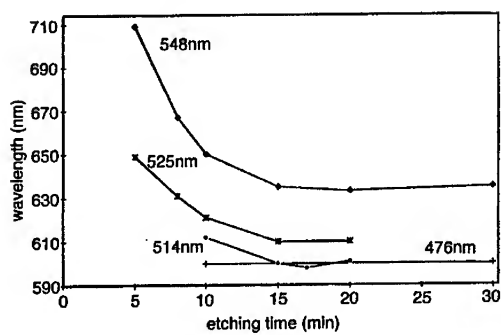


Figure 2. The effect of using different irradiant wavelengths on n-Si during the electrochemical etching process.

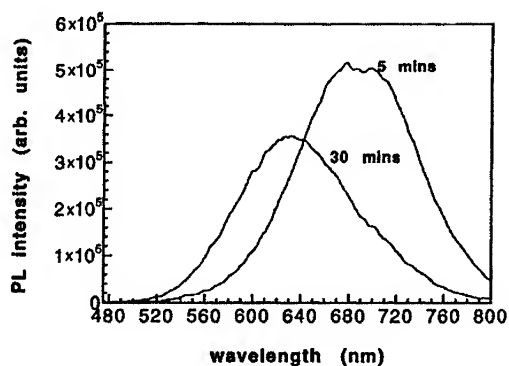


Figure 3. PL spectra for n-Si after 5 minutes and 30 minutes of photoelectrochemical etching.

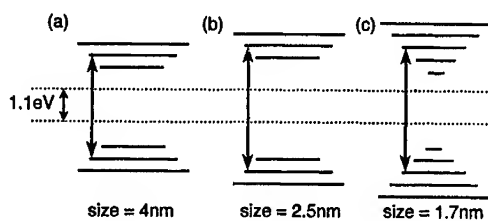


Figure 4. Variation of the surface state positions as the size of the crystallites decreases.
 (a) shows the bandgap before saturation
 (b) shows the bandgap at the critical point
 (c) shows the bandgap at saturation
 The dotted line shows the bandgap of bulk silicon.

A LUMINESCENCE STUDY OF SILICON-RICH SILICA AND RARE-EARTH DOPED SILICON-RICH SILICA

A.J. Kenyon, P.F. Trwoga and C.W. Pitt

*Dept. Electronic & Electrical Engineering,
University College London
Torrington Place
London
WC1E 7JE*

ABSTRACT

Light emission from silicon has long been a goal of the electronics industry, the realisation of which would open up the possibility of true large-scale optoelectronic integration. Current hybrid technologies suffer from processing complexity and lattice mismatch which would be avoided if a suitable silicon-based luminescent material were developed. To this end, there has recently been considerable interest in light emission from new forms of silicon. Research has been primarily concentrated on porous silicon, but there is a growing body of work on related materials such as nanocrystalline silicon and silicon-rich silica. The latter exhibits similar optical properties to porous silicon without the associated problems of stability.

We have produced by Plasma Enhanced Chemical Vapour Deposition a number of silicon-rich silica films which contain silicon nanoclusters as-grown of the order of 2nm diameter. Using photoluminescence spectroscopy, ESR and FTIR studies we have investigated the influence of post-process annealing on the optical and physical properties of the material. We have been able to identify two separate luminescence bands which appear to arise from different mechanisms: defect luminescence and exciton confinement in nanoscale silicon clusters.

We have doped samples of silicon-rich silica with erbium ions and have shown that strong luminescence from the rare-earth ion is obtained even when excited away from characteristic absorption bands; the luminescence intensity is largely independent of excitation wavelength below 514nm. We ascribe this to a carrier-mediated excitation of the rare-earth ions via the silicon microclusters. This is in accordance with recent results in the literature on erbium implanted porous silicon. The very broad absorption of this material opens up the possibility for flashlamp-pumped optoelectronic devices.

We also present electroluminescence spectra from simple metal-insulator-silicon test devices which employ silicon-rich silica as the luminescent layer.

I. INTRODUCTION

The drive towards low-cost optoelectronic and display technologies has generated a huge interest in the development of silicon-based electroluminescent materials. This has been particularly the case since the discovery by Canham in 1990 of bright visible photoluminescence from porous silicon [1]. Bulk silicon is an indirect bandgap material and therefore an inefficient light source. However, investigation of the optical properties of porous silicon and related materials has shown that the problem of low efficiencies may be overcome through the use of new low-dimensional forms of silicon. Porous silicon has been shown to emit light efficiently: photoluminescence quantum efficiencies of up to 10% have been reported and electroluminescent devices have been produced with efficiencies in the region of 0.1% [2]. However, material stability is poor. The nature of the porous silicon surface makes it highly susceptible to both contamination and handling damage. Exposure to the atmosphere can cause degradation of light output in only a few hours.

In contrast, silicon-rich silica (SiO_x , $x < 2$) is a related material which is mechanically and chemically stable. It consists of nanoclusters of silicon embedded in a silica matrix and exhibits visible and near-ir luminescence similar to that seen from porous silicon. Although luminescence was first reported in this material some time ago [3], it is only recently that its optical properties have begun to be thoroughly studied. Photoluminescence has been observed by a number of groups and has been variously identified as arising from quantum confinement of excitons [4], defect luminescence [5], siloxene luminescence [6] or interfacial effects at cluster surfaces [7]. Luminescence studies carried out to date have failed to conclusively identify a unique luminescence mechanism and there are a number of contradictory reports in the literature.

There is good agreement over the physical structure of silicon-rich silica: Transmission Electron Microscopy (TEM) studies have confirmed the presence of clusters of silicon atoms in the SiO_2 matrix [8,9]. As-deposited films generally contain amorphous clusters which crystallise on annealing. Moreover, prolonged annealing and high temperatures serve to increase the mean size of the clusters through diffusion of silicon atoms through the silica matrix. Existing clusters act as nucleation centres for the growth of larger aggregates. This is referred to as 'Ostwald Ripening' and is a key process in inferring the presence of quantum confinement effects. Since the bandgap of clusters with dimensions of the order of the excitonic Bohr radius depends strongly on cluster size, any variation in mean cluster size will be reflected in a corresponding change in both absorption and luminescence spectra. This is the source of the annealing related red-shift in luminescence bands reported as evidence for a quantum confinement origin of luminescence.

In this study we have undertaken a detailed investigation into the luminescence spectra of silicon-rich silica thin films in an attempt to resolve some of the difficulties in assigning a luminescence mechanism. We find that there is more than one mechanism present in most cases, which may be the source of much of the present confusion.

There have been few reports of electroluminescence from silicon-rich silica. However, for device use it is critical to achieve efficient electroluminescence and to understand carrier transport mechanisms. It is a relatively simple process to form good contacts to SiO_x by evaporation: gold, aluminium and ITO have been used successfully. Initial studies of those devices produced to date [8,10] suggest low quantum efficiencies although no detailed measurements have been reported. We report preliminary results of dc electroluminescence studies on material grown using Plasma Enhanced Chemical Vapour Deposition (PECVD). CVD growth avoids many of the problems associated with implantation-related damage and as a result we have been able to demonstrate luminescence in as-grown films.

Light emission from rare-earth doped materials is also an area of great technological importance. With the proliferation of fibre-optic communications systems operating at wavelengths in the near-ir, there is a large and growing need for optical amplifiers, splitters, filters and other active devices. Erbium is a particularly important material as the Er^{3+} ion emits in a broad band around $1.55\mu\text{m}$: a wavelength conveniently positioned within the low loss window of silica optical fibres. For some time, we have been concerned with investigating the inclusion of high concentrations of erbium within silica planar optical waveguide structures. We have been able in past work to increase the concentration of unclustered rare-earth ions by an order of magnitude over conventional glasses [11]. As an extension of this work, we have produced films of erbium-doped silicon-rich silica to investigate the effect of the broad-band absorbing silicon nanoclusters on the optical properties of the erbium ions. We report in this study the observation of a strong interaction between silicon nanoclusters and rare-earth ions. In particular, there is a pronounced excitation exchange mechanism between the two species. This is in agreement with recent results from Polman's work on erbium-doped amorphous silicon showing excitation exchange between the silicon host and the rare-earth ion [12,13].

II. EXPERIMENTAL

A number of silicon-rich silica films were deposited on lightly doped p-type $\langle 100 \rangle$ CZ silicon wafers using PECVD. The sample wafers were first thoroughly cleaned under clean-room conditions using acetone and isopropyl alcohol followed by sulphuric and nitric acids and finally rinsed with deionised water. After placing in the reaction chamber, the wafers were cleaned again with an argon plasma for 5 minutes. A capacitively-coupled deposition chamber was used. Precursor gases were a silane/argon mix (5% silane (SiH_4) in argon) and nitrous oxide (N_2O) as silicon and oxygen sources respectively. The nitrous oxide flow rate was fixed at 10 sccm and the silane/argon mixture flow rate changed from run to run between 240 sccm and 120 sccm. A 13.56 MHz RF generator was used to dissociate the precursor gases, the power being varied from run to run between 10 W and 30 W. Substrate temperature was set in the range 120°C to 350°C .

The erbium doped samples were produced under similar conditions, with the addition of a solid organic chelate precursor: $\text{Er}(\text{thd})_3$ into the reaction chamber. A carrier gas (argon) was used to transport the precursor. The erbium concentration

within the films was 1 at% as measured by secondary ion mass spectrometry (SIMS).

After deposition, each film was divided into a number of pieces which were then annealed under argon for 90 minutes at a series of temperatures between 200 °C and 1000 °C.

Photoluminescence spectra were measured for each film using a Coherent argon-ion laser as the excitation source. Spectra were dispersed using a Bentham M300 monochromator and detection was via a Bentham 231 side window photomultiplier tube, a current preamplifier and lock-in amplifier. For infra-red spectra, the photomultiplier tube was replaced by an InGaAs photodiode. Both the detection electronics and monochromator were computer controlled; care was taken to ensure that the spectra were as accurate and repeatable as possible. A diffraction grating was used as a premonochromator to filter out laser plasma lines and a Schott glass filter (OG495) placed immediately following the collection optics removed any unwanted laser scatter.

A number of films, both as-deposited and post-annealing were studied using electron spin resonance (ESR) in order to investigate the presence of defects.

Selected films were studied using Fourier Transform Infra Red spectroscopy (FTIR). This allowed the determination of such chemical changes as loss of hydrogen and increase in oxidation state of silicon.

Samples of as-grown films were analysed for chemical composition using both SIMS and electron-probe microanalysis. In particular, we were interested in the ratio between elemental and oxidised silicon. This was readily obtained from SIMS data. The films studied contained up to 8 at% elemental silicon; oxygen content was around 55 at% and there was a small amount of nitrogen incorporated: typically around 5 at%.

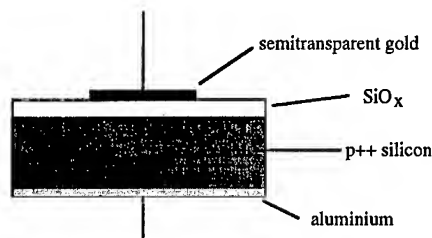


Figure 1: Electroluminescence test structure

A number of silicon-rich silica films were selected for electroluminescence studies on the basis of the strength of photoluminescence signal. In order to ensure efficient conduction through the active layers, sample thicknesses were restricted to approximately 0.1 μm as measured by Talystep. Thin gold electrodes around 50 nm thick and 5 mm diameter were evaporated onto the upper surface of the films

and electrical contact made with needle probes. Figure 1 shows the electroluminescence test structure. The device was placed in the spectroscopic set-up and the electroluminescence spectrum measured.

III. RESULTS AND DISCUSSION

a) Photoluminescence

In general, the photoluminescence spectra of the SiO_x films showed two bands: one around 2 to 2.2 eV and a second around 1.4 to 1.9 eV. The relative strengths and positions of the bands varied between samples and were dependent on post-processing. Figure 2 shows a photoluminescence spectrum of sample SS28 which

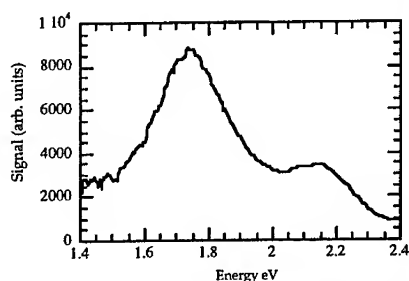


Figure 2: Photoluminescence spectrum of sample SS28 following a 400C anneal

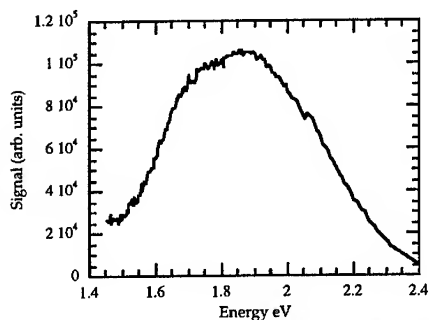


Figure 3: Photoluminescence spectrum of sample SS24 following 400C anneal

clearly shows the two components: compare this with figure 3, a spectrum from sample SS24. The latter spectrum appears asymmetric and can be fitted by two Gaussian curves centred on 2 eV and 1.9 eV. The effects of post-deposition annealing are shown in figure 4 for sample SS24. It is apparent that the two luminescence bands behave very differently under annealing. The higher energy band shows a strong variation in intensity while the lower energy band also exhibits a pronounced shift in energy. This points to the probability of there being two distinct luminescence mechanisms.

The general trend in the annealing behaviour of the two photoluminescence bands across all the samples studied is as follows: the higher energy band, if present, remains at a fixed energy around 2 to 2.2 eV regardless of annealing temperature and becomes completely quenched at temperatures above 600 to 800 °C, following an initial

rise at $T_a < 500$ °C. The lower energy band is present even in samples annealed at

temperatures up to 1000 °C and shows a red shift with increasing annealing temperature, the magnitude of which varies from sample to sample.

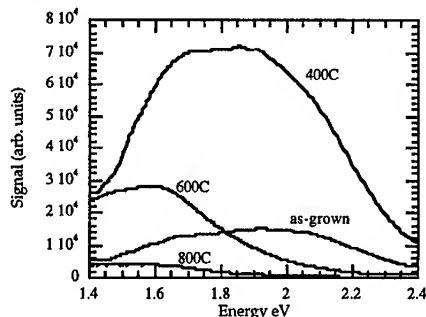


Figure 4: Photoluminescence spectra of sample SS24 following anneals at temperatures indicated

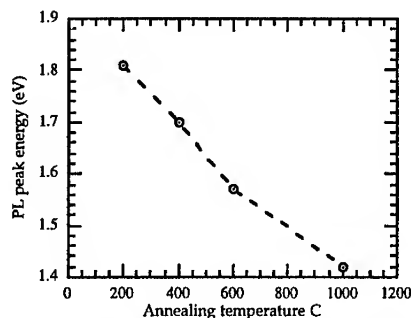


Figure 5: low energy PL band peak energy as a function of annealing temperature for sample SS28

The red shift of the low energy band is a strong indication of a quantum confinement effect. It has been well established by a number of groups that annealing silicon-rich silica films at temperatures in excess of 600 °C results in accretion of excess silicon atoms and aggregates to form progressively larger clusters [14]. If annealed at a high enough temperature for a sufficient time, the larger silicon clusters will tend to incorporate the smaller ones, resulting ultimately in macroscopic inclusions of 'bulk' silicon within the SiO₂ matrix. As an increase in cluster size results in a narrowing of the optical bandgap, observation of annealing-related red-shifts in luminescence spectra is taken to be good evidence in support of the quantum confinement hypothesis. The dependence of the photoluminescence energy on cluster size is well established and formulae have been published which quantify the relationship between cluster size and bandgap energy

[15,16]. In its most simple form, this dependence can be modelled using the 'particle in an infinite well' model and writing out the appropriate expressions for the wavefunction of a confined particle. This yields a $1/r^2$ dependence of band gap energy on cluster size. More detailed models ranging from those based on the Effective Mass Approximation to full density of states calculations have been developed, but the $1/r^2$ dependence is a good working approximation. Figure 5 shows a plot of photoluminescence peak energy for the low energy band as a function of annealing temperature for sample SS24. The quantum confinement model also predicts an increase in luminescence intensity with decreasing cluster size

due to an increased oscillator strength. This may help to explain the reduction in photoluminescence intensity accompanying the red-shift of the low energy band on annealing at $T_a > 600^\circ\text{C}$.

For the case of the high energy band, the absence of an annealing-related red-shift makes it unlikely that this band is the result of recombination of confined excitons. However, luminescence around 1.9 and 2 eV has been noted before in both amorphous silica and quartz. This is generally associated with defect states produced by implantation or irradiation, although there are a number of possible defect species that emit in this region and there has been considerable debate in the literature over the origin of these luminescence bands in silica [17,18]. Current opinion suggests that they are due to emission from non-bridging oxygen hole centres (NBOHCs) [17]. Such defects are usually associated with the radiolysis of hydroxyl groups or the cleavage of strained silicon-oxygen bonds by irradiation; however, there is evidence for the presence of NBOHCs in as-grown CVD oxide films [19].

b) FTIR

Figure 6 shows FTIR data for sample SS26 as-grown and following anneals at the temperatures indicated. Table 1 gives the assignments of FTIR bands observed in SiO_x samples.

Table 1: FTIR bands and assignments

Frequency (cm^{-1})	1050	1100	2150	2200	2250
Assignment	Si-O-Si	Si-O-Si	Si-H	Si-H ₂	Si-H ₃

The Si-H_x stretch bands around 2200 cm^{-1} are shifted up in energy by approximately 100 cm^{-1} with respect to the corresponding bands in hydrogenated amorphous silicon. This can be ascribed to the effect of the SiO_2 matrix. stretches respectively. From Petrova-Koch *et al* [20], it can be inferred that the separation of the Si-H_x band into its three components, Si-H, Si-H₂ and Si-H₃, implies clusters with a diameter greater than 20 Å. Conversely, the broadening of the bands by the local electric field around 'small' clusters (<20 Å diameter) tends to yield spectra with a broad Si-H_x band. We may expect further inhomogeneous broadening of the FTIR bands due to the extended SiO_2 matrix, so this estimate of the transition between 'small' and 'large' clusters can only be an approximate guide. However, it is a reasonable conclusion that the broadening of the Si-H_x band observed for our samples implies the presence of silicon clusters which are of approximately the same size as Petrova-Koch's estimate: *i.e.*: less than 100 Å in diameter.

Of key importance to understanding the chemical changes in the films brought about by annealing is a study of the temperature dependence of the FTIR bands. Figure 7

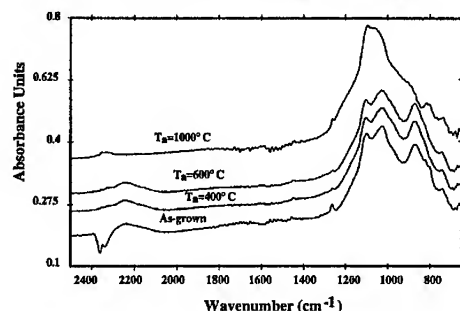


Figure 6: FTIR spectra of sample SS26 following anneals as indicated

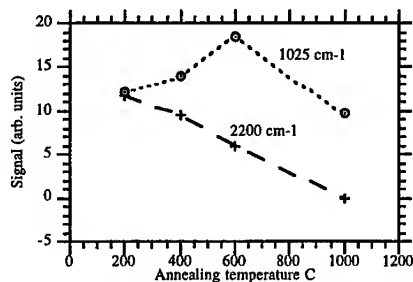


Figure 7: Dependence of 1025cm⁻¹ and 2200cm⁻¹ FTIR bands on annealing temperature. The signal intensities for the 2200cm⁻¹ band have been magnified by a factor of 3 for clarity

shows the variation in intensity with temperature of the bands at 2200 cm⁻¹ (Si-H_x) and 1025 cm⁻¹ (Si-O-Si) for sample SS26. There is a clear reduction in the hydrogen content of the film as T_a increases, and the Si-H_x band completely disappears following a 1000 °C anneal. Accompanying this is an increase in the Si-O-Si band up to T_a=600 °C, implying an annealing out of oxygen vacancies by diffusion of interstitial oxygen. It is not clear what the cause of the subsequent decrease in these bands at T_a=1000 °C is, but it is likely to be due to growth of silicon clusters.

c) ESR

Figure 8 shows ESR spectra for a control sample of cut silicon and similar sized pieces of sample SS26 annealed over a range of temperatures. The absence of a signal in the control sample eliminates the possibility that it is due to dangling bonds formed by cleaving the silicon substrate. The g-value of the peak observed (2.0055) is characteristic of P_b centres in silica, or their analogue in amorphous silicon, the D centre. Both of these defects consist of an unpaired spin located on a silicon atom bonded to three further silicon atoms (Si₃=Si[•]). In the case of amorphous silicon, such defects are characterised as dangling bonds at the surface [21], whilst in the case of silica films on silicon, P_b centres can often be associated with oxygen

vacancies at the Si/SiO₂ interface [22]. It may therefore be the case that the paramagnetic centres in our samples are located at the cluster/silica interface. Studies of the passivation and depassivation of P_b centres in thin film SiO₂ have demonstrated an increase in P_b content on annealing at T>500 °C in vacuum, argon, nitrogen and air [21]. Further annealing at higher temperatures can reduce defect concentration by compensating dangling bonds with interstitial oxygen and water. The rapid increase in ESR signal above T=500 °C agrees well with other observations of the annealing behaviour of the P_b centre. The decrease between T=200 °C and 500 °C may be due to an initial uptake of interstitial hydrogen

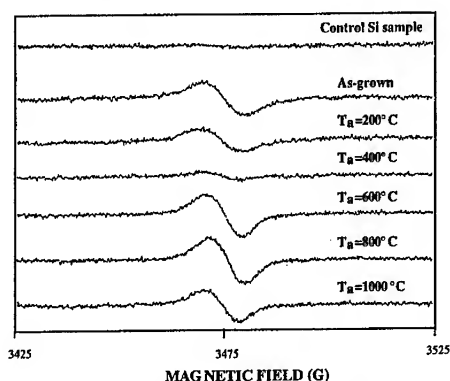


Figure 8: ESR spectra as a function of annealing temperature for sample SS26. The top trace is from a control sample of silicon

Looking at sample SS24, we observe a concentration of 5×10^{16} spins per gramme in the as-grown film. However, comparison of the annealing behaviour of the 2 eV luminescence band with that of the P_b centres shows that it is unlikely that these defects are responsible for the emission. For sample SS26, between 200 °C and 600 °C, the photoluminescence signal increases by a factor of 2 whilst the ESR signal at g=2.0055 falls sharply. Annealing at temperatures in excess of 600 °C leads to complete quenching of the 2 eV band but this is the range over which the ESR signal is strongest.

In the present study, it is puzzling that we do not see the characteristic ESR signal due to the NBOHC at g=2.001; it may however be that some other, non-paramagnetic defect is responsible for the 2 eV band. Certainly, on the basis of our data, we can not conclusively identify it. There is some evidence that the electron trap Si₃- defect luminesces at these energies [17], but the presence of this defect in our samples remains speculation at present. However, the annealing behaviour and lack of red-shift in the case of the 2 eV band suggests a defect origin. The observation that in all cases the 2 eV photoluminescence band is completely

quenched following anneals in excess of 600°C indicates that the quenching mechanism is tied in with the filling of oxygen vacancies in the silica matrix by diffusion of interstitial oxygen and water. However, the low-temperature anneal behaviour of the 2 eV band requires further investigation.

It would initially be expected that removal of hydrogen from hydrogen-rich SiO_x films would produce a large number of dangling bonds which act as non-radiative recombination centres, thus quenching luminescence [23]. However, there is a clear increase in photoluminescence intensity from the 2 eV band following low temperature annealing at $T_a < 600^\circ\text{C}$. Evolution of hydrogen from the films at $T_a < 600^\circ\text{C}$, as confirmed by FTIR increases the population of optically active defects. However, the nature of the defect responsible for the 2 eV band is not clear. We propose that it is produced by the cleavage of Si-H or O-H bonds and may be generically similar to the NBOHC, although it does not appear to be ESR active.

d) Rare-earth doped silicon-rich silica

Figure 9 is a photoluminescence spectrum of an erbium-doped silicon-rich silica sample excited at 514.5nm. It exhibits a strong band around 1535nm characteristic of the $^4\text{I}_{13/2} \rightarrow ^4\text{I}_{15/2}$ Er^{3+} transition. Moreover, it appears that it is possible to obtain fluorescence from Er^{3+} even when the pump wavelength is away from the characteristic erbium absorption bands. Figure 10 shows a photoluminescence spectrum of the same sample excited at 476nm, a wavelength which does not lie within any of the erbium absorption bands. Compare this with figure 11 which shows photoluminescence spectra for an erbium-doped stoichiometric silica film pumped at the same wavelengths. Note the very weak luminescence from this sample under 476nm excitation. Even more striking is the observation that the intensity of fluorescence remains largely unchanged with decreasing pump wavelength. Figure 12 illustrates the normalised integrated fluorescence intensity as a function of excitation wavelength for the erbium-doped SiO_x sample and a reference erbium doped stoichiometric silica fibre. In the case of the fibre, the fluorescence intensity shows a good correlation with the absorption spectrum of erbium in silica [24]. This is in marked contrast to the silicon-rich sample which exhibits fluorescence at 1535nm that is largely independent of excitation wavelength.

The presence of Si microclusters in these samples can be inferred from the luminescence data and from the presence of an abrupt band-edge in the absorption spectra. The marked difference between the fluorescence in our erbium-doped samples and that from the fibre cannot be explained by a change in the erbium absorption or emission cross-sections, for which there is no supporting evidence in the literature. However, if bands due to silicon microclusters and excited levels of

the erbium ion overlap, it is possible that photons with energies to the blue of the absorption edge of the films are absorbed by the silicon aggregates and the energy transferred non-radiatively to the excited states of the erbium.

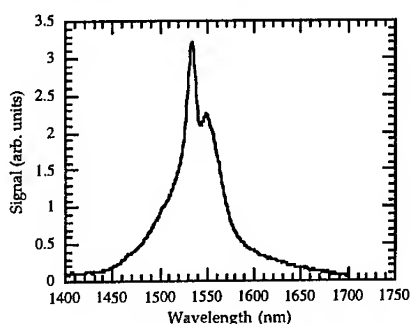


Figure 9: Photoluminescence spectrum of erbium-doped silicon-rich silica film. Excitation wavelength: 514.5 nm

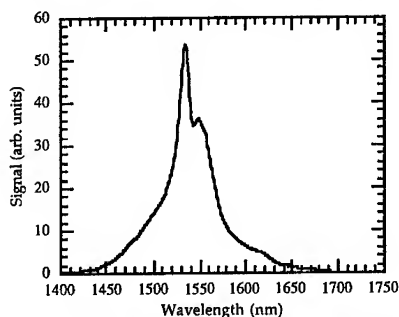


Figure 10: As figure 9, pump wavelength 476nm

the absorber, implying the rare-earth ions are situated within very close proximity to the silicon nanoclusters.

The absorption spectra of the erbium-doped SiO_x films exhibit strong absorption band edges in the visible region of the spectrum similar to those of the non-Er doped samples. Moreover, it appears that the characteristic absorption bands of the rare earth ion at 450nm, 490nm, 520nm, 635nm and 980nm are very much weaker than the absorption due to the silicon aggregates. Hence there appears to be a strong energy exchange mechanism between silicon nanoclusters and the rare-earth ions which seems similar to that observed in rare-earth doped amorphous silicon. If this is a Förster-type transfer with a $1/r^6$ dependence, the emitting species must be very close to

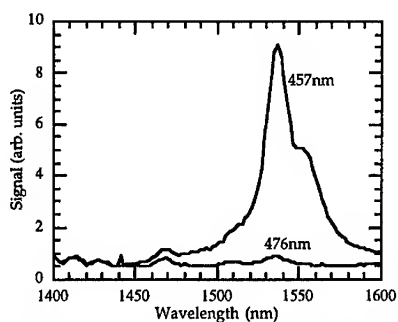


Figure 11: Photoluminescence spectra of an erbium-doped stoichiometric silica film excited at the wavelengths indicated.

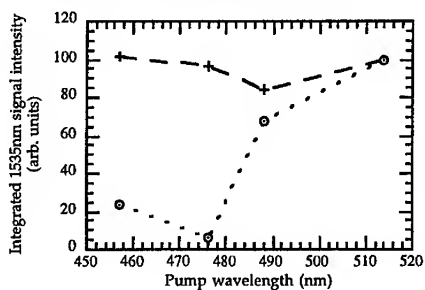


Figure 12: Normalised integrated 1535nm PL intensity as a function of pump wavelength
Crosses: SiO_x film
Circles: reference stoichiometric fibre

e) Electroluminescence

Electroluminescence from the test devices could be observed by eye in a darkened room and was stable for periods of up to six hours. The devices operated under both forward and reverse bias, although luminescence was brighter in the former case. In forward bias, light emission was initiated at a voltage of around 1.5 V and a current of 70 mA. Figure 13 shows a representative electroluminescence spectrum. The spectrum has not been corrected for the absorption of the gold layer. The electroluminescence signal was very much weaker than photoluminescence obtained from the same sample; we estimate the quantum efficiency of electroluminescence to be of the order of 10^{-5} %, which, whilst low, is comparable with figures quoted for porous silicon devices at a similar stage in their development.

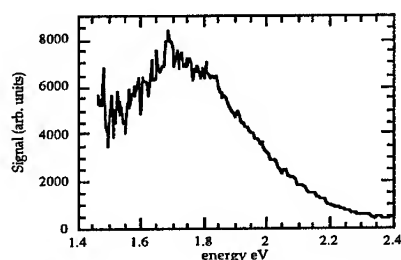


Figure 13: Electroluminescence spectrum of silicon-rich silica thin film

IV. CONCLUSIONS

We have shown that photoluminescence from silicon-rich silica films is the result of two separate mechanisms: defect luminescence, possibly from non-bridging oxygen centres or related oxygen vacancies, and radiative recombination of confined excitons. Our results are in broad agreement with others in the literature [25,26,27]. We propose a mechanism for defect production within hydrogen-rich SiO_x films which involves evolution of hydrogen at a faster rate than the diffusion of interstitial oxygen to compensate the resultant dangling bonds. Evidence for this mechanism comes from photoluminescence and FTIR data which indicate a decrease in hydrogen content accompanied by an increase in photoluminescence intensity for $T_a < 600^\circ\text{C}$. Above this temperature, annealing of oxygen vacancies leads to a reduction in defect luminescence and a growth of silicon clusters as reflected in a red shift of the low-energy photoluminescence peak. However, we are unable at this stage to conclusively identify the luminescent defects. This scheme may help to explain some of the apparently contradictory photoluminescence results published elsewhere.

We have produced by PECVD rare-earth doped silicon-rich silica thin films that exhibit characteristic erbium 1535nm fluorescence even when the sample is excited at wavelengths away from erbium absorption bands. The fluorescence yield appears to be largely independent of the pump wavelength over the range studied. This contrasts with data presented for both an erbium doped silica fibre and for rare-earth doped stoichiometric silica. We propose that our results are consistent with studies on erbium-doped amorphous silicon which indicate carrier mediated excitation of the rare-earth ion [12,13]. This suggests that the rare-earth ions are either sited within or in very close proximity to the silicon nanoclusters.

We report preliminary results of dc electroluminescence of silicon-rich silica, demonstrated in a simple MOS device. We believe this to be the first report of dc electroluminescence from this material: previous studies have used pulsed or ac excitation. Although luminescence is weak, there remains much work to be carried

out on this material; in particular a thorough investigation of carrier transport mechanisms. This material may make a significant contribution to the field of light emission from silicon, and we hope to demonstrate soon that silicon-rich silica is a promising technology which avoids the stability and contamination problems inherent in porous silicon.

V. ACKNOWLEDGEMENTS

We would like to express our thanks to the Engineering and Physical Sciences Research Council, UK, for financial support. Thanks also to Dr Oduwole of Queen Mary and Westfield College, London, for the ESR scans and Dr J. Milledge of the Department of Crystallography, UCL, for FTIR data.

REFERENCES

- [1] L.T. Canham, Appl. Phys. Lett. **57**, 1046, (1990)
- [2] A. Bsiesy, J.C. Vial, F. Gaspard, R. Herino, M. Ligeon, F. Muller, R. Romestain. Semiconductor-Silicon Ed. H.R. Huff, W. Bergholz, K. Sumino, p475, (1994)
- [3] D.J. DiMaria, J.R. Kirtley, E.J. Pakulis, D.W. Dong, T.S. Kuan, F.L. Pesavento, T.N. Theis, J.A. Cutro and S.D. Brorson, J. Appl. Phys. **56**, 401, (1984)
- [4] L.T. Canham, Physica Status Solidi B-Basic Research **190**, 9, (1995)
- [5] B.H. Augustine, E.A. Irene, Y.J. He, K.J. Price, L.E. McNeil, K.N. Christensen and D.M. Maher J. Appl. Phys. **78**, 4020, (1995)
- [6] M. Stutzmann, M.S. Brandt, M. Rosenbauer, H.D. Fuchs, S. Finkbeiner, J. Weber and P. Deak, J. Luminesc. **57**, 321, (1993)
- [7] Y. Kanemitsu, T. Ogawa, K. Shiraishi and K. Takeda, Phys. Rev. B, **48**, 4883, (1993)
- [8] G.S. Tompa, D.C. Morton, B.S. Sywe, Y. Lu, E.W. Forsythe, J. A. Ott, D. Smith, J. Khurgin and B. A. Khan, Mat. Res. Symp. Proc. **358**, 701, (1995)
- [9] D. Rodichev, Ph. Lavallard, E. Doorh  e, A. Slaoui, J. Perriere, M. Gandais and Y. Wang, Nucl. Instrum Meth. Phys. Res. B, **107**, 259, (1996)
- [10] G.G. Qin, A.P. Li, B.R. Zhang and Bing-Chen Li, J. Appl. Phys. **78**, 2006, (1995)
- [11] I. Massarek, PhD thesis, University of London, (1993)
- [12] A. Polman, G.N. Van Den Hoven, J.S. Custer, J.H. Shin, R. Serna And P.F.A. Alkemade, J. Appl. Phys. **77**, 1256, (1995)
- [13] G.N. Van Den Hoven, J.H. Shin, A. Polman, S. Lombardo And S.U. Campisano, J. Appl. Phys. **78**, 2642, (1995)
- [14] T. Komoda, J.P. Kelly, A. Nejim, K.P. Homewood, P.L.F. Hemment and B.J. Sealy, Mat. Res. Symp. Proc. **358**, 163, (1995)
- [15] M. Lannoo, C. Delerue, G. Allan and E. Martin, Mat. Res. Symp. Proc. **358**, 13 (1995)
- [16] N.A. Hill and K.B. Whaley, Mat. Res. Symp. Proc. **358**, 477, (1995)
- [17] M.A. Stevens Kalceff and M.R. Phillips, Phys. Rev. B, **52**, 3122, (1995)
- [18] S. Muneke, T. Yamanaka, Y. Shimogaichi, R. Tohmon, Y. Ohki, K. Nagasawa and Y. Hama, J. Appl. Phys. **68**, 1212, (1990)
- [19] H. Koyama, J. Appl. Phys. **51**, 2228, (1980)
- [20] V. Petrova-Koch, T. Muschik, G. Polisski and D. Kovalev, Mat. Res. Symp. Proc. **358**, 483, (1995)
- [21] E.H. Poindexter, Z. Naturforsch. **50**, 653, (1995)
- [22] D.L. Griscom, J. Elect. Mat. **21**, 763, (1992)

-
- [23] M. Lannoo, C. Delerue and G. Allan, *J. Luminesc.* **57**, 243, (1993)
[24] W.J. Miniscalco, *J. Lightwave Tech.* **9**, 234, (1991)
[25] T. Shimizu-Iwayama, K. Fujita, S. Nakao, K. Saitoh, T. Fujita and N. Itoh, *J. Appl. Phys.* **75**, 7779, (1994)
[26] T. Komoda, J.P. Kelly, A. Nejim, K.P. Homewood, P.L.F. Hemment and B.J. Sealy, *Mat. Res. Symp. Proc.* **358**, 163, (1995)
[27] T. Fischer, T. Muschik, R. Schwarz, D. Kovalev and F. Koch, *Mat. Res. Symp. Proc.* **358**, 851, (1995)

Size dependence of superlinear photoluminescence of CdS_{0.5}Se_{0.5} nanocrystallites in glass

E.B. Stokes, GE Corporate R&D, One research Circle, Bldg. K1, Room 2A40, Schenectady, NY 12309
P.D. Persans, Rensselaer Polytechnic Institute, Troy, NY

Abstract

Photoluminescence emission spectra were acquired on CdS_{0.5}Se_{0.5} doped glass at 77K. Four samples were analyzed, each with a different average nanocrystallite size between 1.1 and 8.4 nm. The photoluminescence emission fluence is superlinear in pulsed excitation fluence. The superlinearity results from the transition from geminate to non-geminate recombination with increasing average number of electron-hole pairs per nanocrystallite. Samples with larger particles are more likely to contain multiply excited nanocrystallites at a given excitation fluence, and hence exhibit a higher degree of superlinearity than samples with smaller particles. The lifetime of the photoluminescence emission decreases with increasing particle size, and the lifetime of non-geminate recombination is less than that of geminate recombination.

Introduction

Photoluminescence emission bands in Cd(S,Se) doped glass typically consist of: (1) a fast doublet near the absorption band edge and (2) a broader and slower red shifted band.¹ In commercial "color filter glass", these bands are inhomogeneously broadened due to the broad distribution of particle sizes. The lifetime and bandwidth of the fast states are of order 10 ns and 100 meV respectively, while those of the slow states are 1 μ s and 400 meV. At low excitation densities, the fast doublet emission is dominated by the lower energy band which results from recombination through saturable shallow traps. At higher excitation densities, the fast doublet is dominated by the higher energy band which results from direct band-band recombination.²

The fast photoluminescence emission band in several types of commercial cutoff filter glass is superlinear in pulsed laser excitation fluence over the range 0.1 to 4 mJ/cm².^{3,4} Over the same range, the slow band is linear while the fast band is superlinear⁵ (though at a lower range of excitation fluence, less than 0.001 mJ/cm², the slow band is sublinear while the fast band is superlinear⁶). In this paper, we report the dependence of the fast photoluminescence intensity in CdS_{0.5}Se_{0.5} doped glass on (1) excitation fluence over the range 0.2 to 8 mJ/cm² and (2) particle size over the range 1.1 to 8.4 nm.

The fast photoluminescence emission results from radiative band to band recombination in the nanocrystallites. For simplicity, we assume that the excitation laser pulse deposits all its energy simultaneously into a cylindrical volume τ :

$$\tau = \frac{A}{\alpha(\lambda)} \quad (1)$$

where α is the bulk absorption coefficient of the semiconductor doped glass
 λ is the excitation wavelength
 A is the cross sectional area of the excitation pulse

The total excited volume of nanocrystallites only is:

$$\tau_N = \left(\frac{A}{\alpha} \right) f_N \quad (2)$$

where f_N is the volume fraction of nanocrystallites.

The number N_{NC} of nanocrystallites in the volume τ is:

$$N_{NC} = \frac{6Af_N}{\alpha\pi d^3} \quad (3)$$

Following absorption of a laser excitation pulse, the average number Q_x of excited electron-hole pairs per nanocrystallite is:

$$Q_x = \frac{\alpha\pi d^3}{6f_N h\nu} F_x \quad (4)$$

In figure 1, F_x is plotted as a function of nanocrystallite diameter for $Q_x = 2$ electron-hole pairs per nanocrystallite. Higher excitation fluence is required to generate multiple electron-hole pairs in smaller nanocrystallites than in larger nanocrystallites.

The absorption coefficient α in (4) is generally a non-linear function of excitation intensity which saturates at higher intensities due to band-filling⁷ and/or absorption by electrons trapped in the host glass.⁸

$$\alpha = \frac{\alpha_0}{1 + \frac{F_x}{F_s}} \quad (5)$$

Substitution of (5) into (4) yields the expression for the average number of electron-hole pairs per nanocrystallite as a function of particle size and excitation fluence, and including a mechanism for absorption saturation.

$$Q_x = \frac{\alpha_0\pi d^3}{6f_N h\nu} \left[\frac{F_x F_s}{F_x + F_s} \right] \quad (6)$$

where F_s is a saturation excitation pulse fluence.

Each nanocrystallite can only contain an integral number of photoexcited electron-hole pairs 0, 1, 2... at a particular time. The number of particles with j excitations is:

$$N(j) = N_{NC} P(j) \quad (7)$$

The probability of a *particular* nanocrystallite having j electron-hole pairs when the *average* number of electron-hole pairs per particle is Q_x is:

$$P(j) = \frac{Q_x^j e^{-Q_x}}{j!} \quad (8)$$

Equation (8) is the Poisson distribution for random partitioning of a quantity of electron-hole pairs into a quantity of available nanocrystallites⁹, plotted in figure 2 for several values of j . We have assumed in (8) that the probability of a particular excitation photon being absorbed by a particular nanocrystallite is independent of the nanocrystallites size and electron-hole pair population; in other words, that the absorption coefficient α is not a function of d or a function of j . These are reasonable assumptions as long as the excitation wavelength is deep in the absorption band, a region where α is very large. Note that the first term in equation (8) is the zero population term and does not contribute to radiative recombination. If the particles containing j electron-hole pairs recombine with an efficiency of ϕ_j , then the radiative recombination rate should scale as follows.

$$L(Q_x) \sim e^{-Q_x} \sum_{j=1}^{\infty} \frac{\phi_j Q_x^j}{j!} = e^{-Q_x} \left(\phi_1 Q_x + \frac{\phi_2 Q_x^2}{2} + \dots \right) \quad (9)$$

For Cd(S,Se) at low photoexcitation fluence, radiative recombination of electron-hole pairs is *geminate* and scales linearly with the minority carrier concentration. At higher photoexcitation density, radiative recombination is *non-geminate* and scales quadratically with minority carrier concentration.¹⁰ For n-type¹¹ Cd(S,Se), the radiative recombination rate can be written:

$$L(p) = ap + bp^2 \quad (10)$$

where p is the minority carrier density
 a is the geminate coefficient
 b is the non-geminate coefficient

Note that equation (10) is essentially the first two terms of equation (9), and should be valid for excitation fluences resulting in the majority of nanocrystallites having two or fewer electron-hole pairs. Since p in equation (10) scales with Q_N in equation (6), equation (10) can be rewritten as an explicit function of excitation fluence including absorption saturation:

$$L(F_x) = A(d) \left[\frac{F_x F_s}{F_x + F_s} \right] + B(d) \left[\frac{F_x F_s}{F_x + F_s} \right]^2 \quad (11)$$

where $A(d)$ is the size dependent geminate coefficient
 $B(d)$ is the size dependent non-geminate coefficient.

Figure 1 - Excitation fluence required to generate an average of two electron-hole pairs per nanocrystallite as a function of particle size - Samples with smaller particles require a higher level of excitation fluence in order to generate multiple excitations per nanocrystallite.

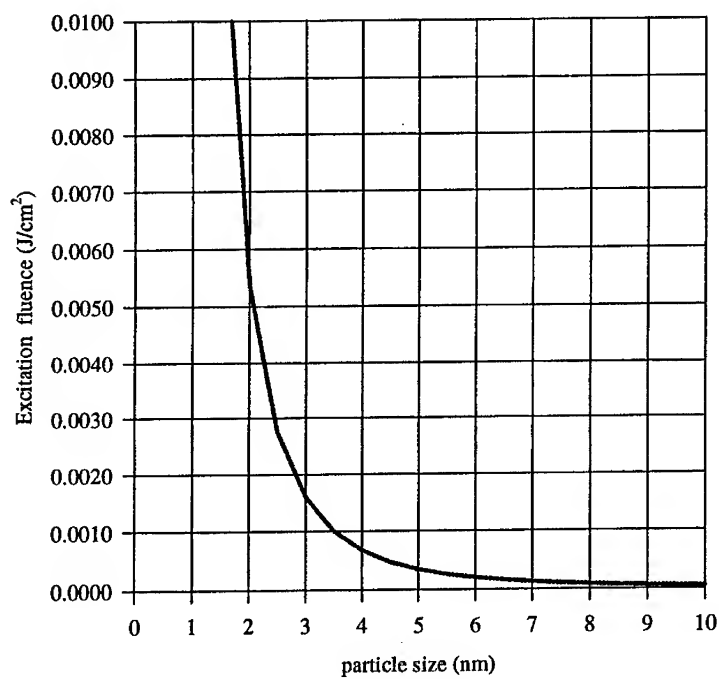
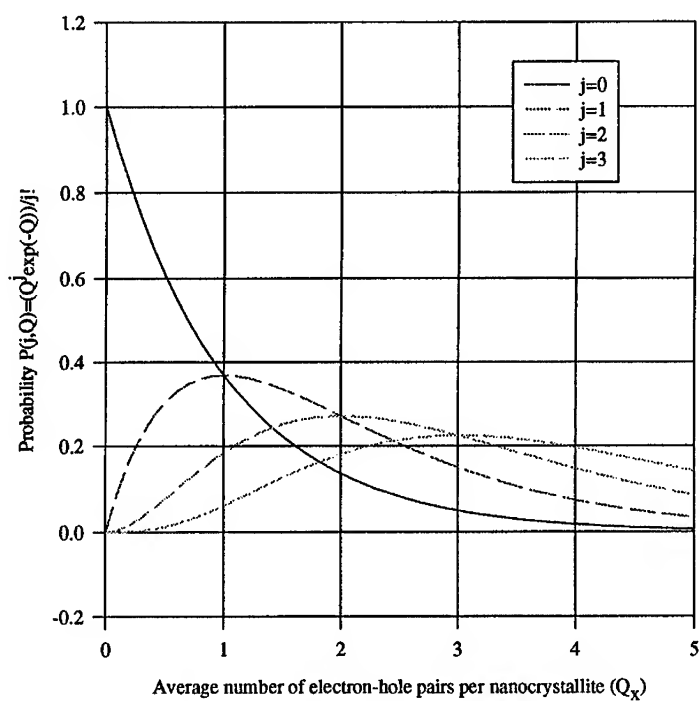


Figure 2 - Poisson distribution - Poisson counting statistics were used to calculate the probability that a particular nanocrystallite contains j electron-hole pairs when the average number of electron-hole pairs per nanocrystallite is Q .



Experimental

Samples of several mm square area and about 100 μm thick were cut from a single large slab¹² of unstruck of $\text{CdS}_{0.5}\text{Se}_{0.5}$ doped glass. Three samples were annealed for one hour at 625, 650, and 700 degrees C, resulting in different particle size distributions. The average particle size of the three samples was measured with x-ray diffraction to be 1.1, 4.5, and 5.4 nm respectively. In addition, a sample of as-received Schott RG630 with the same composition was used; this sample had an average particle size of 8.4 nm. Absorption spectra were measured with a scanning uv/vis spectrophotometer. The samples were mounted in a 77K liquid nitrogen cryostat and the photoluminescence emission spectra were measured as a function of excitation fluence using a nitrogen pumped dye laser at 564 nm (2.20 eV) for the RG630 sample and 440 nm (2.82 eV) for the others. Fast emission was separated from slow emission through time gating. The full details of the experimental setup have been previously described.¹³

Results and discussion

Normalized absorption and photoluminescence emission spectra for the four samples are shown in figure 3. The integrated photoluminescence emission intensities are shown in figure 4 as a function of excitation fluence. Note that the sample with the largest particles is the most superlinear in the fast photoluminescence emission channel. The integrated intensity of the slow channel for one of the samples is also plotted on the same graph.

The data in figure 4 was fit to equation (11) using least squares. The resulting coefficients are summarized in table 1 and plotted vs. particle size in figure 5. For comparison, a cuvette of rhodamine dye was scanned at 298K and fit to equation (11); the photoluminescence was linear over the entire range. Note that the geminate coefficient is dominant for smaller particle sizes and the non-geminate coefficient is dominant for larger particle sizes. Two sets of coefficients were obtained by fitting two independent sets of excitation fluence scans; only one scan per sample is shown in figure 4.

Table 1 - Best fit parameters resulting from least squares fit of data in figure 4 to equation (11)

sample	size (nm)	A_{NC}	B_{NC}	$F_0 (\text{J/cm}^2)$
rhodamine		$9,100 \times 10^3$		
RG630 fast	8.4	0	130×10^6	0.01
RG630 slow	8.4	85×10^3	1.2×10^6	0.1
700C #1	5.6	0	180×10^6	0.0062
700C #2	5.6	0	110×10^6	0.0062
650C #1	4.5	3.8×10^3	120×10^6	0.0022
650C #2	4.5	0	17×10^6	0.025
625C #2	1.1	70×10^3	14×10^6	0.044
625C #2	1.1	18×10^3	13×10^6	0.012

Figure 6 shows the full width at half maximum (FWHM) of the photoluminescence emission pulse as a function of excitation fluence. Our measurement electronics is not fast enough to measure actual decay lifetimes, but the FWHM scales with lifetime. Note that the FWHM decreases as the emission evolves from geminate to non-geminate. Figure 7 shows the average FWHM, read from figure 6, as a function of particle size for the geminate and non-geminate cases.

Figure 3 - Absorption and photoluminescence emission spectra - The normalized absorption spectrum is shown for each sample along with the fast component of the photoluminescence emission spectrum. Since the photoluminescence was done at 77K and the absorption was done at 298K, the absorption spectra were blue shifted by 0.11 eV prior to plotting. The 8.4 nm sample was excited at 564 nm, all others were excited at 440 nm.

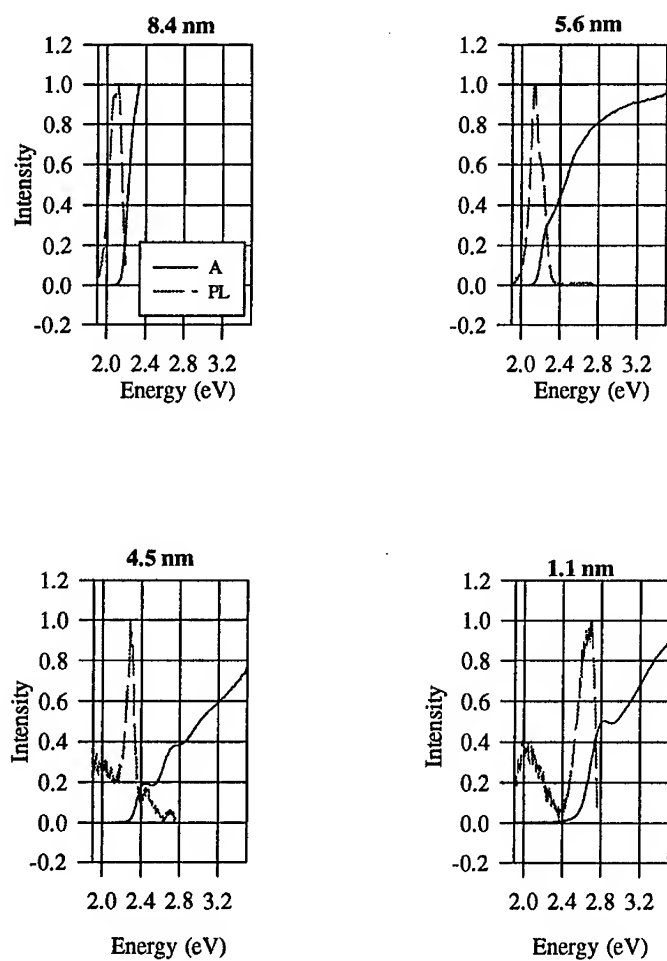


Figure 4 - Fast PL fluence vs. excitation fluence - The integrated fast photoluminescence emission fluence is plotted as a function of excitation fluence for all four samples. The slow component is plotted for the 8.4 nm sample. The curves are the result of least squares fitting to equation (11).

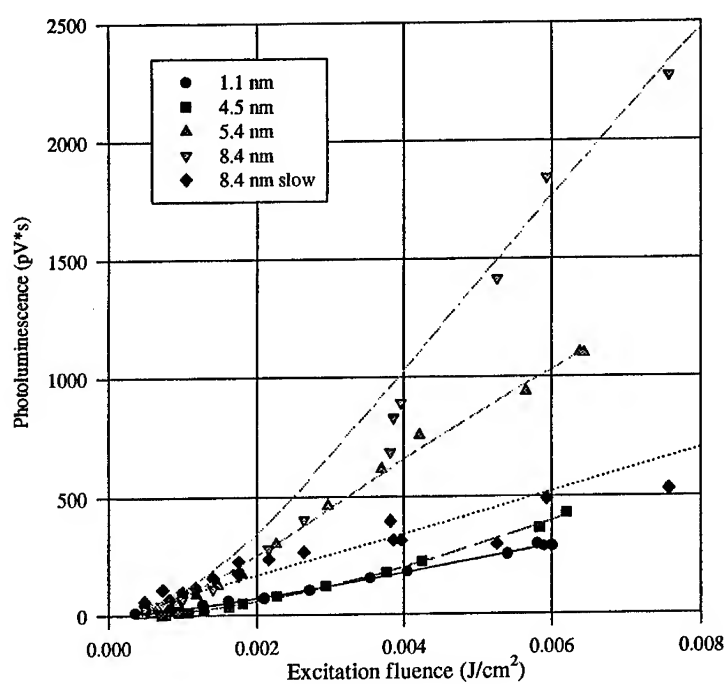


Figure 5 - Geminate and non-geminate coefficients A and B vs. particle size - The coefficients A and B in equation (11) were obtained by least squares fitting the data in figure 4. Two independent sets of data were fit for the three smaller samples, so two values of A and B are shown. Only one data set is plotted in figure 4.

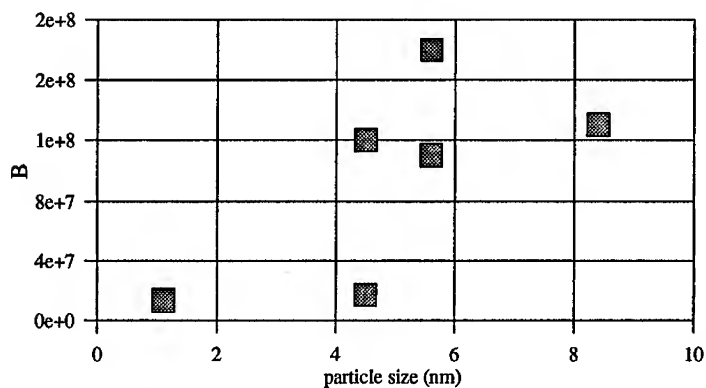
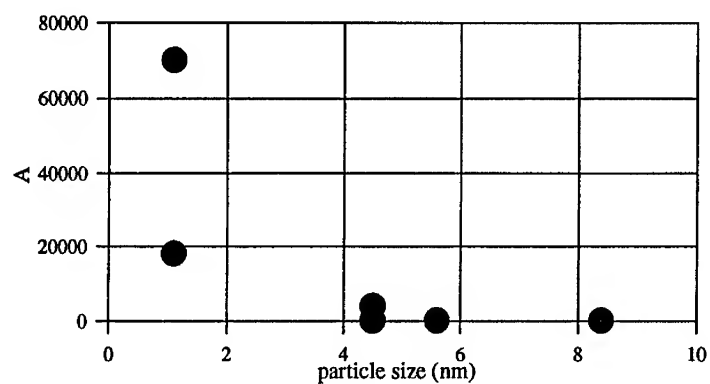


Figure 6 - FWHM vs. excitation fluence - The transition from geminate to non-geminate recombination is marked by a decrease in photoluminescence lifetime.

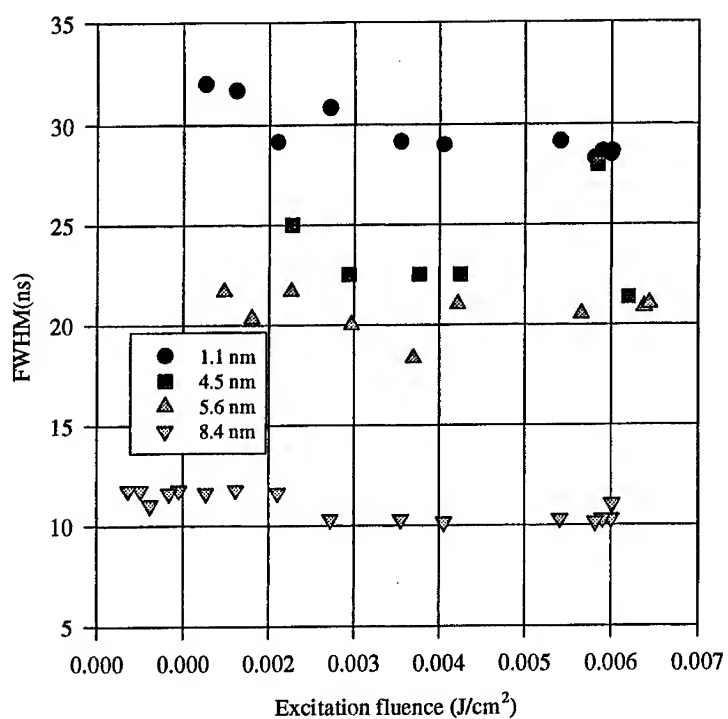
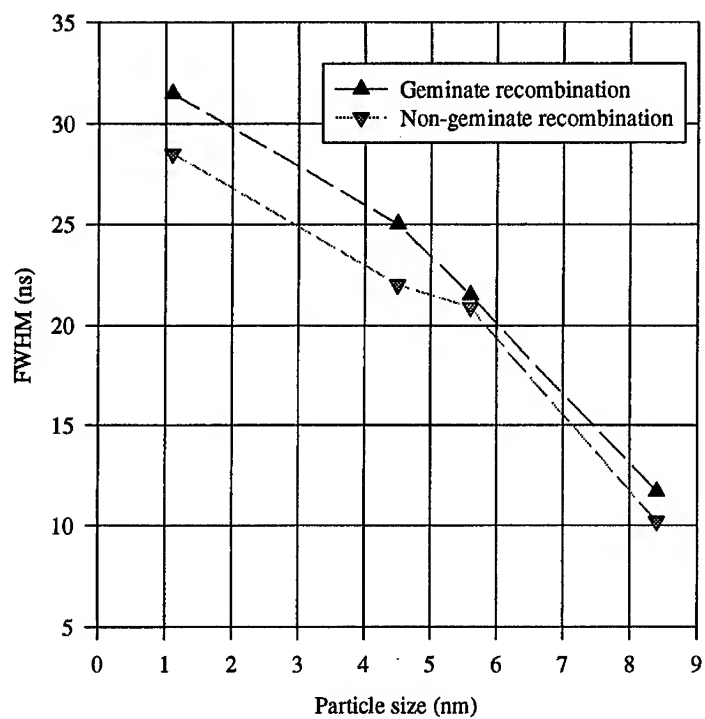


Figure 7 - FWHM vs. particle size for geminate and non-geminate recombination - The average FWHM for geminate and non-geminate recombination was read from figure 6 for each particle size. The smaller particles have a longer observed lifetime.



Summary

Photoluminescence emission fluence from 1.1 to 8.4 nm Cd(S,Se) nanocrystallites in glass is superlinear in pulsed excitation fluence over the range 0.2 to 8 mJ/cm^2 . The superlinearity results from a transition from geminate to non-geminate recombination as the number of electron-hole pairs per nanocrystallite increases. Over the range investigated, larger nanocrystallites exhibit the highest degree of superlinearity, since for a given excitation fluence larger nanocrystallites are more likely to be multiply excited. The photoluminescence lifetime decreases with the onset of superlinearity for all nanocrystallite sizes, and smaller nanocrystallites exhibit a longer lived excited state.

References

- ¹Zheng, J.P., and H.S. Kwok, *J. Opt. Soc. Am. B*, **9**, 2047 (1992).
- ²Hache, F., M.C. Klein, D. Ricard, and C. Flytzanis, *J. Opt. Soc. Am. B*, **8**, 1802 (1992).
- ³Zheng, J.P., L. Shi, F.S. Choa, P.L. Lium and H.S. Kwok, *App. Phys. Lett.*, **53**, 643 (1988).
- ⁴Kull, M., and J-L Coutaz, *J. Opt. Soc. Am.*, **7**, 1463 (1990).
- ⁵Stokes, E.B., PhD dissertation, Rensselaer Polytechnic Institute, Troy, NY, August 1996.
- ⁶Tomita, M., T. Matsumoto, and M. Matsuoka, *J. Opt. Soc. Am. B*, **6**, 165 (1989).
- ⁷Shimizu, A., and K. Fujii, *Nonlinear Optics*, **1**, 149 (1991).
- ⁸Gomes, A.S.L., R.M. Balachandran, and N.M. Lawandy, *J. Lum.*, **60/61**, 640 (1994).
- ⁹Matthews, J., and R.L. Walker, *Mathematical Methods of Physics*, Addison-Wesley, Redwood City, CA, p. 379 (1970).
- ¹⁰Kull, M., and J-L Coutaz, *J. Opt. Soc. Am.*, **7**, 1463 (1990).
- ¹¹Devlin, S.S., "Transport properties", in *Physics and chemistry of II-VI compounds*, edited by M. Aven and J.S. Prener (North-Holland, Amsterdam, 1967), p.588.
- ¹²Schott Glass Technologies, Duryea, PA.
- ¹³Stokes, E.B., P.D. Persans, and K.L. Stokes, *Electrochem. Soc. Proc.*, **95-17**, 248 (1996).

Optical properties of PbS nanocrystals

M.Sirota*, E. Lifshitz*, M.Folman*, R. Chaim[#]

*Department of Chemistry, #Department of Materials Engineering,
Technion - Israel Institute of Technology, Haifa, 32000, Israel

ABSTRACT

Nanometer sized particles of Lead Sulfide were grown under excess sulfur conditions and were embedded in polyacrylamide films. The particles show spherical shape with cubic crystal structure. The absorption and photoluminescence excitation spectra show a substantial blue shift (up to 2 eV) with decreasing particle size, due to a strong quantum size effect. The photoluminescence (PL) spectra consist of exciton and surface imperfection bands. The emission decay curves of the latter PL band suggest a donor-acceptor or trapped electron-hole recombination mechanisms. The trapping sites are associated with stoichiometric defects.

INTRODUCTION

The nanometer size particles (nanoparticles) of Lead Sulfide, PbS, have shown an increase interest in the last decade, due to their unique physical properties. PbS nanoparticles have been prepared in colloidal solutions [1-5], or embedded in transparent solid media (glass, zeolite and polymers) [6-10]. Bulk PbS has a cubic (rock salt) crystal structure and a narrow direct band gap (0.41 eV) at the L point of the Brillouin zone [1,2,11,12]. This point is well separated from all the other bands, thus size quantization will influence mainly the valence and conduction band edges. Moreover, the high dielectric constant (17.3), the narrow band and the small electron effective mass ($<0.1 m^*$) [1,2,5,6] creates an exciton with large effective Bohr radius (180 Å) and relatively weak binding energy [1,5,11]. The aforementioned properties suggest that size quantization possesses strong influence on the electronic properties of PbS nanoparticles.

The present report describes an investigation of PbS nanoparticles prepared under excess sulfur conditions and embedded in poly(acrylamide-co-acrylic acid) (PAA) polymer films. This paper emphasizes the optical properties of the studied materials, utilizing absorption, photoluminescence (PL), PL excitation and time resolved PL spectroscopy.

EXPERIMENTAL

Sample preparation:

PbS nanoparticles were embedded in polymer films and were deposited on a glass substrate, according to the procedure described in reference [6]. Initially, solution A was prepared by dissolving 1 g of PAA in 225 ml distilled water. Solution B was made by dissolving 1 g. of $\text{Pb}(\text{NO}_3)_2$ in 200 ml distilled water. Solution C was prepared by mixing 2 ml of solution B with 2.5-2.7 ml of solution A and diluted with distilled water. Then, a solution of Tio-UREA ($\text{H}_2\text{N}\cdot\text{CS}\cdot\text{NH}_2$) was added to solution C to obtain a molar ratio of $\text{Pb}^{2+}/\text{S}^{2-}=1/20$. The mixed solution was spread on a glass substrate and the excess water was evaporated by heating the covered substrate at a temperature of 348K, for 12 hours. The evaporation was done either under vacuum or in air. The anhydrous product was a PAA film, incorporating the PbS nanoparticles.

Instrumental:

The shape and the size of the particles were determined by transmission electron microscopy (TEM, JEM FX-2000), while the crystallographic structure was determined by electron diffraction.

The absorption or emission spectra were recorded by immersing the sample in a cryogenic dewar. The samples were excited either by a Xenon arc lamp or by an Ar⁺ laser. The transmitted or emitted light was passed through a monochromator and was detected by a PMT or PbS detector. The emission decay curves were recorded by scanning a synchronized gated window utilizing a box car averager.

RESULTS

PbS nanoparticles, embedded in the PAA polymer films were prepared with various average particles size. The latter were controlled by changing the concentration of the primary solutions and the excess solvent vaporization procedure. The transmission electron micrographs (TEM) indicated that the average size of several specimens was in the range of 8 to 2000 Å, with Gaussian distribution and standard deviation of about 20%. The color of the film changed gradually from -brown to dark-yellow, as the average particles' size decreased. Moreover, the TEM images indicated that the particles were spherical, regardless of their size. The electron diffraction indicated that the nanoparticles had a cubic (rock salt) crystal structure, with high degree of crystallinity.

The absorption spectra of the various samples were recorded at room temperature. Representative spectra of samples with average radius of 8 Å and 21 Å are shown in figure 1, by the solid lines. The spectra consist of a long featureless tail, mainly in the visible and UV region. Only few spectra contain a weak exciton shoulder at the bottom of the tail. However, most of the absorption curves are overlapped by a pronounced band, centered at 3.45 eV. The absorption tails show pronounced blue shift with decreasing particle size. On the contrary, the position of the 3.45 eV band is independent of the particle size. Representative photoluminescence excitation (PLE) spectrum of the 21 Å sample is shown in figure 1, by the dashed line. The latter show strong similarity to the corresponding absorption spectrum.

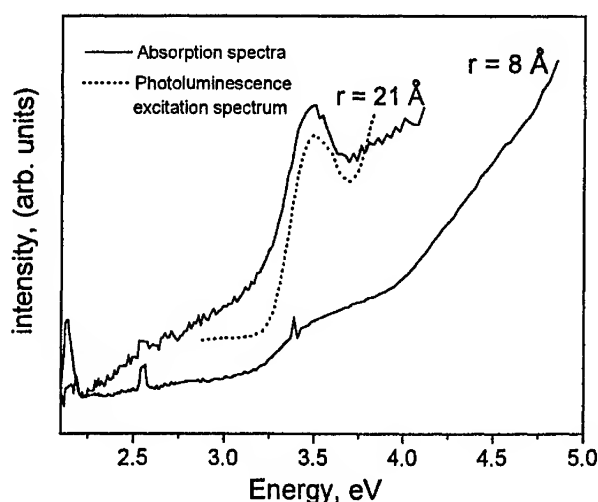


Figure 1: The absorption (solid line) and photoluminescence excitation (dashed line) spectra of PbS nanoparticles with average particles' radius as indicated in the figure.

The PL spectra of the prepared samples were recorded in the temperature range 1.4K to 250K and were excited either with UV (3.35-3.65 eV) or visible (2.7 eV) light. Representative spectra of a sample with 21 Å average particle size and excited with a UV light, are shown in figure 2.

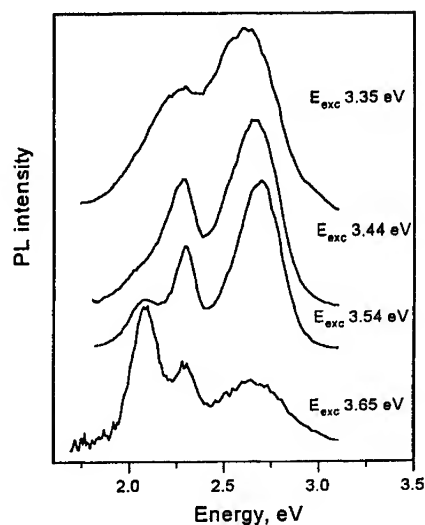


Figure 2: Photoluminescence spectra of PbS nanoparticles with mean radius of 21Å, excited with UV light source, as indicated in the figure.

These spectra consist of three bands centered at 2.74 eV (blue), 2.25 eV (green) and 2.06 eV (red). It should be noted that the intensity of the blue band is enhanced when the excitation is nearly in resonance. Excitation in the visible range leads to substantially different emission spectra. Comparison of the PL curves, excited in the visible and UV are shown in figure 3. The latter are recorded on samples with various average radii, at 77 K. The spectrum on the left corresponds to excitation at 2.71 eV, while the right column of the figure corresponds to excitation at 3.65 eV. The series of spectra on the right indicate that the intensity of the 2.52 eV (blue) and 2.25 eV (green) bands decreases, while the intensity of the 2.06 eV (red) band increases with decreasing particle size. Moreover, the high energy band is blue shifted between 2.52 to 2.74 eV with decreasing particle size, while this shift is not pronounced in the deeper emission bands. Excitation at 2.71 eV leads to PL spectra that consist of a dominating broad band, covering the visible red or near IR region.

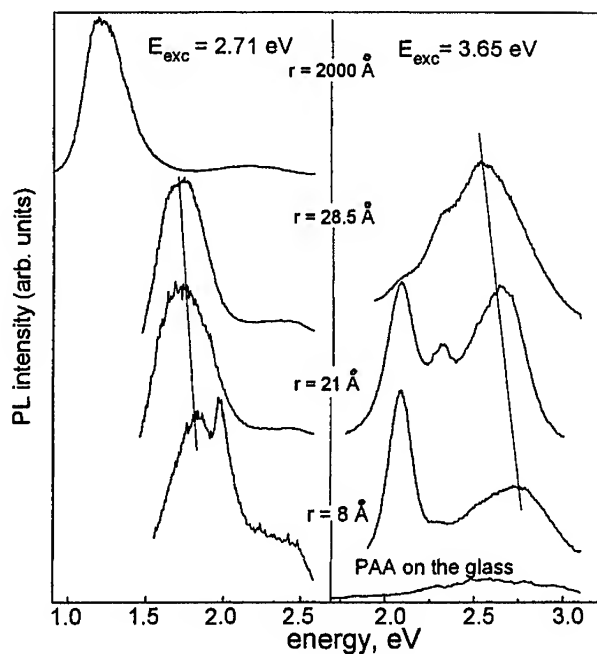


Figure 3: Photoluminescence spectra of PbS nanoparticles with various mean radii, excited with UV (right side) and visible (left side) light.

The emission of the PAA deposited on a glass substrate was recorded as a reference and is shown at the bottom of figure 3. This control experiment confirms that the aforementioned PL spectra correspond entirely to the PbS nanoparticles.

The insert in figure 4 shows representative PL spectra of a sample with an average particle size of 21 Å, recorded at various temperatures and excited with 3.65 eV. The dependence of the integrated intensities of the various bands on the inverse of the temperature is shown in figure 4. The figure shows that the blue band intensity decreases with the increase in temperature. On the contrary, the green and red bands show enhancement of the luminescence intensity followed by quenching with the increase in temperature.

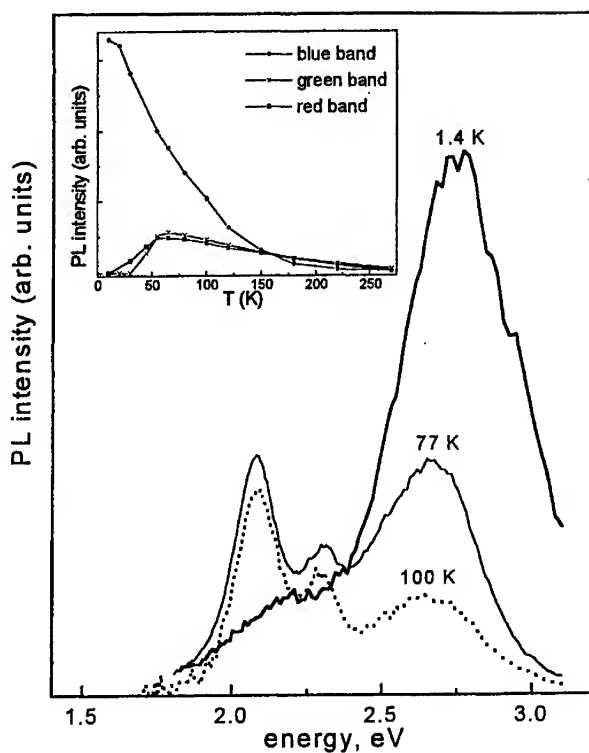


Figure 4: Photoluminescence temperature dependence of the 21 Å particles' sample. Insert: Intensity of the photoluminescence bands versus temperature.

The decay of the luminescence processes were examined in the microsecond range at the temperature of 77K. Representative decay curves recorded at various energies within the red-IR band are shown in figure 5. Obviously, the high energy sites of the band decay faster than the low energy site of that band.

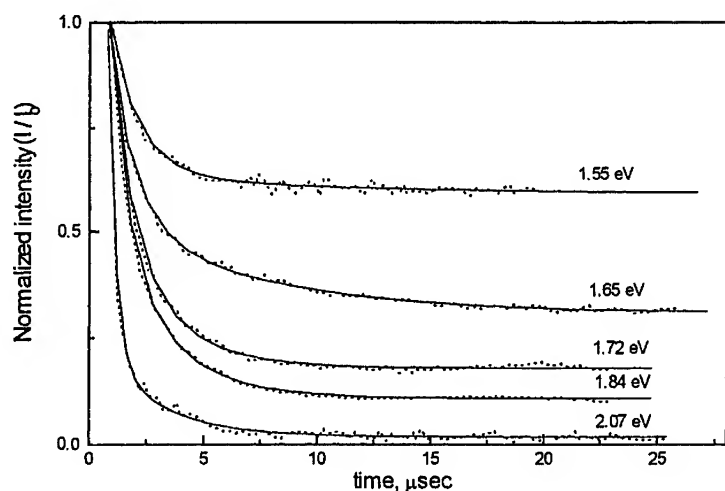


Figure 5: Plot of luminescence intensity versus decay time after a laser pulse (decay curves) as recorded at various energies within the IR luminescence band.

DISCUSSION

The TEM and electron diffraction data indicated that the nanoparticles of PbS, embedded in PAA polymer films, preserve their rock salt crystal structure with relatively high degree of crystallinity.

As indicated in the introduction, bulk PbS is a narrow band semiconductor with a gap energy of 0.41 eV. Moreover, the top of the valence and the bottom of the conduction band consist of a wave-function that is separated from the adjacent ones. Therefore, the reduction of particle size mainly influences the separation between the band edges. Due to the large Bohr radius of the exciton in the bulk (about 180 Å), reduction of particle size in the range 8 Å to 28 Å, oppose strong quantum confinement. This is strongly pronounced as a blue shift of the absorption tail as shown in figure 1. The lack of an exciton shoulder at the edge of the tail may stem from the following reasons: (1) inhomogeneous broadening due to size distribution, (2) quenching of the exciton due to the large dielectric constant, small effective electron mass and relatively large Bohr radius. The fact that the 3.45 eV

absorption band position does not depend upon the particle size suggests that it does not have an excitonic character. Instead this band can be associated either with the molecular transition [8,13,15] or contamination of other Pb^{2+} byproduct in the medium [8,14]. The comparison of the absorption spectra with those of monomolecular PbS demonstrates that the 3.45 eV can be tentatively identified as the transition to the excited singlet molecular orbital $\pi^3\sigma^2\pi$, $^1\Sigma^+$ [13]. The effective photoluminescence excitation at 3.45 eV (shown in figure 2 and 3) may support the existence of molecular transitions too. Indeed, the strong confinement in the present case, may create a transition from a bulk to cluster and to molecular like particles, with decreasing particle size.

The photoluminescence contour shape depends on the energy of excitation. Excitation in the UV revealed an exciton emission in the blue region and two additional nonexcitonic bands. The high energy bands correspond to relatively shallow states and therefore, they are influenced by the quantum shift of the valence and conduction bands. The latter is pronounced as a blue shift of the emission bands. The red and green bands, on the other hand, are independent of the particle size due to their deepness within the gap. In addition, the intensity of the red band is enhanced at the smallest particles. This suggests, that this band is associated with surface defects, since the small particles represent relatively large surface site concentration. The green band may be associated with trapped electron-hole recombination at defect site located at the interior part of the nanoparticle. The latter is reduced with decreasing particle size, as shown in the right column in figure 3. The IR emission band, created due to excitation in the visible region, is associated with deep centers and therefore, show minor changes with a change in particle size in the range between 8 Å to 28 Å. Its origin is not clear at the moment, however, the decay curves shown in figure 5, suggest that the latter band has a donor-acceptor type mechanism (vice infra).

The temperature dependence of the PL spectra reveals information on the relaxation processes and the mutual interaction among the states. The continuous decrease of the luminescence intensity of the blue band with the increase in temperature suggests a coupling to lattice phonon that enable a transfer of carriers into nonradiative states. The increase in luminescence intensity of the green and red emission band up to 65 K, suggest that the corresponding states are populated by carrier transfer from exciton states. The latter process is thermally activated. Then above 65 K this thermal activation is competing with population quenching by nonradiative transitions, and thus, the intensity of the green and red bands decreases with further increase in the temperature. The aforementioned thermal activation model has been suggested in the past for several other nanoparticle semiconductors [16-18].

So far, the decay curves of the IR emission band have been examined. These decay curves have been fitted to a theoretical model, given by the solid lines in figure 5. It should be noted that the experimental decay could not be fitted to a

single exponential, however a sum of two exponents already gave quite a good fit. The latter may suggest at least a double or even multi recombination processes. The simulation suggests that the first process has a lifetime between 0.45-1.06 microseconds, while the second process has a lifetime of 5.3-1.19 microseconds, when measured at an energy between 1.55 - 2.07 eV, respectively. Moreover, the contribution of the first process is dominated at the high energy site of the IR emission band, while it is minor in the low energy sites. Therefore, the effective lifetime at the high energy site seems to be shorter than those at lower energies. The high energy site can correspond to a donor-acceptor recombination with relatively short distance between the recombining site, while the low energy site can correspond to the same donor-acceptor pair with relatively large distance between them. The lifetime measurements of the other luminescent bands and their analysis will be further investigated in the near future. Furthermore, the nature of the deep recombining site will be identified by utilizing optically detected magnetic resonance spectroscopy. The latter method is widely applied to many other nanoparticle samples in our laboratory at the Technion.

ACKNOWLEDGMENTS

This work was supported by Israel Ministry of Science and USA-Israel Binational foundation.

REFERENCES

1. R.Rossetti, R.Hull, J.M.Gibson and L.E.Brus, J. Chem. Phys. 83, 3, 1406 (1985).
2. A.J.Nozik, F.Williams, J. Phys. Chem. 89, 397 (1985).
3. J.L.Machol, F.W.Wise, R.Patel, D.B.Tanner, Physica A, 207, 427 (1994).
4. M.Gao, Y.Yang, B.Yang and J.Shen, X.Ai, J. Chem. Soc. Faraday Trans. 91, 22, 4121 (1995).
5. T.Kyprianidou-Leodidou, W.Caseri, and U.W.Suter, J. Phys. Chem. 98, 8992 (1994).
6. M.Mukherjee, A.Datta, and D.Chakravorty, Appl. Phys. Lett. 64, 9, 1159 (1994).
7. W.Chen, Z.Wang, Z.Lin, J.Qian, and L.Lin, Appl. Phys. Lett. 68, 14, 1990 (1996).
8. Y.Wang, A.Suna, W.Mahler, and R.Kasowski, J. Phys. Chem. 87, 12, 7315 (1987).
9. Y.Wang and N.Herron, J. Phys. Chem. 95, 525 (1991).
10. Hirokazu Miyoshi, Mikio Yamachika and Hiroshi Yoneyama, Hirotaro Mori, J. Chem. Soc. Faraday Trans. 86, 5, 815 (1990).
11. Y.Wang and N.Herron, J. Phys. Chem. 91, 257 (1987).
12. R.S.Kane, R.E.Cohen, and R.Silbey, J. Phys. Chem. 100, 7928 (1996).

-
13. D.E.Biss, J.P.Wilcoxon, P.P. Newcomer and G.A.Samara, Mater. Res. Soc. Symp. Proc. 358 (Microcrystalline and Nanocrystalline Semiconductors), 265, (1995)
 14. S.Gallardo, M.Gutierrez, A.Henglein, and E.Janata, Ber. Bunsenges. Phys. Chem. 93, 1080 (1989).
 15. C.Y.Yang and S.Rabii, J. Chem. Phys., 69, No 6, 15 September (1978)
 16. E.Lifshitz, M.Yassen, L.Bykov, I.Dag, J. of Luminescence 70, 421 (1996).
 17. A.Eychmuller, A.Hasselbarth, L.Katsikas, and H.Weller, Ber. Bunsenges. Phys. Chem. 95, 79 (1991).
 18. M.O'Neil, J.Marohn, and G. McLendon, J. Phys. Chem. 94, 4356 (1990).

QUANTUM CONFINEMENT IN SILICON

Raphael Tsu, Adam Filios, Clay Lofgren, Jinli Ding and Qi Zhang
University of North Carolina at Charlotte, Charlotte NC 28223 USA

Jonder Moraes
UNICAMP, Fisica Aplicada, Campinas, Brazil
and

C.G.Wang
Nanodynamics, Inc., New York NY 10021, USA

ABSTRACT

Quantum confinement in silicon is demonstrated in the following cases: (1) A superlattice barrier consisting of thin silicon epitaxial layers sandwiched between adsorbed oxygen up to an exposure of 10 Langmuirs shows an effective barrier height. Modeling the measured I-V as a function of temperature gives an effective barrier height of 0.5eV at room temperature. This SLB, superlattice barrier, allowing the continuous epitaxial growth, forms the basis of silicon quantum devices. (2) A superlattice consisting of nanoparticles of silicon embedded in an oxide matrix, the Si/Interface adsorbed Gas, Si/IAG multilayer structure shows visible luminescence, including the case where the silicon sandwiched between adsorbed oxygen layers is amorphous. (3) Comparison of PL with nanoscale silicon clusters embedded in an oxide matrix fabricated by co-sputtering.

INTRODUCTION

The lack of a suitable heterojunction barrier for silicon has prevented silicon from playing a significant role in quantum devices. Short period strain-layer superlattice (SLS) of Si/Ge [1] showed high quality and defect free epitaxial growth on Ge(001) substrate. However, the low value for the barrier height limits the utility to low temperature applications. Besides, the carrier confinement is in the Ge layers. Silicon dioxide with a barrier height of 3.2 eV in the conduction band of silicon is amorphous, preventing the building of a quantum well structure on top of the a-SiO₂ barrier. Several years ago, it was proposed that the oxides of one or two monolayers may allow the continuation of epitaxy [2]. In trying to realize the SLB (Superlattice Barrier) with thin silicon layers separated by thin oxides, a new method involving the exposure of oxygen followed by epitaxial growth of silicon using the RHEED as a measure of epitaxy was introduced. [3] It was established that with several L (Langmuir) of oxygen exposure, the silicon reconstructed 1X2 surface RHEED pattern may disappear, particularly after several

monolayers of silicon is deposited. However, the 1×2 surface reconstruction can reappear after several more monolayers of silicon are deposited. What is important to note is the fact that epitaxial growth of silicon can indeed be continued. We have not established whether the continuation of epitaxy is because the adsorbed oxygen does not provide a full coverage, or the oxygen in the interface forms a strain-layered oxide. Although this is of fundamental importance, the appearance of a barrier is technologically important regardless what is exactly the mechanism. We are not satisfied with obtaining the effective barrier height by fitting the I-V as done previously[3]. In this work we present a new method to measure the barrier height using the Arrhenius plot of the temperature dependent I-V. We found that the barrier height is lower than what was obtained previously, nevertheless, a value up to 0.5eV or more is obtained.

We have previously reported the observation of photoluminescence, PL from a multilayers of silicon separated by adsorbed gases such as oxygen and oxygen+ hydrogen, in what we called Si/IAG, silicon / interface adsorbed gas superlattice[4]. In this scheme, the deposition of silicon is usually at room temperature so that the deposited silicon is amorphous separated by adsorbed oxygen. Upon annealing at 800-850 C, nanoscale silicon particles are produced. Since in this case, the silicon layer is amorphous, we usually expose to oxygen up to 100L. In fact we stopped at 100 L because it takes too long to prepare the sample, because we usually prepare at least 9 period to augment the total volume for higher PL. What is new in the present work is the inclusion of amorphous superlattice by eliminating the annealing as reported by Lockwood et. al.[5]. Also we have raised the temperature for both deposition and gas adsorption. We found that PL for the former, from thin amorphous region, is not as strong as that of the latter, where the deposited silicon is crystalline. It is possible that the higher temperature process allows more oxygen to reach the cluster of silicon by surrounding the cluster for better quantum confinement.

Thirdly, we have included the cluster deposition employed by Zhang [6] for comparison purposes. Although the basic mechanism of quantum confinement is the same, the cluster formation is radically different from Si/IAG. In this case, diffusion and original defect centers dictate the cluster size, while the superlattice cases, adsorbed gases serve to limit the grain growth.

DETERMINATION OF THE BARRIER HEIGHT OF THE Si SLB

It seems so straightforward to measure the current at some fixed voltage at various temperature. An Arrhenius plot would directly give the value of an activation energy, which should be the barrier height. In reality, due to the barrier height of 0.5eV or higher, it is necessary to make measurements at too high temperatures. We have developed a method to deal with this problem. The detail will appear elsewhere [7]. For convenience, we shall sketch the salient procedure here. Since the superlattice barrier is formed similar to a double barrier quantum well structure where the ground state energy level is raised to E_1 . We shall show that the measured activation energy is closely approximated by $E_a = E_1 - eV/2$, where V is the voltage applied to a symmetric system of a double barrier structure[8],and

$$E_a = \int E_1 j(E_1) dE_1 / \int j(E_1) dE_1 \quad , \quad (1)$$

in which E_t is the longitudinal energy perpendicular to the layers, and $j(E_t)$ is the current at E_t . If we approximate the transmission probability in Ref. 8 by a Lorentzian centered at the given quantum state superimposed on an exponential which describes the background tunneling at finite temperature, we found that

$$E_a(T) = E_t - eV/2 + c_2 T, \quad kT > E_t - eV/2 - E_f. \quad (2)$$

Next we calculate $E_a(T)$ directly using $E_a(T) = -\partial \ln I / \partial (1/kT)$. At $T=0$, the direct calculation of $E_a(T)$ is $E_t - eV/2$ which shows that the activation energy is nothing but the averaged energy of the energy flow defined by (1). Using this model, we proceeded to measure $I(T)$ typically for $T \sim 300$ - 500 K, and using the Arrhenius plot to determine $E_a(T)$ experimentally, and thus E_a and the barrier height $E_b = E_a(V=0)$.

Typically we expose the clean silicon surface to oxygen up to 10L (1 Langmuir is 10^{-6} Torr of oxygen at 100 sec.), and epitaxial silicon is grown at a deposition temperature of 550 C at a rate of 0.4 \AA/s . Our typical diode structure consists of 200Å of Sb doped silicon buffer on 0.01 Ωcm (100) n-type silicon wafer, followed by oxygen exposure and 11Å of silicon deposition, and second oxygen exposure and followed by 200Å of Sb doped silicon, and topped by an aluminum contact for I-V measurements. The diode size varies between $10 \mu\text{m} \times 10 \mu\text{m}$ to $40 \mu\text{m} \times 40 \mu\text{m}$. Figure 1a shows our typical I-V for an exposure of L of oxygen. The measured I-V for $T=300$ K to 500K is shown in Fig. 1b, and the determined effective barrier height versus oxygen exposure is shown in Fig. 1c.

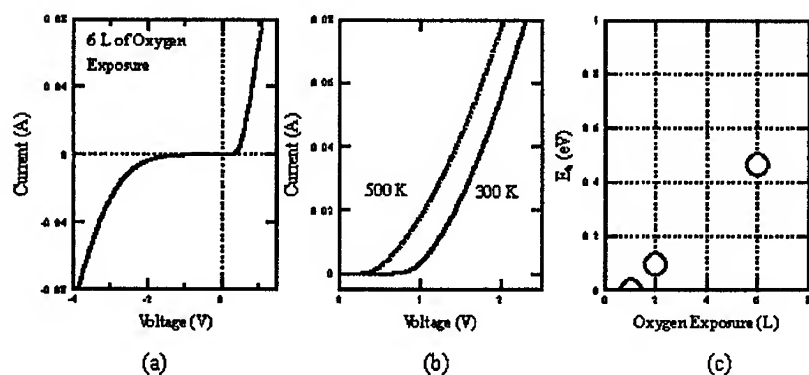


Fig. (1). (a) Current vs Voltage of a SLB with 6L oxygen exposure, (b) Temperature dependent I-V, and (c) Effective Barrier-height E_b vs Oxygen Exposure in L

Note that the activation energy depends on the voltage, and the barrier height E_b is E_t . In other words, the effective barrier height is nothing but the first quantum states of the quantum confined system, in this case, the first energy state of the double barrier structure.

PHOTOLUMINESCENCE IN Si/IAG

Previously we have reported visible luminescence in multilayer structure consisting of nanoscale silicon particles sandwiched between adjacent adsorbed gases such as oxygen and oxygen + hydrogen[4]. The main idea is to use the adsorbed oxygen to break up the a-Si into layers. Upon annealing, the particle size will be limited by the distances between these adsorbed oxygen layers. Since it is known that whenever the layers are too thin, usually below 10nm, it is increasingly difficult to crystallize the a-Si layers [9]. Therefore in the reported work (Ref. 4), the a-Si layer was typically 10nm or more. Figure 2a shows the cross-section TEM of a nine period sample on (100) silicon substrate, with 10nm for the nominal thickness of the silicon layers separated by adsorbed gases, in this case, oxygen and hydrogen. The PL spectrum is shown in Fig.2b, with preparation similar to that of Fig.2a except the substrate is fused quartz. In all cases, annealing is performed at 800C for 10 to 30 minutes in oxygen or oxygen + hydrogen. In general, the addition of hydrogen results in higher PL efficiency presumably due to passivation of dangling bond defects. Figure 2c shows the progression of crystallization of amorphous silicon taken from Hernandez et al.[10], which will be used in later discussions.

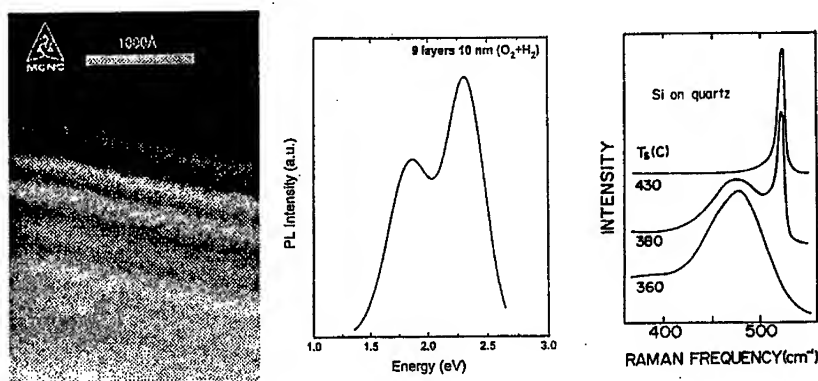


Fig.(2a) Cross-section TEM of a 9-period Si/IAG superlattice
 (2b) PL of the same sample
 (2c) Progression of crystallization taken from Ref.10

As we are partly motivated by the work reported in Ref. 5, and it seems that there is no obvious reason to insist on the crystallinity of the silicon cluster, we proceeded to reduce the thickness of the silicon layer to as thin as 1.2nm. Although we are aware of the constraints presented by the proximity of the adjacent adsorbed gases in trying to form crystallized silicon clusters as described in Ref. 9, it is important to find out what happens even the ultra thin silicon sandwiched between adjacent adsorbed gases is only partially crystalline or even fully amorphous as reported in Ref. 5. Figure 3 shows the PL versus photon energy for six samples with the thickness of the silicon layers 1.2 nm and 2.0 nm, separated by 100 L of oxygen exposure, and deposited at three temperatures, 30C, 300C and 550C, followed by annealing in hydrogen at 420C. Before the hydrogen anneal, PL intensity is very weak. Note that at 30C, according to Fig. 2c, the silicon is primarily amorphous, and therefore the PL peak should show a blue shift, as indicated in the two top curves. Our PL peak at 2.3eV compared closely to that reported in Ref. 5, however, at 2nm, the down shift due to larger dimension is quite small possibly due to a combination of dimensionality of the quantum confinement and the proximity effects of the adsorbed oxygen. Raman scattering shows some crystallinity[11]. The two bottom curves shows the PL for the same samples deposited at 550C. In this case, Raman shows significant crystallization [11], resulted in a red shift from the two top curves. This red shift may be explained in terms of the increased crystallization and subsequent increase in the cluster size. In fact, the bottom curve at 2nm has the PL peak 0.2eV higher, showing that at 2nm either the dimensionality or the crystal size results in higher degree of confinement than the 1.2nm sample. We want to emphasize that this result is consistent with the constraint point of view in Ref. 9. Figure 4 shows the same sample: 30C, 1.2nm after annealing in hydrogen at 420C, in nitrogen at 850C and oxygen at 800C. Note that a blue shift of more than 0.25eV in going from hydrogen to oxygen anneal, indicates the size reduction by oxygen anneal.

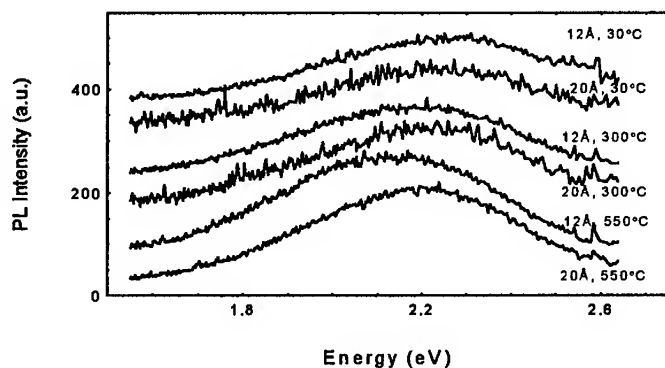


Fig.(3) PL intensity vs Photo energy after H_2 anneal at 420C for 20 min, of Si/IAG samples, with silicon thicknesses, and deposition temperature as shown.

We have shown that the Si/IAG superlattice consisting of thin layers of silicon sandwiched between adsorbed gases serving to limit the grain growth as well as passivation of defects is a powerful new method to take advantage of inducing optical transition in silicon. Thus far, we have a fair qualitative understanding, but somewhat limited in quantitative details. Since all preparation of samples are usually in UHV system, it is possible to acquire more detailed role of defects and impurities.

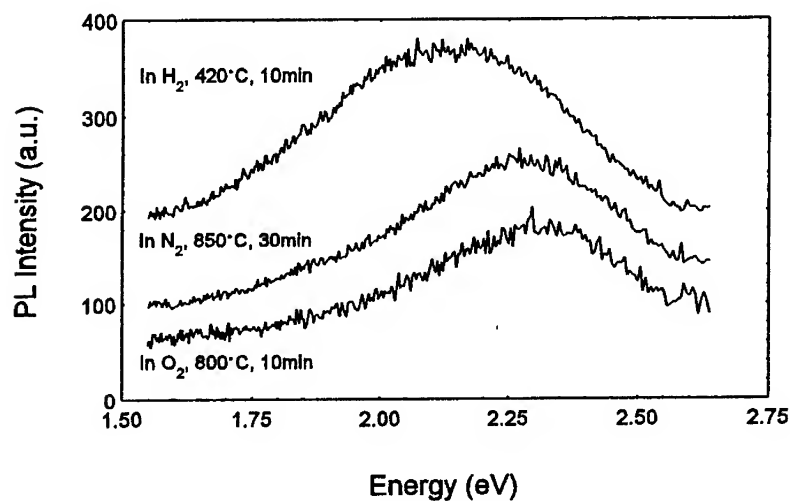


Fig.(4) PL vs Photon energy for the same sample as in Fig.(3) annealed in various gases

SILICON CLUSTERS

Intense visible photoluminescence from red to blue has been observed from annealed Si [12], C [13], and Ge [14], nano-clusters or nanocrystallites (quantum dots) embedded in SiO₂ matrices. The samples of silicon cluster are deposited by rf co-sputtering in a system with base pressure of 2×10^{-6} Torr. The procedure involves the placing of 3 to 20 silicon pieces from silicon wafer, with dimension, $10 \times 10 \times 0.3$ mm³, on a SiO₂, 8 in. target to produce samples of films of Si-cluster for PL response. The typical deposition condition is 2×10^{-4} - 5×10^{-3} Torr of Ar, at 400 W rf power without substrate heating on Si wafer. Samples of up to a micrometer thick are subsequently annealed at 800C for 20 to 30 min in N₂ and at a flow rate of 3 l/min. In addition to PL measurements, TEM is used for the determination of cluster size and EXAFS with the total-yield technique is employed to determine their local structures in terms of types of bond, coordination number and bond length.

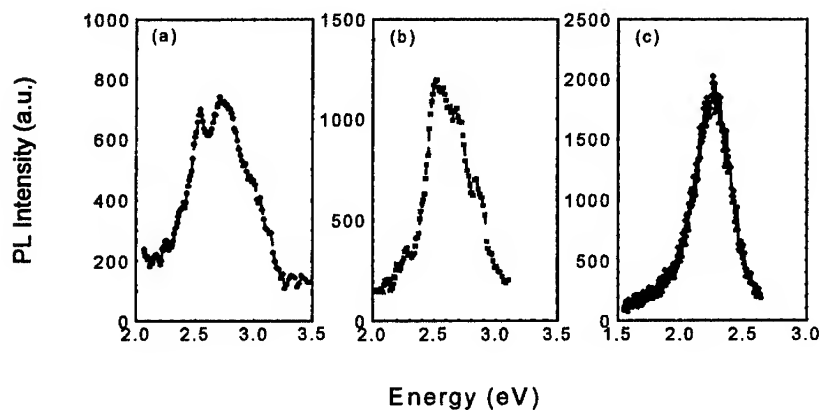


Fig.(5) PL vs Photon Energy for 3 Si-cluster samples with increasing supply of silicon from (5a) to (5c)

Figure (5) shows the typical PL with increasing Si to oxide ratio from (a) to (c), after annealing at 800C for 20-30 minutes. In Fig.(5a), the PL peak is located near 2.7 eV; in Fig.(5b), at 2.55 eV; and in Fig. (5c), at 2.3 eV. These results show that more Si results in larger clusters, and less quantum confinement. The PL intensity is much lower without annealing. Qualitatively, we understand the trend: Assuming that sputtering is involved with the arrival of silicon clusters fairly uniformly distributed, nucleation centers are determined by the defect sites on the substrate; impurities in the plasma which are affected by the rf power; the base pressure; the gas purity; as well as the substrate temperature and the annealing temperature. Therefore, to optimize the process, it is indeed a formidable task, no less complicated than any plasma assisted deposition.

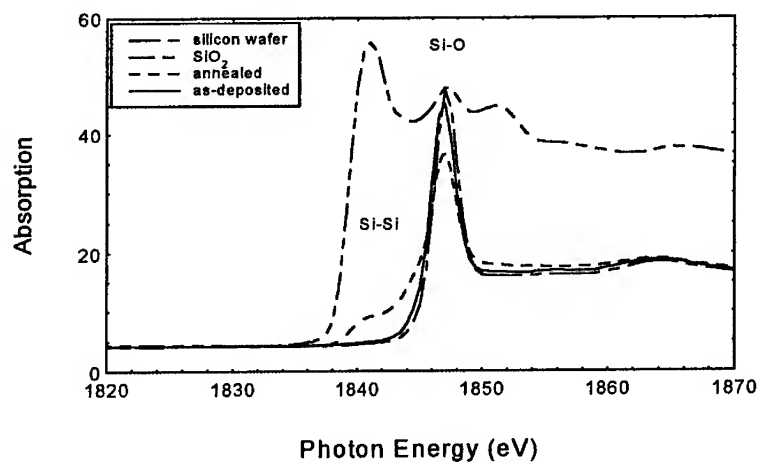


Fig.(6) EXAFS of as-deposited and annealed Si-cluster samples compared to SiO₂ and silicon wafer

EXAFS provides a unique way to examine the detailed local structure. Figure (6) shows the near edge x-ray absorption fine structure (NEXAFS) of a typical sample of Si cluster, both as-deposited and after annealing at 800°C. Data from a Si wafer and SiO₂ are also shown for comparison. As-deposited film shows no contribution from the Si substrate, which means that the film is sufficiently thick to insure reliable measurement of NEXAFS from the films. The spectrum of as-deposited film is very close to that of

pure SiO_2 film with only one absorption peak at about 1847 eV which is the signature of Si-O bonds. After annealing at 800°C, however, this peak decreases and the characteristic absorption of Si-Si bond shows up at about 1841 eV. This indicates that Si clusters are formed from the amorphous as deposited SiO_x ($x < 2$) during the annealing process. The Fourier transforms from the EXAFS data confirms the Si-Si bonding for annealed films and suggests that the nearest neighbor partial coordination number of Si-Si bonds increases from zero for the as-deposited films to 0.6-1 after annealing. The Fourier transforms also indicates that the Si-Si bond length in the annealed films is $2.35 \pm 0.002 \text{ \AA}$ as expected, whereas the Si-O bond length is somewhat shorter, at 1.58 Å instead of 1.62 Å for pure SiO_2 [6],[15]. This is clearly caused by the large difference in the thermal expansion between the Si substrate and the matrix film. Our overall understanding may be summarized by the fact that the films are Si-rich SiO_x before annealing, and after annealing, the O atoms are driven out of the clusters. The PL peak position versus size obtained theoretically [16], agrees quite well with the TEM determination of the cluster size (not shown here), confirming the quantum confinement model.

CONCLUSION

We have covered the subject of quantum confinement in silicon. The SLB is potentially very important to future generation of quantum devices, and even 3-dimensional integration. The main finding is that it is possible to grow epitaxial silicon beyond several Langmuirs of oxygen exposure. The superlattice barrier height has been determined by a new method of analyzing the I-V at moderate temperature range. The effective barrier height is nothing but the ground state energy of the quantum well structure. By repeating the process to many periods, we have shown that the resulting nanoscale silicon particles in the layers separated by adsorbed gases in what we call the Si/IAG superlattice, produce visible photoluminescence. This process also include the thin amorphous silicon with or without annealing. However, hydrogen passivation is important to serve as passivation. On the other hand, the formation of silicon clusters in an oxide matrix is somewhat different in principle because diffusion plays a more prominent role. This last approach is simpler than the Si/IAG, particularly from the technological point of view. However, unlike the latter, sputtering is required rather than MBE, which may not be readily incorporated into the standard silicon processing technology.

REFERENCES

1. W. Wegscheider, K. Eberl, H. Cerva and H. Oppolzer, *Appl Phys. Lett.* **55**, 448 (1989)
2. R. Tsu, *Nature* **364**, 19 (1993).
3. R. Tsu, A. Filios, C. Lofgren, D. Cahill, J. VanNostrand and C.G. Wang, *Solid-State Electronics*, **40**, 221 (1996).
4. R. Tsu, J. Morais, A. Bowhill, *Mat. Res. Soc. Symp. Proc.* **358**, 825 (1995).
5. For example, see Z.H. Lu, D.J. Lockwood and J.M. Baribeau, *Nature* **378**, 258 (1995).
6. Qi Zhang, S. C. Bayliss and D. A. Hutt, *Appl. Phys. Lett.* **66**, 1977(1994).
7. J.L. Ding and R. Tsu, unpublished
8. R. Tsu and L. Esaki, *Appl. Phys. Lett.* **22**, 562 (1973).
9. D. Allred, J.Hernandez and V.Nguyen, "Multilayered Article Including Crystallization Inhibition Layer", *US Patent 4,792,501*, Dec. 20, (1988)
10. J. G. Hernandez, D. Martin, S.S.Chao, and R. Tsu, *Appl Phys. Lett.* **45**, 101,(1984)
11. Raman scattering is ideal to show partial crystallization in a quantitative way. It is not shown due to space limitation.
12. T. Ito, T. Ohta and A. Hiraki. *Jpn. J. Appl. Phys.* **31**, L1(1992).
13. S. Hayashi, M. Kataoka and K. Yamamoto, *Jpn. J. Appl. Phys.* **32**, 1274(1993).
14. Y. Maeda, *Phys. Rev. B* **51**, 1658(1995).
15. Qi Zhang, S. C. Bayliss and W. Frentrop, *Solid State Comm.* **99**,883(1996).
16. C. Delerue, M.Lannoo and G.Allan, *J.Lumin.* **57**,247(1993).

ACKNOWLEDGMENTS

We are pleased to acknowledge the support of MBDO and ARO for the SLB work, and ONR for the Si/IAG. One of us, Q.Zhang wishes to thank Dr. Bayliss.

Quantum Wires: Optical Properties

Nonlinear Optical Properties of Semiconductor Quantum Wires.

T.Dneprovskaya, V.Dneprovskii and E.Zhukov

Moscow St. University, Dept. of Physics, 119899 Moscow, Russia;

Fax: 7-095-9393731; E-mail: dnepr@scond.phys.msu.su

Nonlinear optical absorption at discrete frequencies has been observed in semiconductor quantum wires crystallized in transparent dielectric matrix (inside chrysotile asbestos nanotubes). The induced changes of absorption in quantum wires have been explained by filling of the size-quantized energy bands with nonequilibrium carriers (dynamic Burstein-Moss effect); renormalization of the one-dimensional energy bands at high density of the induced plasma; phase space filling, quantum-confined Stark effect and screening of excitons. The measured values of exciton binding energies are much greater than that of the corresponding bulk semiconductors. The increase of the exciton binding energy may be attributed not only to the quantum confinement but also to the "dielectric confinement" – the increase of electron-hole attraction because of the difference in dielectric constants of semiconductor nanowires and dielectric matrix.

I. Introduction.

In recent years semiconductor nanostructures in which the movement of carriers is restricted to two dimensions – quantum wires (QWRs) – are attracting much interest not only from the viewpoint of fundamental physics, but also from their potential application in electronics and optoelectronics. As the dimensionality is reduced from two to one dimension, giving QWRs, the density of states becomes sharper and narrower instead of a step-like. Additional carrier confinement should lead to a narrower gain spectrum, higher differential gain [1], to an increased exciton binding energy and lasing from excitons [2], to enhanced optical nonlinearities [3]. Therefore, application of QWRs promises improvements in performance of lasers (lower threshold, increased modulation bandwidth, reduced threshold temperature sensitivity), of transistors (application of extremely high electron mobility channels), and of optical switching devices (low switching energy, fast switching). This paper reports the observation of nonlinear optical absorption at discrete frequencies of GaAs and CdSe QWRs in a transparent matrix, excited by

powerful picosecond laser pulses. It may be attributed to the filling of the size-quantized (one-dimensional) energy bands with nonequilibrium carriers; renormalization of the energy bands at high density of the induced plasma; phase space filling, quantum-confined Stark effect in the presence of high density plasma and screening of excitons.

II. Experiment.

The existing methods for semiconductor QWRs fabricating include molecular beam epitaxy (MBE) or metal-organic chemical vapor deposition (MOCVD) together with etching, the application of prepatterned substrates, and cleaving of a conventional 2D-structure perpendicular or at slight angle to the surface [4]. They don't allow to prepare samples with suitable volume and density of nanostructures for optical absorption and nonlinear optical absorption measurements. We have used samples prepared by a different method [5] where the sample's size and the concentration of QWRs allow the spectra of both linear and nonlinear absorption to be measured. Molten semiconductor material was injected and crystallized in the hollow cylindrical 6 nm diameter channels of crysotile-asbestos nanotubes. The sample is a regular close packed structure of parallel crysotile-asbestos 30 nm diameter nanotubes filled with ultrathin crystalline wires of GaAs or CdSe. The diameter of the wires is comparable with the de Broglie wavelength of the electron. For nonlinear absorption measurements, QWRs were excited by ultrashort pulses at the second harmonic of a mode-locked Nd:YAG laser, with a photon energy 2.33 eV. The duration of an individual pump pulse was about 20 ps, and its intensity reached 100 MW/cm^2 . The exciting beam was directed along the normal to the surface of the sample and was focused into a spot $\approx 200 \mu\text{m}$ in diameter. It was polarized parallel to the wire axis. The central part of the excitation region was probed by an oppositely directed focused beam of "white" light. An ultrashort pulse of "white" light was produced by sending a part of the laser beam at the fundamental frequency into a cell filled with heavy water. An optical delay line made it possible to delay the probing pulse with respect to the exciting pulse and to measure the kinetics of the induced absorption. The probing light was detected in front and behind the sample by multichannel optical analyzer, with accumulation of 50 pulses and with energy selection of the ultrashort excitation pulses

within an error $\pm 10\%$. In these experiments we measured the differential transmission spectra [6]:

$$DT(\lambda) = \frac{T(\lambda) - T_0(\lambda)}{T_0(\lambda)}, \quad (1)$$

where $T(\lambda)$ and $T_0(\lambda)$ are the transmission spectra of the excited and unexcited sample, respectively. So it was possible to eliminate the spurious effect of the spectral characteristics of the photodetectors and to reduce the role played by an instability of the spectral composition of the probing light. Transmission spectra normalized to the reference spectra of the probing pulse were used in (1)

III. Results and discussion.

Bleaching bands have been observed in the differential transmission (DT) spectra of GaAs QWRs (Fig.1). The low energy band (1.67 eV) has been registered only for some parts of the samples (the exciting and probing beams could be scanned along the surface of the samples). The energy positions of these bands coincide with corresponding "hills" and "shoulder" in the linear absorption (LA) spectra. The induced bleaching bands at 1.85 eV (Fig.2.a) and 2.15 eV disappear over 50 ps. The relaxation time of the lower energy 1.67 eV band (Fig.2.b) is shorter and could not be measured because of insufficient time resolution of our system.

In QWRs different nonlinear processes may compete and coexist: the dynamic Burstein–Moss saturation effect, renormalization of the energies of one dimensional gaps at a high density of the excited carriers, bleaching and broadening of the exciton absorption line due to the phase space filling and screening of excitons, etc [7–9].

The hills in the LA and bleaching bands at 1.85 eV and 2.15 eV in DT spectra may be attributed to the optical transitions (and saturation of these transitions) between the one dimensional energy bands of cylindrical QWRs [10,11]. Within effective mass approximation combined with assumption of infinitely deep cylindrical potential well and negligible role of Coulomb interaction between carriers, the energies of transitions between space quantization levels in corresponding valence bands and conduction band are given by [12]:

$$E_i = E_g^i + \frac{X_{01}^2 \hbar^2}{2\mu_i \rho^2}, \quad (2)$$

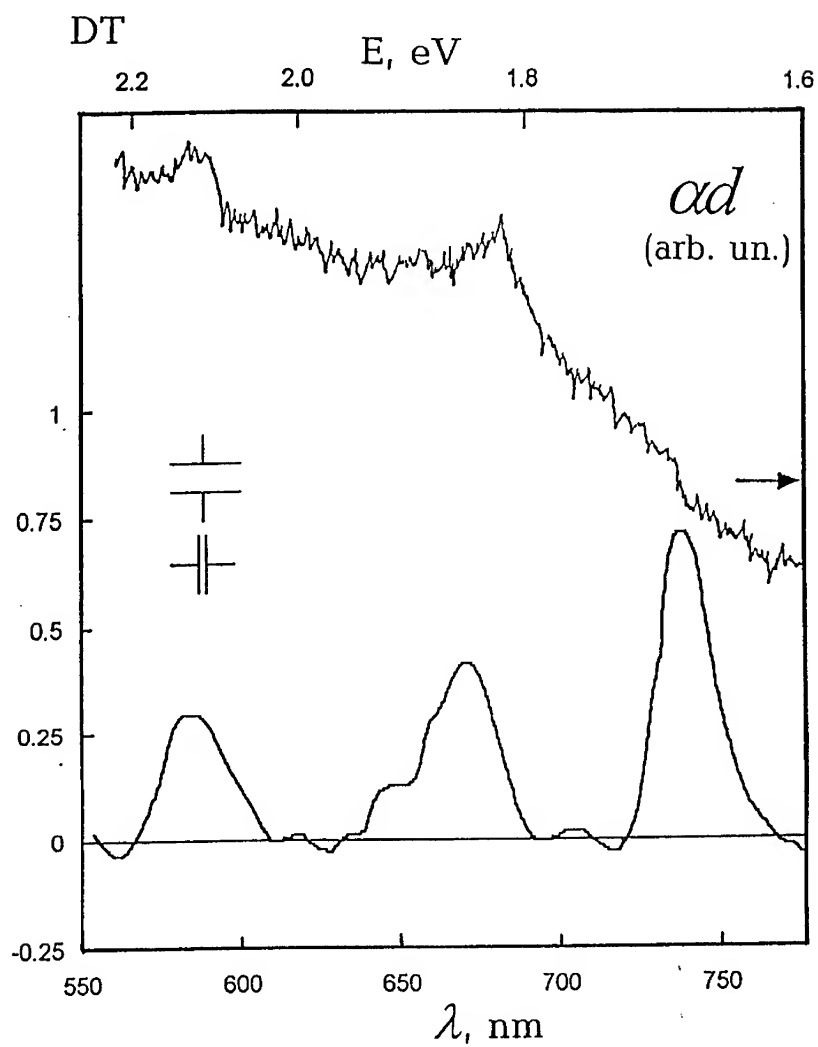


Fig.1. The linear absorption and differential transmission (zero delay between the pumping and probing pulses) of GaAs QWRs crystallized in crysotile asbestos nanotubes.

where E_g^i is an energy gap (index "i" defines the corresponding valence band); $X_{01} \cong 2.4$; ($J_0(X) = 0$, J_0 is the Bessel function);

$\mu_i = \frac{m_e m_h^i}{m_e + m_h^i}$; m_e, m_h^i — the effective masses of electrons and holes; and ρ is the radius of QWR.

Using (2) it is easy to show that for GaAs QWRs of 6 nm diameter, the bleaching bands 1.85 eV and 2.15 eV (Fig.1) correspond to the saturation of the transitions between the heavy hole subband and the lowest conduction subband as well as to the split off by spin orbit coupling valence subband and the lowest conduction subband.

As can be seen in Fig.2.a, the 1.85 eV bleaching band of DT spectrum broadens — the low energy side shifts to the longer wavelength part at higher excitation. The values of the energy shifts depend upon the delay between the pumping and probing pulses and attain maximum at zero delay (at the highest plasma density). One may attribute these energy shifts to the band gap renormalization that arises at high density of the optically excited nonequilibrium carriers. It is possible to estimate the band gap shrinkage using the results obtained by S. Benner and H. Haug [7]. They have calculated the band gap shrinkage for GaAs QWRs in the presence of high density electron-hole plasma using random phase approximation. For the densities of plasma attained in our experiment ($\leq 2 \cdot 10^6 \text{ cm}^{-3}$) the maximum band gap shrinkage (Fig.1 in [7]) is about 33–40 meV.

Thus the nonlinear absorption of GaAs QWRs in the vicinity of 1.85 and 2.15 eV may be explained by the state filling and renormalization of one dimensional energy band gaps. The width of the bleaching bands is too great (50–70 meV) to be attributed to the state filling by laser excited nonequilibrium carriers and is probably determined by inhomogeneous broadening due to the size dispersion of QWRs crystallized in crysotile asbestos nanotubes.

The registered bleaching band at 1.67 eV in the low energy part of the DT spectra (Fig.1 and 2.b) may be attributed to the "saturation" of excitons in GaAs QWRs (phase-space filling effect). The presence of high density electron-hole plasma causes a bleaching of excitonic resonance while reducing the effective electron-hole attraction by screening and phase-space filling. Phase-space filling is more efficient in QWRs than Coulomb screening [7,8]. The phase-space filling effect arises because an exciton consists of an electron and a

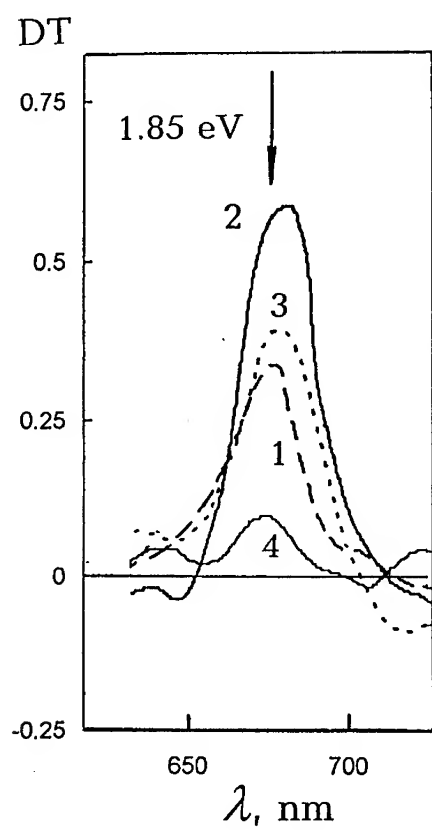


Fig.2.a. The differential transmission spectra of GaAs QWRs (1.85 eV bleaching band) at different delays between the pumping and probing pulses: (-13 ps) -1, 0 ps -2, 20 ps -3, 50 ps -4.

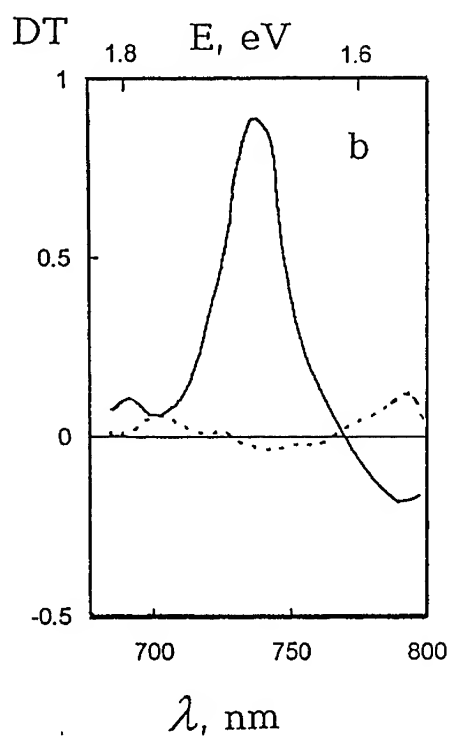


Fig.2.b. The differential transmission spectra of GaAs QWRs ("excitonic band") at zero and 15 ps delays between the pumping and probing pulses.

hole, each of which obeys the Pauli exclusion principle. Hence only those electron–hole states may be used for the exciton creation that are not yet occupied by free carriers. The screening effect leads to the spatial rearrangement of the electrons and holes which is strongly restricted in QWRs.

The energy position of the excitonic bleaching band allows to estimate the binding energy of exciton of GaAs 3 nm radius QWRs in dielectric (crysotile asbestos) matrix. It is about 130–160 meV. This value is much greater than the binding energy of excitons in GaAs QWRs formed by T-shaped intersection of two GaAs/AlGaAs 7 nm quantum wells [3]. In a case of QWRs in dielectric matrix the increase of the excitonic binding energy may be explained not only by quantum confinement (excitons become one dimensional) but also by the “dielectric confinement” [13,14,]. The image potentials that arise due to the difference in the dielectric constants of semiconductor QWR and dielectric matrix become essential. They result in the marked increase of the electron–hole attraction and in so called dielectric amplification of excitons (dielectric confinement). The binding energies of excitons in the cylindrical QWRs have been culculated in [15,16] as a function of the wire’s radius and dielectric constants of semiconductor and surrounding dielectric. For GaAs QWRs in dielectric matrix with dielectric constant $\epsilon \approx 2.3$, the culculated binding energy of exciton is about 130–140 meV. The measured value of the exciton binding energy of GaAs QWRs in crysotile asbestos nanotubes is in good agreement with that culculated in [15,16].

As pointed out the 1.67 eV bleaching band, which is attributed to the phase–space filling of excitons, has been observed only for some parts of the excited samples. It may be explained by nonuniform filling of crysotile asbestos nanotubes with crystallized GaAs [17]. Only some parts of the samples contain nanowires whose length exceeds the Bohr radius of exciton considerably. The observed induced bleaching of GaAs QWRs in crysotile asbestos nanotubes at the frequency of the heavy hole – the first electron subband (1.85 eV bleaching band) allows us to determine the third order nonlinear susceptibility $\chi^{(3)}$ [6]*:

$$\text{Im} \chi^{(3)}(\omega) = \frac{c^2 n_0^2 \Delta \alpha(\omega)}{8 \pi^2 \omega l(\omega)} \quad (3)$$

In (3) $\Delta\alpha$ is the change of the absorption coefficient induced by the resonant monochromatic field of the intensity $I(\omega)$; n_0 is the linear refraction index. For quasistationary conditions the radiation intensity $I(\omega)$ may be expressed in terms of the number of photoexcited electron-hole pairs per one QWR n_e :

$$I(\omega) = \frac{n_e N d h \omega}{(1 - T_0(\omega) - r) \tau}, \quad (4)$$

where N is the concentration of QWRs in crysotile asbestos matrix, τ is the recombination time of the photoexcited carriers, T_0 and r — the transmission and reflection of the sample, d is its thickness.

The $\Delta\alpha(\omega)$ spectrum may be directly determined from the corresponding $DT(\lambda)$ spectrum:

$$\Delta\alpha = -\ln(1 + DT) / d \quad (5)$$

Substituting in (3) the maximum value of $\Delta\alpha$ at the frequency of the lower optical interband transition, as well as the measured relaxation time of the induced changes in the absorption coefficient, one may obtain: $\text{Im } \chi^{(3)} \cong -4.10^{-8}$ e.s.u. (the relaxation time is about 30 ps).

For CdSe QWRs in crysotile asbestos nanotubes the LA and DT spectra are shown in Fig.3. The energy position of the "hills" of LA spectrum and the bands of DT spectrum (1.7 eV and 2.05 eV) allow us to attribute them to the linear and nonlinear absorption of excitons (with binding energy about 200 meV) in 3 nm radius cylindrical CdSe QWRs (1.7 eV) and to the linear and nonlinear absorption (state filling) at the frequency of the optical transition heavy holes of one dimensional energy band — the first subband of electrons (2.05 eV).

 * So called strong (resonant) dynamic (inertial) nonlinearities have been examined that arise in the case of absorption of light in semiconductor nanostructures [18]. In contrast to "classical" nonlinearities in transparent medium strong nonlinearities arise from free carriers via a real exchange of energy from optical field to the medium. The relaxation time of strong dynamic nonlinearities is determined by the recombination process of nonequilibrium electrons, excitons, etc. In 1926 S.I. Vavilov and V.L. Levshin discovered strong optical nonlinearity of uranium glass in the case of its resonant excitation [19] — the saturation of optical transition (saturation of a two-level system).

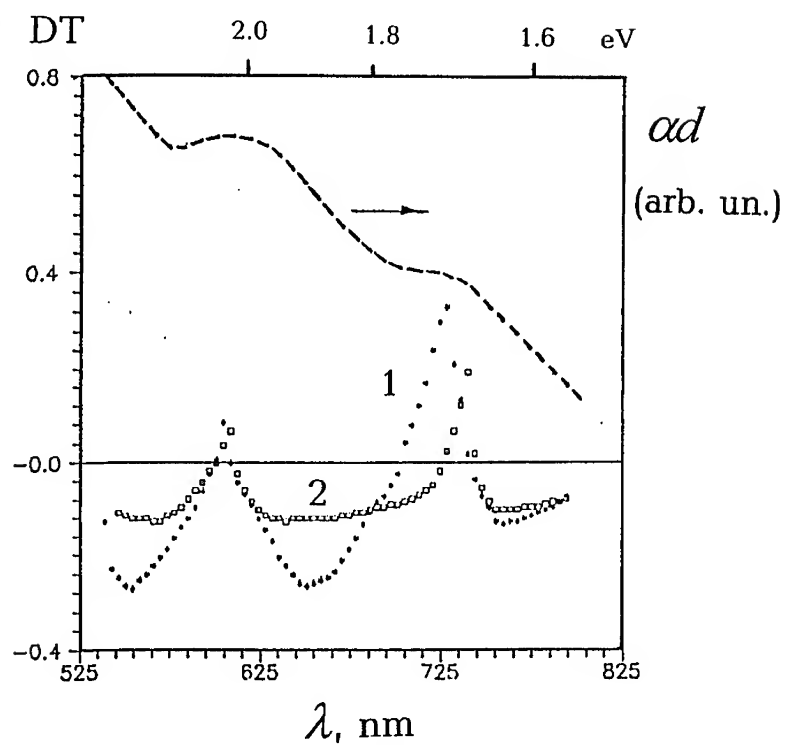


Fig.3. The linear absorption and differential transmission (at zero (1) and 7 ps (2) delay between the pumping and probing pulses) of CdSe QWRs crystallized in crysotile asbestos nanotubes.

The blue shift and the increase of absorption in the vicinity of the "excitonic" 1.7 eV band of the DT spectrum, in the case of higher density of the excited plasma (compare the DT spectra in Fig.3 obtained with different optical delays between the pumping and probing pulses), may be explained following [8] by the joint action of the electric field and high density electron-hole plasma. The electric field probably arises due to carriers localized in the lateral barrier region that contain imperfections and impurities [8,20]. Without excited electron-hole plasma, the low electric field cause the reduction of the exciton binding energy due to the reduced electron-hole overlap. So the blue shift of the excitonic resonance may exceed the Stark shift of excitons and the red shift of one-dimensional energy gap. For the large lateral electric field the Stark effect dominates and the exciton absorption peak shifts towards red. For increasing high density of a thermal electron-hole plasma, and with applied electric field, the Hartree term (the reduction of the electron-hole interaction) shifts the excitonic absorption peak to higher energies due to the violation of charge neutrality [8].

The results of [8] allow to estimate the approximate value of the plasma density at which the Hartree term (it is proportional to NE^2 , where N is the number of excited carriers, E is the lateral electric field) compensates the red Stark shift of the excitonic resonance that is proportional to E^2 :

$$\frac{N}{L} = \frac{\epsilon \mu^3 (\Delta_e + \Delta_h)^3}{4e^2 (m_e + m_h)^2} \left(\frac{1}{m_e \Delta_e^2} + \frac{1}{m_h \Delta_h^2} \right) \quad (6)$$

In (6) L is the wire's length, ϵ represents the static dielectric constant of the wire's material, μ is the reduced electron-hole mass, m_j is the electron (hole) mass, Δ_j are the intersubband spacings that arise due to the quantum confinement for electrons and holes. Thus the estimated value of the plasma density for 3 nm radius CdSe QWRs is about 10^6 cm^{-1} . The plasma densities obtained in our experiment exceed this value.

In summary, we have investigated the physical processes that may be the reason of the observed nonlinear absorption at discrete frequencies in semiconductor quantum wires crystallized inside transparent dielectric nanotubes. The peculiarities of the nonlinear absorption at high excitation by powerful picosecond laser pulses and its kinetics may be explained by several competing and coexisting nonlinear processes: the state filling and renormalization of one-

dimensional energy bands at high density of nonequilibrium carriers; phase-space filling of excitons; quantum-confined Stark effect of excitons in the presence of high density plasma and lateral electric field. The increase of the exciton binding energy of GaAs and CdSe nanowires in dielectric matrix have been attributed to joint influence of quantum confinement and "dielectric confinement".

This research was made possible in part by Grant 96-2-17339 of the Russian Foundation for Fundamental Research and Grant of the Russian Ministry of Science program "Physics of Solid Nanostructures". We thank V.V. Poborchii for the samples of nanostructures crystallized in crysotile asbestos nanotubes.

References.

- [1] Y. Arakawa and A. Yariv, IEEE J. Quantum Electron. 22, 1887 (1986)
- [2] W.Weigscheider, L.N. Pfeiffer, M.M. Dignam, A. Pinczuk, K.W. West, S.L. McCall, and R. Hull, Phys. Rev. Lett. 71, 4071 (1993)
- [3] S. Schmitt-Rink, D.A.B. Miller, and D.S. Chemla, Phys. Rev. B 35, (1987)
- [4] M.S. Sundaram, S.A. Chalmers, P.F. Hopkins, A.C. Gossard, Science 254, 1326 (1991)
- [5] V.V. Poborchii, M.S. Ivanova, I.A. Salamatina, Superlattices and Microstr. 16, 133 (1994)
- V.N. Bogomolov, Usp. Fiz. Nauk 124, 171 (1978)
- [6] V.S. Dneprovskii, V.I. Klimov, D.K. Okorokov, Yu.V. Vandyshev, Solid State Commun. 81, 227 (1992)
- [7] S. Benner and H. Haug, Europhys. Lett. 16, 579 (1991)
- [8] S. Benner and H. Haug, Phys. Rev. B 47, 15750 (1993-I)
- [9] K.H. Wang, M. Bayer, A. Forchel, P. Iles, S. Benner, H. Haug, Phys. Rev. B 53, R10505 (1996-II)
- [10] N.V. Gushchina, V.S. Dneprovskii, E.A. Zhukov, O.V. Pavlov, V.V. Poborchii, I.A. Salamatina, JETP Lett. 61, 507 (1995)
- [11] V. Dneprovskii, N. Gushina, O. Pavlov, V. Poborchii, I. Salamatina, E. Zhukov, Phys. Lett. A 204, 59 (1995)
- [12] H. Zarem, K. Vahala, A. Yariv, IEEE J. Quantum Electron. 25, 705 (1989)
- [13] N.S. Rytova, Dokl. Akad. Nauk SSSR 163, 118 (1965)
- [14] L.V. Keldysh, JETP Lett. 29, 716 (1979)

-
- [15] E.A. Muliarov, S.G. Tihodeev, "Dielectric strengthening of excitons in semiconductor quantum wires", Preprint of General Physics Inst., Moscow (1995)
 - [16] E.A. Muliarov, S.G. Tihodeev, JETP 111 (1), (1997)
 - [17] V.V.Poborchii, private communication
 - [18] P.N. Butcher, D. Cotter "The Elements of Nonlinear Optics", Cambridge University Press, (1990)
 - [19] S.I.Wawilow, W.L. Lewschin, Z. Phys.35, 932 (1926)
 - [20] D.J.Norris, A.Sacra,C.B.Murray, M.G.Bawendi, Phys.Rev.Lett. 72, 2612 (1994)

LUMINESCENCE CHARACTERIZATION OF SELFORGANIZED GaAs QUANTUM WIRES: CARRIER CAPTURE AND THERMALIZATION

P. Fischer ^a, J. Christen ^a
M. Takeuchi ^b, H. Nakashima ^b, K. Maehashi ^b, K. Inoue ^b
G. Austing ^c
M. Grundmann ^d, D. Bimberg ^d

a „Otto von Guericke“ University of Magdeburg, Faculty of Natural
Science, Institute of Experimental Physics, PO box 4120,
39016 Magdeburg, Germany

b ISIR, Osaka University, 8-1 Mihogaoka, Ibaraki, Osaka 567, Japan

c NTT Basic Research Laboratories, 3-1, Morinosato Wakamiya,
Atsugi-shi, 243-01 Japan

d Technical University of Berlin, Hardenbergstrasse 36, 10623 Berlin,
Germany

ABSTRACT

GaAs quantum wires were grown on vicinal substrates using gas source molecular beam epitaxy with different growth conditions. The quantum wires were investigated by means of (micro-) photoluminescence and cathodoluminescence. Stochastic thickness fluctuations occur from wire to wire as well as along each single quantum wire. Using a two-step growth mode leads to an improved homogeneity of the quantum wires. The maximum carrier capture efficiency into the quantum wires is found in the temperature range from 70K to 100K.

I. INTRODUCTION

Using the selforganization of quantum wires (QWRs) provides a promising technique to reproducibly grow QWRs. By means of optical investigations we investigated the quality of selforganized GaAs QWRs. In this paper we address two of the most important questions for QWR device applications:

1. Reproducibility and homogeneity from wire to wire as well as along a single QWR are crucial parameters for lateral arrays of selforganized low dimensional structures.

Statistical size- and compositional fluctuations may lead to dramatic energetical broadening of the one dimensional Eigenstates, possible smearing out the one dimensional bandstructure.

2. The majority of excess carriers are generated or injected not in the QWRs themselves but in the surrounding barrier material, thus carrier capture into the wires is essential.

In this paper we present a systematic luminescence investigation of QWRs grown by gas source molecular beam epitaxy using one- and two-step growth mode. By means of temperature dependent photoluminescence we studied the carrier capture efficiency into the QWRs. Micro-photoluminescence and highly spatially resolved cathodoluminescence allowed us to investigate the quality of single QWRs.

II. EXPERIMENTAL

The selforganized GaAs QWRs investigated in this work were grown on vicinal (110) GaAs tilted towards (111)A by 3° and 6°, respectively, using gas source molecular beam epitaxy. The QWRs were naturally formed induced by the coherently aligned giant growth steps, due to compositional modulation of AlGaAs barrier layers as well as thickness modulation of GaAs single quantum well (SQW) at the giant growth step edges [1]. The quantum wires run along the [-110] direction.

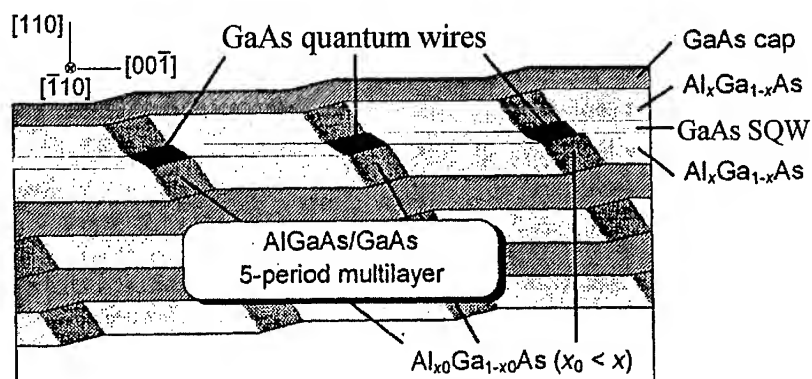


Figure 1: Schematic illustration of GaAs quantum wire structure.

The epilayer structure consist of a 5 period AlGaAs (30nm) / GaAs (30nm) multi quantum well (MQW), followed by a GaAs SQW with a nominal thickness t of 1nm, 2nm or 3nm, respectively, embedded in AlGaAs (30nm) barriers [2].

The growth temperature of barriers and SQW was varied between 500°C to 550°C. In case of changing the growth temperature for the SQW before starting to grow the first barrier we will refer to as two-step growth mode. In this paper we will focus on samples with a SQW grown at 500°C, 530°C and 550°C.

Details of experimental setup are given elsewhere [3,4]. Metal masks on top of quantum wires structured by means of electron beam lithography were applied to measure photoluminescence and cathodoluminescence of single resolved QWRs.

500°C - 550°C	20 nm GaAs	Single Quantum Well
	30 nm Al _{0.5} Ga _{0.5} As	
	t GaAs	
	30 nm Al _{0.5} Ga _{0.5} As	
500°C	30 nm GaAs	Multi Quantum Well
	30 nm Al _{0.5} Ga _{0.5} As	
	30 nm GaAs	
	30 nm Al _{0.5} Ga _{0.5} As	
	30 nm GaAs	
	30 nm Al _{0.5} Ga _{0.5} As	
	30 nm GaAs	
	30 nm Al _{0.5} Ga _{0.5} As	
	30 nm GaAs	
	30 nm Al _{0.5} Ga _{0.5} As	
	200 nm GaAs	
	vicinal GaAs (110) substrate	

Figure 2: Sample structure.

III. RESULTS

Figure 3 shows a typical surface of a GaAs quantum wire sample.

The quantum wires are naturally formed along the step edges of the coherently aligned steps. Although the homogeneity is very high and the steps seem to be equidistant, there still are fluctuations from wire to wire as well as along each single quantum wire. Furthermore a few steps are not running through the whole field of view.

Laterally integrated photoluminescence (PL) at 5K using an Ar⁺ Laser was used first to investigate the influence of changing the growth temperature. Figure 4 shows photoluminescence from samples grown on 3°

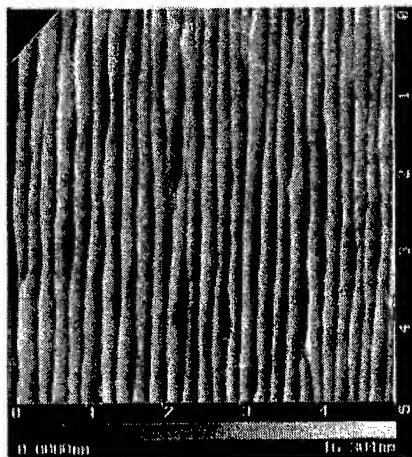


Figure 3: Atomic Force Microscopy image of a GaAs QWR sample.

tilted substrates from both, the GaAs layers in the MQW and the GaAs QWRs embedded in the GaAs SQW.

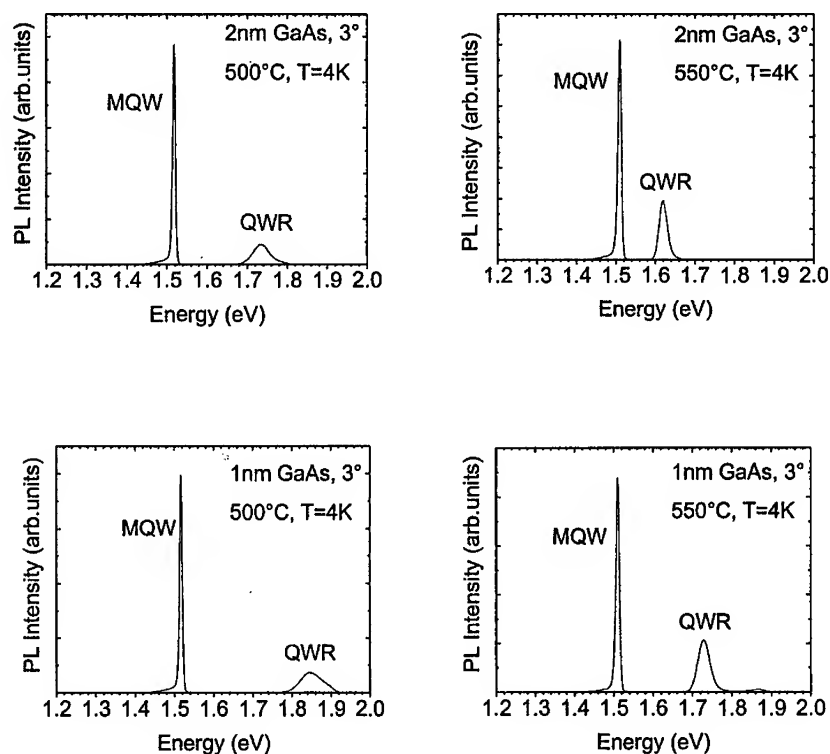


Figure 4: PL of QWR samples with a nominal QW thickness of 1nm and 2nm, respectively.

The higher intensity and smaller full width at half maximum (FWHM) of QWR photoluminescence of samples with a SQW grown at 550°C clearly shows the higher uniformity of quantum wires grown in two-step growth mode. The results of low temperature photoluminescence are summarized in figure 5.

To compare one- and two-step growth mode the FWHM of the QWR peak is plotted as a function of QWR emission peak position. The FWHM is a good measure for statistical inhomogeneities along and between the QWRs. In figure 5 QWR samples grown on 3° and 6° tilted substrates are compared. The QW thickness printed is the nominal thickness. Thinner samples are more effected by thickness fluctuations. A direct comparison of FWHM can be applied for samples with the same emission peak position. Obviously the samples (2nm,500°C) and (1nm,550°C) have the same thickness, and it is clearly visible that the latter one is much more homogeneous.

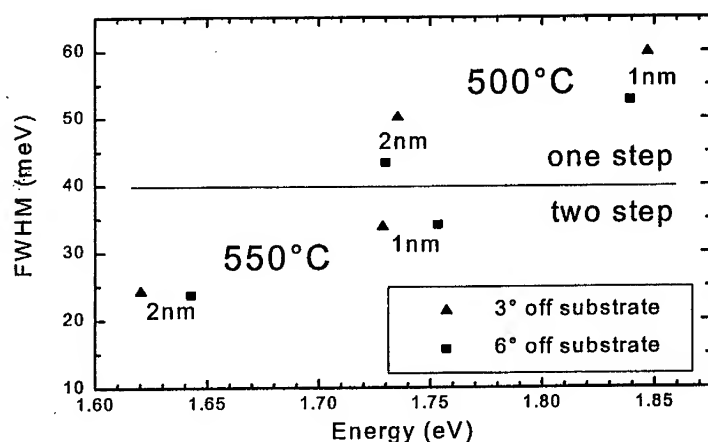


Figure 5: Comparison of one- and two-step growth mode.

In any case the FWHM of PL of the two-step growth mode samples (550°C) is significantly lower than for those grown in one-step growth mode (500°C). Even with a thicker QW the one-step growth mode samples with a nominal 2nm QW seem to have more fluctuations than the two-step growth mode samples at the same energetic position.

To investigate properties of single QWRs we applied metal masks on top of the QWRs structured by means of electron beam lithography and evaporating.

Figure 6 shows a Ti / Au mask with covered and uncovered open areas on top of the sample. The large rectangles are used for orientation and called box in the following. According to the lateral distance of the QWRs of 150-300nm, different slits with a width of 200-350nm were used parallel and perpendicular to QWRs.

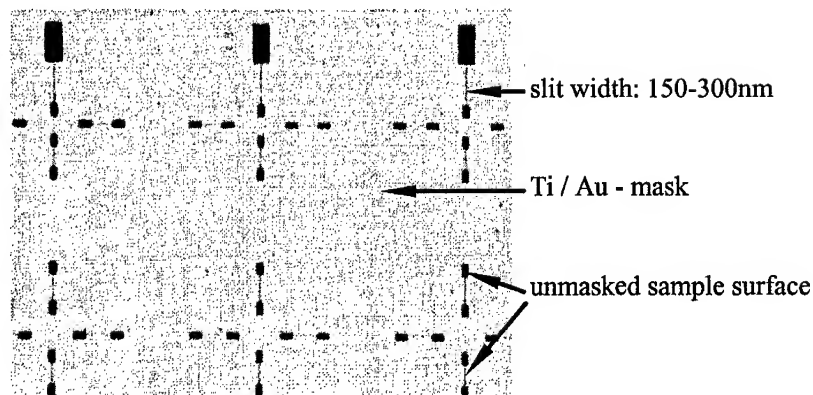


Figure 6. Metal mask to investigate SQWRs.

First we measured micro-PL using an Ar⁺ Laser with a spot diameter of 5 μm . Figure 7 shows PL from an uncovered area from both the MQW and the QWRs. Using a laser with an excitation area of 5 μm diameter leads to a broad QWR luminescence peak. The broadening of the QWR peak due to integrating over approximately 25 wires with statistical thickness fluctuations is clearly seen. Figure 8 shows luminescence from QWRs covered by a mask with a width of 250 nm perpendicular to the QWRs. 7 different peaks are observed. This is in perfect agreement with the QWR pitch of 220 nm for this sample (spotsize / pitch = 1.5 μm / 220nm \Rightarrow 7 QWRs). However, there is still the possibility for thickness fluctuations along the QWR within the 350nm slit

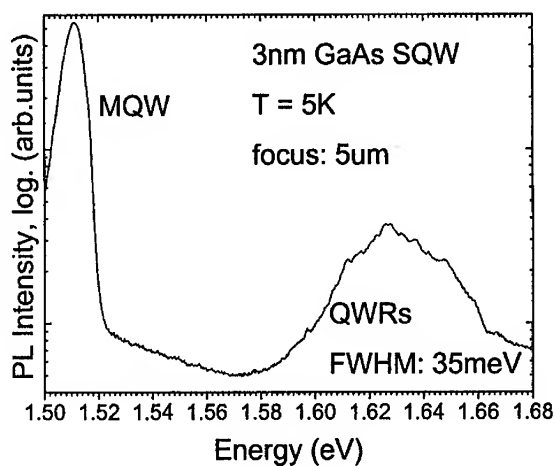


Figure 7: PL laterally integrated over approx. 25 QWRs.

Figure 9 shows both, luminescence from a box area applying a 5 μm laser spot together with a sharp luminescence peak coming from a 200 nm slit area parallel to a single QWR. If the fluctuations only occur from wire to wire only one sharp peak from one isolated QWR under a slit is expected. The „broadening“ of this peak has its origin in fluctuations around the main thickness of the single QWR within the excited slit length of 1.5 μm .

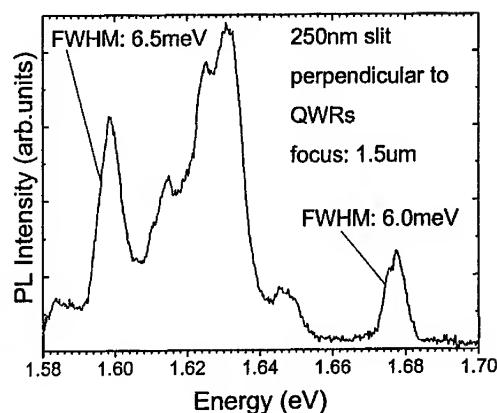


Figure 8: Photoluminescence from different single QWRs.

Next, highly spatially resolved cathodoluminescence microscopy (CL) was used to produce quantitative mappings of the lateral confinement potential. Here we will report from the same masked GaAs QWR sample with a 3nm SQW grown at 530°C investigated by micro-photoluminescence. The left part of figure 10 shows an SEM image of the investigated area. We clearly see the transition from slit to box and the steps running parallel to the slit. The surface steps running from the upper left to the lower right corner can be observed. The left part of this image shows an uncovered area, part of the box. The right part shows a very thin slit covering one step. This field of view gives us the possibility to investigate both, single quantum wire (below the slit) and neighbored quantum wires. The second image is a so called CLWI (cathodoluminescence wavelength image) recorded at the same time. It shows the wavelength at maximum intensity for the chosen wavelength win-

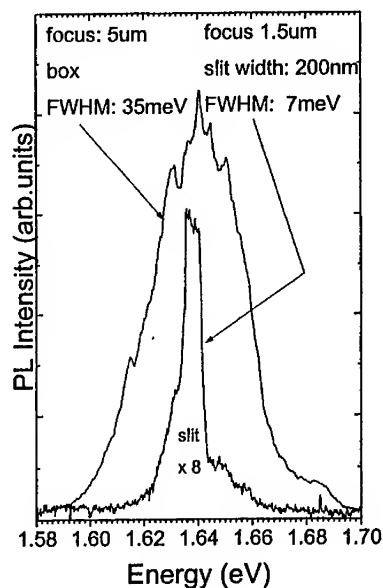


Figure 9: PL from a single QWR.

dow as a function of position in the investigated area. This image was recorded for the wavelength window of the GaAs layers in the multi quantum well. They are expected to emit light at a wavelength of 820nm, like in the box. If the surrounding area is covered by a mask the emission shifts to 824nm. Obviously we have to consider wavelength shift because of strain induced by the metal mask. This shift is not important for the characterization of single QWRs, because we still can observe the fluctuations, even if the emission wavelength is shifted.

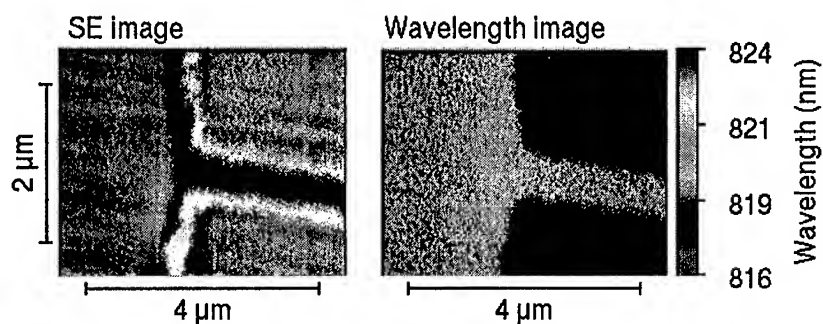


Figure 10: SEM image and CLWI of a transition from a covered to an uncovered area.

Figure 11 shows the CLWI for the QWR luminescence of the same sample area. Wavelength fluctuations along the wire under the slit as well as from wire to wire in the box, mainly caused by thickness fluctuations, are found.

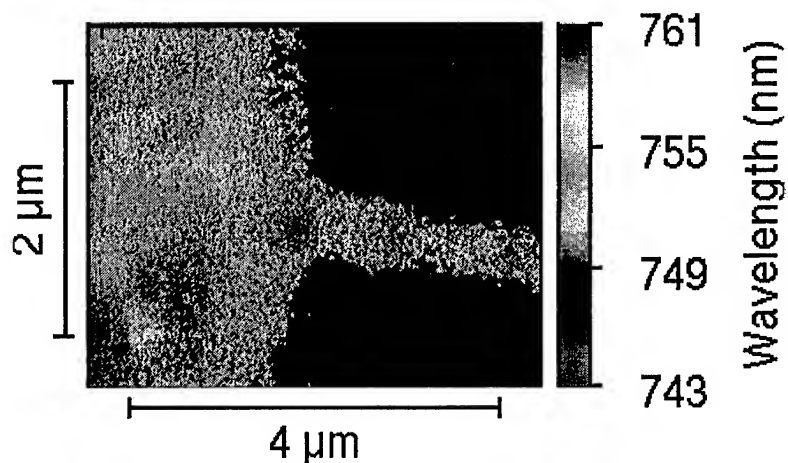


Figure 11: CL wavelength image of QWR.

Figure 12 shows the changes in local cathodoluminescence spectra from spot to spot along the wire. Again we can clearly observe fluctuations in the CLWI and in the local cathodoluminescence spectra taken at different locations. Furthermore we took CL spectra separately integrated over the box and the slit, marked by arrows. Obviously the FWHM of the spectrum taken from the complete slit area ($4\mu\text{m} \times 300\text{nm}$) does not differ from the FWHM of the spectrum taken from the box area with 40meV . The broadening of spectra is caused by fluctuations along the wire as well as by fluctuations from wire to wire, both participating equally.

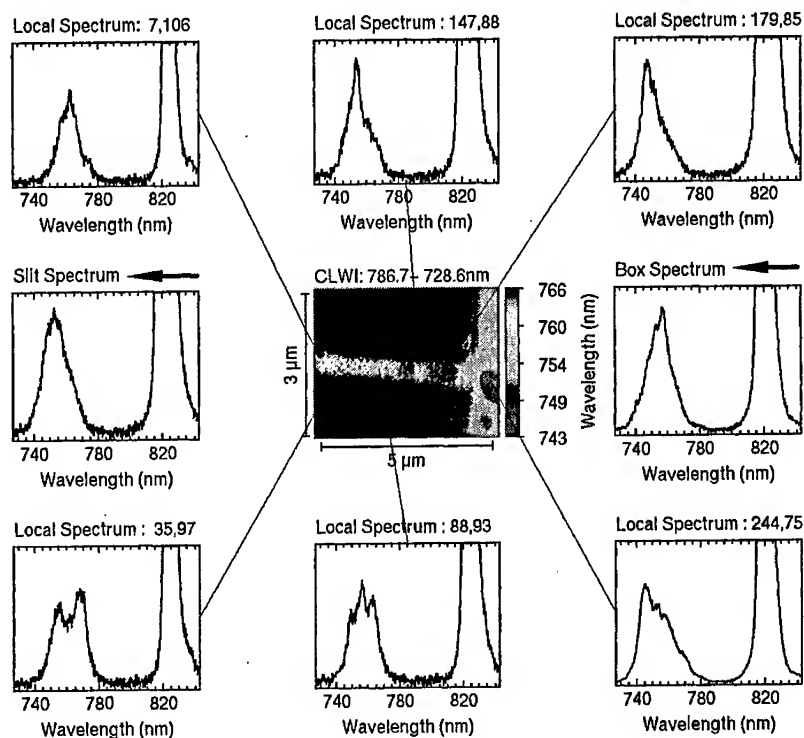


Figure 12: Local CL spectra and CLWI of masked GaAs QWRs.

Looking at the geometry of sample structure (fig.1.) it is obvious that the majority of excess carriers is generated or injected not in the QWRs themselves but in the surrounding barrier material, thus carrier capture into the QWRs is essential. We have to distinguish between the vertical transport process of generated carriers from the barriers into the quantum well and the transport along the SQW into the QWRs. The vertical transport is well known to be very efficient and fast, which is confirmed in our investigation by the fact that no luminescence from AlGaAs barriers is observed.

Temperature dependent PL allows to discuss the transport along the (110) plane of the single quantum well into the quantum wire. Figure 13 shows the temperature dependence of the normalized QWR photoluminescence intensity for a complete set of samples, grown by one- and two-step growth mode. Using the ratio of QWR and MQW photoluminescence intensity (fig.13) is a good measure to determine the most efficient temperature range for carrier transport along the SQW. For all samples the carrier capture process is most efficient in the temperature range of 70K-100K. Generally the samples grown by two-step growth mode show a more efficient carrier capture.

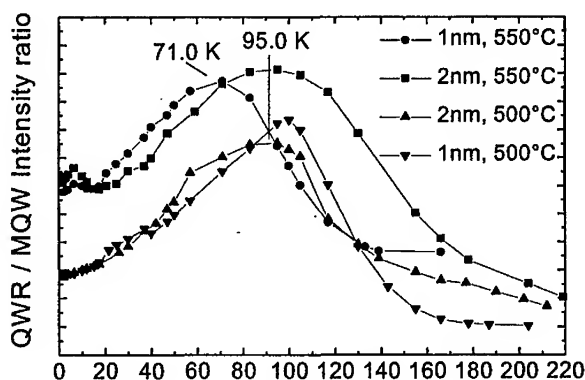


Figure 13: Carrier capture into the QWRs.

A high energetic luminescence shoulder (fig. 14.) in the vicinity of quantum wire peak additionally appears in photoluminescence and cathodoluminescence spectra. These peaks mainly occurred in spectra of samples with a 1nm thick single quantum well. These peaks disappear if the temperature is raised above 50K. This is caused by thermal activation so carriers are able to leave local potential minima.

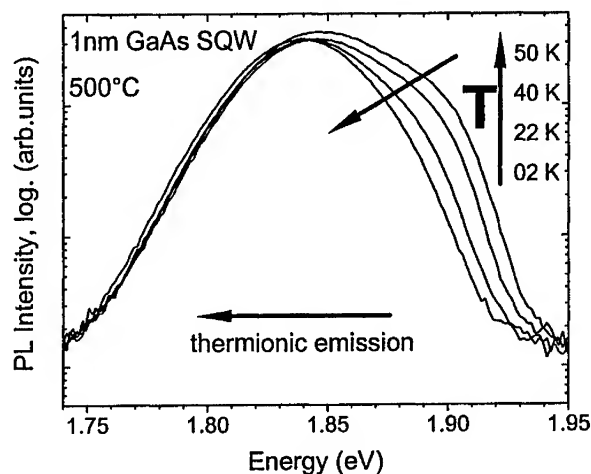


Figure 14: Thermal activation of local potential minima in the vicinity of QWRs.

IV. CONCLUSION

Using a two-step growth mode leads to an improved homogeneity of selforganized GaAs QWRs grown by gas source molecular beam epitaxy. Stochastic thickness fluctuations occur from wire to wire as well as along a single quantum wire. The FWHM of 7 meV obtained from micro-photoluminescence of a single GaAs QWR shows that there are very few modulations along a SQWR within 1.5 μm . Investigating an area of 4 μm of a SQWR by cathodoluminescence shows that there are the same thickness fluctuations within this range of a SQWR as from wire to wire. Temperature dependent photoluminescence allows to discuss the transport along the (110) plane of the SQW into the QWR. The maximum carrier capture efficiency into the quantum wires occurred in the temperature range from 70K to 100K. This is the same temperature range Hillmer found in /5/ for GaAs QWs. Higher energetic luminescence peaks additionally appeared in both the photoluminescence and cathodoluminescence spectra. These peaks mainly occurred in spectra of samples with a 1nm thick single quantum well. They were found to have their origin from recombination in local potential minima in

the vicinity of QWRs. Obviously, part of the generated excess carriers freezed in local potential minima at low temperatures. The carriers are able to leave these local potential minima by thermal activation at temperatures higher than 50K.

ACKNOWLEDGEMENTS

One of the authors, Peter Fischer, likes to thank the ISIR, Osaka University, and NTT Basic Research Laboratories, Atsugi, for their hospitality during his stays in Japan. This work is partially supported by a Grand-in-Aid for Scientific Research on Priority Areas, „Quantum Coherent Electronics“ from Ministry of Education, Science and Culture, Japan.

REFERENCES

1. M. Takeuchi, K. Shiba, K. Sato, H.K. Huang, K. Inoue, H. Nakashima, Proceedings of International Workshop on Mesoscopic Physics and Electronics 1995, Tokyo, Japan
2. M. Takeuchi, T. Takeuchi, Y. Inoue, T. Kato, K. Inoue, H. Nakashima, P. Fischer, J. Christen, M. Grundmann, D. Bimberg, Proceedings of International Conference on Superlattices, Microstructures and Microdevices (ICSMM-9), Belgium (1996)
3. J. Christen, M. Grundmann, D. Bimberg, J. Vac. Sci. Technol. **B 9** (4) (1991), 2358
4. H. Nakashima, M. Takeuchi, K. Inoue, T. Takeuchi, Y. Inoue, P. Fischer, J. Christen, M. Grundmann, D. Bimberg, Physica **B 227** (1996), 291
5. H. Hillmer, dissertation, University of Stuttgart (1989)

RESONANT ABSORPTION OF FAR-INFRARED
RADIATION IN QUANTUM WIRES
AT STRONG MAGNETIC FIELDS

W. Xu^{a)}, P. Vasilopoulos^{b)}, F.M. Peeters^{c)}
and C. Zhang^{a)}

^{a)}*Department of Physics, University of Wollongong
Wollongong, NSW 2522, Australia*

^{b)}*Department of Physics, Concordia University
Montreal, Canada H3G 1M8*

^{c)}*Department of Physics, University of Antwerp (UIA)
B-2610 Antwerpen, Belgium*

ABSTRACT

When the rate $1/\tau$ of electron scattering by impurities and/or phonons is comparable to the frequency ω of an electromagnetic radiation, the electron transitions among different states are accompanied by absorption of radiation. Far-infrared resonant absorption of radiation in a quantum wire (QW) at strong magnetic fields B is studied. The radiation is taken polarised along the QW (x axis) and B is applied normal to it (z axis). The confining potential along the y and z axes is assumed parabolic and triangular, respectively. The results show that: 1) similar to the case of a two-dimensional electron gas (2DEG), resonant absorption occurs in a QW when the electron temperature T_e is in the range from 80 K to 150 K; 2) one absorption peak can be observed at $f = \omega/2\pi \sim 0.1$ THz for $T_e \sim 80$ K, whereas for a 2DEG, at the same T_e , it occurs at $f = \omega/2\pi \sim 0.5$ THz; 3) with increasing T_e the peak shifts to higher frequencies and broadens markedly; 4) with increasing B , the peak shifts to higher frequencies and the absorption intensity first increases and then decreases; 5) the application of B does not result in a significant broadening of the absorption peak. As a result, applying a strong B -field to a QW provides a means of controlling the rate $1/\tau$ and leads to a frequency-tunable resonant absorption.

I. INTRODUCTION

With the development of novel means of investigation, such as free-electron-lasers (FELs), it has become possible to study the transport and optical properties of electronic devices subjected to intense far-infrared (FIR) or terahertz (THz) electromagnetic (EM) radiations. The FELs can provide the source of the linearly polarised FIR radiation which can be very useful in the investigation of novel condensed-matter materials such as low-dimensional electronic structures (LDESs). For a LDES realised from, e.g., III-V compounds using techniques such as Molecular Beam Epitaxy or Metallo-Organic Chemical Vapour Deposition, the conducting electrons in the system are confined within distances on the nanometer scale. The resulting energies, e.g., Fermi energy, electronic subband separation, etc., are on the meV scale. Noting that an energy $\hbar\omega \sim \text{meV}$ corresponds to a frequency $\omega \sim \text{THz}$, FIR EM waves may couple strongly to LDESs and this gives the possibility to observe photon-induced quantum resonance effects such as magneto-photon-phonon resonances [1]. Moreover, for a semiconductor GaAs-based LDES, the rate of electronic transitions due to scattering by impurities and/or phonons may be on the THz scale, i.e., 10^{12} s^{-1} [2,3]. As a result, the FIR EM radiation will modify strongly the processes of momentum and energy relaxation for excited electrons. This implies that GaAs-based LDESs can serve as THz devices operating in the linear and nonlinear response regimes.

Recently, nonlinear transport and optical properties have been studied experimentally [4,5] in THz-driven 2DEGs using FELs. Correspondingly, theoretical calculations have been performed [2,6] in order to account for the experimental observations. The results obtained have indicated that when a 2DEG is subjected to intense THz or FIR EM radiations, the electrons in the system will be heated by the EM field and the scattering rate $1/\tau$ will be influenced by the strength and frequency of the EM radiation field. This and the fact that nonradiative electronic transitions may be accompanied by the emission and absorption of EM radiation, may lead to resonant absorption of THz radiation when the rate $1/\tau$ of electronic scattering is comparable to the frequency ω of the EM radiation. Experimental data and theoretical results have shown that for GaAs-based 2DEGs, resonant absorption can be observed around a frequency $f = \omega/2\pi \sim 0.5 \text{ THz}$ for an electron temperature $T_e \sim 80 \text{ K}$. The physical reason for this was discussed in Ref. [2].

Since the FELs can provide linearly polarised EM radiations, one would expect that the resonant absorption seen in 2DEGs may also be observed in a QW when the FIR or THz radiation is polarised along its direction. In this paper we study in detail the conditions under which resonant FIR absorption in one-dimensional electron gases (1DEGs) can be observed. In search of an extra means of controlling the nonradiative scattering processes and consequently the resonant absorption, we consider a situation where a strong magnetic field B is applied to the QW.

II. ONE-ELECTRON QUANTUM WIRE CHARACTERISTICS

We consider a 1DEG along the x axis produced by a lateral confinement of a 2DEG that we model by a harmonic potential $U(y) = m^* \omega_0 y^2 / 2$; ω_0 is the characteristic frequency and m^* the effective electron mass. When the magnetic field B is applied along the z axis (growth direction of the 2DEG), the one-electron energy spectrum and the wavefunction of the 1DEG system are given, respectively, by

$$E_\alpha(k_x) = E_{Nn}(k_x) = \frac{\hbar^2 k_x^2}{2m_B^*} + \varepsilon_\alpha = \frac{\hbar^2 k_x^2}{2m_B^*} + \left(N + \frac{1}{2}\right) \hbar \omega_B + \varepsilon_n, \quad (1)$$

and

$$|k_x, \alpha\rangle = |k_x, N, n\rangle = e^{ik_x x} \phi_{Nk_x}(y) \psi_n(z). \quad (2a)$$

Here, $\alpha = (N, n)$, k_x is the electron wavevector, $m_B^* = m^*[1 + (\omega_c/\omega_0)^2]$ with $\omega_c = eB/m^*$ the cyclotron frequency, $\omega_B = (\omega_c^2 + \omega_0^2)^{1/2}$, and

$$\phi_{Nk_x}(y) = (2^N N! \pi^{1/2} l_B)^{-1/2} e^{-\xi^2/2} H_N(\xi) \quad (2b)$$

with $l_B = (\hbar/m^* \omega_B)^{1/2}$, $\xi = y/l_B - (\omega_c/\omega_B) l_B k_x$ and $H_N(x)$ the Hermite polynomials. In Eqs. (1) and (2), $\psi_n(z)$ and ε_n , the solutions of the 1D Schrödinger equation along the z axis, are independent of B . Furthermore, the density of states for noninteracting electrons at the energy level $\alpha = (N, n)$ is given by

$$D_\alpha(E) = \frac{g_s}{\pi} \sqrt{\frac{2m_B^*}{\hbar^2}} \frac{\Theta(E - \varepsilon_\alpha)}{\sqrt{E - \varepsilon_\alpha}}, \quad (3)$$

where $g_s = 2$ accounts for the spin degeneracy and $\Theta(x)$ is the unit step function.

Equations (1)-(3) are valid when the EM radiation is absent. In this paper we consider EM radiation energies much smaller than those given by Eq. (1) so that the effect of the radiation on the subband structure can be ignored. This can be expressed as $eE_0 k_x / m^* \omega^2 \ll 1$, with E_0 being the strength of the EM field for radiations polarised along the QW.

III. MOMENTUM-BALANCE EQUATION

It has been demonstrated [2] that the momentum-balance equation proposed by Lei and Horing [8] (LH) provides a useful tool for studying nonlinear transport and optical properties in 2DEGs driven by intense EM radiations. This approach is based on a high-frequency approximation with $eE_0 k_x / m^* \omega^2 \ll 1$, when the radiation is polarised along the x -direction of a 2DEG. It can be proven that the

results of the LH theory in the linear response limit are in essence a limiting case of the high-frequency transport theory proposed by Tzoar [9] using a Kubo formula approach. The LH momentum-balance equation for electron-phonon scattering can be obtained from Eqs. (2.33) and (2.33') of Ref. [9] by taking the phonon propagator to be a δ -function, ignoring the effect of screening due to the self-consistent field, and by introducing an electron temperature into the electron density-density (d-d) correlation function.

In this paper we derive a momentum-balance equation for a 1DEG. When the EM radiation is polarised along the QW, the effect of *direct* optical absorption via intersubband electronic transitions can be ignored. The EM field with a frequency ω can be represented by an ac electric field $E = E_0 e^{-i\omega t}$. In the experiments conducted in Refs. [4,5] the ac driving field ($E_0 \sim \text{kV/cm}$) is much larger than the dc exploring field ($E_{dc} < 2 \text{ V/cm}$), so the effect of E_{dc} in the measurement can be ignored. The steady-state electron velocity corresponding to the ac field is then of the form $v = v_0 e^{-i\omega t}$. This approach has been used by Peeters and Devreese [10] in deriving, e.g., the Thornber-Feynman theory for electron-LO-phonon interactions in low-density 3D systems. Considering electron interaction only with LO-phonons and following Ref. [8], we derive the momentum-balance equation and from that the frequency-dependent magnetoconductivity in the form of the Drude formula

$$\sigma_{xx}(\omega) = \frac{n_e e^2}{m^*(\omega)} \frac{\tau}{1 - i\omega\tau}, \quad \text{Re}\sigma_{xx}(\omega) = \frac{n_e e^2}{m^*(\omega)} \frac{\tau}{1 + (\omega\tau)^2}. \quad (4)$$

Here n_e is the electron density of the 1DEG, $m^*(\omega) = m^*[1 + M_1(\omega)/\omega]$ is the frequency-dependent effective electron mass, $\tau = [m^*(\omega)/m^*]/M_2(\omega)$ is the frequency-dependent electron relaxation time, and $M(\omega) = M_1(\omega) + iM_2(\omega)$ is the memory function embodying the different scattering mechanisms. For interactions with LO-phonons the memory function is given by

$$M(\omega) = \frac{N_0 - N_\omega}{m^* n_e \omega} \sum_{\alpha', \alpha, \mathbf{Q}} q_x^2 |u^{LO}(\mathbf{Q})|^2 F_{\alpha'\alpha}(\mathbf{Q}) \Pi(\alpha', \alpha, q_x, \omega_{LO} - \omega), \quad (5)$$

where $N_0 = [e^{\hbar\omega_{LO}/k_B T} - 1]^{-1}$ is the LO-phonon occupation number with $\hbar\omega_{LO}$ the LO-phonon energy, $N_\omega = [e^{\hbar(\omega_{LO}-\omega)/k_B T_e} - 1]^{-1}$ is the effective LO-phonon occupation number in the presence of radiation, and T_e the electron temperature. Further, $\mathbf{Q} = (q_x, q_y, q_z)$ is the phonon wavevector, $F_{\alpha'\alpha}(\mathbf{Q})$ the form factor for interaction with bulk phonon modes, $\Pi(\alpha', \alpha, q_x, \omega) = \Pi_1(\alpha', \alpha, q_x, \omega) + i\Pi_2(\alpha', \alpha, q_x, \omega)$ the Fourier transform of the electron density-density correlation function, and $|u^{LO}(\mathbf{Q})|^2$ the square of the electron-LO-phonon interaction matrix element. The effects of electron-electron interactions and of photon emission have been neglected. Using the Fröhlich Hamiltonian for electron-LO-phonon scattering, we have

$$|u^{LO}(\mathbf{Q})|^2 = 4\pi\alpha_{LO} L_0 (\hbar\omega_{LO})^2 / Q^2, \quad (6)$$

where α_{LO} is the coupling constant and $L_0 = (\hbar/2m^*\omega_{LO})^{1/2}$ the polaron radius. With the wavefunction given by Eq. (2) the form factor takes the form

$$F_{\alpha'\alpha}(\mathbf{Q}) = G_{n'n}(q_z) C_{N',N} \left(\frac{l_B^2}{2} \left[\left(\frac{\omega_c}{\omega_B} \right)^2 q_x^2 + q_y^2 \right] \right), \quad (7)$$

with $G_{n'n}(q_z) = |\langle n' | e^{iq_z z} | n \rangle|^2$, $C_{N',N}(x) = [N!/(N+J)!] x^J e^{-x} [L_N^J(x)]^2$, and $L_N^J(x)$ the associated Laguerre polynomial. Further, with the energy spectrum given by Eq. (1), the imaginary part of the electron density-density correlation function is obtained as

$$\Pi_2(\alpha', \alpha, q_x, \omega) = -\frac{m_B^*}{\hbar^2 |q_x|} \left[f\left(\epsilon_{\alpha'} + \frac{(\epsilon_x - \epsilon_{\alpha'\alpha})^2}{4\epsilon_x}\right) - f\left(\epsilon_{\alpha} + \frac{(\epsilon_x + \epsilon_{\alpha'\alpha})^2}{4\epsilon_x}\right) \right], \quad (8)$$

where $\epsilon_x = \hbar^2 q_x^2 / 2m_B^*$, $\epsilon_{\alpha'\alpha} = \epsilon_{\alpha'} - \epsilon_{\alpha} + \hbar\omega$, and $f(x) = [e^{(x-E_F)/k_B T} + 1]^{-1}$ is the Fermi-Dirac function with E_F the Fermi energy.

For THz EM radiations we have $M_1(\omega) \ll \omega$ and this results in $m^*(\omega) \simeq m^*$. As is usual in the experiments, we consider the case when only the lowest subband in the z-direction is occupied and describe it with the usual variational wavefunction [11]. This gives $G_{00}(q_z) = [1 + (q_z/b)^2]^{-3}$, where $b = [(48\pi m^* e^2 / \kappa \hbar^2)(N_d + (11/32)N_e)]^{1/3}$ with κ the dielectric constant and N_d and N_e , respectively, the depletion charge density and the electron density of the 2DEG.

IV. RESULTS AND DISCUSSIONS

We perform the calculations for AlGaAs/GaAs QWs with the following parameters: effective mass $m^* = 0.0665m_e$ with m_e the electron rest mass, dielectric constant $\kappa = 12.9$, LO-phonon energy $\hbar\omega_{LO} = 36.6$ meV, and electron-LO-phonon coupling constant $\alpha_{LO} = 0.068$. Other typical parameters are the electron densities of the 1DEG $n_e = 2 \times 10^6$ cm $^{-2}$ and of the 2DEG $N_e = 2 \times 10^{11}$ cm $^{-2}$, the depletion charge density $N_d = 5 \times 10^{10}$ cm $^{-2}$, and the characteristic energy of the 1D confinement $\hbar\omega_0 = 5$ meV. The Fermi energy is determined by electron number conservation.

In Fig. 1, we plot the real part $\text{Re}\sigma_{xx}(\omega)$ of the conductivity and the inverse of the scattering rate $1/\tau$ as a function of the radiation frequency for different temperatures T_e at a fixed magnetic field. $\text{Re}\sigma_{xx}(\omega)$ describes the absorption of the EM wave in the QW. In the low- (high-) frequency regime, we have $\text{Re}\sigma_{xx}(\omega) \sim \tau$ ($\text{Re}\sigma_{xx}(\omega) \sim 1/\tau$). Since $1/\tau$ always decreases with ω , the competition between ω and $1/\tau$ results in a changeover of the dependence of the optical absorption on ω . Consequently, a peak in the resonant absorption can be observed. From Fig. 1(a), we see that: 1) similar to the case of 2DEGs [2], an absorption peak can be observed when T_e is in the range from 80 K to 150 K; 2) the absorption peak appears around

$f_p = \omega_p/2\pi \sim 0.1$ THz, whereas for 2DEGs it appears at $f_p \sim 0.5$ THz; 3) as in 2DEGs, with increasing T_e (or radiation intensity), the peak broadens and its position is shifted to higher frequencies; and 4) as in 2DEGs, the absorption peak cannot be observed at very low and very high excitation frequencies. In Fig. 1 (b) we see that, in a QW, $1/\tau$: i) increases rapidly with increasing T_e , ii) is comparable to the radiation frequency ω , and iii) decreases with increasing ω . These are the conditions under which resonant absorption of EM radiations can be observed, as discussed in Ref. [2] for a 2DEG.

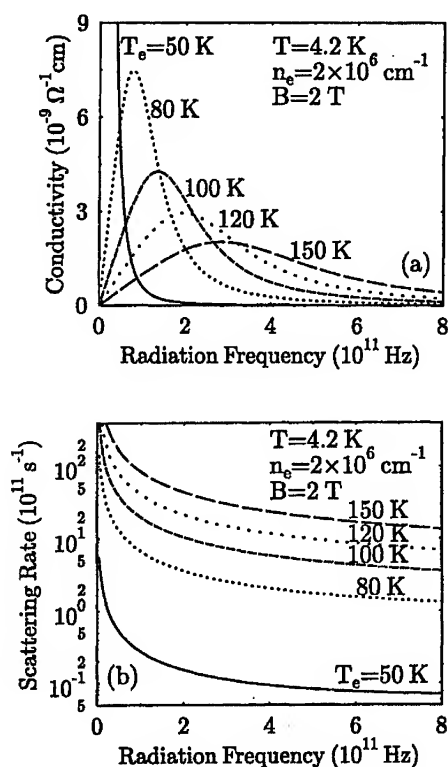


Fig. 1. (a) Real part of the conductivity ($\text{Re}\sigma_{xx}(\omega)$) and (b) scattering rate $1/\tau$ as a function of the radiation frequency $f = \omega/2\pi$ for different electron temperatures (T_e) at fixed lattice temperature (T) and magnetic field (B).

In Fig. 2 the real part of the conductivity and the inverse of the relaxation time are shown as a function of ω for different B and a fixed T_e . As can be seen, 1) for low (high) magnetic fields, e.g., $B < 2$ T ($B > 3$ T) at $T_e = 100$ K, due to the features of the relaxation time shown in Fig. 2(b), the absorption peak shifts to lower (higher) frequencies relative to that for $B = 0$; 2) with increasing B , up to about 6 T, the absorption peak first increases and then decreases; 3) FIR resonant absorption can be observed at relatively low B fields; and 4) the application of B does not result in a significant broadening of the peak. These results show that applying a magnetic field to a QW leads to a control of the electronic scattering rate and, consequently, provides a means of controlling FIR resonant absorption.

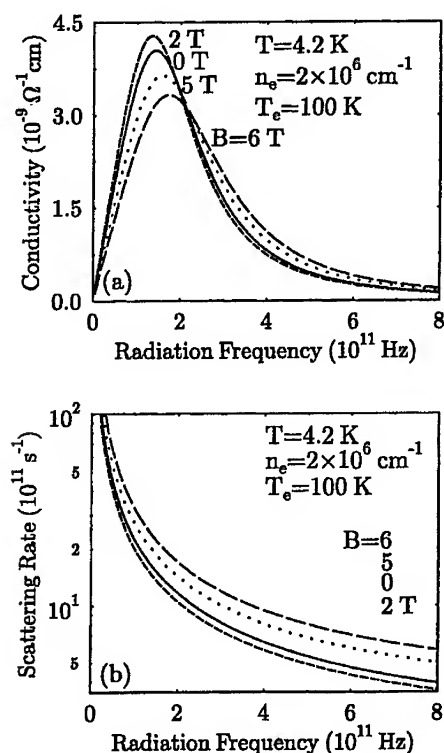


Fig. 2. (a) Real part of the conductivity and (b) scattering rate $1/\tau$ as a function of the radiation frequency $f = \omega/2\pi$ for different magnetic fields and with fixed electron and lattice temperatures.

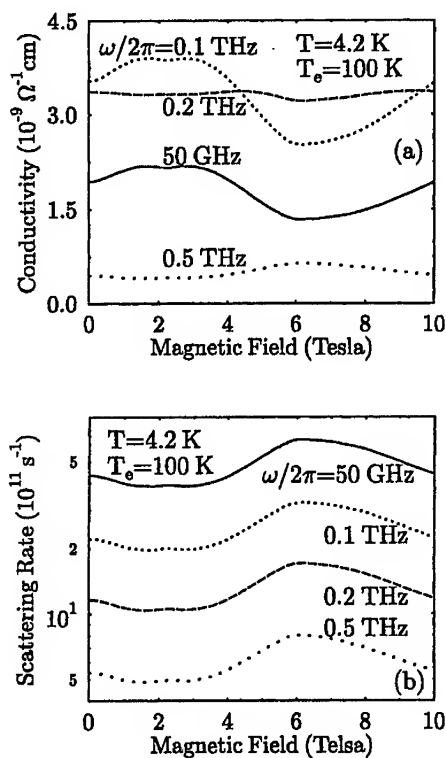


Fig. 3. (a) Real part of the conductivity and (b) scattering rate $1/\tau$ as a function of magnetic field for different radiation frequencies and with fixed electron and lattice temperatures.

From Figs. 1 and 2 one can find that $\text{Re}\sigma_{xx}(\omega) \rightarrow 0$ when $\omega \rightarrow 0$ at relatively high T_e . This is in contrast with the experimental observations [4]. The main reason is that the momentum-balance equation was based on a high-frequency approximation for evaluating the diagrams for the contributions to the high-frequency conductivity proposed by Tzoar [9]. In the low-frequency (LF) regime, particularly when $\omega \rightarrow 0$, this approach may break down. When $eE_0k_x/(m^*\omega^2) \gg 1$, one should evaluate the LF conductivity diagrammatically but this complicates the calculations considerably. We do not attempt such an evaluation here. Furthermore,

in our model only single-photon processes are taken into account. In a QW under intense LF EM radiations channels for multiphoton absorption will open up leading to an increase in the conductivity in the LF regime. It should be noted that the LF and/or $\omega \rightarrow 0$ conductivity was also discussed by PD in Ref. [10] for electron-LO-phonon interactions. To calculate correctly the LF conductivity one has to sum an infinite number of diagrams; the results obtained have been documented in Ref. [10].

The real part of the conductivity and the scattering rate $1/\tau$ are shown in Fig. 3 as a function of magnetic field B for different radiation frequencies ω with fixed electron T_e and lattice T temperatures. The peaks appearing around 6 T, in Fig. 3(b), are the usual magneto-phonon resonances (here $3\omega_B \simeq \omega_{LO}$) [7]. For fixed T_e , the rate $1/\tau$ decreases with increasing ω for all B fields. From Fig. 3(a) we note that for low ω ($\omega/2\pi < 0.2$ THz) absorption peaks can be observed at low B and a magneto-phonon minimum appears around $B \sim 6$ T. When $\omega/2\pi > 0.2$ THz there is no absorption peak as a function of B up to 10 T, and the conductivity is rather featureless. These results suggest that in the presence of B resonant absorption of relatively low-frequency FIR radiations can be observed by measuring the dependence of the dc conductivity (or mobility) on the field B for fixed frequency and intensity of the radiation field.

V. SUMMARY

We have studied resonant absorption of FIR radiation by hot electrons in QWs in the presence of strong perpendicular magnetic fields. Similar to the case of 2DEGs, we have found that resonant absorption in a QW can be observed when the rate $1/\tau$ of electron scattering by LO-phonons is comparable to the radiation frequency ω if the electron temperature is in the range from 80 K to 150 K. In contrast with 2DEGs, where the resonant absorption peak appears at about $f \sim 0.5$ THz, the same peak in QWs occurs at about $f \sim 0.1$ THz at $T_e \sim 80$ K. If we apply a magnetic field parallel to the QW, the position and the intensity of the FIR absorption can be varied. Thus, the applied magnetic field provides a means of controlling the electronic scattering and, consequently, a means of controlling the optical absorption. The results presented here need to be tested experimentally.

ACKNOWLEDGEMENT

This work was supported by the Australian Research Council (WX, CZ) and by NSERC Grant No. OGP0121756 (PV). One of us (FMP) is a Research Director with the FWO-VL (Flemish Science Foundation).

References

- [1] W. Xu and C. Zhang, *Phys. Rev. B* **54**, 4907 (1996).
- [2] W. Xu and C. Zhang, *Appl. Phys. Lett.* **68**, 3305 (1996).
- [3] W. Xu, F.M. Peeters, and J.T. Devreese, *Phys. Rev. B* **48**, 1562 (1993).
- [4] N.G. Asmar, J. Černe, A.G. Markelz, E.G. Gwinn, M.S. Sherwin, K.L. Campman, and A.C. Gossard, *Appl. Phys. Lett.* **68**, 829 (1996).
- [5] N.G. Asmar, A.G. Markelz, E.G. Gwinn, J. Černe, M.S. Sherwin, K.L. Campman, P.F. Hopkins, and A.C. Gossard, *Phys. Rev. B* **51**, 18041 (1995).
- [6] W. Xu and C. Zhang, *Phys. Rev. B* **55**, 5259 (1997).
- [7] P. Vasilopoulos, P. Warmenbol, F.M. Peeters, and J.T. Devreese, *Phys. Rev. B* **40**, 1810 (1989).
- [8] X.L. Lei and N.J.M. Horing, *Phys. Rev. B* **36**, 4238 (1987).
- [9] N. Tzoar and Chao Zhang, *Phys. Rev. B* **35**, 7596 (1987).
- [10] F.M. Peeters and J.T. Devreese, *Solid State Phys.* **38**, 82 (1984)
- [11] T. Ando, A.B. Fowler, and F. Stern, *Rev. Mod. Phys.* **54**, 437 (1982).

Infrared Second Harmonic Generation in Magnetic-Field-Biased Quantum Wires

A. Svizhenko, A. Balandin, and S. Bandyopadhyay
Department of Electrical Engineering
University of Nebraska
Lincoln, Nebraska 68588

Abstract

We have theoretically studied non-linear frequency conversion in a semiconductor quantum wire biased with a magnetic field. In these systems, efficient second harmonic generation occurs as a result of the large value of the second-order dielectric susceptibility $\chi^{(2)}$ arising from dipole transitions between magneto-electric subbands. The magnitude and peak frequency of $\chi^{(2)}$, as well as the absorption and refractive index associated with $\chi^{(2)}$, can be tuned with the magnetic field. This allows one to achieve low insertion loss and efficient phase matching by manipulating the absorption and refractive index with a magnetic field.

I. Introduction

Most ordinary solids are not efficient frequency converters because they exhibit extremely small even-order dielectric susceptibilities. Ideally, even-order susceptibilities vanish in solids with inversion symmetry.¹ Consequently, a semiconductor structure can exhibit a large value of the second order susceptibility $\chi^{(2)}$ only if the inversion symmetry of the conduction-band potential is broken artificially either by an external electric field, or by the intentional growth of an asymmetric structure. Obviously, the former is the preferred method since an electric field can be varied continuously and

this allows one to tune the degree of symmetry-breaking and the magnitude of $\chi^{(2)}$. However, an electric field has a practical shortcoming. In a quantum confined structure, it tilts the potential barriers confining the photogenerated carriers. As a result, carriers can escape by tunneling or thermionic emission and this is especially serious in *GaAs/AlGaAs* systems where the barrier height is relatively small. Indeed, it has been pointed out that the electronic states in a quantum confined system biased by a transverse electric field are never true bound states since the particles can always lower their energy by escaping from the well². Consequently, optical transitions (and their higher order harmonics) associated with these states have inconveniently large linewidths and small oscillator strengths.

Recently, we proposed magnetostatic biasing as an attractive alternative to mitigate this problem.³ We showed that a magnetic field can break inversion symmetry in a quantum wire without tilting potential barriers. A transverse magnetic field, applied to a wire, exerts a Lorentz force on an electron moving along the length. As a result, its wave function (in any magneto-electric subband) will be skewed towards one edge of the wire. This skewing does not tilt potential barriers to first order (the barriers may tilt slightly because of a second-order effect associated with space-charges and the self-consistent (Hall) electric field). However, it effectively breaks inversion symmetry since it causes net charges to accumulate at either edge of the wire. This leads to a non-vanishing even-order susceptibility in an otherwise symmetric structure. The skewing has another subtle effect. The degree to which the wave function is skewed is *different in different subbands* since an electron has different kinetic energies (and hence experiences different Lorentz forces) in different subbands. As a result, transitions between subbands whose wave functions have the same parity - which are forbidden without a magnetic field - are now allowed since the parities are altered by different amounts in different subbands. This effect has some similarity with the quantum confined Lorentz effect (QCLE) previously examined by us⁴ in

the context of interband transitions between conduction and valence band states.

In this paper, we first calculate the second-order susceptibility $\chi^{(2)}$ in a symmetric quantum wire whose inversion symmetry (along the width) has been broken with a magnetic field. We restrict ourselves to narrow GaAs wires with a width of about 150\AA . The energy spacing between the first and second subband is $\Delta E_{12} \approx 72\text{ meV}$. This choice of the wire dimension puts the resonant frequency (for transitions between the lowest subbands) in the mid-infrared spectral region. The wavelength of the second harmonic component of this transition is about $8.6\text{ }\mu\text{m}$. Here we will be mainly interested in $\chi^{(2)}$ arising from resonant and near-resonant inter-subband transitions which are governed by the interplay of dipoles and resonant excitations. In contrast, Ref. [3] focussed on the off-resonance regime which was governed solely by the dipoles. We will also calculate absorption and refractive index in the frequency region of interest for both pump and second harmonic frequencies and show how they can be manipulated with an external magnetic field to realize low insertion loss and efficient phase matching.

The rest of the paper is organized as follows. In the next section, we describe the theoretical formulation, followed by results. Finally, in section IV, we present the conclusions.

II. Theory

We consider a generic GaAs quantum wire (as shown in the inset of Fig. 1) with a magnetic field applied along the z direction. The thickness along the z direction is so small (and consequently the subband separation in energy in this direction is so large) that for the range of photon energies considered, an electron cannot be excited (by real transition) into a subband which has more than two nodes along the z -direction. In other words, such a transition will not be accessible in energy. This restriction, coupled with the fact that a magnetic field does not affect the z -component of the electron wave function, allows us to drop the z -component from further consideration. The width

of the wire along the y-direction is however large enough ($W = 150\text{\AA}$) that subbands with more than two nodes along the y-direction are accessible in energy.

In systems without inversion symmetry, the lowest order optical nonlinearity is of the second order and is expressed by

$$P^{(2)}(\vec{k}, \omega) = \chi^{(2)}(\omega; \omega_1, \omega_2) \vec{E}_1(\vec{k}_1, \omega_1) \vec{E}_2(\vec{k}_2, \omega_2), \quad (1)$$

where \vec{P} is the polarization caused by two electric fields \vec{E}_1 and \vec{E}_2 that are associated with the electromagnetic fields of either two frequency components of the same light beam or two different coherent beams with frequencies ω_i and wave vectors \vec{k}_i . It is well known that the third-ranked tensor $\chi^{(2)}$ will vanish in any structure with inversion symmetry. A quantum confined structure may lack inversion symmetry for two main reasons. (i) the semiconductor material by its intrinsic chemical and crystalline structure may lack inversion symmetry,⁵ and this is the case in most III-V, II-VI, and I-VII compounds along certain crystallographic directions, or (ii) the quantum confining potential well may be asymmetric (e. g. triangular potential well, asymmetric double square well potential, etc.). In the first case, the asymmetry is related to the intracell charge asymmetry and is not affected by the confinement since the latter extends over several unit cells. In the second case, the asymmetry is artificially imposed and therefore can be engineered. It clearly depends on the confining potential. Insofar as an applied electric field can alter the potential, it can change the degree of symmetry-breaking and hence modulate $\chi^{(2)}$.

In the present work we restrict ourselves to the second case and do not consider intrinsic second order nonlinearities which can be quite large in some materials (the nonlinear susceptibility of bulk GaAs is $\chi_{14}^{(2)} = 3.8 \cdot 10^{-10} \text{ m/V}$).⁶ As mentioned before, we avoid the use of a symmetry-breaking electric field since it promotes carrier escape. Instead, we consider a magnetic field. Although a magnetic field does not directly affect the potential, it leads to an *uneven charge distribution* along the width (*y - axis*) of the wire because of

the different degrees of skewing of the wave functions in different magnetoelectric subbands. This has the effect of breaking inversion symmetry.

As mentioned before, a magnetic field induces forbidden transitions between subbands of the same parity. The large magnitude of the dipoles associated with these transitions and their extreme sensitivity to the field open up the possibility of *controllable* second harmonic generation (SHG) that can be manipulated by the magnetic field. In order to evaluate the magnitude and dependence of SHG on the biasing field and wire geometry, we calculate the second order susceptibility using the formula¹

$$\chi^{(2)}(2\omega; \omega; \omega) = \frac{Ne^3}{\epsilon\epsilon_0 2\hbar^2} \hat{S}_T \sum_{abc} \frac{d_{ab}^\mu d_{bc}^\alpha d_{ca}^\beta}{(\Omega_{ba} - \omega - i\gamma)(\Omega_{ca} - 2\omega - i\gamma)}, \quad (2)$$

where N is concentration (number density) of conduction electrons, γ is a damping factor associated with elastic and inelastic scattering, $\hbar\Omega_{ba} \equiv \hbar\Omega_{ba}(B, W, k)$ is the energy spacing between the b -th and a -th magnetoelectric subbands which depends on the applied magnetic field, wire width and electron wave vector and $d_{mn} \equiv d_{mn}(B, W, k)$ is a dipole element of transitions between different subbands. The total symmetrisation operation \hat{S}_T indicates that the expression which follows is to be summed over all permutations of the pairs $(\mu, 2\omega), (\alpha, \omega), (\beta, \omega)$. Since \hat{S}_T involves a summation over all possible permutations, it is clear that $\chi_{\mu\alpha\beta}^{(2)}(2\omega; \omega; \omega)$ is invariant under any of them.

In order to calculate dipole elements $d_{mn}(B, W)$, we proceed as in Ref. [3]. Under the electric dipole approximation, the matrix element of photoinduced inter-subband transitions within the conduction band is given by⁷

$$d_{f,i}(k, B) = e \int \chi_f(y, k, B) \hat{n} \cdot \vec{r} \chi_i(y, k, B) d\vec{r} \int u_f^*(x, y, k) u_i(x, y, k) d\Omega \quad (3)$$

where $d\Omega$ is a volume element, \hat{n} is the unit vector along the direction of the incident photon polarization, $\vec{r} = x\vec{a}_x + y\vec{a}_y$ is the two-dimensional radius vector, and subscripts i, f stand for initial and final states respectively. Now, if we assume that the incident light is polarized along the y -direction so that

$\hat{\eta} = \hat{d}_y$, the above equation simplifies to

$$d_{f,i}(k, B) = e \langle \chi_f | y | \chi_i \rangle = e \int_{-W/2}^{W/2} y \chi_f(y, k, B) \chi_i(y, k, B) dy, \quad (4)$$

where W is the width of the quantum wire along the y -direction. One should note here, that if there is no magnetic (or electric) field applied, the envelope functions χ_i are just particle-in-box states and the dipole moment in Eq. (4) is non zero only for the transitions between subband states of opposite parity. However, this is obviously not the case when a magnetic field is present. It is clear from Eq. (4) that to calculate the dipole moments in the presence of a magnetic field, all we need to compute are the wave functions $\chi_{f,i}(y, k, B)$ at a given magnetic field B , for given magnetoelectric subbands f and i , and for a given wave vector k . This is achieved via a numerical (finite difference) solution of the Schrödinger equation for the y -component of the wavefunction

$$\frac{\partial^2 \chi(y)}{\partial y^2} + \frac{2m^*}{\hbar^2} E \chi(y) - \left(\frac{y}{l}\right)^2 \chi(y) + 2\frac{y}{l^2} k \chi(y) - k^2 \chi(y) = 0 \quad (5)$$

with l being the magnetic length given by $l = \sqrt{\hbar/eB}$, assuming hardwall boundary conditions

$$\chi(y = W/2) = \chi(y = -W/2) = 0 \quad (6)$$

and following the prescription of Ref. [8]. Once this is done, we can calculate the dipole moment in Eq. (4) for any chosen intersubband transition, at any chosen magnetic field and for any chosen wave vector.

The absorption of both the fundamental frequency (pump) and its second-order harmonic is very important when considering frequency conversion with *low insertion loss*. In general, it is desirable to have large absorption coefficient $\alpha(\omega)$ for the pump frequency and small $\alpha(2\omega)$ for the converted frequency so that the latter is not re-absorbed to cause large insertion loss. In order to obtain the absorption coefficients in the whole range of frequencies and for different values of a magnetic flux density, we need to calculate the first-order susceptibility as follows

$$\chi^{(1)}(\omega) = \frac{Ne^2}{\epsilon\epsilon_0\hbar} \sum_{ab} \frac{(d_{ab})^2}{\Omega_{ba} - \omega - i\gamma}, \quad (7)$$

where we have used the same notation as in Eq. (2). The imaginary part of $\chi^{(1)}(\omega)$ is related to the absorption coefficient while the real part is related to the refractive index.

II. Results

We now present results of our calculations. The physical parameters used for the numerical calculations are relevant for a *GaAs* quantum wire with relative dielectric constant $\epsilon_r = 12.9$, and effective masses $m_e = 0.067m_0$ and $m_h = 0.5m_0$ where m_0 is the free electron mass.

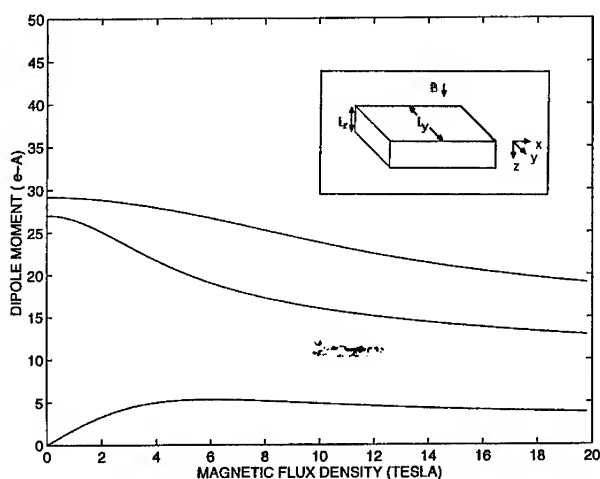


Figure 1: The dipoles of three inter-subband transitions as functions of the applied magnetic field. The induced dipole d_{e1-e3} peaks at a magnetic flux density of 5.3 tesla.

Fig. 1 presents the dipole moments for the lowest intraband transitions as a function of magnetic flux density. At zero magnetic field, a non-vanishing dipole matrix element occurs only for transitions between states of opposite parity (e1-e2, e2-e3) as expected from Eq. (4). Transition dipole d_{e3-e1}

has a non-monotonic dependence on the magnetic field. This transition is forbidden at zero field since the wave functions of the first and third subband have the same parity. At low and moderate magnetic fields, the parities are altered by the skewing of the wavefunctions. The skewing effect of the wave functions of the first and the third subbands is shown in Fig. 2 (top). Its degree depends on a subband number, which causes a breaking of inversion symmetry and, consequently, non-zero value of dipole matrix element d_{e3-e1} for otherwise forbidden transition.

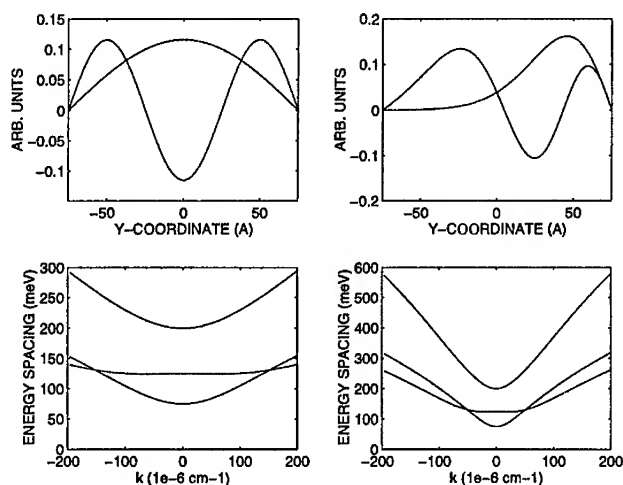


Figure 2: (Top left and right). Skewing of the wave functions of the first and third subbands in a magnetic field. The left panel corresponds to zero magnetic flux density and the wave functions are particle-in-a-box states. The right panel corresponds to a flux density of 3 tesla and the wave functions are those of "edge states". (Bottom left and right). The energy spacing $\hbar\Omega_{mn}$ between the m th and n th subbands vs. wave vector k at a magnetic flux density $B=1$ tesla (left) and $B=3$ tesla (right). The lowest curve (at $k=0$) corresponds to $e1-e2$, the intermediate curve to $e2-e3$, and the highest to $e1-e3$.

The dipole moment reaches a maximum of about 6 e-Å and then de-

creases. This later decrease is related to the following effect. For some fixed wave vector k (electron velocity), a sufficient increase in the flux density B forces the traversing states ("skipping orbits" or "edge states") to condense into closed cyclotron orbits (Landau levels) which are no longer skewed by the magnetic field to the wire edge since they have no translational velocity and hence experience no Lorentz force. While edge states have a skewed wave function which is not symmetric in space, cyclotron orbits have a wave function that is symmetric about the orbit center. Note that the orbit center's coordinates depend only on k and B . Therefore, at a fixed k , the wave functions of the first and third Landau levels are symmetric about a *common* center. Whenever this kind of symmetry holds, d_{e3-e1} vanishes. Therefore, the dipole moment d_{e3-e1} decreases gradually to zero at high magnetic field with the onset of Landau condensation (5 tesla for this wire dimensions).

In Fig. 3, we plot the absolute values of $\chi^{(2)}$ as a function of photon energy for two different values of the magnetic field. In our numerical calculations we have used a dilute carrier concentration of $N=10^{17} \text{ cm}^{-3}$ which allows us to neglect high density effects such as screening and bandgap renormalization. Both susceptibility curves have pronounced three-peak resonant structure which corresponds to two one-photon transitions e1-e2 (at 72 meV) and e2-e3 (at 124 meV) and one two-photon transition e1-e3 (at 100 meV) between magneto-electric subbands. These three peaks have different broadenings because the sum in Eq. (2) represents an integral effect of all direct transitions with different values of electron wave vector k and because of the complex dependence of the subband spacing $\hbar\Omega_{mn}$ on k and B (see Fig. 2 (bottom)). The latter also gives rise to an unevenness in the second order susceptibility peaks. The peak value of the second order susceptibility is $\chi^{(2)} = 14.5 \text{ \AA/V}$ for 1 tesla field (left panel); and $\chi^{(2)} = 43.1 \text{ \AA/V}$ for 3 tesla (right panel). For comparison, the nonlinear susceptibility of electric field biased GaAs quantum wells ($W=92 \text{ \AA}$) - calculated theoretically and measured experimentally in Ref. [9] - was $\chi^{(2)}=240 \text{ \AA/V}$ for an electric field of 36

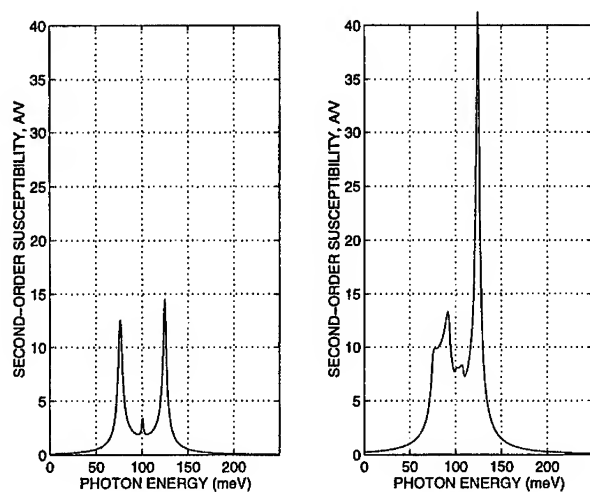


Figure 3: Second order susceptibility as a function of the photon energy for two values of the biasing magnetic field. The left panel corresponds to a magnetic flux density $B=1$ tesla, the right panel to $B=3$ tesla. The maximum values of the $\chi^{(2)}$ curves are 14.5 \AA/V for 1 tesla field and 43 \AA/V for 3 tesla field.

kV/cm. The carrier concentration used in their calculations was $N=5 \times 10^{17} \text{ cm}^{-3}$. Adjusted to that carrier concentration, the second order susceptibility for a 3-tesla magnetic field is about 215 \AA/V compared to 240 \AA/V of Ref. [9]. This shows that relatively weak magnetic fields in quantum wires can produce similar magnitudes of $\chi^{(2)}$ as rather strong electric fields in quantum wells.

Fig. 4 shows the dependence of the imaginary part of the first-order susceptibility $\text{Im}(\chi^{(1)})$ as a function of photon energy for two different values of the magnetic field. We have used the same wire dimensions and carrier concentrations for this plot as in the previous one. The same physics pertinent to the previous plot explains different broadening; however, the peaks are now attenuated because of averaging over different transition probabilities.

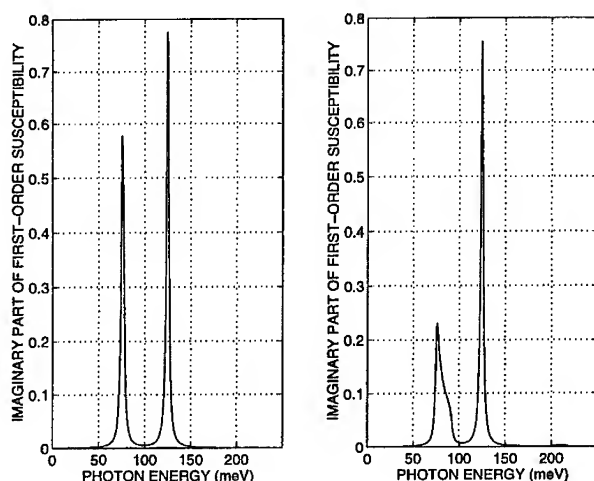


Figure 4: Imaginary part of the first-order susceptibility as a function of the photon energy for B=1 tesla (left panel) and B=3 tesla (right panel).

Since $Im(\chi^{(1)})$ is related to the absorption coefficient $\alpha(\omega)$ as

$$\alpha(\omega) = \frac{4\pi\omega}{c} Im(\chi^{(1)}), \quad (8)$$

one can estimate the absorption over the whole frequency range. At resonant photon energies of 72 meV and 124 meV, the absorption coefficient $\alpha = 1.5 \cdot 10^4 \text{ cm}^{-1}$ and $\alpha = 4.5 \cdot 10^4 \text{ cm}^{-1}$, respectively. It is clear from the figure, that the absorption coefficient at twice these frequencies, $\alpha(2\omega)$ is much less. This implies that a large portion of the pump energy at these resonant frequencies will be absorbed by the structure and converted into second harmonic signal which will not be significantly re-absorbed.

Another important factor for efficient second harmonic generation is *phase matching*. Since the refractive index $n(\omega)$ of most materials is frequency dependent, the following inequality holds $n(\omega) \neq n(2\omega)$. As a result, the coherence length $l_{coh} = \lambda_\omega / 4(n_{2\omega} - n_\omega)$ for *GaAs* (typical non-birefringent crystal)

varies between $10\mu\text{m}$ and $100\mu\text{m}$. The efficiency of nonphase-matched interactions are about 10^{-5} times less than that of the phase-matched interactions over a length scale of 1 cm.

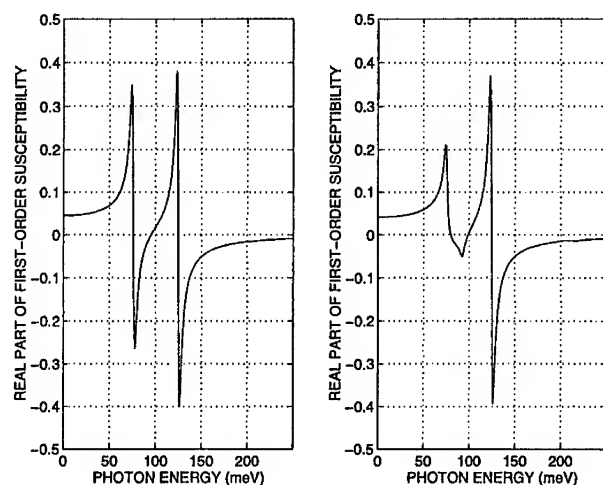


Figure 5: Real part of the first-order susceptibility as a function of the photon energy for $B=1$ tesla (left panel) and $B=3$ tesla (right panel).

Using a magnetic field as an additional degree of freedom, we may try to adjust $n(\omega)$. In Fig. 5 we present the dependence of the real part of the first-order susceptibility $Re(\chi^{(1)})$ as a function of photon energy for two different values of the magnetic field. Using the relation

$$\Delta n(\omega) = 2\pi Re(\chi^{(1)}), \quad (9)$$

and Eq. (8), one can determine the frequencies where two conditions simultaneously hold: $n(\omega) \approx n(2\omega)$ and $\alpha(\omega) \gg \alpha(2\omega)$. For the 3-tesla field, this frequency $\hbar\omega$ corresponds to 75 meV.

IV. Conclusion

We have theoretically studied second harmonic generation in a semiconductor quantum wire biased with a magnetic field. A strong second-harmonic component of the dielectric susceptibility, due to the dipoles associated with transitions between magneto-electric subbands, is found. We have also calculated absorption coefficient and refractive index in the appropriate frequency range to assess the efficiency of frequency conversion and insertion loss. We have shown that a magnetic field can be used as an additional degree of freedom in optimizing second harmonic generation efficiency. This may have important applications in nonlinear optics.

Acknowledgement

This work is supported by the US Army Research Office under contracts DAAH04-95-1-0586 and DAAH04-95-1-0527. The authors are indebted to the Electrochemical Society, Inc. for partial travel support.

REFERENCES

- [1] see for example P.N. Butcher, D. Cotter, *The Elements of Nonlinear Optics*, (Cambridge University Press, 1990); A. Yariv, *Quantum Electronics*, (Wiley, N.Y., 1989); or Y.R. Shen, *The Principles of Nonlinear Optics*, (Wiley, N.Y., 1984).
- [2]. E.J. Austin and M. Jaros, *Phys. Rev. B* **31**, 5569 (1985).
- [3]. A. Svizhenko, A. Balandin and S. Bandyopadhyay, *J. Appl. Phys.*, (in press, 1997).
- [4]. A. Balandin and S. Bandyopadhyay, *J. Appl. Phys.*, **77**, 5924 (1995); A. Balandin, Ph.D. dissertation, University of Notre Dame, 1996.
- [5] This lack of symmetry is due to the transfer of a valency charge from one atom to the other bond-forming atom and resultant uneven charge distribution along the bond axis.

[6] *Handbook of Lasers*, Edited by R.J. Pressley (Chemical Rubber Co., Cleveland, 1971), p. 504.

[7]. Claude Weisbuch and Borge Vinter, *Quantum Semiconductor Structures: Fundamentals and Applications*, (Academic Press, Boston, 1991).

[8] S. Chaudhuri and S. Bandyopadhyay, *J. Appl. Phys.*, **71**, 3027 (1992).

[9]. M.M. Fejer, S.J.B. Yoo, R.L.Byer, A. Harwit, J.S. Harris, *Phys. Rev. Lett.*, **62**, 1041 (1989).

Optical Characterization of Semiconductor Nanowires Fabricated by Electrodeposition into Porous Alumina

Ivan Avrutsky¹, D. Routkevitch^{2,1}, M. Moskovits², Jimmy Xu¹

University of Toronto

¹ Department of Electrical and Computer Engineering

² Department of Chemistry

10 King's College Road, Toronto, ON M5S 3G4

³ Nanomaterials Research Corp.

2849 E. Elvira Road, Tucson, AZ 85706

1. Introduction

Low-dimensional semiconductors have attracted increasing interest from both fundamental and applied fronts. Non-lithographic fabrication of nanostructured materials based on electrochemical (EC) deposition into the pores of anodic aluminum oxide is a promising technique allowing the creation of periodically disposed and uniform nanowire arrays of high spatial density [1,2]. Starting with very clean (99.99%) aluminum plates polished to achieve a mirror surface and using a two-stage anodization process, it is possible to produce an ideally ordered hexagonal honeycomb structure of close-packed cylindrical pores [3]. Porous films filled by metals exhibited highly anisotropic absorption, being transparent to light polarized vertically to the metal columns, and absorptive to parallel polarization [4]. The optical properties of nanowires, especially semiconductor nanowires, are of particular interest for applications in optoelectronic devices.

In this paper we discuss the optical characterization of the material quality as well as of the degree of confinement and anisotropy in CdS nanowire arrays using photoluminescence (PL) and resonant Raman (RR) spectroscopies. We consider also how luminescent properties are affected by annealing at different temperatures and ambient atmospheres.

2. Sample preparation

CdS nanowires have been successfully fabricated by means of electrodeposition into porous alumina template [5]. Typical wire diameter was in the range of few to tens of nanometers depending on conditions of preparation, and wire length was about 1 μm . Pores diameters were determined by direct imaging with scanning electron microscope. The sample parameters are listed in Table.

To improve the crystalline quality of the nanowires we subjected them to annealing in inert atmosphere (Ar) and hydrogen enriched atmosphere (5 vol. % H_2 in Ar). It has been reported in the literature for CdS nanocrystals in SiO_2 glass matrix, produced by segregation from oversaturated solid solution, that during annealing hydrogen penetrates into SiO_2 film and passivates nonradiative recombination centers in CdS [6]. To prevent sulfur sublimation, we covered samples by 40nm SiO_2 film using plasma enhanced chemical vapor deposition. The samples were annealed up to 530-650C for 5 min. We were able to observe that hydrogen indeed penetrates through covering film: the samples annealed in hydrogen at temperature >600C

changed their color, while annealing in pure argon at the same temperature the sample did not. We tried also very long annealing ranging from 1 to 5 hr, and we found that the annealing temperature rather than time is a determining parameter. Annealing temperature is limited by the melting point of Al substrate, 660C.

3. Photoluminescence

Photoluminescence measurements were performed with 1m focal length SPEX monochromator under cw excitation by 458nm Ar-laser line of 0.1W power. The samples temperature varied from 10 to 300K.

The onset of the quantum confinement phenomena is expected to be observed when nanowire diameter approaches the Bohr diameter of the exciton (~4nm for CdS). On the other hand, optical properties of the larger nanowires may also differ from that of bulk CdS due to deviation from the bulk crystal structure. Bulk CdS exhibits strong band-edge green ($\lambda \sim 500\text{nm}$) luminescence both at room and low temperature (Figs. 1a, 2b). There is normally a weak and very wide luminescent peak in red-infrared region ($\lambda \sim 700\text{-}800\text{nm}$), which is typically attributed to recombination with deep acceptors created by crystal defects or impurities. Its amplitude was found to be three orders of magnitude smaller than the band-edge peak in bulk CdS.

Electrochemical deposition, generally speaking, does not by itself produce high crystal quality of a deposited material. EC deposition can result in a high quality material when conducted on the single crystal substrate with favorable epitaxial conditions. Using underpotential deposition of monolayers (electrochemical atomic layer epitaxy, ECALE [7]), well ordered epitaxial thin films of CdS have been produced [7], which show strong band-edge luminescence at room temperature. In one case, CdS films deposited on Pt substrate showed only red luminescence (Fig. 1a). In the case of material deposited into pores, where the amorphous alumina does not facilitate epitaxial growth, as-deposited samples reveal a broad-band defect-induced luminescence in red-infrared region (0.7-0.9 μm) not only at room temperature (Figs. 1b, 1c) but also at temperatures down to 10K (Figs. 3, 4, 5). The situation improves considerably when samples are annealed.

Samples #16 and #14 with relatively large pores diameters (35 and 78 nm respectively) were annealed in Ar atmosphere. Annealing at 530C for 5hr did not produce much changes in PL spectra. Additional annealing at 600C for 1hr gave rise to band-edge luminescence peak (Figs. 1b, 1c). In the meantime, red peak becomes a little stronger, wider, and shifted to longer wavelengths. For some samples it extended to at least to 1100nm. A periodic modulation of the spectrum with a period of 50-100nm is seen and is caused by interference in the aluminum oxide film. Very similar modulation takes place in transmission spectra of free standing films.

At low temperature green luminescence becomes much stronger than defect related radiation (Fig. 2a). Nevertheless, there is a significant difference between bulk CdS and nanowires PL spectra in the band-edge region. Low temperature PL spectrum of nanowires in band-to-band region is a single peak of 40-75 meV width while a bulk CdS sample reveals under the same conditions clearly resolved narrow (<10meV) peaks corresponding to free excitons (X), neutral donor and neutral acceptor bounded excitons (D^0, X), (A^0, X), their phonon replicas and other features typical for low temperature PL (Fig. 2b). For nanowires of 30-70 nm in diameter, when quantum confinement is negligible, the PL peak location is 15-30 meV lower in energy

than the strongest peak in bulk PL spectrum recognized as (D^0,X). This may be attributed to rather large disordering in nanowires. We have also observed a macroscopic nonuniformity of the samples resulted in slightly different PL spectra measured at different locations.

Samples #31, #37, and #62 with pores diameters 12nm, 22nm, and 40nm respectively were divided into a number of parts and annealed in Ar or H_2 /Ar atmosphere at temperature up to 530-650C for 5min. The low temperature photoluminescence spectra of the annealed samples are presented in Figs. 3, 4, 5. In general, the higher the temperature the stronger is the band-edge luminescence.

On all the samples we observed that annealing in hydrogen produces better results. Moreover, for small diameter samples (12nm and 22nm) annealing without hydrogen does not improve photoluminescence (Figs. 3a, 4a). It suggests that in small diameter nanowires ($d \leq 22$ nm) the band-edge luminescence is significantly influenced not only by crystal defects but also by nonradiative recombination through surface states which could be passivated by hydrogenation. In the case of thick wires ($d \geq 35$ nm) hydrogen atmosphere is not as important, it is, nevertheless, helpful.

Photoluminescence measurements of nanowires are obscured by the photo-darkening phenomenon. It is well-established (see, for example, [8]), that nanoparticles in glass suffer photo-structural changes under light illumination. We observed photo-darkening of nanowires in porous alumina by measuring temporal dependence of the PL intensity (Fig. 6). For relatively thick wires (sample #14) PL intensity dropped few times in several minutes under cw excitation by 458nm Ar-laser line of 100mW power focused onto 0.1-0.3mm spot. In the case of wires with smaller diameter the photo-darkening was much stronger.

4. Resonant Raman spectroscopy

Clearly resolved RR spectra were registered for annealed samples. The spectra were dominated by a progression in the longitudinal optical phonon mode (Fig.7). The LO phonon frequency, overtone ratio and the overall RR intensity were found to be wire-diameter dependent. Analysis of relative intensities of the members of the progression as a function of excitation wavelength was done to estimate exciton energies of nanowires. A small blue shift in exciton energy with decreasing the wire diameter down to 10-15 nm was observed [10].

The RR spectra showed no anisotropy, however, which was likely due to the low aspect ratio of the nano-crystallites composing the nanowire [5]. Annealing increased the intensity and the number of observed overtones, suggesting an improved crystallinity and a reduced concentration of defects.

The broadening parameter as deduced from RR spectra is in good correspondence with PL spectrum linewidth. Broadening is possibly due to the interactions at the CdS/oxide interface or with neighboring crystallites within the nanowires as well as due to the scattering at the remaining structural imperfections. This is supported by the observation that the intensity of the CdS nanowire luminescence increases with increasing diameter.

A significant degree of crystalline disorder in nanowire was also implied by the results of resistivity measurements of Ni nanowires using an STM tip as a contacting probe [3]. The resistance of a single nanowire before annealing was found to be at least an order of magnitude higher than that expected from bulk conductivity values.

It should be noted, that no special care was taken to eliminate impurities in our samples. Using higher-purity materials in the electrodeposition should improve the quality of the nanowires and reduce the non-radiative recombination caused by impurities.

5. Conclusions

Novel arrays of CdS nanowires were successfully fabricated nonlithographically in Al_2O_3 nanopores template, and being investigated by a variety of techniques. Optical characterization offered first insights to the wire structure and crystallinity in both as deposited and annealed states, in addition to confirming the intuitively expected size dependence. Quenching of the red band PL in CdS wires by hydrogenation and size dependence provides a strong evidence of the existence of interface states at the wall surface of the wires.

More specifically, it has been found that the higher the annealing temperature the better is the PL performance, at least up to the melting temperature of aluminum substrate (660C). It appears worthwhile to try annealing of free standing porous films at higher temperature.

It is important to close pores by thin layer of SiO_2 or, maybe, by other material to prevent CdS sublimation during the annealing.

Annealing of nanowires of $>35\text{nm}$ in diameter in Ar atmosphere produces considerable and qualitative change in PL spectra, and band-edge transitions become prominent in PL at low temperature. This can be attributed to improvement of crystalline quality of the nanowires.

Nanowires of 12-22nm in diameter show green luminescence only after annealing in hydrogen enriched atmosphere. It may be explained by hydrogen passivation of surface (interface) states. Nonradiative recombination through these states is considerably stronger for small diameter nanowires.

Nanowires, like nanocrystals in glass, reveal photo-darkening, which is more significant for small diameter nanowires.

The small blue shift in exciton energy with decreasing wire diameter calculated from Raman spectra demonstrated the onset of quantum size effects. The lack of polarization dependence is tentatively attributed to the fact that nanowires are comprised of microcrystallites with low aspect ratios.

6. Acknowledgment

I. A. is grateful to Paul Zhang for measuring of PL spectra of some samples.

References

- [1] D. Routkevitch, A. Tager, J. Haruyama, D. Al-Mawlawi, M. Moskovits, and J. M. Xu, *IEEE Trans. Electron Dev.*, 43(10), 1646-1658 (1996).
- [2] A. A. Tager, D. Routkevitch, J. Haruyama, D. Al-Mawlawi, L. Ryan, M. Moskovits, J. M. Xu. "Nonlithographical fabrication and physics of nanowires and nanodot array devices - present and future", in "Future Trends in Microelectronics. Reflections on the Road to Nanotechnology", ed. by Serge Luryi, Jimmy Xu, Alex Zaslavsky, Kluwer Academic Publishers, 1996, pp.171-183.
- [3] Hideki Masuda and Masahiro Saton, *Jpn. J. Appl. Phys.*, 35, Pt. 2 (No. 1B), L126-L129, 1996.
- [4] M. Saito, M. Kiriara, T. Taniguchi, and M. Miyagi, *Appl. Phys. Lett.*, 55(7), 607-609, 1989.
- [5] D. Routkevitch, T. Bigioni, M. Moskovits, and J. M. Xu, *J. Phys. Chem.*, 100, 14037-14047 (1996).
- [6] A. Ekimov, *J. of Luminescence*, 70, 1-20, 1996.
- [7] B. Edward Boon and Curtis Shannon, *J. Phys. Chem.*, 100, 9480-9484, 1996.
- [8] V. Jungnickel, F. Henneberger, *J. of Luminescence*, 70, 238-252, 1996.
- [9] D. N. Davydov, D. Routkevitch, J. Haruyama, B. W. Statt, M. Moskovits, and J. M. Xu, 191-th Meeting of Electrochemical Society, Montreal, 1997.
- [10] D. Routkevitch, T. L. Hasfett, L. Ryan, T. Bigioni, C. Donketis, M. Moskovits, *Chem. Phys.*, 210, 343-352, 1996.

Table. The samples parameters and the annealing conditions.

Sample No	Pores diameter, nm	Annealing conditions
# 14	78	530C for 5 hr & 600C for 1 hr.
# 16	35	
# 31	12	530-650C for 5 min. In Ar or H ₂ /Ar atmosphere
# 37	22	
# 62	40	

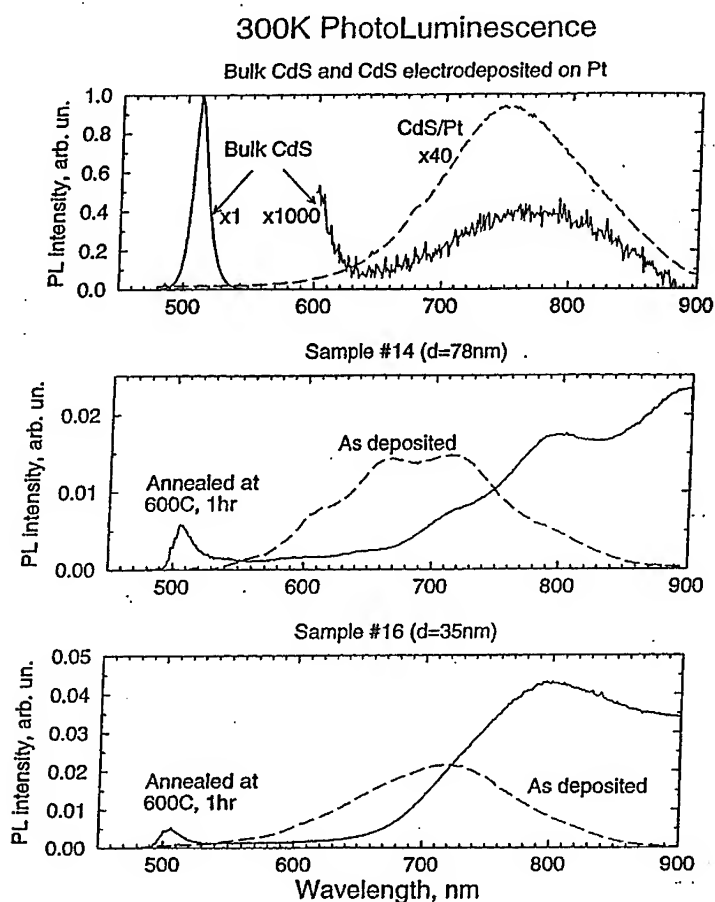


Fig.1. Room temperature photoluminescence of:

- a) bulk CdS and CdS electrodeposited on Pt substrate;
- b) sample #14 (pores diameter d=78nm) before and after annealing in Ar at 600C for 1h;
- c) sample #16 (pores diameter d=35nm) before and after annealing in Ar at 600C for 1h.

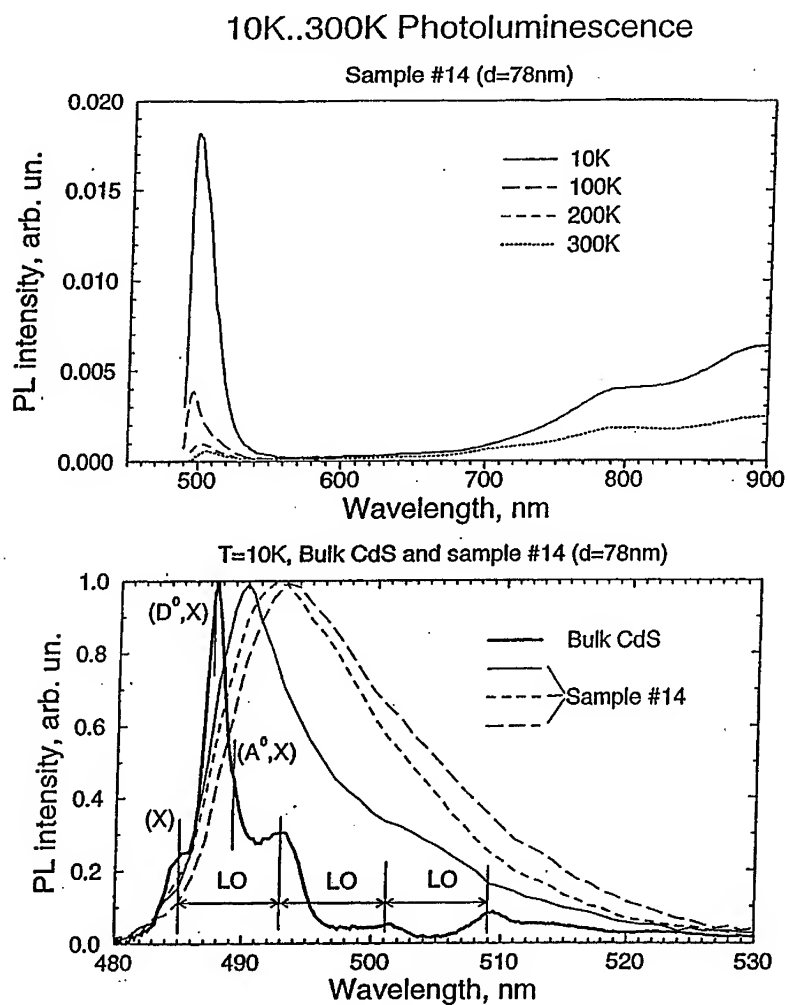


Fig.2. Variable temperature photoluminescence of sample #14 (pores diameter d=78nm):
a) PL spectra at different temperatures;
b) band-edge low-temperature spectra of bulk CdS and sample #14.

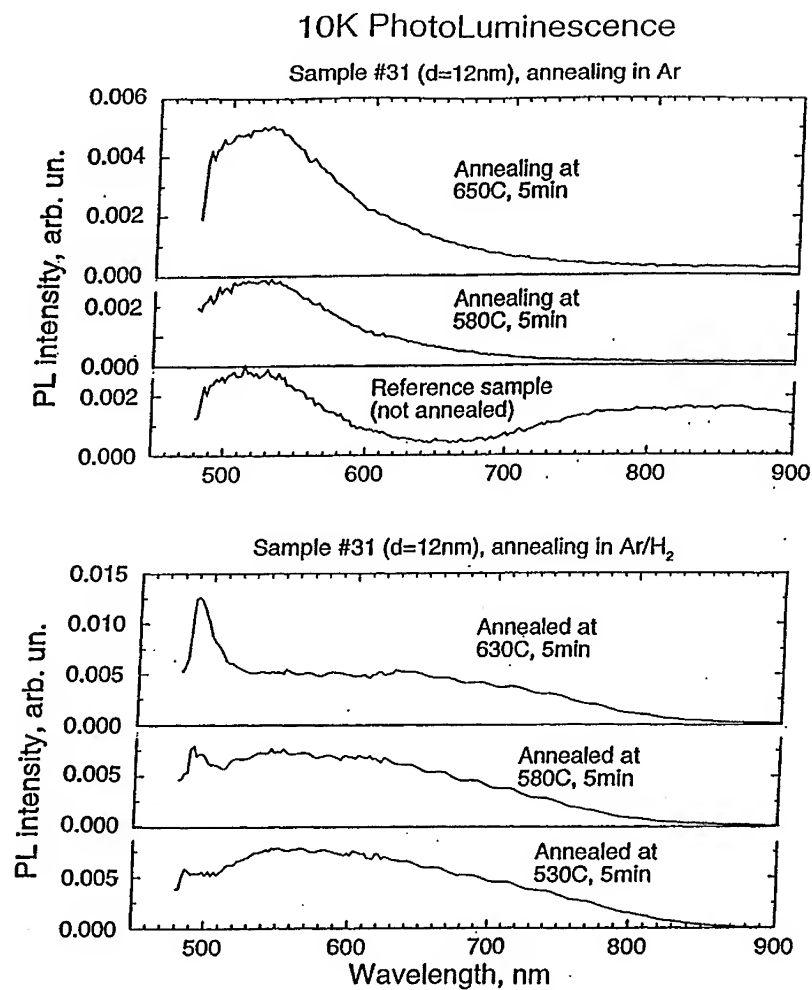


Fig.3. Low temperature PL spectra of the sample #31 (pores diameter $d=12\text{nm}$):

- a) annealing in Ar;
- b) annealing in H₂/Ar.

Annealing temperature is indicated on the graphs.

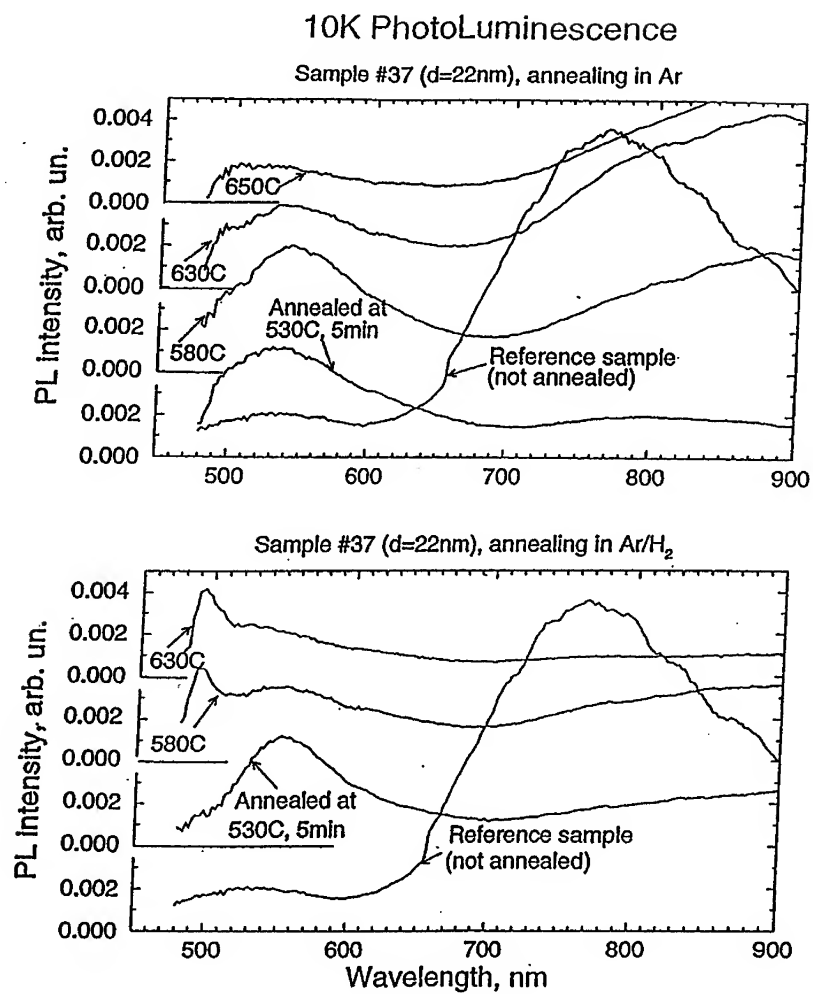


Fig.4. The same as Fig.3, but for sample #37 (pores diameter d=22nm).

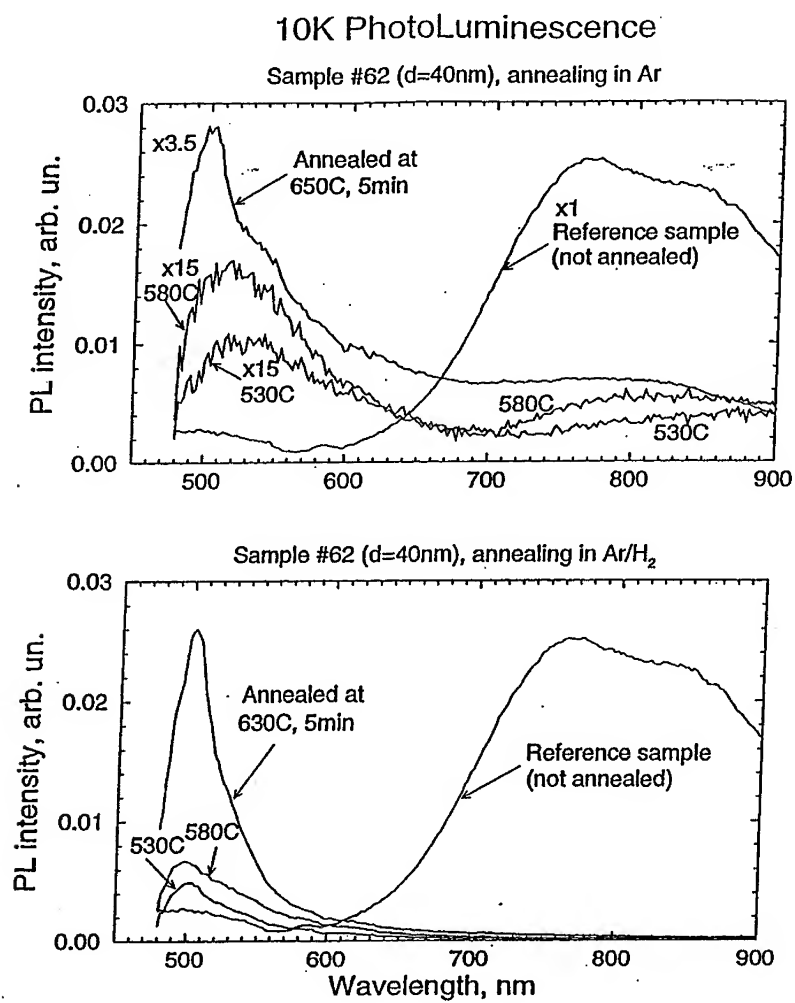


Fig.5. The same as Fig.3, but for sample #62 (pores diameter d=40nm).

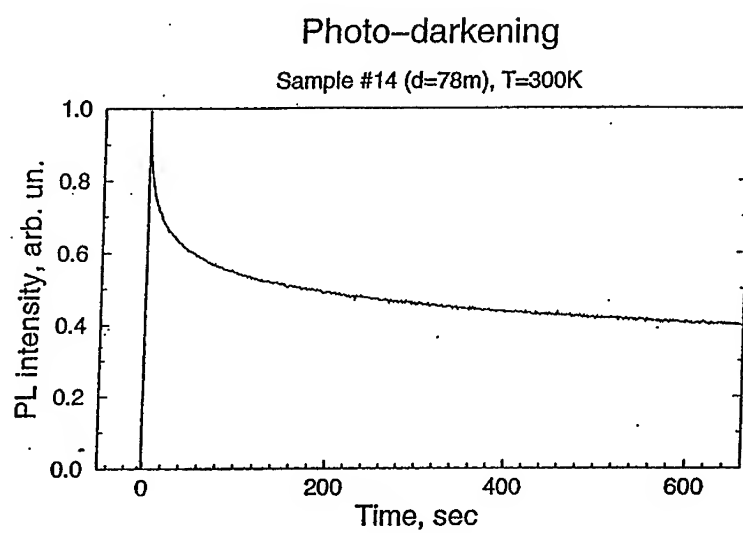


Fig.6. Photo-darkening: PL intensity degradation under long term illumination.

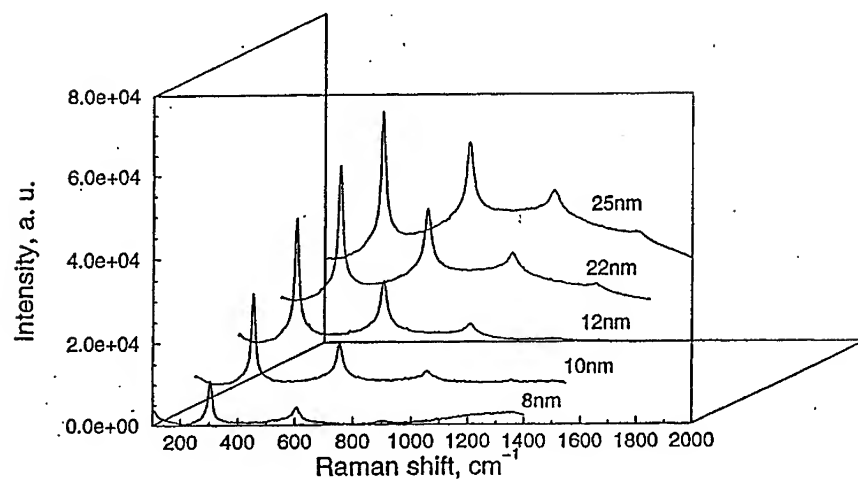


Fig.7. Resonance Raman spectra of CdS nano-wires of different diameters excited with an s-polarized 488nm Ar-laser line.

Quantum Structures and Devices

Optical and Electrical Properties of Si/Ge Quantum Confinement Structures

Y. Shiraki, N. Usami, H. Sunamura, E. S. Kim, A. Yutani,
and S. Fukatsu*

Research Center for Advanced Science and Technology

**Department of Pure and Applied Sciences*

The University of Tokyo

4-6-1 Komaba, Meguro-ku, Tokyo 153, Japan

ABSTRACT

Si/Ge quantum confinement structures, not only conventional type-1 quantum wells but also new structures called NCSs, were successfully fabricated by MBE. Moreover, Ge quantum wires and dots were formed on Si substrates in self-assemble manner and luminescence properties of QWRs were shown to very different from those of QWs. Well controlled QWRs and QDs were formed on patterned Si substrates and their unique optical properties were observed. Modulation doping structures were successfully grown on relaxed SiGe buffer layers. The extremely high mobilities were obtained and mechanisms governing the conduction were clarified in this system.

1. INTRODUCTION

Si/Ge quantum confinement structures have high potential not only to improve present electronic devices but also to realize new optoelectronic devices based on silicon. Thanks to the development of sophisticated crystal growth techniques such as molecular beam epitaxy (MBE) and modified chemical vapor deposition, lattice mismatched systems can be well handled and strain effects are well exploited. The research is now extended to quantum wires and dots. However, comprehensive studies on optical properties as well as electrical ones of these structures are still lacking. In this report, after the promising gas source MBE (GSMBE) for formation of quantum structures is introduced as well as unique optical properties of grown structures, interesting optical properties of quantum wires and dots in this system are reviewed. The modulation doping structures which provide extremely high mobilities are also demonstrated and the transport mechanisms are discussed.

2. GAS SOURCE MBE AND TYPE-1 QUANTUM WELLS

Silicon GSMBE growth with disilane gas is strongly dependent on growth conditions reflecting

chemical reactions on Si surfaces [1]. Below 700 C, the growth rate exponentially decreases with decreasing temperature with an activation energy of 47 Kcal/mol corresponding to the hydrogen desorption. The growth rate is found to be larger on (100) surfaces than those on other surfaces. Introduction of GeH_4 , moreover, changes reaction kinetics and the activation energy is decreased depending on the content of GeH_4 .

Luminescence from quantum wells (QWs) reflects the distortion of the potential shape due to surface segregation and type-1 SiGe/Si QWs grown by the conventional solid source MBE show significant energy deviation to higher energies from the theoretical well width dependence due to Ge surface segregation. However, GSMBE was found not to show such an energy shift and to provide the well width dependence expected from the square-well potential calculation [1]. This is due to the surfactant effect of a large amount of atomic hydrogen which is constantly supplied to the growth front.

The coupling of QWs grown by this method is well understood based on effective mass approximation and the increase in the number of coupled wells resulted in superlattices the peak energy of which follows a simple Kronig-Penny type calculation [2].

3. NEIGHBORING CONFINEMENT STRUCTURES (NCSs)

The band alignment of SiGe/Si type-1 quantum wells is very similar to that of AlGaAs/GaAs QWs. However, it is a disadvantage of the former that the band offset almost resides at the valence band and the offset at the conduction band is negligibly small and electrons cannot be well confined in the well region. In order to overcome this problem, we proposed a new type of quantum wells called Neighboring Confinement Structures (NCSs) where a pair of tensily strained Si layer and compressively strained SiGe layer is sandwiched by relaxed SiGe alloy layers as shown in Fig. 1 [3]. To realize such a structure on Si substrates, fully relaxed SiGe buffer layers should be grown. The formation of relaxed SiGe buffer layers with high quality is obtained by using GSMBE with step grading Ge concentration [4].

Various QWs including NCS were grown on this buffer layer and their luminescence spectra are shown in Fig. 2 [3]. Although distinct luminescence peaks originating from QWs are seen in all structures, the type-2 QWs show poor luminescence efficiency compared with the type-1 QW. It is remarkable that the luminescence intensity, especially no-phonon one, is strongly enhanced in the case of NCS structures. This is believed to be brought from significant confinement of both electrons and holes and overlapping of their wavefunctions in the well region. The reason for the selective enhancement of NP lines was shown to be localization of excitons at heterointerfaces [5]. Systematic energy shift was also observed as shown in Fig. 3 [3] when the thickness of the pair layers was changed, indicating that the band diagram which we expect is correct.

4. FORMATION OF QUANTUM WIRES AND DOTS

The strain energy due to lattice mismatch is basically released by introducing misfit dislocations which deteriorate optical as well as electrical properties of heterostructures. However, it has been recognized recently that another pathway to release strain without introducing misfit dislocations, that is, formation of islands, is possible. In the case of deposition of pure Ge on Si substrates, the situation is drastic. When pure-Ge layers are embedded in Si, well resolved edge emissions are

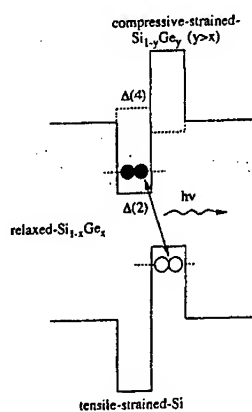


Fig. 1 Schematic band alignment of NCS. A pair of carrier confining layers for electrons and holes is sandwiched by barrier layers.

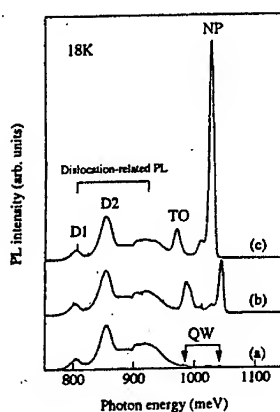


Fig. 2 PL spectra of (a) type-2 QWs with 10Å strained-Si layers, (b) type-1 QWs with 10Å strained-SiGe layers, and (c) NCS.

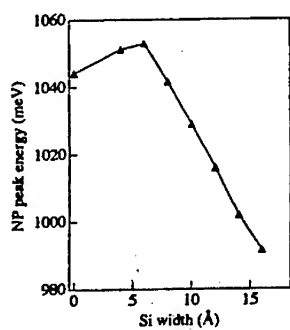


Fig. 3 Si width dependence of NP lines of NCS samples.

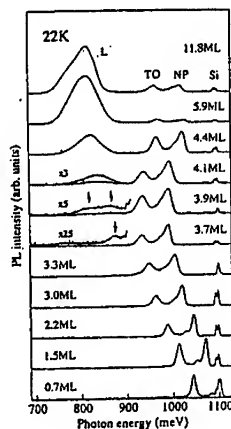


Fig. 4 Well width dependence of PL spectra of Si/pure-Ge/Si QWs

observed and they shift toward lower energies with increasing Ge width, showing quantum confinement of Si/Ge/Si QWs as seen in Fig. 4 [6]. When Ge exceeds 4 MLs, however, a new broad peak is seen to appear in the lower energy region along with edge emissions. Emergence of this broad peak was found to well correspond to the formation of islands from TEM measurements. The peak was stable against temperature and was observed even at room temperature. It is, moreover, noteworthy that the edge emissions of QWs show the blue shift to the energy corresponding to Ge 3 MLs during evolve of islands. This indicates that excess Ge atoms more than 3 MLs are consumed to form islands, and Ge wet layers with 3 MLs and islands coexist in this system. In other words, the Ge thickness of 3 MLs is the equilibrium critical thickness. This was confirmed by the growth interrupting experiment where PL peaks with 3 MLs were stable against increase of interruption period while the peaks with excess Ge showed big energy shift due to formation of islands.

QWs with Ge less than 1 ML were found to give rise to sufficient intensity of luminescence and the energy monotonically increased with decreasing Ge thickness as shown in Fig. 5 [7]. Plan view TEM measurements revealed that Ge wires were formed at the step edges of Si surfaces in this region and PL could be attributed to emissions from Ge quantum wires (QWRs) embedded in Si crystals. The luminescence properties of these wires are much different from those of QWs as shown in Fig. 6 [7]. Band filling effect which is generally seen in indirect QWs is absent in the case of wire structures, probably reflecting the high density of states of QWRs. Moreover, a new peak is observed to develop on the lower energy side of the original peak as the excitation intensity is increased. From the excitation intensity dependence, this peak is speculated as luminescence of biexcitons created due to high density of states of QWRs as well as long life time of excitons in indirect band gap materials.

5. FORMATION OF QUANTUM STRUCTURES ON PATTERNED SUBSTRATES

QWRs are also formed in a controlled manner on patterned substrates. When SiGe/Si QWs were formed on V-groove of Si substrates, crescent-shaped SiGe features were found to be grown in the bottom region of the V-groove apart from QWs on the top (100) surface and (111) side walls [8]. These three quantum structures give rise to different luminescence as shown in Fig. 7 and cathode luminescence patterning well distinguishes their positions [9]. It is quite interesting that these luminescence peaks show different decay times and especially the luminescence from the (111) side wall strongly depends the pattern size as shown in Fig. 8 [8]. Moreover, the temperature dependence of the decay time is completely different among them and that of the (111) side wall QW decreased with increasing temperature while the others showed the increase. This is due to exciton diffusion from the side wall to (100) and bottom regions. From this temperature dependence, the diffusion length of excitons can be deduced and its temperature dependence is shown in Fig. 9 where it monotonically increases with increasing temperature.

The cross-sectional emission from QWRs shows polarization characteristics reflecting wire geometry [10]. That is, no polarization is seen in luminescence emitted from the side of the sample while strong polarization is observed in the emission from the surface in the case of the wire structure. It is significant that QWRs show a large blue shift of PL peaks [10]. However, the energy shift is too big to be explained in terms of quantum confinement. The main cause of the energy shift may be the change in the strain distribution, from two-dimensional compression to hydrostatic pressure, which provides comparable energy shift.

Ge islands are randomly formed on the wetting layer when the thickness exceeds the critical

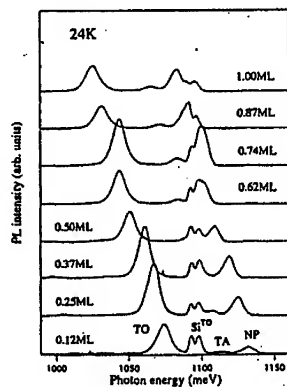


Fig. 5 PL spectra of Si/pure-Ge/Si structures with submonolayers of Ge

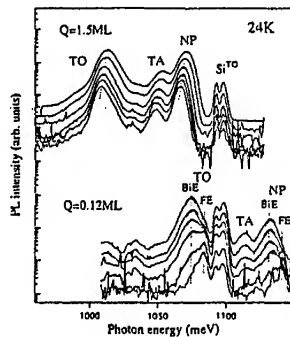


Fig. 6 Excitation intensity dependence of PL spectra of (upper) Si/Ge/Si QWs and (lower) quantum wires

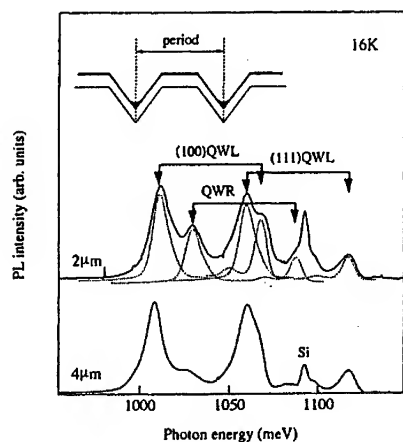


Fig. 7 PL spectra of SiGe/Si heterostructures grown on V-groove patterned substrates with different periods.

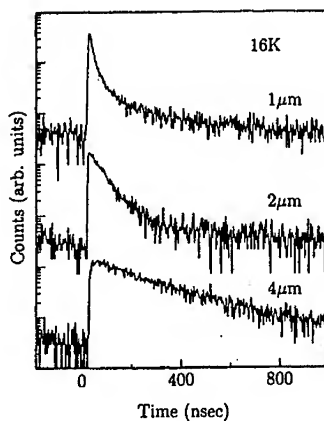


Fig. 8 The temporal profiles of the luminescence from (111) QWs with different periods.

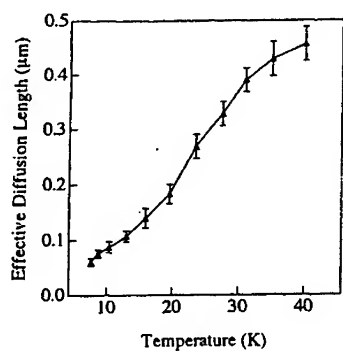


Fig. 9 Temperature dependence of the exciton diffusion length.

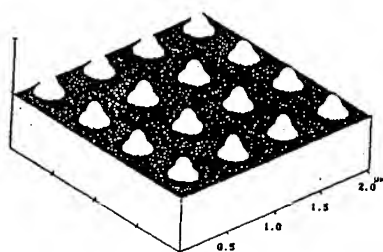


Fig.10 AFM images of Ge islands formed on patterned Si substrates with SiO₂ films.

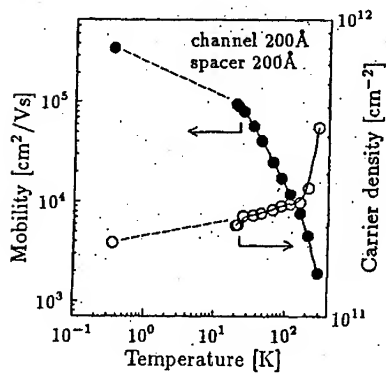


Fig.11 Temperature dependence of mobility and carrier density of SiGe/Si modulation doping structures.

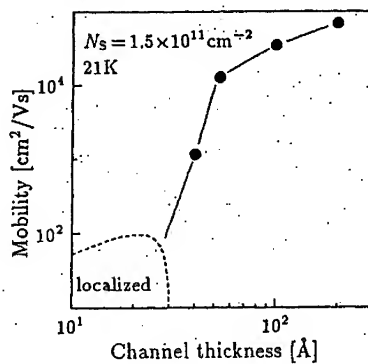


Fig.12 Channel width dependence of the mobility of SiGe/Si modulation doping structures.

thickness. In order to control their position and size, Ge layers were deposited on Si substrates covered with SiO₂ films with small holes patterned by electron beam lithography. Since GSMBE has growth selectivity between Si and dielectric materials, Ge islands were formed only in the holes in the controlled manner as seen in Fig. 10 [11]. The number of islands depends on the hole size and it was seen in AFM images that only one island was formed when the hole size was less than 200 nm. Well resolved NP and TO peaks were observed in these quantum dots and their peak position was seen to shift depending on the island size.

6. MODULATION DOPING AND ITS MOBILITY

Formation of the type-2 SiGe/Si heterostructure is important to make the conduction band offset high enough to realize such high speed devices as modulation-doping field-effect-transistors (MODFETs). After optimizing growth conditions as well as the structure formed on the relaxed SiGe buffer layers, temperature dependence of mobilities of the modulation doping structure was carefully examined as a function of channel width [12]. It was found that the sample with thicker well widths gave rise to high mobility and that it increased with decreasing temperature, exceeding 360,000 cm²/Vsec around 1 K as shown in Fig. 11 which has never been realized in Si-MOS structures. Another interesting feature is that the mobility decreases with decreasing well width as seen in Fig. 12 [12]. This tendency was revealed to reflect the fact that the dominating mechanism of mobility is the interface roughness scattering of carriers in this well width regime. The mobility of samples with much narrower well width is extremely low and the conduction was found to be governed by variable range hopping of carriers in the two dimension. The localization of carriers might be brought by the interface roughness the effect of which increases with decreasing well width.

7. CONCLUSION

Various Si/Ge quantum structures were fabricated by using MBE technique. Not only conventional type-1 quantum wells with high luminescence efficiency were grown but also new structures, NCSs, were proposed to overcome the demerit of SiGe/Si type-1 quantum wells and shown to enhance luminescence efficiency. Ge quantum wires and dots were formed on Ge wetting layers in self-assemble manner and luminescence properties of QWRs were shown to very different from those of QWs reflecting the change of density of states. Well controlled QWRs and QDs were formed on patterned Si substrates and their unique optical properties were observed. Modulation doping structures were successfully grown on relaxed SiGe buffer layers and the extremely high mobilities were obtained. Mechanisms governing the conduction were clarified in this system. These results well demonstrate high potential of Si/Ge quantum confinement structures and their device applications for not only electronic devices but also optical devices are well expected.

REFERENCES

- [1] S. Fukatsu, N. Usami, Y. Kato, H. Sunamura, Y. Shiraki, H. Oku, T. Ohnishi, Y. Ohmori, and K. Okumura; *J. Crystal Growth* **136**, 315 (1994)

-
- [2] S. Fukatsu; Solid-State Electronics **37**, 817 (1994)
 - [3] N. Usami, F. Isshiki, D. K. Nayak, Y. Shiraki, and S. Fukatsu; Appl. Phys. Lett. **67**, 524 (1995)
 - [4] D. K. Nayak, N. Usami, S. Fukatsu, and Y. Shiraki; Appl. Phys. Lett. **63**, 3509 (1993)
 - [5] N. Usami, Y. Shiraki, and S. Fukatsu; Appl. Phys. Lett. **68**, 2340 (1996)
 - [6] H. Sunamura, N. Usami, S. Fukatsu, and Y. Shiraki; Appl. Phys. Lett. **66**, 3024 (1995)
 - [7] H. Sunamura, Y. Shiraki, and S. Fukatsu; Solid-State Electronics **40**, 693 (1996)
 - [8] N. Usami, H. Akiyama, Y. Shiraki, and S. Fukatsu; Phys. Rev. B **52**, 5132 (1995)
 - [9] V. Higgs, E. C. Lightowers, N. Usami, Y. Shiraki, T. Mine, and S. Fukatsu; J. Crystal Growth **150**, 1070 (1995)
 - [10] N. Usami, T. Mine, S. Fukatsu, and Y. Shiraki; Appl. Phys. Lett. **64**, 1126 (1994)
 - [11] E. S. Kim, N. Usami, Y. Shiraki, and K. Momma; unpublished
 - [12] A. Yutani and Y. Shiraki; Semicond. Scie. and Technol. **11**, 1009 (1996)

Sub-500 nm RITD fabrication

K. Shiralagi, R. Tsui, and H. Goronkin

Motorola Inc., Phoenix Corporate Research Labs, 2100 E. Elliot Road, Tempe, AZ
85284

Abstract

Epitaxial regrowth on patterned substrates which results in well defined crystallographic facets is utilized for a novel contacting and fabrication scheme to make sub-500 nm InAs/AlSb/GaSb resonant interband tunneling diodes. The facet termination, obtained during regrowth by choosing the orientation of the device, is utilized to make contact to the device in desired directions and isolate contacts in all other directions. Sidewall spacer technology is used to define the device active region. Device and contact fabrication are achieved without using any fine-line lithography. Results of this fabrication scheme and the effect of geometry on the I-V characteristics of the device are reported.

1. Introduction

Resonant interband tunneling diodes (RITDs) based on the InAs/AlSb/GaSb material system have been shown to exhibit high peak-to-valley current ratios (PVCRs) at room temperature [1]. RITDs integrated with a heterojunction field effect transistor have been demonstrated in the past [2,3] as useful building blocks for a new generation of quantum functional devices [4,5]. The conventional approach to large dimension RITD fabrication consists of standard optical lithography, evaporating the top ohmic contact for the RITD, lift-off and a subsequent etch with the contact as a mask [6]. Our earlier approach to reduce device dimensions consisted of etching a double-step mesa on a GaAs substrate and then regrowing a RITD structure with layer thicknesses chosen so that the RITD can be fabricated on the middle ledge [7]. The active region of the RITD has an AlSb/GaSb/AlSb quantum well cladded on both sides by InAs contacting layers. The top contacting InAs layer of the RITD on the ledge connects to the bottom layer on the top mesa and the bottom contacting InAs layer connects to the top layer below the ledge, resulting in contacts to RITD on the middle ledge. Thus a small device on the middle ledge can easily be contacted by large pads above and below the ledge. This approach yielded working diodes as long as the middle ledge width was wider than 1-2 μm . Attempts were made to narrow the ledge width first by lithography and later by using a sidewall spacer approach. The latter method resulted in ledge widths on the order of 100 nm to 300 nm. However, since the surface migration lengths of In atoms during InAs growth were much larger than the ledge dimensions, the RITD growth behavior (facet) was very different from that seen on wide ledges. Attempts to control the growth conditions to reduce the migration of In atoms proved to be unsuccessful and so we developed a new approach reported here. Now, the RITD structure was grown on a GaAs substrate patterned with a single mesa and using a SiO_2 sidewall spacer at the vertical growth facet located at the mesa edge, as shown in Fig. 1. The spacer was used as a mask to etch down and define the RITD width. Metalization on the top and at the bottom of the mesa serve as contacts for the RITD so defined. Thus, epitaxial regrowth on patterned substrates combined with sidewall spacer technology is used to define the device dimensions in the sub-500 nm regime. The concept, fabrication process and current-voltage (I-V) characteristics of the device, as well as a comparison with RITDs

fabricated in a conventional manner, are reported here.

2. Experiments

Semi-insulating (100) GaAs substrates were patterned by reactive ion etching through a silicon nitride mask using a $\text{CH}_4/\text{H}_2/\text{Ar}$ mixture [8]. The mask was removed in a SF_6/O_2 plasma after dry etching. The device structure was grown in a Fisons V90H chemical beam epitaxy system using cracked arsine and trimethylindium as source materials for InAs and elemental Si as the n-type dopant. For the growth of AlSb and GaSb, elemental Al, Ga and Sb were used. In the present study the layers were grown at 495 °C and at rates of 1.816, 1.524 and 1.78 Å/s, respectively, for the InAs, GaSb and AlSb. The RITD, consisting of top and bottom Si-doped ($1 \times 10^{18}/\text{cm}^3$) InAs contacting layers and an active region of 15Å AlSb/ 65Å GaSb/15Å AlSb, was grown with a 100Å thick not-intentionally-doped InAs isolation layer between each of the doped InAs contacting layer and the active region.

3. Results and Discussion

The starting GaAs mesa height used in this study was approximately 850 nm and the top and bottom InAs regrown contacting layer thicknesses were carefully chosen so that they make electrical contact at the edge of the mesas oriented along the [011] direction, as shown in Fig. 1(a). Figures 2 (a) and (b) contain cross-sectional SEM photographs that show the connection of layers in the [011] direction and discontinuous layers in the perpendicular direction ([0 $\bar{1}\bar{1}$] in the case of a square shaped feature), respectively. The samples were stained prior to SEM imaging to enhance the contrast of the various layers. Contact isolation is obtained for lines in the [0 $\bar{1}\bar{1}$] direction as a result of the formation of {111} and other higher index facets. Thus, regrowth on a square shaped mesa will result in proper RITD contacts for lines along the [011] direction and isolation in the other perpendicular direction. The vertical growth facet obtained for lines along the [011] direction makes it suitable for the formation of a sidewall spacer. This was formed by uniform SiO_2 deposition and an anisotropic etch-back of the oxide to leave behind oxide spacers only at the vertical walls. After sidewall spacer formation and an InAs etch to define the active region, complete isolation was obtained between the top and bottom of the mesa in all other directions. Ohmic contacts to n-InAs were made at the top and bottom of the mesa by conventional evaporation and lift-off techniques using Au, Ge and Ni metals.

Figure 3 shows a SEM cross-section of a RITD defined by a sidewall spacer. The SiO_2 sidewall mask was diminished due to its slow etching during the InAs etch process to define the active region. The RITD width is defined by the width of the SiO_2 sidewall and hence is approximately 100 nm as seen in the picture. The active region was designed to be located slightly below the top of the GaAs mesa. Otherwise, leakage would occur in the diode current. Figure 4 shows the room temperature I-V characteristics of a diode defined by the width of the side wall spacer and the length of a 50 μm x 50 μm square mesa. The device exhibits a negative differential resistance region as shown. Leakage on the sides of the GaAs mesa and the high density of dislocations present in the active region contribute to high valley currents and hurt the peak-to-valley current ratio (PVCR) of the diode. The 7% lattice mismatch between the GaAs substrate and the bottom InAs contact layer of the RITD gives rise to a high

concentration of misfit dislocations. From our earlier studies of the growth of InAs on GaAs, we have determined the dislocation density to be in the $10^{11}/\text{cm}^2$ range at the substrate/epitaxial layer interface, decreasing by about two orders of magnitude for an epitaxial thickness of about 2 μm [9]. A RITD with an InAs buffer 1 μm thick grown on a planar GaAs substrate and processed in a conventional manner would yield a PVCR of greater than 10, whereas an increase in valley current in these diodes results in a lower PVCR as shown in the I-V curve. In fact, dislocations originating at the interface that propagate through the QW region have been observed in cross-sectional TEM analysis of these diodes.

Figure 5 shows a processed device structure on a square shaped mesa with all sides oriented at 45° to the wafer flats. It shows complete isolation between top and bottom contact layers of the mesa. Now, to control the device width even further, the starting GaAs mesa shape was chosen such that majority of the mesa consisted of sidewalls oriented in the 45° directions except for one corner where there is a small region of sidewall aligned along the [011] direction. This way, the active region of the device was defined by lithography to approximately 500 nm in one direction and by a sidewall spacer to 100-200 nm in the other direction. Diodes with different shapes and sizes have been fabricated and their I-V characteristics measured. The current in the active region of the device is defined by the narrow [011] facet whereas the leakage current is a contribution of the current all around the mesa. Thus, the small PVCR in the narrow active region is superimposed by all-around leakage that contributes to high valley current, and no significant PVCR were seen in these diodes. Diodes of a lattice matched material system such as InAlAs/InGaAs on InP substrates in which no diode leakage occurs and where high PVCRs have already been demonstrated would be suitable candidates for a continuation of this study.

4. Summary

In conclusion, we have demonstrated a novel fabrication method of sub-500 nm RITDs which make use of epitaxially grown contacting layers on non-planar substrates. The approach utilizes the formation of specific growth facets at the pattern edges during epitaxial growth on patterned wafers. Our concept is demonstrated by forming a functional RITD having a width of 100 nm without using any fine-line lithography. The PVCR of the device is low as a result of the high density of dislocations in the mismatched epitaxial layers. A further decrease in device dimension in the other lateral direction to less than 1 μm did not result in a diode with a significant PVCR. The decrease in the ratio of the active to passive regions of the device, and the high density of dislocations in the active region contribute to an increase in valley current, in turn resulting in a poor PVCR. We believe this approach however, will eventually allow one to obtain devices with lateral dimensions in all directions in the sub-200 nm regime without the use of fine-line lithography.

Acknowledgement

This work was performed in part under the management of FED (the R&D Association for Future Electron Devices) as a part of the R&D of Basic Technology for Future Industries supported by NEDO (New Energy and Industrial Technology Development Organization, Japan).

References

- [1] S. Tehrani, J. Shen, H. Goronkin, G. Kramer, M. Hoogstra, and T. X. Zhu, "AlAs hole barriers in InAs/GaSb/AlSb interband tunnel diodes," *Inst. Phys. Conf. Ser. No. 136* (IOP, Bristol, 1994), pp. 209-214.
- [2] S. Tehrani, H. Goronkin, G. Kramer, R. Tsui, and T. X. Zhu, "Resonant Interband Tunneling FET," *IEEE Electron Device Lett. EDL-16*, pp. 557-559 (1995).
- [3] K. J. Chen, K. Maezawa, and M. Yamamoto, "Novel current-voltage characteristics in an InP-based resonant-tunneling high electron mobility transistor," *Appl. Phys. Lett.* **67**, pp. 3608-3610 (1995).
- [4] J. Shen, S. Tehrani, H. Goronkin, G. Kramer, and R. Tsui, "An Exclusive-Nor Based on Resonant Interband Tunneling FET's," *IEEE Electron Device Lett. EDL-17*, pp. 94-96 (1996).
- [5] J. Shen, S. Tehrani, H. Goronkin, and G. Kramer, "Resonant Tunneling Devices and Circuits," *Soc. Photo-Optical Instrum. Engr. Proc. Series Vol. 2694* (SPIE, Bellingham, 1996), pp. 90-99.
- [6] H. Goronkin, G. Kramer, R. Tsui, M. Peffley, J. Shen, S. Tehrani, T. X. Zhu and M. Hoogstra, "Interband tunneling structures for quantum multifunction transistors," *Extended Abstracts 11th Symposium on Future Electron Devices* (Tokyo: R&D Assoc. for FED, 1992), pp. 207-210.
- [7] R. Tsui, M. Walther, K. Shiralagi, and H. Goronkin, "Facet terminated growth of quantum functional devices on patterned substrates," *Inst. Phys. Conf. Ser. No. 145* (IOP, Bristol, 1996), pp. 1283-1288.
- [8] M. Walther, G. Kramer, R. Tsui, H. Goronkin, M. Adam, S. Tehrani, S. Rogers, and N. Cave, "Growth of GaSb/AlSb heterostructures on patterned substrates by molecular beam epitaxy," *J. Crystal Growth* **143**, 1 (1994).
- [9] G. D. Kramer, M. S. Adam, R. K. Tsui, and N. D. Theodore, "Characterization of dislocation reduction in MBE-grown (Al,Ga)Sb/GaAs by TEM," *Inst. Phys. Conf. Ser. No. 136* (IOP, Bristol, 1994), pp. 727-732.

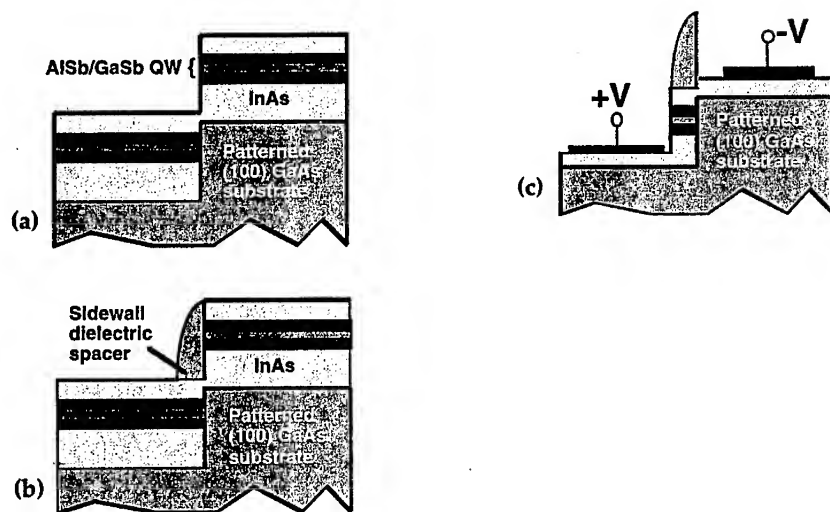


Fig. 1. Schematic illustration of the growth and fabrication process to form a sub-500 nm RITD.

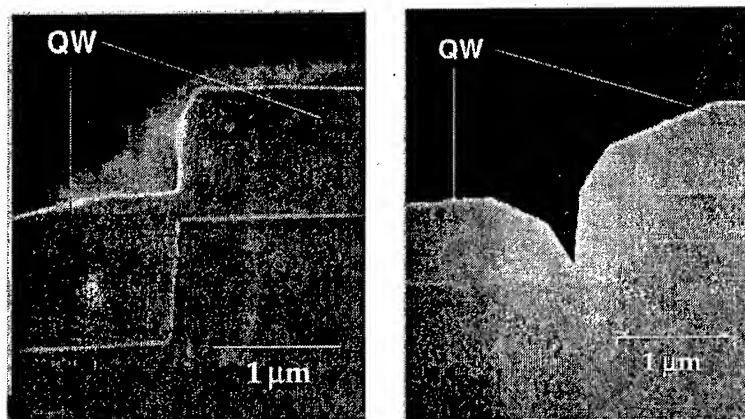


Fig. 2. SEM cross-section of a RITD structure for, (a) a line along the $[011]$ direction, showing a vertical growth facet with the appropriate layers connected between top and bottom of the mesa, (b) a line along the $[0\bar{1}\bar{1}]$ direction, showing the layer isolation between the top and bottom of the mesa.

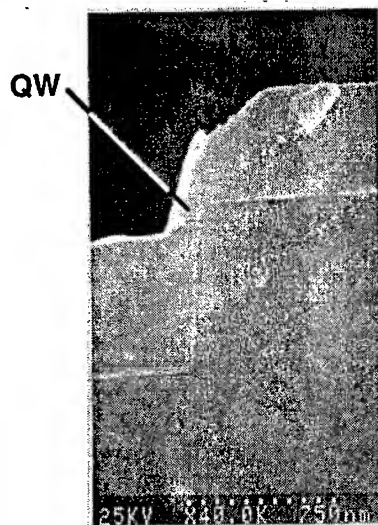


Fig. 3. SEM cross-section of a sidewall spacer defined active region of the RITD.

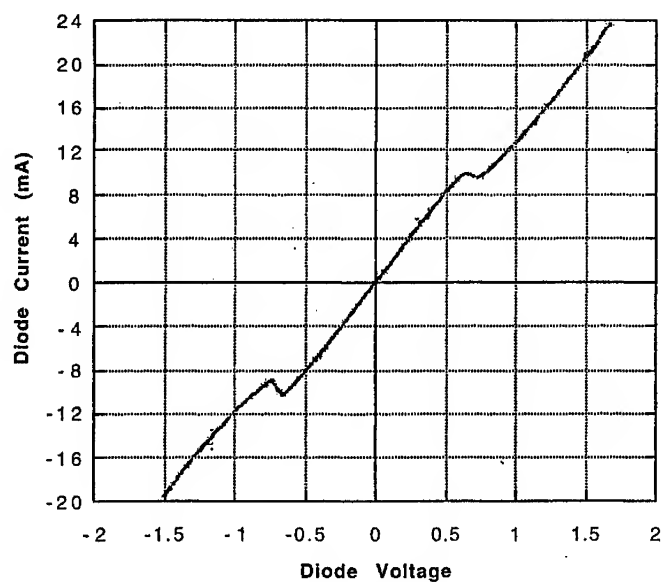


Fig. 4. Room temperature I-V characteristics of a sidewall RITD on a square mesa 50 μm on a side showing negative differential resistance. The device is on two sides of the square mesa with the other two sides of the mesa isolated.

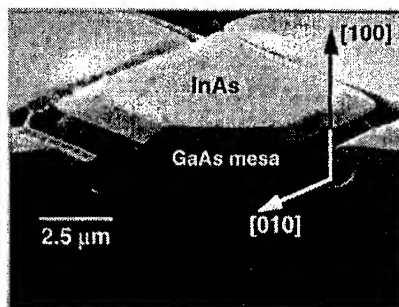


Fig. 5. SEM cross-section of a 5 μm x 5 μm square shaped mesa, oriented at 45° to the wafer flats, with a RITD structure regrown on it and showing complete contact isolation between top and bottom.

REACHING THE FUNDAMENTAL TRANSISTOR SIZE LIMIT: MOSFETs WITH 10 nm EFFECTIVE CHANNEL LENGTH

C. H. Yang and James Wang
Elec. Eng. Dept., University of Maryland, College Park, MD 20742
M. J. Yang and B. R. Bennett
Naval Research Laboratory, Washington, D.C. 20375
R. A. Wilson and D. R. Stone
Laboratory for Physical Sciences, College Park, MD 20740

ABSTRACT

A MOSFET suffers from the short-channel effects when its effective channel length is downsized to sub-0.1 μm . Nanometer-scale transistors that could survive the short-channel effects are therefore of interest for VLSI applications. In this paper, simulation results of two nanometer-scale tunneling field-effect transistors (TFETs) are presented. Both are based on tunneling: the electron tunneling probability from the source to the drain is strongly controlled by the gate voltage. By strategically placing the three terminals, we find that nanometer-scale TFETs can display desirable transistor characteristics while the short-channel effects are inherently avoided. Finally, one type of TFETs has been experimentally demonstrated with a channel length of 25 nm.

INTRODUCTION

In the past, scaling has proven useful in increasing the complexity and the performance of integrated circuits. For example, with a gate length of approximately 0.1 μm , a MOSFET operated at room temperature has shown a unity-gain cutoff frequency of 116 GHz (1). For VLSI applications, the effective-channel length is expected to be reduced to 0.1 μm by the year 2007 (2). Beyond 0.1 μm , however, the scaling approach has its physical limit (2) due to both the material properties and the fundamental operating principles of MOSFETs (3). To overcome the short-channel effects, there have been many investigations on alternative, non-conventional MOSFET structures (4) as well as new fabrication technologies. For example, using solid-state diffusion to define ultra-shallow junctions, a 40 nm gate-length MOSFET has recently been achieved (5). However, its effective channel length, defined to be the length of the channel region in which the carrier concentration is strongly modulated by the gate voltage, is in theory greater than ~ 70 nm (6). In addition, there are also efforts in using quantum effects, e.g., single-electron transistors (7), interference

effect transistors (8) and quantum computing systems (9).

To develop new nanometer-scale transistors, we first observe that in metals the screening length is only angstroms, e.g., 0.55 Å in copper. In semiconductors, however, electric field can easily induce or deplete carriers, and the Debye length ranges from tens of nanometers to microns. Furthermore, doping is no longer a reliable scheme to control the characteristics of nanometer-scale transistors. For example, at a doping level of $10^{18}/\text{cm}^3$, the average spacing between dopants is already 10 nm. Thus, any nanometer-scale device must exclude the use of pn junctions. In addition, randomly spaced dopants create a random local field, which disturbs electron transport. Finally, if the new transistor is to be used as a digital switch in conventional VLSI circuits, it is expected to display impedance isolation and signal gain — both are strongly desirable for circuit designers.

In view of the above observations and the practical difficulties, we have designed new transistors based on tunneling: *the electron tunneling current between the source and the drain is strongly controlled by the gate bias.*

LATERAL TUNNELING MOSFET

One approach to avoid pn junction as the carrier injector is to use tunneling junctions (10). A recent proposal using SiGe/Si heterojunctions (11) to reduce the punchthrough current in deep submicron MOSFETs. In other MOSFETs where tunneling injectors are used (12–15), the source is typically a reverse-biased Schottky barrier, and the drain has been assumed to be as a perfect ohmic contact. Based on numerical simulations, a minimum channel length of approximately 250 Å has been determined (12). There are also experimental investigations (14–15). Our model structure is shown in Fig. 1(a). It is similar to that of a conventional MOSFET, but instead of using heavily doped silicon, the source and drain regions are now completely replaced by thin, metallic material. Unlike the other transistors using tunneling injectors (12–15), our new transistor makes the drain-to-channel contact an integral part of the tunneling injector, i.e., two back-to-back Schottky barriers form a tunneling barrier separating the source and the drain. The drain current in this new MOSFET is dominated by electron tunneling through the entire barrier.

We have developed a two-dimensional numerical simulator specifically for our lateral TFET structure. The current conduction mechanisms include thermionic emission, quantum tunneling, as well as drift and diffusion. In previously published works, the tunneling current was only estimated by a post-processing quantum tunneling model (11), or based on an approximated formula for the Schottky barrier tunneling injector (12). Our two-dimensional simulation consists of a self-consistent loop for the solution of the Poisson equation and the current continuity equations. The boundary conditions used in simulations are similar to those for conventional

MOSFETs, as discussed in (16).

Realistic material parameters are used in the calculation, including an oxide thickness of 3 nm (17), a supply voltage of 1.0 V, a junction depth of 10 nm, a channel length of 20 nm, an interface-state density of $6 \times 10^{13}/\text{cm}^2$ at Schottky barriers (from the donor-like states and the acceptor-like states, located at 0.62 eV and 0.5 eV above the valence band top, respectively).

Band bendings for different biasing conditions are calculated. Under zero bias ($V_g = 0\text{V}$, $V_{ds} = 0\text{V}$), there is no current flowing between the source and the drain because of the thick potential barrier in the channel (see Fig. 1(b)). When the drain is positively biased, the potential barrier under zero gate voltage is still tall enough to block electrons flowing from the source to the drain. These two cases correspond to the "OFF" state of the transistor, where the Fermi level remains strongly pinned, and the Schottky barrier height is unchanged. A positively biased gate induces electrons in the middle of the "square" quantum barrier at the Si/SiO₂ interface. As a result, a much thinner tunneling barrier is formed between the source and the drain, resulting in a significantly enhanced channel conductance. The current will flow when a drain bias is applied, corresponding to the "ON" state. Band bendings for drain voltages at 0 V and 0.2 V are shown in Fig. 2(a) and (b), respectively. The Schottky barrier height is reduced when the lateral TFET is turned on, from ~ 0.6 eV by a few tenths of an eV, because of electron accumulation at the Schottky interface. The reduction in barrier height helps to increase the drain current when the transistor is turned on. The transistor operates as a three-terminal switch. Fig. 3(a) plots the calculated transistor I-V characteristics. When the gate voltage is zero, the net current is approximately zero. As the gate voltage is increased, the tunneling current gradually dominates. Finally, when the transistor is fully turned on at $V_g = 1$ V, the tunneling current can be tens of times higher than the thermionic-drift-diffusion component.

Unlike the typical I-V characteristics of conventional MOSFETs, but consistent with our operating principle, the drain current initially increases exponentially with the drain bias, and saturates at high drain voltages. The transfer characteristics, $\log(I_d)$ versus V_g , are shown in Fig. 3(b). When the lateral TFET is turned on ($V_g > 0$), I_d shows an exponential dependence on V_g , originating from the tunneling mechanism. The dependence is found to be about 130 mV/decade, i.e., a change of gate voltage by 130 mV can induce a modulation in drain current by 10 times. When the lateral TFET is turned off, the thermionic current through the bulk (behind the electron gas at the channel) is responsible for the leakage current. The leakage current has dependence on the drain bias, the residue/substrate doping, and the junction depth.

An inverter is simulated using n-type and p-type lateral TFETs. Assuming that a p-channel lateral TFET has matching characteristics to its n-channel counterpart, the calculated transfer function of an inverter is shown in Fig. 4(a). According to our

calculation, the inverter offers a noise margin greater than 0.4 V (30 % of the power supply voltage when 1 V is used), suitable for circuit integration. Similarly, we can build a CMOS-like NAND gate with two n-type transistors connected in series as the "pull-down" and two p-type transistors connected in parallel as the "pull-up."

The channel length can be downscaled to approximately 10 nm, only limited by the direct tunneling through the channel. Keeping all the parameters the same as before, except that the channel length is changed to 10 nm, we have calculated the transistor and the implied inverter characteristics. As shown in Fig. 4(b), the drain leakage current becomes discernible at $V_g = 0$ and $V_d = 1$ V, due to the thinner tunneling barrier at the channel. The inverter transfer relation also shows a reduced noise margin of 0.3 V. When channel length is decreased from 20 nm to 10 nm, the drain current at $V_d = 1$ V and $V_g = 1$ V decreases, because the band bending is strongly influenced by the pinned potential at the Schottky boundary. A similar explanation can be reached from the dependence of the transistor characteristics on the Schottky barrier height, density of interface states, temperature, junction depth, and substrate doping.

VERTICAL TUNNELING MOSFET

Modeling of Vertical Tunneling MOSFETs

Another tunneling MOSFET has a vertically-stacked structure. (18-19) Fig. 5 shows the schematic structure and the associated energy band diagram. The silicon-based heterostructure includes silicon, silicon-germanium alloy, SiO_2 , and silicides. The top two electrodes are the source and the drain. The bottom electrode is the backgate. The conduction channel is a quantum well (QW) sandwiched by a thin tunneling barrier and a gate dielectric. The current conduction between the source and the drain is through a sequential process including (i) source electrons tunnel into the QW; (ii) the electrons drift laterally in the QW; and (iii) QW electrons tunnel to the drain. A gate bias (V_{gs}) modulates two-dimensional electron concentration (n_{2D}) in the QW by a capacitive coupling, as in a typical MOSFET. As n_{2D} is changed, so is the tunneling current since the number of available final states is also modified. For example, when n_{2D} is depleted, the current must be zero.

Since the current flow is continuous, depending upon the structural specifics, if the tunneling process dominates, the tunneling transmission coefficient is strongly modulated by the gate bias, and the drift current has to follow the change of the tunneling current to satisfy the current continuity. On the other hand, when the drift process dominates, the source-drain current is linearly proportional to the n_{2D} . By definition, $n_{2D} = \int_{E_0}^{\infty} D(E)f(E)dE$, where $D(E)$ is the two-dimensional density of states, and $f(E)$ is the Fermi-Dirac distribution function. The threshold voltage, V_{th} , is defined here as V_{gs} at which $E_F = E_0$. The subthreshold region

is defined to be the condition when $V_{gs} < V_{th}$. In addition, when $E_F - E_0 \ll -3kT$, $n_{2D} \approx (m^*/\pi\hbar^2)kT \exp((E_F - E_0)/kT)$. We find that the vertically-stacked MOSFET has the same subthreshold characteristic as that of ideal, long-channel MOSFETs. Under the biasing condition that $V_{ds} \ll V_{gs} - V_{th}$, n_{2D} is approximately uniform along the QW channel and the current conduction can be represented as $I_d = n_{2D}qvW$, where q is the electron charge, v is the electron drift velocity, and W is the channel width. The subthreshold swing, S , defined as the gate-voltage swing required to reduce I_d by one decade, can then be evaluated by $S = \ln(10)(dV_{gs}/d\ln(I_d)) = \ln(10)(dV_{gs}/d\ln(n_{2D})) = \frac{kT}{q} \ln(10)(dV_{gs}/d(\frac{E_F - E_0}{q}))$. To the limit where $dV_{gs}/d(\frac{E_F - E_0}{q}) = 1$, which can be achieved by using a thin gate dielectric, $S = \frac{kT}{q} \ln(10)$, approximately 60 mV/decade at room temperature.

Experimental Realization of Vertical TFET

While new techniques for growing silicon-based QW systems are still under development, we have taken advantage of the mature Molecular Beam Epitaxy (MBE) technique and chosen to work on the InAs/AlSb heterojunction system. Grown on heavily n-doped GaAs substrate, the sample has an insulating buffer layer ($\sim 2.5 \mu\text{m}$), a 50 nm AlSb Bottom Barrier, an 8 nm InAs QW, a 5 nm AlSb Tunneling Barrier, and a 3 nm InAs surface capping layer. More information on sample structure, fabrication process and characteristics are reported in Ref. (20). We have fabricated a series of vertical TFETs with 25 nm metallurgical channel length, defined as the spacing between the metallic (150 nm Au) source and drain,

At $T < 200$ K, the backgate bias, V_{gs} , up to ± 10 V can be applied with a negligible leakage current. Fig. 6(a) shows the 77 K I_d - V_{ds} characteristics of the 25 nm channel-length vertical TFET. The applied gate bias range has been restricted to be within $-10 \text{ V} < V_{gs} < 10 \text{ V}$, because beyond this range, an undesirable hysteresis loop will appear in the I_d - V_{gs} transfer characteristic due to the complex gating effect in the AlSb bottom barrier (22). The transistor cannot be completely turned off at $V_{gs} = -10 \text{ V}$ because V_{th} has been shifted to be approximately -40 V , due to an increase of the InAs surface Fermi level pinning energy resulting from the surface damage induced by the plasma-ashing process. The ashing-induced V_{th} shift has been identified by our extensive magnetotransport experiments (20) and numerical simulations.

To understand the subthreshold characteristics for the specific experimental system, we have performed one-dimensional numerical analysis along the sample growth direction (22). The self-consistent solution is obtained by solving the Poisson equation and the Schroedinger equation iteratively (18,23). For each V_{gs} , the spatial charge distribution and the corresponding potential profile are first obtained by solving the Poisson equation numerically without considering the size quantization effects. This potential profile is then used to calculate the energy positions of the

quantum states (E_0, E_1 , etc.) in the QW region by employing the transfer matrix method (24–25). From the energy difference between E_F and E_0 , n_{2D} can be calculated by $n_{2D} = (m^*/\pi\hbar^2)kT\ln(1 + \exp((E_F - E_0)/kT))$ as described earlier. Since the wave function of the ground state in a QW is approximately a cosine function, the equivalent QW charge distribution in three-dimension (3D) is expressed as: $n_{3D}(x) = n_{2D}|\cos(\frac{\pi x}{L})|^2/L$, where the QW extends from $x = -\frac{L}{2}$ to $\frac{L}{2}$. The updated charge distribution is then fed back to the Poisson equation to calculate the new potential profile, which is subsequently used to update the energy positions of the quantum states. The calculated results are in excellent agreement with experiments. Fig. 6(b) and (c) show the 77 K $I_d - V_{ds}$ and $I_d - V_{gs}$ characteristics of an unashed vertical TFET with a 0.7 μm channel length, respectively. Fig. 6(b) also shows the simulated $\log(n_{2D})$ versus V_{gs} at 77K. In the range $-3 \text{ V} < V_{gs} < 10 \text{ V}$, S is measured and calculated to be 5 V/decade. The large S is a result of the thick 2.6 μm gate dielectric. When $V_{gs} < -3 \text{ V}$, the measured transfer characteristic deviates from what simulated, because there is a leaky, parallel conduction path between the source and the drain through the imperfect AlSb bottom barrier. (22)

Since the aforementioned numerical analysis can successfully interpret the measured transfer characteristic of the vertical TFET, we further used the same simulation routine to estimate the vertical TFET's performance by taking an optimized structure with thinner gate dielectric. Fig. 7 (a) shows the band-bending of a generic structure at $V_{gs} = 0 \text{ V}$. Two parameters are defined here: t_d , the gate dielectric thickness; and t_p , the distance from the surface to the left edge of the quantum well. In simulation, the tunneling barrier thickness is kept constant at 5 nm, and the surface Fermi-level pinning energy is assumed to be 200 meV above the InAs conduction band minimum. The "ON" state transfer ratio $\Delta n_{2D}/\Delta V_{gs}$ and the S in the subthreshold region are calculated for structures with different t_d and t_p . Results are summarized in Fig. 7(b) and 7(c). We find that a thinner t_d results in higher $\Delta n_{2D}/\Delta V_{gs}$ and a smaller S . The "ON" state $\Delta n_{2D}/\Delta V_{gs}$ is only a weak function of t_p , while S is strongly dependent on t_p . According to the simulated results, by extrapolating t_p to ∞ (corresponding to cases where the surface is either at a distance or the surface Fermi level is unpinned), S approaches 60 mV/decade, similar to that of the ideal, long-channel MOSFETs. As for intrinsic transconductance, $g_m = (\Delta n_{2D}/\Delta V_{gs})qv$, if a 2 nm gate dielectric is used and 10^7 cm/sec saturation velocity is assumed (26) the g_m is found to be 1.3 S/mm. Based on simulation, a vertical TFET operated at room temperature with $t_d = 5 \text{ nm}$ and $t_p = 100 \text{ nm}$ should display an S of 100 mV/decade with g_m of 1 S/mm. The channel length can be downscaled to nanometers, limited by direct tunneling of electrons in between the source and the drain.

CONCLUSION

We have presented two tunneling transistors. The lateral TFET has about one

fourth the driving current (27) of that of a $0.1\text{-}\mu\text{m}$ conventional MOSFET, the speed is comparable, because of its smaller gate capacitance. The vertical TFET is also attractive, particularly because the operation is demonstrated in an FET with only 25 nm channel-length. The silicon version using Si-based quantum well structures with front gate will be investigated.

When scaled in both lateral dimensions, the semiconductor region of both TFETs ultimately can be of 10 nm by 10 nm in area. We do not anticipate that size quantization would significantly affect the operation of the transistor at room temperature, because the energy breadth of the quantum states is broadened to be comparable to the thermal energy (26 meV at 300K).

While the discussed TFETs will face the same challenges in fabrication as other newly proposed alternatives, their strength is in the scalability: the ultimate effective channel length in principle can be continuously downscaled to $0.01\text{ }\mu\text{m}$.

REFERENCES

1. R.H. Yan, K.F. Lee, Y.O. Kim, D.Y. Jeon, D.M. Tennant, and E.H. Westerwick, OSA Proceed. Ultrafast Electronics and Optoelectronics, 1993, Vol. 14, eds. J. Shah and U. Mishra, Optical Soc. Am., (1993).
2. *SIA Semiconductor Technology-Workshop Working Group Reports*, Semiconductor Industry Association (1994).
3. S.M. Sze, *Physics of Semiconductor Devices*, p. 77, 2nd edition, Wiley, New York, (1981).
4. For a recent review, see, e.g., C. H. Wann, K. Noda, T. Tanaka, M. Yoshita, and C. Hu, IEEE Trans. Electron Devices, 43, 1742 (1996).
5. M. Ono, M. Saito, T. Yoshimoto, C. Fiegna, T. Ohguro, and H. Iwai, IEEE Trans. Electron Devices, 42, 1822 (1995). In this work, the shallow junction's sheet resistance is experimentally measured to be approximately $6\text{ kohm}/\square$ after $1000^\circ\text{C}/10\text{ sec}$ RTA, which implies an LDD series resistance of 150 ohms . But, the measured transistor data shows a turn-on resistance (at $V_{\text{gate}} = 2\text{V}$) of only 88 ohm . Therefore, only by assuming an effective channel length of approximately 80 nm can we come up with a consistent explanation.
6. This is because when the conducting channel is switched from on to off, the quasi-Fermi level in the silicon channel is swept from band edge to mid-bandgap. The effective channel length should be therefore at least twice (source-side and drain-side combined) of the depletion length of a pn junction, in order to avoid the source-drain punch-through (when there is effectively no barrier between

the source and the drain). Even with very high doping levels ($N_A = N_D = 10^{18}/\text{cm}^3$), the depletion length is found to be $\sqrt{\frac{2\epsilon}{q}(\frac{N_A+N_D}{N_A N_D})}\phi_i \sim 360 \text{ \AA}$, where ϵ is the dielectric constant of silicon, q is electron charge, N_A and N_D are the doping concentrations of the channel and the source/drain, respectively, and ϕ_i (0.6 eV, half of the bandgap) is the built-in potential. Therefore, a MOSFET that uses a homojunction as the carrier injector will necessarily make the channel length greater than $\sim 720 \text{ \AA}$.

7. For single-electron transistors, see, e.g., Y. Takahashi, H. Namatsu, K. Kurihara, K. Iwadata, M. Nagase, and K. Murase, *IEEE Trans. Electron Devices*, 43, 1213 (1996); and M.A. Kastner, *Rev. of Modern Phys.*, 64, 849 (1992).
8. S. Datta, *Superlattice and Microstructures*, 6, 83 (1989); and F. Sols, M. Macucci, U. Ravaioli, and K. Hess, *Appl. Phys. Lett.*, 54, 350 (1989).
9. D.P. DiVincenzo, *Science*, 270, 255 (1995), and references therein.
10. M.P. Lepselter and S.M. Sze, *Proc. IEEE*, 56, 1088 (1968).
11. S.A. Hareland, A.F. Tasch, and C.M. Maziar, *Proc. Int. Symp. Compound semicond.* 1994, Inst. Phys. Conf. Ser. No. 141, p. 806, IOP Publishing Ltd., (1995); and Hareland, S.A., Tasch, A.F., and Maziar, C.M., *Electronics Letters*, 29, 1894 (1993). Since the commercial package, SEMICAD, does not account for the tunneling mechanism in the transistor, the device was not simulated with the tunneling current in the calculation loop.
12. J.R. Tucker, C. Wang, and P.S. Carney, *Appl. Phys. Lett.* 65, 618 (1994). Although a contour plot of tunneling barrier was provided, the authors did not specify if their self-consistent simulation loop was two-dimensional or not. We believe that a two-dimensional simulation is necessary here to get accurate results.
13. R. Hattori, A. Nakae, and J. Shirafuji, *J. Appl. Phys.* 31, L1467 (1992); and Hattori, R., Nakae, A., and Shirafuji, J., *Jap. J. Appl. Phys.* 33, 612 (1994).
14. N. Kimura, and T. Matsudate, *IEEE Electron Device Lett.* 15, 412 (1994).
15. J.P. Snyder, C.R. Helms, and Y. Nishi, *Appl. Phys. Lett.* 67, 1420 (1995).
16. S. Selberherr, *Analysis and Simulation of Semiconductor Devices*, Springer-Verlag, New York, (1984).
17. Chenming, Hu, *Semiconductor International*, 105 (1994).
18. W. E. Zhang, F.-C. Wang, and C. H. Yang, *IEEE Trans. Electron Devices*, 43, 1441 (1996).

19. W. Saitoh, K. Yamazaki, M. Asada, and M. Watanabe, *Jpn. J. Appl. Phys.*, part 2, 35, L1104 (1996).
20. F.-C. Wang, W.E. Zhang, C.H. Yang, M.J. Yang, B.R. Bennett, R.A. Wilson, and D. Stone, to be published in *Applied Physics Letters* (June 1997).
21. J. Chung, M.-C. Jeng, J. E. Moon, A. T. Wu, T. Y. Chan, P. K. Ko, and C. Hu, *IEEE Electron Device Lett.*, 9, 186 (1988).
22. F.-C. Wang, W. E. Zhang, C. H. Yang, M. J. Yang, and B. R. Bennett, *Appl. Phys. Lett.*, 69, 1417 (1996).
23. J. Chen, C. H. Yang, and R. A. Wilson, *J. Appl. Phys.*, 71, 1537 (1992).
24. R. Tsu and L. Esaki, *Appl. Phys. Lett.*, 22, 562 (1973).
25. M. J. Yang and C. H. Yang, *J. Appl. Phys.*, 70, 2208 (1991).
26. T. Mizuno, R. Ohba, and K. Ohuchi, *Appl. Phys. Lett.*, 69, 106 (1996).
27. C.K. Huang, W. E. Zhang and C.H. Yang, unpublished.

FIGURES

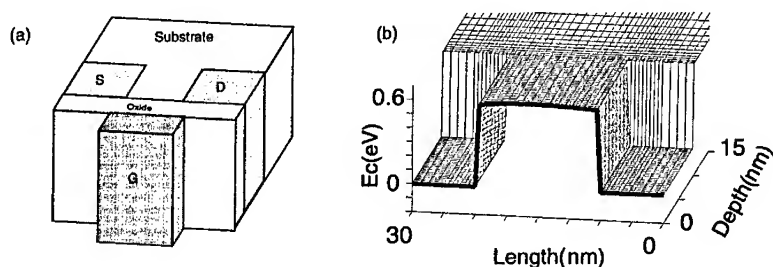


Fig. 1: (a) The schematic model structure of a lateral TFET. (b) Calculated band bending (conduction band minimum) for the model structure at zero bias in two-dimensions along the source-drain direction (Length) and toward the substrate (Depth). Zero depth is defined to be at the Si/SiO₂ interface, and the zero in length is arbitrarily set at 20 nm away from the source/channel interface. The thick, solid line depicts the potential profile at the Si/SiO₂ interface.

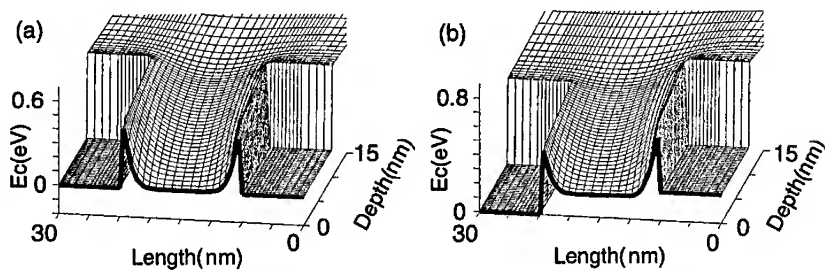


Fig. 2: Calculated band bending at (a) $V_d = 0$ V, $V_g = 1$ V; and (b) $V_d = 0.2$ V, $V_g = 1$ V.

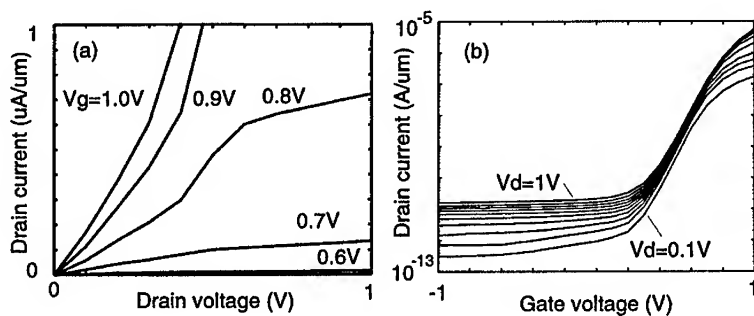


Fig. 3: (a) Calculated transistor characteristics, with the gate voltage evenly stepped from 0 to 1 V. (b) Calculated transfer characteristics for the model structure.

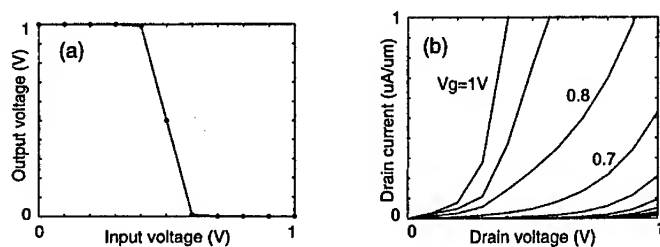


Fig. 4: (a) Calculated transfer characteristic of an inverter built by using two lateral TFETs, where an n-channel TFET is in series with a p-channel TFET. (b) Calculated

transistor characteristics for a 20 nm channel length lateral TFET.

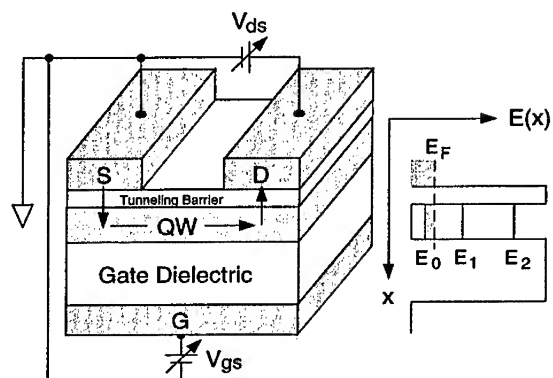


Fig. 5: Schematic vertical TFET structure and the associated energy band diagram. The design requires four materials: small bandgap semiconductor for the QW, large bandgap gate dielectric, tunneling barrier, and metallic electrodes.

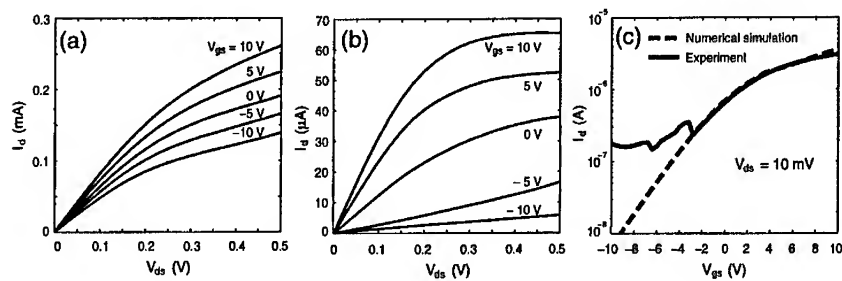


Fig. 6: (a) The 77 K I_d - V_{ds} characteristics of the 20 nm channel-length vertical TFET. (b) The 77 K I-V characteristics of an unashed TFET with a 0.7 μm channel length: I_d - V_{ds} characteristic; and (c) I_d - V_{gs} characteristic. The dashed line is from calculation.

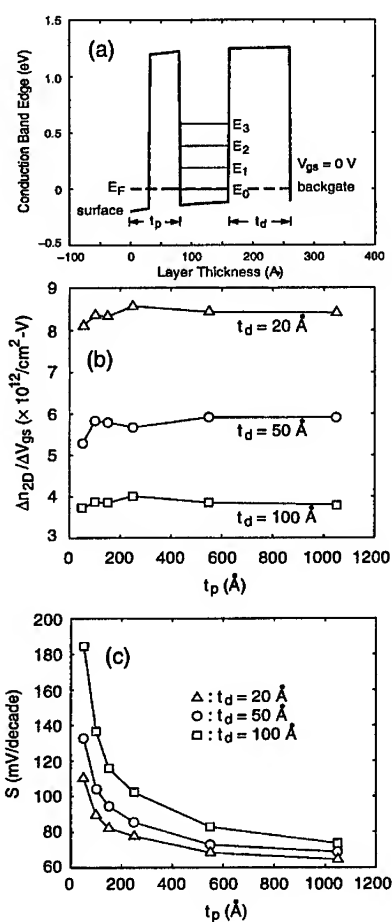


Fig. 7: (a) Calculated conduction band profile of an InAs/AlSb vertical TFET at $V_g = 0$ V. $T = 300$ K. The simulated results: (b) The "ON" state carrier transfer ratio $\Delta n_{2D}/\Delta V_{gs}$, and (c) S in the subthreshold region, plotted as a function of the gate dielectric thickness (t_d) and the distance from the surface to the QW (t_p).

BIAS DEPENDENCE OF THE TRANSMISSION
COEFFICIENT OF HOLES THROUGH THE ABRUPT
EMITTER-BASE JUNCTION OF A
 $In_{0.52}Al_{0.48}As/In_{0.53}Ga_{0.47}As$
Pnp HETEROJUNCTION BIPOLAR TRANSISTOR

T. Kumar, M. Cahay, and K. Roenker
Department of Electrical Engineering
University of Cincinnati, Cincinnati, Ohio 45221

ABSTRACT

Starting with the 4X4 Luttinger-Kohn Hamiltonian, a scattering-matrix approach is used to calculate the transmission coefficients of holes across the abrupt junction of a $In_{0.52}Al_{0.48}As/In_{0.53}Ga_{0.47}As$ heterojunction bipolar transistor (HBT). The tunneling coefficients of heavy and light holes are calculated for the upper and lower 2X2 Hamiltonians obtained through a unitary transform of the 4X4 Luttinger-Kohn Hamiltonian. The importance of band mixing between heavy and light holes is calculated as a function of the forward emitter-base bias and as a function of the hole wavevector parallel to the emitter-base interface. For holes injected from the emitter into the base, the probability of heavy to light hole conversion is shown to be quite different when calculated with the upper and lower Hamiltonians. On the other hand, the amount of light to heavy hole conversion is nearly the same for the upper and lower Hamiltonians. The consequences of these results on the emitter efficiency and high frequency performance of abrupt Pnp HBTs are briefly discussed.

INTRODUCTION

The development of Pnp InP based HBTs has received increased interest only over the last few years [1]. There have been only a few reports of Pnp HBTs while high performance Npn transistors have been widely reported [2, 3]. Stanchina et al. have obtained a current gain of 25, an f_T of 10 GHz and an f_{max} of 27 GHz

at $7 \times 10^3 \text{ A/cm}^2$ for an initial, conservatively designed, single heterojunction AlInAs/GaInAs Pnp transistor [4]. In view of their potential for a wide variety of applications, there is a need to develop accurate models of the device physics of Pnp HBTs. While the importance of electron tunneling through the emitter-base spike of Npn HBTs has been investigated by several groups [5, 6, 7, 8], the importance of hole tunneling across the emitter-base junction of abrupt and graded Pnp HBTs has not been addressed so far. This paper deals with the coherent transport of holes across the abrupt heterointerface between the emitter-base region of a typical abrupt $\text{In}_{0.52}\text{Al}_{0.48}\text{As}/\text{In}_{0.53}\text{Ga}_{0.47}\text{As}$ HBT. We study both the importance of the anisotropy of the dispersion relation of holes and the effects of band mixing on the tunneling of holes across the emitter-base junction. A preliminary account of the scattering-matrix approach used here has been reported recently [9]. In our earlier study, we started with the 4x4 Luttinger-Kohn Hamiltonian [10, 11] to develop a scattering-matrix approach to study coherent hole transport through abrupt and graded Pnp HBTs. The scattering-matrix was developed after reducing the 4x4 Hamiltonian to two 2x2 Hamiltonians (referred as upper and lower Hamiltonian in the literature) through a unitary transformation originally developed by Broido and Sham [12]. Because the Kramers degeneracy is lifted for holes tunneling through the highly asymmetric valence band profile across a forward bias emitter-base junction in an abrupt HBT, the tunneling coefficients for heavy and light holes are expected to be different when calculated starting with the upper or lower Hamiltonian [13]. This is illustrated in this paper for a specific $\text{In}_{0.52}\text{Al}_{0.48}\text{As}/\text{In}_{0.53}\text{Ga}_{0.47}\text{As}$ abrupt Pnp HBT.

II. APPROACH

Following Chuang [13], we start with the well-known Luttinger-Kohn Hamiltonian [11] describing the top of the valence band while ignoring the split-off band

$$H = \begin{bmatrix} P+Q & -S & R & 0 \\ -S^\dagger & P-Q & 0 & R \\ R^\dagger & 0 & P-Q & S \\ 0 & R^\dagger & S^\dagger & P+Q \end{bmatrix} \quad (1)$$

where \dagger stands for the complex conjugate. In writing the Hamiltonian above, the energy of holes is measured positive as indicated in Fig.1. The explicit expressions for the above matrix elements are

$$P = \Gamma_1(k_x^2 + k_y^2 + k_z^2), Q = \Gamma_2(k_x^2 + k_y^2 - 2k_z^2) \quad (2)$$

$$R = -\sqrt{3}\tilde{\Gamma}(k_x - ik_y)^2 + \sqrt{3}\left[\frac{\Gamma_3 - \Gamma_2}{2}\right](k_x + ik_y)^2, S = 2\sqrt{3}\Gamma_3(k_x - ik_y)k_z \quad (3)$$

where $\Gamma_1 = \hbar^2\gamma_1/2m_0$, $\Gamma_2 = \hbar^2\gamma_2/2m_0$, $\Gamma_3 = \hbar^2\gamma_3/2m_0$ and $\tilde{\Gamma} = (\Gamma_2 + \Gamma_3)/2$, the γ_i 's are the Luttinger parameters [11], and m_0 is the free electron mass.

The Hamiltonian in Eq.(1) is a 4x4 matrix in the basis ($|\frac{3}{2}, \frac{3}{2}\rangle, |\frac{3}{2}, \frac{1}{2}\rangle, |\frac{3}{2}, -\frac{1}{2}\rangle, |\frac{3}{2}, -\frac{3}{2}\rangle$) of the four degenerate Bloch wavefunctions at the center of the Brillouin zone. These basis functions are given explicitly in the appendix of ref. [12, 13]. The 4x4 Luttinger-Kohn Hamiltonian (1) can be block diagonalized using a unitary transformation [13]:

$$H = \begin{bmatrix} H^U & 0 \\ 0 & H^L \end{bmatrix}$$

where the upper and the lower blocks are given by

$$H^\sigma = \begin{bmatrix} P \pm Q & \tilde{R} \\ \tilde{R}^\dagger & P \mp Q \end{bmatrix} \quad (4)$$

where $\sigma = U$ (or L) refers to the upper (or lower) \pm signs. In the expressions of H^L and H^U , \tilde{R} is equal to $|R| - i|S|$, where R and S have been defined above.

In the numerical examples below, the diagonal elements in Eq.(4) will usually contain an extra potential energy term which can easily be incorporated in the expressions given below for the energy eigenvalues and corresponding wavevectors for heavy and light holes. Hereafter, we focus only on the H^U part of the Hamiltonian whose eigenvalues are given by

$$E(k) = Ak^2 \pm [B^2k^4 + C^2(k_x^2k_y^2 + k_y^2k_z^2 + k_x^2k_z^2)]^{1/2} \quad (5)$$

where $A = \Gamma_1$, $B = 2\Gamma_2$, $C^2 = 12(\Gamma_3^2 - \Gamma_2^2)$ and $k^2 = k_x^2 + k_y^2 + k_z^2$ and the + and - sign refers to light (LH) and heavy (HH) holes, respectively. For simplicity, we consider the (k_x, k_z) plane, and set k_y equal to zero. As a result, rearranging Eq.(5), we get

$$k_x^2(k_x, E) = \frac{1}{A^2 - B^2} \left\{ AE - \left(A^2 - B^2 - \frac{C^2}{2} \right) k_x^2 \mp \left[B^2 E^2 + AC^2 E k_x^2 - C^2 \left(A^2 - B^2 - \frac{C^2}{4} \right) k_x^4 \right]^{1/2} \right\} \quad (6)$$

where the + is for the heavy hole and the - is for the light hole. We chose the z axis as the direction of growth of the heterostructure and we focus on hole injection from emitter to base.

The corresponding eigenvectors for the HH and LH wavefunctions are [13]

$$\psi_{HH}(r) = \frac{1}{N} \begin{bmatrix} U \\ -\tilde{R}^\dagger \end{bmatrix} = \begin{bmatrix} F_{1H} \\ F_{2H} \end{bmatrix} e^{i\vec{k}\cdot\vec{r}} \quad (7)$$

and

$$\psi_{LH}(r) = \frac{1}{N} \begin{bmatrix} \tilde{R} \\ U \end{bmatrix} = \begin{bmatrix} F_{1L} \\ F_{2L} \end{bmatrix} e^{i\tilde{k} \cdot r} \quad (8)$$

where

$$U = (Q^2 + \tilde{R}\tilde{R}^\dagger)^{1/2} - Q = \begin{Bmatrix} P - Q - E(HH) \\ E - P - Q(LH) \end{Bmatrix} \quad (9)$$

and

$$N = (|U|^2 + |\tilde{R}|^2)^{1/2} \quad (10)$$

is a normalization constant.

An arbitrary valence band energy profile can always be approximated as a series of small steps in which the valence band edge is assumed to be a constant. While considering tunneling between the contacts sandwiching an arbitrary heterostructure, the wavefunction of a heavy hole incident from the left contact can be written [13]

$$\psi_{HH}(\vec{r}) = \begin{bmatrix} F_{1H} \\ F_{2H} \end{bmatrix} e^{i(k_x x + k_z^{(H)} z)} \quad (11)$$

where $F_{1H} = U_H/N_H = (P_H - Q_H - E)/N_H$, $F_{2H} = -\tilde{R}_H^\dagger/N_H$, and $N_H = \sqrt{|P_H - Q_H - E|^2 + |\tilde{R}_H|^2}$. The quantities P_H , Q_H , U_H , and \tilde{R}_H are the expressions given above evaluated for $k_z = k_z^{(H)}$ in Eq.(6). The reflected wave can be written as

$$\psi_{refl}(\vec{r}) = \Gamma_{HH} \begin{bmatrix} F_{1H} \\ F_{2H} \end{bmatrix} e^{i(k_x x - k_z^{(H)} z)} + \Gamma_{LH} \begin{bmatrix} F_{1L} \\ F_{2L} \end{bmatrix} e^{i(k_x x - k_z^{(L)} z)} \quad (12)$$

where Γ_{HH} and Γ_{LH} are the reflection amplitudes for the heavy hole and light hole, respectively, $F_{1L} = \tilde{R}_L(-k_z^{(L)})/N_L$, $F_{2L} = -\tilde{R}_L^\dagger(-k_z^{(L)})/N_L$, and $F_{2L} = U_L/N_L$. The quantities P_L , Q_L , R_L , U_L and N_L are the values of the (P, Q, R, U, N) expressions evaluated for $k_z = k_z^{(L)}$. On the other hand, the transmitted wave function can be written

$$\psi_{trans}(\vec{r}) = \tau_{HH} \begin{bmatrix} F_{1H}^t \\ F_{2H}^t \end{bmatrix} e^{i(k_x x + k_z^{(H)} z)} + \tau_{LH} \begin{bmatrix} F_{1L}^t \\ F_{2L}^t \end{bmatrix} e^{i(k_x x + k_z^{(L)} z)} \quad (13)$$

where the superscript t is a reminder that the quantities must be evaluated in the transmitted region (the base of the transistor in our case). In Eq. (13), τ_{LH} and τ_{HH} are the transmission coefficients for the light hole and heavy hole, respectively.

At the interface between any two steps approximating the valence band energy profile, the envelope functions $F_{1,2}(z)$ must be chosen such that

$$\begin{bmatrix} F_1(z) \\ F_2(z) \end{bmatrix} \text{ and } \begin{bmatrix} (\Gamma_1 - 2\Gamma_2) \frac{\partial}{\partial z} & \sqrt{3}\Gamma_3 k_x \\ -\sqrt{3}\Gamma_3 k_x & (\Gamma_1 + 2\Gamma_2) \frac{\partial}{\partial z} \end{bmatrix} \begin{bmatrix} F_1(z) \\ F_2(z) \end{bmatrix} \quad (14)$$

are continuous [14]. Similarly, for the lower Hamiltonian, the envelope functions $F_{3,4}(z)$ must be such that

$$\begin{bmatrix} F_3(z) \\ F_4(z) \end{bmatrix} \text{ and } \begin{bmatrix} (\Gamma_1 + 2\Gamma_2)\frac{\partial}{\partial z} & -\sqrt{3}\Gamma_3(k_x - ik_y) \\ \sqrt{3}\Gamma_3(k_x + ik_y) & (\Gamma_1 - 2\Gamma_2)\frac{\partial}{\partial z} \end{bmatrix} \begin{bmatrix} F_3(z) \\ F_4(z) \end{bmatrix} \quad (15)$$

must be continuous [14]. In this case, the analysis outlined above must be repeated with the explicit forms of the eigenvectors of the lower Hamiltonian given in Table I of ref. [15].

Applying the boundary conditions given above across each potential step in the valence band, the unknown reflection and transmission amplitudes $\Gamma_{HH}, \Gamma_{LH}, \tau_{HH}$ and τ_{LH} for the upper and lower Hamiltonian can then be found as solutions of a matrix equation

$$M [\Gamma_{HH}, \Gamma_{LH}, \tau_{HH}, \tau_{LH}]^T = \vec{V}_h \quad (16)$$

where T stands for the transpose operation and the explicit forms of M and \vec{V}_h are given in [16]). Repeating the analysis above while shooting the heavy hole from right to left, the corresponding reflection and transmission amplitudes can be found to obey an equation similar to Eq. (16). We denote these reflection and transmission coefficients with a prime. After repeating that analysis for a light hole incident from either side, we then can form the scattering matrix across a potential step which relates the incoming and outgoing amplitudes of the hole wavefunctions on either side of each potential step as follows

$$S = \begin{bmatrix} \tau & \rho' \\ \rho & \tau' \end{bmatrix} \quad (17)$$

where

$$\tau = \begin{bmatrix} \tau_{HH} & \tau_{LH} \\ \tau_{LH} & \tau_{LL} \end{bmatrix} \text{ and } \rho = \begin{bmatrix} \Gamma_{HH} & \Gamma_{LH} \\ \Gamma_{LH} & \Gamma_{LL} \end{bmatrix} \quad (18)$$

The matrices τ' and ρ' can be defined similarly by priming all the elements in Eq. (17). In the matrices above, the first index characterizes the hole character upon reflection or transmission and the second index is a reminder of which hole is incident on the interface, The overall scattering matrix across the emitter-base junction is then obtained using the cascading rules for scattering matrices described in [17]. As mentioned above, the valence band must first be approximated by segmenting the potential energy profile in a number of small intervals in which the potential is approximated as a constant. Intervals should be sufficiently small to accurately represent the potential profile. At the interface between steps, the scattering matrix must be determined as outlined above. For the regions where the valence band is approximated by a constant, the scattering matrices have only non-zero elements on the diagonal which are the corresponding phase-shifts for the heavy and light holes.

In order to calculate the transmission and reflection coefficients for heavy and light holes incident from the emitter, the probability current density must be calculated along the growth direction (selected to be the z axis). This expression has been derived previously [13, 18]

$$j_{z,\alpha} = Re \frac{2}{\hbar} \{ [(|F_{1,\alpha}|^2 + |F_{2,\alpha}|^2)\Gamma_1 - (|F_{1,\alpha}|^2 - |F_{2,\alpha}|^2)2\Gamma_2]k_{z,\alpha} + 2i\sqrt{3}k_x\Gamma_3F_{1,\alpha}F_{2,\alpha}^* \} \quad (19)$$

where $\alpha = H$ or L for incident heavy and light hole, respectively. Using Eq.(19), the reflection and transmission coefficients for a heavy hole incident from the left are calculated as follows [18]

$$T_{HH} = \frac{|\tau_{HH}|^2 j_{z,H}^{trans}}{j_{z,H}^{inc}}, \quad T_{LH} = \frac{|\tau_{LH}|^2 j_{z,L}^{trans}}{j_{z,H}^{inc}}, \quad (20)$$

and

$$R_{HH} = -\frac{|\Gamma_{HH}|^2 j_{-z,H}^{inc}}{j_{z,H}^{inc}}, \quad R_{LH} = -\frac{|\Gamma_{LH}|^2 j_{-z,L}^{inc}}{j_{z,H}^{inc}}. \quad (21)$$

where $\alpha = L, H$ for light-hole and heavy-hole, respectively. In the expression above, the labels *trans* and *inc* mean that the probability current density must be evaluated in the transmitted and incident regions, respectively. Furthermore, the following relation $j_{-z,\alpha} = -j_{z,\alpha}$ holds between the probability current densities corresponding to left ($j_{-z,\alpha}$) and right ($j_{z,\alpha}$) propagating states. Current conservation further requires that $T_{HH} + T_{LH} + R_{HH} + R_{LH} = 1$, which is helpful to check the accuracy of the numerical simulations.

The formalism described above can be modified readily to handle the case of an incident light hole. Since we will be looking at the coherent transport of holes across the emitter-base junction of a Pnp HBT under forward bias, we will only consider the case of heavy and light holes incident from the left contact hereafter.

III. RESULTS

For simplicity, we assume in all the numerical examples below that $k_y = 0$. First, the valence band energy profile for a given structure is computed as a function of the forward emitter-base bias using the program FISH1D [19]. We approximate a given valence band energy profile as a series of small steps 10 Å wide. The valence band energy profile in the emitter is used as the zero of energy and the valence band energy is assumed to be constant throughout the heavily doped base. This amounts to neglecting the band bending in the base at the proximity of the emitter-base junction. This is a good approximation at large forward emitter-base bias as illustrated in Fig. 1. All calculations are performed assuming room temperature operation for all devices.

The Pnp HBT studied here is similar to the one investigated by Stanchina and coworkers [4]. The emitter consists of a $1,100\text{\AA}$ P-type *InAlAs* region doped at $8 \times 10^{17} \text{cm}^{-3}$ on top of a 300\AA wide base doped N-type at $7 \times 10^{18} \text{cm}^{-3}$. The valence band energy profile across the emitter-base junction was computed over a set of forward biases ranging from 0.0 to 0.9 V and the results are displayed in Fig.1. The following Luttinger parameters were used: $\gamma_1 = 6.85$, $\gamma_2 = 2.1$, $\gamma_3 = 2.9$ for GaAs, $\gamma_1 = 20.4$, $\gamma_2 = 8.3$, $\gamma_3 = 9.1$ for InAs [15], and $\gamma_1 = 3.45$, $\gamma_2 = 0.68$, $\gamma_3 = 1.29$ for AlAs [13]. The corresponding values for *In_{0.52}Al_{0.48}As* and *In_{0.53}Ga_{0.47}As* were obtained by linear interpolation.

First, we plot in Fig. 2 the real (Re) and imaginary (Im) parts of the heavy-hole wave number $k_z^{(H)}$ in the *In_{0.52}Al_{0.48}As* region as a function of energy; $\text{Re}k_z^{(H)}$ and $\text{Im}k_z^{(H)}$ for a transverse wavevector k_x equal to $4 \times 10^{-2}(2\pi/a)$, where $a = 5.65\text{\AA}$ is the lattice constant of GaAs. Figure 2 also shows the corresponding real and imaginary parts of the light-hole wave number $k_z^{(L)}$ in the *In_{0.53}Ga_{0.47}As* base. In Fig. 2, the zero of energy is the top of the valence band in the emitter region and the bias across the emitter-base junction is assumed to be 0.9 V.

The critical energies (E_h^- , E_h^+ , E_1) at which there is a sudden break in the energy dependence of the real and imaginary wavevector components of the heavy and light holes were calculated explicitly in ref. [18]. These expressions are repeated here for the sake of completeness:

$$E_1 = (\gamma_1 + 2\gamma_2) \frac{\hbar^2 k_x^2}{2m_0}, \quad (22)$$

$$E_h^+ = (\gamma_1 - 2\gamma_2) \frac{\hbar^2 k_x^2}{2m_0}, \quad (23)$$

and

$$E_h^- = \Gamma^+ \frac{\hbar^2 k_x^2}{2m_0}, \quad (24)$$

where

$$\Gamma^+ = \frac{3}{2} \frac{\gamma_1(\gamma_3^2 - \gamma_2^2)}{\gamma_2^2} \left\{ -1 + \left[1 + \frac{4}{3} \frac{\gamma_2^2}{\gamma_1^2(\gamma_3^2 - \gamma_2^2)} (\gamma_1^2 - \gamma_2^2 - 3\gamma_3^2) \right]^{1/2} \right\}. \quad (25)$$

The energies E_h^- , E_1 are the energy thresholds for the existence of propagating heavy and light holes, respectively, as a function of k_x . The energy range (E_h^- , E_h^+) corresponds to a small range of energy for which $\text{Re}k_z^{(L)}$ is negative while $\text{Im}k_z^{(L)}$ is zero [18]. A plot of (E_h^- , E_h^+ , E_1) is shown in Fig. 3 for the *InAlAs/InGaAs* structure considered here. From Fig.2, we expect the probability of conversion from heavy to light hole while crossing an *InAlAs/InGaAs* interface to be small since, for a given energy above the threshold E_1 for light hole propagation, $\text{Re}k_z^{(L)}$ in the *InGaAs* region is much smaller in magnitude than $\text{Re}k_z^{(H)}$ in the *InAlAs*

region. This is illustrated in Fig.4 where we plot the transmission coefficients (T_{HH}, T_{LH}) as a function of energy for a heavy hole incident from the emitter in the abrupt *InAlAs/InGaAs* Pnp HBT considered here. We used $k_x = 0.04(2\pi/a)$ and the emitter-base voltage $V_{EB} = 0.9$ V. The full and dashed lines show the results obtained with the upper and lower Hamiltonians, respectively. $T_{I,J}$ is the probability for transmission of a J-type hole into a I-type hole while tunneling across the emitter-base junction. Figure 5 is a similar plot for the light hole transmission coefficients T_{LL} and T_{HL} . Figure 4 shows that the tunneling coefficients for heavy holes are markedly different whether calculated with the upper or lower Hamiltonians. The difference is less dramatic for the light hole transmission coefficients. Furthermore, Fig. 4 indicates that the probability of heavy to light hole transition reaches a maximum of 30% and 10% for the upper and lower Hamiltonians, respectively. The probability of light to heavy hole transmissions is nearly the same when calculated with the upper and lower Hamiltonians, as shown in Fig. 5.

The sensitivity of (T_{HH}, T_{LH}) on the choice of the upper or lower Hamiltonian is further illustrated in Fig. 6. This figure shows that the coefficient T_{LH} is more sensitive to the emitter-base bias for the lower Hamiltonian. Also, T_{LH} increases slightly with the forward emitter-base bias.

Finally, Figures 7 and 8 show the tunneling coefficients T_{HH} and T_{LL} calculated with the upper and lower Hamiltonians for three different values of k_x . The emitter-base bias is set equal to 0.9 V. A comparison of Figures 7 and 8 shows that, as a function k_x , T_{HH} is more sensitive than T_{LL} to the choice of the upper and lower Hamiltonian.

The transmission coefficients of both light and heavy holes starting with the upper and lower Hamiltonians must be calculated accurately in order to estimate the total current densities of heavy and light holes across an emitter-base junction as a function of bias. For the holes incident from the emitter, the overall scattering matrix for propagation across the emitter-base junction must be found using the prescription outlined in this paper. Then, the appropriate current densities must then be evaluated following Chao and Chuang [16]:

$$J_{HH} = \frac{e}{4\pi^3} \int_{\Omega_{h1} + \Omega_{h2} + \Omega_{h3}} [f(E) - f(E + eV)][T_{HH \rightarrow HH}(\vec{k}) + T_{HH \rightarrow LH}(\vec{k})]v_{zHH}(\vec{k}) \\ + \frac{e}{4\pi^3} \int_{\Omega_{h4}} [f(E) - f(E + eV)][T_{LH \rightarrow HH}(\vec{k}) + T_{LH \rightarrow LH}(\vec{k})]v_{zHH}(\vec{k}) \quad (26)$$

and

$$J_{LH} = \frac{e}{4\pi^3} \int_{\Omega_l} [f(E) - f(E + eV)][T_{LH \rightarrow HH}(\vec{k}) + T_{LH \rightarrow LH}(\vec{k})]v_{zLH}(\vec{k}) \quad (27)$$

where a summation over the contribution of the lower and upper Hamiltonians must be carried out. The different domains of integration defined in Eqns.(26-27) are illustrated in Fig. 9 [16]. In the current expressions above, $T_{HH \rightarrow HH}$ stand

for the transmission coefficient from HH-in to HH-out, etc., and v_{zHH} is the group velocity of the incident HH, etc., $f(E)$ is the Fermi-Dirac distribution function, and V is the emitter-base junction potential. The above three-dimensional integrals must be carried out numerically over the regions illustrated in Fig.3 [16]. This burden is quite time consuming and can be reduced somewhat by using the axial approximation [12] while applying the scattering-matrix formalism outlined in this paper. Results for the emitter-bias dependence of the emitter currents for heavy and light holes calculated using Eqns.(26) and (27) will be reported in a forthcoming publication.

IV. CONCLUSIONS

We have used the 4x4 Luttinger-Kohn Hamiltonian to develop a scattering-matrix approach to study coherent hole transport through both abrupt and graded Pnp HBTs. The scattering-matrix was developed after reducing the 4X4 Hamiltonian to two 2x2 Hamiltonians (referred as upper and lower Hamiltonian in the literature) through a unitary transformation originally developed by Broido and Kohn [12]. Because the Kramers degeneracy is lifted for holes tunneling through the highly asymmetric valence band profile across a forward bias emitter-base junction in an abrupt HBT, the tunneling coefficients for heavy and light holes are expected to be different when calculated starting with the upper or lower Hamiltonian. This was illustrated by calculating the transmission coefficients for the upper and lower Hamiltonians as a function of the emitter-base bias and as a function of k_x , the wavevector component of the incident hole perpendicular to the axis of growth of the heterostructure. We have found that the transmission coefficients for heavy holes are quite different when calculated with the upper and lower Hamiltonians, but that the difference is much smaller for light holes.

ACKNOWLEDGEMENT

This work is supported by the National Science Foundation (ECS-9525942). We also acknowledge the Ohio-Cray supercomputing center for the use of their facilities.

References

- [1] M. E. Kim, B. Bayraktaroglu, and A. Gupta, Chapter 5, in *HEMTs and HBTs: Device, Fabrication, and Circuits*; F. Ali and A. Gupta, Eds. Artech House, Boston (1991).
- [2] J. F. Jensen, W. E. Stanchina, R. A. Metzger, D. B. Rensch, R. F. Lohr, R. W. Quen, M. W. Pierce, Y. K. Allen, and P. F. Lou, *IEEE Journal of Solid State Circuits*, Vol. 26, p. 415 (1991).
- [3] W. L. Chen, J. P. Sun, G. I. Haddad, M. E. Sherwin, G. O. Munns, J. R. East, and R. K. Mains, *Appl. Phys. Letters*, Vol. 61, p.189 (1992).
- [4] W. E. Stanchina, R. A. Metzger, D. B. Rensch, L. M. Burns, J. F. Jensen, R. H. Walden, L. E. Larson, and P. T. Greiling, *GOMAC-91 Digest* (1991).
- [5] R. J. Ferro, R. G. Wilson, J. F. Jensen, D. B. Rensch, W. E. Stanchina, R. A. Metzger, M. W. Pierce, T. V. Kargodorian and Y. K. Allen, *Solid State Electronics*, 34(12), 1319 (1991).
- [6] A. Das and M.S. Lundstrom, *Journal of Applied Physics*, 66(5), 2168 (1989).
- [7] T. Kumar, M. Cahay, S. Shi, K. Roenker, and W. E. Stanchina, *Journal of Applied Physics*, 77(11), 5786 (1995).
- [8] T. Kumar, M. Cahay, S. Shi, and K. Roenker, *Journal of Applied Physics*, 78(11), 6814 (1995).
- [9] T. Kumar, M. Cahay, and K. Roenker, "Hole Tunneling Through the Emitter-Base Junction of a Heterojunction Bipolar Transistor", submitted to *Physical Review B*.
- [10] E. O.Kane, in *Physics of III-V Compounds*, edited by R. K. Willardson and A. C. Beer, *Semiconductors and Semimetals*, Vol.1 (Academic, New York, 1966), p.75.
- [11] J. M. Luttinger and W. Kohn, *Phys. Rev.* 97, p.869 (1955).
- [12] A. D. Broide and J. L. Sham, *Phys. Rev. B*, Vol. 31, p. 888 (1985).
- [13] S. L. Chuang, *Phys. Rev. B*, Vol. 40(15), p.10379 (1989).
- [14] L. C. Andreani, A. Pasquarello, and F. Bassani, *Phys. Rev. B*, vol.36(11), p.5887, 1987.
- [15] S. L. Chuang, *Phys. Rev. B*, Vol.43(12), p.9649 (1991).

- [16] C.Y. Chao and S.L. Chuang, Phys. Rev. B, vol.43, no.9, 7027, 1991.
- [17] M. Cahay, M. McLennan, and S. Datta, Phys. Rev. B, vol.37, no.17, pp.10125, 1988.
- [18] Sanchez. A.D., Proetto. C.R., J. Phys. Condens. Matter, vol.7, pp.2059, 1995.
- [19] The energy band diagram through the emitter-base junction is calculated using the program FISH1D released by Purdue University. Copies of the program can be obtained by contacting M. Lundstrom at lundstro@ecn.purdue.edu.

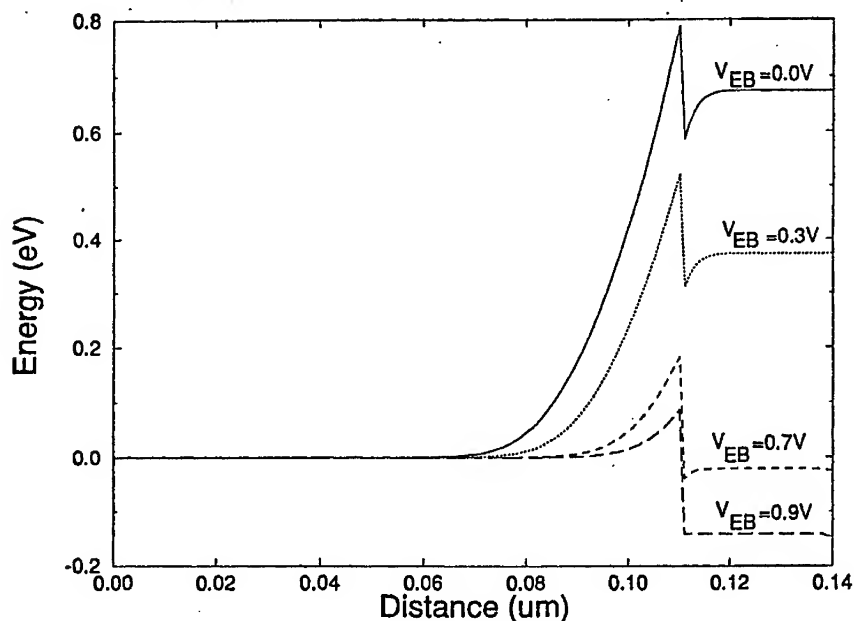


Figure 1: Valence band energy profile across the emitter-base junction of a typical *InAlAs/InGaAs* abrupt Pnp HBT. The emitter consists of a 1,100Å P-type *InAlAs* region doped at $8 \times 10^{17} \text{ cm}^{-3}$ on top of a 300Å wide base doped N-type at $7 \times 10^{17} \text{ cm}^{-3}$. The valence band energy profile across the emitter-base junction is shown for several values of the emitter-base bias. Hole energies are measured positive as indicated on the figure while taking the valence band energy profile in the bulk of the emitter region as the zero of energy.

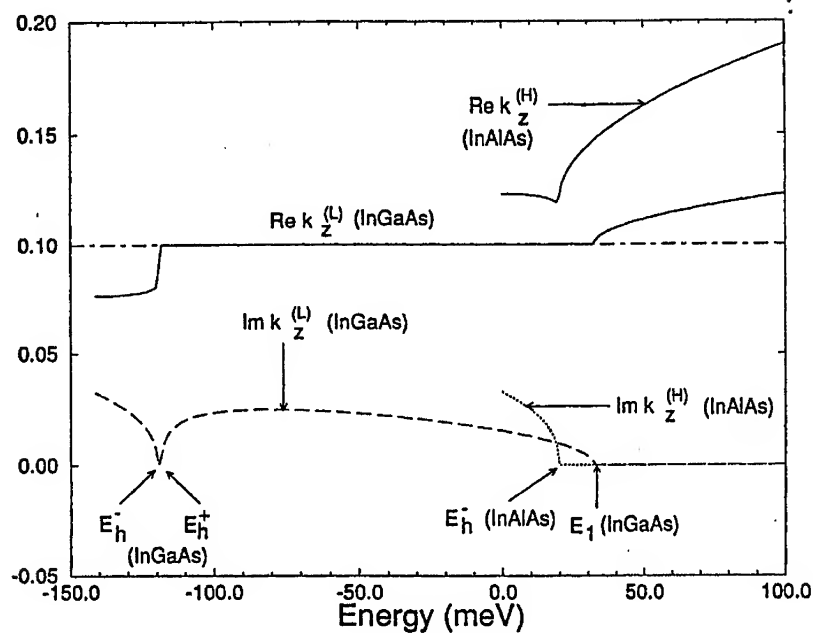


Figure 2: Real and imaginary parts of the heavy-hole wave number $k_z^{(H)}$ in the $\text{In}_{0.52}\text{Al}_{0.48}\text{As}$ emitter region as a function of energy for a value of $k_x = 0.04$ ($2\pi/a$). Also shown are the real and imaginary parts of the light-hole wavevector in the $\text{In}_{0.53}\text{Ga}_{0.47}\text{As}$ base region. A bias of 0.9 V is applied across the emitter-base junction of the structure considered. The zero of energy is the top of the valence band in the emitter region. The real and imaginary parts of both heavy and light holes are expressed in units of $2\pi/a$, where $a = 5.65 \text{ \AA}$ is the lattice constant of GaAs. For clarity, the real parts have been shifted vertically by an amount equal to 0.1 ($2\pi/a$).

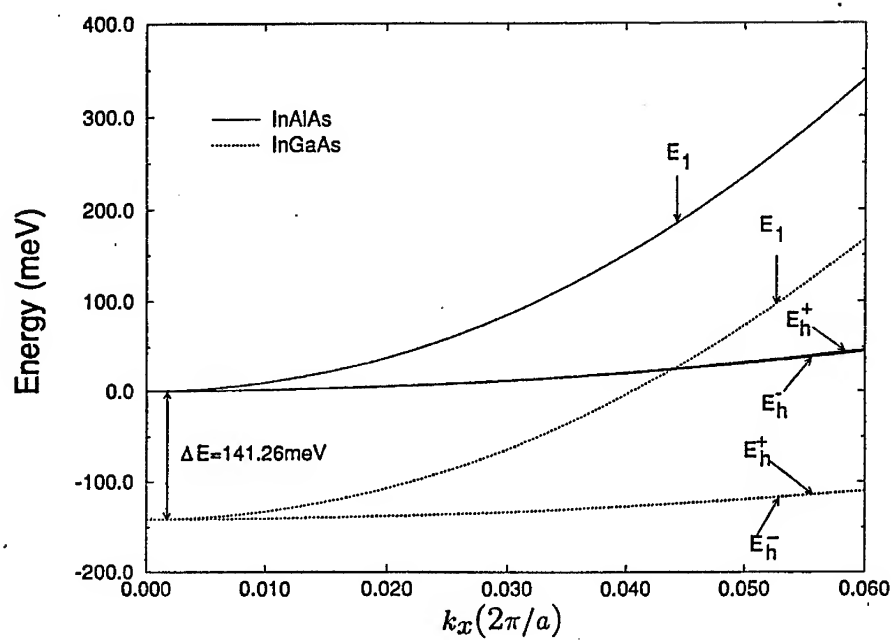


Figure 3: k_x dependence of the energies (E_h^- , E_h^+ , E_1) defined in the text. The full lines are the energies in the $In_{0.52}Al_{0.48}As$ emitter and the dotted lines are the values in the $In_{0.53}Ga_{0.47}As$ base. The lower curves are shifted by an amount of 141.26 meV which corresponds to the difference in energy of the top of the valence band in the bulk of the emitter and base regions for a bias V_{EB} of 0.9 V across the emitter-base junction.

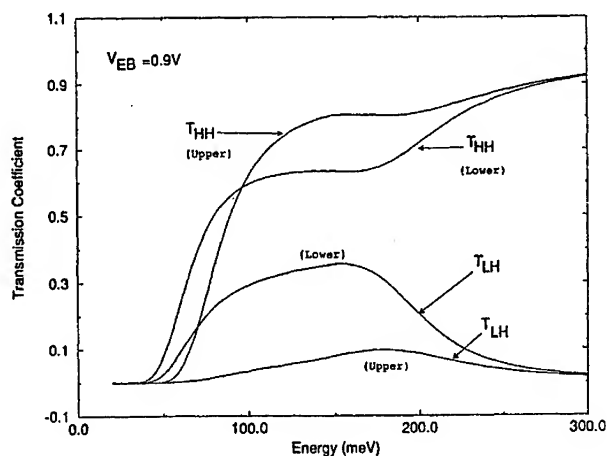


Figure 4: Plot of the transmission coefficients (T_{HH}, T_{LH}) as a function of energy for a heavy hole incident from the emitter in the abrupt $InAlAs/InGaAs$ Pnp HBT considered here. We used $k_x = 0.04(2\pi/a)$ and the emitter-base voltage $V_{EB} = 0.9$ V. The results are shown for the upper and lower Hamiltonians. The zero of energy is the top of the valence band in the emitter. $T_{I,J}$ is the probability for transmission of a J-type hole into a I-type hole while tunneling across the emitter-base junction.

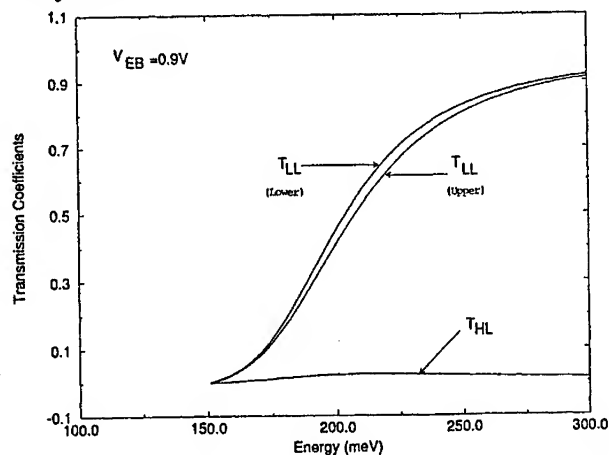


Figure 5: Same as Fig.4 for the light hole transmission coefficients (T_{LL}, T_{HL}).

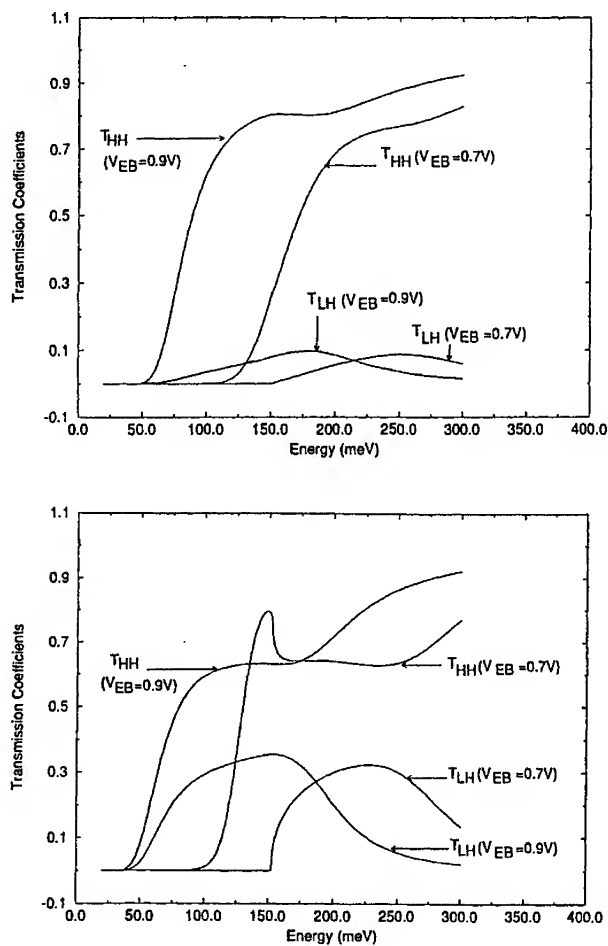


Figure 6: Bias dependence of the transmission coefficients T_{HH} and T_{LH} for heavy hole incident from the emitter across the abrupt $In_{0.52}Al_{0.48}As/In_{0.53}Ga_{0.47}As$ emitter-base junction. The wavevector k_x was set equal to $0.04(2\pi/a)$. The results obtained with the upper and lower Hamiltonians are shown in the top and bottom figures, respectively. The zero of energy is the top of the valence band in the emitter.

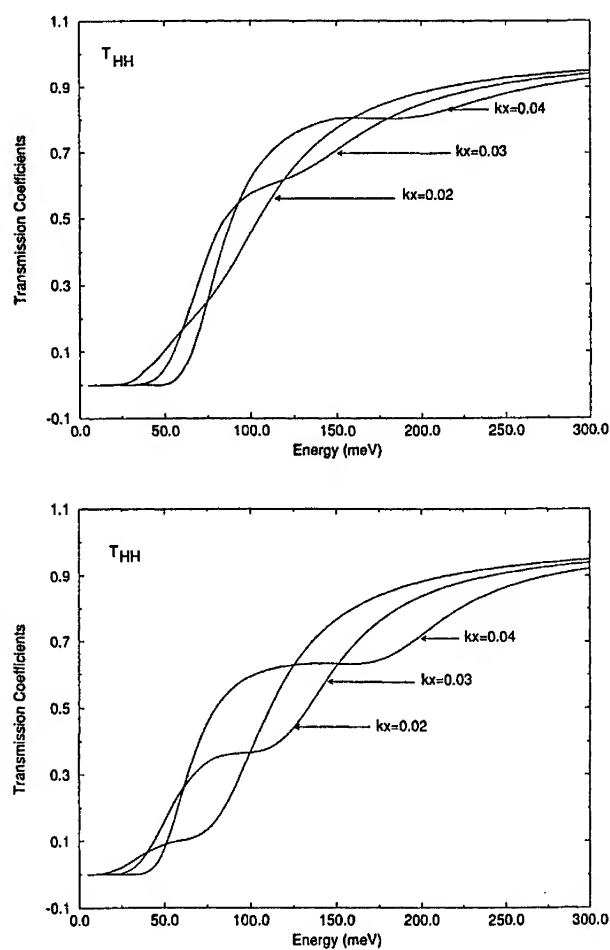


Figure 7: Energy dependence of the transmission coefficient T_{HH} for heavy holes from emitter to base across the abrupt emitter-junction shown in Fig. 1. The bias across the emitter-base junction was set equal to 0.9 V. T_{HH} is plotted for several values of k_x . The results obtained with the upper and lower Hamiltonians are shown in the top and bottom figures, respectively. The zero of energy is the top of the valence band in the emitter.

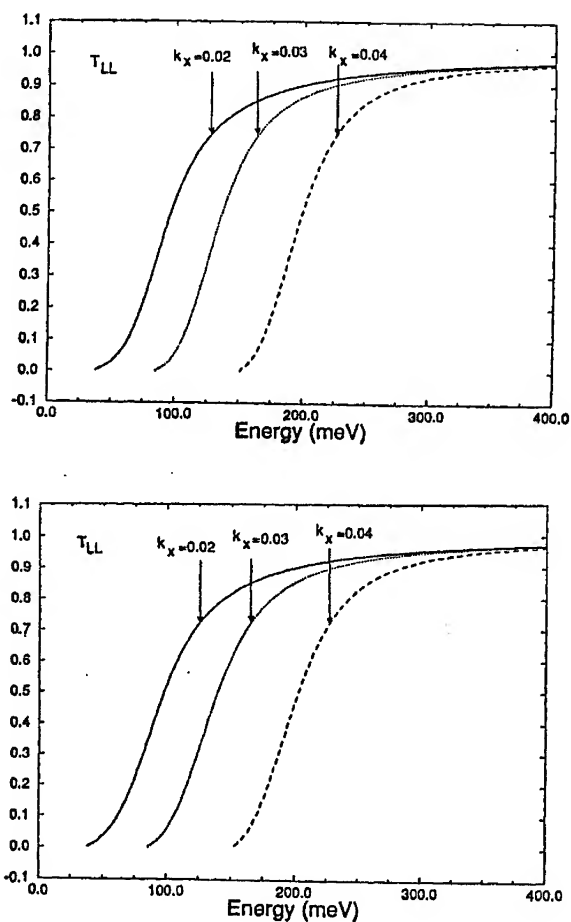


Figure 8: Same as Fig.7 for the transmission coefficient T_{LL} . The top and bottom figures show the results obtained with the upper and lower Hamiltonians, respectively. The difference between the values of T_{LL} obtained with the upper and lower Hamiltonians is less drastic than for heavy holes (See Fig. 7). The zero of energy is the top of the valence band in the emitter.

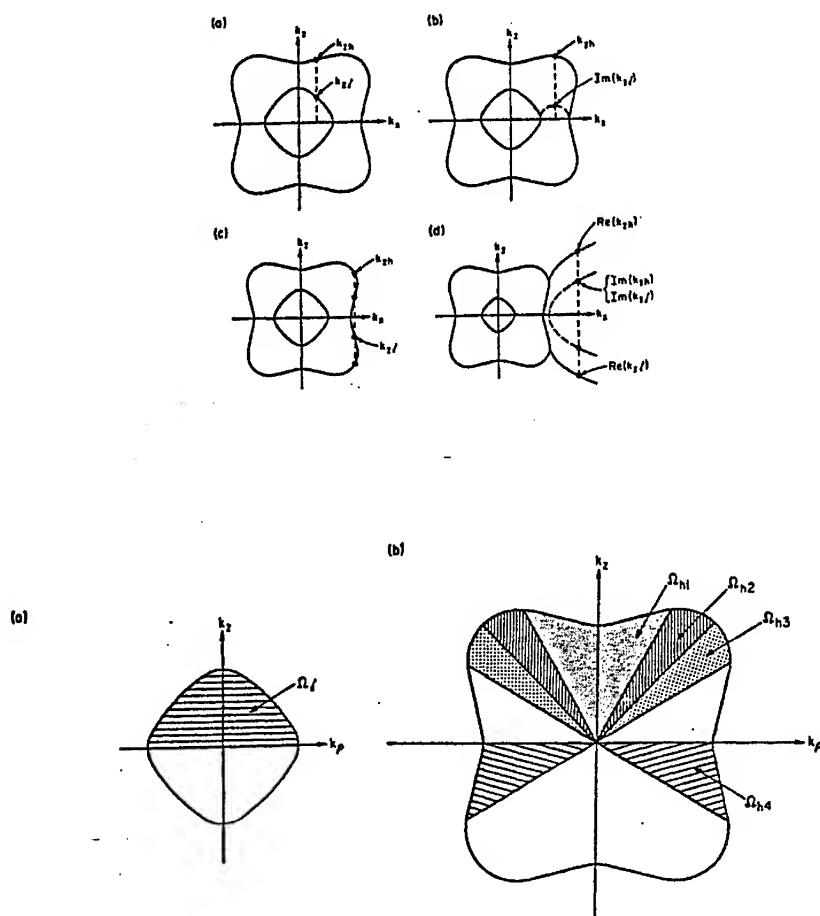


Figure 9: (a) Solutions for k_z obtained from Eq.(6). for fixed k_x (assuming $k_y = 0$). and total energy E . (b) Domains of integration in \vec{k} space for calculating the emitter currents for heavy (Eq.(26)) and light (Eq.(27)) holes. The domains Ω_l and Ω_{h1} correspond to the condition in frame (a) of the top figure. The region Ω_{h2} corresponds to quadrant (b), whereas Ω_{h3} and Ω_{h4} correspond to quadrants (c) and (d), respectively (After Chuang [15]).

RESONANT TUNNELING IN QUASI- ONE- DIMENSIONAL MULTIPLE WELL STRUCTURES WITH VERTICALLY UNIFORM GATING

V.R. Kolagunta^{a)}, D.B. Janes, M.R. Melloch,
School of Electrical and Computer Engineering,
Purdue University, West Lafayette IN 47907-1285.

^{a)}Electronic Mail: kolagunt@ecn.purdue.edu

C. Youtsey
Department of Electrical Engineering,
University of Illinois,
Champaign, IL61801

ABSTRACT

In this paper we present the study of gating effects in double well resonant tunneling heterostructures with sub-micron minimum feature widths. Resonant tunneling through one- dimensional states in the wells is observed as the device approaches pinch-off at temperatures as high as 77K. This is the first demonstration of gating effects in double well structures and first observance of such confinement effects at 77K.

I. INTRODUCTION

Vertical gated heterostructures are interesting in their applications in multi valued logic systems and study of quantization effects with possible applications in single electron transistors. RT devices have been shown to oscillate at frequencies of a few hundred Gigahertz and hence are suitable for high speed circuits [1]. Other applications of such three terminal resonant tunneling devices include oscillators and high frequency switching circuits [2]. Most previous resonant tunneling gated structures have demonstrated pinch-off of the resonance peak at liquid helium temperatures or below and have involved a lateral Schottky gating technique. These devices have suffered from the problems of inhomogeneous gating along the heterostructure. The problem of an uneven gating field along the heterostructure has been alleviated by the use of a sidewall gate [3, 4]. Using this self-aligned sidewall gating technique we have demonstrated the ability to fabricate Resonant Tunneling Transistors with self-aligned sidewall gates and minimum features in the sub-micron regime that permit pinch-off of the resonant peak at room temperature

[5]. Even gating field and a higher gating efficiency has been demonstrated in a recently published work comparing similar sidewall gated devices and previously used lateral gating techniques [4].

Fixed width, one-dimensional (1D) structures in single well RTDs, wherein the carriers are confined in two dimensions, have been fabricated using i) a focused Gallium ion beam technique and ii) a novel etch technique [6, 7]. In these devices, transitions through the various sub-bands caused by the lateral confinement were observed. These transitions are manifested as a series of sub-peaks instead of a single large RT peak of a large area (2D) diode. The increased separation between the sub-peaks with decreasing width of the device corresponds to the stronger confinement and thus an increased separation between the sub-bands. Additional fine structure is observable in the sub-peaks in the case of the etched 1D structures and corresponds to the weaker lateral confinement in the emitter [8]. One should note that the length of these wire like structures was of the order 500 nm while the widths were between 200 and 75 nm. Also, in the case of the etched wire structures, while a varying magnetic field parallel to the direction of the current was used to confirm that the fine structure was caused by the lateral confinement, thermal broadening beyond 20K washes out this fine structure [8].

In this paper we shall demonstrate the ability to laterally confine electrons in vertical double well RT heterostructures using the self-aligned sidewall gating technique. In addition to room temperature pinch-off of the various RT peaks [9], clear 1D tunneling characteristics at temperatures as high as 77K is observed. All the devices presented herein were fabricated in a single run with a range of sub-micron minimum physical widths (0.9 μm to 0.5 μm) thus permitting observation of transformation of the tunneling characteristics from a 2D-RTD to a 1D-RTD [9].

The heterostructure grown on a semi-insulating substrate in a GEN II MBE system is shown in Fig 1. The asymmetric double wells are 180Å and a 100Å wide with a 60Å *AlGaAs* barrier in between. The two i-GaAs wells are separated from the top and bottom contact n-GaAs regions using a 35Å *AlGaAs* barrier and a 100Å undoped GaAs spacer layer. The access channels to the spacer layer from the n+ GaAs regions are graded to prevent breakdown of the gate Schottky barrier. The top-contact structure is a non-alloyed contact structure and uses the low-temperature grown GaAs (LTG:GaAs) capping technique [10]. Fabrication details of these devices are presented elsewhere [9].

II. CONDUCTION IN 1D STRUCTURES

The main energy levels ($E_z^{m,well}$) of the two wells due to the *Al_{0.3}Ga_{0.7}As* confinement in the vertical direction (z-axis) calculated using the SEQUAL simulator are shown in Fig. 1 [11]. As is well known, when a resonant energy level in each well lines up with the conduction band edge in the emitter a RT peak in conduc-

tance occurs. For example, with the bottom contact as emitter (Source) and the top contact as collector (Drain), the first resonance peak in the positive bias region occurs when levels 1 (lowest level in the 100 Å well) and 2' (second level in the 180 Å well) line up with the conduction band edge in the bottom contact. The inter-well potential differences at which any two resonant levels line up are; i) in the positive bias regime 18 meV (1-2'), 76 meV (2-4'), 84 meV (1-3') and 167 meV (1-4') and ii) in the negative bias regime 17 meV (3'-2'), 20 meV (1'-1), 81 meV (2'-2), 92 meV (4'-3) and 119 meV (1'-2). It is important to note that when two different sets of levels (e.g. 1-3' and 2-4') line up at almost the same inter-well potential difference the contribution to the tunneling current from the pair of higher resonances (2-4') is determined by the occupation of the higher level and goes down considerably at lower temperatures [12].

The relatively thick inter-well barrier (60 Å) causes the de-coupling of the states in the two wells and a large portion of the potential drop to occur across this barrier. If all tunneling is elastic, the effective widths of the resonances in such double well structures is a convolution of the resonance widths in each well and hence is expected to be sharper than in the case of single well RTDs [12]. This leads to higher peak to valley ratios with the valley current being weakly dependent on temperature [13, 14]. In an ideal double well structure the line-widths are of the order of 0.1 meV but the roughness introduced at the interfaces in MBE grown structures causes broadening of the intrinsic energy line-width in each well leading to eventual broadening of the measured resonant peak width.

In the case of the gated 1D structures, we approximate the potential along the width (y-axis) of the device at any given gate bias as a parabolic potential of the type $U(y) = m^* \omega_0^2 y^2 / 2$ where ω_0 is determined by the potential on the gate electrode. The energy levels for such a confining potential are then given as $E_y^{n,well} = (n + 1/2) \hbar \omega_0 / 2\pi$ for $n=0,1,2,3,\dots$ where \hbar is Planck's constant. The energies of the various sub-bands formed due to the confinement in both the z and y axis is then given as $E_{tot}^{m,n,well} = E_z^{m,well} + E_y^{n,well}$. The numbers "well" corresponds to the well number, "m" corresponds to the quantum number of the main resonance peak in a 2D-RTD and "n" corresponds to the quantum number of the sub-band caused by the confining potential along the y axis. If the gating in both quantum wells is identical, sub-bands of the main resonant levels that are formed near pinch-off due to the one-dimensional quantization would be identical (i.e. $E_y^{n,1} = E_y^{n,2}$). This would allow one to observe resonant tunneling through these sub-bands with maximum tunneling conductance (current) occurring when all sub-bands of one main resonant peak in one well align with the corresponding sub-bands of the main resonant peak in the other well [17, 8]. If the linewidths of the sub-bands are as sharp as that of the main levels (i.e. ≤ 0.1 meV), clear delineation of the interaction between the various sub-bands leading to the observance of corresponding sub-peaks should be possible. In addition, near extreme

pinch-off, one should be able to see quantization effects in the two access channels manifesting itself as fine structure in each sub-peak [8]. It has been demonstrated that the gating (confinement) in the access channels is weaker than in the wells in such sidewall gated structures [5, 9, 4]. It is important to note that variation in the confinement along the length of the device or in the two wells causes broadening of the effective linewidth of the energy levels in the wells. While for the devices presented in the following sections, we have used length of 10 μm or more to make sure that single electron charging effects are negligible, variation along the length of the device is expected and would result in broadening of the states in the well [8].

III. DEVICE CHARACTERISTICS

All measurements presented herein are made using a HP 4145 parameter analyzer and measurements at 77K are made by dipping the mounted device into a liquid nitrogen dewar. The fabricated devices had nominal minimum widths of 0.5, 0.7, 0.9 μm and lengths of 10, 20, 30, 40 μm . The variation in the minimum widths was to allow one to observe the transition in the conduction properties in these devices from that of a 2D-RTD characteristic to that of a 1D-RTD characteristic. The description of resonant tunneling characteristics in the following sections assumes the bottom contact as the emitter (Source) and the top-contact as the collector (Drain). All biases are relative to the source, which is grounded at all times. Further, the nomenclature for the various resonant peaks are: i) peak A corresponds to the first resonant peak in the negative bias region (1'-1); ii) peak B corresponds to the first resonant peak in the positive bias region (1-2') and iii) peak C corresponds to the second resonant peak in the positive bias region (1-3').

Fig 2 and Fig 3 show the measured DC characteristics at 77K of a $0.7 \times 30 \mu\text{m}$ device (Device I) in both the positive and negative bias regions for various gate biases. The I-V curves show clear indication of multiple sub-peaks in case of Peaks A and C. Fine structure in each of these multiple sub-peaks is seen especially in the case corresponding to Peak A (1'-1). As shown in the inset of Fig 2, no sub-peak formation is observed in the case of the RT Peak B (1-2'). The fine structure that is observed in the case of Peak B is similar to the fine structure observed in the sub-peaks of Peaks A and C. In addition the peak value of the RT current is much smaller in the case of Peak B than either Peak A or Peak C. Fig 5 is a plot of the dI/dV of the measured I-V and shows the presence of a series of conductance peaks similar to those observed in etched single well devices that have been studied earlier [15, 8]. The position of the first conductance peak moves further from zero bias with increasing negative gate bias. Also, the separation between the various conductance peaks shown in Fig 5 increases with increasing negative gate bias.

IV. DISCUSSION

In the study of triple barrier sub-micron quasi-zero-dimensional devices it has been noted that the peak current densities relating to tunneling between main levels in the two wells of different parity (i.e. odd to even parity) is much lower than in the case of tunneling between levels of similar parity (i.e. odd to odd or even to even) [16]. A similar reasoning is applied to explain the drastic reduction in RT currents with increasing negative gate bias in the case of Peak B when compared to Peaks A and C. Hence we shall compare the characteristics of the Peaks A and C to illustrate the observance of 1D quantization in these devices. As has been noted earlier in this paper, in the case of 1D structures one observes the RT current through sub-band mixing. Similar sub-peak formation can occur due to other inelastic processes like phonon assisted tunneling. In the case of the inelastic processes it has to be noted that the separation between the current sub-peaks has to be relatively independent of gate biases.

Fig 4 shows the position of the the first two RT current sub-peaks corresponding to Peaks A and C for Device I at various gate biases. Clear shift in the position of the first peak away from zero bias with increasing negative gate bias is observed. More importantly the separation between the first and the second sub-peak increases with increasing negative gate bias. Quantization along the y-axis due to the confining potential ($m^*\omega_y y^2/2$) causes the lowest sub-band in each well to be shifted by a value of $\hbar\omega_y/4\pi$. Assuming that the confinement in the emitter is independent of gate bias, the shift of the first current sub-peak is attributable to the fact that with increasing confinement an additional bias has to be applied between the emitter and the first well to line up the lowest sub-band of a main resonance in the well with the conduction band edge in the emitter. The same reasoning is used to explain the increased separation between the first and the second current sub-peak. Here the increased confinement causes a corresponding increase in the separation between two sub-bands of a main resonant level in the well. One thus needs to apply a higher bias to line up with the next higher sub-band of a main resonant level in the well.

To illustrate that the observed sub-peaks are due to 1D quantization in the wells, a simple picture using a parabolic potential for the conduction band edge, shown in Fig 6(a), is used. In this picture it is assumed that at the sidewall, the Schottky gate pins the surface of the GaAs well at midgap and that the potential in the middle of the well along the y-axis is controlled by the Fermi-level in the emitter regions. The parabolicity (ω_y) of the potential field $U(y)$ is now determined by: i) physical width of the mesa L_w ; ii) the potential difference in the conduction band edge between the center of the mesa and the sidewall and iii) the applied gate bias. The parabolicity is directly related to the energy separation between the sub-bands of the main resonance formed due to the lateral confinement along the y-axis. Fig 6(b) and Fig 6(c) shows the calculated values of the energy level separation ($\hbar\omega_y/2\pi$) for two different configurations. In Fig 6(b) the mesa widths are kept

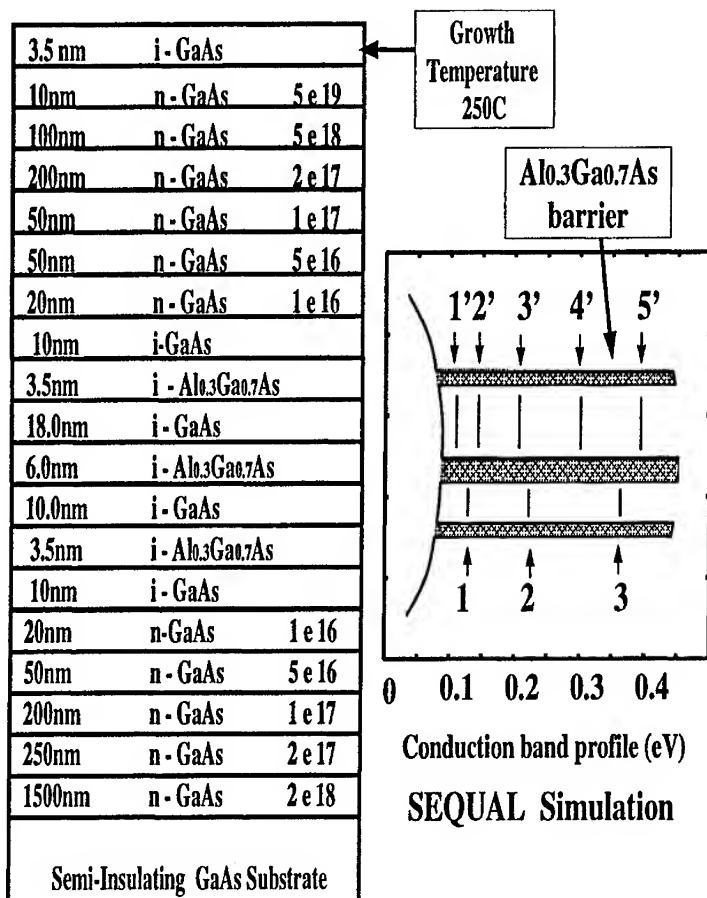
constant and the applied bias at the sidewall gate is changed while in the case of Fig 6(c) the mesa widths are modified and the gate voltages are kept constant. As shown, the separation between sub-bands is of the order of 2-10 meV in either case and the separation is more pronounced only at mesa widths around $0.5\ \mu\text{m}$. It is important to note that these values are much smaller than the LO phonon energy in GaAs ($\approx 36\text{meV}$) and the smallest separation between two energy levels in any well. The inter-well potential difference at which levels 1' and 1 line up (Peak A) is approximately 20 meV with the corresponding potential across the whole device being about 100 mV. If we assume that the ratio of the inter-well potential to the applied device bias is same for all biases, we can estimate the interwell potentials corresponding to the difference in position of the sub-peaks. In the case of Device I (Peak A), the separation of the current sub-peaks goes from 23 mV @ $V_g = +0.5\text{V}$ to 88mV @ $V_g = -1.0\text{V}$. This corresponds to inter-well potential differences of 4.6 meV @ $V_g = +0.5\text{V}$ and 17.6 meV @ $V_g = -1.0\text{V}$. The sub-peak separation energies are hence: i) much smaller than the LO phonon energy ii) much smaller than the energy difference between any two levels in a well and iii) larger than the thermal energy of the electrons ($k_B T \approx 6.6\text{meV}$). This change in the separation between the sub-peaks clearly demonstrates that the sub-peaks are not caused by inelastic tunneling mechanisms like phonon assisted tunneling but rather due to resonant tunneling through sub-band mixing of the main resonant levels in the two wells.

V. CONCLUSIONS

We have demonstrated the ability to fabricate vertical quasi- one- dimensional resonant tunneling devices that show clear 1-D quantization at temperatures as high as 77K. Fine structure corresponding to resonant tunneling through the various sub-bands formed in the well has been observed. Also since such strong quantization is observed in the study presented above, three terminal quasi- 0D structures using the same sidewall gating technique should make vertical Single Electron Transistors a possibility.

ACKNOWLEDGEMENT

We would like to thank Prof. S. Datta and Dr. G.L. Chen for motivating this work. We also acknowledge Prof. I. Adesida for providing the etching facilities. This work was supported in part by ARO, DARPA and NSF-MRSEC.



MBE grown structure

Figure 1: The asymmetric double well structure grown on a insulating GaAs substrate. Also shown is the band profile at zero applied bias for the structure calculated using the SEQUAL simulator. Peaks in the transmission probabilities corresponding to the various levels (1, 2, 3 and 1', 2', 3' 4', 5') in the two well are also shown.

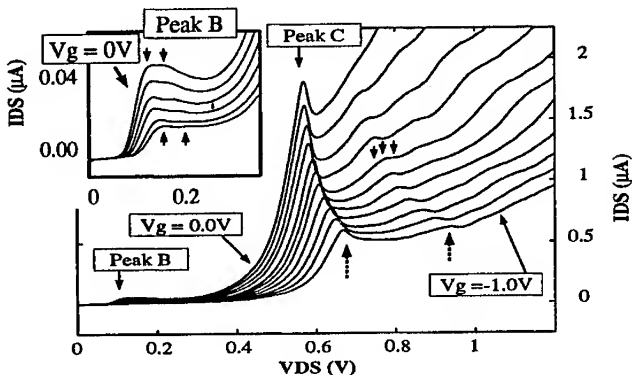


Figure 2: Measured DC characteristics at 77K for positive Drain-Source biases at gate biases 0 to -1.0 V stepped at -0.1V for Device I. Inset shows I-V characteristics of Peak B at gate voltages of 0, -0.1, -0.2, -0.3, -0.4 and -0.5 Volts. The small arrows indicate the fine structure in the sub-peaks. The dashed arrows indicate the position of the sub-peaks.

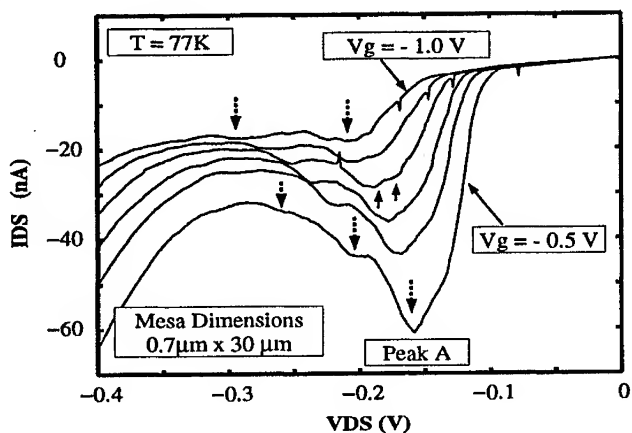


Figure 3: Measured DC characteristics showing the I-V curves around Peak A at gate biases -0.5 to -1.0 V stepped at -0.1V for Device I. The small arrows indicate the fine structure in the sub-peaks. The dashed arrows indicate the position of the sub-peaks.

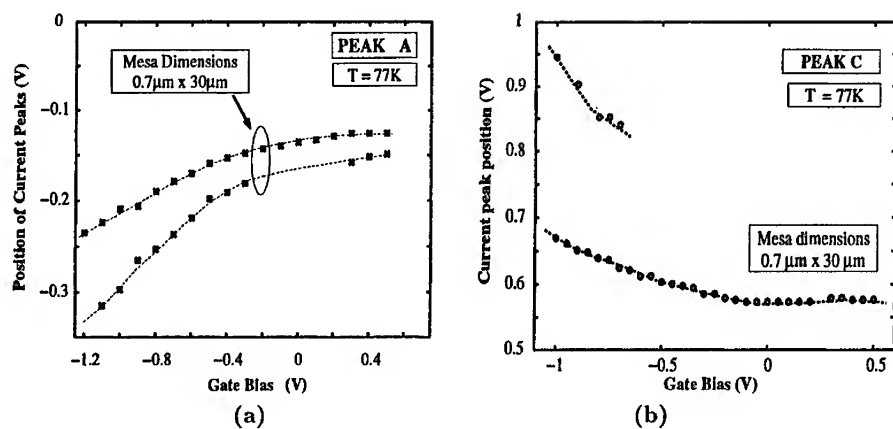


Figure 4: (a) Position of current maxima corresponding to the first and second sub-peak of Peak A. (b) Position of current maxima corresponding to the first and second sub-peak of Peak C. Dotted lines are drawn for visual reference.

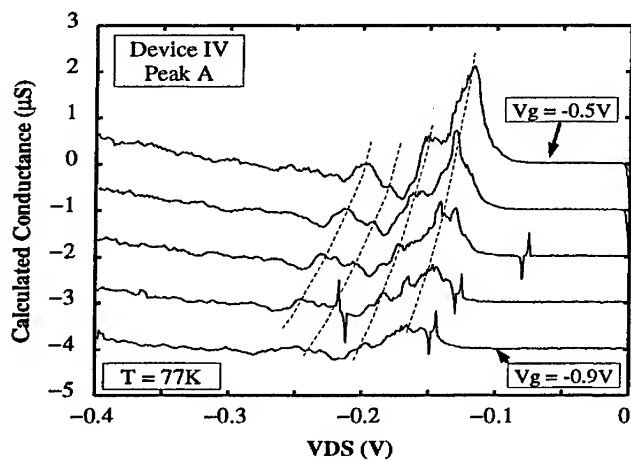


Figure 5: dI/dV curves of the measured DC I-Vs for gate biases of -0.5, -0.6, -0.7, -0.8, -0.9 Volts showing the presence of multiple conductance peaks. Dotted lines are shown for visual reference.

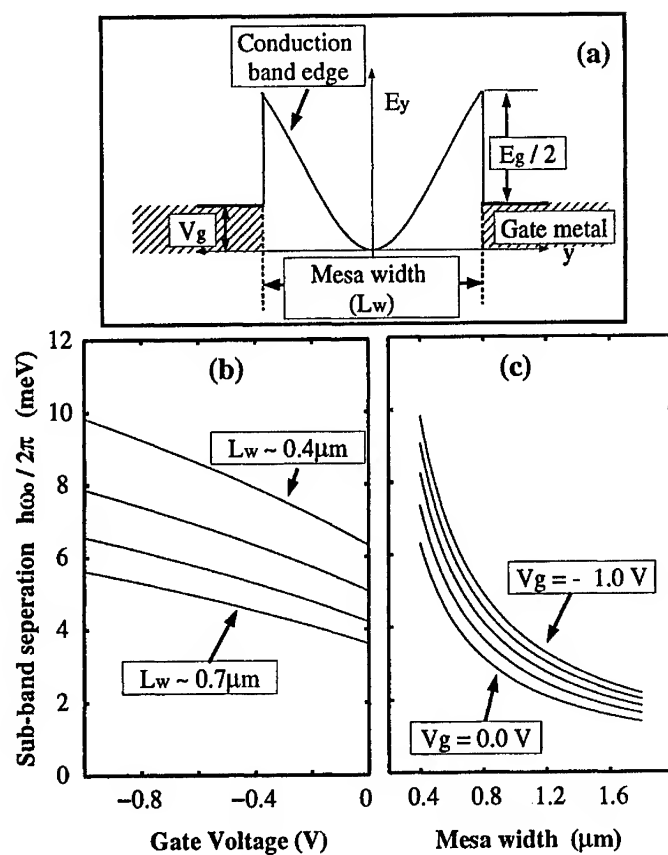


Figure 6: Plots of sub-band level separation of the main resonance band caused by the confinement in the y-axis. (a) shows the parabolic potential field used to model the confinement in along the y-axis. (b) plots the sub-band energy separation with changing sidewall gate bias for mesa widths of 0.4, 0.5, 0.6 and 0.7 μm . (c) plots the sub-band energy separation for varying mesa widths and at gate biases of 0, -0.25, -0.5, -0.75 and -1.0 Volts.

REFERENCES

- [1] E.R. Brown, C.D. Parker, A.R. Calawa, and M.J. Manfra. *Appl. Phys. Lett.*, 62(23):3016, 1993.
- [2] T. Way. PhD thesis, School of Electrical Engineering, PURDUE University, 1995.
- [3] V.R. Kolagunta, G. Chen, D.B. Janes, K.J. Webb, and M.R. Melloch. *Superlatt. and Microstruct.*, 17(4):339, 1995.
- [4] D.G. Austing, T. Honda, and S. Tarucha. *Semiconductor Technology*, 11:388-391, 1996.
- [5] V.R. Kolagunta, G. Chen, D.B. Janes, K.J. Webb, M.R. Melloch, and C. Youtsey. *Appl. Phys. Lett.*, 69(3):374, 1996.
- [6] S. Tarucha, Y. Hirayama, and Y. Tokura. *Superlatt. and Microstruct.*, 9(3):341, 1991.
- [7] P.H. Beton, J. Wang, N. Mori, L. Eaves, P.C. Main, T.J. Foster, and M. Henini. *Phys. Rev. Lett.*, 1995.
- [8] J. Wang, P.H. Beton, N. Mori, L. Eaves, H. Buhmann, L. Mansouri, P.C. Main, T.J. Foster, and M. Henini. *Phys. Rev. Lett.*, 73(8):1146, 1994.
- [9] V.R. Kolagunta, D.B. Janes, M.R. Melloch, and C. Youtsey. submitted to. *Appl. Phys. Lett.*
- [10] M.P. Patkar, T.P. Chin, J.M. Woodall, M.S. Lundstrom, and M.R. Melloch. *Appl. Phys. Lett.*, 66:1412, 1995.
- [11] M. McLennan. Master's thesis, School of Electrical Engineering, Purdue University, 1987.
- [12] T. Nakagawa, T. Fujita, Y. Matsumoto, T. Kojima, and K. Ohta. *Appl. Phys. Lett.*, 51(6):445-447, 1987.
- [13] D.A. Collins, D.H. Chow, D.Z.Y. Ting, E.T. Yu, J.R. Soderstrom, and T.C. McGill. *Solid-State Elect.*, 32(12):1095-1099, 1989.
- [14] T. Nakagawa, T. Fujita, Y. Matsumoto, T. Kojima, and K. Ohta. *Jap. J. Appl. Phys.*, 26(6):L980, June 1987.
- [15] J. Wang, P.H. Beton, N. Mori, H. Buhmann, L. Mansouri, L. Eaves, P.C. Main, T.J. Foster, and P. Henini. *Appl. Phys. Lett.*, 65(9):1124, 1994.

-
- [16] M. Tewordt, R.J.F. Hughes, L. Martin-Moreno, J.T. Nicholls, H. Asahi, M.J. Kelly, V.J. Law, D.A. Rithcie, J.E.F. Frost, G.A.C. Jones, and M. Pepper. *Phys. Rev. B*, 49(12):8071–8075, 1994.
- [17] N. Mori, P.H. Beton, J. Wang, and L. Eaves. *Phys. Rev. B*, 51(3):1735, 1995.

SCARRING EFFECTS IN OPEN QUANTUM DOTS

R. Akis and D. K. Ferry
Center for Solid State Electronics Research
Arizona State University, Tempe, AZ 85287

J. P. Bird
Frontier Research Program, RIKEN, 2-1 Hirosawa,
Wako, Saitama 351-01, Japan

ABSTRACT

Solving Schrödinger's equation on a discrete lattice, we have performed numerical simulations of open ballistic quantum dots of several different shapes, including squares, stadiums, triangles and variations thereof. We have found that *scarring* of the total wave function is present in these open dots, with this scarring effect corresponding to the enhancement of the wave function amplitude along the remnants of classical orbits. The calculated magneto-conductance fluctuations yield periodicities in excellent agreement with the experiments on stadium and square shaped dots. The scarring effects are also seen to be periodic, with periodicities that are in good correspondence with the fluctuations, thus providing support for the assertion that the transport is dominated by the orbits we observe.

I. INTRODUCTION

The electrical properties of mesoscopic devices are well known to be influenced by electron interference [1]. In disordered systems, electronic motion is diffusive and a significant understanding of the processes affecting the interference has already been achieved. Recent advances in semiconductor micro-processing technology now enable the fabrication of sub-micron scale quantum dots, in which electronic motion is predominantly ballistic [2-4]. While precise details such as dot shape differ between experiments, the devices usually consist of some central scattering region, patterned on a length scale smaller than the elastic mean free path, and connected to source and drain reservoirs via tunable quantum point contact leads. Large angle scattering of electrons is restricted to the boundaries of these devices and, until recently, relatively little was known about the details of electron interference within them.

Recent experiments on nominally square and stadium shaped dots suggest however, that their electrical properties are dominated by a characteristic *periodicity* in their magnetoconductance. These in turn yield strong peaks at just a few discrete frequencies in the Fourier power spectrum of the fluctuations [2,4]. In an earlier study, it was tentatively suggested that this periodicity arises from the remnants of regular, semi-classical orbits within the dots [2]. In order to investigate this effect, we have modeled ballistic quantum dots of varying shapes, by solving the quantum mechanical problem on a discrete lattice using an iterative matrix method that is a numerically stabilized variant of the transfer matrix approach [5]. The details of this method are summarized in the next section. The section following that presents our theoretical results as well as a comparison with experiments. Simulating dots of comparable size, we are able to reproduce the periodicity of the fluctuations found experimentally. Moreover, reconstructing the quantum probability density inside the dots, we find that the wave functions of these open structures can in fact be heavily scarred by periodic orbits, with certain scars recurring periodically in magnetic field, in good correspondence with selected peaks in the power spectra. Based on comparisons with closed dots as well as with *classical* simulations, we argue that these results are in large part due to the collimation effect of the quantum point contacts, which define the entrance and exit ports of the cavities. Importantly, since they support very few modes, the electrons enter the dot at an angle due to waveguiding effects. The paper concludes with a summary.

II. METHOD OF CALCULATION

For our simulations, the general situation is one in which ideal quantum wires, which extend outward to $\pm\infty$, are connected to a quantum dot by entry and exit ports that support a small number of propagating modes. A schematic picture of a square dot is displayed in Fig. 1. This quantum mechanical problem can be solved by using an iterative matrix method [5] applied to the discretized version of the Schrödinger equation, obtained by keeping terms up to first order in the approximation of the derivative:

$$(E_F - \mathbf{H}_j)\psi_j + \mathbf{H}_{j,j-1}\psi_{j-1} + \mathbf{H}_{j,j+1}\psi_{j+1} = 0 \quad (1)$$

where ψ_j is a M -dimensional vector containing the amplitudes of the j th slice. The problem is solved on a square lattice of lattice constant a with the wires extending M lattice sites across in the y direction and the region of interest being broken down into a series of slices along the x direction. In this equation, the \mathbf{H}_j matrices represent Hamiltonians for individual slices and the matrices $\mathbf{H}_{j,j-1}$ and $\mathbf{H}_{j,j+1}$ give the inter-slice coupling. By approximating the derivative, the kinetic energy terms of Schrödinger's equation get mapped onto a tight-binding model with $t = -\hbar^2/2m^*a^2$ representing nearest neighbor hopping. The confining potential simply adds to the on site energies. The places where the confining potential is high are indicated by the blackened regions in the figure.

Assuming electron waves are only incident from the left, equation (1) can be used to derive a transfer matrix which allows us to translate across the system and thus

calculate the transmission coefficients which enter the Landauer-Büttiker formula to give the conductance. Transfer matrices however are notoriously unstable due to the exponentially growing and decaying contributions of evanescent modes. This difficulty can be overcome by performing some clever matrix manipulations and calculating the transmission by an iterative procedure rather than just multiplying transfer matrices together. The full details of this technique are given in ref. [5]. This method in some ways is quite similar to the recursive Green's function techniques [6,7] that typically are used to solve these problems, and a comparison has shown good agreement between the two methods [5]. However the iterative matrix method is simpler both conceptually and in its implementation. The amplitudes of the wave functions at specific values of x and y can be found easily by backward substitution after the iteration is performed.

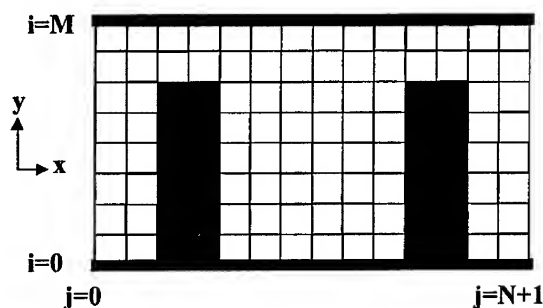


Fig. 1. The geometry of a square quantum dot, and quantum point contacts, that are considered in this study. The grid represents the underlying mesh on which the calculations are performed, though in practice the mesh is much finer.

III. THEORETICAL RESULTS

We begin by presenting an illustrative example of our calculations. In Fig. 2, we show the results of the conductance fluctuations for a $0.3 \mu\text{m}$ square dot with $0.04 \mu\text{m}$ port openings, which allow two modes to enter and exit the dot. The magnetic field is applied normal to the plane of the dot, and the carrier density is taken to be $4 \times 10^{11} \text{ cm}^{-2}$ in order to compare with the experiments of ref. [4]. These fluctuations are obtained after subtracting out an average background conductance [4]. Instead of a random aperiodic variation with magnetic field, a series of quasi-periodic oscillations is evident (these are more clear if the resonances are subtracted out). Also apparent are several resonance features. In particular, we point out a set of resonances at $B \sim 0.069, 0.173, 0.283$, and 0.397 T (while the feature is difficult to see at $B = 0.173 \text{ T}$, it appears as a small "glitch" in the curve). These are marked with arrows. Note here that these features occur with

virtually periodic spacing ($\Delta B \sim 0.11$ T). The wave functions corresponding to these four resonances are also displayed at the bottom of the figure.

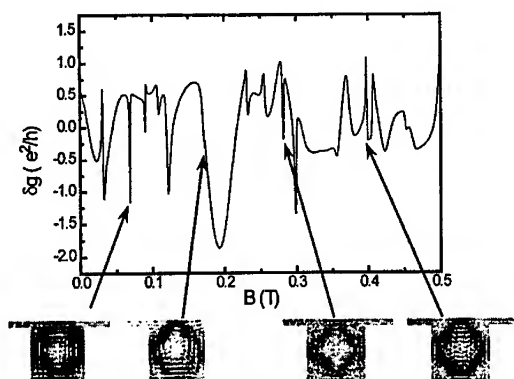


Fig. 2. The conductance fluctuations vs. magnetic field for the $0.3 \mu\text{m}$ dot discussed in the text. Four resonance features that appear in the curve are also indicated, and $|\psi(x,y)|$ vs. x and y in the quantum dot plotted for each of these features. Darker shading corresponds to higher amplitude.

What is shown in each case is $|\psi(x,y)|$, with the darker shading corresponding to higher wave function amplitude. Strikingly, essentially the same diamond-shaped pattern occurs in each case. This pattern is highly reminiscent of the "scars" that have been observed in calculations performed for *closed*, classically chaotic cavity structures [8,9] (in particular the stadium), in that the quantum mechanical amplitude appears to follow a single underlying classical orbit. However, unlike the stadium, our structure is ostensibly regular. The fact that there appears to be a correspondence to the classical picture is not as much of a surprise since the wave functions should be concentrated along the projections of the invariant tori of the regular trajectories in classical phase space. However, it is worth pointing out that this result *differs radically* from what one expects in a *closed* dot, in which the amplitude for the eigenstates tends to be distributed much more uniformly and one *can not* make an association with a single orbit. To emphasize this point, in Fig. 3(a), we plot $|\psi(x,y)|$ for a $0.3 \mu\text{m}$ dot formed by two tunneling barriers, with the barrier height equal to the Fermi energy of the previous example and a barrier width of $0.05 \mu\text{m}$. The conductance as a function of B for this case consists of a series of very sharp tunneling peaks, so the dot is a very close approximation to a closed system. The wave function in this image corresponds to a resonant tunneling peak at $B = 0.165$ T, and is a

fairly typical result. Comparing (a) with the wave functions displayed in Fig. 2, it is clear that the results are quite different.

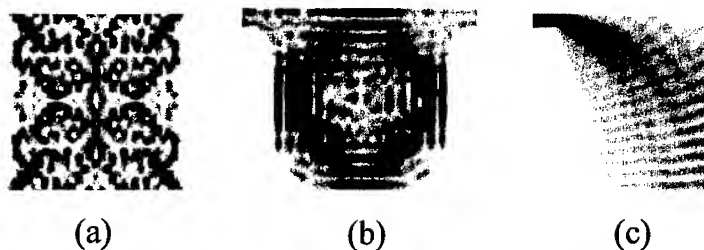


Fig. 3. $|\psi(x,y)|$ vs. x and y is plotted. Darker shading corresponds to higher amplitude. The three pictures correspond to: (a) a square dot completely enclosed by tunneling barriers, (b) a rounded dot still showing the diamond "scar", and (c) a collimated beam exiting a quantum point contact.

In Fig. 3(b), $|\psi(x,y)|$ is plotted for $B = 0.282$ T, but in the case of a rounded dot. Here, the bottom corners of the dot are of the form of quarter-circles of radius $0.1 \mu\text{m}$, while the entry ports are also rounded with radius $0.05 \mu\text{m}$, though the narrowest width of the opening is the same as in the original example. We see that rounding does not prevent the diamond "scar" from forming. This result is reassuring, since one does not expect the experimental dots to be perfectly square in shape. Generally, we find that the presence of some rounding by itself does not destroy the resonance effects (in fact, some of the resonances are even stronger in this case), nor does it strongly affect the basic underlying periodicity. Eventually of course, if the rounding is increased, the scarring patterns are disrupted. Importantly, if the dot shape is held fixed while the rounding of the leads is increased, one finds the diamond patterns will simply shift in magnetic field. On the other hand, rounding of the bottom corners yields a more fundamental effect, with the diamond pattern disappearing completely when the bottom is almost semicircular. The differences between a closed dot with tunneling barriers and our open dots and our results with rounding of the leads can be understood in part by considering the effect produced by the quantum point contact. In Fig. 3(c), we show an isolated point contact of the same width as those connected to the quantum dots in the previous examples. As is apparent, this quantum point contact effectively collimates the electron waves into a relatively narrow *beam*. What we are seeing here is the result of the waveguiding effects of the contact. With very few modes present in the leads (in this case two), the entry angle of the electrons becomes strongly restricted by the *quantization* of the wave-vectors in the y -direction. It should be emphasized that this picture corresponds to the zero field case. Thus, the rotation of the electron beam away from the x -axis can not be attributed to the

bending of the electron trajectories by the magnetic field. It is this collimation that is important for selecting or exciting the regular orbits of the electrons. This explains the difference between the open and closed dot cases, as well as the shifting in magnetic field of the scarring pattern when making changes to the leads such as rounding. In the latter case, one is simply changing the aim of the collimated beam.

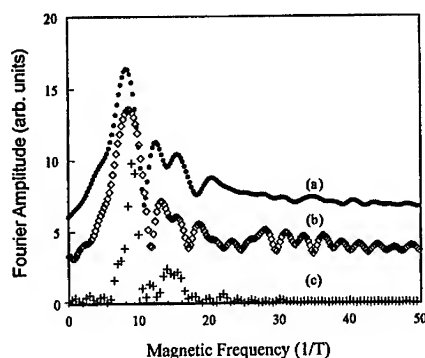


Fig. 4. a comparison of the Fourier spectra of the conductance fluctuations for an experimental dot (a), the quantum simulation (b), and a classical simulation with collimation (c), all for an effective dot size of $0.3 \mu\text{m}$. The curves are offset for clarity.

The periodicities evident in the conductance fluctuations such as those shown in Fig. 2 can be quantified by looking at the Fourier spectrum, which is shown in Fig. 4 (a). In addition to the result from the quantum mechanical simulation, which is curve (b), are results obtained from an analysis of experimental data [4], curve (a) in the figure. The experiments in question were carried out at a temperature of 10 mK with a split-gate quantum dot fabricated in GaAs/AlGaAs heterojunction formed using standard lithographic techniques. After low temperature illumination, the carrier density and mobility were found to be $5.1 \times 10^{11} \text{ cm}^{-2}$ and $70 \text{ m}^2/\text{Vs}$, respectively. The effective dot size, after accounting for depletion, was found to be approximately $0.3 \mu\text{m}$. It is clear that the transport is dominated by probably a single, or a very few, orbits, and the agreement between the two curves is remarkable. Equally remarkable is the agreement with curve (c), which is the result of a purely *classical* calculation. This curve is the Fourier transform of a correlation function based on the quantity, $2T-1$, T being the fraction of classical electrons that exit out the right port, a quantity which removes most of the background average conductance and highlights the fluctuations. In order to achieve this agreement, two restrictions are *absolutely necessary* for the classical calculations: 1) the electron beam *must be collimated*, which is done by fixing the size of the port openings (in this case $0.05 \mu\text{m}$), and, equally important, 2) the beam must enter

at an *angle* (here $\theta = -67$ degrees, measured with respect to the x -axis). This result underlines the importance of beam collimation. Finally, we note that the peak at 9 T^{-1} that occurs in these Fourier spectra correlates well with the periodicity of the diamond shaped scar-like features, which had a period of $\Delta B \sim 0.11 \text{ T}$. Thus, it appears we can make a firm correspondence between a Fourier peak and a particular periodic orbit in this case.

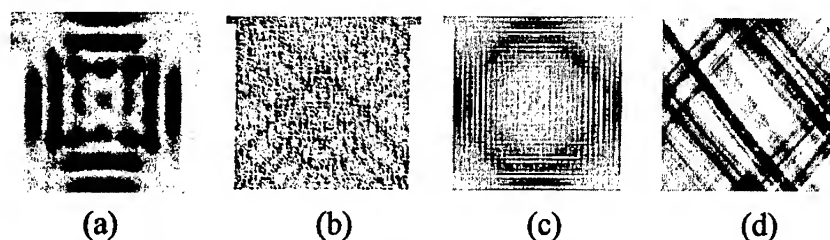


Fig. 5. $|\psi(x,y)|$ vs. x and y is plotted, with darker shading corresponding to higher amplitude, for (a) a $0.15 \mu\text{m}$ dot at $B=1.02 \text{ T}$, (b) a $0.8 \mu\text{m}$ dot at $B=0.0156 \text{ T}$ and (c) a $0.8 \mu\text{m}$ dot at $B=0.002 \text{ T}$. In panel (d), the classical electron distribution vs. x and y for an entry angle of 36 degrees, a port opening of $0.03 \mu\text{m}$ and $B = 0.025 \text{ T}$. Darker shading corresponds to higher electron concentration.

For a $0.3 \mu\text{m}$ dot, we found that diamond-shaped orbit was the most prominent (although it must be mentioned that several other orbits were found in that case [10]). Now we consider the effect of size. In Fig. 5(a), we plot $|\psi(x,y)|$ vs. x and y for a dot $0.15 \mu\text{m}$ square, a quarter of the area of the dot studied previously, at $B=1.02 \text{ T}$. Though much less well resolved than in Fig. 2 and Fig. 3(b), the wave function here shows an example of a diamond-shaped scar. The lack of resolution is due to the comparatively large value that the Fermi wavelength has in comparison to the dot size in this case. As in the case of the larger dot, the diamond features recur periodically, with a similar wave function occurring at $B=1.24 \text{ T}$. This yields a periodicity of $\Delta B=0.22 \text{ T}$, which happens to be exactly *twice* that observed in the larger dot. This indicates that the period is determined by the *length* of the periodic orbit. Thus, $1/\Delta B$ follows $A^{1/2}$, A being the area of the dot. This is consistent with the *experimental* observation [11], made by comparing dots of four different sizes, that the position of the fundamental peak in the Fourier spectrum follows $A^{1/2}$.

As the dot size is reduced below $0.15 \mu\text{m}$, the diamond shape fails to be resolved (although precursors are evident). Contrasting, as the dot is made larger, the diamond-shaped scar remains, but progressively more complicated orbits also start appearing in the wave functions. Correspondingly, the Fourier spectrum shows more peaks indicating

additional periodicities are appearing in the conductance fluctuations (observed both in the experiments and in the simulations). However, as the situation becomes more complicated, the periodic scarring effects tend to become weaker, and it becomes more difficult to see a scar reoccur. An example of a much more complicated (and fainter) scar is shown in Fig. 5(b). The parameters used here are the same as in the previous example, except that the dot is now much larger, $0.8 \mu\text{m}$, and $B=0.0156 \text{ T}$. The diamond pattern in this case appears at a very low magnetic field, $B=0.002 \text{ T}$, and is shown in Fig. 5(c). What is interesting here is that the diamond pattern actually looks like it is composed of several diamonds, slightly out of phase with each other. An easy way of understanding this is that, since the electrons here eventually must exit from one lead or the other, the electrons cannot be retracing exactly the same orbit as they go around the dot. The electrons enter the dot and traverse the diamond orbit. However, each orbit is slightly different from the previous one, so that eventually the electrons "kick" themselves out of the pattern and subsequently leave the dot. In this regard, it should be noted that calculations in which phase breaking was introduced into the dots indicated that phase coherence must be maintained over many orbits (of the order of 40 for the $0.3 \mu\text{m}$ dot) in order for the scar to appear [12]. Thus the electrons must spend a considerable amount of time in the dot. For comparison, Fig. 5(d) shows a distribution of *classical* electrons within a square cavity. For this simulation, we have injected 2000 electrons into the cavity, each made to obey Newton's laws. To generate the picture, the cavity was broken down into a 100×100 grid, and we have counted the number of times an electron passes through a grid element, the darker shading corresponding to higher counts. As in the classical results of Fig. 4, the electrons enter the cavity in an angled, collimated beam from the left and the field is 0.025 T . This classical distribution bears a strong resemblance to the "fuzzy" diamond pattern evident in the preceding wave-function plot and is consistent with our assertion that the electrons take "quasi-periodic" paths around the dot.

Thus far, we have concentrated on nominally square dots. The correspondence between periodicities in the conductance and scarring effects was first suggested as a possibility in the context of stadium shaped quantum dots by Marcus *et al.* [2]. Provided an ensemble average was not performed, they found that a Fourier analysis of their conductance fluctuations revealed the presence of strong peaks at a few discrete frequencies. The stadium is of particular interest, since its closed, classical analog is well known to be chaotic. As such, one might expect the behavior to reflect ergodicity, or phase space filling. Such behavior is only recovered after ensemble averaging over many conductance traces (each obtained by altering the gate voltage). Importantly, such averaging has the effect of returning the dot, and its point contact leads, to the classical regime, since the quantization is averaged out, and the proper quantum behavior is masked.

The results of such an analysis are shown in Fig. 5(a) as curve (a), taken from ref. [2]. In the inset is a micrograph of the actual dot on which the experiments were

performed. As shown, the input and output leads were at right angles to each other. The dot size was approximately $0.4 \times 1.0 \mu\text{m}$ and the electron density was $3.6 \times 10^{11} \text{ cm}^{-2}$. Curve (b) is the Fourier power spectrum obtained from a simulation of a similar sized dot (after accounting for depletion). Both the experiment and the simulation show strikingly similar harmonic content, with well defined peaks at $f \sim 20, 33$ and 65 T^{-1} in both cases. For the simulation, four modes were allowed to propagate in the leads. Making minor structural alterations (eg. narrowing the leads), we find that the relative weighting of the peaks can be significantly altered but that their *positions* are quite stable. This is consistent with the experimental results, which showed the peak positions remaining essential fixed, but reweighted, when gate voltage was changed [2]. In addition to the periodicity, we have also found evidence of scarring in our simulations of the stadium. Fig. 5(b) shows a representative example, a "bow-tie" scar, apparent at $B=0.229 \text{ T}$, which is strikingly similar to a scar observed in the *closed* stadium (see Fig. 2 of ref. [9]). Unfortunately, it is difficult to establish a specific period to the scars we see in this example, and thus establish a connection with a particular power spectrum peak, since similar looking scars can be resolved only at a very few other values of field.

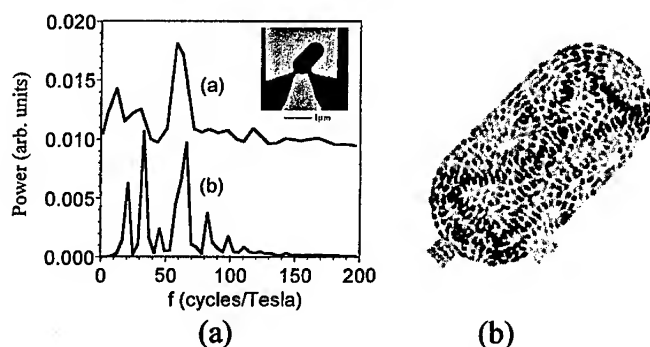


Fig. 5. In panel (a), the Fourier power spectrum of the conductance fluctuations is plotted. The curve labeled (a) is for the experimental stadium dot shown in the inset (from ref. [2], with permission). Curve (b) is the result of the quantum simulation. Panel (b) show a "bow-tie" scar that appears in this configuration for the stadium.

Fig. 6 shows a stadium example in which the correspondence between a specific power spectrum peak and scarring is particularly strong. This stadium has centrally *aligned* leads, dimensions of $0.4 \mu\text{m} \times 0.8 \mu\text{m}$ and an electron density of $4 \times 10^{11} \text{ cm}^{-2}$. Here we plot the conductance fluctuations for this configuration and the corresponding

power spectrum is shown in the left inset. A single peak at 47 T^{-1} clearly dominates. The corresponding magnetic field period is 0.021 T , in good agreement with the spacings between successive minima in the fluctuations. The solid circles correspond to values of B where a "whispering-gallery" scar was observed in the wave function, an example of which is shown in the left inset, where $|\psi(x,y)|$ vs. x and y is plotted for $B=0.288 \text{ T}$. This orbit is excited by an angled beam coming out of the left contact [13] and should not be confused with the "skipping" orbits one associates with edge states (those occur at significantly higher fields for the parameters we have chosen). These scars appear at very nearly periodic intervals, with the period also being 0.021 T , though one period is missed (a scar is expected at $B \sim 0.26 \text{ T}$). As with the diamond patterns shown in Fig. 2, the wave functions at the indicated points are very similar, but not precisely identical. A phase breaking analysis in this case indicates that the electrons make several trips around the dot before exiting to form each scar [13], consistent with the earlier results for the square dot. It is possible that the closely related scars we have found may be classified as "cousins", to borrow a term of Heller *et al.* [14]. They made the observation for closed stadiums that there is a difficulty in making a correspondence between a scarred wave function and a *specific* orbit. Each simple orbit has a large number of similar but more complex "cousins", consisting of progressively more bounces, only matching up with themselves after several trips around the stadium.

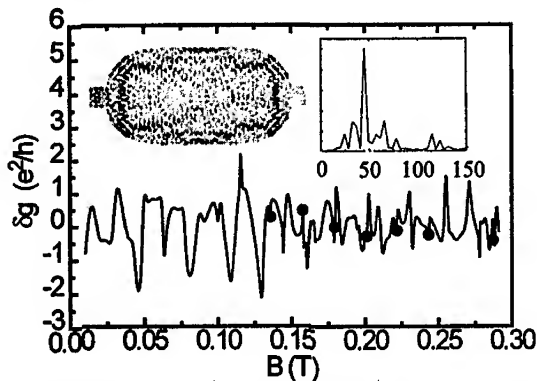


Fig. 6. Conductance fluctuations, δg , are plotted as a function of magnetic field for a stadium quantum dot with aligned leads. The right inset shows the corresponding power spectrum. The left inset shows a "whispering gallery" scar that recurs at the points indicated by the solid dots.

We have seen many other scars [12] familiar from the literature on stadiums [8,9,14] (for example, "the bouncing ball"). Some scars do recur, while many others do

not. When there is recurrence, typically it is not easy to assign a periodicity (if it in fact exists) since the scars do not recur with the same intensity each time and some periods are apparently missed. In this regard, we note that the energy levels are broadened in *open* dots, so there is a question of whether the scars correspond to eigenstates of particular energy levels, or averages over broadened and overlapping levels. It is difficult to answer this question conclusively. It is possible that some levels are still being resolved since the level spacing is not even and indeed all the scars shown here correspond to points in the conductance where there was some sharp resonance feature. Thus, the missing of periods may be due to uneven broadening effects, which smear some resonances but not others. That being said, we have found that narrowing the leads and, thus, reducing the expected broadening, does not necessarily give sharper scars. We also point out that while, for example, the scarred stadium wave functions plotted by Heller *et al.* [14] do correspond to individual eigenstates, Bogomolny [15] has shown that scarring can be a property of *energy averaged* wave functions.

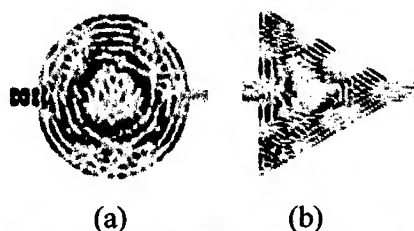


Fig. 7. Scarring effects in other shapes- (a) a triangular "scar" in a circular dot and (b), a skipping orbit in a triangular quantum dot.

Finally, we conclude by showing some examples of what can occur in other quantum dot shapes. Fig. 7 (a) shows a triangular "scar" that occurs in a circular dot of radius $0.3 \mu\text{m}$. Here the carrier density is $4 \times 10^{11} \text{ cm}^{-2}$, $B=0.2 \text{ T}$, and two modes propagate in the leads. What is interesting here is that can trace the origin of the orbit to the downward pointing collimated beam exiting the left lead. In Fig. 7 (b), the wave function reveals a "skipping" orbit in an equilateral triangular dot of dimension $0.45 \mu\text{m}$, density $2 \times 10^{11} \text{ cm}^{-2}$ and $B=0.78 \text{ T}$. Experiments have been performed such triangular structures [16], and these show prominent peaks in the *resistance*. Using a classical analysis, these peaks have been attributed to commensurate skipping orbits that fit in the structure in such a way that they manage to exit out of the entrance lead [16]. Fig. 7 (b) looks not unlike one of the orbits that was used in this analysis, but there is a clear difference- the orbit revealed by the wave function clearly *misses* the left lead. Thus, this feature shares a property of the other wave functions we have plotted here, that being that

the electrons must make several circuits around the dot before the underlying classical orbit becomes resolved.

IV. SUMMARY

We have performed numerical simulations of the magnetoconductance and corresponding wave functions of open ballistic quantum dots using several different shapes. Not only do we see clear evidence of scarring in these open structures, but a close association can be made with the certain scars and peaks in the Fourier spectrum of the conductance fluctuations. Our results are in good agreement with the experiments performed on square and stadium shaped dots.

ACKNOWLEDGEMENT

This work was supported in part by the Office of Naval Research and the Advanced Research Projects Agency. We thank Charles Marcus for the use of his data and figure.

REFERENCES

- [1] For a review see, S Washburn and RA Webb, *Adv. Phys.* **35**, 375 (1986).
- [2] C. M. Marcus, A. J. Rimberg, R. M. Westervelt, P. F. Hopkins, and A. C. Gossard, *Phys. Rev. Lett.* **69**, 506 (1992); C. M. Marcus, R. M. Westervelt, P. F. Hopkins, and A. C. Gossard, *Chaos* **3**, 643 (1993).
- [3] J. P. Bird, K. Ishibashi, Y. Aoyagi, T. Sugano, and Y. Ochiai, *Phys. Rev. B* **50**, 18678, (1994); J. P. Bird, K. Ishibashi, D.K. Ferry, Y. Ochiai, Y. Aoyagi, and T. Sugano, *Phys. Rev. B* **51**, 18037 (1995).
- [4] J. P. Bird, D. K. Ferry, R. Akis, Y. Ochiai, K. Ishibashi, Y. Aoyagi, and T. Sugano, *Europhys. Lett.* **35**, 529 (1996).
- [5] T. Usuki, M. Saito, M. Takatsu, R. A. Keihl, and N. Yokoyama, *Phys. Rev. B* **52**, 8244, (1995).
- [6] T. Ando, *Phys. Rev. B* **44**, 8017 (1991).
- [7] H. U. Baranger, D. P. Vincenzo, R. A. Jalabert, A. D. Stone, *Phys. Rev. B*, **44**, 10637, (1991).
- [8] E. J. Heller, *Phys. Rev. Lett.* **53**, 1515 (1984).
- [9] E. J. Heller, and S. Tomsovic, *Physics Today* **46**, (7), 38 (1993).
- [10] R. Akis, D.K. Ferry, and J.P. Bird, *Phys. Rev. B* **54**, 17705 (1996).
- [11] J.P. Bird, R. Akis, D. K. Ferry, Y. Aoyagi, and T. Sugano, *J. Phys. Cond. Matt.*, *in press*.
- [12] R. Akis, J.P. Bird, and D.K. Ferry, *J. Phys. Cond. Matt.* **8**, L667, (1996).
- [13] R. Akis, D.K. Ferry, and J.P. Bird, *to be published*.
- [14] E. J. Heller, P. W. O' Connor, and J. Gehlen, *Physica Scripta* **40**, 354 (1989).
- [15] E. B. Bogolmolny, *Physica D* **31**, 169 (1988).
- [16] H. Linke, L. Christensson, P. Omling, and P. E. Lindelof, *Phys. Rev. B*, *in press*.

AUTHOR INDEX

Aigouy, L., 146	Henderson, D.O., 100
Akis, R., 474	Hieke, K., 221
Akisuka, J., 65	Hirschman, K.D., 134
Allen, L.H., 59	Holden, T., 146
Austing, G., 366	Inoue, K., 366
Avrutsky, I., 402	Janes, D.B., 462
Balandin, A., 242, 388	Ji, Z.-L., 231
Bandyopadhyay, S., 242, 388	Jorne, J., 298
Bellani, V., 269	Kahn, S.U.M., 65
Bennet, B.R., 432	Kamada, H., 155
Bimberg, D., 146, 366	Kelley, D.F., 16
Bird, J.P., 474	Kenyon, A., 304
Boilot, J.P., 35	Kim, E.S., 417
Bovin, J.-O., 79	Kofman, R., 269
Braun, P.V., 3	Kohlert, P., 134
Cahay, M.M., 444	Kolagunta, V.R., 462
Chaim, R., 331	Kop'ev, P.S., 146
Chen, J., 100	Kubiak, C.P., 211
Cheyssac, P., 269	Kumar, T., 444
Christen, J., 366	Labbe, H.J., 155
Counio, G., 35	Lai, S.L., 59
Datta, S., 211	Lakshmi, B.B., 47
Deppert, K., 79	Leburton, J.P., 165
Ding, J., 341	Ledentsov, N.N., 146
Dneprovskaya, T., 353	Li, L.S., 3
Dneprovskii, V., 353	Li, Xi, 100
Dutttagupta, S.P., 134	Lifshitz, E., 331
Farias, G.A., 185, 197	Lockwood, D.J., 134, 155
Fauchet, P.M., 134, 287	Lofgren, C., 341
Ferry, D.K., 474	Magnusson, M.H., 79
Filios, A., 341	Maehashi, K., 366
Fischer, P., 366	Malm, J.-O., 79
Folman, M., 331	Malone, C., 298
Freire, V.N., 185, 197	Martin, C.R., 47
Fukatsu, S., 417	McCaffrey, J., 134
Gacoin, T., 35	Melloch, M.R., 462
Goronkin, H., 425	Morais, J., 341
Grundmann, M., 366	Morisaki, H., 177
Gu, Z., 100	Moskovits, M., 402
Hawrylak, P., 117, 155	Mu, R., 100

Nagaraaja,S.,165	Trwoga,P.,304
Nakashima,H.,366	Tsybeskov,L.,134
Nozaki,S.,177	Tsu,R.,341
Osenar,P.,3	Tsui,R.,425
Palm,T.,221	Tung,Y.S.,100
Parsapour,F.,16	Ueda,A.,100
Peeters,F.M.,378	Usami,N.,417
Persans,P.D.,319	Ustinov,V.M.,146
Pickup,P.G.,28	Vasilopoulos,P.,255,378
Pitt,C.W.,304	Wang,C.G.,341
Pollak,F.H.,146	Wang,J.,432
Potemski,M.,155	Weman,H.,155
Pralle,M.U.,3	Wesström,J.-O.J.,221
Qi,Z.,28	White,C.W.,100
Roenker,K.,444	Wilcoxon,J.,16
Routkevitch,D.,402	Wilson,R.A.,432
Samuelson,L.,79	Wu.M.,100
Sato,S.,177	Xu,J.,402
Schmidt,M.,287	Xu,W.,255,378
Shi,J.-M.,185,197	Yutani,A.,417
Shiralagi,K.,425	Yang,C.H.,432
Shiraki,Y.,417	Yang,M.,J.,432
Sirota,M.,331	Youtsey,C.,462
Sprung,D.W.L.,231	Zacharias,M.,134,287
Stalnacke,B.,221	Zhang,C.,255,378
Stella,A.,269	Zhang,Qi,341
Stokes,E.B.,319	Zhu,J.G.,100
Stolz,B.,221	Zhukov,E.,353
Stone,D.R.,432	Zuhr,R.,100
Stupp,S.L.,3	
Sunamura,H.,417	
Svensson,C.,79	
Svizhenko,A.,388	
Takeuchi,M.,366	
Tamamura,T.,155	
Temmyo,J.,155	
Tew,G.,3	
Thean,V.Y.A.,165	
Tian,W.,211	
Tognini,P.,269	

SUBJECT INDEX

abrupt heterojunction,444
 aerotaxy method,79
 anatase,47
 bandgap shrinkage,357
 blue luminescence,287
 blue shift,331
 capacitance spectroscopy,117
 carrier capture,366
 cathodoluminescence,366
Cd_{1-x}Mn_xS nanoparticles,35
CdS nanocrystallites,35
CdS nanowire arrays,402
CdS_{0.5}Se_{0.5} nanocrystallites,319
 chrysotile asbestos nanotube,353
 cluster-beam evaporation,177
 conducting polymers,28
 confined magneto-polariton,242
 coupled quantum dots,146
 defect luminescence,309
 delta-doped nanostructures,165
 dielectric confinement,353
 dielectric susceptibility,388
 differential scanning calorimetry,59
 dopant disorder,165
 dynamic Burnstein-Moss effect,353
 electrodeposition,402
 electroluminescence,313
 electron-electron interaction,117,155
 electron-hole pairs,319
 electron-hole recombination,331
 electron interference,474
 electroreflectance,146
 emitter-base junction,444
 emitter efficiency,444
 exciton,353
 exciton-exciton interaction,117
 exciton-polariton resonance,242
 far-infrared radiation,378
 flat-band potential,65
 fractional charge state,211
 frequency conversion,388
 Friedel sum rule,211
Ga nanoparticles,269
GaAs quantum well,366
 gated dots,117
 gas source MBE,417
Ge and *GeO₂* nanocrystallites,287
 geminate recombination,319
 graded spherical dots,185,197
 Hartree,117
 Hartree-Fock,117
 heterojunction bipolar transistor,444
 hole conversion,444
 in-plane gate,221
 interband tunneling,425
 interface disorder,165
 interface roughness,185
 Kane model,185
 Kronig-Penny model,417
 Langmuir,341
 light emission from *Si*,304
 Luttinger-Kohn Model,444
 magnetic superlattice,231
 magnetoconductance,231
 magneto-luminescence,155
 magneton sputtering,287
 mesh gate device,165
 mesoscopic device,474
 metallic nanocrystal,269
 minigaps,231
 molecular wire,211
 molecular nanostructure,211
MoS₂ nanocluster,16
 nanocalorimetry,59
 nanocrystal,79,100
 nanoscale *Si* clusters,341
 nanostructure,47
 nc-*Si/SiO₂* superlattice,134
 non-geminate recombination,319
 non-linear absorption,353

n-TiO₂/Mn₂O₃ films,65
 open ballistic quantum dot,474
 oxide matrix,287,341
PbS nanocrystals,331
 photocatalysis,47
 photoconversion efficiency,65
 photoelectrochemical etching,298
 photoelectrolysis,65
 photoluminescence,307
 photoredox reactions,16
 pinch-off,462
 plasma enhanced CVD,306
 plasmon lineshape,269
 platinum nanoparticles,28
 platinum oxide nanoparticles,28
 Pnp HBT,444
 polyacrylamide film,331
 polypyrrole particles,28
 porous alumina,402
 porous silicon,298
 porous vycor glass,100
PtO₂ nanoparticles,28
 quantum-confined Stark effect,353
 quantum confinement,308
 quantum confinement in *Si*,341
 quantum dot,3
 quantum well,417
 quantum wire,255,366,378
 quantum wire waveguide,242
 rare earth emission,312
 recrystallization,134
 regrowth,425
 resonant absorption,378
 resonant interband tunneling diode,425
 resonant Raman spectroscopy,402
 resonant tunneling,462
 scarring effect,474
 second harmonic generation,388
 self-assembled,3
 self-assembled quantum disks,155
 self-consistent modeling,165
 self-organized *GaAs* quantum wires,366
 self-organized growth,79
 semiconductor quantum well,353
 semiconducting nanocrystals,269
 semiconductor nanowire,402
 shallow donor,185
 short-channel effects,432
 sidewall spacer,425
Si/Ge nanostructures,417
Si quantum device,341
 Silicon quantum dots,134
 Silicon nanoclusters,306
 Silicon nanocrystals,134
 single-electron transistor,462
 single-mode transport,211
 sol-gel,35,47
 sol-gel silica matrix,35
 stadium shaped dots,474
 stoichiometric defects,331
 Stokes shift,298
 strain-layer superlattice,341
 Stranski-Krastanov growth,79
 sub-0.1 μm MOSFET,432
 sub-500 nm transport,425
 superlattice barrier,341
 supramolecular materials,3
 surface plasmon resonance,100
 surface state model,298
 surface voltage spectroscopy,146
 template synthesis,47
 tetragonal *Ge* nanostructure,177
 tilted magnetic field,255
 tunneling,444
 tunneling field-effect transistor,432
 ultra-shallow junction,432
 ultrasonic phonon,255
 unity-gain cutoff frequency,432
 vertical gated heterostructure,462
 Y-branch switch,221